DISSERTATION ZUR ERLANGUNG DES DOKTORGRADES

DER FAKULTÄT FÜR CHEMIE UND PHARMAZIE

DER LUDWIG-MAXIMILIANS-UNIVERSITÄT MÜNCHEN

HIGH ENERGY DENSITY MATERIALS BASED ON TETRAZOLE AND NITRAMINE COMPOUNDS

–

SYNTHESIS, SCALE-UP AND TESTING

VORGELEGT VON

JAN J. WEIGAND

AUS

REISBACH

2005

Erklärung

Diese Dissertation wurde im Sinne von § 13 Abs. 3 bzw. 4 der Promotionsordnung vom 29. Januar 1998 von Prof. Dr. Thomas M. Klapötke betreut.

Ehrenwörtliche Versicherung

Diese Dissertation wurde selbständig, ohne unerlaubte Hilfsmittel erarbeitet.

München, den 27. März 2005

…………………………………………

(Jan J. Weigand)

Dissertation eingereicht am:	27.04.2005
1. Gutachter	Prof. Dr. Thomas M. Klapötke
2. Gutacher	PD Dr. Axel Schulz
Mündliche Prüfung am	25.05.2005

Mom, I love you!

THOMAS, NIELS, ROSEMARIE,
DOMINIK, RENATE, PETER,
HARTMUT AND ZACHARY

Thank you!

Acknowledgement

I would like to thank *Prof. Dr. Thomas M. Klapötke* for all his guidance and encouragement during this study and for his invaluable mentorship.

I would like to thank the group of Prof. Klapötke and the members of the Department of Chemistry and Biochemistry for support.

JJW thanks for a FCI scholarship, DO 171/46

Axel, Thank you!

TABLE OF CONTENTS

Page

TABLE OF CONTENTS…..…...…………………………………………………… i

LIST OF TABLES………………………………………………………...…… viii

LIST OF FIGURES……………………………………………………………..xi

LIST OF SCHEMES…………………………………………………………… xvi

CHAPTER

I INTRODUCTION

1. Classification of explosives …………………………………………….. 1

1.1 High Explosives……………………………………………….5

1.2 Propellants…………………………………………………… 6

1.3 Pyrotechnics…………………………………………………...7

2. Drawbacks of Explosives……………………………………………….. 7

2.1 Pyrotechnic Compositions…………………………………… 7

2.2 Gas Generators………………………………………………...8

2.3 Liquid Propellants……………………………………………..9

2.4 Primary Explosives……………………………………………9

2.5 Tetrazene as Sensitizer………………………………………...10

3. High Energy Density Materials − A Solution ?…………………….…… 10

3.1 Relationship between Guanidines and Tetrazoles……………….. 12

3.2 Goals of this Study……………………………………………….14

3.3 Experimental Techniques……………………………………...20

3.3.1 Thermal Analysis……………………………………...20

TGA……………………………………………………..20

DSC…………………………………………………….. 21

Bomb Calorimetry……………………………………… 24
Explosion experiments…………………………………..24
3.3.2 Sensitivity Tests……………………………………….25
Impact Sensitivity……………………………………….26
Friction Tester…………………………………………...27
Koenen Test……………………………………………..28
4. References………………………………………………………. 30

II 5-AMINOTETRAZOLE AND AZOTETRAZOLATES
1. Introduction……………………………………………………... 34
1.1 Tetrazoles……………………………………………………...34
1.1.1 Tautomerism……………………………………………..35
1.1.2 Stability…………………………………………………. 36
1.1.3 Acid/base properties…………………………...……... 37
1.1.4 5-Aminotetrazole monohydrate (**5-AT, 13**) ……………..38
1.2 Azotetrazolates………………………………………………...39
2. Azidoformamidinium and Guanidinium 5,5'-Azotetrazolate Salts……... 41
2.1 Synthesis of **AFZT**, **GZT**, **AGZTH**, **DAGZT** and **TAGZT**……41
2.2 Result and Discussion…………………………………….... 43
2.2.1 Raman, IR and NMR Spectroscopy………..…………43
2.2.2 Crystal structure of **AFZT** and **AGZTH**………………...45
2.2.3 Thermodynamic aspects………………………………… 48
Heats of formation……………………………………… 48
Detonation pressure (*P*) and velocities (*D*)……………... 49
Impact and friction sensitivities………………………… 50
2.2.4 Thermal behavior……………………………………...50
DSC…………………………………………………….. 51
Explosion products……………………………………... 52
2.3 Conclusion……………………………………………………. 55
2.4 Experimental…………………………………………………..56

CHAPTER Page

3. Hydrazinium 5,5'-Azotetrazolate Salts......61

3.1 Synthesis of **HZT** (**26**), **HZTH** (**27**), and **DAD** (**28**)......62

3.2 Patent...... 63

3.3 High Temperature and Pressure FTIR study of **DAD** (**28**)...... 78

3.3.1 Experimental Method...... 78

3.3.2 Experimental Results 80

3.3.3 Discussion...... 88

3.3.4 Conclusion......90

4. STANAG 4147 and 4582......91

4.1 Compatibility tests of **HZT** and **HZTH** with TLPs......92

4.2 Compatibility tests of **TAGZT** with TLPs......95

4.3 Conclusion......97

5. References......99

III *N,N*-BIS-(1(2)*H*-TETRAZOL-5-YL)-AMINE HYDRATE (**BTA**)

1. Introduction...... 102

1.1 Pyrotechnic composition and primers 102

1.2 Synthesis of $\mathbf{H_2bta}$ (**30**)...... 104

2. The Dianion of 5-Cyanoiminotetrazoline: $C_2N_6^{2-}$ (**CIT, 33**)...... 105

2.1 Introduction......105

2.2 Results and Discussion......107

2.2.1 Synthesis and properties of **CIT** salts 107

2.2.2 DSC of Cs_2CIT (**34**)...... 108

2.2.3 In Situ X-ray Powder Diffraction of Cs_2CIT (**34**) 109

2.2.4 X-ray Structure of $(^{i}PrNH_3)_2$**CIT**•MeOH (**35**) and **34**......110

2.2.5 Structure and bonding of the **CIT** dianion......113

2.2.6 Crystal Structure of $[Pd(C_2N_6)(NH_3)_3]\cdot H_2O$ (**36**)...... 115

2.2.7 The reaction of Cs_2CIT with SO_2...... 118

2.2.8 Crystal Structure of $Cs_2CIT\text{-}SO_3\bullet SO_2$ (**37**)......119

2.2.9 **CIT** *versus* $\mathbf{CITSO_3}$...... 121

2.3 Conclusion......122

2.4 Experimental...... 123

CHAPTER Page

3. H_2bta as HNC ligand system....... 127

3.1 Alkali and alkaline earth metal salts....... 127

3.1.1 Raman spectroscopy....... 128

3.1.2 Crystal structure of Li_2**bta***$5H_2O$ (**40**)....... 130

3.1.3 Crystal structure of Na_2(**bta**)*$2H_2O$ (**42**)....... 132

3.1.4 Crystal structure of CsH**bta***H_2O (**39**), Rb_2**bta***H_2O (**43**) and Cs**bta***H_2O (**44**)....... 134

3.1.5 Crystal structure of Cabta*$5H_2O$ (**45**) and and Babta*$5H_2O$ (**46**)....... 136

3.1.6 Experimental....... 138

3.2 H_2**bta** / $(NH_4)_2[Cu(NH_3)_6]$ System....... 143

3.2.1 Introduction....... 143

3.2.2 Synthesis of $Cu(bta)(NH_3)_2$ (**47**), $Cu(bta)(NH_3)_2$*H_2O (**48**) and $(NH_4)_2Cu(bta)_2$*$2.5H_2O$ (**49**)....... 143

3.2.3 Crystal structure of **47** and **48**....... 144

3.2.4 Magnetic properties of **47**, **48** and **49**....... 150

3.2.5 Thermal decomposition and thermodynamic aspects....... 152

3.2.6 Conclusion....... 154

3.2.7 Experimental....... 155

3.3 H_2**bta** / CuX_2 ($X = Cl^-$, ClO_4^-) System....... 158

3.3.1 Introduction....... 158

3.3.2 Synthesis....... 158

3.3.3 Molecular structure of $[CuCl_2(H_2$**bta**$)(H_2O)]$*$2H_2O$ (**50**)....... 159

3.3.4 Molecular structure of $[CuCl(H_2$**bta**$)_2]Cl$ (**51**)....... 160

3.3.5 Molecular structure of $[CuCl_2(H_2$**bta**$)_2]$*$2H_2O$ (**52**)....... 162

3.3.6 Molecular structure of $[Cu(H_2$**bta**$)_2](ClO_4)_2$*H_2O (**53**)....... 162

3.3.7 Discussion....... 163

3.3.8 Experimental....... 166

3.4 Conclusion....... 167

4. References....... 168

IV 1,5-DIAMINO-1*H*-TETRAZOLE (DAT)
1. Introduction………………………………………………………….. 173
1.1 **DAT** ……………………………...…………………….. 173
1.2 Energetic salts…..……………………………..…………… 174
1.3 Crystal building units…...………………………..…………… 175
2. HDAT$^+$ / MeDAT$^+$ salts……………………………………………… 177
2.1 Synthesis……………………………………………………… 178
2.2 IR spectroscopy…….……..…………….…..…………………179
2.3 ^{15}N Chemical Shifts and ^{1}H-^{15}N Coupling Constants…………… 182
2.4 ^{1}H and ^{13}C NMR spectra………………………………………184
2.5 Molecular structure of $HDATNO_3$ (**59a**), $HDATClO_4$ (**59b**),
$MeDATNO_3$ (**61b**) and $MeDATN_3$ (**61d**)……………………...186
2.6 Crystal structure of **59a**, **61b**, **59b** and **61d**………………………189
2.7 $MeDATN(NO_2)_2$ (**61c**)…………………………………...…194
2.7.1 Crystal structure of **61c**………………………………..…195
2.7.2 Closed-shell interaction in **61c**……………………….………. 197
2.8 Thermodynamic aspects…..……………………………...…199
2.8.1 Heats of formation and detonation…...…………….……199
2.8.2 Detonation pressures and velocities………..…………..……202
2.8.3 Sensitivity test………………………………………... 202
2.8.4 Koenen test of **59c**……………………………….……203
2.9 Thermal behavior …….………………………………...… 204
2.9.1 DSC and TGA……………………...………………..…… 205
2.9.2 Activation energy………...…………....………………..…… 208
2.9.3 Decomposition experiments.……......…………………..…… 208
Possible decomposition scheme for **61d**………..…...….. 208
Possible decomposition scheme for **61b**……......……….. 212
Possible decomposition scheme for **61c**……..…………..215
2.10 Conclusion……...……..……..…………………………...… 217
2.11 Experimental….....……..……..…………………………...… 218
3. References…..……………...……………………………………..…... 224

CHAPTER Page

V 1,4-BIS-[TETRAZOL-5-YL]-1,4-DIMETHYL-2-TETRAZENES

1. Introduction.. 229

1.1 Synthesis.. 230

1.1.1 **A**: Building of Nitrogen Chains.......................................230

1.1.2 **B**: Exchange of substituents..232

1.2 Stability of 2-tetrazenes..233

1.3 1,4-Bis-[1-methyltetrazolyl-5-yl]-1,4-dimethyl-2-tetrazene (**84**)...233

2. Substituted hydrazine derivatives.. 235

2.1 From cyanohydrazines...235

2.2 From thiosemicarbazides...236

2.2.1 Possible mechanism of hydrazine decomposition.......... 240

2.2.2 Properties of **88a-d**..243

2.2.3 Mass spectrometry of **88d**... 244

2.2.3 Raman and IR spectroscopy... 246

2.2.4 Crystal structure of **88a** and **88b**. 246

3. Oxidation of hydrazine derivatives **88a-d**.................................. 249

3.1 Characterization of **84a-d**...254

3.1.1 Raman and IR spectroscopy... 254

3.1.2 Mass spectrometry of **84b**... 255

3.1.3 Mass spectrometry of **84d**... 256

3.2 Molecular and Crystal structures of **84d** and **104**....................257

4. Decomposition experiments of **84a** and **84b**.............................. 261

5. Conclusion..262

6. Experimental..263

7. References.. 272

VI NITRAMINES

1. *N*-Nitroso- and *N*-Nitraminotetrazoles.. 275

1.1 Synthesis and properties of *N*-Nitroso- a. *N*-Nitraminotetrazoles.. 276

1.2 Molecular Structures..278

1.3 NBO analysis..283

1.4 ^{15}N Chemical Shifts and ^{1}H-^{15}N Coupling Constants............... 285

1.5 ^{1}H and ^{13}C NMR spectra……………………………………………287
1.6 Raman and IR spectroscopy…………………………………………...289
1.7 N,N Rotational Barriers………………………………………………289
1.8 Thermochemistry……………………………………………………...292
1.9 Conclusion……………………………………………………………294
1.10 Experimental…...…………………………………………………...294
2. Mono- and Dinitrobiuret........……..............…………………………... 300
2.1 Synthesis of **MNB** (113) and **DNB** (114)…………...………... 302
2.2 Raman and IR spectroscopy of **MNB** and **DNB**…….…………….. 302
2.3 NMR spectroscopy of **MNB** and **DNB**…….………..………..303
2.4 Molecular structure of **MNB**, **DNB*H₂O** and **DNB**…....………..306
2.5 Reaction of **DNB** with base……………………………………... 308
2.5.1 Synthesis of **DNB** salts…………………………………..308
2.5.2 IR spectroscopy………………………………………………309
2.5.3 Molecular structure of dipotassium dinitrobiuretate (**117**) 310
2.5.4 ^{1}H and ^{13}C NMR of **DNB** and **DNB** salts………………..311
2.6 Decomposition of **DNB** in solution……………………............311
2.7 Thermochemistry of **MNB** and **DNB**……….……………........314
2.7.1 Thermal behavior…...……………………….………..314
2.7.2 IR spectroscopy……….………………………..……….. 318
2.7.3 Mass spectrometry...…..…………………………..………..321
2.7.4 Discussion……….....…..……………………..………..322
2.8 Explosive properties……………..……………….……………........324
2.9 Conclusion………..……………..……………….……………........ 325
2.10 Experimental...…..………………..……………….……………........ 326
3. Sachstandsbetricht zur Studie E/E210/4D004/X5143..………..………... 329
4. References…………………………………….....………..………... 362

APPENDIX A……………..……………………………………………………… 367
APPENDIX B……………..……………………………………………………… 384
Full List of Publications
CV

LIST OF TABLES

TABLE Page

1.1 Pyrotechnic composition generating different colored smoke…………………… 6

1.2 Impact sensitivity of selected examples……………………………………….. 26

1.3 Friction sensitivity of selected examples……………………………………….28

1.4 Fragmentation degree …………………………………………………………….29

1.5 Sensitivity guidelines………………………………………………………….. 29

2.1 Selected bond length and angles of the cations in **AFZT** and **AGZT**…………… 46

2.2 Hydrogen bond geometry (Å, °) of **AFZT** and **AGZTH**…………………….. …..47

2.3 Summary of the physico-chemical properties of the investigated salts…………... 49

2.4 Peak positions and total shifts for peaks moving with pressure from *Figure 2.11*.. 81

2.5 Peak positions and total shifts for peaks moving with pressure from *Figure 2.13*.. 84

2.6 Peak positions and total shifts for peaks moving with pressure from *Figure 2.14*.. 84

2.7 Measured samples and sample amount…………………………………………... 92

2.8 Evolved energy and evaluated measurement time……………………………….. 93

2.9 Maximum heat flow [μW g^{-1}]………………………………………………………. 93

2.10 Compatibility of **HZT** and **HZTH** toward STAB-0-DPA; t = 5 days…………… 94

2.11 Measured samples and sample amounts………………………………………….95

2.12 Results of the measurement……………………………………………………… 96

3.1 Comparison of selected interatomic distance (Å) and bond angles (°) of the C_2N_6 111

3.2 Observed Cs-N contacts and calculated vaelency units in **34**…………………… 112

3.3 Selected structural parameters (Å, °) of **36**……………………………………..... 117

3.4 Hydrogen bond geometry (Å, °) of **36**…………………………………….... … 117

3.5 Selected geometric parameters (Å, °) of **37**…..…………..…………………….120

3.6 Observed Cs-N contacts and calculated valency units in **37**…..………………… 121

3.7 Selected geometric parameters (Å, °) of **40** and **42**…………………………… 131

3.8 Hydrogen bond geometry (Å, °) of **40 a**nd **42**…………………………….... 134

3.9 Selected geometric parameters (Å, °) of **47** and **48**……………………………145

3.10 Hydrogen bond geometry (Å, °) of **47** and **48**…………………………...…..147

3.11 Physico-chemical properties of **47** and **48**………………………………….. 153

4.1 Calculated and experimental IR and Raman data of **55**, **59a** and **61a**…………..…182

4.2 ^{15}N and ^{13}C NMR chemical shifts………………………………………... 184

4.3 Comparison of Selected Interatomic Distance…………………………………… 188

4.4 Hydrogen bond geometry (Å, °)…………………………………………………. 196

4.5 Bond Critical Points in **61c**……………………………………………...…….. 198
4.6 Thermochemical Results of the Synthesized Salts **59a**, **59b** and **61b-d**…………..... 200
4.7 Explosive Properties and Initial Safety Testing.…………………………………. 202
4.8 Properties of the salts **61b-d** related to the DSC and TGA measurements………..205
4.9 Maximum exothermic responses of **61b-d** as a function of scan speed………….. 207
4.10 Observed mass (*m/z*) in the decomposition experiments of **61d**……….………… 208
4.11 Vibrational frequencies (cm^{-1}) of the exp. observed molecules in the gas phase… 211
5.1 Yields and mobile phase for the purification of **88a-d**………………………….....240
5.2 Comparison of selected interatomic distance……………………………………..247
5.3 Oxidations methods……………....…………………………………………….250
5.4 Selected structural parameters of different tetrazenes……...……………………..259
6.1 Synthesis of the 5-aminotetrazole derivatives **109a-c**, **111a**, **111c** and **112a-c**…...278
6.2 Comparison of selected interatomic distances (Å)………………………………..279
6.3 Comparison of selected calculated Wiberg bond indices…………………………284
6.4 Summary of the NBO Analysis of **111a**,**c** and **112a-c**…………………………...….284
6.5 ^{15}N and ^{13}C NMR chemical shifts……………………………………………...285
6.6 Potential Energy Barriers[a] (Kcal mol^{-1}) for the Rotation about the N−N Bond….. 290
6.7 Thermochemical properties of **112a** and **112c**…………………………...…….293
6.8 NMR data of biuret, **MNB** and **DNB**….……………….……………………...…..304
6.9 IR frequencies and modes in **116** and **117**……………………………….……. 310
6.10 ^{1}H and ^{13}C NMR of **DNB** and deprotonated species……………………………...312
6.11 Residual products after the first decomposition step of **MNB**…………………… 317
6.12 Maximum exothermic responses of **MNB** and **DNB** as a function of scan speed.. 317
6.13 Vibrational frequencies (cm^{-1}) of the experimentally observed molecules………. 322
A-1 Frequency analysis of **CIT** dianion (**33**): B3LYP/aug-cc-pvDZ………………….367
A-2 Frequency analysis of Cs_2CIT (**33**): B3LYP/aug-cc-pvDZ……………………….368
A-3 Frequency analysis of CIT•SO_3 (**37**): B3LYP/aug-cc-pvDZ…………………….. 369
A-4 NPA Charges (B3LYP/aug-cc-pvDZ) [e]……………………………………....369
A-5 AIM and NBO charges……………………………………………………….... 370
A-6 Cartesian coordinates from X-ray structure determination……………………… 371
A-7 Parameters of the critical point analysis………………………………………..372
A-8 G2/G3 method………………………………………………………………… 374
A-9 Mulliken and NBO (in brackets) charges [*e*]………………...…………………... 377
A-10 Absolute Energies (in au) for Ground State and Transition States………………..378

A-11 Absolute Energies (in au) for Ground State and Transition States………………..378
A-12 Absolute Energies (in au) for Ground State and Transition States………………..379
A-13 Calculated and experimental IR and Raman frequencies of **MNB**………………. 380
A-14 Calculated and experimental IR and Raman frequencies of **DNB.**………………. 381

LIST OF FIGURES

FIGURES Page

1.1 Classification of *Explosives*……..………………………………………………. 2

1.2 Structures of commonly used *Explosives*……..……………………………..... 2

1.3 HEDMs and insensitive LPEMs……………………………………………… 3

1.4 HEDMs with a combination of an acyclic and cyclic moiety……………………. 12

1.5 Nitrogen content of certain Tetrazoles and Salts………………………………… 15

1.6 BAM drop hammer……………………………………………………………….25

1.7 BAM friction tester……………………………………………………………….27

1.8 Koenen Test……...…………………………………………………………….28

2.1 A view of the molecular structure of **AFN**……………………………………..28

2.2 Raman spectra of 5,5-azotetrazolate salts……………………………………... 44

2.3 A view of the molecular structure of **AFZT**…………………………………... 45

2.4 A view of the molecular structure of **AGZTH**……………………………….….. 46

2.5 DSC thermograph of the investigated salts ($\beta = 10°C\ min^{-1}$)……………………..51

2.6 Gas phase spectra of the decomposition products of the **ZT** salts………………...52

2.7 Dihydrazinium salt of $[N_4C\text{-}N{=}N\text{-}CN_4]^{2-}$……………………………………... 61

2.8 Original preparation procedure of dihydrazinium salt of $[N_4C\text{-}N{=}N\text{-}CN_4]^{2-}$…….. 62

2.9 Bassett-type HDAC experimental setup……………………………………… 79

2.10 Background file from the HDAC with no gasket and no sample………………… 80

2.11 Room temperature pressure increase after a previous pressure cycle……………..81

2.12 Spectra from temperature increase……………………………………………..82

2.13 Compression and decompression cycle at room temperature……………………..83

2.14 Compression and decompression cycle at room temperature……………………..85

2.15 Spectra from temp. increase where the pressure was initially set to 2.12 Gpa…… 86

2.16 Spectra from temp. increase where the pressure was initially set to 5.25 GPa……87

2.17 Spectrum from a sample with no gasket……………………………………… 88

2.18 Decomposition temperature versus pressure…………………………………...90

2.19 **HZT**, STAB-0-DAP and mixture and STAB-0-DPA + **HZTH**…………………94

2.20 **HZTH**, STAB-30-DAP and mixture…………………………………………….. 95

2.21 **TAGZT**, STAB-0-DAP and mixture…………………………………………...96

2.22 **TAGZT**, STAB-15-DAP and mixture……………………………………………97

3.1 Promising HNC high energy materials…………………………………….... 102

3.2 Selected carbon-nitrogen anions……………………………………………. 106

3.3 DSC experiments showing the decomposition of β-$Cs_2C_2N_6$ 108
3.4 Temperature-dependent X-ray diffraction measurement 109
3.5 Formula unit and labeling scheme for **35** 110
3.6 Formula unit and labeling scheme for **34** 111
3.7 Molecular model and numbering scheme of the C_2N_6 112
3.8 View of cesium coordination environment in Cs_2CIT 113
3.9 Nine possible Lewis representations 114
3.10 π-Type MOs (B3LYP/aug-cc-pvTZ) of **CIT** displaying the *10π*-8c-bond 115
3.11 The dimer $[Pd(C_2N_6)(NH_3)_3]\bullet H_2O$ (**36**) 116
3.12 Formula unit and labeling scheme for **37** 120
3.13 View of cesium coordination environment in Cs_2CIT-$SO_3\bullet SO_2$ (**37**) 121
3.14 Best Lewis representation of **$CITSO_3$** 122
3.15 Subunit of the crystal structure in **38** along the [100] axis 128
3.16 Raman spectra of alkaline **bta** salts 129
3.17 Coordination environment of the two Li^+ cations 130
3.18 Part of the crystal structure of **42** 132
3.19 Part of the crystal structure of **42** showing the formation of the (010) sheet 133
3.20 Main graphs sets in the 1D subunit of **39** 135
3.21 View along the [100] axis in **44** 135
3.22 View of the dimeric unit in **45** 136
3.23 View of the extended dimeric unit in **46** 137
3.24 The coordination environment of the Cu^{II} ion in **47** 144
3.25 Crystals structure of **48** 146
3.26 Crystals structure of **48** 148
3.27 View of the chain like structure in **49** 149
3.28 Plot of $\chi_M T$ vs. T for **47** (A) and **48** (B) under an applied magnetic field of 0.5 T 150
3.29 Plot of $\chi_M T$ vs. T for **49** under an applied magnetic field of 0.5 T 151
3.30 DSC thermographs of **47** (left) and **49** (right) 152
3.31 The coordination environment of the Cu^{II} ion in **47** 159
3.32 The hydrogen-bonding system in **50** 160
3.33 The coordination environment of the Cu^{II} ion in **51** 161
3.34 The coordination environment of the Cu^{II} ion in **52** 162
3.35 View of the molecular structure of **53** 163
3.36 IR spectra of **50**, **51**, **52** and **30** 164

3.37 Raman experiment of **52**……………………………………………………….…… 165
3.38 Molecular arrangement of **54**……………………………………………………….. 167
4.1 Aminotetrazoles………………………………………………………………………….. 173
4.2 Scheme of the 2D organization pattern of [$HGN^+NO_3^-$]………………………… 176
4.3 Reaction products of **DAT**……………………………………...…………….…….. 177
4.4 IR spectra of **61a-d** recorded in KBr…………………………………………………...181
4.5 Proton broadband decoupled and coupled ^{15}N NMR spectra of **55**……………….183
4.6 ^{1}H-HMBC NMR spectrum of **61a**………...………………………………...……… 185
4.7 Formula unit and labeling scheme for **59a**………………………………………….. 186
4.8 Formula unit and labeling scheme for **59b**…………………………………………...187
4.9 Formula unit and labeling scheme for **61b**…………………………………………...187
4.10 Formula unit and labeling scheme for **61d**…………………………………………...189
4.11 Surrounding of the NO_3^- anion in the structure of **59a**…………………………..... 190
4.12 Surrounding of the NO_3^- anion in the structure of **61b**………………………….....192
4.13 Surrounding of the ClO_4^- anion in the structure of **59b**…………………………....193
4.14 Surrounding of the N_3^- anion in the structure of **61d**……………………………....194
4.15 Formula unit and labeling scheme used for **61c**……………………………….... 195
4.16 View of the strand formed by alternating cations (MeDAT) and anions (DN)…... 196
4.17 Koenen test of **59c** (d = 2 mm)………...……………………………………… 203
4.18 Koenen test of **59c** (d = 6 mm)……………...…………………………………… 204
4.19 DSC and TGA thermographs of **61b** (β = 10°C/min)………..…………………...205
4.20 DSC and TGA thermographs of **61c** (β = 10°C/min)………..…………………... 206
4.21 DSC and TGA thermographs of **61d** (β = 10°C/min)………..…………………...206
4.22 Gas phase IR spectrum of the decomposition products of **61d**…......………….... 209
4.23 Infrared spectroscopic evolved gas analysis of **61d**……………………………… 211
4.24 Infrared spectroscopic evolved gas analysis of **61b**……………………...….. 212
4.25 Gas phase IR spectrum of the decomposition products of **61b**…………...…… 213
4.26 Mass spectrum of the decomposition products of **61b**…...………...…………..… 213
4.27 ^{13}C-NMR spectra of decomposition products of **61b** recorded in [d6]-DMSO…...215
4.28 Infrared spectroscopic evolved gas analysis of **61c**……………..………………...216
4.29 Gas phase IR spectrum of the decomposition products of **61c**…...………………216
5.1 Five possibilities for the linkage of four di- and/or three-coordinated N-atoms…..229
5.2 1,4-bis-[tetrazolyl-5-yl]-2-tetrazenes……………………………………………….. 234
5.3 DEI^+ mass spectrum of **88b**……………………………………………..…….. 245

5.4 Formula unit and labeling scheme for **88a**..246
5.5 Formula unit and labeling scheme for **88b**..247
5.6 Crystal arrangement of **88a** viewed along the [100] axis..............................248
5.7 Crystal arrangement of **88b** viewed along the [010] axis..............................249
5.8 Molecular structure of **105a**...253
5.9 DEI+ mass spectrum of **84b**...255
5.10 DEI+ mass spectrum of **84d**..256
5.11 ORTEP plot of the molecule structure of compound **84d**...............................258
5.12 View of the crystal structure of **84d** along the [100] axis..........................259
5.13 View of the molecular arrangement of **104**...260
5.14 IR spectra of evolved gases from pyrolysis experiments of **88a** and **88b**...........261
6.1 Secondary explosives..275
6.2 Connectivity and numbering scheme..279
6.3 Molecular structures and labeling scheme for **109a**, **111a** and **112a**............280
6.4 Molecular structures and labeling scheme for **109c**, **111c** and **112c**............281
6.5 Molecular structure and labeling scheme **112b**...282
6.6 Lewis representation of the donor-acceptor interaction of p-LP(N5)......................283
6.7 Connectivity and numbering scheme..284
6.8 Temperature depended ^{1}H and ^{13}C{^{1}H} NMR spectra of **112b**...............288
6.9 Resonance in *N*-nitrosamines...289
6.10 Optimized structures and transition states of *N*-nitrosoaminotetrazoles...............291
6.11 Examples of nitroureas...301
6.12 **MNB** and **DNB**...301
6.13 ^{14,15}N NMR spectra of biuret, **MNB** and **DNB**..................................305
6.14 Formula unit and labeling scheme for **MNB**..306
6.15 Formula unit and labeling scheme for **DNB*H$_2$O**.....................................307
6.16 Formula unit and labeling scheme for **DNB**..308
6.17 View of the molecular structure of **117**..309
6.18 View of the molecular structure of **117**..310
6.19 Decomposition of **DNB** in [d6]-DMSO solution..313
6.20 DSC thermographs of **MNB** (β = 5, 10, 15 and 20°C/min)................................314
6.21 TGA and DTGA thermograph of **MNB**..315
6.22 ^{13}C-NMR spectra of decomposition products of **MNB**...............................315
6.23 DSC thermographs of **DNB**...317

6.24 TG and DTG thermograph of **DNB**……………………………………...……. 318
6.25 Infrared spectroscopic evolved gas analysis of **MNB**………………...……….. 319
6.26 Infrared spectroscopic evolved gas analysis of **DNB**………………...………….... 320
6.27 IR spectra of HNCO and decomp. gases of **MNB** (190°C) and **DNB** (130°C)…...320
6.28 EI-mass spectrum (70 eV) of the decomposition gases of **MNB**……………...…. 321
6.29 EI-mass spectrum (70 eV) of the decomposition gases of **DNB**………………….322
6.30 Koenen test with **DNB**…………………………………………………...……….325
A-1 Numbering scheme of **61c** used in calculation……………………………………371
A-2 The electron density plot, ρ(r), and the Laplacian plot ρ(r), $-\nabla^2\rho$(r)…………...373
A-3 ESP mapped onto electron density surface of **111c**……………………………… 375
A-3 ESP mapped onto electron density surface of **111a**……………………………… 375
A-3 ESP mapped onto electron density surface of **112c**……………………………… 376
A-3 ESP mapped onto electron density surface of **112b**………………………………376
A-3 ESP mapped onto electron density surface of **112a**……………………………… 377

LIST OF SCHEMES

SCHEMES Page

1.1 Relationship between Guanidines and Tetrazoles …………………….……………13

2.1 Tautomerism of Tetrazole……………………………………………………………...34

2.2 Tautomerism of 5-Aminotetrazole and related derivatives…………...………….. 35

2.3 Imidoyl azide − Tetrazole equilibrium…………………………………………....…36

2.4 Typical decomposition pathway of 1,5-disubstituted tetrazoles………………….. 37

2.5 Synthesis of **5-AT** (**14**)………………………………………………………... 38

2.6 Oxidation of **5-AT** to **Na_2ZT**……………………………………………………..39

2.7 Reaction of **BaZT** with $(N_2H_5)_2SO_4$…………………………………………... 40

2.8 **5-AT** monohydrate………………………………………………………………. 41

2.9 Synthesis of Azidoformamidinium and Guanidinium 5,5'-Azotetrazolate Salts… 42

2.10 Simplified scheme of the initial decomposition pathway of the **ZT** salts………... 53

2.11 Simplified scheme of the decomposition pathway of the **AF** cation……………...54

2.12 Simplified scheme of the decomposition pathway of the guanidinium cations…...54

3.1 Synthesis of **H_2bta** (**30**)…………………………………………………….. 104

3.2 Synthesis of **CIT** (**33**)…………………………………….…………………… 107

3.3 Attempted synthesis of **37**……………………………………….………………..118

3.4 H_2**bta** (**30**) with two reversible types of protonated and deprotonated mode……..127

3.5 H_2**bta** / CuX_2 (X = Cl^-, ClO_4^-) System…………………………………………158

4.1 Reaction of 5-AT (14) with HOSA under base condition ……..……………….173

4.2 Synthesis of DAT (**55**) according Gaponik et al………………………………….174

4.3 Reaction products of **DAT**……..……………………………………………….....177

4.4 Synthesis of the metal salt of azidotetrazole…………………………………... 178

4.5 Improved synthesis of **55**…………………………..……………………….. 178

4.6 Synthesis of **61a-d**……………………………...………………………... 179

4.7 General Born-Haber energy cycle for the reactions [1]-[4]……………………….199

4.8 Possible decomposition pathway of **61d**……..……………………………..….210

4.9 Possible decomposition pathway of **61b**……..…………………….……….214

4.10 Possible decomposition pathway of **61c**………..……………………..……... 217

5.1 Preparation of tetrazenes………………………………………………………….230

5.2 Preparation of tetrakis(trimethylsilyl)-2-tetrazene…………….……………… 231

5.3 Tetrazadiene complexes………………………………………………………...231

5.4 From two "N1" and one "N2" or one "N3" and one "N1" fragment…..…………… 232

5.5 Exchange of substituents.......232
5.6 Decomposition pathways of 2-tetrazenes.......233
5.7 One-pot synthesis of **84b**....... 234
5.8 Synthetic targets.......235
5.9 Synthesis of **88a**.......235
5.10 Alkylation of **88a**....... 236
5.11 Synthesis of **88a** from 2-methyl-thiosemicarbazide.......237
5.12 Preparation of substituted thiosemicarbazide.......238
5.13 Imidoyl azide-tetrazole ring-chain isomerism.......239
5.14 Preparation of 1,3-substituted thiosemicarbazides....... 239
5.15 Preparation of the substituted hydrazine derivatives **88a-d**....... 240
5.16 Oxygen induced formation of diazene **I** and hydroperoxide **II**.......241
5.17 Methyl group transfer of diazene **I** yielding **III** and **IV**....... 242
5.18 Dimerization of diazene **I**.......243
5.19 Formation of nitrosoamines **VI**.......243
5.20 Proposed fragmentation path of **88b**....... 245
5.21 Oxidation of **88a** to **84a**....... 249
5.22 Oxidation of **88a** to **104**....... 251
5.23 Oxidation of **88b-d** to **84b-d**.......252
5.24 Acid catalyzed decomposition of **88a-d**.......253
5.25 Possible fragmentation pathway of **84b**.......255
5.26 Possible fragmentation pathway of **84d**.......257
6.1 Synthesis of *N*-nitroso- and *N*-nitraminotetrazoles.......277
6.2 Condensation of DNU with an alcohol to keto-RDX (K-6).......300
6.3 Synthesis of MNB and DNB.......302
6.4 Preparation of mono or doubly deprotonated **DNB** salts....... 308
6.5 Possible decomposition pathway of DNB monitored in [d6]-DMSO solution....... 312
6.6 Possible decomposition pathway of **MNB** and **DNB**.......323

C h a p t e r   I

INTRODUCTION

1 Classification of explosives

Energetic materials (explosives, propellants and pyrotechnics) are used for both civilian and military applications. Ongoing worldwide research projects are currently developing pyrotechnics with reduced smoke and new explosives and propellants with higher performance or enhanced insensitivity to thermal or shock insults. An *explosive substance* is a solid or liquid substance (or mixture of substances) which is in itself capable by chemical reaction of producing gas at such a temperature and pressure and at such a speed as to cause damage to the surroundings. Pyrotechnic substances are included even when they do not evolve gases.

> ***NOTE**: The use of the word "explosive" can have different meanings and interpretations. Reference to "an explosive" or "explosives" is commonly understood to mean substances or articles in Class 1 of the scheme of the UN Recommendations on the Transport of Dangerous Goods, that is those which are intentional explosives or have properties which when assessed under the test procedure of the Manual of Tests and Criteria place them in UN Class 1.*[1]

Depending on their purpose, explosives are divided into three main types: high explosives, propellants and pyrotechnics (*Figure 1.1*). The output of a pyrotechnic produces some sort of audio-visual effect (based on a redox reaction of inorganic reducing agents and oxidizer compounds), whereas the output of high explosives is a detonation, and propellants serve to accelerate either projectiles, missiles or rockets.

1.1 High Explosives

High explosives (*Figure 1.1*) can be grouped into *primary* and *secondary explosives*. *Primary explosives* are considered sensitive *explosives* in that they will detonate when subjected to a spark, flame, friction or a heated wire which causes a crystal to reach its ignition temperature. The most frequently used *primary explosives* are lead azide, lead trinitroresorcinate (lead styphnate), and tetrazolyl guanyltetrazene hydrate (tetrazene). In earlier times, mercury fulminate was also used (*Figure 1.2*).

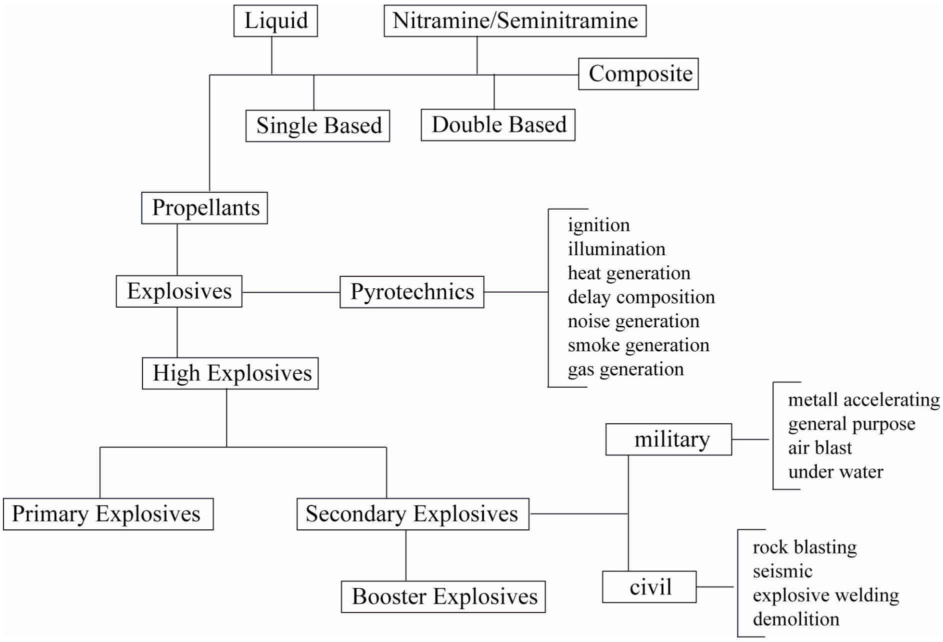

Figure 1.1. Classification of *explosives*

A common problem for most primary *explosives* is the presence of lead, due to its corresponding environmental impact when the *primary explosives* are brought to function. Therefore lead-free primary *explosives*, e.g. 1,3,5-triazido-2,4,6-trinitrobenzene (TATNB),[2] are preferred. The reaction of a *primary explosive* starts with a deflagration but within a few milliseconds or less becomes a detonation.

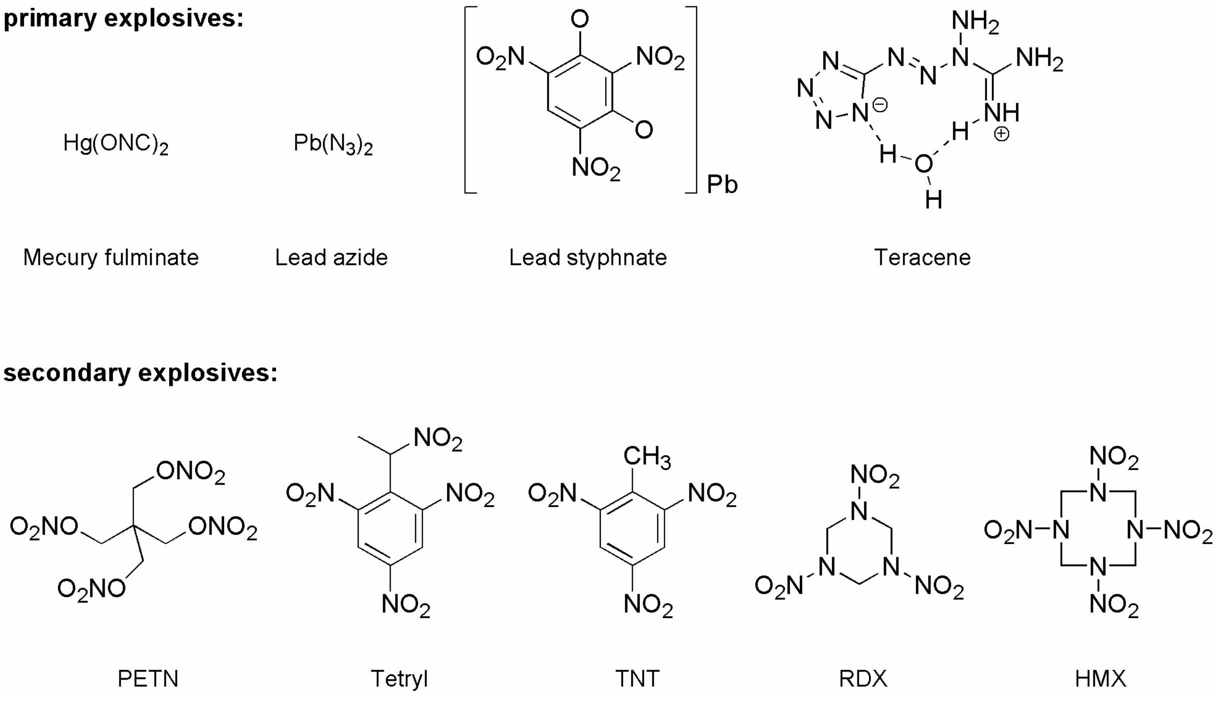

Figure 1.2. Structures of commonly used *explosives*.

This detonation is taken up by booster *explosives* (belonging to *secondary explosives*), which amplify the detonation and transmit it further to the main charge. Main charge explosives (e.g. Tetryl, TNT or PETN)[3] produce the final effect (*Figure 1.2*). More modern ones are based on nitramine compounds like hexahydro-1,3,5-trinitro-*S*-triazine (RDX)[4] or octahydro-1,3,5,7-tetranitro-1,3,5,7-tetrazine (HMX).[5] Main charge *explosives* can differ greatly and their composition depends strongly on their application. In the most cases those systems also contain special binders where the amount of binder can be as low as 5%. Blasting *explosives* can be very heterogeneous, *e.g.* ammonium nitrate (AN) used as oxidizer for a liquid fuel. Between these examples nearly every combination can be found.

In the field of main charge *explosives*, especially in military applications, many new energetic molecules have been synthesized (*Figure 1.3*).[6] Based on computational simulations,[7] as well as experiences from the field of organic chemistry, high density *explosive* target molecules (so called high energy density materials: HEDMs) have been defined and can be achieved if the molecular structure contains fused ring and/or strained ring systems.

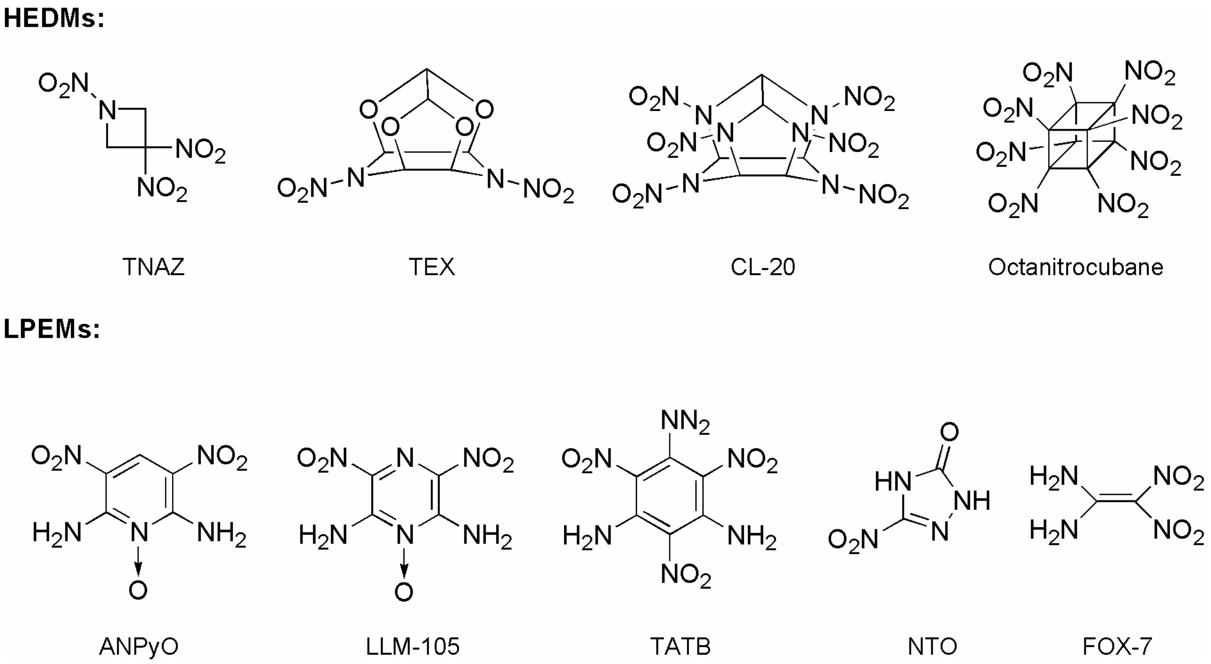

Figure 1.3. HEDMs and insensitive LPEMs.

Target molecules, like nitrated cubanes, are predicted to be shock-insensitive and very dense (1.9 − 2.2 g cm^{-3})[8] with great potential as an explosive and a propellant. Although octanitrocubane has been synthesized recently, cubane chemistry is too complicated to produce quantities for use in corresponding charges (*Figure 1.3*).[9] Another interesting cage structure, which can be synthesized quite easily, is based on the isowurtzitanes (*Figure 1.3*). The two most important molecules representing this class are the 2,4,6,8,10,12-(hexanitro-hexaaza)-tetraazayclododecane (HINW, CL-20)[10] and 4,10-dinitro-2,4,8,12-tetraoxa-4,10-diaza-tetracyclododecane (TEX).[11] CL-20, in its ε-crystal polymorph, has a density of 2.04 g cm^{-3}, a decomposition temperature of 228 °C and a drop hammer height of 12−18 cm (e.g. PETN = 10 cm). Highly nitrated small ring heterocycles and carbocycles are interesting as energetic materials too, because of the increased performance expected from the additional energy release (manifested in a higher heat of formation) upon opening of the strained ring system during decomposition. The most widely studied energetic small-ring compound to date is 1,3,3-trinitroazetidine (TNAZ), a potentially melt-castable explosive that has been investigated as a possible replacement for TNT. TNAZ has a melting point of 103–104 °C, a crystal density of 1.84 g cm^{-3} and thermal stability of >240 °C. TNAZ was first synthesized by Archibald et al.[12]

A different area of interest, which has been in focus for the last two decades, is the so called insensitive, less powerful (low performance) high explosive molecules (LPEMs). The field of the chemical base structures of these materials is very manifold, and therefore only a few prominent examples are given (*Figure 1.4*). The most traditional insensitive high explosive, 1,3,5-triamino-2,4,6-trinitrobenzene (TATB), has an aromatic base structure and is currently the standard for heat resistant, insensitive explosives.[13] Newer ones are related to the work of Pagoria et al. and Ritter et al., and are illustrated by two examples of dinitro-substituted pyridine and pyrazine heterocycles (*Figure 1.3*). Pagoria et al. synthesized 2,6-diamino-3,5-dinitropyrazine-1-oxide (LLM-105)[14] which has a density of 1.918 g cm^{-3} and a decomposition point of 354 °C. Ritter and Lichter reported the synthesis of 2,6-diamino-3,5-dinitropyridine-1-oxide (ANPyO) with a density of 1.878 g cm^{-3} and an mp of >340 °C (dec.).[15] 3-Nitro-1,2,4-triazole-5-one (NTO), easily synthesized in two steps,[16] is used in many new high explosive applications, especially in combination with RDX, designed to be less sensitive.[17] One of the most promising new insensitive explosive is the recently reported 1,1-diamino-2,2-dinitroethylene (FOX-7 or DADE) with a density of 1.885 g cm^{-3} and a drop hammer height value of 72 cm (HMX = 32 cm).[18] It has the same oxygen balance as HMX and is predicted to have 85% of its performance.

1.2 Propellants

Propellants (Figure 1.1) differ from *primary* and *secondary explosives* in that their prime objective is to deflagrate. By deflagrating, *propellants* build up relatively high pressures without the presence of a higher velocity shock wave. This allows work to be performed by the pressure increase and does not cause fracturing of the containment chamber. For example, if PETN were used in a rifle, the barrel would shatter, whereas black powder burns in a way that the pressure build up accelerates the bullet out of the barrel. For *propellants*, the chemistry of the compounds can be divided into three groups. Single based (SB), double based (DB) and semi-nitramine/nitramine *propellants* belonging to the gelatinized nitrocellulose-based *propellants* (NC-based), which are most widely used in gun applications.[19] Additionally to NC, DB *propellants* contain stabilized nitroglycerine (NG), or other nitroglycol compounds, so that the energy output of such charges can be enhanced. In the case of semi-nitramine/nitramine the same effect is established by adding certain nitramines to the NG matrix. A further group of *propellants* is based on a synthetic polymer binder system with an inorganic oxidizing system, commonly a perchlorate, and called composite *propellant*. Composite *propellants* are widely used for rocket propulsion.

Finally there are the liquid *propellants*, which are mainly used in space exploration and technology. Liquid *propellants* are divided into mono- and bi-*propellants*. Hydrazine, monomethylhydrazine (MMH), and unsymmetric dimethylhydrazine (UDMH) are liquid rocket fuels. They are used in a wide variety of rocket engines requiring high performance and long storage times. Hydrazine is most often used as a monopropellant (without an oxidizer) by decomposing it into hot gas with a catalyst. Up to 50% hydrazine is often mixed with MMH or UDMH fuels in order to improve performance. At room temperature and pressure, the hydrazine family of fuels is hypergolic (self-igniting) when mixed with various oxidizers such as N_2O_4, HNO_3, Cl_2, or F_2. When used in a bipropellant system, hydrazine releases about half of its energy by decomposing into a hot gas and half by burning with an oxidizer. Although hydrazine can be burned with an oxidizer, safe combustion is difficult to achieve. Thus, it is not widely used in conjunction with an oxidizer; however, it is often used as an additive to enhance performance of the more stable-burning MMH and UDMH fuels. MMH and UDMH, which remain liquid over a –50 to +70°C temperature range, are high-performance fuels used for missiles.[20]

1.3 Pyrotechnics

Pyrotechnics (*Figure 1.1*), the expression comes from the Greek words '**pyros** → fire, heat' and '**techne** → art',[21] is one of the closely related subjects: *high explosives*, *propellants* and *pyrotechnics* itself. Since these three subjects have a more or less common physico-chemical background, their function and purpose also overlap. But for *pyrotechnics*, the most obvious typical manifestation is that pyrotechnic composition produces beautiful optical and acoustical effects. *Optical effects*: Motion (rockets, fire wheels, bombs); Color (stars, different colored smoke); Sparks (candles, volcanoes, fountains). *Acoustic effects*: Bang ('swissbanger', thunderbangers, crackers); Whistle (wailing banshees, sirens); Rustle (cracklestars).[22] A pyrotechnic process differs from ordinary combustion by not requiring the presence of ambient air.[23] The exothermic reactions used in *pyrotechnics* are based on simple chemical redox reactions. For a long time experience was the fundamental base of *pyrotechnics*. By clever choice of reducing agents and oxidizers, as well as variation of the composition, the redox reaction can be influenced to obtain the desired, well-defined effects. In pyrotechnics the expression 'effect' includes: reaction rate, heat of reaction, reaction temperature, gas production, reaction products/glowing particles and colored light.

Table 1.1. Pyrotechnic composition generating different colored smoke

Substance/Color	**Yellow**	**Red**	**Green**	**Blue**
$KClO_3$ [wt. %]		25	28	28
KNO_3 [wt. %]	25			
S_8 [wt. %]	16			
Wheat flour [wt. %]		15	15	15
Sudan yellow [wt. %]	59		10	
Rhodamine B [wt. %]		24		
Para Red [wt. %]		36		
Methylene Blue [wt. %]			17	17
Indigo Pure [wt. %]			30	40

Fireworks projectiles for example, typically include two components, an initial burst and a main burst. Black powder is one of the oldest pyrotechnic compositions and is typically used in both the initial and the main burst. The main burst includes smaller color-producing pellets referred to as "stars". Igniting these stars during detonation of the main burst provides the light and color of a fireworks display. Typical compositions for a red star include: (1) potassium chlorate, strontium carbonate, charcoal, red gum (shellac), dextrin (or rice starch); (2) potassium perchlorate, strontium carbonate, charcoal, red gum (or shellac), dextrin (or ice starch) and polyvinyl chloride; or (3) strontium nitrate, red gum (or shellac), magnalium (an alloy of

aluminium and magnesium) and Parlon® chlorinated rubber $(C_6H_6Cl_4)_n$. *Table 1.1* gives examples for pyrotechnic compositions generating different collared smoke.[24]

2 Drawbacks of Explosives

Since the drawbacks of explosives omnipresent and they strongly depend on the purpose of the corresponding materials, only a few examples are given below.

2.1 Pyrotechnic Compositions

The burning of large quantities of conventionally *pyrotechnics*, for example used in propelling charges of fireworks projectiles, generates large amounts of smoke, and depending upon the particular weather conditions, such as wind direction, wind speed and relative humidity, the smoke can block the view of further fireworks or can envelop the audience. Most *pyrotechnics* compositions show a very high sensitivity to electrostatic discharge and friction, and as the distribution of particle size, and the morphology affect the sensitivity and the reactivity of pyrotechnic composition systems, special manufacturing demands makes the production difficult and dangerous. For example, the electrostatic charge of a human being is strong enough to initiate a tripping of certain pyrotechnic redox reactions. Furthermore, coloring of pyrotechnics is still a difficult subject as the absence of any metal ions (transition metals) is better for control of the fireworks color and eliminates any ash residue. Therefore, ammonium perchlorate and ammonium nitrate are preferred oxidizers. Although chlorates may be employed as an oxidizer, they are not preferred due to their extreme sensitivity. With respect to color, blue (in most cases resulting from copper salts) is difficult to realize. The other colors are easily produced by certain alkali or earth-alkali metals (e.g. red (strontium salts), green (barium alts), yellow (sodium salts)) which do not produce ash residue.

Low-smoke pyrotechnic composition including a high-nitrogen content, low carbon content energetic material together with the replacement of previous used colorants, e.g. cupric oxide (blue), by transition metal complexes with high-nitrogen, energetic ligands are sought.

2.2 Gas Generators

There are several gas-generators for sudden pressurization or inflation, such as seat-belt tensioners,[25] fire fighting equipment[26] and inflating vehicle occupant passive restraint systems (known colloquially as "air bags").[27] One kind of known inflators utilizes a quantity of stored compressed gas which is selectively released to inflate the air bag. A related type of inflator generates a gas source from a combustible gas-generating material which, upon ignition, provides a quantity of gas sufficient to inflate the air bag. Another inflator (known as a hybrid inflator), the air bag inflating gas is provided by the combination of a stored compressed gas and the combustion products of a gas generating material. Inflators which depend entirely or partially on the generation of gases by virtue of combustion of combustible materials have several disadvantages. For example, the burning of the propellant and the initiator materials in such inflators results in the production of undesired particulate matter. Thus, using inflators that are particulate-containing or which generate particulates upon combustion as part of a passive restraint system in a vehicle might result in undesirable particulates being released into the occupant zone of the vehicles and thereby inhaled by the occupants. In particular, asthmatic reactions may be caused by inhalation of particulate matter, creating a health risk for the occupants. For this reason, automobile manufacturers limit the quantity and type of particulates released by the inflator system. Insoluble particulates are preferred over soluble particulates, as the latter are believed to cause greater reaction. Particulates may arise from certain components of solid rocket propellants or gas generators and ignition systems, as well as through secondary combustion of inert components used in rocket and inflation systems. Reduction in the contribution of particulates from one or more of these components will result in a beneficial reduction in visible ("smoke-like") particulates for the whole assembly. Another problem is the toxicity of the released gases after the ignition of the gas generator (*e.g.* NH_3, HCN, NO_x, CO). In small gas generators sodium azide is often used. Unfortunately, this chemical exhibits drawbacks concerning toxicity and yield of gas. Other classical gas-generating agents are double base propellants. However, they deliver toxic and reactive gases and their combustion temperatures are high. Alternative gas-generating compounds have been proposed, fuelled with double base propellants (DB), azodicarbonamide (ADCA), nitroguanidine or guanidine nitrate and oxidized with potassium nitrate (KNO_3) or potassium perchlorate ($KClO_4$).[28]

These systems show only partly improved properties with respect to the mentioned problems, and therefore the demand of new systems is imperative.

2.3 Liquid Propellants

Hydrazines are used in propellant scenarios, whether as boost materials or in altitude control devices. Hydrazines, like hydrazine itself, MMH, UDMH and DMH have several shortcomings, most of which are inherent to the basic properties of the materials. They have relatively high vapor pressures at ambient temperature (e.g. hydrazine 12-14 torr), which leads to vapor toxicological problems, as they are extremely toxic, carcinogenic and mutagenic. The specific gravities are comparably low, approximately 1.0 g/cm^3 at ambient temperature, which is related to storage problems. In contact with certain metals and oxygen, they tend to decompose easily, and under certain conditions, explosively. All of these properties can be significantly improved upon, with the use of new materials in monopropellant formulations.

There is a need and market for energetic propellant ingredients which are easily synthesized in high yield that have reduced vapor pressure at ambient temperature and otherwise overcome the above prior art shortcomings.

2.4 Primary Explosive

Modern *primary explosives* may be represented by lead azide as the main filling for detonators, and by lead styphnate as the main filling for primers, usually associated with tetrazene as a sensitizer.[29] Lead azide ranked top amongst the conventional initiators, and is being most widely used in service detonators. In spite of its best initiating and filling properties, it suffers from certain drawbacks like, (a) high friction sensitivity, (b) tendency to undergo hydrolysis in the presence of moisture, (c) rapid deterioration in a carbon dioxide environment, and (d) incompatibility with copper (a component of the detonator fuze casing). Environmental impact of the presence of heavy metals when they are brought to function, is also major drawback of those primers. For example, those primers are responsible for the dangerously high level of lead found at some firing ranges. A 1991 survey, for instance, found that employees who had just cleaned a range run by FBI in Quantico, Virginia, had levels of lead in their blood almost ten times a high as US government health limit.[30,31]

Therefore high-energy-capacity transition metal complexes are sought to replace the conventional initiators to reduce the risks involved.

2.5 Tetrazene as Sensitizer

Tetrazene (*Figure 1.2*) is slightly hygroscopic and stable at ambient temperature. It hydrolyses in boiling water evolving nitrogen gas. Its ignition temperature is lower than that of mercury fulminate, and it is slightly more sensitive to impact than mercury fulminate. The detonation properties of tetrazene depend on the density of the material, *i.e.* its compaction. Tetrazene will detonate when it is not compacted, but when pressed, it produces a weaker detonation. These compaction properties make the transition burning to detonation very difficult. Therefore, tetrazene is unsuitable for filling detonators. Tetrazene is used in ignition caps where a small amount is added to the explosive composition to improve its sensitivity to percussion and friction.[32]

A priming compound suitable for making percussion caps which meets military standards for example, including stability and sensitivity, and which compromises no toxic heavy metals, comprises 21-52 wt.% of an explosive compound. The explosive compound comprising ≥ 85 wt.% potassium dinitrobenzofuroxan (KDNBF) as a main energetic ingredient and ≤ 15 wt.% tetrazene as a sensitizer, 48-70 wt.% anhydrous strontium nitrate and/or potassium nitrate as an oxidant. Optionally ≤ 15 wt.% of a fuel such as calcium silicide can be added.[33]

However, the use of tetrazene is diminished in some way due to its hygroscopic property and the low "melting point" of between 128-132 °C, which is comparatively low and unwanted. Tetrazene does not actually have a "melting point" but rather a decomposition point (decomposition point is the point at which the compound is separated into its constituents through chemical reaction). It is the decomposition point and the hygroscopic property which goes along with the longevity of ammunition.

Therefore an alternative to tetrazene is important.

3 High Energy Density Materials − A Solution?

Since the generation of molecular nitrogen as an end product of a propulsion or explosion is highly desired in order to avoid environmental pollutions, health risks, as well as untraceable signatures, compounds containing a backbone of directly linked nitrogen atoms (nitrogen catenation) are of great interest. Compounds fulfilling these requirements could be regarded as a new generation of HEDMs (high energy density materials), which might be used as propellants,

explosives or gas generators, and therefore might serve as solutions for certain problems related to explosives, already pointed out in *Drawbacks of Explosives (Chapter I, 2)*.

Up To date, there is no example of a neutral homopolyatomic nitrogen compound which could be used as HEDM, since neither thermodynamic nor kinetic stabilization with respect to decomposition into N_2 has been achieved. Therefore, experimental investigations[34] are elusive compared to the large number of theoretical studies.[35] It seems that in the near future the azide anion and the more exotic species N_5^+ [36] and possibly N_5^- [37] are the only accessible homopolyatomic nitrogen species (beside N_2). _Note_: The polymerization of nitrogen in sodium azide at pressures as high as 120 GPa was reported.[38] Although the polymeric form was preserved on decompression in the diamond anvil cell, transformation back to the starting azide form occurred under ambient conditions. Quite recently, a single-bonded cubic form of nitrogen was observed. This material was synthesized directly from molecular nitrogen at temperatures above 2000 K and pressures above 110 GPa in a laser-heated diamond-cell.[39] Although theory predicts that the *cg*-N could be metastable at atmospheric pressures, the authors of the high pressure study found that at room temperature *cg*-N is metastable only at pressures above 42 GPa. Only further experiments can show whether this new form of poly-nitrogen may ever be suitable for use as a high energy density material (HEDM).

An approach to overcome the thermodynamic and kinetic problems represents the modification of homoleptic polynitrogen compounds, by substitution of a nitrogen atom by a CR group (e.g. R = H, alkyl, aryl etc.). In such compounds the endothermic and highly energetic properties are conserved, however with larger activation barriers to decomposition. Compounds of this class are composed of nitrogen chains which may be (i) entirely acyclic, (ii) a combination of an acyclic and cyclic moiety; (iii) entirely cyclic or (iv) singly joined, non-fused rings (cyclic-cyclic).[40,41]

The synthesis of these materials is very challenging because the reactants, intermediates, and desired products can have high endothermicities. These high endothermicities might make many of these compounds shock sensitive and extremely difficult to handle. Examples for known compounds, for example with a combination of an acyclic and cyclic moiety with six contiguous nitrogen atoms containing double bonds and tetrazolyl substituents, are the poorly described 1,6-bis-[tetrazoly-5-yl]-1,5-hexadiene[42] and 1,3,4,6-tetrakis-[2-methyl-tetrazole-5-yl]-1,5-hexadiene[43] which tend to explode violently upon heating, friction or impact (*Figure 1.4*).

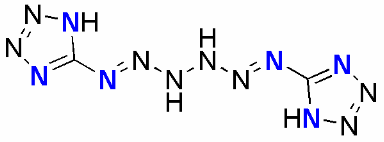

1,6-bis-[tetrazolyl-5-yl]-1,5-hexadiene

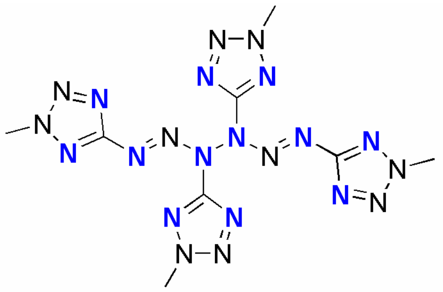

1,3,4,6-tetrakis-[2-methyl-tetrazolyl-5-yl]-1,5-hexadiene

Figure 1.4. HEDMs with a combination of an acyclic and cyclic moiety

The goal of exploiting the potential of polynitrogen compounds for HEDM applications requires research to identify new target molecules that possess sufficient energy and kinetic stability to warrant attempts at their synthesis, to develop new methodology for their preparation, and to prepare amounts sufficient for the determination of their structures and properties.

Since new HEDMs are thought to be manageable with respect to the application in new propellants, primers, gas generators or pyrotechnics, the base structure of those compounds has to be chosen carefully to avoid any risks.

The enthalpy criteria of energetic materials are governed by their molecular structure, and therefore, the move to heterocycles with a higher nitrogen content (e.g. from imidazole ($\Delta_f H^\circ_{cryst}$= 14.0 kcal/mol)[44], over 1,2,4-triazole ($\Delta_f H^\circ_{cryst}$= 26.1 kcal/mol) to tetrazole ($\Delta_f H^\circ_{cryst}$= 56.7 kcal/mol)[45]) the trend in the heats of formation is obvious. The base structure of those stabilized potential polynitrogen compounds was chosen to be that of tetrazoles, particularly 5-amino-1*H*-tetrazoles, since these groups of compounds shows reasonable stability with a huge variety of different (including energetic) substituents.

3.1 Relationship between Guanidines and Tetrazoles

The chemistry of aminotetrazoles is related to the chemistry of guanidines, and therefore the latter serves as suitable precursors. Guanidine chemistry has extended over a period of more than 100 years, and many useful compounds have been identified. The uses of these compounds are highly diverse, ranging from biologically active molecules to highly energetic materials,

thus indicating the manifold usability of the guanidine moiety as building block.[46] Thiele was the first to prepare guanidine derivatives, e.g. aminoguanidine in 1892, and has to be seen as the founder of the modern nitrogen-based high energy density materials.[47]

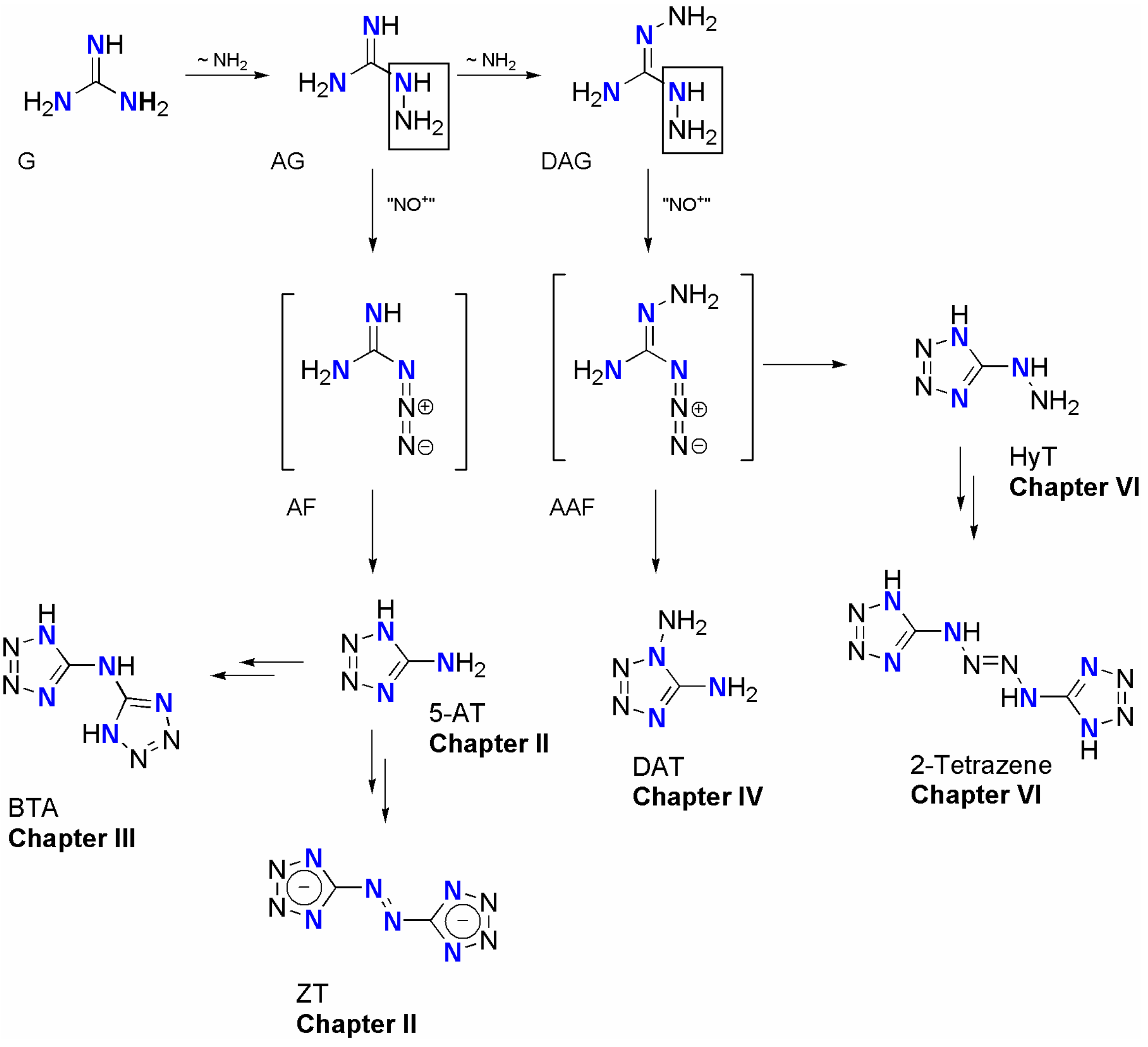

Scheme 1.1. Relationship between Guanidines and Tetrazoles

The formal exchange of a hydrogen atom of guanidine successively by NH_2 group leads to the family of guanidines: guanidine (**G**), aminoguanidine (**AG**), diaminoguanidine (**DAG**) and triaminoguanidine (**TAG**). In *Scheme 1.1* (**TAG** not shown), the connectivity of guanidines and corresponding tetrazoles are displayed (corresponding nitrogen atoms are in bold) with respect to the later discussed fields of research (*Chapter I, 3.2*). In general, the reaction between HNO_2 ("NO^+") and a hydrazine moiety (*Scheme 1.1*) can formally yield the corresponding

azide, in the case of AG → azidoformamidine (**AF**) and for **DAG** (only one equivalent HNO_2) → *N*-amino-azidoformamidine (**AAF**). **AF** and **AAF** are only stable in their protonated forms (**AAF** only in solution) and undergo ring closure to the corresponding tetrazole derivative.[48] For **AF**, 5-amino-1*H*-tetrazole (**5-AT**) is formed, and in the case of **AAF**, depending on how the ring closure proceed, formally 1,5-diamino-1*H*-tetrazole (**DAT**) or 5-hydrazino-1*H*-tetrazole (**HyT**) is obtained. The latter process is related to the Dimroth rearrangement − imidoyl azide-tetrazole ring-chain isomerism − which was found to be typical for 1,5-diaminotetrazoles.[49] Azotetrazolates (**ZTs**) and 2-tetrazenes are obtained by a formal oxidation reaction, and *N*,*N*-bis-(1(2)*H*-tetrazol-5-yl)-amine (**BTA**) is a derivative of **5-AT** (*Chapter III*).

3.2 Goals of this Study

The concept of a new class of high nitrogen content high energy material (HNC-HEMs) as an energetic component of propellants has evinced great interest recently. Presence of N–N and C–N bonds in HNC compounds confers positive heat of formation on them. Furthermore, HNC-HEMs produce more nitrogen gas per gram than most of the HEMs, resulting in inherently cooler combustion products, which is an attractive feature for gun propellants and gas generators. Low percentage of carbon and hydrogen in these compounds reduces the proportion of oxidized combustion products in comparison to conventional HEMs, resulting in formation of low mean molecular mass combustion products like methane.

The goal of this PhD thesis can be shortly summarized by the following expression:

- *Develop methods for the synthesis of the proposed target compounds or develop new synthesis and scale-up procedures for known materials.*
- *Prepare sufficient amounts of material on the laboratory scale to allow the determination of the structure and the chemical and physical properties of these new materials.*
- *Evaluate the potential of the known or new compounds for HEDM applications.*

The concept of this thesis is partly summarized in *Figure 1.5*, which is related to the nitrogen content of certain tetrazole derivatives.

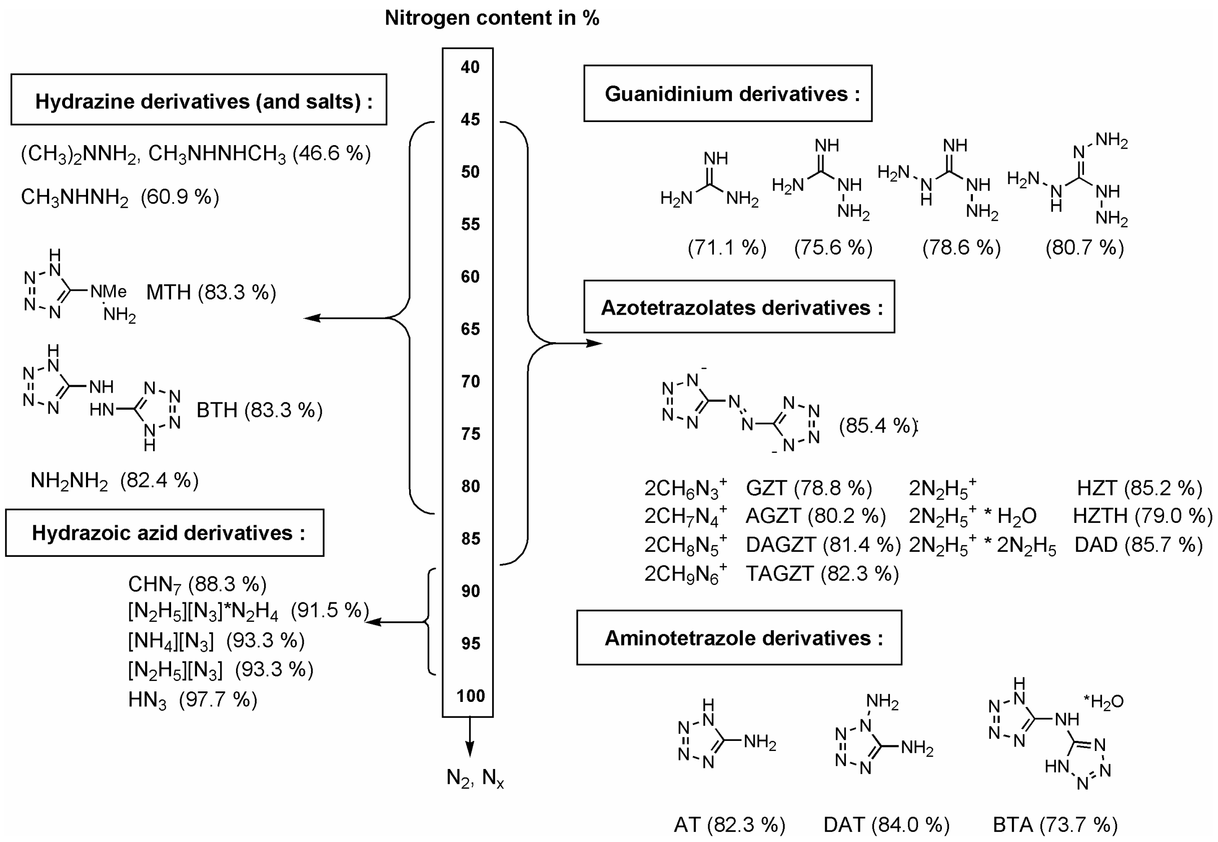

Figure 1.5. Nitrogen content of certain Tetrazoles and Salts

Chapter II:

The first part of *Chapter II* deals with energetic salts of the 5,5'-azotetrazolate anion with different guanidinium cations, including (bis(guanidinium) 5,5'-azotetrazolate (**GZT**), bis(aminoguanidinium) 5,5'-azotetrazolate (**AGZT**), bis(aminoguanidinium) 5,5'-azotetrazolate monohydrate (**AGZTH**), bis(diaminoguanidinium) 5,5'-azotetrazolate (**DAGZT**) and bis(triaminoguanidinium) 5,5'-azotetrazolate (**TAGZT**)) and (bis(azidoformamidinium) 5,5'-azotetrazolate (**AFZT**)). **AGZT** was obtained according to the literature as the monohydrate (**AGZTH**) and **DAGZT** was synthesized for the first time. All salts were fully characterized by vibrational spectroscopy (IR, Raman), multinuclear NMR spectroscopy and elemental analysis. Safety testing (impact and friction sensitivity) was performed to find safe handling procedures. The crystal structures of **AFZT** and **AGZTH**, which crystallize in the monoclinic space groups $P2_1/n$ and $C2/c$, were determined. The thermal decomposition of the salts was monitored by differential scanning calorimetry (DSC) and the gaseous products of the explosions of all compounds were identified with mass spectrometry and IR spectroscopy. The second part describes a new and safe synthesis of hydrazinium azotetrazolate in form of a patent. In the

third part the results of a high temperature and pressure FTIR study on dihydrazinium azotetrazolate dihydrazinate (**DAD**) will be discussed. The last part of *Chapter II* presents the results of compatibility as well stability tests of dihydrazinium azotetrazolate hydrate (**HZTH**), dihydrazinium azotetrazolate (**HZT**) and **TAGZT** in combination with certain propellant charges according STANAG 4582.

Chapter III:

Several salts (alkali, Cu, Ni, Pd and $^{i}PrNH_2$) of 5-cyanoiminotetrazoline ($C_2N_6^{2-}$, 5-cyanoiminotetrazolinediide **CIT**) were investigated. A full characterization by means of X-ray, Raman, NMR techniques, mass spectrometry and elemental analysis is presented for the $^{i}PrNH_2$, Cs and Pd salts. The **CIT** dianion represents a nitrogen rich binary CN dianion and the cesium forms monoclinic crystals (a = 7.345(2) Å, b = 9.505(2) Å, c = 10.198(2) Å, β = 92.12(3) °, space group $P2_1$/n, Z = 4). DSC and *in situ* temperature-dependent X-ray diffraction measurements of the cesium salt revealed an astonishing thermal stability accompanied by a reversible phase transition from the low temperature α modification to the metastable β modification at 253 °C. Above the melting point (334 °C), the cesium salt decomposes yielding cesium azide and cesium dicyan amide which decomposes under further heating under release of nitrogen. The reaction of Cs_2CIT with SO_2 resulted in the surprising formation of a new cesium salt with the 5-cyaniminotetrazoline-1-sulfonate dianion ($Cs_2CIT\text{-}SO_3{\cdot}SO_2$). This salt crystallizes in the monoclinic space group $P2_1$ with one SO_2 solvent molecule (a = 8.0080(2) Å, b = 8.0183(2) Å, c = 9.8986(3) Å, β = 108.619(1) °, Z = 2). The structure and bonding of the 10π dianion are discussed on the basis B3LYP/aug-cc-pvTZ computations (MO, NBO) and the three-dimensional array of the cesium salts with respect to the $Cs^{\delta+}$–$N^{\delta-}$ in Cs_2CIT compared to the $Cs^{\delta+}$–$N^{\delta-}$ and $Cs^{\delta+}$–$O^{\delta-}$ in $Cs_2CIT\text{-}SO_3{\cdot}SO_2$ is discussed. Due to the expected rich bonding modes of the CIT anions, the coordination chemistry with palladium was also studied, yielding monoclinic crystals of $[Pd(CIT)(NH_3)_3]{\bullet}H_2O$ (a = 7.988(2) Å, b = 8.375(2) Å, c = 13.541(3) Å, β = 104.56°, space group $P2_1$/n, Z = 4). In the solid state, the complex is composed of dimers, showing two agostic interactions and an unusual close interplanar π-π stacking of the tetrazole moiety of **CIT** ligand. The second part introduces the alkaline and alkaline earth metals salts of BTA. Since Cupric oxide is one of the most important additives used to a) catalyze decomposition reaction in gas generators in order to obtain cooler reaction gases b) as burning enhancer for AP based composite *propellants* and c) as coloring agent in *pyrotechnics* the H_2bta

ligand system was investigated in this context. The third part discusses the reaction of Cu^{2+} ions in aqueous ammonia solution with H_2**bta**. Depending on the reaction conditions three complexes were obtained: $Cu(bta)(NH_3)_2$ (**47**), $Cu(bta)(NH_3)_2$*H_2O (**48**) and $(NH_4)_2Cu(bta)_2$*$2.5H_2O$ (**49**). The crystal structures of **47** and **48** are discussed with respect to the coordination mode of bta, which mediates in the case of **47** and **48** weak superexchange interactions between the adjacent magnetic transition metal Cu^{II} cations. This antiferromagnetic interactions result from 1D copper chains over a disguised azide end to end bridge. Interestingly, the structural arrangement of **47** completely changes in the present of crystal water. Moreover, some physicochemical properties (e.g. heat of formation, friction and impact sensitivity, DSC) of these complexes with respect to high energetic materials are discussed. The last part of *Chapter III* discusses the H_2**bta** / CuX_2 (X = Cl^-, ClO_4^-) system, and it will be derived that H_2**bta** might serve as ligand in new High-Energy-Capacity Copper(II) **bta** salts suitable for safe non-toxic PC formulations, as possibly photosensitive compounds utilized in laser detonators as well as colorants in pyrotechnic formulations.

Chapter IV:

The first part of *Chapter IV* discusses the synthesis of 1,5-Diamino-1*H*-tetrazole (**55**, **DAT**) and certain salts. **DAT** can easily be quaternized by the reaction with strong mineral acids yielding the poorly investigated 1,5-diaminotetrazolium nitrate (**59a**) and perchlorate (**59b**). A new synthesis for **55** is introduced avoiding lead azide as hazardous byproduct. The reaction of 1,5-diamino-1*H*-tetrazole with iodomethane (**61a**) followed by the metathesis of the iodide (**61a**) with silver nitrate (**61b**), silver dinitramide (**61c**) or silver azide (**61d**) leads to a new family of heterocyclic-based salts. In all cases, stable salts were obtained and fully characterized by vibrational (IR, Raman), multinuclear NMR spectroscopy, mass spectrometry, elemental analysis, X-ray structure determination, as well as initial safety testing (impact and friction sensitivity). Most of the salts exhibit good thermal stabilities and the perchlorate (**59b**) as well as the dinitramide (**59c**) have melting points well below 100°C, yet high decomposition onsets, defining them as new (**59c**), highly energetic ionic liquids. Preliminary sensitivity testing of the crystalline compounds indicates for all compound rather low impact sensitivities, the highest being that of the perchlorate (**59b**) and the dinitramide (**61c**) with a value of 7 J. In contrast, friction sensitivities of the perchlorate (**59b**, 60 N) and the dinitramide (**61c**, 24 N) are relatively high. The enthalpies of combustion ($\Delta_c H^\circ$) of **61b-d** were determined

experimentally using oxygen bomb calorimetry: $\Delta_c H^\circ$ (**61b**) = -2456 cal g^{-1}, $\Delta_c H^\circ$ (**61c**) = -2135 cal g^{-1} and $\Delta_c H^\circ$ (**61d**) = -3594 cal g^{-1}. The standard enthalpies of formation ($\Delta_f H^\circ$) of **61b-d** were obtained on the basis of quantum chemical computations using the G2 (G3) method: $\Delta_f H^\circ$ (**61b**) = 41.7 (41.2) kcal mol^{-1}, $\Delta_f H^\circ$ (**61c**) = 92.1 (91.1) kcal mol^{-1} and $\Delta_f H^\circ$ (**61d**) = 161.6 (161.5) kcal mol^{-1}. The detonation velocities (*D*) and detonation pressures (*P*) of **59b** and **61b-d** were calculated using the empirical equations by Kamlet and Jacobs: *D*(**59b**) = 8383 m s^{-1}, *P*(**59b**) = 32.2 GPa; *D*(**61b**) = 7682 m s^{-1}, *P*(**61b**) = 23.4 GPa; *D*(**7c**) = 8827 m s^{-1}, *P*(**7c**) = 33.6 GPa; *D*(**59d**) = 7405 m s^{-1}, *P*(**59d**) = 20.8 GPa. For all compounds a structure determination by single crystal X-ray diffraction was performed. **61a** and **61b** crystallize in the monoclinic space groups *C*2/c and $P2_1$/n, respectively. The salts of **55** crystallize in the orthorhombic space groups $Pna2_1$ (**59a, 59d**), and *F*dd2 (**61b**). The hydrogen bonded ring motifs, in the formalism of graph-set analysis of hydrogen-bond patterns is discussed and compared in the case of **59a**, **59b** and **61b**. The second part of *Chapter IV* presents the thermal decomposition of the highly energetic 1,5-diamino-4-methyl-1*H*-tetrazolium nitrate (**61b**), 1,5-diamino-4-methyl-1*H*-tetrazolium dinitramide (**61c**) and 1,5-diamino-4-methyl-1*H*-tetrazolium azide (**61d**) were investigated by thermogravimetric analysis (TGA) and differential scanning calorimetry (DSC). Mass spectrometry and IR spectroscopy were used to identify the gaseous products. Decomposition appears in the cases of **61c** and **61d** to be initiated by a proton transfer to form the corresponding acid HN_3 and HN_3O_4 whereas in the case of **61b** a methyl group transfer to $MeONO_2$ is observed as initial process. The gaseous products after the exothermic decomposition are comparable and are in agreement of the proposed decomposition pathways. The decomposition temperatures of **61b** and **61c** are significantly higher than that of **61d** and were supported by evaluation the values of the activation energy according the method of Ozawa and Kissinger.

Chapter V:

Chapter V represents the continued work of the diploma thesis. The reduction of the eight-step-reaction for the preparation of the 1,4-bis-(1-dimethyl-1*H*-tetrazol-5-yl)-1,4-dimethyl-2-tetrazene (**84b**) was reduced to a three step synthesis. The obtained overall yield of 26% exceeds the former synthesis, which yielded 4%. Moreover, a general synthesis for the preparation of substituted (R = H, Me, allyl, cyclohexyl) 1,4-bis-(1R-1*H*-tetrazol-5-yl)-1,4-dimethyl-2-tetrazene will be introduced. Two new products could also be confirmed by means

of single X-ray crystal structure determination. A new route to 1-methyl-1-tetrazolylhydrazines is introduced, which themselves are interesting compounds.

Chapter VI:

Since the search of new energetic compounds with increased performance is progressing relatively slow, the trend in the development of 'New Products' has rather to be seen in the manufacturing of blended and polymer-bonded explosives. In particular, extremely insensitive formulations are thought to meet the international standards. They are currently made by formulation of nitramine compounds, like RDX or HMX, and special additives. *N*-nitraminotetrazoles are potentially interesting materials as they might be used as modifiers of the combustion rates in rocket propellants, as cool gas generators or as additives in insensitive explosive formulations. The first part of *Chapter VI* discusses certain substituted *N*-aminotetrazoles (with low carbon content). In the case of corresponding *N*-nitrosoaminotetrazoles (**111a**, **111c**) and secondary *N*-nitraminotetrazoles (**112a-c**) experimental data are in the most case not available and therefore these compounds are fully characterized by vibrational (IR, Raman) and multinuclear NMR spectroscopy ($^{14}N/^{15}N$, ^{1}H, ^{13}C), mass spectrometry and elemental analysis. For most of the compounds the molecular structure in the solid state was determined by single crystal X-ray diffraction. In the case of two *N*-nitraminotetrazoles (**112a,c**) the physicochemical properties (e.g. D, P, $\Delta_f H^{\circ}$) were evaluated. The heat of formation was calculated to be positive for **112a** and **112c** (+2.8 and +85.2 Kcal mol^{-1}, respectively) and the calculated detonation velocity with 5988 (**112a**) and 7181 (**112c**) m s^{-1} reaches values of TNT and nitroglycerin. The second part reports the investigation of mono- (**MNB**) and dinitrobiuret (**DNB**). Both compounds are for the first time structurally characterized and the initial safety testing has been performed indicating, that DNB is highly explosive. The thermal decomposition of two highly energetic materials, mononitrobiuret (MNB) and 1,5-dinitrobiuret (DNB) were investigated by thermogravimetric analysis (TGA) and differential scanning calorimetry (DSC) and are discussed in the third part of *Chapter VI*. Mass spectrometry and IR spectroscopy were used to identify the gaseous products. Decomposition appears in both cases to be initiated by the release of nitramine. The gaseous products after the exothermic decomposition are similar for MNB and DNB, but the decomposition temperature of MNB is significantly higher and leads to the formation of urea, biuret (imidodicarbonic diamide), triuret (diimidotricarbonic diamide), tetrauret

(triimidotetracarbonic diamide) and cyanuric acid (*s*-triazine-2,4,6(1*H*,3*H*,4*H*)-trione). The last part reports the synthesis of three novel nitramines.

3.3 Experimental Techniques

There are a variety of experimental techniques to characterize and quantify the physico-chemical properties of explosives. Experimentation provides a better understanding of the energy content, the release of energy of a substance under various conditions. Such information is extremely important in assessing reactive hazards and managing risks; moreover, they are important to make a correct classification of certain explosives and help to understand the decomposition processes involved.

3.3.1 Thermal Analysis

An explosion, deflagration or other reactivity hazard involves conversion of stored chemical energy of the component into mechanical or heat energy, and it is the uncontrolled release of this stored energy that causes the damage in a reactive chemical incident, volitional in the case of high energetic materials. The reactivity of a substance is normally assessed by performing calorimetric measurements.[50] Information about the amount of energy released and the rate of energy released for a energetic material can be obtained by performing calorimetric tests. There are several various calorimetric measurements possible. Moreover decomposition experiments are also important.

TGA:

The thermogravimetric Analysis (TGA) provides a graph of mass loss *vs.* temperature over a specified temperature range (up to 2000 °C). This analytical technique is widely used in polymer science, inorganic chemistry, fuel science, and geology to measure the loss of volatile components or thermal stability of a sample and can also be used for the investigation of *explosives*. The experiments are usually run with a temperature ramp of 5 or 10 °C min^{-1} and can be carried out in inert atmospheres, such as nitrogen, to study thermal stability or volatility, or in oxidizing atmospheres to study oxidative decomposition. The mass losses can be

characteristic of a material and, where the losses are in discrete steps, the TGA experiment can offer quantitative data on the course of a decomposition. The TGA also can be run in an isothermal mode, where the rate of weight loss at a fixed temperature is measured. This type of experiment can be used to predict loss rates of volatiles or decomposition rates for materials.

The following procedure describes a general TGA experiment, measurements deviating from this procedure will be stated: The samples were subjected to TGA analysis in a nitrogen atmosphere in open Al_2O_3 crucibles (sample weight ~ 1 − 5 mg) at a heating rate of 5 °C min^{-1} with a thermogravimetric analyzer (Setaram DTA−TGA 92)[51] in the temperature range from 30°C − 750 °C. For the removal of moisture, the samples were dried *in vacuo* (if possible) for 24 h at 40°C.

DSC:

A differential scanning calorimetry (DSC) can provide an overall indication of exothermic activity of the composition activity of the compound being tested and can help to assess potential reactive hazards. In a DSC, a sample and a reference are subjected to a continuously increasing temperature, and heat is added to the reference to maintain it at the temperature as the sample. This added heat compensates for the heat lost or gained as a consequence of an overall endothermic or exothermic reaction. When the heat generation (Watts) in the sample exceeds a particular value, the heat supply to the sample is cut-off, and this additional heat gain is attributed to exothermic activity within the sample. This cut-off value depends on the sensitivity of the particular instrument. In the case of an exothermic (endothermic) reaction, a peak is observed in a DSC thermograph. A base line is constructed from the initial heating mode, and another line is drawn to coincide with the initial rise due to the exotherm (endotherm). The temperature at the intersection of the two lines is called the onset temperature and corresponds to a detectable level of heat due to a chemical reaction. The energy released (-ΔH) during the process is calculated as the area under the heat-supplied (Watts) and time curve. DSC is a popular screening tool because it is safe, since it involves a small amount of sample (for energetic materials less than 1mg is appropriate).

The kinetics of exothermic reactions are important in assessing the potential of materials and systems for thermal explosion. These parameters are for example accessible from the onset temperature (T_{onset}) determined by DSC, since it denotes a rate of chemical reaction. The

detected onset temperature is thus a measure of the reaction kinetics. There is considerable argument about such interpretation[52], and therefore we decided to use the Standard Test Method for Arrhenius Kinetic Constants for Thermally Unstable Materials from American Society for Testing and Materials (ASTM) according to the ASTM protocol E 698 – 99 to estimate parameters like activation energy (E_a).[53] The theoretical background of this procedure is based on the work of Ozawa[54] and Kissinger[55].

Autocatalytic and *n*th-order kinetics are the main features of decomposition reactions. They can be expressed as follows: For *n*th order kinetics,

$$\frac{d\alpha}{dt} = k(1-\alpha)^n \tag{1}$$

where α, the extent of decomposition, is defined as $\alpha = \Delta H_t / \Delta H_{Total}$, were ΔH_t and ΔH_{Total} are the enthalpy of the decomposition reaction at time t and the enthalpy of the decomposition reaction at the end of the decomposition, respectively; they can be determined from DSC thermograms (Peak maxima). The rate constant (k) can be expressed as

$$k = Ae^{-E_a/RT} \tag{2}$$

where A is the frequency factor. Then,

$$\ln k = \ln \frac{(d\alpha / dt)}{(1-\alpha)^n} = \ln A - \frac{E_a}{RT}. \tag{3}$$

When the order of this reaction is properly assumed, a plot of ln k versus $1/T$ provides A and E_a. Kissinger[55] proposed that

$$E_a \beta (RT_p^2) = Ae^{-E_a/RT_p} \tag{4}$$

where $\beta = dT/dt$ is the heating rate. By taking the logarithm of Eq. (4), we obtain the Kissinger equation:

$$-\ln(\beta / T_p^2) = \ln \frac{AR}{E_a} + (1/T_p)(E_a / R) \tag{5}$$

From a plot of $-\ln(\beta / T_p^2)$ versus $1/T_p$, where T_p is the peak temperature, and fitting to a straight line, the activation energy E_a can be calculated from the slope. The general equation for the reaction rate under isothermal conditions has been written as:

$$\frac{d\alpha}{dt} = f(\alpha) A T^n e^{-E_a/RT} \tag{6}$$

Under non-isothermal condition, at a constant heating rate β = *dT/dt*, an explicit temporal dependence of Eq. (6) can be derived, and together with Doyle's approximation[56] the linear equation of Ozawa-Flynn-Wall[54] can be obtained:

$$E_a = -\frac{R}{0.4567} \frac{d \log \beta}{d(1/T_p)} \tag{7}$$

From a plot of $\log \beta$ versus $1/T_p$ and fitting a straight line, the activation energy, E_a, can also be obtained from the slope. By using the Kissinger as well as the Ozawa method the activation energy can be determined without knowing the order of reaction.

In most cases of the investigated compounds, it is assumed that the rate constant follows the Arrhenius law and that the exothermic reaction can be considered as a single step; certainly the conversion at the maximum rate is independent of the heating rate, when this is linear. In order to get a better agreement of the activation energies determined according the Kissinger and Ozawa method, following the ASTM protocol, a refinement of the Kissinger activation energy (7) according (9)

$$E_a = \left(-2.303 \frac{R}{D} \right) \left[\frac{d(\log_{10} \beta)}{d(1/T)} \right] \tag{9}$$

using given D factors in [53] leads to very close agreements.

The following procedure describes a general DSC experiment, measurements deviating from this procedure will be stated: Samples (~ 0.3 − 1.5 mg) for DSC measurement were analyzed with a nitrogen flow of 20 mL/min in closed Al-containers with a hole (1 µm) on the top for gas release and a 0.003*3/16-in. disk was used to optimize good thermal contact between the sample and container (according ASTM E 698 – 99)[53]. The reference sample was an Al-container with air. Measurements were recorded between 30°C−400 °C. The sample and

the reference pan were heated in a differential scanning calorimeter (Perkin-Elmer Pyris 6 DSC,[57] calibrated by standard pure Indium and Zinc) at heating rates of 2, 5, 10, 15 and 20 °C. In the most cases the decomposition points are given at a scan rate of 10°C/min. For the removal of moisture, the samples were dried (if possible) *in vacuo* for 2 h at an appropriate.

Bomb calorimetry

For all calorimetric measurements a Parr 1356 bomb calorimeter (static jacket) equipped with a Parr 207A oxygen bomb for the combustion of highly energetic materials was used.[58] The samples (ca. 80 – 100 mg) were loaded in (energetically) calibrated Parr gelatine capsules (0.9 mL) and a Parr 45C10 alloy fuse wire was used for ignition. In all measurements a correction of 2.3 (IT) calories per cm wire burned has been applied and the bomb was examined for evidence of noncombusted carbon after each run. A Parr 1755 Printer was furnished with the Parr 1356 calorimeter to produce a permanent record of all activities within the calorimeter. The reported values are the average of three single measurements. The calorimeter was calibrated by combustion of certified benzoic acid (SRM, 39i, N.I.S.T) in oxygen atmosphere at a pressure of 3.05 MPa. Typical experimental results of the constant volume combustion energy ($\Delta_c U_m$) of the compounds are summarized in corresponding *Chapters* and are assigned. The standard molar enthalpy of combustion ($\Delta_c H_m^\circ$) was derived from $\Delta_c H_m^\circ = \Delta_c U_m + \Delta nRT$ ($\Delta n = \sum n_i$ (products, g) $- \sum n_i$ (reactants, g); $\sum n_i$ is the total molar amount of gases in products or reactants). The enthalpy of formation, $\Delta_f H^\circ$, for each of the corresponding salts were calculated at 298.15 K using designed Hess thermochemical cycles.

Explosion experiments

For the analysis of the explosion gases of all compounds, a specially equipped IR-cell was loaded with about ~ 2 mg of the sample and evacuated. The sample holder of the IR cell was heated rapidly to 450°C to initiate the explosion. The explosion products were allowed to expand into the gas cell and the IR spectrum was recorded. For the recording of the mass spectra, a sample of about 1 mg of the compounds was rapidly heated to 450°C to initiate the explosion in a one side closed glass tube (length: 500 mm; diameter: 5 mm) connected to the reservoir of the mass spectrometer. The explosion gases were then analyzed by mass

spectrometry (JEOL MStation JMS 700)[59] using electron impact (EI) mode (mass range 1 – 120; 1 scans per second). In order to analyze the gases from the stepwise decomposition of the compounds, a specially equipped IR-cell was loaded with the compounds (~ 2 mg) and evacuated. The sample holder of the IR cell was heated at a rate of 1°C/min (CARBOLITE 900°C Tube Furnace type MTF 9/15)[60] and the reaction products were allowed to expand continuously into the gas cell. During this heating, IR-spectra were recorded continuously as a function of the heating rate using a Perkin-Elmer Spektrum One FT-IR[57] instrument.

3.3.2 Sensitivity Test[1]

Calorimetric tests capture temperature-time response of a substance and are performed to detect thermal instability. However, the energy stored within the substance can be released by a variety of stimuli. Sensitivity is defined as the ease with which a substance subjected to external stimuli, such as shock, impact or heat, can undergo detonation.[61] A few of the techniques used to determine the sensitivity[1] of a material are discussed below.

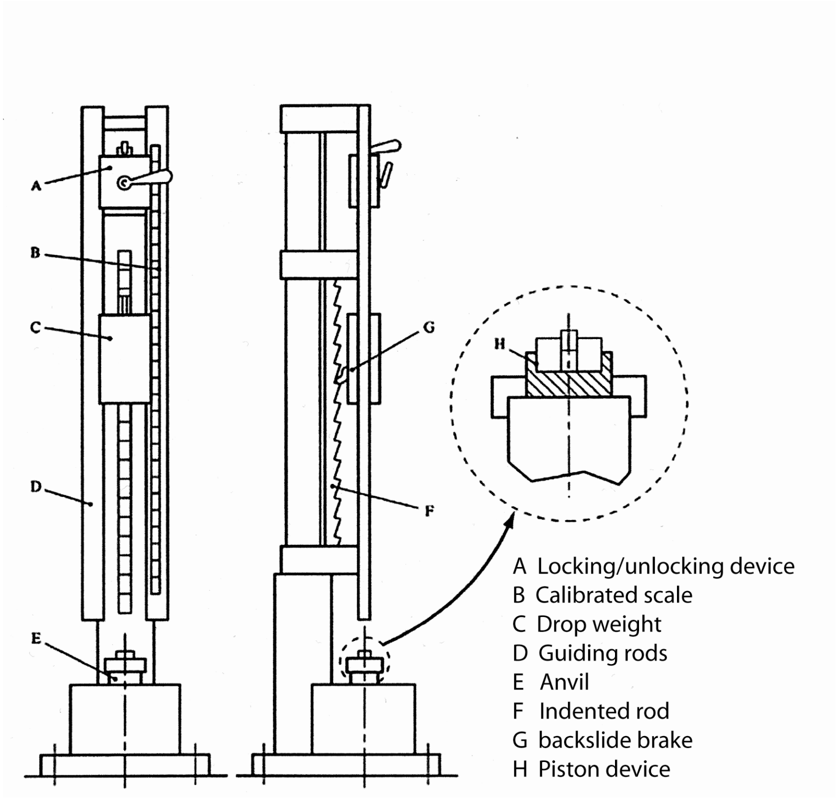

Figure 1.6. BAM drop hammer

Impact Sensitivity

During impact tests, the impact of a drop-weight on a substance is assessed. The sample, placed between two flat, parallel, hardened steel surfaces, is subjected to an impact by dropping a weight. The impact may result in initiation depending on the sensitivity of the material, weight mass, and its drop height (impact energy). Initiation is observed by sound, light effects, smoke, or by inspection. The BAM impact apparatus, known to give fairly reproducible results, is shown in *Figure 1.6*. Typically drop weights having a mass of 1, 2, 5 or 10 kg are used and the lowest energy required to create a detonation is recorded. Thus drop-weight and drop-height at which the initiation of the sample occurs are the main parameters determined from impact testing. The drop height at which detonation is observed is thus a measure of impact sensitivity of an *explosive*. A typical experiment runs as following: A small amount of pre-weighed sample, usually around 20 mg, is placed in a brass cup for each test. 6 μm HMX was tested previously as a standard, giving value of 34 kg cm for five consecutive negative results. Drop heights are measured with falling of 1 and 5 kg mass and a minimum drop height considered for six consecutive drops at a specific height and mass with no change in sample. The result is rated as "+", if the lowest impact energy an explosion occurred (in six single trials) is ≤ 2 J. "+" indicates that the corresponding compound is too dangerous for transport. In the case of no explosion or impact > 2 J the result is rated as "-". *Table 1.2* gives some examples.

Table 1.2. Impact sensitivity of selected examples

Substance	Impact energy [J]	result
Ethylnitrite	1	+
$N_2H_5ClO_4$ (dry)	2	+
$Pb(N_3)_2$	2.5	-
Lead styphnate	5	-
Nitroglycerin (NG), liquid	1	+
$Hg(ONC)_2$	1	+
PETN (dry)	3	-
RDX (dry)	5	-
Tetryl (dry)	4	-

Friction Tester

The sample is placed on a rough ceramic plate and a force (created by different weights on the lever) is loaded on the sample trough a stationary pin in contact with the plate. The plate is motor driven trough a complete cycle pass beneath the pin. The test sample is subjected to the friction created by the rubbing of the pin against the plate. Normally the test is run with a pin load of 5 − 10 − 20 − 40 − 60 − 80 − 120 − 160 − 240 − 360 N or values in between depending of the weight and the used groove. Each experiment is evaluated with respect to "no reaction", decomposition (change of color, smell) or explosion (bang, crackle, spark formation, ignition) and continued, by changing the pin load, until no explosion occurred within six single tests. A compound is classified as not friction sensitive if each single test with a friction load of 360 N was evaluated as decomposition or "no reaction". The result is rated as "+", if the lowest friction load an explosion occurred (in six single trials) is < 80 N. "+" indicates that the corresponding compound is too dangerous for transport. In the case of no explosion or friction ≥ 80 N the result is rated as "-". *Table 1.3* gives some examples.

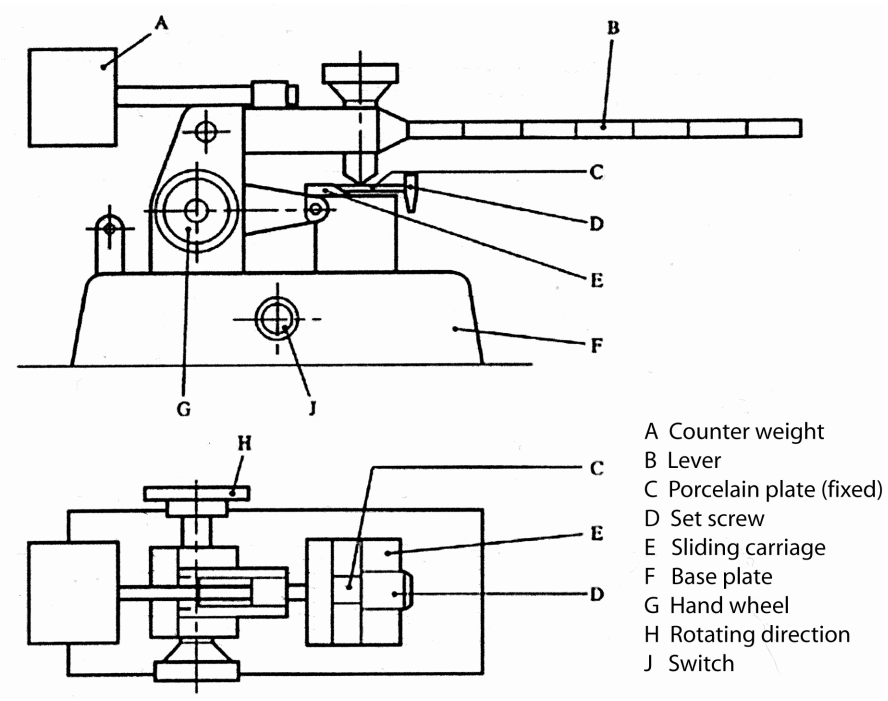

Figure 1.7. BAM friction tester

Table 1.3. Friction sensitivity of selected examples

Substance	Friction energy [N]	result
HMX (dry)	80	-
$N_2H_5ClO_4$ (dry)	10	+
$Pb(N_3)_2$ (dry)	10	+
Lead styphnate	2	+
TNT	360	-
$Hg(ONC)_2$	10	+
PETN (dry)	60	+
RDX (dry)	120	-
Hexanitrostilben	240	-

Koenen Test

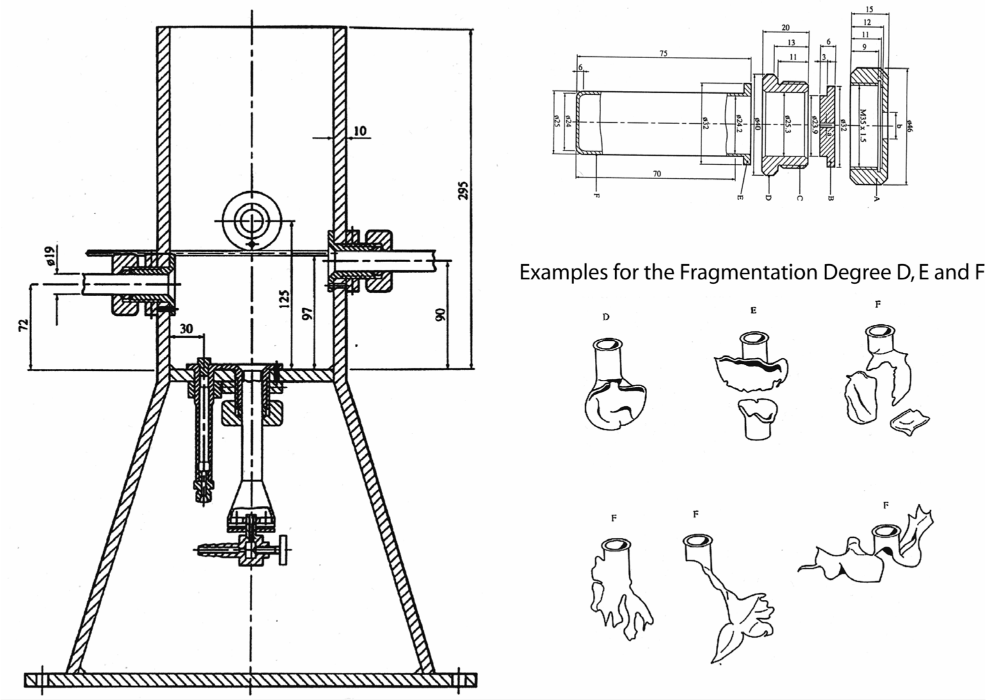

Figure 1.8. Koenen Test

The Koenen Test measures the effect of strong heating under confinement. The sample is contained in a drawn steel tube (27 cm^3) equipped with an closure, which allows orifice plates with various apertures of diameters 1.0, 1.5, 2.0, 2.5, 3.0, 5.0, 8.0, 12.0 o 20.0 mm (*Figure 1.8*). The tube is heated with four calibrated propane burners. The result reported from such a test is the largest size orifice at which the tube is fragmented.

Table 1.4. Fragmentation degree

Types of Fragments	Description	result
0	Thimble is unchanged	−
A	T. plate is dented in	−
B	T. plate and sides are dented in	−
C	T. plat is broken	−
D	T. is teared up	−
E	T. is put in two parts	−
F	T. is destroyed in three or more big pieces, which can be connected	Explosion
G	T. is destroyed into little pieces, top is undamaged	Explosion
H	T. is damaged in a lot of little pieces, the top is damaged too	Explosion

The first experiment is performed with a nozzle plate of any diameter. If an explosion occurs the next test will be done with an orifice plate with a 50 % bigger port diameter. This procedure is repeated until no explosion occurs. The appearance of the fragmentation degree decides if an explosion occurred or not. *Table 1.4* shows the possible outcomes. A decomposition which leads to a partitioning of the thimble in three or more fragments is called an explosion. The valuation of a substance in order to its thermal sensitivity is combined in *Table 1.5*.

Table 1.5. Validation guidelines

Valuation	**Port diameter [mm]**
non sensitive	$\varnothing < 2$
few sensitive	$2 \leq \varnothing < 10$
sensitive	$10 \leq \varnothing < 16$
very sensitive	$16 \leq \varnothing < 20$
extreme sensitive	$\varnothing \geq 20$

4. References

[1] 'Recommendations on the Transport of Dangerous Goods, Manual of Tests and Criteria', fourth revised edition, United Nations Publication, New York and Geneva, **2003**.

[2] Adam, D.; Karaghiosoff, K.; Klapötke, T. M.; Holl, G.; Kaiser, M. *Propellants, Expl. Pyrotech.* **2002**, *27*, 7.

[3] Köhler, J.; Meyer, R., 'Explosivstoffe', Wiley-VCH, D-Weinheim, D, 9. Auflage, **1998**.

[4] Deal, W. E. *J. Chem. Phys.* **1957**, *27(1)*, 796.

[5] Mader, C. L. Report LA-2900, *Los Alomos Scientific Laboratory, Fortran BKW Code for computing the detonation properties of explosives*, Los Alamos, NM, July **1963**.

[6] Pagoria, P. F.; Lee, G. S.; Michell, A. R.; Schmidt, R. D. *Thermochim. Acta* **2002**, *384*, 187.

[7] a) Anderson, E. *Prog. Astronout. Aeronout.* **1993**, *155*, 81; b) Kempa, P. A.; Kerth, J. *32th Int. Annual Conf. of ICT*, Karlsruhe, Germany, **2001**, P147; c) Akutsu, Y.; Che. R.; Tamura, M. *J. Energ. Mater.* **1993**, *11*, 173; d) Kamlet, M. J.; Hurwitz, H. *J. Chem. Phys.* **1968**, *23*, 3685; e) Rothstein, L. R.; Peterson, R. *Propellants, Expl. Pyrotech.* **1979**, *4*, 56; d) Spear, R. J.; Dagley, I. J. *in Organic Energetic Compounds* (Marinkas P. L. (ed.)), Nova, Commack, NY, **1996**, chap. 2.

[8] a) Kitaigorodsky A. I. *Molecular Crystals and Molecules*, Academic Press, New York, **1973**; b) Immirzi, A.; Perini, B. *Acta Cryst.* **1977**, *33(A)*, 216; c) Cady, H. H. *Estimation of the Density of Organic Explosives from Their Structural Formulas*, Report #LA-7760-MS, Los Alamos National Laboratory, Los Alamos, NM, **1979**; d) Cichra, D. A.; Holden, J. R.; Dickinson, C. *Estimation of "Normal" Densities of Organic Explosives from Empirical Atomic Volumes*, Report #NSWC-TR-79-273, Naval Surface Warfare Center (White Oak), Silver Spring, MD, **1980**; e) Stine, J. R. *Prediction of Crystal Densities of Organic Explosives by Group Additivity*, Report #LA-8920, Los Alamos National Laboratory, Los Alamos, NM, **1981**; f) Alster, J.; Iyer, S.; Sandus O. in Chemistry and Physics of Energetic Materials (Bulusu S. N. (ed.)), Kluwer, Dordrecht, **1990**, chap. 28; g) Holden, J. R.; Du, Z.; Ammon, H. L. *J. Comput. Chem.* **1993**, *13*, 422; h) Jayasuriya, K. *Computational Investigation of New Potential Explosive and Propellant Molecules*, 14th Annual Working Group Institute on HEDMs, Kiamesha Lake, NY, **1995**, 2943; i) Murray, J. S.; Brinck, T.; Politzer, P.; *Chem. Phys.* **1996**, *204*, 289.

[9] a) Zhang, M.-A.; Eaton, P. E.; Gilardi, R. *Angew. Chem. Int. Ed.* **2000**, *39(2)*, 401; b) Zhang, M.-A.; Eaton, P. E. *Propellants, Expl. Pyrotech.* **2002**, *27*, 1.

[10] a) Sollott, G. P.; Alster, J.; Gilbert, E. E.; Sandus, O.; Slagg, N. *J. Energ. Mater.* **1986**, *4*, 5; b) Boileau, J.; Emeury, L.; Kehren, J.-P. United States Patent 4,487,938, **1984**; c) Nielsen, A. T. Unites States Patent 5,693,794, **1997**.

[11] Hanks, J.; Highsmith, T.; Sanderson, A.; Warner, K.; Worthington, J. *33th Int. Annual Conf. of ICT*, Karlsruhe, Germany, **2002**, P129.

[12] Doddi, G.; Mencarelli, P.; Razzini, A.; Stegel, F. *J. Org. Chem.* **1979**, *44*, 2321.

[13] a) Rice, S.F.; Simpson, R.L. Lawrence Livermore National Laboratory, Report UCRL-LR-103683, Livermore, CA, **1990**; b) Mitchell, A. R.; Pagoria; P. F.; Schmidt, R. D. Unites State Patent 6,069,277, **2000**.

[14] Pagoria, P.F.; Mitchell, A.R.; Schmidt, R.D.; Simpson, R.L.; Garcia, F.; Forbes, J.; Cutting, J.; Lee, R.; Swansiger, R.; Hoffman, D.M. *Presented at the Insensitive Munitions and Energetic Materials Technology Symposium*, San Diego, CA, **1998**.

[15] Ritter, H.; Licht, H.H.; *J. Heterocycl. Chem* **1995**, *32*, 585.

[16] Basal, A. R.; Zbarsky, V. L.; Zhilin, V. F. *32th Int. Annual Conf. of ICT*, Karlsruhe, Germany, **2001**, P73.

[17] Becuwe, A.; Delcos, A. *Propellants, Expl. Pyrotech.* **1993**, *18*, 1.

[18] a) Latypov, N. V.; Bergman, J.; Langlet, A.; Weller, U.; Bemm, U. Tetrahedron **1998**, *54*, 11525; b) Östmark, H.; Bergman, H.; Bemm, U.; Goede, P.; Holgrem, E.; Johannson, M.; Langlet, A.; Latypov, N. V.; Pettersson, A.; Pettersson, M.-L.; Wingborg,N.; Vörde, C.; Stenmark, H.; Karlsson, L.; Hihkiö, M. *32th Int. Annual Conf. of ICT*, Karlsruhe, Germany, **2001**, V26.

[19] Urbanski, T. 'Chemistry and technology of explsoives', Pergamon Press, England, **1985**.

[20] a) Schimdt, E. W., *Hydrazine and Its Derivatives, Vol. 2*, 2nd ed., Wiley, Chichester, New York, **2001**, chap. 6.2, 1475; b) Catoire, L.; Chaumeix, N.; Paillard, C. *J. Prop. Pow*er **2004**, *20*, 87; c) Catoire, L.; Swihart, M. T. *J. Prop. Pow*er **2002**, *18*, 1242; d) Christos, T.; Niron, Y.; James, H.; Perlee, H. *J. Spacer. Rockets* **1967**, *4*, 122; e) Nonnenberg, C.; Frank, I. Klapötke, T. M. *Angew. Chem. Int. Ed.* **2004**, *43*, 4586 and references therein.

[21] Ellern, H. *Military and Civilian Pyrotechnics*, Chemical Publishing Company Inc., New York, USA, **1968**.

[22] Shimizu, T. *Fireworks − Art, Science and Technique*, Maruzen Co Ltd., Tokyo, J, **1981**.

[23] Lancaster, R.; Shimizu, T.; Butler, R. E. A.; Hall, R. G. *Fireworks − Principle and Practise*, Chemical Publishing Company Inc., New York, USA, **1974**.

[24] Ineichen, H.; Berger, B. *Chimia*, **2004**, *58*, 369.

[25] Cord, P. P.; Labourdique, A.; Fauconnier, A.; Rouby, T. *16th Int. Annual Conf. of ICT*, Karlsruhe, Germany, **1985**, 44/1.

[26] a) Reed, R.; Brady, V. L.; Hirtner, J. M. *20th International Pyrotechnics Seminar*, Colorado Springs, Colorado, USA, IPSUSA, Inc. **1994**, 815; b) Galbraith, L. D. Unites States Patent 5,449,041, **1995**; c) Engelen, K.; Lefebvre, M. H. *Proceeding of Eurofire '98 on CD*, Brussels, Belgium, **1998**.

[27] a) Lane, G. A.; Torkleson, T. R.; Dergarzarian, T. E.; Staudacher, G. R. *3rd International Pyrotechnics Seminar*, Colorado Springs, Colorado, USA, IPSUSA, Inc. **1972**, 25; b) Nilsson, K. E.; Zeuner, S. *16th Int. Annual Conf. of ICT*, Karlsruhe, Germany, **1985**, 30/1; c) Bramilla, L. *18th Int. Annual Conf. of ICT*, Karlsruhe, Germany, **1987**, 29/1; d) Berger, J. M.; Butler, P. B. *Combust. Sci. Technol.* **1995**, *104*, 93.

[28] Engelen, K.; Lefebvre, M. H. *Propellants, Expl. Pyrotech.* **2003**, *28(4)*, 201.

[29] Akhavan, J. *The Chemistry of Explosives*, RCS Paperbacks, Cambridge, **1998**.

[30] Giles, J. *Nature* **2004**, *427*, 580.

[31] Barsan, M. E.; Miller, A. *Lead Hazard Evaluation HETA Report No. 91-0346-2572*, National Institute for Occupational Safety and Health, Cincinnati, Ohio, *1996*.

[32] a) Bloss, K. H. *Deutsches Patent* Nr. 2 217 780, **1972**; b) Bloss, K. H. *Deutsches Patent* Nr. 2 142 578, **1973**; c) Redecker, K. *Deutsches Patent* Nr. 19 505 568, **1996**; c) Gawlick, H. *Deutsches Patent* Nr. 1 805 358, **1970**.

[33] Scott, H. A. PCT WO 99/14171, **1999**.

[34] a) Huisgen, R.; Ugi, I.; *Angew. Chem. Int. Ed.* **1956**, *68*, 736; b) Wallis, J. D.; Dunitz, J. D.; *J. Chem. Soc., Chem. Commun.* **1983**, 910; c) Workentin, M. S.; Wagner, B. D.; Negri, F.; Zgierski, M. Z.; Lusztky, J.; Silberand, W.; Wyner, D. D. M. *J. Phys. Chem.* **1995**, *99(1)*, 94; d) Workentin, M. S.; Wagner, B. D.; Lusztyk, J.; Wayner, D. D. M. *J. Am. Chem. Soc.* **1995,** *117*, 119.

[35] a) Buenker, R. J.; Peyerimhoff, S. D. *J. Chem. Phys.* **1968**, *48*, 354; b) Murray, J. S.; Seminario, J. M.; Lane, P.; Politzer, P. *J. Mol. Struct. (THEOCHEM)* **1990**, *66(3-4)*, 193; c) Engelke, R. *J. Chem. Phys.* **1992**, *96*, 10789; d) Engelke, R. *J. Am. Chem. Soc.* **1993**, *115*, 2961; e) Klapötke, T. M. *J. Mol. Struct. (THEOCHEM)* **2000**, *499*, 99; f) Michels, H. H.; Montgomery, J. A.; Christe, K. O.; Dixon, D. A. *J. Phys. Chem.* **1995**, *99*, 187; g) Klapötke, T. M.; Harcourt, R. D. *J. Mol. Struct. (THEOCHEM)* **2001**, *541*, 237; h) Gagliardi, L.; Orlandi, G. *J. Chem. Phys.* **2001**, *114*, 10733; i) Strout, D. L. *J. Phys. Chem. A* **2002**, *106*, 816; j) Fau, S.; Wilson, K. J.; Bartlett, R. J. *J. Phys. Chem. A* **2002**, *106*, 4639; k) Hammerl, A.; Klapötke, T. M.; Schwerdtfeger, P. *Chem. Eur. J.* **2003**, *9(22)*, 5511.

[36] a) Christe, K. O.; Wilson, W. W.; Sheehy, J. A.; Boatz, J. A. *Angew. Chem. Int. Ed.* **1999**, *38 (13/14)*, 2004; b) Vij, A.; Wilson, W. W.; Vij, V.; Tham, F. S.; Jeffrey, V; Christe, K. O. *J. Am. Chem. Soc.* **2001**, *123(26)*, 6308; c) Dixon, D. A.; Feller, D.; Christe, K. O.; Wilson, W. W.; Vij, A.; Vij, H. D.; Brooke, H. D. B.; Olson, R. M.; Gordon, M. S. *J. Am. Chem. Soc.* **2004**, *126(3)*, 834.

[37] Hahma, A.; Holmberg, E.; Hore, N.; Tryman, R.; Wallin, S.; Östamrk, H.; *33th Int. Annual Conf. of ICT*, Karlsruhe, Germany, **2002**, 62/1; b) Vij, A.; Pavlovich, J. G.; Wilson, W. W.; Vij, V.; Christe, K. O. *Angew. Chem., Int. Ed. Engl.* **2002**, *41(16)*, 3051; c) Östamark, H.; Wallin, S.; Brinck, T.; Carlqvist, P.; Claidge, R.; Hedlun, E.; Yudina, L. *Chem Phys. Let.* **2003**, *379(5,6)*, 539; d) Carlqvist, P.; Östmark, H.; Brinck, T. *J. Org. Chem.* **2004**, *69(9)*, 3222.

[38] a) Eremets, M. I.; Popov, M. Yu.; Trojan, I. A.; Denisov, V. N.; Boehler, R.; Hemley, R. J. *J. Chem. Phys.* **2004**, *120 (22)*, 10618.

[39] Eremets, M. I.; Gavriliuk, A. G.; Trojan, I. A.; Dzivenko, D. A.; Boehler, R. *Nature*, **2004**, July 4, in press.

[40] a) Pottie, I. R.; Vaughan, K.; Zaworotko, M. J. *J. Chem. Cryst.* **2001**, *31(3)*, 143; b) Schmid, R.; Straehle, J. *Z. Anorg. Allg. Chem.* **1989**, *575*, 187; c) Benson, F. R. *The High Nitrogen Compounds*, Wiley, Chichester, New York, **1983**.

[41] Weigand, J. J. *1,4-Bis(1'-methyltetrazolyl)-1,4-dimethyl-2-tetrazene and other nitrogen rich high energy density materials* Diploma thesis, Ludwig-Maximilian University, **2002**.

[42] Hofmann, K. A.; Hock, H. Chem. *Ber.* **1912**, *44*, 2946.

[43] Butler, R. N.; Garvin, V. C. *J. Chem. Res. (S)* **1982**, 183.

[44] West, R. C.; Selby, S. M. *Handbook of Chemistry and Physics*, 48th ed.; The Chemical Rubber Co.; Cleveland, OH, 1967-1968; pp D22-D51.

[45] Ostrovskii, V. A.; Pevzner, M. S.; Kofman, T. P.; Tselinskii, I. V. *Targets Heterocycl. Syst.* **1999**, *3*, 467.

[46] a) Fukumoto, S.; Imamiya, E.; Kusumoto, K.; Fujiwara, S; Watenabe, T.; Shiraishi, M. *J. Med. Chem.* **2002**, *45(14)*, 3009; b) Jedidi, I.; Therond, P.; Zarev, S.; Cosson, C.; Couturier, M.; Massot, C.; Jore, D.; Gardes-Albert, M.; Legrand, A.; Bonnefondt-Rousselot, D. *Biochemistry* **2003**, *42(38)*, 11356; c) Schug, K. A.; Lindner, W. *Chem. Rev.* **2005**, *105(1)*, 67; d) Nineham, A. W. *Chem. Rev.* **1955**, *55(2)*, 355; e) Brothrton, T. K.; Lynn, J. W. *Chem. Rev.* **1959**, *59(5)*, 841; f) Neutz, J; Grosshardt, O.; Schäufele, S.; Schnuppler, H.;

Schweikert, W. *Prop. Explos. Pyrotech.* **2003**, *28(4)*, 181; g) Wingborg, N.; Latypov, N. *Prop. Explos. Pyrotech.* **2003**, *28(6)*, 314.

[47] Thiele, J. *Justus Liebigs Ann. Chem.* **1892**, *270*, 54-63.

[48] Perrott, J. R.; Stedman, G.; Uysal, N. *Dalton Trans.* **1976**, *20*, 2058.

[49] Moderhack, D.; Goos, K. H.; Preu, L. *Chem. Ber.* **1990**, 1575.

[50] Grewer, T. *Thermal Hazards of Chemical Reactions*, Elsevier Science, Amsterdam, Netherlands, **1994**.

[51] http://www.setaram.com/.

[52] Hoeflich, T.C.; LaBarge, M. S. *Journal of Loss Prevention in the Process Industries* **2002**, *15*, 163.

[53] Standard Test Method for Arrhenius Kinetic Constants for Thermally Unstable Materials, ASTM Designation E698-99, **1999**.

[54] Ozawa, T. Bull. *Chem. Chem. Soc. Jpn.* **1965**, *38*, 1881.

[55] Kissinger, H. E. *Anal. Chem.* **1957**, *29*, 1702.

[56] a) Doyle, C. D. *J. Appl. Polym. Sci.* **1961**, *38*, 1881; b) Doyle, C. D. *Nature* **1965**, *207*, 240.

[57] http://www.perkinelmer.com/.

[58] http://www.parrinst.com/.

[59] http://www.jeol.co.kr/.

[60] http://www.carbolite.com/.

[61] Iyer, S.; Slagg, N. *Molecular Aspects in Energetic Materials. Molecular Structure and Energetics, Structure and Reactivity,* (Liebman, J.; Greenberg, A. (ed.)), VCH publisher, New York, **1988**.

Chapter II

5-AMINOTETRAZOLE AND AZOTETRAZOLATES

1 Introduction

The following introduction gives a short overview recording the properties of mono- and disubstituted tetrazoles and in particular, for 5-amino-1*H*-tetrazoles substituted at N1 and the oxidation of the parent 5-amino-1*H*-tetrazoles to the 5,5'-azotetrazolate dianion.

1.1 Tetrazoles

Tetrazoles survive a wide range of chemical environments such as strongly acidic and basic media, as well as oxidizing and reducing conditions. Therefore, these compounds are a unique family of heterocycles widely used in material science and many pharmaceutical applications.[1] They can serve as metabolically stable surrogates for the carboxylic acid group,[2] as precursors to a variety of nitrogen-containing heterocycles by the Huisgen rearrangement,[3] as simple lipophilic spacers displaying two substituents in the appropriate manner, and not last, as basic structures for the here discussed highly energetic materials.

Tetrazoles are five-membered, fully unsaturated 6π-heterocycles with one carbon and four nitrogen atoms. For the tetrazole itself, there are three different tautomers possible (I (1*H*-tetrazole), II (2*H*-tetrazole) and III (5*H*-tetrazole)) which can interconvert by an [1,5]-sigmatropic proton migration. The 5*H*-tetrazole III is not a stable member of this family, as it does not posses aromatic character (*Scheme 2.1*).

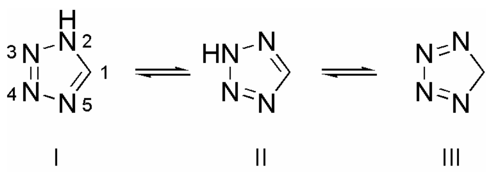

Scheme 2.1. Tautomerism of Tetrazole

1.1.1 Tautomerism

The tautomerism of 5-aminotetrazoles has been studied by Murphy[4] and Katritzky.[5] One of the regular features of heteroaromatic tautomerism is that amino-compounds exist predominantly as such with large K_T values. This indicates that the 5-aminotetrazoles exist in the amino **1** rather than in the imino-form **2** (*Scheme 2.2*). Although the solvent can have significant effects on tautomeric equilibria,[6] a change of the magnitude postulated for such a relatively minor change in solvent composition would be unprecedented. Finally, those equilibria, which involve two tautomers that are interconvertible by the breaking and forming solely of N-H or O-H bonds, are normally fast at RT on the NMR time scale, and time-averaged NMR spectra are found.

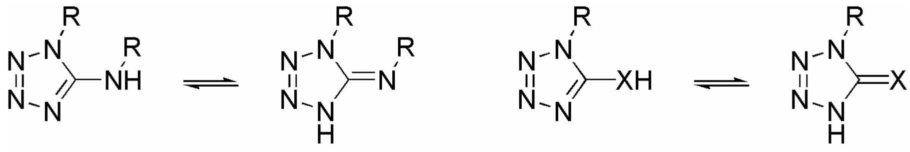

1 **2** **3** **4**

Scheme 2.2. Tautomerism of 5-aminotetrazole and related derivatives

In contradiction to the exocyclic O- and S- species (**3**, X = O, S) which predominantly possesses the dihydrotetrazole structure **4** (*Scheme 2.2*), structural limitation with the predominance of the imino-form **2** for tetrazoles is stringent. Thus, for the alkyl substituted aminotetrazoles the amino form should be observed in the crystal structure determination in all cases as this pattern is connected with the aromatic and other mesomeric stabilisation energies of these compounds in a rational manner and agrees with the observation obtained during this work.

An interesting case is the imidoyl azide (**5**) − tetrazole (**6**) tautomerism, which is found especially for the orthocondensed tetrazoloheterocycles (*Scheme 2.3*). The transformation of a heterocyclic azide in the tetrazole isomer has been described in the literature as a case of tautomerism, as an azidoazomethine-tetrazole (imidamide-tetrazole) equilibria, as a 1,5-dipolar cyclization, and as a valence isomerization.[7] It is well known that compounds with an azido group adjacent to a ring nitrogen atom may spontaneously cyclize to give a polycycle with a fused tetrazole ring or, at least, an equilibrium mixture of both. Especially in the case of 1,5-diaminotetrazole, this tautomerism, know as Dimroth rearrangement, is important and will be pointed out in the corresponding *Chapters*.

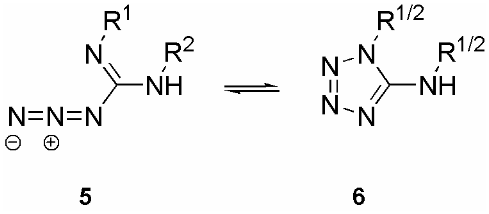

Scheme 2.3. Imidoyl azide – Tetrazole equilibrium

In the case of the substituted azidoformamidine derivatives (**5**) which do not contain a ring nitrogen atom, an equilibrium between the open chain **5** and closed chain **6** isomers is often observed (*Scheme 2.3)*. Substituents R^1, R^2 with electron withdrawing properties favor the azide form whereas substituents with donor abilities favor the tetrazole.[8] Therefore, it may be expected that for small alkyl substituents R^1, R^2 only the tetrazole will be observed. As the ring opening process is endothermic,[9] raising the temperature should increase the amount of the open chain isomers. The polarity of solvent also has an influence on the equilibrium: polar solvents favor tetrazole and nonpolare favor azide formation.[10] Dipolar aprotic solvents are particularly suitable for resulting in ring closure.[11] Acidic solutions, in which the imino nitrogen atom is protonated, stabilise the open chain isomer, while basic media stabalizes the tetrazole isomer.

1.1.2 Stability

Most of the 1,5- and 2,5-disubstituted tetrazoles are stable crystalline substances at RT. The melting points of the 1- and 2-unsubstituted derivatives are considerably higher than those of the corresponding 1,5- and 2,5-disubstituted compounds due to H-bridging. Inductive effects are responsible for the higher melting points of the 1-substituted compounds in comparison with to the 2-substituted isomers.[12] Tetrazoles are quite polar and normally show good solubility in polar solvents.[13] They show relatively high enthalpies of formation, for example for 1*H*-tetrazole a value of 28.1 eV (648 Kcal mol^{-1}) was found, which fits well with the calculated value of 27.7 eV.[14] Therefore, tetrazoles represent energy-rich molecules. In most cases, tetrazoles are not stable at high temperatures and often start to decompose near their melting points. The ease of decomposition and the type of products formed during the thermal decomposition strongly depend on the character and the position of the substituents on the tetrazole ring (*Scheme 2.4*).

The thermolysis of the 1,5-disubstituted tetrazoles **7** proceeds in most cases via a ring opening to the α-azido-imines **8** and loss of N_2, with the formation of an imino nitrene **9** (*Scheme 2.4*). Most of the isolated products, such as carbodiimids **10** and ortho-condensed imidazoles **11** can be derived from this intermediate.[15]

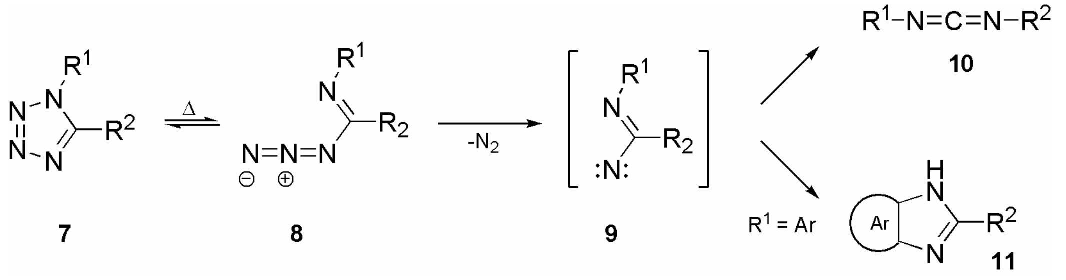

Scheme 2.4. Typical decomposition pathway of 1,5-disubstituted tetrazoles

The thermolysis of certain tetrazole derivatives can run completely different and *Scheme 2.4* shows only one possibility. Since the stability of tetrazoles with respect to temperature are quite different, different decomposition pathways are expected and also observed during this study and are going to be highlighted in the corresponding *Chapters*.

1.1.3 Acid/base properties

Tetrazole and the 5-substituted derivatives are weak acids with pK_a-values in the range of 1,1 – 6,3, which is comparable with that of carbonic acids.[16] The acidity increases in the case of 5-arylsubstituted tetrazoles because of a better resonance stabilization of the anion. In the case of strong π-delocalization in the anion, e.g. 5-azido-1*H*-tetrazole,[17] the acidity approaches that of a strong acid. The tetrazole ring itself shows a basicity lower than that of aniline. Typical pK_b-values are found in the range of 9,7 (1-methyl-1*H*-tetrazol) to 12,9 (5-amino-1-phenyl-1*H*-tetrazole). Protonation takes place preferentially at N4.[18] Electrophiles attack tetrazoles usually at one of the ring nitrogen atoms.[19] While acylation[20] of 5-monosubstituted tetrazoles proceed in the most cases selectively at N(2), alkylation is not selective and yields mixtures of 1,5- and 2,5-disubstituted tetrazoles.[21] The position attacked by the electrophile strongly depends on the substituent at C5, the reaction conditions, and the reagent.

1.1.4 5-Aminotetrazole monohydrate (**5-AT**, **14**)

5-Aminotetrazole (**5-AT, 14**) is a valuable intermediate in the preparation of tetrazole compounds because of its varied reactions and its ease of preparation. It is obtained by the reaction of nitrous acid with aminoguanidine (*Scheme 2.6*, **A**)[22] or by the reaction of hydrazoic acid with dicyandiamide (*Scheme 2.5*, **B**)[23]. The first reaction (**A**) forms azidoformamidinium nitrate (**AFN**, **13**) (starting from aminoguanidinium nitrate **AGN**, **12**) which after deprotonation rearranges to **5-AT**. In the second reaction (**B**) the dicyandiamide (**15**) depolymerises to cyanamide (**16**), which then reacts with hydrazoic acid to give **5-AT**. In both cases, **5-AT** is obtained as monohydrate.

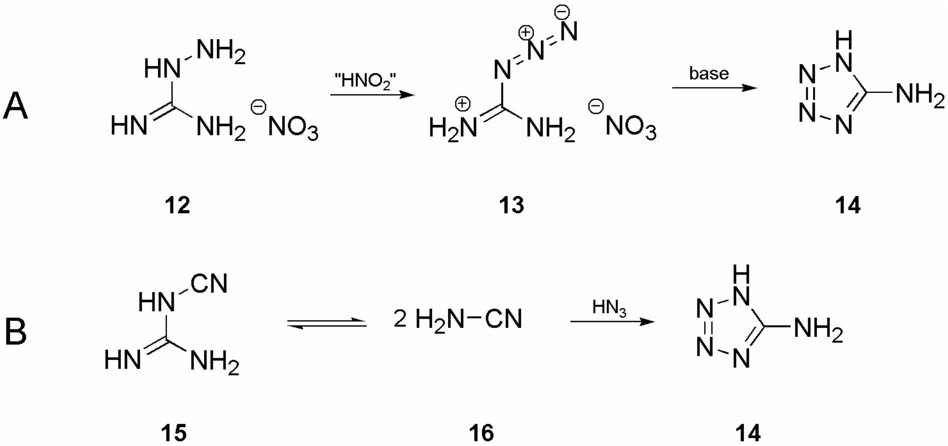

Scheme 2.5. Synthesis of **5-AT** (**14**)

Interestingly, although **13** has been known for a long time, no investigation with respect to the molecular structure is reported. During the investigation colorless crystals of **13** were obtained, suitable for a structure determination, and a few of the molecular graphs of **13** can be depicted from *Figure 2.1*. Only a short description of the structure is given below.

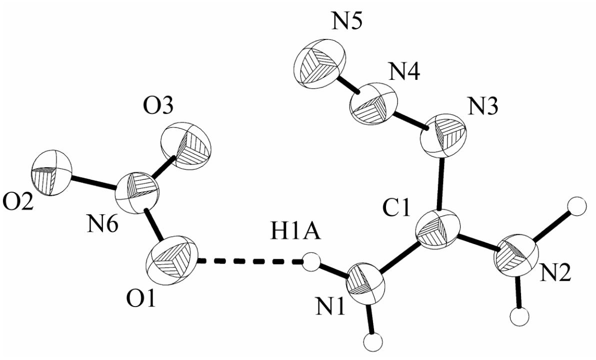

Figure 2.1. A view of the molecular structure of **AFN**. Displaced ellipsoid are drawn at the 50 % probability level and hydrogen atoms are shown as small spheres of arbitrary radii.

AFN crystallizes in the monoclinic space group $P2_1/c$ with four formula units in the cell. The azidoformamidinium moiety is almost planar with C–N distances and interatomic angles similar to those found in the 1972 by Bärnigausen investigated azidoformamidinium chloride (torsion angle N1–N2–N3–N4 is 3.95(1)°).[24] The nitrate and azidoformamidinium moieties are approximately coplanar, and within the same plane the nitrate groups are linked trough hydrogen bonds to the N atoms of the cations, forming sheet like layers. The crystal structure of **AFN** is related to the crystal structure of aminoguanidinium nitrate showing a closer packing of 1.640 g cm^{-3} *vs.* 1.566 g cm^{-3}, respectively.[25]

1.2 Azotetrazolates

5-AT is a comparable weak acid (K_a = 10^{-6}).[26] It can be easily oxidized under base condition, to corresponding azotetrazolate salts (**ZT**). At present, the most important reaction related to azotetrazolate is depicted in *Scheme 2.6* and shows the oxidation of **5-AT** in the presence of sodium hydroxide as base and potassium permanganate as oxidant.[22] The product, disodium azotetrazolate pentahydrate (**Na_2ZT**, **17**) is at the moment the most important starting material used for preparation of a series of different types of azotetrazolates which might find application in new *propellants*, additives or *explosives*.

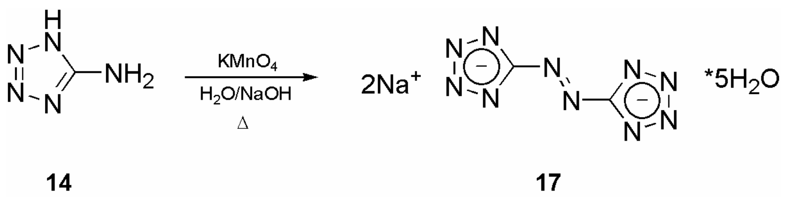

Scheme 2.6. Oxidation of **5-AT** to **Na_2ZT**

With respect to the oxidation of amino substituted azoles, the stability of corresponding azo compounds is related to the number of heterocyclic nitrogen atoms present. Thus, the parent azotetrazole could not be isolated yet,[27,28] but azotriazoles[29] could be prepared. In the case of the corresponding salts, the stability of those compounds is completely different, and although most of these salts possess comparable high endothermicities they show unexpectedly high stabilities toward heat, friction and impact. The presence of the azo group as well as many donor sites of the anion for either van der Waals interaction or hydrogen bridges, dramatically increases the melting points and stabilities of corresponding salts and gives rise, in combination with certain

cations, to much higher positive heats of formation compared to salts of aminotetrazoles, polynitro and other nitrogen compounds. In principal, 5,5'-azotetrazolates are considered to belong to the field of high nitrogen content energetic materials and exciting, developing new field of HEDMs.

With respect to the previous work by Dr. Anton Hammerl during his PhD,[30] the chemistry of disodium azotetrazolate pentahydrate (**Na_2ZT**, **17**) was investigated. The former work was mainly based on metathetical reactions of the barium 5,5'azotetrazolate pentahydrate (**BaZT**, **18**) with corresponding sulphates (*e.g.* $(N_2H_5)_2SO_4$; *Scheme 2.6*) yielding in most cases the expected products and barium sulphate as by-product. Since this method has some drawbacks, such as a) barium salts are problematic for an industrial up-scale, b) an additional preparation step (Na_2ZT → BaZT) and c) $BaSO_4$ turns out to be problematic during the purification step, **17** was expected to be an appropriate replacement.

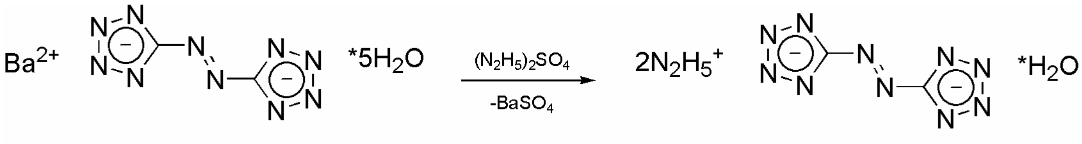

18

Scheme 2.7. Reaction of **BaZT** with $(N_2H_5)_2SO_4$

2 Azidoformamidinium and Guanidinium 5,5'-Azotetrazolate Salts

Los Alamos National Laboratory (LANL), USA, reported the synthesis of three unique HNC materials based on azotetrazolate anion in combination with ammonium, guanidinium and triaminoguanidinium cationic species.[31] These compounds are reported to have a combination of high positive heat of formation and insensitivity. The reported heat of formation for ammonium (**AZT**), guanidinium (**GZT**, **20**) and triaminoguanidinium azotetrazolate (**TAGZT**, **23**) salts are 98, 106 and 257 Kcal mol^{-1}, respectively. Many other institutions all over the globe have been actively involved in the research and development work on azotetrazolate based HEMs.[32] Still, additional work has to be done on these compounds in view of their increasing importance to complete the data of guanidinium derivatives of 5,5'-azotetrazolate as it has been realized that some compounds have not been investigated yet or are only insufficiently characterized. Bis(azidoformamidinium) 5,5'-azotetrazolate (**AFZT**, **19**), bis(guanidinium) 5,5'-azotetrazolate (**GZT**, **20**), bis(aminoguanidinium) 5,5'-azotetrazolate (**AGZT**, **22**) and bis(triaminoguanidinium) 5,5'-azotetrazolate (**TAGZT**, **24**) have already been described,[32b,32b,g,f] but **AFZT** has not been sufficiently characterized and the connectivity of the nitrogen atoms has not yet been unambiguously clarified. **AGZT**, which was synthesized according to [32f], was obtained as its monohydrate (**AGZTH**, **21**), and bis(diaminoguanidinium) 5,5'-azotetrazolate (**DAGZT**, **23**) has not been reported yet.

2.1 Synthesis of AFZT, GZT, AGZT, AGZTH, DAGZT and TAGZT

The starting material, **5-AT**, can readily be obtained by a) interaction of dicyandiamide with sodium azide and hydrochloric acid or b) by the reaction of aminoguanidinium salts (e.g. nitrate) with HNO_2 (*Scheme 2.8*).[33]

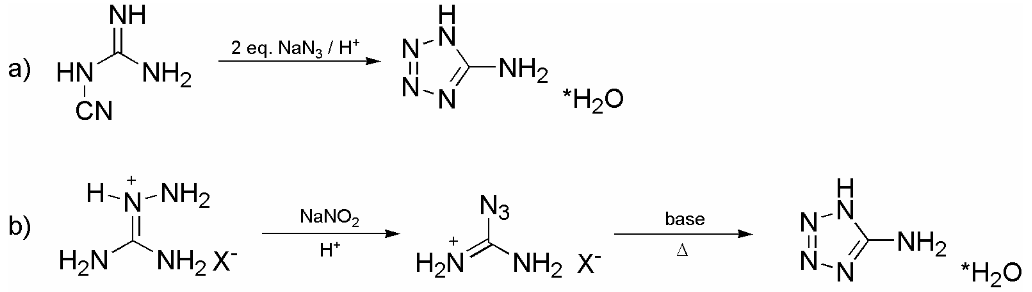

Scheme 2.8. **5-AT** monohydrate

Following the path b) in reaction *Scheme 2.8*, it is possible to isolate azidoformamidinium chloride, sulfate or nitrate depending on the aminoguanidinium salt and the acid used and yields the corresponding azidoformamidinium salt for the later described synthesis of **AFZT**.

The oxidation of **5-AT** with potassium permanganate in basic aqueous solution according to Thiele yields disodium 5,5'-azotetrazolate pentahydrate (**Na_2AT**, *Scheme 2.9*).[34] **Na_2AT** is the source from which all the other azotetrazolates were synthesised. They were obtained from the reaction of the respective guanidium salts (**AFZT**, **GZT**, **AGZTH**, **DAGZT** and **TAGZT**) by adding a hot, aqueous solution of the guanidinium salt (e.g. X^- = Cl, NO_3) to a hot, aqueous solution of **Na_2AT** followed by fractional crystallization of the azotetrazolates.[32b] In the case of **GZT** and **AGZTH** a yellow precipitate was formed almost immediately, whereas for **DAGZT** and **TAGZT,** the products crystallized from cold solution with the best results at a temperature of 5°C. Yields between 90-95% were obtained.

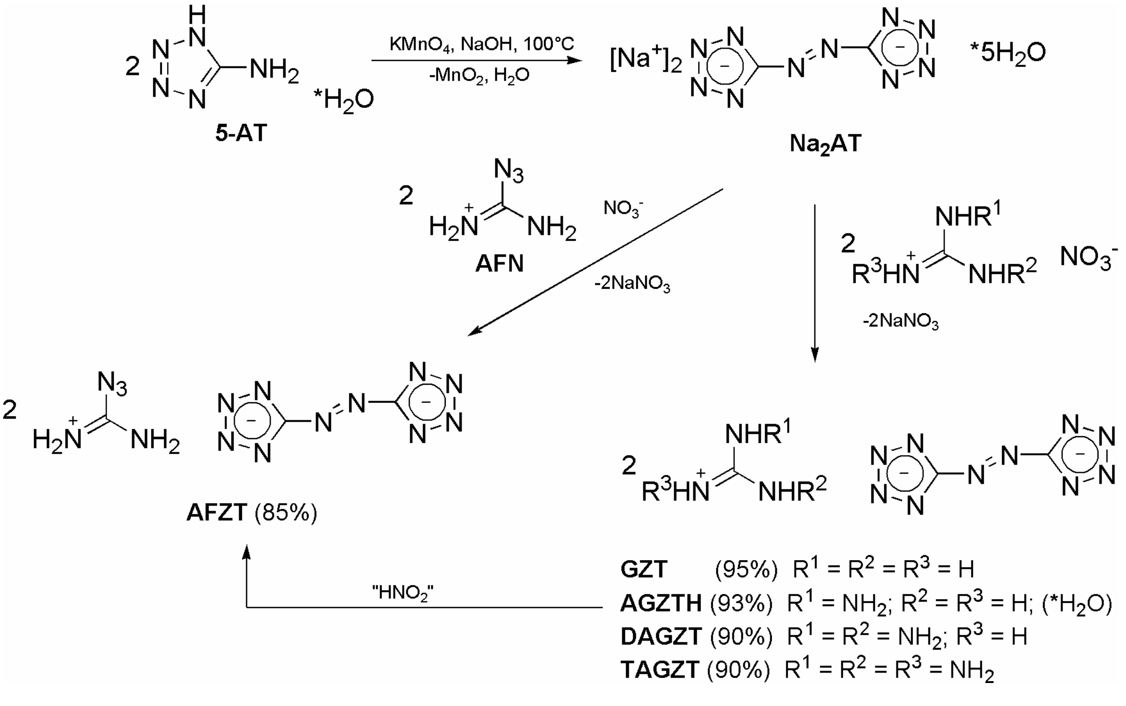

Scheme 2.9. Synthesis of Azidoformamidinium and Guanidinium 5,5'-Azotetrazolate Salts

AGZT is formed in quantitative yield by dehydration of **AGZTH** *in vacuo* at a temperature of 100°C. Further recrystallization from hot water marginally increases the purity

accompanied by the loss of yield. **AFZT** was prepared from azidoformamidinium nitrate (**AFN**) and **Na_2AT** with a yield of ~85 %. Here the temperature has to be carefully controlled, and the product has to be isolated very rapidly after crystallization as the product decomposes in solution. **AFZT**, dissolved in DMSO completely decomposes within 10 minutes under formation of nitrogen. **AFZT** also can be prepared from **AGZTH** by reaction of nitrous acid, which is formed *in situ* from ethylnitrite. Here the yield of **AFZT** is with 32 % (*Scheme 2.9*) much lower compared to the synthesis from **AFN** and **Na_2AT,** as **AFZT** decomposes in solution.

2.2 Result and Discussion

The 5,5'-azotetrazolate salts were characterized and unequivocally identified by Raman and IR spectroscopy, NMR spectroscopy and elemental analysis. The crystal structures of **GZT** and **TAGZT** have already been reported.[32h] The crystal ctructures of **AFZT** and **AGZTH** were determined, while the structure of **DAGZT** could not be solved successfully due to a twin problem.

2.2.1 IR and Raman Spectroscopy

The 5,5'-azotetrazolate salts can be easily and rapidly identified by Raman and IR spectroscopy. Due to the C_i symmetry of the the 5,5'-azotetrazolate anion in the solid state, the symmetric C-N_{azo} vibration is found around 1384 cm^{-1} and the $N_{acyclic}$=$N_{acyclic}$ stretching mode of the diazo group around 1480 cm^{-1} in the Raman spectrum (*Figure 2.2*). The azide vibration of **AFZT** is split due to the C_i symmetry of the crystal system. The Raman spectra are dominated by the vibrations of 5,5'-azotetrazolate, and therefore the IR spectra are better suited for the characterization of the cations. In the IR spectra, the asymmetric C-N_3 stretching vibration of the 5,5′-azotetrazolate anion appears at ~1390 cm^{-1} and the asymmetric C-N_2 stretching mode of the azo group at ~735 cm^{-1}.The IR spectra of the guanidinium 5,5'-azotetrazolate salts contain a set of characteristic absorption bands: 3400-3000 cm^{-1} [ν(NH_2), ν(NH)], 1680-1550 cm^{-1} [δ(NH), δ(NH_2)], 1550-1350 cm^{-1} [ν tetrazolate ring, δ(NH)], 1350-700 cm^{-1} [ν(NCN), ν(NN), ω(NNH_2), γ(CN), δ tetrazolate ring], <700 cm^{-1} [δ out of plane bend (N–H), ω(NH_2)]. The asymmetric stretching vibrations of the azide group in **AFZT** are found at 2177 and 2120 cm^{-1} and the symmetric stretching vibration at 1240 cm^{-1}.

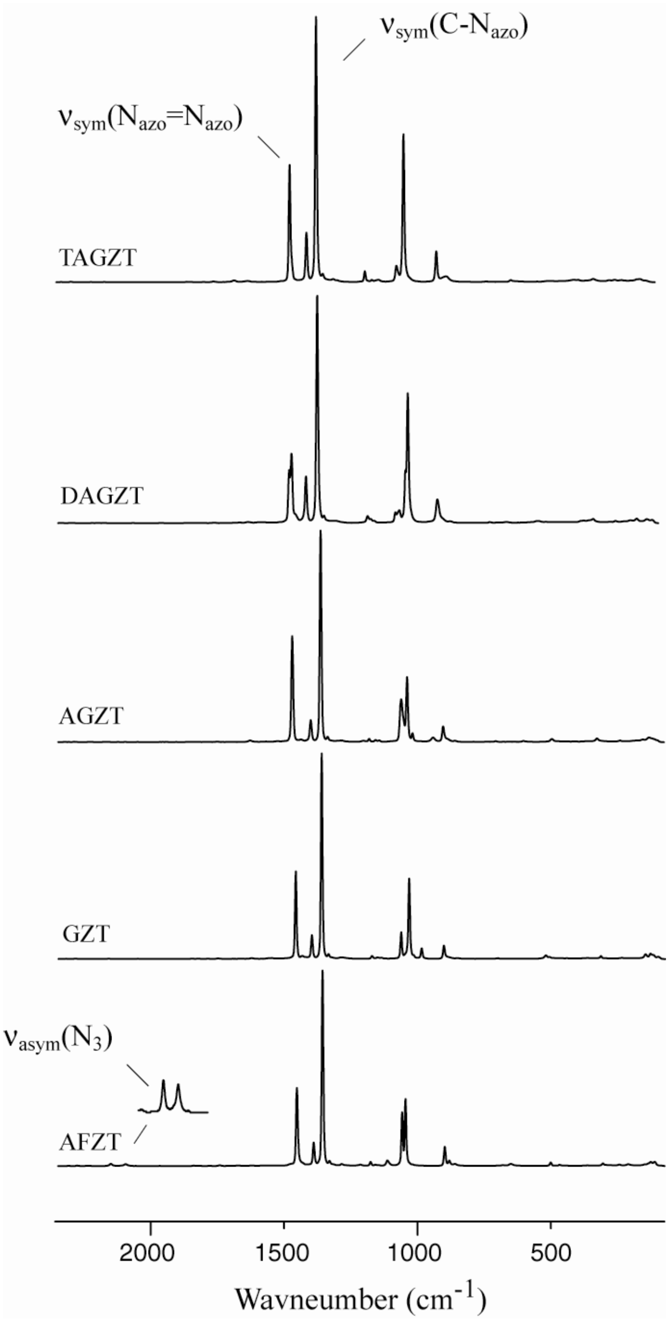

Figure 2.2. Raman spectra of 5,5-azotetrazolate salts

In the [1]H NMR the signals for NH and NH_2 groups are found at the expected region as a singlet, while for **DAGZT** a dynamic behavior of the protons has been observed. In the [13]C NMR the corresponding shifts for the carbon of the guanidinium moiety are found in the expected region, and the carbon resonances for the anion are found around 173 ppm, similar to the shifts previously reported.[32] The molar peaks of all guanidinium cations as well as the azidoformamidinium cations were also detected in a FAB^+ mass spectrometry experiment. The elemental analyses show excellent agreement with the calculated values.

2.2.2 Crystal structure of **AFZT** and **AGZTH**

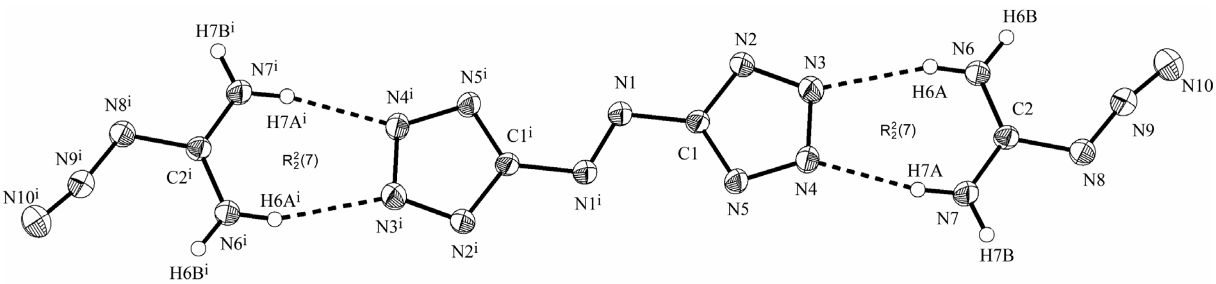

Figure 2.3. A view of the molecular structure of **AFZT**, showing the atom-labeling scheme. The inversion centre in the middle of the molecule makes half of the molecule independent. Displacement ellipsoids are drawn at the 50% probability level and hydrogen atoms are shown as small spheres of a arbitrary radii. [Symmetry code: (i) -x, -y, -z.]

AFZT crystallizes in the monoclinic space group $P2_1/n$ with 2 formula units per unit cell (*Figure 2.3*); **AGZTH** crystallizes in the monoclinic space group C 2/c with four formula units per unit cell (*Figure 2.4*). The bonding parameters of the 5,5'-azotetrazolate anion are in accordance with reported values of other 5,5'-azotetrazolate salts, and therefore a detailed discussion is abstained. Selected bond lengths and angles for the cations are presented in *Table 2.1*.[32c] The azidoformamidinium cation of **AFZT** is a member of the series of (*poly*)azido derivatives of the guanidinium cation, in which the amino groups are successively replaced by N_3-groups finally leading to the triazidocarbonium cation.[24] As mentioned above, the aminoguanidinium cation can easily be transformed to the corresponding azide. As only few structures of this kind have been reported, a more detailed discussion is presented.[35] The C–N bond lengths and angles of both cations are found to be shorter (1.308(4) – 1.388(4) Å) than the bond length of a C–N single bond (1.47 Å, *Table 2.1*), indicating the stabilization of the cations by the formation of a delocalized π system with a weak participation of the N_3-group in the case of the azidoformamidinium cation. The bond angles around the planar C atom (sum of angles 360°) in both cations are different, and for the aminoguanidinium cation they are slightly distorted. Here N6–C2–N6 is significantly larger and N6–C2–N8 and N7–C2–N8 significantly smaller than 120°. The distortion may be caused by the C2–N8 bond, which is significantly longer than the C2–N6 and C2–N7 bonds. Analysis of 177 reports on the dimension of the $(NH_2)_2$–C–NH– fragment in the Cambridge Structural Database[36] reveals a mean $d_{C–N}$ = 1.323(1) Å for the equivalent of the present C2–N6 and C2–N7 bonds and a mean $d_{C–N}$ = 1.335(1) Å for the equivalent of the C2–N8 bond. The latter is in good agreement with the bond lengths given in *Table 2.1*, but the C2–N6 and C2–N7 bond length in the table are shorter than

the mean values from the database. This may be explained by the intramolecular interactions of H6B with N9 (N6–H6B····N9, 2.665(5) Å) and the α-effect of the $N9H_2$ amino group, which is also consistent with a shorter C2–N7 (1.312(2) Å) bond length compared to the longer C2–N6 (1.328(3) Å) bond length.

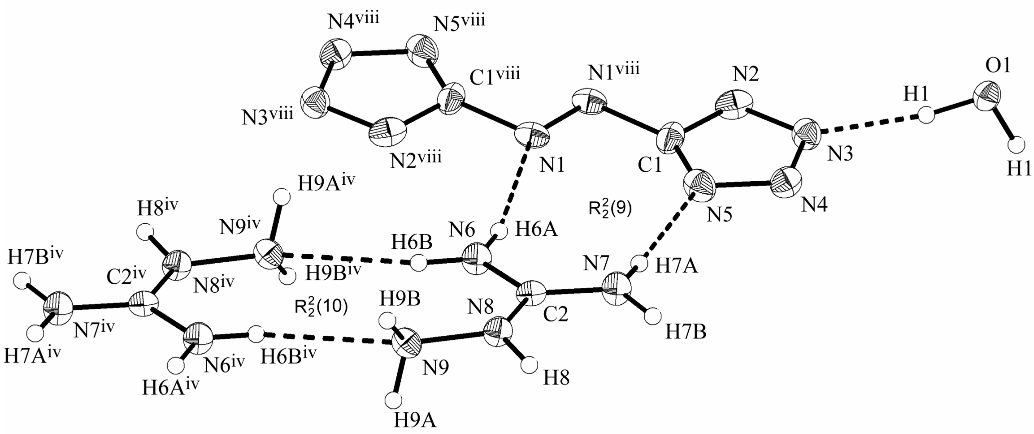

Figure 2.4. A view of the molecular structure of **AGZTH**, showing the atom-labeling scheme. Displacement ellipsoids are drawn at the 50% probability level and hydrogen atoms are shown as small spheres of a arbitrary radii. [Symmetry code: (iv) 1-x, -y, 1-z; (viii) 0.5-x, 1.5-y, 1-z; (ix) –x, y, 0.5-z]

Table 2.1. Selected bond length and angles of the cations in **AFZT** and **AGZT**

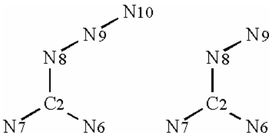

	AFZT	AGZTH
Å		
C2–N6	1.308(4)	1.328(3)
C2–N7	1.303(4)	1.312(2)
C2–N8	1.388(4)	1.341(3)
N8–N9	1.255(4)	1.414(2)
N9–N10	1.112(4)	-
°		
N6–C2–N7	123.1(3)	122.2(2)
N6–C2–N8	123.9(3)	118.5(2)
N7–C2–N8	113.5(2)	119.3(2)
C2–N8–N9	116.2(2)	118.9(2)
N8–N9–N10	169.8(3)	-

For the azidoformamidinium cation in **AFZT**, the situation is different and can be explained by the electron withdrawing effect of the azide group and the absence of intramolecular hydrogen bonds. The two almost identical C2–N6 and C2–N7 bonds lengths (1.308(4) Å and 1.303(4) Å, respectively) show that the delocalization of the π system over the molecule is restricted to the formamidinium part of the cation and indicate a weak π-interaction with the N_3-group. The bond angles N6–C2–N7 and N6–C2–N8 are very similar (~ 123°) and greater than the N7–C2–N8 angle (~ 113°). The azido group is rotated out of the molecular plane by approximately 6° (C2–N6–N7–N8). The N–N bond lengths are in agreement with those found in other azides which are covalently bound to carbon.[37]

Table 2.2. Hydrogen bond geometry (Å, °) of **AFZT** and **AGZTH**.

D–H···*A*	*D*–H	H···*A*	*D*···*A*	*D*–H···*A*
AFZT				
N6–H6A···N3	0.86	2.1706(5)	2.9976(5)	161.230(9)
N6–H6B···N5^{i}	0.86	2.1358(5)	2.9633(6)	161.313(8)
N7–H7A···N4	0.86	2.0600(4)	2.9037(5)	166.69(1)
N7–H7B···N2^{ii}	0.86	2.0688(4)	2.9120(6)	166.511(8)
AGZTH				
O1–H1···N3	0.97(3)	1.88(3)	2.842(2)	172(3)
N8–H8···O1^{iii}	0.89(2)	2.07(2)	2.884(2)	152(2)
N6–H6B···N9^{a}	0.90(2)	2.29(2)	2.665(3)	105(2)
N6–H6A···N1	0.82(3)	2.40(3)	3.201(2)	165(3)
N6–H6B···N9^{iv}	0.90(2)	2.43(2)	3.247(3)	151(3)
N7–H7A···N5	0.87(3)	2.07(3)	2.933(3)	170(2)
N7–H7B···N4^{v}	0.89(2)	2.05(2)	2.944(2)	179(3)
N9–H9A···N8^{vi}	0.90(3)	2.49(3)	3.288(2)	148(2)
N9–H9B···N2^{vii}	0.90(3)	2.29(2)	3.156(3)	162(2)

[a] intramolecular hydrogen bond;
Symmetry codes for **AFZT**: (i) 0.5+x, -0.5-y, 0.5+z; (ii) -0.5+x, -0.5-y, 0.5+z; **AGZTH**: (iii) 0.5-x, 1.5+y, 0.5-z; (iv) 1-x, -y, 1-z; (v) 0.5-x, -0.5+y, 0.5-z; (vi) 1-x, 1-y, 1-z ; (vii) -0.5+x, 0.5+y, z.

The analysis of the crystal packing in **AFZT** and **AGZTH** shows the existence of numerous N–H···N hydrogen bonds, which are well within the sum of the van der Waals radii of two nitrogen atom ($r_{A(N)} + r_{D(N)}$ = 3.10 Å).[38] The N–H–N bond angles indicate a strongly directional rather than a purely electrostatic interaction (*Table 2.2*). In **AFZT**, the hydrogen atoms H7A on N7 and H7B on N6 form two intermolecular N6–H6A···N3 and N7–H7A···N4 hydrogen bonds with the external nitrogen atoms (N3, N4) of the 5,5'-azotetrazolate anion, yielding cation/anion pairs as depicted in Figure 2. The hydrogen bond ring motif, in the

formalism of graph-set analysis of hydrogen-bond patterns[39] of the cation/anion pairs is characterized as $R_2^2(7)$ graph set. The center of the molecular unit contains the inversion centre. Together with two further hydrogen bonds, N6–H6B····N5^{i} and N7–H7B····N2^{ii}, a three-dimensional supramolecular network is formed [symmetry code: (i) 0.5+x, -0.5-y, 0.5+z; (ii) -0.5+x, -0.5-y, 0.5+z]. The hydrogen bond network of **AGZTH** is more complicated. The two main graph sets are characterized as $R_2^2(10)$ and $R_2^2(9)$ (*Figure 2.4*), forming strands which are connected to a three-dimensional network by the water molecule and the amino group ($N9H_2$).

2.2.3 Thermodynamic aspects

Heats of formation

The heats of combustion for the compounds **AFZT**, **AZTH** and **DAGZT** were determined experimentally, and the molar enthalpy of formation of these samples were calculated from a designed Hess thermochemical cycle according to reactions [1-3] and are summarized in *Table 2.3*.

AFZT: $C_4H_8N_{20}$ (s) + 6 O_2 → 4 CO_2 (g) + 4 H_2O (l) + 10 N_2 (g) [1]

AGZTH: $C_4H_{16}N_{18}O$ (s) + 7.5 O_2 → 4 CO_2 (g) + 8 H_2O (l) + 9 N_2 (g) [2]

DAGZT: $C_4H_{16}N_{20}$ (s) + 8 O_2 → 4 CO_2 (g) + 8 H_2O (l) + 10 N_2 (g) [3]

$$\Delta_f H_m^\circ = x\Delta_f H_m^\circ(CO_2, g) + y\Delta_f H_m^\circ(H_2O, l) - \Delta_c H_m^\circ$$

The heats of formation for **GZT**, **AGZT** and **TAGZT** have been taken from references [32b,g,40] and are also presented in *Table 2.3*. With an increase in nitrogen atoms (> 75%), the standard enthalpies of formation of the 5,5'-azotetrazolate salts increase significantly. The enthalpy criteria of energetic materials are governed by their molecular structure, and therefore, the move to heterocycles with a higher nitrogen content (e.g. from imidazole ($\Delta_f H_{cryst}^\circ$ = 14.0 Kcal mol^{-1})[41] over 1,2,4-triazole ($\Delta_f H_{cryst}^\circ$ = 26.1 Kcal mol^{-1}) to tetrazole ($\Delta_f H_{cryst}^\circ$ = 56.7 Kcal mol^{-1})[42]) the trend in the heats of formation is obvious. The highest heats of formations of the investigated salts were found for **TAGZT** and **AFZT** with $\Delta_f H_{cryst}^\circ$ = 257 Kcal mol^{-1} and $\Delta_f H_{cryst}^\circ$ = 247.8 Kcal mol^{-1}, respectively, and are in accordance with the increase in nitrogen atoms.

Detonation pressure (*P*) and velocities (*D*)

From the obtained heats of formation and the densities obtained from the crystal structure determinations, some thermochemical properties have been calculated using the ICT-Thermodynamic code.[43] The heats of combustion (*Table 2.3*) have been used to calculate the expected detonation pressures (*P*) and detonation velocities (*D*), using the semi-empirical equations suggested by Kamlet and Jacobs (Eqs. [4] and [5], *Table 2.3*).[44,45,46]

Table 2.3. Summary of the physico-chemical properties of the investigated salts

	AFZT	**GZT**	**AGZTH**	**AGZT**	**DAGZT**	**TAGZT**
Formula	$C_4H_8N_{20}$	$C_4H_{12}N_{16}$	$C_4H_{16}N_{18}O$	$C_4H_{14}N_{18}$	$C_4H_{16}N_{20}$	$C_4H_{18}N_{22}$
Molar Mass	336.24	284.14	332.18	314.16	344.19	374.33
N [%]	83.31	78.84	75.87	80.22	81.36	82.32
Ω [%][a]	-57.1	-78.8	-72.2	-76.4	-74.4	-72.7
β[°C]:						
2	128.81	144.05	-	208.63	185.93	191.63
5	135.92	253.70		217.46	194.14	201.63
10	141.69	261.51		223.44	200.93	209.20
15	145.49	266.13		226.54	205.08	213.74
20	148.22	268.35		230.27	208.24	217.05
T_{int}[b]	127-145	250-265	215-230	215-230	191-208	193-212
$\Delta_{max}H$[c] [J g^{-1}]	-850.62	-1364.2	-	-1446.7	-1490.5	1599.2
E_a [Kcal mol^{-1}][d]	38.18 ± 0.84	49.64 ± 0.49	-	50.50 ± 1.56	43.51 ± 0.25	39.18 ± 0.20
	38.02 ± 0.63	49.21 ± 1.07		49.90 ± 1.48	43.15 ± 0.55	39.07 ± 0.19
$-\Delta_C U_m$ [cal g^{-1}][e]	2672.1	-	3058.4	-	3178.9	-
$-\Delta_C H_m°$ [Kcal mol^{-1}][f]	897.3	-	1013.6	-	1094.5	-
$\Delta_f H_m°$ [Kcal mol^{-1}][g]	+247.8	+98	+90.9	+104	+169.4	+257
$-\Delta_E H_m°$ [Kcal kg^{-1}][h]	772.6	426.1	474.5	418.0	585.1	784.1
Density [g cm^{-3}]	1.624	1.538[m]	1.559	1.540[n]	1.599[o]	1.602[m]
Impact [J][i]	3	32	> 40	15	4	4
Friction [N][j]	12 (+)	> 360 (-)	> 360 (-)	> 360 (-)	> 360 (-)	60 (+)
P [GPa][k]	215.6	154.0	181.4	165.6	204.5	241.7
D [m s^{-1}][k]	7201	6192	6690	6418	7045	7654
Gas volume (25°C)[l] [ml g^{-1}][m]	911	975	1101	999	1026	1058

[a] Oxygen balance; [b] Range of decomposition (β = 10°C); [c] Heat of combustion from maximum exothermic step (DSC); [d] Ozawa and refined Kissinger activation energy according ASTM E 698–99 see ref. [54]; [e] Experimental constant volume combustion energy; [f] Experimental molar enthalpy of combustion; [g] Molar enthalpy of formation; [h] Calculated molar enthalpy of detonation, ICT Thermodynamic code see ref. [43]; [i] see *Chapter I*; [j] see *Chapter I*; [k] calculated from semi-empirical equations suggested by Kamlet and Jacobs see ref. [44-46]; [l] Assuming only gaseous products, ICT Thermodynamic code see ref. [43]; [m] ref. [32h]; [n] ref. [50]; [o] estimated from a structure determination.

The calculated detonation pressures lie in the range of TNT (*P* = 20.6 GPa)[47] and the detonation velocities in the range of nitroglycerol for **TAGZT** (7610 ms^{-1} *versus* 7654 ms^{-1}, respectively),[48] similar to the calculated detonation pressures and velocities of hydrazinium 5,5′-azotetrazolate.[32c] The calculated detonation pressures and detonation velocities increase in

the order of the densities of the 5,5'-azotetrazolate salts (**GZT** (1.417) < **AGZT** (1.540) ~ **AGZTH** (1.559) < **DAGZT** (1.599) < T**AGZT** (1.602) ~ **AFZT** (1.624)). Under the assumption that only gaseous products are formed, all salts show high calculated gas yields per gram (~ 1000 ml g^{-1}) under standard temperature and pressure.

$$P[10^8 Pa] = K\rho^2\varphi \qquad [4]$$

$$D[mm\mu s^{-1}] = A\varphi^{1/2}(1 + B\rho) \qquad [5]$$

Impact and friction sensitivities

Impact testing was carried out on a "BAM Fallhammer" in accordance to BAM regulations (see *Chapter I, 3.3.2*). Form *Table 2.3* it can be depicted that the impact sensitivities increase from insensitive for **AGZTH** (>40 J) to sensitive for **DAGZT** (4 J) and **TAGZT** (4 J) to very sensitive **AFZT** (3 J), which is comparable to the highly used dry explosives RDX (5 J), Tetryl (4 J) or the more sensitive PETN (3 J).[49] Interestingly, the friction sensitivities, which were determined with the BAM friction tester (see *Chapter I, 3.3.2*), are greater than 360N for **GZT**, **AGZTH**, **AGZT** and **DAGZT** > 360 N (*Table 2.3*) and lower than expected. For **TAGZT** (60 N) the friction sensitivity is similar to the very sensitive PETN (dry, 60N). **AFZT** possesses the highest friction sensitivity with a value of 12 N, similar to lead azide (10 N). Therefore, **AFZT** should be classified as primer.

2.2.4 Thermal behavior

The thermal behavior of the salts has been investigated using Differential Scanning Calorimetry (DSC). The gaseous explosion products were detected by means of gas phase IR spectroscopy and mass spectrometry. Characteristic temperatures were identified by systematic variation of the heating rate (β = 2, 5, 10, 15 and 20 °C min^{-1}) in the DSC experiments, and the energies of activation were calculated following the ASTM protocol. The estimated energies of activation of **AFZT** and **TAGZT** (Ozawa: 38.18 ± 0.84 kcal mol^{-1} and 39.18 ± 0.20 kcal mol^{-1}, respectively) are in accordance with the observed sensitivities toward friction and impact (*Table 2.3*). The higher activation energies for the decomposition of the other compounds is confirmed by their decreased sensibility (*Table 2.3*). Normally, one would expect that the formation of hydrogen bonds would stabilize the molecule and therefore lower the sensitivity. Thus an

increased number of NH groups in the series **GZT**, **AGZT**, **DAGZT** and **TAGZT**, should lead to decreased sensitivity, but, interestingly, the sensitivity increases with an increase of inherently energetic N-N bonds as well as the increase of density, yielding the observed sensitivity rank: **AFZT** > **TAGZT** > **DAGZT** >> **AGZT** > **GZT** > **AGZTH**. The small deviation by **AGZTH** is caused by the stabilization effect of the crystal water.

DSC

Figure 2.5 shows characteristic DSC thermographs of **AFZT**, **GZT, AGZTH**, **DAGZT** and **TAGZT** (β = 10 °C min^{-1}). All five compounds show a distinctive exothermic step. The highest was found for **GZT** (T_{max} 262 °C) and the lowest for **AFZT** (T_{max} 142 °C). All compounds decompose almost free of solid residue under the formation of only gaseous products in the temperature range depicted in *Table 2.3*. The crystal water of **AGZTH**, is easily removed by simply heating the compound *in vacuo* above 100 °C as indicated by an endoterhmic signal in *Figure 2.5*, yielding **AGZT** in quantitative yields.

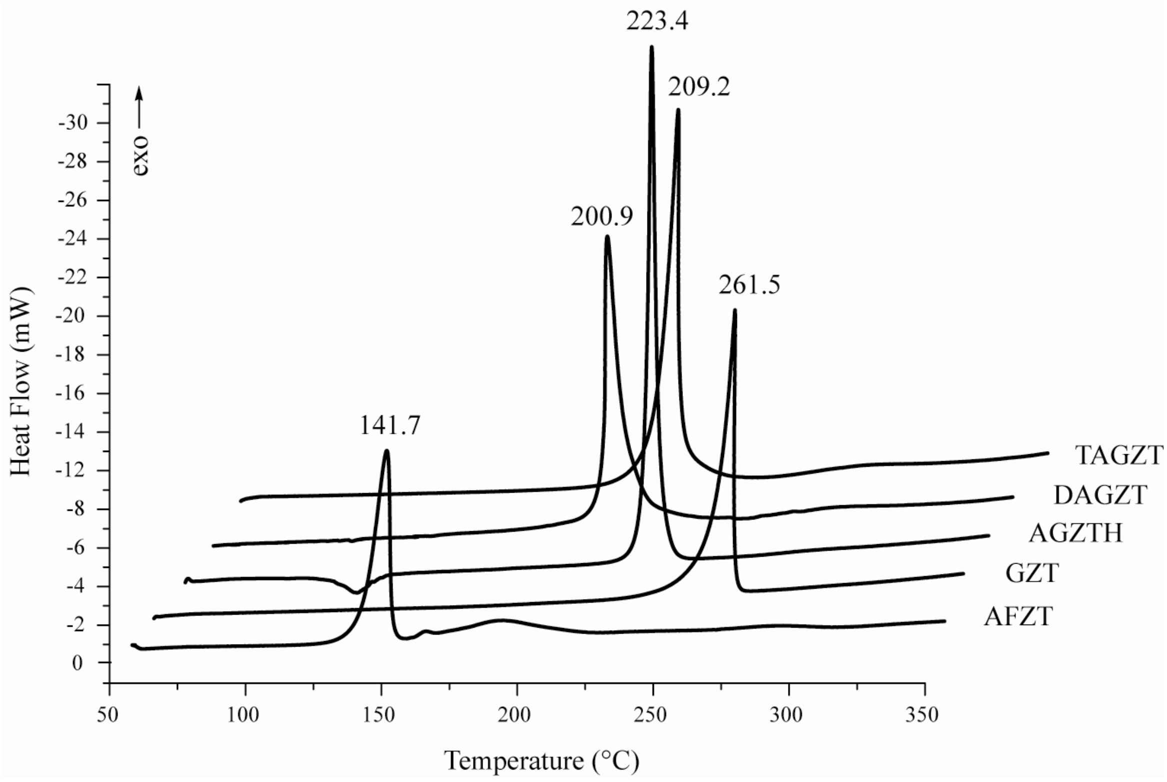

Figure 2.5. DSC thermograph of the investigated salts (β = 10°C min^{-1})

Explosion products

In all cases the major explosion product is nitrogen N_2, which was identified with mass spectrometry by its characteristic mass fragment *m/z* 28, as well as by its characteristic purple gas-phase discharge color using a high-frequency brush electrode (Tesla coil). *Figure 2.6* shows the explosion gases detected by gas-phase IR spectroscopy. For **AFZT** only hydrogen azide HN_3, hydrogen cyanide HCN and traces of ammonia NH_3 were detected as IR-active gaseous decomposition products. Surprisingly, the gas-phase IR spectra of the other salts are almost identical, indicating a similar explosion process. Small amounts of hydrogen cyanide HCN were identified and in the IR spectra by a band at 2137 cm^{-1}, a band at 1320 cm^{-1} indicates the formation of carbodiimide HNCNH rather than cyanamide (ν = 2364, 2328 cm^{-1}). In the explosion of **GZT**, **AGZT**, **DAGZT** and **TAGZT**, HN_3 has not been observed.

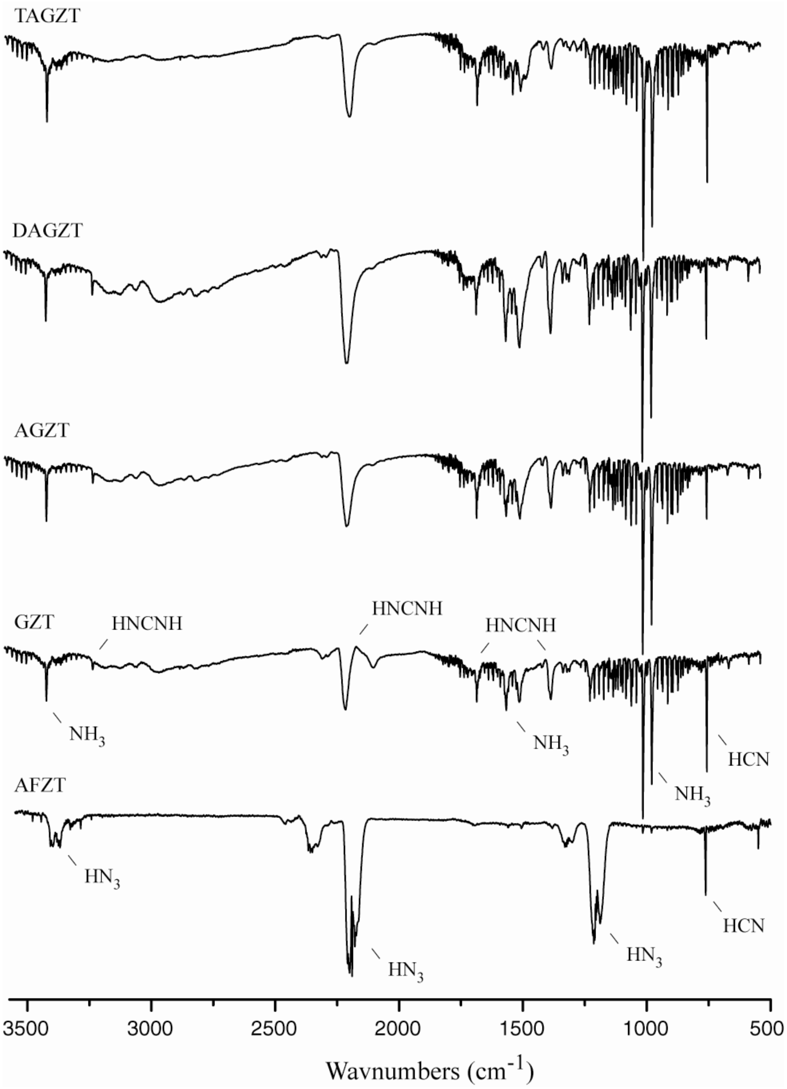

Figure 2.6. Gas phase spectra of the decomposition products of the **ZT** salts

The mass fragments *m/z* 14 (N^+, N_2^{++}), 16 (NH_2^+), 17 ($NH_3^{\cdot +}$), 26 (CN^+), 27 ($HCN^{\cdot +}$) and 28 ($N_2^{\cdot +}$, $NCNH^+$) were detected in the explosion gases of all compounds. Together with the fragments *m/z* 43 ($HN_3^{\cdot +}$) for **AFZT** and *m/z* 42 ($HNCNH^{\cdot +}$) for **GZT**, **AGZT**, **DAGZT** and **TAGZT**, the gaseous products NH_3, HCN, HNCNH and HN_3 identified by IR spectroscopy can be confirmed. Traces of oxygen containing species like H_2O or CO_2 were not found.

The main difference in the composition of the gaseous explosion products of **AFZT** and the other 5,5'-azotetrazolate salts is the occurrence of HN_3 for **AFZT** and the occurrence of carbodiimide for the other salts. The observed explosion products can be explained by a similar decomposition mechanism. The decomposition of the 5,5'-azotetrazolates anion proceeds via the protonated species. Previous investigations have shown that the decomposition of tetrazoles is initiated by ring opening reactions,[50] in which the tetrazole ring decomposes either to the corresponding nitrile under release of hydrogen azide (*Scheme 2.10*, **a**)) or to the nitrilimines under release of elemental nitrogen (*Scheme 2.10*, **b**)). The latter seems to be the main decomposition step, due to the absence of HN_3 in the IR as well as the mass spectra of **GZT**, **AGZT**, **DAGZT** and **TAGZT**.

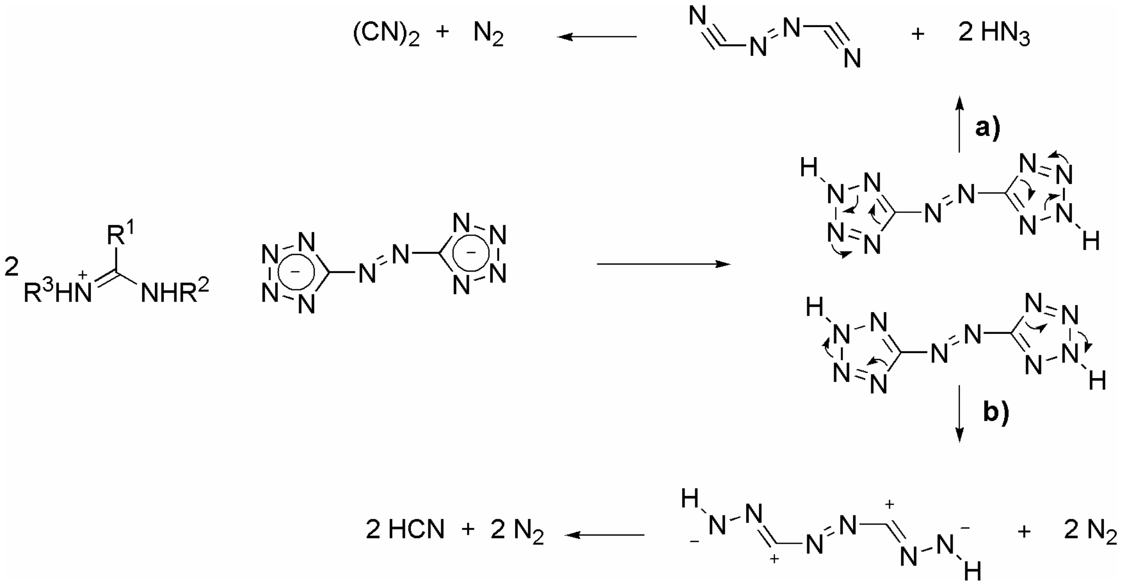

Scheme 2.10. Simplified scheme of the initial decomposition pathway of the **ZT** salts

HN_3 found after the explosion of **AFZT** can be explained by the *in situ* formation of 5-amino-1*H*-tetrazole (**5-AT**), which decomposes under these conditions via a formal elimination of HN_3 and cyanamide. Under the reaction conditions the cyanamide is not stable and decomposes to NH_3, HCN and N_2 (*Scheme 2.11*, **a**)). The small amounts of ammonia in the IR as well as the mass spectra can be explained by the recombination of HN_3 and NH_3 to NH_4N_3 (*Scheme 2.11*, **b**)) and its following decomposition to form N_2, H_2 and trace amounts of NH_3.

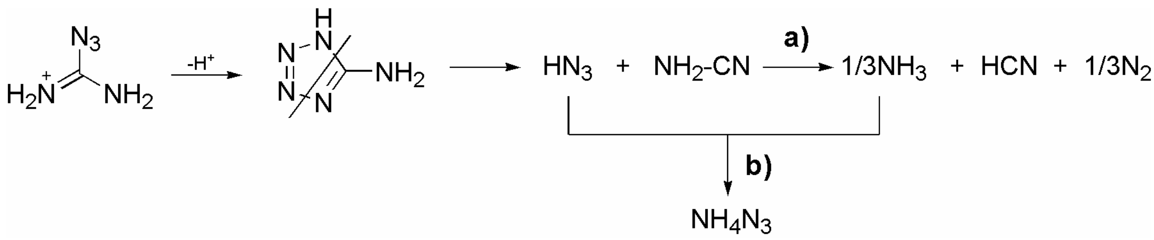

Scheme 2.11. Simplified scheme of the decomposition pathway of the **AF** cation

The decomposition of the guanidinium cations is started by the elimination of either ammonia (**GZT**) or hydrazine (**AGZT**, **DAGZT** and **TAGZT**), yielding the observed carbodiimide (*Scheme 2.12*, **a**)). The elimination of hydrazine was confirmed by the observation of *m/z* 32 ($N_2H_4^{\cdot+}$) in the mass spectra of **AGZT**, **DAGZT** and **TAGZT**. Hydrazine is not stable under the reaction conditions and decomposes according to known mechanisms[51] to form N_2, H_2 and small amounts of ammonia and was therefore not observed in the IR spectra. According to *Scheme 2.12* (**b**), consecutive gas phase decomposition reactions of carbodiimide leads to the evolution of more NH_3, HCN and N_2, as identified in the gaseous explosion products of the investigated salts.

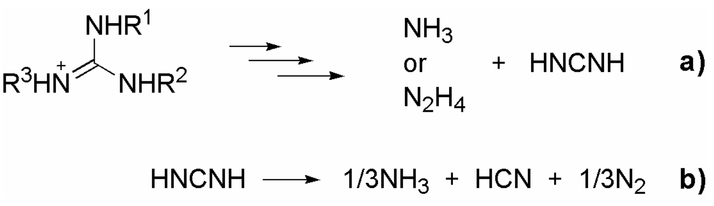

Scheme 2.12. Simplified scheme of the decomposition the guanidinium cations

2.3 Conclusion

AFTZ and the investigated guanidinium 5,5'-azotetrazolates are interesting and useful high energetic materials, which are either already in use (**GZT** and **TAGZT**) or may yet find a wide application as gas generators for airbags, initiators or additives in solid rockets as low-smoke *propellant* ingredients. In general, these salts exhibit good to reasonable physical properties, like high densities (> 1.50 g cm^{-3}), good thermal stabilities (especially for guanidinium 5,5'-azotetrazolate), and distinctive decomposition temperatures between 140 and 260°C. Depending on their properties, these salts can be seen as examples of safe, manageable gas generators (**GZT**, **AGZTH**, **AGZT**) as their friction and impact sensitivities do not exceed values prescribed by the UN Recommendations on the Transport of Dangerous Goods. **DAGZT** and **TAGZT** have the sensitivity of *secondary explosives* and **AFZT** is a *primary explosive*. All compounds have calculated detonation velocities and detonation pressures similar to already used explosives such as nitroglycerin. The molar enthalpies of formation were calculated from the combustion energy obtained from the combustion with oxygen in a bomb calorimeter. In all cases, high combustion energies and high molar enthalpies of formation were obtained. A complete summary of explosive properties has been given and the crystal structure for **AFZT** and **AGZTH** have been reported for the first time and analysed in the formalism of graph-set analysis of hydrogen-bond patterns, indicating distinctive intermolecular hydrogen bonding playing an important role for the crystal packing.[52]

2.3 Experimental

CAUTION: Azotetrazolates are highly energetic materials and tend to explode under certain conditions. Appropriate safety precautions should be taken, especially when these compounds are prepared on a larger scale. Laboratories and personnel should be properly grounded, and safety equipment such as Kevlar® gloves, leather coat, face shield and ear plugs should be worn at all times, especially in the case of ***AFZT*** *and* ***TAGZT****.*

General Method

All chemical reagents and analytical grade solvents were obtained from Sigma-Aldrich Fine chemicals Inc. and used as supplied. MeOH and EtOH were dried according to known procedures, freshly distilled and stored under nitrogen. The ^{1}H and ^{13}C NMR spectra were recorded on a JEOL Eclipse 400 instrument in [d_6]-DMSO at 25°C. The chemical shifts are given relative to external tetramethylsilane (^{1}H, ^{13}C). Infrared (IR) spectra were recorded on a Perkin-Elmer Spektrum One FT-IR instrument as KBr pellets at 20°C. Raman spectra were recorded on a Perkin Elmer Spectrum 2000R NIR FT-Raman instrument equipped with a Nd:YAG laser (1064 nm). The intensities are reported in % relative to the most intense peak and given in parenthesis. Elemental analyses were performed with a Netsch Simultanous Thermal Analyser STA 429.

Bomb Calorimetry

For all calorimetric measurements a Parr 1356 bomb calorimeter (static jacket) equipped with a Parr 207A oxygen bomb for the combustion of highly energetic materials was used.[53] The samples (ca. 80 – 100 mg) were loaded in (energetically) calibrated Parr gelatine capsules (0.9 mL) and a Parr 45C10 alloy fuse wire was used for ignition. In all measurements a correction of 2.3 (IT) calories per cm wire burned has been applied and the bomb was examined for evidence of noncombusted carbon after each run. A Parr 1755 Printer was furnished with the Parr 1356 calorimeter to produce a permanent record of all activities within the calorimeter. The reported values are the average of three single measurements. The calorimeter was calibrated by combustion of certified benzoic acid (SRM, 39i, N.I.S.T) in oxygen atmosphere at a pressure of 3.05 MPa.

DSC experiments

Samples (~ 0.35 mg) for DSC measurement were analyzed with a nitrogen flow of 20 mL min^{-1} in closed Al-containers with a hole (1μm) on the top for gas release, and a 0.003*3/16-in. disk was used to optimize good thermal contact between the sample and container (according ASTM E 698 – 99).[54] The reference sample was an empty Al-container in atmosphere. Measurements were recorded between 30°C-350°C. The sample and the reference pan were heated in a differential scanning calorimeter (Perkin-Elmer Pyris 6 DSC, calibrated by standard pure Indium and Zinc) at heating rates of 2, 5, 10, 15 and 20 °C. The decomposition points are given at a scan rate of 10°C min^{-1}. For the removal of moisture, the sample were dried *in vacuo* for 2 h at RT. **AGZT** was obtained by heating the corresponding hydrate, **AGZTH**, *in vacuo* for 4h at 110°C. The activation energy for the decomposition step was estimated by the method of Ozawa[55] and Kissinger[56] by following the differential heating rate method of the American Society for Testing and Materials (ASTM) according to the ASTM protocol E 698 – 99.[54]

Explosion experiments

For the analysis of the explosion gases of all compounds a specially equipped IR-cell was loaded with about ~2 mg of the sample and evacuated. The sample holder of the IR cell was heated rapidly to 450 °C to initiate the explosion. The explosion products were allowed to expand into the gas cell and the IR spectrum was recorded. For the recording of the mass spectra a sample of about 1 mg of the compounds was rapidly heated to 450°C to initiate the explosion in a one side closed glass tube (length: 500 mm; diameter: 5 mm) connected to the reservoir of the mass spectrometer. The explosion gases were then analyzed by mass spectrometry (JEOL MStation JMS 700) using electron impact (EI) mode (mass range 1 – 120; 1 scans per second).

X-ray Crystallographic Analyses.

A X-ray quality crystal of **AFZT** (CCDC 266607) was mounted in a Pyrex capillary and the X-ray crystallographic data collected on a Nonius Mach3 diffractometer with graphite-monochromated MoK_{α} radiation (λ = 0.71073 Å). The X-ray crystallographic data for

AGZTH (CCDC 266608) was collected on a Enraf-Nonius Kappa CCD diffractometer using graphite-monochromated MoK_α radiation (λ = 0.71073 Å). Unit cell parameters for **AFZT** were obtained from setting angles of a minimum of 25 carefully centered reflections having 2θ > 20°; the choice of the space group was based on systematically absent reflections and confirmed by the successful solution and refinements of the structures. The structures were solved by direct methods (SHELXS-86, SHELXS-97)[57] and refined by means of full-matrix least-squares procedures using SHELXL-97. Empirical absorption correction by Psi-scans was used for **AFZT**. In the case of **AGZTH** no absorption correction was applied. Crystallographic data are summarized in *Appendix B*. Selected bond lengths and angles are given in *Table 2.1*. All non-hydrogen atoms were refined anisotropically. In the case of **AFZT** the hydrogen atoms were included at geometrically idealized positions and refined. They were assigned fixed isotropic temperature factors with the value of $1.2B_{eq}$ of the atom to which they were bonded. The hydrogen atoms of compound **AGZTH** were located from the difference electron-density map and refined isotropically. The azo group in **AGZTH** is disordered with a site occupation factor (SOF) ratio of 1:1. Further information on the crystal-structure determinations (excluding structure factors) has been deposited with the Cambridge Crystallographic Data Centre as supplementary publication no. 266607 and 266608.[58]

5,5'-Azotetrazolate salts GZT, **AGZTH**, **DAGZT** and **TAGZT** were prepared according to a modified, previously published procedure [31] as follows: To a hot solution (~ 70 – 80 °C) of sodium 5,5'azotetrazolate pentahydrate (20 mmol) in 18 mL water a hot solution of the corresponding guanidinium salt (10 mmol, Cl^- or NO_3^-) in 35 mL water was added. While **GZT** and **AGZTH** precipitated immediately, while **DAGZT** and **TAGZT** crystallized after 3h at 5 °C. All products, which were purified by recrystallization from a minimum amount of water, were obtained with yields higher than 90 %.

Bis(guanidinium) 5,5'-azotetrazolate (GZT): 95 % yield; m.p. 242 °C (T_{onset}, decomp.); IR (KBr, cm^{-1}): $\tilde{\nu}$ = 3445 (s), 3396 (s), 3198 (s), 3089 (s), 2825 (m), 2232 (w), 2083 (w), 1697 (m), 1653 (s), 1585 (m), 1570 (m), 1399 (s), 1196 (w), 1049 (w), 768 (w), 737 (m), 576 (m), 532 (s), 398 (w); Raman (200mW, 25 °C, cm^{-1}) $\tilde{\nu}$ = 3207 (1), 1483 (42), 1459 (2), 1422 (12), 1386 (100), 1361 (3), 1197 (2), 1088 (13), 1058 (39), 1011 (5), 928 (7), 546 (2), 339 (1), 172 (2), 154 (3); ^{1}H-NMR ([d6]-DMSO) δ: 7.12 (s, 6H, NH_2); ^{13}C-NMR ([d6]-DMSO) δ: 157.6

(C), 172.6 (C); $C_4H_{12}N_{16}$ (284.25): Calcd. C, 16.9; H, 4.3; N, 78.8 %; Found: C, 16.7; H, 4.3; N, 78.7 %.

Bis(aminoguanidinium) 5,5'-azotetrazolate monohydrate (AGZTH): 93 % yield; m.p. 218 °C (T_{onset}, decomp.); IR (KBr, cm^{-1}): $\tilde{\nu}$ = 3420 (s), 3335 (s), 3275 (s), 3058 (s), 2788 (m), 2215 (w), 2095 (w), 1673 (s), 1645 (s), 1398 (s), 1203 (m), 1177 (w), 1164 (w), 1116 (M), 1054 (w),1013 (w), 769 (m), 739 (s), 639 (m), 563 (m), 478 (s); Raman (200mW, 25 °C, cm^{-1}) $\tilde{\nu}$ = 3268 (1), 1492 (50), 1422 (10), 1385 (100), 1360 (3), 1204 (2), 1180 (1), 1084 (20), 1062 (31), 1041 (4), 946 (2), 926 (7), 519 (2), 350 (2), 155 (2); ^{1}H-NMR ([d6]-DMSO) δ: 3.40 (s, 2H, H_2O), 4.78 (s, 1H, N*H*), 7.40 (s, 6H, NH_2); ^{13}C-NMR ([d6]-DMSO) δ: 159.3 (C), 173.4 (C); $C_4H_{16}N_{18}O$ (333.18): Calcd. C, 14.4; H, 4.9; N, 75.9 %; Found: C, 14.2; H, 4.8; N, 75.9 %.

Bis(aminoguanidinium) 5,5'-azotetrazolate (AGZT): **AGZT** was obtained in quantitative yield by dehydration of **AGZTH** in vacuo at a temperature of 100°C. $C_4H_{14}N_{18}$ (314.16): Calcd. C, 15.3; H, 4.5; N, 80.2 %; Found: C, 15.1; H, 4.6; N, 80.5%.

Bis(diaminoguanidinium) 5,5'-azotetrazolate (DAGZT): 90 % yield; m.p. 196 °C (T_{onset}, decomp.); IR (KBr, cm^{-1}): $\tilde{\nu}$ = 3354 (s), 3324 (s), 3229 (s), 3131 (s), 2391 (w), 2195 (w), 1690 (s), 1643 (s), 1595 (m), 1444 (m), 1397 (s), 1371 (m), 1330 (m), 1187 (s), 1175 (s), 1027 (m), 996 (s), 958 (s), 765 (m), 740 (s), 668 (m), 564 (s), 360 (w); Raman (200mW, 25 °C, cm^{-1}) $\tilde{\nu}$ = 3268 (2), 1482 (24), 1473 (31), 1419 (21), 1377 (100), 1352 (3), 1188 (5), 1084 (5), 1070 (2), 1047 (24), 1038 (57), 927 (11), 343 (2), 180 (2), 142 (2); *The compound exhibits dynamic behaviour in solution*; ^{1}H-NMR ([d6]-DMSO) δ: 4.67 (s, 4H), 7.28 (s, 2H), 8.74 (s, 2H,); ^{13}C-NMR ([d6]-DMSO) δ: 160.4 (C), 173.7 (C); $C_4H_{16}N_{20}$ (344.19): Calcd. C, 14.0; H, 4.7; N, 81.4 %; Found: C, 13.8; H, 4.9; N, 81.5 %.

Bis(triaminoguanidinium) 5,5'-azotetrazolate (TAGZT): 90 % yield; m.p. 203 °C (T_{onset}, decomp.); IR (KBr, cm^{-1}): $\tilde{\nu}$ = 3352 (m), 3335 (s), 3214 (s), 2397 (w), 2211 (w), 1680 (s), 1587 (m), 1571 (m), 1386 (m), 1335 (m), 1186 (w), 1139 (s), 999 (s), 945 (s), 770 (w), 732

(m), 637 (m), 590 (m), 560 (m), 426 (w), 401 (w); Raman (200mW, 25 °C, cm^{-1}) $\tilde{\nu}$ = 3338 (1), 3239 (2), 1471 (44), 1408 (19), 1371 (100), 1347 (3), 1189 (4), 1138 (1), 1071 (6), 1045 (56), 921 (12), 884 (2), 642 (1), 333 (1), 158 (1); ^{1}H-NMR ([d6]-DMSO) δ: 4.48 (s, 6H, N*H*$_2$), 7.59 (s, 3H, N*H*); ^{13}C-NMR ([d6]-DMSO) δ: 159.6 (*C*), 173.9 (*C*); $C_4H_{18}N_{22}$ (374.33): Calcd. C, 12.8; H, 4.9; N, 82.3 %; Found: C, 12.7; H, 4.8; N, 81.2 %.

Bis(azidoformaidinium) 5,5'-azotetrazolate (AFZT): *Method 1:* To a hot solution (~ 70 °C) of sodium 5,5'azotetrazolate pentahydrate (3.001 g, 10 mmol) in 35 mL water was added a hot solution of azidoformamidinium nitrate (2.964 g, 10 mmol) in 15 mL water. The orange solution was then cooled in an ice bath and the resulting orange crystals were immediately separated by filtration and washed with EtOH and Et_2O yielding 2.85g AFZT (84.8 %). *Method 2:* To a warm solution (40 °C) of AGZTH (3.32 g, 10 mmol) in 40 mL water ethylnitrite (1.5 mL) was slowly added. The solution was kept at 40°C for 1h and then cooled to 5°C. Orange crystals were obtained and separated by filtration, washed with EtOH and Et_2O yielding 1.08 g AFZT (32 %). During the crystallization process the formation of nitrogen was observed; m.p. 134 °C (T_{onset}, decomp.); IR (KBr, cm^{-1}): $\tilde{\nu}$ = 3410 (m), 3219 (s), 3124 (s), 2980 (s), 2791 (m), 2181 (s), 2120 (m), 1716 (s), 1495 (s), 1390 (s), 1243 (s), 1132 (m), 1061 (m), 906 (w), 773 (w), 735 (s), 696 (m), 559 (w), 524 (m); Raman (200mW, 25 °C, cm^{-1}) $\tilde{\nu}$ = 2174 (1), 2119 (1), 1477 (40), 1414 (12), 1381 (100), 1355 (3), 1309 (1), 1201 (2), 1138 (3), 1083 (28), 1070 (34), 923 (10), 906 (3), 676 (1), 526 (2), 330 (1), 235 (1), 151 (2), 136 (2); ^{1}H-NMR ([d6]-DMSO) δ: 6.42 (s, 4H, N*H*$_2$); ^{13}C-NMR ([d6]-DMSO) δ: 159.6 (*C*), 169.6 (*C*); *m/z* (FAB^+, xenon, 6keV, m-NBA matrix): 86 $[CH_4N_5]^+$; $C_4H_8N_{20}$ (336.24): Calcd. C, 14.3; H, 2.4; N, 83.3 %; Found: C, 14.1; H, 2.8; N, 83.3 %.

3 Hydrazinium 5,5'-Azotetrazolate Salts

It is known that 5,5'-azotetrazolate ($[N_4C\text{-}N{=}N\text{-}CN_4]^{2-}$) salts decompose in acidic media under nitrogen evolution and formation of 5-hydrazino-1*H*-tetrazole (**HyT**, **25**).[59] Therefore, in the case of basic counterions like certain ammonium and guanidinium cations (*Chapter II, 2*), it was found that those salts are stable in the solid state and in most cases also in solution.[32c-f,g,h] The energy content of HNC materials is directly related to high heats of formation, which is attributed to increasing numbers of inherently energetic N−N and C−N bonds. Therefore, counterions with additional energetic N−N and possible no C−N bonds are sought. The simplest example of such a cation is the mono-protonated hydrazinium cation, $N_2H_5^+$. A series of interesting compounds, based on the $N_2H_5^+$-cation was recently developed by Hammerl *et al.*[32c] He described the synthesis of the dihydrazinium salt of $[N_4C\text{-}N{=}N\text{-}CN_4]^{2-}$ (**HZT**, **26**), its monohydrate (**HZTH**, **27**), and its dihydrazinate (**DAD**, **28)** (*Figure 2.7*).

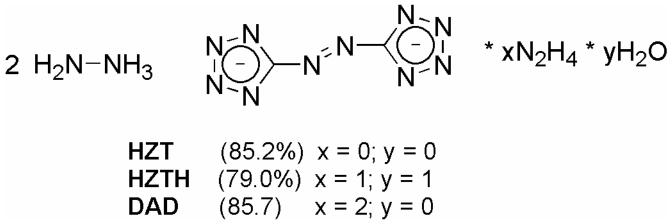

Figure 2.7. Dihydrazinium salt of $[N_4C\text{-}N{=}N\text{-}CN_4]^{2-}$

The compounds **26-28** are stable at room temperature and stored on air. They show reasonable insensitivity toward friction and impact, but detonate violently when the explosion is initiated, e.g. by rapid heating over the decomposition temperature or by using an initiator. These compounds appear to be quite promising for use as *propellants*. They represent new HEDMs with one of the highest nitrogen contents reported (79.0 % to 85.7 %). The applicability of these compounds as *propellants* is currently being tested in collaboration with the WIWEB, the ICT and the Indian Head Division, Naval Surface Warfare Centre. Since, for this purpose larger amounts of material are necessary and as the initial used synthesis procedures are not suitable for the preparation on a larger scale, the preparation of these compounds was reinvestigated.

3.1 Synthesis of **HZT**, **HZTH**, and **DAD**

The original synthetic procedure from [32c] (*Figure 2_8*) suffers from some drawbacks related to the disadvantageous use of BaZT in its hydrated as well dehydrated form, as well as the use of the very problematic anhydrous hydrazine:

Results and Discussion

Synthesis and Properties of Dihydrazinium 5,5′-Azotetrazolate Salts. The reaction of barium azotetazolate with $[N_2H_5]^+{}_2[SO_4]^{2-}$, generated from commercially available $[N_2H_6]^{2+}[SO_4]^{2-}$ [22] with $N_2H_4{\cdot}H_2O$ in water, gave a yellow solution. After filtration, water was allowed to evaporate. Yellow needles of dihydrazinium 5,5′-azotetrazolate dihydrate (**2**) were isolated. By heating **2** to 100 °C in vacuo for 2 days, the water was removed to form dihydrazinium 5,5′-azotetrazolate **1**. Reaction of $[N_2H_6]^{2+}[SO_4]^{2-}$ with barium 5,5′-azotetrazolate carried out in anhydrous hydrazine gave, after filtration, a yellow solution that was concentrated in vacuo and was allowed to crystallize at low temperature. Yellow needles of dihydrazinium 5,5′-azotetrazolate dihydrazinate (**3**) were isolated. The quality of all elemental analyses suffers because of the difficulty of obtaining correct values for compounds with extremely high nitrogen content.[9]

Figure 2.8. Original preparation procedure of dihydrazinium salt of $[N_4C\text{-}N{=}N\text{-}CN_4]^{2-}$; 1 → HZT; 2 → HZTH (dihydrate is erroneous); 3 → DAD; published in Inorg. Chem. 2001 ref [32c].

The main disadvantages of the original synthesis are the use of anhydrous hydrazine as solvent and water free barium azotetrazolate **(BaZT)**. Both compounds are quite hazardous. Anhydrous hydrazine is difficult to handle as it is extremely poisonous and tends to decompose explosively, especially in the presence of traces of metals. Water-free **BaZT** is extremely explosive and is difficult to prepare since it tends to explode during the dehydration process. It is known that heavy metal salts of 5,5'-azotetrazolates, particularly lead 5,5'azotetrazolate dihydroxide,[34a,60] have been investigated for use as initiators. An industrial synthesis of **132** on a large scale is not practical using the original method.

The modified synthesis, which is based on the reaction of **NaZT** with appropriate hydrazine precursors was combined in a patent and filed as an application for a patent. The patent is currently being under examination at the Deutsche Patent und Markenamt.

3.2 Patent

Patentansprüche

1. Verfahren zur Herstellung einer Verbindung der Reihe Dihydrazinium 5,5'-Azotetrazolat * x-Hydrazinat * y-Hydrat ($0 \leq x \leq 2$, $0 \leq y \leq 1$) derart, dass die Verbindung als Produkt aus der Reaktion der beiden Edukte Alkalimetall 5,5'-Azotetrazolat und Hydraziniumsalz erhalten wird und dass diese Reaktion in einem wässrigen Reaktionsmedium duchgeführt wird.

2. Verfahren nach Anspruch 1, bei dem das Edukt Alkalimetall 5,5'-Azotetrazolat ein Dinatrium 5,5'-Azotetrazolat * x-Hydrat ($x \leq 5$) ist.

3. Verfahren nach Anspruch 2, bei dem das Dinatrium 5,5'-Azotetrazolat * x-Hydrat ($x \leq 5$) aus einer vorgeschalteten Stufe erhalten wird, bei dem 5-Amino-1H-tetrazol * x-Hydrat ($x \leq 1$) mit Natronlauge und Kaliumpermanganat umgesetzt wird.

4. Verfahren nach einem der Ansprüche 1 bis 3, bei dem das im Anspruch 1 genannte wässrige Reaktionsmedium kein Hydrazin aufweist.

5. Verfahren nach einem der Ansprüche 1 bis 3, bei dem das im Anspruch 1 genannte Reaktionsmedium ein Hydrazin/Wasser-Gemisch umfasst.

6. Verfahren nach Anspruch 5, bei dem während der Reaktion der Hydrazingehalt eingestellt werden kann.

7. Verfahren nach Anspruch 5 oder 6, bei dem während der in Anspruch 1 genannten Reaktion dem Reaktionsmedium wasserentziehende Salze zugesetzt werden.

8. Verfahren nach einem der Ansprüche 1 bis 7, bei dem nach Erhalt der Verbindungen aus der Reihe Dihydrazinium 5,5'-Azotetrazolat * x-Hydrazinat * y-Hydrat ($0 \leq x \leq 2$, $0 \leq y \leq 1$) die Nebenprodukte durch Sublimation im Vakuum entfernt werden.

Verfahren zur Herstellung von Explosivstoffen

Die Erfindung betrifft die Herstellung von Explosivstoffen mit hohem Stickstoffgehalt.

Die Salze der Reihe Dihydrazinium 5,5'-Azotetrazolat * x -Hydrazinat * y-Hydrat ($[N_2H_5]_2^+[N_4C\text{-}N\text{=}N\text{-}CN_4]_2^-$ * xN_2H_4 * yH_2O, wobei: $0 \leq x \leq 2$, $0 \leq y \leq 1$) stellen stickstoffreiche energetische Verbindungen dar, die in Kombination mit diversen Oxidationsmitteln zur Herstellung von Treibmitteln mit einem weitgehend rückstandslosen Abbrand verwendet werden können.

Aus einem Fachaufsatz (A. Hammerl, T. M. Klapötke, H. Nöth, M. Warchhold, Inorg. Chem. 2001, 40, 3570-3575) ist ein Verfahren zur Herstellung von Verbindungen der vorgenannten Reihe Dihydrazinium 5,5'-Azotetrazolat * x -Hydrazinat * y-Hydrat ($0 \leq x \leq 2$, $0 \leq y \leq 1$) bekannt geworden.

In dem Fachaufsatz ist dargelegt, dass man die in Rede stehenden Verbindungen als Produkt aus der Reaktion der beiden Edukte Barium 5,5'-Azotetrazolat und Hydraziniumsulfat erhält (Seite 3571, Spalte 1, Absatz der Überschrift „Synthesis and Properties of Dihydrazinium 5,5'-Azotetrazolate Salts"). Ferner heißt es, dass das Hydraziniumsulfat ($[N_2H_5]_2^+[SO_4]_2^-$) gebildet wird aus dem kommerziell erhältlichen $[N_2H_6]_2^+[SO_4]_2^-$ und einem Equivalent N_2H_4*H_2O (Hydrazinhydrat) in Wasser.

Im Fachaufsatz ist ferner dargelegt (Seite 3575, zweite Spalte), dass je nach Reaktionsführung die nachfolgenden 3 Verbindungen, die in dieser Anmeldung als HZT, HZTH und DAD bezeichnet sind, erhalten werden:

- HZT, ebenso Dihydrazinium 5,5'-Azotetrazolat, ebenso $[N_2H_5]_2^+[N_4C\text{-}N\text{=}N\text{-}CN_4]_2^-$, ebenso $[N_2H_5]_2^+[N_4C\text{-}N\text{=}N\text{-}CN_4]_2^-$ * xN_2H_4 * yH_2O mit $x = 0$ und $y = 0$:
  - HZT erhält man durch eine thermische Behandlung von HZTH.
- HZTH, ebenso Dihydrazinium 5,5'-Azotetrazolat * Monohydrat, ebenso $[N_2H_5]_2^+[N_4C\text{-}N\text{=}N\text{-}CN_4]_2^-$ * $1H_2O$, ebenso $[N_2H_5]_2^+[N_4C\text{-}N\text{=}N\text{-}CN_4]_2^-$ * xN_2H_4 * yH_2O mit $x = 0$ und $y = 1$:
  - Erhalt von HZTH aus Barium 5,5'-Azotetrazolat und $[N_2H_6]_2^+[SO_4]_2^-$ in Wasser mit einem <u>Equivalent</u> Hydraziniumhydrat.

- Im Fachaufsatz wird das HZTH als Dihydrat vorgestellt (x = 0, y = 2); dabei handelt es sich allerdings um einen Fehler. Der richtige Wassergehalt dieser Verbindung entspricht dem eines Monohydrates, was durch Kristallstrukturanalyse, TGA und Elementaranalyse bestätigt werden konnte.

- DAD, ebenso Dihydrazinium 5,5'-Azotetrazolat * Dihydrazinat, ebenso $([N_2H_5]_2^+[N_4C\text{-}N{=}N\text{-}CN_4]_2^-$ * $2N_2H_4$, ebenso $[N_2H_5]_2^+[N_4C\text{-}N{=}N\text{-}CN_4]_2^-$ * xN_2H_4 * yH_2O mit x = 2 und y = 0:
  - DAD erhält man aus Barium 5,5'-Azotetrazolat und $[N_2H_6]_2^+[SO_4]_2^-$ in wasserfreiem Hydrazin.

Im Falle des DAD muss, wie zuvor dargelegt, in hochexplosivem, wasserfreiem Hydrazin gearbeitet werden, welches zum Zwecke der Produktisolierung nach schwieriger Abtrennung des ausgefallenen Bariumsulfates abdestilliert werden muss.

Bei den im Fachaufsatz vorgestellten Reaktionen handelt es sich um eine Fällungsreaktion, bei der durch Umsetzung von wasserfreiem Barium 5,5'-Azotetrazolat mit einem Hydraziniumsulfat durch Ausfällung des schwerlöslichen Bariumsulfates das Dihydrazinium 5,5'-Azotetrazolat in Lösung erhalten wird. Die Darstellung des Barium 5,5'-Azotetrazolat erfolgt in einer vorgeschalteten Reaktion, die nicht näher im Fachaufsatz beschrieben ist. Das wasserfreie Barium 5,5'-Azotetrazolat reagiert äußerst empfindlich auf Reibung, Schlag und Temperatur und ist daher extrem explosiv.

Das bekannte, sehr aufwendige Verfahren basiert auf der Umsetzung des entsprechenden Barium 5,5'-Azotetrazolat. Bei Barium handelt es sich um ein Erdalkalimetall, welches zu den Schwermetallen zu zählen ist. Barium ist in Form seiner löslichen Salze hoch giftig und daher in großtechnische Synthesen zu vermeiden. Zudem ist Barium im Vergleich zu Natrium ausgesprochen teuer. Bei der Fällungsreaktion, ausgehend vom Bariumsalz, entsteht als Abfallprodukt Bariumsulfat, was ein Problem in Hinblick auf die Entsorgung darstellt.

Der Erfindung liegt die Aufgabe zugrunde, ein weiteres Verfahren zur Herstellung von stickstoffreichen Explosivstoffen zu schaffen, welches effizient und ökonomisch

arbeitet und bei dem solche Edukte eingesetzt werden, die eine großtechnische, gefahrlose Synthese ermöglichen.

Diese Aufgabe wird erfindungsgemäß durch die Merkmale des Patentanspruches 1 gelöst.

Die Synthese einer Verbindung der Reihe $[N_2H_5]_2^+[N_4C\text{-}N\text{=}N\text{-}CN_4]_2^-$ * xN_2H_4 * yH_2O ($0 \leq x \leq 2$, $0 \leq y \leq 1$) erfolgt durch Metathesereaktion von einem Alkalimetall 5,5'-Azotetrazolat (vorzugsweise dem Dinatrium 5,5'-Azotetrazolat Pentahydrat) und einem Hydraziniumsalz (vorzugsweise NO_3^- oder Cl^-). Im Vergleich zu der im Fachaufsatz beschriebenen Fällungsreaktion, handelt es sich bei dem neuen Verfahren um eine fraktionierte Kristallisation. Beide Edukte sind auch in großtechnischem Maßstab gut zu handhaben.

Ein großer Vorteil liegt in der effizienten Ausgestaltung des Verfahren.

In einem ersten Schritt wird ein Alkalimetall 5,5'-Azotetrazolat * x-Hydrat (vorzugsweise das Dinatrium 5,5'-Azotetrazolat * x-Hydrat ($x \leq 5$)) aus einer vorgeschaltenen Stufe erhalten (beispielsweise gemäß einem Unteranspruch).

In einem zweiten Schritt wird das erhaltene Alkalimetall 5,5'-Azotetrazolat * x-Hydrat (vorzugsweise das Dinatrium 5,5'-Azotetrazolat * x-Hydrat ($x \leq 5$)) in einem entsprechenden Lösungsmittelgemisch umgesetzt, wobei das entsprechende Produkt aus der Reaktionslösung beim Abkühlen auskristallisiert. Das Produkt kann durch einfache Filtration vom Reaktionsgemisch abgetrennt werden. Es wird in hohen Ausbeuten und einem hohen Reinheitsgrad erhalten. Bei den Nebenprodukten handelt es sich, je nach eingesetztem Hydraziniumsalz, um Natriumchlorid oder Natriumnitrat, welche keine Probleme in Hinblick auf eine Entsorgung darstellen.

Das zweistufige Verfahren ist dadurch möglich, dass als eines der beiden Edukte ein Alkalimetall 5,5'-Azotetrazolat verwendet wird. Der Vorteil der Alkalimetall 5,5'-Azotetrazolat-Salze gegenüber den Erdalkalimetallsalze ist deren bessere Löslichkeit in wässriger bzw. hyrdazinhaltigen-wässrigen Lösungen. Im Gegensatz dazu weisen die Hydrazinium Azotetrazolate ebenfalls eine schlechtere Löslichkeit auf, was eine

fraktionierte Kristallisation ermöglicht. Beim Bekannten führt eine gleiche Umsetzung von Hydraziniumsalzen mit Barium 5,5'-Azotetrazolat in wässriger bzw. hyrdazinhaltigen-wässrigen Lösungen zu einer Mischkristallisation von entsprechenden Barium- und Hydraziniumsalzen, und liefert daher keine phasenreine Produkte.

Eine aufwendige Abtrennung von Nebenprodukten, wie zum Beispiel des $BaSO_4$ beim bekannten Verfahren, wird vermieden. Zusätzlich liegt ein weiterer Vorteil in der sehr hohen Ausbeute und der Möglichkeit zur ökonomischen, industriellen Herstellung von hydrazinfreien Verbindungen, z.B. von Dihydrazinium 5,5'-Azotetrazolat * Monohydrat (HZTH, x = 0, y = 1) und Dihydrazinium 5,5'-Azotetrazolat (HZT, x = 0, y = 0). Denn bezüglich der toxikologischen Einstufung weisen die Salze mit variierendem Hydrazingehalt eine Sicherheitsproblematik auf, die durch die Gesundheitsgefahren von Hydrazinlösungen im Syntheseschritt ausgehen. Deshalb sind die vorgenannten hydrazinfreien Verbindungen HZT und HZTH von besonderem technischen Interesse.

Eine Belastung durch eventuell abgegebenes Hydrazin aus DAD und anderen hydrazinhaltigen Salzen der Reihe $[N_2H_5]_2^+[N_4C\text{-}N{=}N\text{-}CN_4]_2^- * xN_2H_4 * yH_2O$ ($0 \leq x \leq 2$, $0 \leq y \leq 1$) ist nicht gegeben, da Stabilitäts- und Druckbelastungstest bestätigen, dass auch unter extremen Drücken und Temperaturen nahe dem Zersetzungspunkt eine Abgabe von Hydrazin nicht statt findet.

Die Reaktion der beiden Edukte Alkalimetal 5,5'-Azotetrazolat * x-Hydrat (x ≤ 5) und Hydraziniumsalz wird in einem wässrigen Reaktionsmedium durchgeführt. Hierdurch erhöht sich die Sicherheit in einem großtechnischen Prozess.

Gemäß einer Ausgestaltung der Erfindung ist das Edukt Alkalimetal 5,5'-Azotetrazolat * x-Hydrat (x ≤ 5) ein Dinatrium 5,5'-Azotetrazolat * x-Hydrat (x ≤ 5). Vorzugsweise wird als Dinatrium 5,5'-Azotetrazolat * x-Hydrat (x ≤ 5) die Verbindung Dinatrium 5,5'-Azotetrazolat * Pentahydrat eingesetzt.

Gemäß einer weiteren Ausgestaltung der Erfindung wird das Dinatrium 5,5'-Azotetrazolat * x-Hydrat (x ≤ 5) aus einer vorgeschalteten Stufe erhalten, bei dem 5-

Amino-1H-tetrazol * x-Hydrat (x ≤ 1) mit Natronlauge und Kaliumpermanganat umgesetzt wird.

Gemäß einer weiteren Ausgestaltung der Erfindung weist das wässrige Reaktionsmedium kein Hydrazin auf. Dies dient der Herstellung von HZTH.

Gemäß einer weiteren Ausgestaltung der Erfindung umfasst das Reaktionsmedium ein Hydrazin/Wasser-Gemisch. Dieses Reaktionsmedium ist sicher zu handhaben (Hydrazingehalt ≤ 64 Vol-%) und kann in geschlossenen Apparaturen eingesetzt werden, was für den entsprechenden Operator keine gesundheitliche Belastung darstellt.

Gemäß einer weiteren Ausgestaltung der Erfindung kann durch Einstellung des Hydrazingehaltes in vorteilhafter Weise der Wassergehalt der Produkte eingestellt werden (siehe die nachfolgende Tabelle 1). Dadurch lassen sich Produkte erhalten, die in Ihrem Stickstoffgehalt um bis zu 7% variieren.

Gemäß einer weitern Ausgestaltung können während der Reaktion wasserentziehende Salze dem Reaktionsmedium zugesetzt werden. In Frage kommen die Salze wie z. B. NaCl oder $NaNO_3$. Durch die Hydratation des entsprechenden Kations (z.B. $[Na(H_2O)_6]^+$) ermöglicht man den Einsatz von verdünnten Hydrazin/Wasser Lösungen. Zusätzlich erzwingt man dadurch die Kristallisation des schlechter löslichen Salzes, hier den entsprechenden Hydraziniumsalzen, da das System mit einer anderen Spezies übersättigt wird (Verdrängungsprinzip).

Gemäß einer weiteren Ausgestaltung der Erfindung werden die Nebenprodukte, wie auch das Wasser und das Hydrazin, durch Sublimation im Vakuum entfernt, um die erforderlichen Reinheiten zu erzielen.

Die Erfindung wird nachfolgend an Hand mehrerer, in den Zeichnungen dargestellter Ausführungsbeispiele näher erläutert. Dabei zeigen:

Fig. 1 nacheinander ablaufende Reaktionsgleichungen, die darlegen, wie man ausgehend vom 5-Amino-1H-tetrazol x-Hydrat (x ≤ 1) zu Verbindungen der Reihe

Dihydrazinium 5,5'-Azotetrazolat * x -Hydrazinat * y-Hydrat ($0 \leq x \leq 2$, $0 \leq y \leq 1$) gelangt;
Fig. 2 eine Reaktionsgleichung, die darlegt, wie man ausgehend von der Reihe Dihydrazinium 5,5'-Azotetrazolat * x -Hydrazinat * y-Hydrat ($0 \leq x \leq 2$, $0 \leq y \leq 1$) zur Verbindung HZT gelangt;
Fig. 3 eine Tabelle, die den Stickstoffgehalt der Verbindungen in Abhängigkeit vom Verhältnis Hydrazin zu Wasser im Reaktionsmedium zeigt.

Die Fig. 1 zeigt ein Verfahren zur Herstellung einer Verbindung der Reihe Dihydrazinium 5,5'-Azotetrazolat * x -Hydrazinat * y-Hydrat ($0 \leq x \leq 2$, $0 \leq y \leq 1$), welche als Produkt aus der Reaktion der beiden Edukte Alkalimetall 5,5'-Azotetrazolat (am Beispiel Dinatrium 5,5'-Azotetrazolat * x-Hydrat ($x \leq 5$)) und Hydraziniumsalz erhalten wird.

Die vorgenannte Reihe weist verschiedene Grenzfälle auf, da, wie zuvor formelmäßig dargelegt, die Variable x Werte von 0 bis 2 und die Variable y Werte von 0 bis 1 aufweisen kann.

Wenn x den Wert von 2 und y den Wert von 0 einnimmt, liegt die Verbindung (I) vor. Die Verbindung (I) weist die chemische Bezeichnung Dihydrazinium 5,5'-Azotetrazolat Dihydrazinat (DAD) auf.

Die Verbindung (II) betrifft den Grenzfall, wonach x den Wert 0 und y den Wert 1 einnimmt. Die zweite Verbindung stellt Dihydrazinium 5,5´-Azotetrazolat Monohydrat (HZTH) dar.

Bei der Verbindung (III) nimmt sowohl x als auch y den Wert von 0 ein. Die dritte Verbindung ist mit Dihydrazinium 5,5´-Azotetrazolat (HZT) bezeichnet.

Als Reaktionsmedium kann Wasser (HZTH) oder ein Hydrazin/Wasser-Gemisch (Salze der Reihe $[N_2H_5]_2^+[N_4C\text{-}N{=}N\text{-}CN_4]_2^-$ * xN_2H_4 * yH_2O ($x \leq 2$, $y \leq 1$)) eingesetzt werden. Dieses Reaktionsmedium ist sicher zu handhaben (Hydrazingehalt ≤ 64 Vol.-%) und kann in geschlossenen Apparaturen eingesetzt werden, was für den entsprechenden Operator keine gesundheitliche Belastung darstellt. Je nach

Anforderung kann der Gehalt an Hydrazin im gewünschten Produkt eingestellt werden. Fig. 3 zeigt das Kristallisationsverhalten der verschiedenen Phasen in Abhängigkeit vom Verhältnis Hydrazin : Wasser im Reaktionsmedium. Werden die Umsetzungen in Wasser als alleiniges Reaktionsmedium durchgeführt, so erhält man als Produkt HZTH **(II)** (N : 79.0 %), aus wasserfreiem Hydrazin würde man DAD **(I)** (N : 85.7%) erhalten. Auf Umsetzungen in wasserfreiem Hydrazin wird verzichtet, da aus konzentrierten, übersättigten Hydrazinhydrat Lösungen ebenfalls DAD (Reaktionsbeispiel **5**) erhalten wird. Spricht man Hydrazinhydrat, so ist N_2H_5OH gemeint. Diese Verbindung ist kommerziell erhältlich und entspricht einem Hydrazingehalt von 64%.

In Abhängigkeit von der Konzentration der eingesetzten Edukte zum Reaktionsmedium, z.B. Hydrazinhydrat (N_2H_4: 64,0%), variiert der Hydrazin/Wassergehalt in den Produkten der allgemeinen Zusammensetzung $[N_2H_5]_2^+[N_4C\text{-}N{=}N\text{-}CN_4]_2^- * xN_2H_4 * yH_2O$ ($0 \leq x \leq 2$, $0 \leq y \leq 1$).

Arbeitet man in Wasser als Lösungsmittel, so erhält man bei der Umsetzung eines entsprechenden Alkalimetall-Azotetrazolats (vorzugsweise dem Natriumsalz) und einem entsprechenden Hydraziniumsalz (vorzugsweise dem Chlorid) bei Temperaturen zwischen 80 und 90°C das HZTH (Synthesebeispiel **1**).

Arbeitet man in einer übersättigten Lösung eines entsprechenden Alkalimetall-Azotetrazolats (vorzugsweise dem Natriumsalz) und einem entsprechenden Hydraziniumsalz (vorzugsweise dem Chlorid) bei Temperaturen zwischen 50 und 90°C in Hydrazinhydrat (Hydrazin/Wasser-Gemisch?), so wird DAD erhalten (Synthesebeispiel **5**).

Die nachfolgende Tabelle 1 gibt Synthesebeispiele mit den entsprechenden Elementaranalysen von den dabei erhaltenen Produkten wieder.

Beispiel	HZT * xN_2H_4 * yH_2O	Elementaranalyse Soll	Ist
1	x = 0, y = 1	N: 79.0 C: 9.7 H: 4.9	N: 79.0 C: 9.7 H: 4.9
			N: 78.6 C: 9.5 H: 4.8
			N: 79.6 C: 9.7 H: 4.9[a]
2	x = 1, y = 1	N: 80.0 C: 8.6 H: 5.7	N: 80.0 C: 8.5 H: 5.2
3	x = 0.5, y = 0.5	N: 82.4 C: 9.4 H: 5.3	N: 82.3 C: 9.6 H: 5.4
			N: 83.3 C: 9.6 H: 5.4
4	x = 1.5, y = 0.5	N: 82.9 C: 8.4 H: 6.0	N: 83.1 C: 8.8 H: 5.8
5	x = 2, y = 0	N: 85.7 C: 8.3 H: 6.0	N: --.- C: 8.3 H: 6.0[b]

[a] Verschiedene Ansätze
[b] Stickstoffwert konnte bei dieser Probe aus technischen Gründen nicht bestimmt werden

Tabelle 1

Hydraziniumchlorid ist kommerziell erhältlich und weist gegenüber dem Hydraziniumnitrat, welches stark hygroskopisch ist, eine bessere Handhabbarkeit auf.

Dem Reaktionsmedium können wasserentziehende Salze (z.B. NaCl, $NaNO_3$) zugesetzt werden, um die Reaktion auch in verdünnten Wasser/Hydrazin-Lösungen durchzuführen. Allerdings beobachtet man dann eine etwas geringere Ausbeute.

Die Kristallisationstemperatur der Produkte hängt von der Konzentration des Hydrazingehaltes ab und liegt bei reinem Wasser bei 5°C und sinkt mit steigendem Hydrazingehalt bis -20°C. Die so erhaltenen Produkte kristallisieren in Form von feinen gelben Kristallen. In jedem Fall erhält man die Produkte in sehr hohen Ausbeuten (abhängig vom Reaktionsmedium zwischen 70 u. 90%) und Reinheiten von meist über 98%. Die Produkte werden durch einfache Saugfiltration vom Reaktionsmedium abgetrennt und mit Alkohol (vorzugsweise EtOH) von anhaftendem Reaktionsmedium befreit. Zur weiteren Trocknung ist eine Behandlung mit Ethern oder andern aprotischen Lösungsmitteln möglich (vorzugsweise Diethylether). Als Nebenprodukt entsteht das entsprechende Alkalimetallsalz (vorzugsweise NaCl bzw. $NaNO_3$), welches im Reaktionsmedium zurück bleibt. Eine Verunreinigung der Produkte mit diesem Alkalimetallsalz ist gering (< 1%), man beobachtet eher eine Verunreinigung

durch die entsprechenden Hydraziniumsalze ($N_2H_5NO_3$ bzw. N_2H_5Cl), wobei die Reinheit für die meisten Anwendungen ausreichend ist.

Das Edukt Alkalimetall-Azotetrazolat ist ein Dinatriumazotetrazolat *x-hydrat ($x \leq 5$), das aus einer vorgeschalteten Stufe erhalten wird, bei dem 5-Amino-1H-tetrazol *Hydrat mit Natronlauge und Kaliumpermanganat umgesetzt wird. Vorzugsweise wird als Dinatriumazotetrazolat *x-Hydrat ($x \leq 5$) die Verbindung Dinatrium 5,5'-Azotetrazolat Pentanhydrat eingesetzt. 5-Amino-1*H*-tetrazol Monohydrat ist kommerziell erhältlich. Bezogen auf das 5-Amino-1H-tetrazol Monohydrat erhält man eine Gesamtausbeute an Dinatrium 5,5'-Azotetrazolat Pentahydrat von bis zu 75%. Die Fig. 1 zeigt Reaktionsgleichungen, die darlegen, wie man ausgehend vom 5-Amino-1*H*-tetrazol Monohydrat zu den Verbindungen des Typs $[N_2H_5]_2^+[N_4C\text{-}N{=}N\text{-}CN_4]_2^-{*}xN_2H_4{*}yH_2O$ ($0 \leq x \leq 2$, $0 \leq y \leq 1$) gelangt.

Ebenso kann in Abweichung zum dargestellten Ausführungsbeispiel das Dinatriumazotetrazolat *x-hydrat ($x \leq 5$) in jeder Form seiner Hydrate verwendet werden ($x \leq 5$).

Die Nebenprodukte, wie auch das Wasser und das Hydrazin, werden durch Sublimation im Vakuum entfernt (vorzugsweise 105°C bei einem Druck von ca. $5{*}10^{-3}$ bar; $N_2H_5NO_3$, mp 70.7°C; N_2H_5Cl, mp 89°C). Dabei erhält man das solventfreie HZT (III), wie in Fig. 2 illustriert ist (Synthesebeispiel **6**).

Beispiel	**HZT * xN_2H_4 * yH_2O**	**Elementaranalyse Soll für HZT**	**Tempern (100°C/$5{*}10^{-3}$bar) Ist**
1	x = 0, y = 1	N: 85.2 C: 10.4 H: 4.4	N: 85.3 C: 10.2 H: 4.2
			N: 85.1 C: 10.2 H: 4.2
2	x = 1, y = 1	-//-	N: 85.1 C: 10.5 H: 4.4
3	x = 0.5, y = 0.5	-//-	N: 86.1[a] C: 10.4 H: 4.5
			N: 86.1 C: 10.4 H: 4.6
4	x = 1.5, y = 0.5	-//-	N: 85.2 C: 10.2 H: 4.4
5	x = 2, y = 0	-//-	N: 85.1 C: 10.3 H: 4.4

[a] Dieser hohe Stickstoffwert lässt sich nicht erklären

Tabelle 2

In der vorhergehenden Tabelle 2 sind die Elementaranalysen aller getrockneten Produkte zusammengefasst, die nach den oben angegebenen Synthesebeispielen erhalten wurden.

Nachfolgend wird die Herstellung verschiedener Verbindungen erläutert:

Beispiel 1 betreffend HZTH (II) (N: 85.2%):

Zu einer heißen (80 – 90°C) Lösung von *di*(Natrium) 5,5'-Azotetrazolat (5,803 g, 20 mmol) in 35 mL H_2O wird eine heiße (60 – 70°C) Lösung von Hydraziniummonochlorid (2,740g , 40 mmol) in 5 ml Wasser gegeben. Bereits nach 5 Minuten beginnt das Produkt aus der Lösung auszukristallisieren. Zur Vervollständigung der Kristallisation lässt man den Ansatz ca. 2h bei 5°C stehen, trennt das Produkt von der Mutterlauge und wäscht mit EtOH und Et_2O (4,871 g, 19,6 mmol, 98% Ausbeute). Das so erhaltene Produkt hat eine hohe Reinheit (> 98%), kann aber durch Umkristallisation aus Wasser weiter gereinigt (> 99%) werden (4,52g, 18,2 mmol, 91% Ausbeute).

Beispiel 2 betreffend $[N_2H_5]_2^+[N_4C\text{-}N{=}N\text{-}CN_4]_2^-{*}N_2H_4{*}H_2O$ (N:80,0%):

Dinatrium 5,5'-Azotetrazole $*5H_2O$ (5.803, 20 mmol) wird zu einer Lösung von 25 mL Hydrazinhydrat (Hydrazingehalt 64%) und 7,5 ml Wasser gegeben und auf 50°C bis 70°C erhitzt. Zu dieser Lösung gibt man auf einmal Hydraziniumchlorid (2,74g, 40 mmol) und rührt die erhaltene Mischung bei ca. 75°C, bis eine klare rot-orangefarbene Lösung entstanden ist. Die Kristallisation des Produktes erfolgt in Form von feinen gelben Nadeln bei – 18°C meist innerhalb von 2h. Die Kristalle werden durch Saugfiltration von der Mutterlauge getrennt und mittels EtOH von anhaftenden Lösungsmittelresten befreit. Waschen mit Et_2O und Trocknung liefert $[N_2H_5]_2^+[N_4C\text{-}N{=}N\text{-}CN_4]_2^-{*}N_2H_4{*}H_2O$ in 98 % Reinheit (3,47 g, 70 % Ausbeute).

Beispiel 3 betreffend $[N_2H_5]_2^+[N_4C\text{-}N{=}N\text{-}CN_4]_2^-{*}0{,}5N_2H_4{*}0{,}5H_2O$ (N:82,4%):

Dinatrium 5,5'-Azotetrazole $*5H_2O$ (4,353, 15 mmol) wird zu einer Lösung von 20 mL Hydrazinhydrat (Hydrazingehalt 64%) und 2.5 ml Wasser gegeben und auf 50°C bis 70°C erhitzt. Zu dieser Lösung gibt man auf einmal Hydraziniumchlorid (2,055g, 30 mmol) und rührt die erhaltene Mischung, bis eine klare rot-orangefarbene Lösung

entstanden ist. Die Kristallisation des Produktes erfolgt in Form von feinen gelben Nadeln bei – 18°C meist innerhalb von 2h. Die Kristalle werden durch Saugfiltration von der Mutterlauge getrennt (3,32g, 13,5 mmol) und aus Hydraziniumhydrat umkristallisiert. Durch Saugfiltration und Waschen mit EtOH und Et_2O erhält man $[N_2H_5]_2^+[N_4C\text{-}N{=}N\text{-}CN_4]_2^-$ * $0{,}5N_2H_4$ * $0{,}5H_2O$ in 99 % Reinheit (2,12 g, 55 % Ausbeute). Aus den Mutterlaugen lassen sich weiter Produktfraktionen gewinnen, die allerdings in Gehalt an Hydrazin/Wasser variieren.

Beispiel 4 betreffend $[N_2H_5]_2^+[N_4C\text{-}N{=}N\text{-}CN_4]_2^-$*$1{,}5N_2H_4$*$0{,}5H_2O$ (N:82,9%):

Dinatrium 5,5'-Azotetrazole *$5H_2O$ (4,353, 15 mmol) wird zu einer Lösung von 25 mL Hydrazinhydrat (Hydrazingehalt 64%) und 1.5 ml Wasser gegeben und auf 50°C bis 70°C erhitzt. Zu dieser Lösung gibt man auf einmal Hydraziniumchlorid (2,055g, 30 mmol) und rührt die erhaltene Mischung bei 75°C, bis eine klare rot-orangefarbene Lösung entstanden ist. Die Kristallisation des Produktes erfolgt in Form von feinen gelben Nadeln bei – 18°C meist innerhalb von 2h. Die Kristalle werden durch Saugfiltration von der Mutterlauge getrennt (3,32g, 90% Ausbeute).

Beispiel 5 betreffend DAD (I) (N:85.7%):

Zu 15 mL Hydrazinhydrat (Hydrazingehalt 64%) wird Dinatrium 5,5'-Azotetrazole *$5H_2O$ (5.803, 20 mmol) gegeben und auf 50°C bis 70°C erhitzt. Zu dieser Lösung gibt man auf einmal Hydraziniumchlorid (2.74g, 40 mmol) und rührt die erhaltene Mischung bei 75°C, bis eine klare, rot-orangefarbene Lösung entstanden ist. Die Kristallisation des Produktes erfolgt in Form von feinen gelben Nadeln bei – 18°C innerhalb von 2h. Die Kristalle werden durch Saugfiltration von der Mutterlauge getrennt und mittels EtOH von anhaftenden Lösungsmittelresten befreit. Waschen mit Et_2O und Trocknung liefert $[N_2H_5]_2^+[N_4C\text{-}N{=}N\text{-}CN_4]_2^-$*$2H_2H_4$ in 99 % Reinheit (4,21 g, 85 % Ausbeute).

Beispiel 6 betreffend HZT (III):

HZT **(III)** wird quantitativ durch Ausheizen im Vakuum bei Temperaturen zwischen 80 und 110°C der nach obigen Verfahren hergestellten Salze des Typs $[N_2H_5]_2^+[N_4C\text{-}N{=}N\text{-}CN_4]_2^-$ * xN_2H_4 * yH_2O ($0 \leq x \leq 2$, $0 \leq y \leq 1$) erhalten. HZT (III) lässt sich mit Oxidatoren verreiben und pressen (z.B. ADN).

Beispiel 7 betreffend DAD (I):

DAD (I) wird in 75% Ausbeute durch Umkristallistation von HZT (III) aus Hydrazinhydrat (> 64%) erhalten. Eine Mischung von 10 g HZT und 15 g Hydrazinhydrat wird so lange erwärmt (70-90°C), bis eine klare gelb-orange Lösung entstanden ist. Beim Abkühlen (-5 °C) kristallisiert das DAD als feine gelbe Nadeln.

Im Gegensatz zu den traditionellen energetischen Materialien (z.B. TNT, RDX oder HMX) verdanken die in Rede stehenden Verbindungen [Stickstoffgehalt variiert zwischen 79.0% (**III**) und 85.7% (**I**)] ihre hohen Energieinhalte hauptsächlich ihren hohen positiven Bildungsenthalpien (**(I)**, 288 kcal/mol; **(III)**, 205 kcal/mol) und nicht der Oxidation des zugrunde liegenden Kohlenwasserstoffgerüsts. Zusätzliche Verwendungsmöglichkeiten sind gegeben als Zusatz für pyrotechnische Formulierungen und Raketentreibstoffe (Hydrazin, MMH, UDMH) sowie als gaserzeugende Komponente in Formulierungen für Gasgeneratoren. DAD (**I**), HZTH (**II)** und HZT (**III)** zeigen gegenüber den meisten Oxidatoren gute Beständigkeiten.

Als Oxidationsmittel können Nitrate, Perchlorate, Dinitramide von Ammonium, Natrium, Kalium, Magnesium, Calcium oder Eisen, und andere, vorzugsweise Ammonium Dinitramid (ADN) oder Peroxide von Zink, Calcium, Strontium oder Magnesium eingesetzt werden. In Bezug auf Treibmittel werden Peroxide dabei mit einem Sauerstoffwert eingesetzt, wie er aus stabilen Verbindungen erhalten werden kann. Für Zinkperoxid liegt dieser bei etwa 11 bis 14 Gew.-%. Das entsprechende Molverhältnis wird entsprechend dem Sauerstoffbedarf der jeweiligen Verbindung (I), (II) oder (III) angepasst und liegt dabei im Bereich von 1 : 2 bis 5,5. Calciumperoxid kann einen aktiven Sauerstoffwert von beispielsweise 18,62 Gew.-% aufweisen und wird vorteilhaft im Molverhältnis HEDM/Peroxid von 1 : 3 eingesetzt. Im allgemeinen können die oben genannten Peroxide im Molverhältnis 1 : 1 bis 20 eingesetzt werden. Es können Mischungen der Peroxide untereinander oder solche mit anderen Oxidationsmitteln eingesetzt werden. Andere Oxidationsmittel sind beispielsweise die oben erwähnten. Im Falle von DAD (I) und HZTH (II) kann es in Kombination mit diversen Oxidatoren zur vorübergehenden Verflüssigung aufgrund des im Kristall enthaltenen Hydrazins (I) bzw. Wassers (II) kommen. Bestimmte Mischungen verfestigen sich nach einer gewissen Zeit wieder (z.B. ADN als Oxidator) oder lassen

sich problemlos trocknen bei Temperaturen von vorzugsweise zwischen 60 und 110°C. Dabei entweicht Hydrazin bzw. Wasser und es bleibt im wesentlichen HZT (III) als Treibstoff wirkende Komponente zurück. Darüber hinaus scheint es für bestimmte Anwendungen zweckmäßiger zu sein, die Salze der Reihe $[N_2H_5]_2^+[N_4C\text{-}N{=}N\text{-}CN_4]_2^-$ $*xN_2H_4*yH_2O$ ($0 \leq x \leq 2$, $0 \leq y \leq 1$) einzusetzen, da HZT (III) eine etwas erhöhte Schlagempfindlichkeit aufweist.

Bei Einsatz von sauer reagierenden Oxidatoren (selten bei basich reagierenden) oder anderen sauer (selten bei basich reagierenden) reagierenden Zusätzen kann es zu Reaktionen mit den Verbindungen (I), (II) oder (III) kommen. Hier ist eine Beschichtung der entsprechenden Komponenten mit anorganischen oder organischen Materialien nach an sich bekannten Verfahren zweckmäßig.
Aufgrund des hohen Stickstoffgehalts der Verbindungen (I), (II) und (III) entstehen im Gemisch, mit oder ohne Oxidator, bei der thermischen/chemischen Umsetzung hauptsächlich N_2 und H_2O, neben wenig CO_2 (schlecht detektierbare Signatur). Die Emissionen von energetischen Stoffen, insbesondere die von gesundheitsgefährdenden Gasen, dürfen bestimmte Grenzwerte der verschiedensten nationalen wie auch internationalen Regelwerke nicht überschreiten. Verbindungen mit hohem Stickstoffgehalt, wie die Verbindung (I), (II) oder (III), können hierzu entscheidend beitragen.

Zusammenfassung

Verfahren zur Herstellung von Explosivstoffen

Es soll ein neues Verfahren zur Herstellung von stickstoffreichen Explosivstoffen geschaffen werden, welches effizient arbeitet und bei dem solche Edukte eingesetzt werden, die eine großtechnische, gefahrlose Synthese ermöglichen.

Das neue Verfahren dient der Herstellung einer Verbindung der Reihe Dihydrazinium 5,5'-Azotetrazolat * x-Hydrazinat * y-Hydrat ($0 \leq x \leq 2$, $0 \leq y \leq 1$). Dabei wird die Verbindung als Produkt aus der Reaktion der beiden Edukte Alkalimetall 5,5'-Azotetrazolat und Hydraziniumsalz erhalten.

Fig. 1

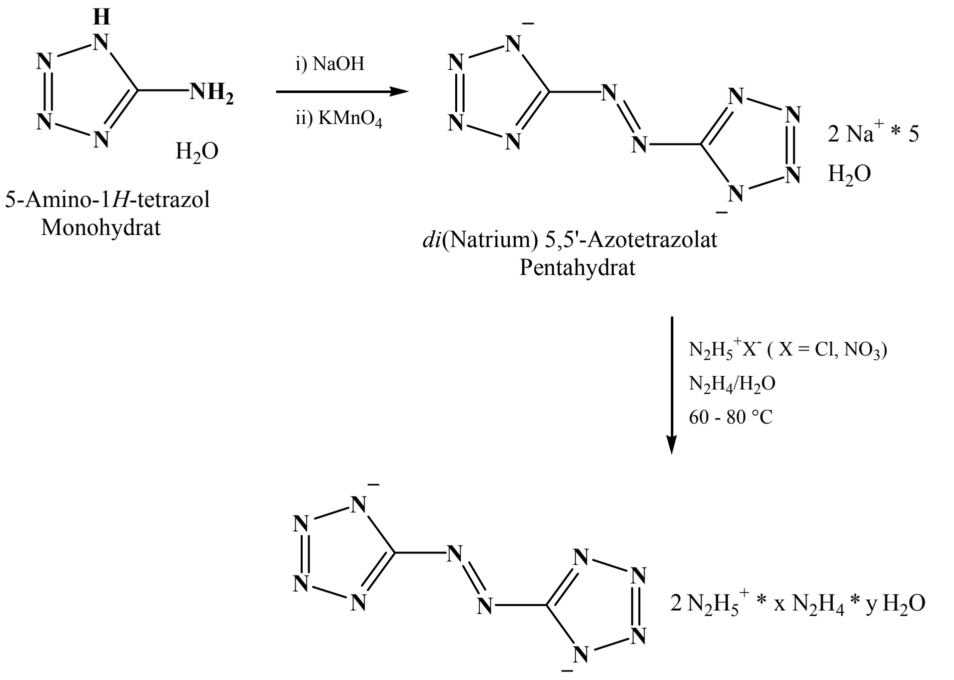

di(Hydrazinium) 5,5'-Azotetrazolat Dihydrazinat (**DAD 1**) x = 2, y = 0

di(Hydrazinium) 5,5'-Azotetrazolat Monohydrat (**HZTH** 2) x = 0, y = 1

Fig 2.

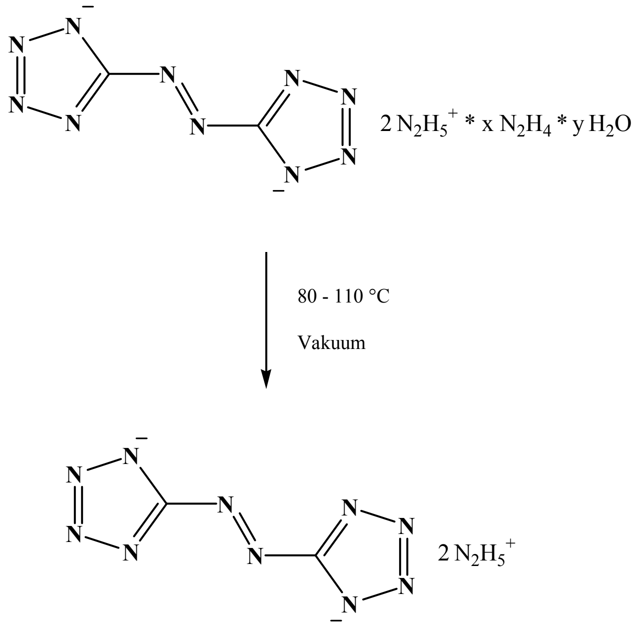

di(Hydrazinium) 5,5'-Azotetrazolat (**HZT 3**)

Fig 3.

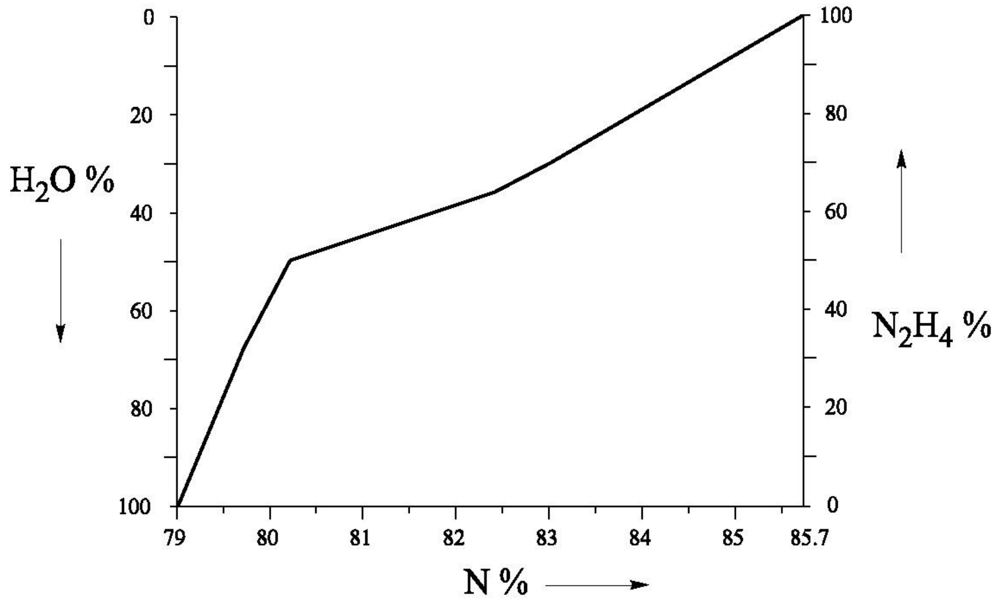

3.3 High Temperature and Pressure FTIR study of **DAD** (**28**)

Hydrazinium **DAD** (**28**) sample were sent to Dr. Kerry A. Clark and Dr. Jared C. Gump from the Indian Head Division, Naval Surface Warfare Center in order to evaluate the stability of DAD towards high temperature and pressure in a Hydrothermal Diamond Anvil Cell (HDAC), monitored by means of FTIR measurements. The sample consisted of yellow rod-like crystals on the order of 150-200 μm in length and approximately 50 μm wide.

3.3.1 Experimental Method

A Hydrothermal Diamond Anvil Cell (HDAC) developed by Bassett[61] was used to compress and heat the sample (*Figure 2.9*). The basic design of this cell consists of two brilliantly cut diamonds with their culets polished flat. The diamonds are positioned so that the culets are facing each other. Heating coils are placed in contact with the table end of each

diamond to provide the heat source and thermocouple tips are placed close to each culet end to monitor the temperature. A metal gasket with a hole in it is inserted between the two diamond culets. The sample is placed inside the gasket hole, and pressure is applied by tightening three screws positioned around the cell, which draws the diamonds together. The HDAC used in these experiments had two type I diamonds. Inconel 600 (nickel-chromium alloy) was used as the gasket material.

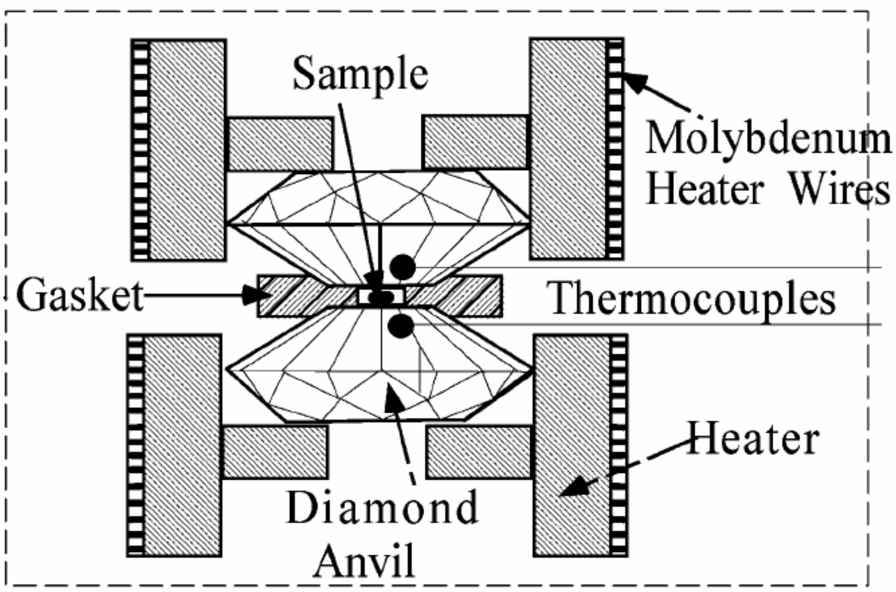

Figure 2.9. Bassett-type HDAC experimental setup; ref [61]

Pressure in the HDAC was monitored using the ruby fluorescence technique.[62] A piece of ruby is placed inside the gasket hole along with the sample. When the pressure of the cell is increased, Raman spectroscopy can be used to observe shifts in the ruby R1 and R2 fluorescence lines. The sensitivity of these lines to pressure is well characterized, which allows the pressure on the sample to be determined.[62]

The FTIR used in these experiments is a ThermoNicolet Nexus 870 spectrometer. The detector was a liquid nitrogen cooled MCT-A detector. The number of scans for each spectrum was 200 with a resolution of 4. A background image was collected from the HDAC cell with no gasket and no sample. This background spectrum is shown in *Figure 2.10*. Due to the natural absorption of a type I diamond, the region from approximately 1100 cm^{-1} to 1335 cm^{-1} is not accessible.[63]

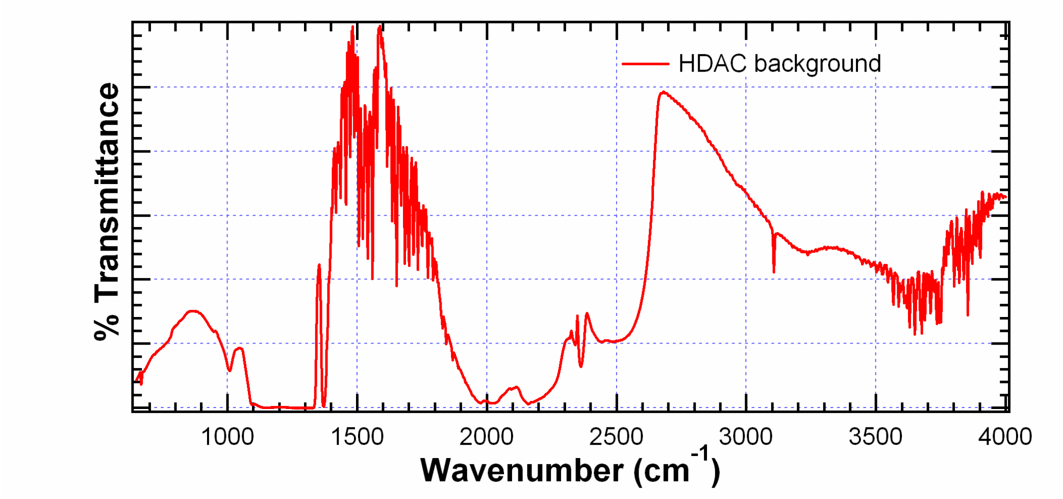

Figure 2.10. Background file from the HDAC with no gasket and no sample. The transmittance spectrum is typical for a type I diamond

3.3.2 Experimental Results

An initial experiment was performed with a 250 μm diameter, 127 μm thick gasket hole. The sample was packed into the hole along with a ruby piece. The IR signal was not able to penetrate this volume of sample. With an increase in pressure some signal was able to penetrate the sample, however the gasket had deformed, limiting any further pressure increase.

To allow more signal to pass through the cell at a lower pressure, the initial gasket thickness was decreased by pre-indenting a 400 μm diameter gasket until the hole closed, then a new hole with a 150 μm diameter was drilled. The original gasket thickness was 127 μm. The thickness of the gasket was found to be unmeasurable, but likely to be in the order of 60-70 μm. The new hole was loaded with sample and a piece of ruby. Without pressure there was still no signal penetrating. Upon increasing pressure the sample began to become visibly more transparent, but very little IR signal was getting through. As pressure continued to increase the sample began to appear darker. The pressure was realized, and it was found that the sample had become visibly much more translucent even at low pressure. From that sample, IR spectra were recorded while the pressure was increasing again. The spectra from the resulting experiment can be depicted from *Figure 2.11*.

There are two regions in *Figure 2.11* where the absorbance is saturated. The region from 1100 cm^{-1} to 1335 cm^{-1} is expected to be saturated in an absorbance plot because of the absorption from a type I diamond. The region from ~ 2000 cm^{-1} to 2300 cm^{-1} is also a region of

high absorption for the type I diamond.[63] Outside of the regions of maximum absorbance multiple peaks are visible. Several of these peaks show changes with pressure. *Table 2.4* lists the peaks that shift position with pressure.

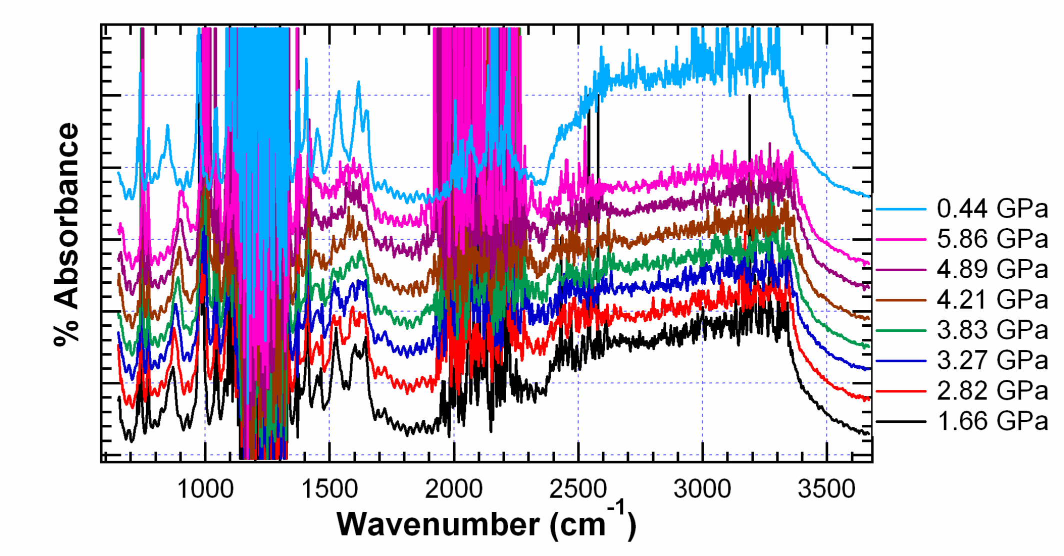

Figure 2.11. Room temperature pressure increase after a previous pressure cycle

All of these peaks move to a higher energy position with an increase in pressure. The total shift over the 4.2 GPa from the initial pressure of 1.66 GPa to the maximum pressure of 5.86 GPa is also shown in *Table 2.4*. Clearly the peak originally at 869 cm^{-1} shows the largest change with pressure. The peak labeled as 985 cm^{-1} is actually a group of peaks that are difficult to distinguish from each other, so the peak's position is a best estimate of the center of the group.

Table 2.4. Peak positions and total shifts for peaks moving with pressure from *Figure 2.11*

Peak Position @ 1.66 GPa	Peak Position @ 5.86 GPa	Total shift over 4.2 GPa
727	732	5
740	748	8
869	904	35
985 (center of group)	1000	15
1049	1056	7
1409	1417	8
1463	1481	18

Besides position changes with pressure, it is noteworthy note that the overall quality of the spectra decreased with increasing pressure. By 5.68 GPa several peaks were no longer able to be resolved due to the increase in background noise.

After reaching a pressure above 5 GPa, the cell was decompressed to determine if the changes due to pressure were reversible. Upon full decompression to room pressure the sample darkened due to grain boundary formation. The pressure was increased to 0.44 GPa to remove grain boundary distortion and "clear" the sample. The decompressed spectrum is represented in *Figure 2.11* by the pattern labeled at 0.44 GPa. The peaks that had shifted to higher energy positions with an increase in pressure did return to positions of lower energy upon decompression. The signal-to-noise level also improved once the pressure was released.

Because this sample was still loaded in the high temperature cell and was now giving strong IR signals, the pressure was left at 0.44 GPa and the temperature was increased. *It is important to note that at this point the sample had already been through two pressure cycles.* The temperature was increased at an approximate rate of 4 ^{o}C /min. Initially a scan was taken after every 5 ^{o}C increase up to 60 ^{o}C. No apparent changes were observed, so the next scan was taken after stabilizing and holding at 70 ^{o}C for one hour.

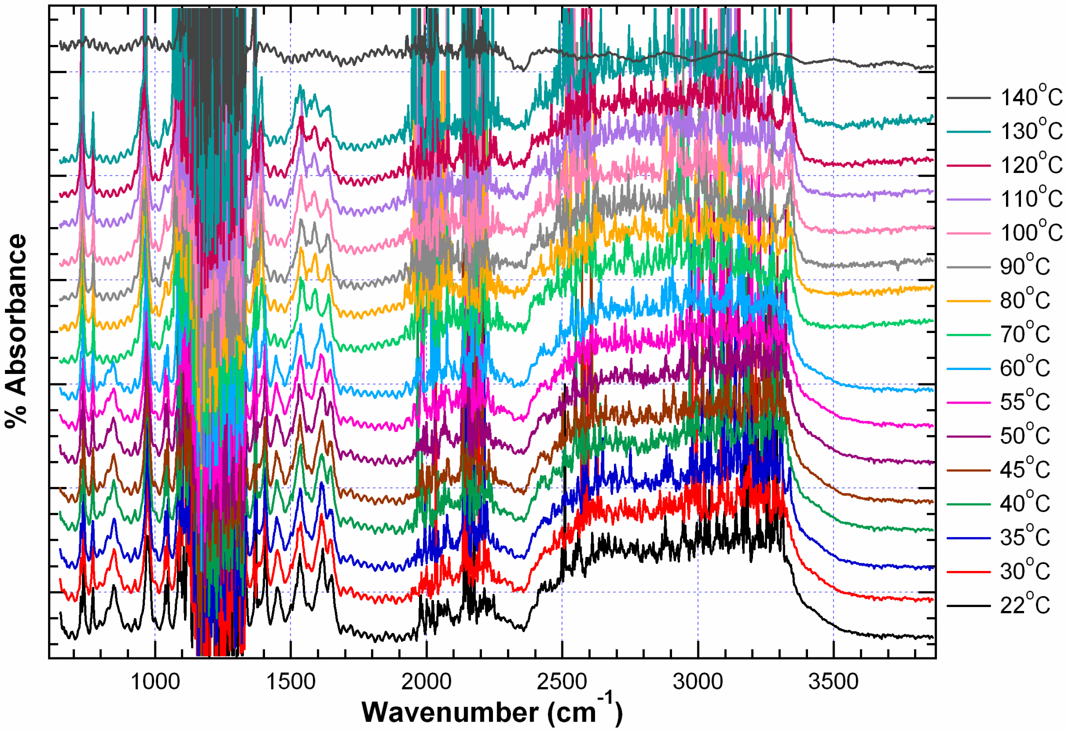

Figure 2.12. Spectra from temperature increase after sample has undergone two pressure cycles and was left at 0.44 GPa. The heating rate was ~4 ^{o}C/min. The sample was held at 70 ^{o}C from one hour before the 70 ^{o}C spectrum was taken.

Three changes were apparent in the 70 °C scan. First, the peak at 848 cm^{-1} was no longer visible above the background noise. Second, the peak at 1452 cm^{-1} also was no longer visible. Finally, the peak originally at 1612 cm^{-1} appeared to shift to a lower energy position at 1587 cm^{-1}. The temperature was again increased at a rate of ~ 4 °C min^{-1} and scans taken at every 10 °C increment. No further changes occurred until the sample thermally decomposed between 130 °C and 140 °C. The spectra from this experiment are shown in *Figure 2.12*.

For the next two experiments, a Merrill-Bassett diamond anvil cell without heating capability was used in order to simplify sample loading and to try to get a couple pressure-only measurements. The gasket for the first cell was pre-indented and redrilled to a 250 μm hole diameter. The sample was packed into the hole along with a piece of ruby. The pressure was increased in the cell until a signal was received by the FTIR detector through the sample. At this point the pressure was already at 6.1 GPa. The spectrum is shown in *Figure 2.13*. At 6.1 GPa the spectrum has a lot of noise.

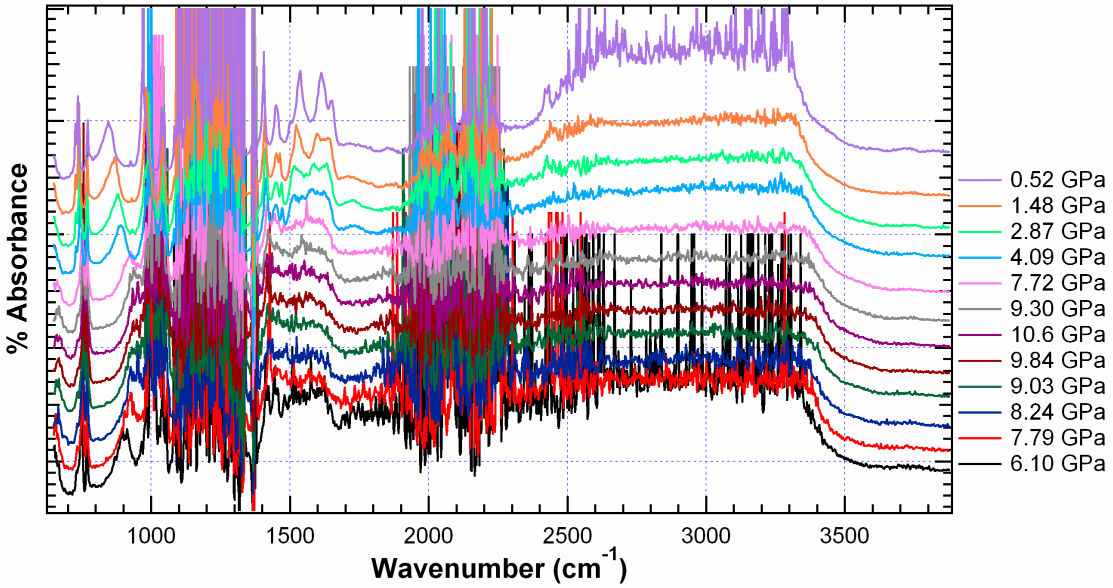

Figure 2.13. Compression and decompression cycle at room temperature

While most of the peak regions that were visible in the first experiment can be seen here, several of the individual peaks are not distinguishable above the noise. This seems to be most apparent from about 1500 cm^{-1} and higher. With an increase in pressure the same peaks from

the first experiment that shift to higher wavenumber with an increase in pressure appear to follow the same trend here. Decompression was performed in smaller steps for this sample. *Table 2.5* lists the shifts for the same peaks that were in *Table 2.4*, except this time the positions are taken from maximum pressure to minimum decompression pressure because all of the peaks become visible on decompression. There is one new peak that appears at the extreme low end of the wavenumber scale. It moves into the detectors range above 6 GPa, but since it is not always visible, it is not included on *Table 2.5*.

Table 2.5. Peak positions and total shifts for peaks moving with pressure from *Figure 2.13* during decompression

Peak Position @ 10.6 GPa	Peak Position @ 0.52 GPa	Total shift over 10.08 GPa
738	727	11
755	736	19
952	846	106
(center of group) shifting but too much noise	970	−
1066 (weak)	1046	20
1419	1405	14
1457 (weak)	1450	7

The second pressure experiment using the Merrill-Bassett cell had a pre-indented gasket with a 150 μm diameter hole. For this sample, some IR signal was reaching the detector by 0.64 GPa. From *Figure 2.14* it is evident that there is still a lot of absorption occurring, but some of the peaks that shift with pressure are already visible. Upon increasing the sample pressure, the shifting of peaks to higher energy is again observed, as well as an increase in the noise. Upon decompression, the noise reduces and the peaks return to their original positions. For *Table 2.6*, only the three lowest energy peaks are shown because they remain distinguishable from the noise.

Table 2.6. Peak positions and total shifts for the three lowest energy peaks moving with pressure from *Figure 2.14* during compression

Peak Position @ 0.64 GPa	Peak Position @ 9.37 GPa	Total shift over 8.73 GPa
726 (weak)	732	6
736	754	18
846	925	79

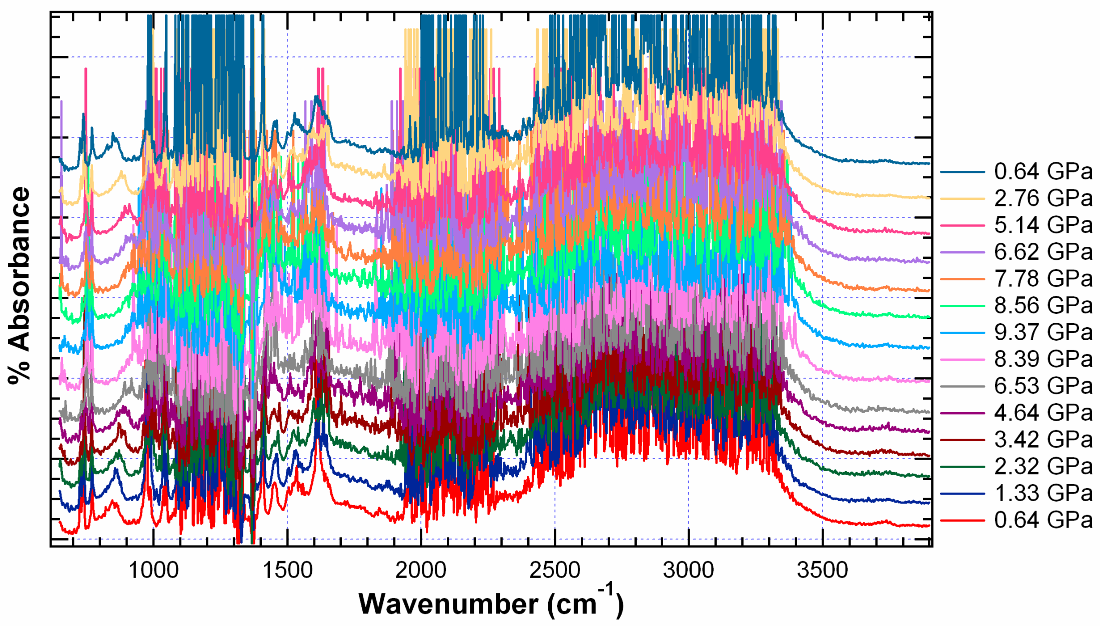

Figure 2.14. Compression and decompression cycle at room temperature

The last three experiments were all performed in the HDAC with temperature. In all three experiments the gasket was pre-indented and redrilled to a hole size of 150 μm in diameter. For the first experiment, the pressure on the sample was increased in steps to 2.12 GPa. The temperature was then increased at ~ 4 ^{o}C min^{-1} without actively changing the pressure. Due to thermal expansion effects the lattice may expand and increase the pressure inside the cell as the temperature increases. With the current experimental set-up, it is not possible to monitor the pressure while the cell is being heated inside the FTIR. Once the cell was cooled and removed from the FTIR, a final pressure reading was taken. For this experiment the cell did not return to 2.12 GPa after cooling, but registered a pressure of 5.37 GPa.

Spectra were collected at 10 ^{o}C intervals. A graph of the spectra is shown in *Figure 2.15*. Clearly there is a lot of noise, especially at the high wavenumber end of the spectra. Increasing the temperature tended to increase the noise level. From the peaks that can be distinguished from the noise, it appears that the temperature has little effect on peak position. In comparison with the results from the temperature experiment shown in *Figure 2.12*, it appears that the same two peaks which disappeared in that experiment at 70 ^{o}C also disappear in this experiment, but at a higher temperature (~100 ^{o}C). It is more difficult to determine whether the peak which shifted position in *Figure 2.12* has done so for this experiment due to the high level of noise in that region. Also of note is the fact that the sample did not thermally decompose even by 170 ^{o}C.

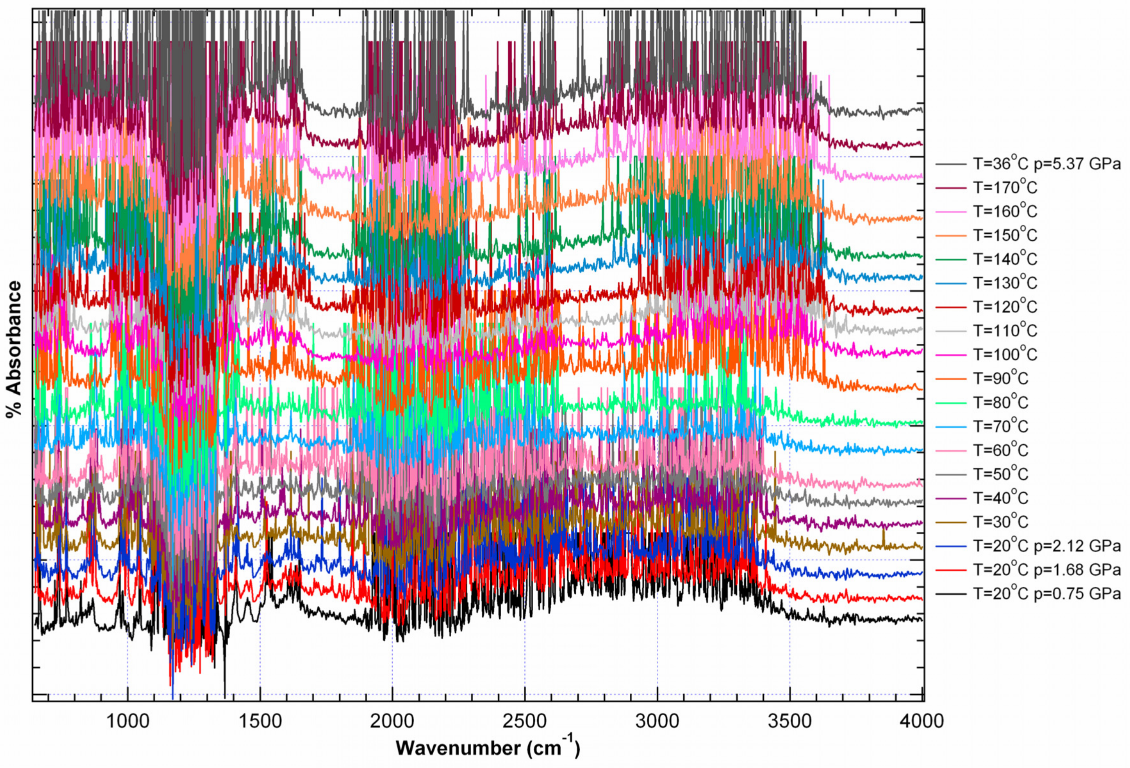

Figure 2.15. Spectra from temperature increase where the pressure was initially set to 2.12 Gpa. The heating rate was ~4 °C/min. Upon cooling the pressure was measured to be 5.37 GPa

The next temperature experiment was performed in the same manner as the last one except that the pressure was initially increased to 5.25 GPa. Once again, the final pressure after cooling was not 5.25 GPa but 8.27 GPa. For this experiment, the higher initial pressure and the noise from the temperature increase makes it difficult to say with certainty whether the two peaks (originally at 857 cm^{-1} and 1149 cm^{-1} at 0.96 GPa) disappear with increasing temperature. Upon cooling, the spectrum clears slightly, and the peak originally at 857 cm^{-1} is visible. For this sample, a spectrum was taken after releasing the pressure, and both peaks (now at 852 cm^{-1} and 1452 cm^{-1}) are visible. Also the sample did not thermally decompose by 140 °C. Spectra from this experiment can be seen in *Figure 2.16*.

The final set of temperature experiments performed was used to determine an approximate temperature for thermal decomposition under ambient pressure. In order to achieve ambient pressure conditions even at high temperatures in the cell, only a small amount of sample was placed in the gasket hole with air gaps present. No ruby was used in this

experiment. The spectra showed almost total absorption until decomposition occurred. The background began to reduce by 120 °C, and by 130 °C the sample had fully decomposed.

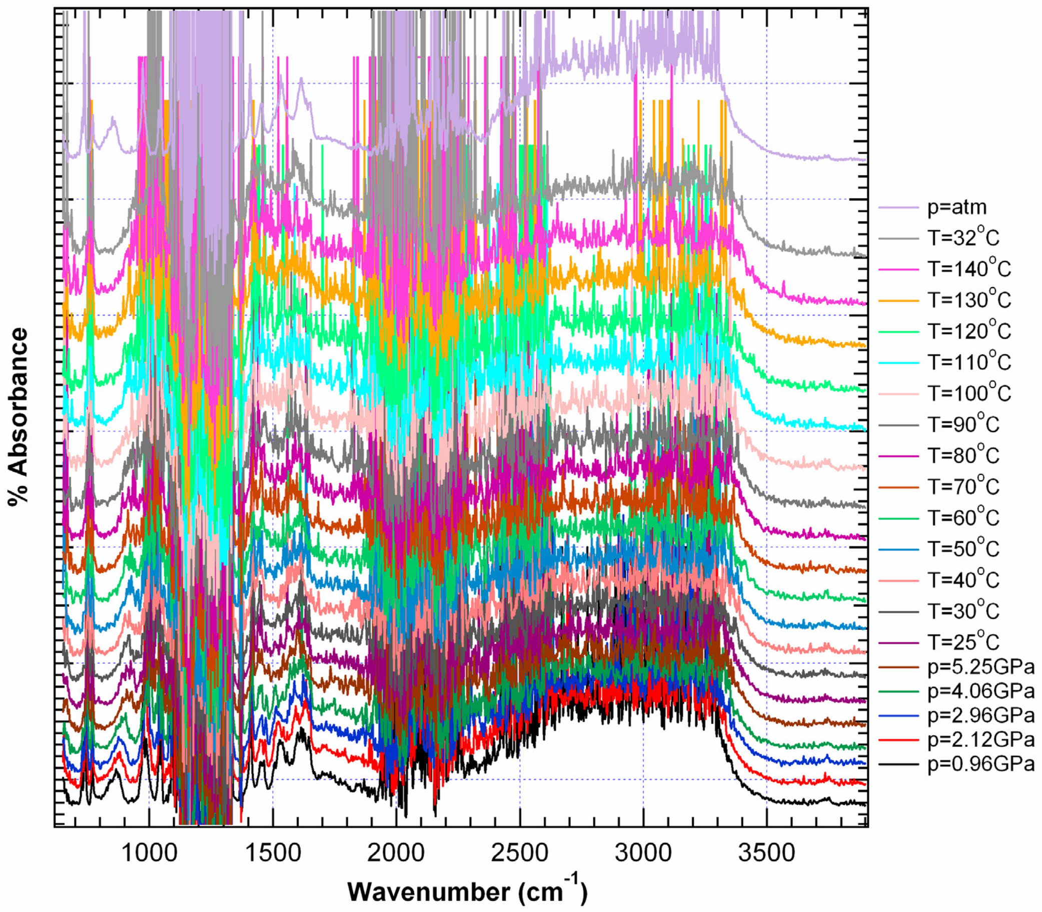

Figure 2.16. Spectra from temperature increase where the pressure was initially set to 5.25 GPa. The heating rate was ~4 °C/min. Upon cooling the pressure was measured to be 8.27 GPa. A final spectrum was obtained at room temperature and pressure.

There was one final spectrum taken of the sample placed directly between the diamond faces with no gasket. This loading allowed the sample to extrude out towards the side of the cell creating the thinnest possible sample layer. This should provide the maximum amount of IR signal through the sample. There is a small amount of pressure on the sample under these conditions. The resulting spectrum is shown in *Figure 2.17*. The typical absorption region from the type I diamond is still apparent from 1100 cm^{-1} to 1335 cm^{-1}. This spectrum shows much more detail in the higher wavenumber region above 2000 cm^{-1}.

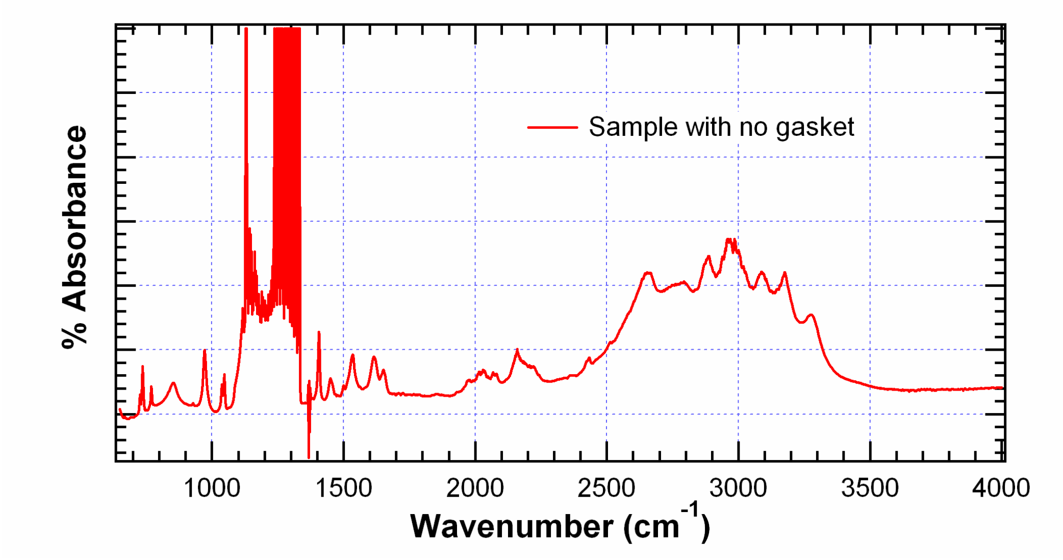

Figure 2.17. Spectrum from a sample with no gasket

3.3.3 Discussion

Identification of the peaks appearing in *Figure 2.17* provides a more useful interpretation of the data obtained in this study. Some comparison with published infrared spectra allows for certain regions to be assigned to specific vibrational modes. The dominant spectral features appear in the region of 3300 cm^{-1} to 2600 cm^{-1}. This region is most likely associated with the stretching vibration of the primary amine salts (NH_3^+), which is reported to have strong, broad absorption from 3200-2800 cm^{-1}. The smaller peaks appearing between 1500-1700 cm^{-1} may be related to the asymmetric and symmetric deformation vibrations of NH_3^+ reported to be around 1625-1560 cm^{-1} and 1550-1505 cm^{-1} respectively. The small, broad peak around 850 cm^{-1} can reasonably be identified as the out-of-plane NH deformation vibration, which is reported to be a broad, medium strong peak appearing around 800 cm^{-1}. Secondary evidence for the assignment of the NH deformation vibration to the 850 cm^{-1} peak comes from the IR data on hydrazinium azotetrazolate. As opposed to the hydrazinium azotetrazolate hydrazinate spectrum, the hydrazinium azotetrazolate spectrum does not show a peak in this region. As the NH deformation would be due to the hydrazinate, it logically follows that if the 850 cm^{-1} peak is from an NH deformation that it should be absent in the hydrazinium azotetrazolate spectrum, which it is.

The pressure data clearly show that the peak most influenced by a change in pressure is the out-of-plane NH deformation (NH d_{op}) peak. Upon increasing pressure, the NH d_{op} peak is shifted to higher energies. A plausible physical interpretation of this phenomenon would be that

as the increase in pressure draws the molecules closer together they will tend to compress perpendicular to the most planar axis, forcing any out-of-plane components to be under a greater strain than components in the plane. Therefore, it is reasonable to assume that being an out-of-plane vibration, NH d_{op} would be influenced to a greater degree by pressure than other vibrations aligned along the plane. The reversibility of the shift upon decreasing pressure implies that no permanent deformation of the molecule occurred up to the maximum pressure attained.

The temperature data appear to show little influence on peak position. The largest change in peak position with temperature was an abrupt jump of the peak around 1612 cm^{-1} to 1587 cm^{-1} when the sample temperature changed from 60 ^{o}C to 70 ^{o}C. Accompanying this jump was the disappearance of the peaks at 848 cm^{-1} (believed to be the NH d_{op}) and 1452 cm^{-1}. The peak jump was not distinguishable from the background noise in the two subsequent temperature scans. The two peaks disappearing did appear to occur when the cell was left at 2.12 GPa and the temperature was increased, but most likely did not occur when the cell was left at 5.25 GPa the temperature was increased. The disappearance of the two peaks could be associated with the removal of the hydrazinate at elevated temperatures. An increase in pressure on the sample may be able to stabilize the hydrazinate in the molecule so it can withstand the temperature increase. This would be a logical extension of the fact that the peak disappeared at a higher temperature when held at 2.12 GPa than at 0.44 GPa. The fact that the sample did not thermally decompose at 130 ^{o}C when held above 2 GPa seems to imply that the molecule as a whole may become more thermally stable at increased pressure.

This is also in accordance with the variable temperature experiments, where the temperatures were increased by 10 ^{o}C increments. The pressures listed on the *Figure 2.18* are the pressures the cells registered before the temperature was increased. Pressure is likely to increase as the temperature is increased due to thermal expansion. Decomposition only occurred for two of the four temperature experiments. At ambient pressure, the spectra showed almost total absorption due to grain boundary scattering until decomposition occurred. The background began to reduce by 120 ^{o}C, and by 130 ^{o}C the sample had fully decomposed. For the 0.44 GPa experiment, full decomposition occurred at 140 ^{o}C. The 2.12 and 5.25 GPa pressure experiments did not decompose by the maximum temperature obtained in their experiments (170 ^{o}C and 140 ^{o}C, respectively), when the cell began to lose temperature stability. The HDAC should be able to achieve temperatures above 200 ^{o}C, but in practice

mechanical failures often inhibit this performance. So at this point, the only conclusion which can be drawn from the pressure experiments above 0.44 is that the decomposition temperature is above the maximum obtained temperature (*Figure 2.18*).

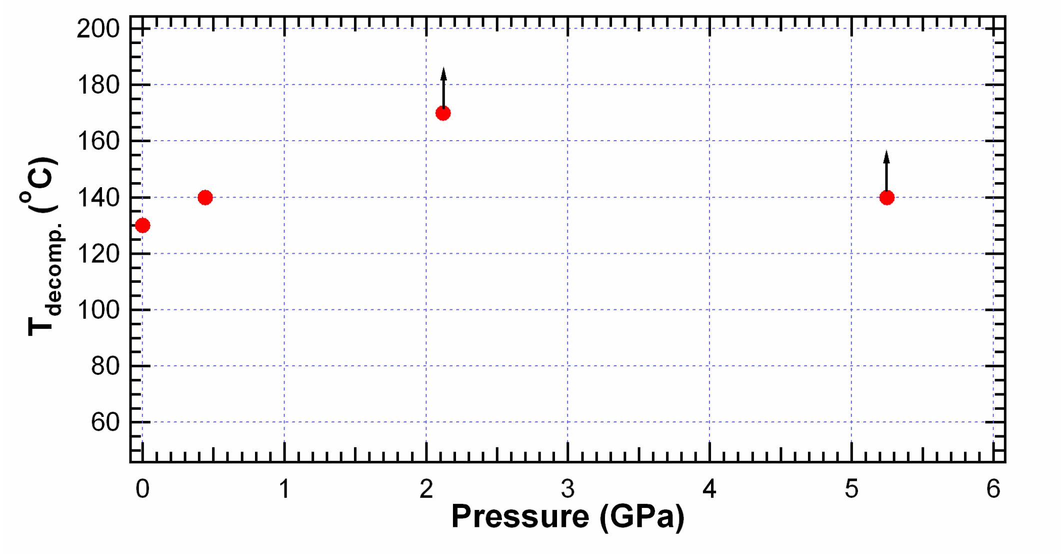

Figure 2.18. Decomposition temperature versus pressure. The 2.12 and 5.25 GPa points have arrows denoting that the decomposition temperature is higher than the temperature shown

3.3.4 Conclusion

Samples of **DAD** were studied with FTIR spectroscopy under various temperature and pressure conditions. An increase in pressure at ambient temperature caused several of the IR peaks to shift towards higher energy. The largest shift occurred for the peak associated with the NH out-of-plane deformation vibration, implying that an increase in pressure imparts stress to that bond as it most likely is forcing it into the plane of the molecule. All of the peaks that shifted under compression would return to their previous positions under decompression.

Increasing the temperature of the sample at room pressure produced thermal decomposition at about 130 °C. Due to scattering of the IR light by grain boundaries, the IR spectra of the sample at ambient pressures showed almost uniform absorption. Therefore, IR spectra from temperature experiments could only be obtained with some initial pressure applied. Temperature experiments were performed at 0.44, 2.12 and 5.25 GPa. Only the 0.44 GPa experiment showed thermal decomposition, and this occurred at about 140 °C. An increase in temperature influenced peak position very little, but the 0.44 and the 2.12 GPa temperature experiments showed the disappearance of two peaks, one of which is the peak associated with

the NH out-of-plane deformation vibration. These peaks did not disappear during the 5.25 GPa temperature experiment. This fact, plus the absence of thermal decomposition at 140 °C for the two higher pressure temperature runs, suggests that an increase in pressure may enhance the thermal stability of the hydrazinium azotetrazolate hydrazinate molecule.

4. STANAG 4147 and 4582

NATO standardisation agreements (STANAG) on the thermal ("chemical") stability of propellants describe mutually acknowledged test procedures to facilitate cross procurement by avoiding repeated testing in different countries. The most important standard, which describes the testing and assessment of chemical compatibility, is STANAG 4147.[64] According to this standard, the purpose of a compatibility test is "to provide evidence that a material may be used in an item of ammunition without detriment to the safety or reliability of an *explosive* with which it is in contact or proximity". The individual compatibility tests are based on the different effects/phenomena, means: Chemical reactions between *explosive* and contact material can, on the *explosive*, increase the rate of binder degradation, stabilizer depletion, heat and gas production and weight loss. Furthermore, the sensitivity of the *explosive* can be increased. On the other hand, also chemical reactions on the contact material can be initiated, such as post curing and decomposition of binders and corrosion process in container materials.

At the moment the STANAG is under revision, since in particular vacuum stability test (VST), heat flow calorimetry test (HFC) and stabilizer depletion test artificially age relatively large amounts (several grams) of explosive, contact material and mixture under sealed (ammunition-like) conditions. All three tests are perfectly suitable for nitrocellulose-based propellants; the VST and HFC tests are also suitable for *high explosive* and *composite propellants*. Due to the large sample masses, however, testing of primary explosives and pyrotechnics is too dangerous with these methods.

On the other hand, thermogravimetric analysis (TGA) and differential scanning calorimetry (DSC) uses very small samples (several milligrams). They are therefore suitable for the testing of *primary explosives* and *pyrotechnics*, whereas their applicability for propellants must be questioned.

In principal HFC methods are suitable to measure the quantity that can lead to thermal explosion, offering a more direct method. Moreover, interrupting an HFC experiment shortly

before an autocatalytical reaction starts allows the determination of relevant limits for the stabilizer consumption methods by analysis. In this contrast, the STANAG 4582 sets the basis for realistic and scientific proven tests times/temperatures than other 'stability STANAGs' (stabilized depletion, vacuum stabiliy). STANAG 4582 is suitable for explosives − NC based propellants stabilized with DPA (diphenylamine) by means of heat flow calorimetric measurements. Only the HFC allows a free choice of test temperature and corresponding test duration. It is based on an Arrhenius extrapolation to 10 years self life at 25 °C by assuming an activation energy of 28.7 Kcal mol^{-1} above 60 °C and 19.1 Kcal mol^{-1} below this temperature.[65]

The compatibility of **TAGZT**, **HZT** and **HZTH** with certain propellant charges "TLPs" has been tested by the WIWB (Dr. Wilker) according STANAG 4582. **TAGZT**, **HZT** and **HZTH** have been microcalorimetrically (HFC) tested as single component and as composite with different TLPs (STAB-0-DPA, STAB-15-DPA, STAB-30-DPA).[66] STAB-0-DPA is a single and STAB-15/30-DPA a double gelatinized-based (NC based) propellant without any additional components, such as graphite, phlegmatizer or plasticizer. STAB-15-DPA and STAB-30-DPA contains diphenylamine (DPA) as stabilizer.

4.1 Compatibility tests of **HZT** a. **HZTH** with TLPs

In the HFC, measurements at 80 °C are performed with the pure test materials and in combination with the corresponding TLPs (STAB-0-DPA, STAB-30-DPA). The sample amounts of **HZT** and **HZTH** are summarized in *Table 2.7*. The test substances have not been incorporated into the TLPs, therefore, any interactions are only possible on the surfaces.

Table 2.7. Measured samples and sample amount

substance	TLP→	STAB-0-DPA	STAB-30-DPA
	single component	mixture	mixture
HZTH	724 mg	TLP 2166 mg, HZTH 412 mg	TLP 2358 mg, HZTH 382 mg
HZT	443 mg	TLP 2327 mg, HZT 345 mg	n. g.
STAB-0-DPA	2886 mg	-	-
STAB-30-DPA	2939 mg	-	-

n.g. = not measured

Table 2.8 summarizes the evolved energy and the evaluated measurement time. According to STANAG 4582, the required measurement time is 10.6 days at a temperature of 80 °C. For the evaluation of the stability of the mixtures the maximum heat flow accounts 114 μW g^{-1} at 80 °C. In all cases, the required measurement time could not be realized, since all mixtures did not show the required stabilities. In the case of **HZTH**/STAB-30-DPA, due to security reasons and to protect the corresponding measurement channel (explosive decomposition), the experiment was aborted already after 0.6 days.

Table 2.8. Evolved energy and evaluated measurement time

substance	TLP→	STAB-0-DPA	STAB-30-DPA
	single component	mixture	mixture
HZTH	14 J/g (5 d) 0.5 J/g (0.6 d)	82 J/g (5 d)	11 J/g (0.6 d)
HZT	58 J/g (5 d)	95 J/g (5 d)	n. g.
STAB-0-DPA	7 J/g (5 d)	-	-
STAB-30-DPA	14 J/g (5 d) 3.3 J/g (0.6 d)	-	-

n.g. = not measured

The maximum heat flow of every experiment is summarized *Table 2.9*. In the case of the TLPs and **HZTH,** the expected maximum heat flow is less than the maximum value of 114 μW g^{-1} at 80 °C, but **HZT** is more than three times higher in value than the limit, indicating already that this compound does not have even as pure substance the required stability.

Table 2.9. Maximum heat flow [μW g^{-1}]. Heat flow of the first Maxima are not recognized (within a value of 5 J g^{-1})

substance	TLP→	STAB-0-DPA	STAB-30-DPA
	single component	mixture	mixture
HZTH	26	367	259
HZT	350	360	n. g.
STAB-0-DPA	12	-	-
STAB-30-DPA	60	-	-

n.g. = not measured

The analysis of the compatibility is summarized in *Table 2.10.* The limit of the interreaction heat (Q_R) has to be lowered from 30 J g^{-1} to 14.2 J g^{-1} since only 5 days measurement time could be realized (extreme gas evolution) compared to the required 10.9 days. The limit of D = mixture / $mixture_{theo}$ is 3.0 and **HZTH** as well as **HZTZ** exceeds this value, indicating the incompatibility with the tested TLPs.

Tabelle 2.10. Compatibility of **HZT** and **HZTH** toward STAB-0-DPA; t = 5 days

	single component	mixture	mixture theo.	Q_R	D
	[J/g]	[J/g]	[J/g]	[J/g]	[-]
HZTH	14	82	12	70	6,8
HZT	58	95	18	77	5,3
STAB-0-DPA	12	-	-	-	-

The corresponding thermographs of the experiments are depicted in *Figure 2.19* and *Figure 2.20.*

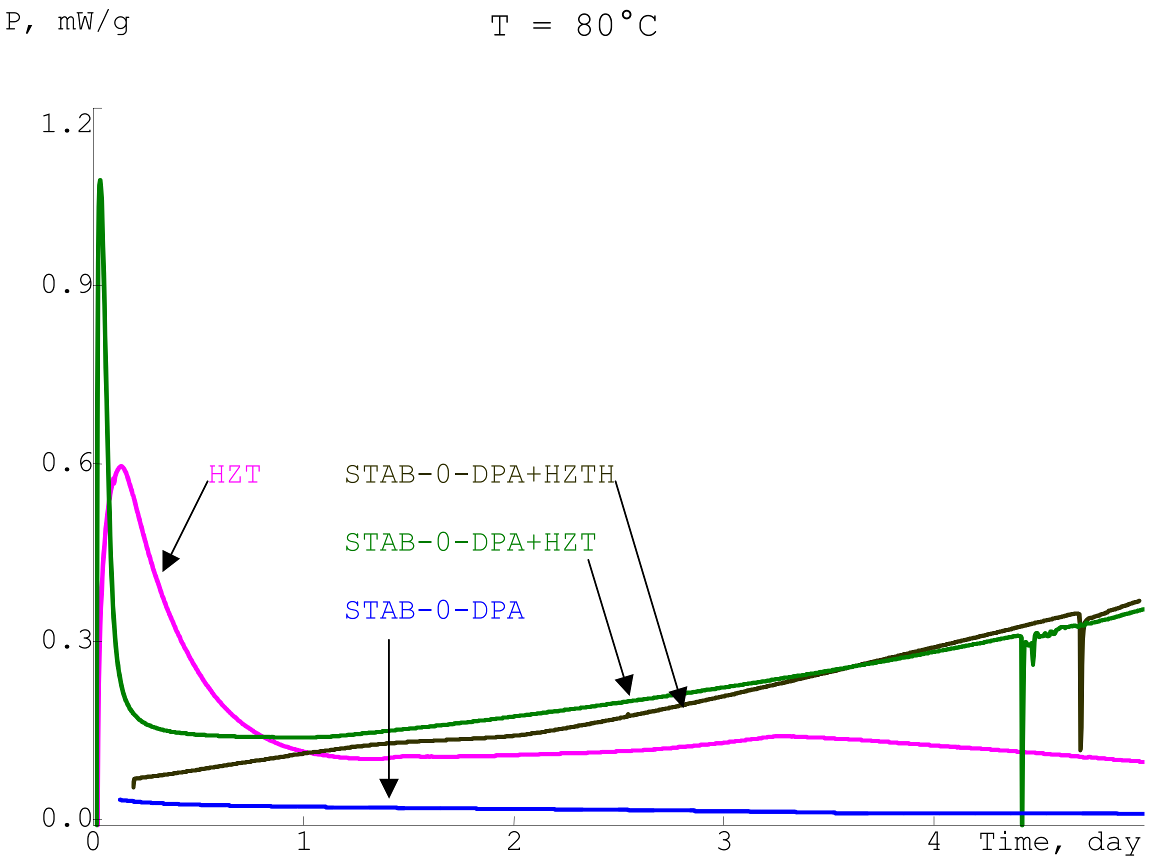

Figure 2.19. **HZT**, STAB-0-DAP and mixture and STAB-0-DPA + **HZTH**

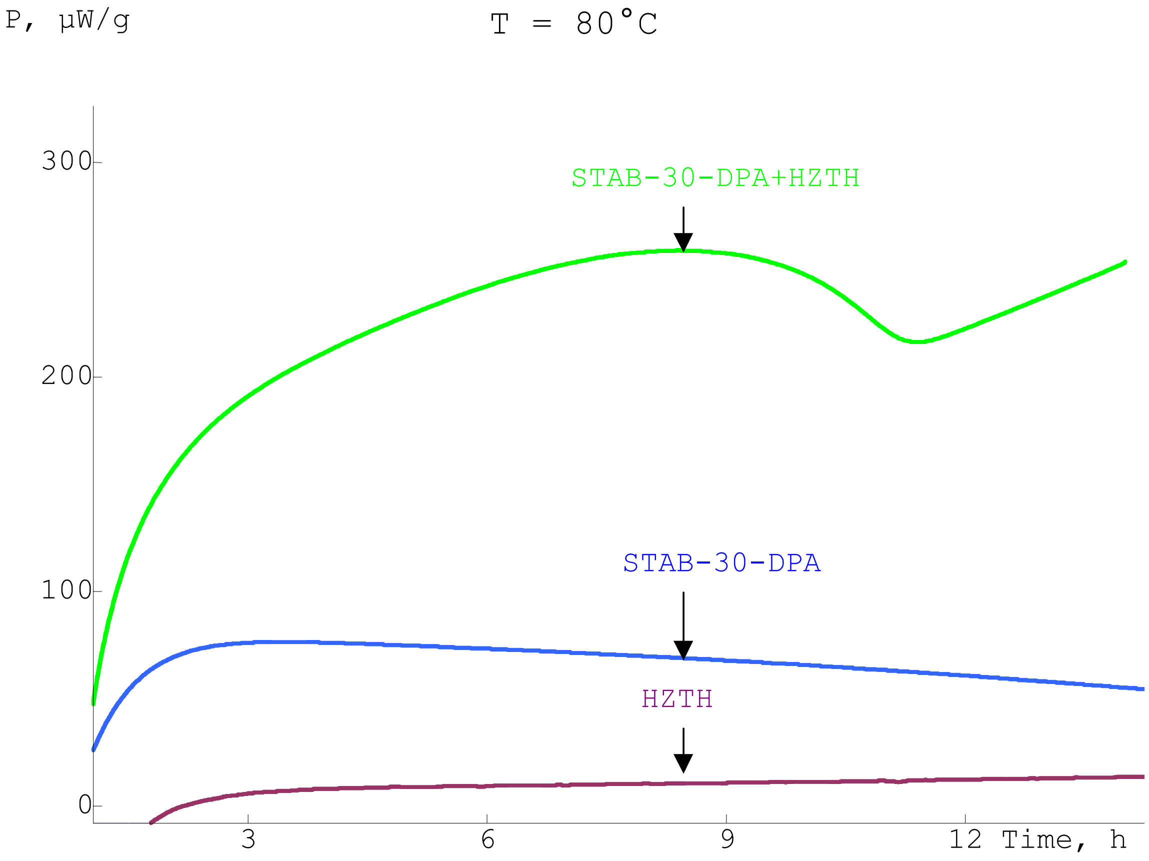

Figure 2.20. **HZTH**, STAB-30-DAP and mixture

4.2 Compatibility tests **TAGZT** with TLPs

In the HFC, measurements at 80 °C are performed with the pure test materials and in combination with the corresponding TLPs (STAB-0-DPA, STAB-15-DPA). The sample amounts are summarized in *Table 2.11*. The test substances have not been incorporated into the TLPs, therefore, any interactions are only possible on the surfaces.

Table 2.11. Measured samples and sample amount

substance 1	Substance 2	weight	weight
STAB-0-DPA	-	2,886 g	-
STAB-15-DPA	-	3,013 g	-
TAGZT	-	0,373 g	-
STAB-0-DPA	TAGZT	2,228 g	0,339 g
STAB-15-DPA	TAGZT	2,219 g	0,268 g

The important parameters of the experiments are summarized in *Table 2.12*, and the corresponding thermographs are depicted in *Figure 2.21* and *Figure 2.22*. From these two experiments, a good stability and compatibility of **TAGZT** with the used TLPs can be derived, indicating **TAGZT** to be a suitable component in new propellant formulation and should be further investigated.

Table 2.12. Results of the measurement

substance 1	substance 2	P_{max} [µW/g]	Q [J/g][1]	Q_R [J/g]	D [-]
STAB-0-DPA	-	8,5	10,5	-	-
STAB-15-DPA	-	22,5	15,5	-	-
TAGZT	-	13,8	7,9	-	-
STAB-0-DPA	TAGZT	18,8	11,9	1,7	1,17
STAB-15-DPA	TAGZT	35,8	21,2	6,5	1,45

[1] Integration from 0 d to 9d 4h (due to defect measurement device)

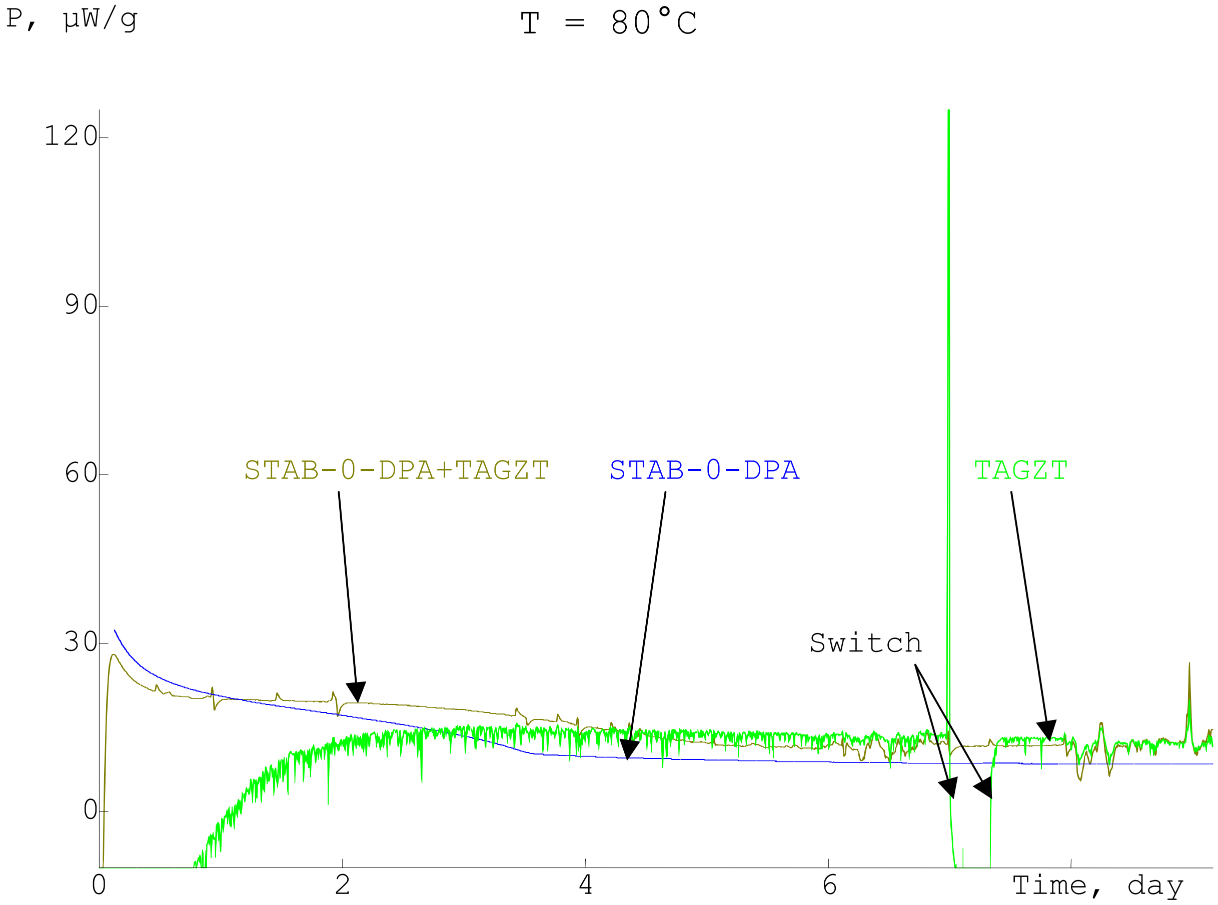

Figure 2.21. **TAGZT**, STAB-0-DAP and mixture

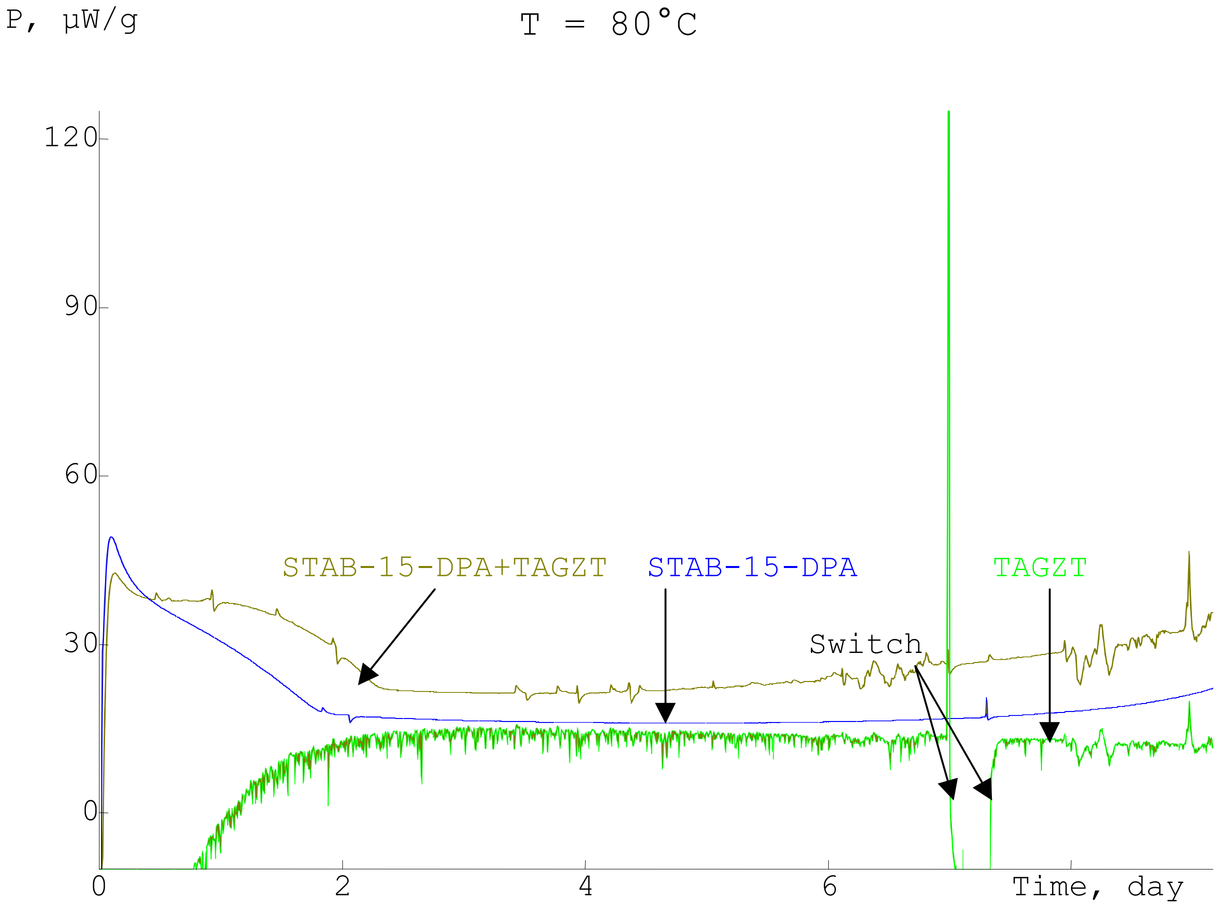

Figure 2.22. **TAGZT**, STAB-15-DAP and mixture

4.2 Conclusion

HZT and **HZTH** are not compatible in mixtures with the discussed TLPs. In both cases the required measurement time of 10.9 days at 80 °C could not be archived since the developed gas blast lead in one case to the damage of the corresponding measurement channel, and the same appeared to happen in the other case and therefore were aborted. However, from the obtained data, the incompatibility as well as the instability of theses components could doubtless be derived. Since the interreaction of **HZTH** with STAB-30-DPA lead to extreme energy release, the test of the contact pair **HZT** / STAB-30-DPA was not conducted, expecting the same outcome. Interestingly, the incompatibility of the double based *propellants* with **HZTH** is more pronounced than compared to the single based STAB-0-DPA. Both *propellants* contain as enrergetic groups nitrates in form of gelatinized NC (single based), and additionally, in the case of double based *propellant*, stabilized nitroglycerin. The reason for this might be

found in the reaction of the hydrazinium cation with the nitrate groups. It seems that for **HZT** and **HZTH,** the hydrazinium ion serves as proton source for the ester cleavage of the nitrate groups rather than as base. This reaction is accelerated when nitroglycerin is present, which is known to decompose more easily than NC with respect to the nitrate groups. The presence of crystal water in **HZTH** compared to **HZT** does not play a significant role as almost an identical behavior in combination with STAB-0-DPA was observed. Therefore, it is questionable if hydrazinium based azotetrazolate salts ever could be used in combination with nitrate based (NC and NG) propellants.

If the assumption above is true, changing the counterion from the hydrazinium ion to the more base TGA cation a higher stability is expected, since the protonation ability of the TGA cation is extremely low. From the experimental point of view exactly this was observed. **TAGZT** is both compatible and stable in combination with the used *propellants*, indicating no interreaction between TGA cation and the NC (STAB-0-DPA) or NC / NG (STAB-15-DPA) based *propellants* occurred. At present, the other members of the guanidinium family are also tested according to STANAG 4582, but test results are not available yet.

5. References

[1] Butler, R. N. In *Comprehensive Heterocyclic Chemistry*; (Katritzky, A. R., Rees, C. W., Scriven, E. F. V. (ed.)); Vol. 4, Pergamon: Oxford, U.K., **1996**.

[2] Singh, H.; Chawla, A. S.; Kapoor, V. K.; Paul, D.; Malotra, R. K. *Prog. Med. Chem.* **1980**, *17*, 151.

[3] Huisgen, R.; Sauer, J.; Sturm, H. J.; Markgraf, J. H. *Chem. Ber.* **1960**, *63*, 2106.

[4] Murphy, D. B.; Picard, J. P. *J. Org. Chem.* **1954**, *19*, 1807.

[5] Bianchi, G.; Boulto, A. J.; Fletcher, I. J.; Katrizky, A. R. *J. Chem. Soc. (B)* **1971**, 2355.

[6] Gordon, A. A.; Katritzky, A. R. *Tetrahedron Letters*, **1968**, 2767.

[7] a) Reimlinger, H. *Chem. Ber.* **1970**, *103*, 1900; b) Huisgen, R. *Angew. Chem.* **1968**, *80*, 329.

[8] a) Norris, W. P.; Henry, R. A. *J. Org. Chem.* **1964**, *29*, 650; b) Atwood, J. L.; Smith, K. D. *J. Am. Chem. Soc.* **1973**, *95*, 1488.

[9] a) McEwan, W. S.; Rigg, M. W. *J. Am. Chem. Soc.* **1951**, *73*, 4725; b) Tišler, M. *Synthesis* **1973**, 123.

[10] Burke, L. A.; Elguero, J.; Levroy, G.; Sana, M. *J. Am. Chem. Soc.* **1976**, *98*, 1685.

[11] Kadaba, P. K. *Synthesis* **1973**, 71.

[12] a) Lounsbury, J. B. *J. Phys. Chem.* **1963**, *89*, 6835; b) Bloor, J. E.; Breen, D. L. *J. Am. Chem. Soc.* **1967**, *89*, 6835.

[13] Benson, F. R. *Chem. Rev.* **1947**, *41*, 1.

[14] Dewar, M. J. S.; Gleicher, G. J. *J. Chem. Phys.* **1966**, *44*, 759.

[15] a) Vaughan, J.; Smith, P. A. S. *J. Org. Chem.* **1958**, *23*, 1909; b) Huisgen, R. *Angew. Chem.* **1960**, *72*, 359.

[16] a) Butler, R. N.; Katritzky, A. R.; Boulton, A. J. *Advances in Heterocyclic Chemistry*, Vol. *21*, 323, Academic Press, New York, **1977**; b) Butler, R. N.; Katritzky, A. R.; Rees, C. W. *Comprehensive Heterocyclic Chemistry*, Vol. *5*, 791, Pergamon Press, Oxford, **1984**.

[17] a) Lieber, E.; Patinkin, S. H.; Tao, H. H. *J. Am. Chem. Soc.* **1951**, *73*, 1792; b) Hammer, A.; Klapötke, T. M.; Mayer, P.; Weigand, J. J. *Propellants, Expl. Pyrotech.* **2004**, *29(6)*, 325 and references therein.

[18] Barlin, G. B.; Batterham, T. J. *J. Chem. Soc. (B)* **1967**, 516.

[19] Sainsburry, M. *Rodd's Chemistry of Carbon Compounds*, Vol IV, Part D, 211, Elsevier, Amsterdam, **1986**.

[20] a) Huisgen, R.; Sauer, J.; Seidel, M. *Chem. Ber.* **1960**, *93*, 2885; b) Martin, D.; Weise, A. *Chem. Ber.* **1966**, *99*, 317.

[21] Markgraf, J. H.; Bachmann, W. T.; Hollis, D. P. *J. Org. Chem.* **1965**, *30*, 3472.

[22] Thiele, J. *Liebigs Ann.* **1892**, *270*, 1.

[23] Stollé, R. *Ber. Dtsch. Chem. Ges.* **1929**, *62*, 1118.

[24] Müller, U.; Bärnighausen, H. *Acta Cryst.* **1970**, *26(B)*, 1671-1679

[25] Akella, A.; Keszler D. A. *Acta Cryst.* **1994**, *C50*, 1974.

[26] Lieber, E.; Patinkin, S. H.; Tao, H. H. *J. Amer. Chem. Soc.* **1951**, *73*, 1792.

[27] Krimen, L.; Baltazzi, E. *Chem. Rev.* **1963**, *63(5)*, 511.

[28] Hammer, A. succeeded in the isolation and structure solution of azotetrazolate, private communication, **2005**.

[29] Thiele, J.; Manchot, W. *Liebigs Ann.* **1898**, *303*, 47.

[30] Hammerl, A. *Hochenergetische, stickstoffreiche Verbindungen* PhD thesis, Ludwig-Maximilian University, **2001**.

[31] Hiskey, M. A.; Goldman, N.; Stine, J. R. *J. Energetic Mater.* **1998**, *16(2 & 3)*, 119.

[32] a) Hiskey, M. A.; Chavez, D. E.; Naud, D. L.; Son, S. F.; Berghout, H. L.; Bolme, C. A. *Proc. Int. Pyrotech. Seminar*, 2000, **27**, 3; b) Hiskey, M. A.; Goldman, N.; Stine, J. R. *J. Energetic Mater.* **1998**, *16(2 & 3)*, 119; c) Hammerl, A.; Klapötke, T. M.; Nöth, H.; Warchhold, M.; Holl, G.; Kaiser M.; Ticmanis, U. *Inorg. Chem.* **2001**, *40*, 3570; d) Hammerl, A.; Holl, G.; Klapötke, T. M.; Mayer, P.; Nöth, H.; Piotrowski, H.; Warchhold, M. *Eur. J. Inorg. Chem.* **2002**, 834; e) Ang, H.; Frank, W.; Karaghiosoff, K.; Klapötke, T. M.; Nöth, H.; Sprott, J.; Suter, M.; Vogt, M.; Warchhold, M. *Z. Anorg. Allg. Chem.* **2002**, *628*, 2901; f) Peng, Y.; Wong, C. *US Patent* **1999**, 5.877.300, CA 130:196656; g) Tremblay, M. *Can. J. Chem.* **1964**, 1154; g) Hammerl, A.; Holl, G.; Kaiser, M.; Klapötke, T. M.; Mayer, P.; Piotrowski, H.; Vogt, M. *Z. Naturforsch.* **2001**, *56(9)*, 847; h) Hammerl, A.; Holl, G.; Kaiser, M.; Klapötke, T. M.; Mayer, P.; Nöth, H.; Piotrowski, H.; Suter, M. *Z. Naturforsch.* **2001**, *56(9)*, 857.

[33] Finnegan, W. G.; Henry, R. A.; Lieber, E. *J. Org. Chem.* **1953**, *18(7)*, 779.

[34] a) Thiele, J.; Marais, J. T. *Liebigs Ann.* **1893**, *273*, 144; b) Thiele, J. *Liebigs Ann.* **1898**, *303*, 57.

[35] Henke, H.; Bärnighausen, H. *Acta Cryst.* **1970**, *28(B)*, 1100.

[36] Allen, F. H.; Kennard, O. *Chem. Des. Autom. News* **1993**, *1*, 66.

[37] Schomaker, V.; Waser, J.; Marsh, R. E.; Bergmann, G. *Acta Cryst.* **1959**, *12*, 600.

[38] Bondi, A. *J. Phys. Chem.* **1964**, *68*, 441.

[39] a) Etter, M. C. *Acc. Hem. Res.* **1990**, *23*, 120; b) Etter, M. C.; MacDonald, J. C. *Acta Crsyt.* **1990**, *B46*, 256.

[40] Sivabalan, R.; Talawar, M. B.; Senthilkumar, N.; Kavitha, B.; Asthana, S. N. *J. Therm. Anal. Cal.* **2004**, *78*, 781-792.

[41] West, R. C.; Selby, S. M. *Handbook of Chemistry and Physics*, 48th ed.; The Chemical Rubber Co.; Cleveland, OH, 1967-1968; pp D22-D51.

[42] Ostrovskii, V. A.; Pevzner, M. S.; Kofman, T. P.; Tselinskii, I. V. *Targets Heterocycl. Syst.* **1999**, *3*, 467-526.

[43] *ICT – Thermdynamic Code*, Version 1.0, Frauenhofer-Institut für Chemische Technologie (ICT). Pfinztal/Berghausen, Germany 1988-2000.

[44] a) Kamlet, M. J.; Jacobs, S. J. *J. Chem. Phys.* **1968**, *48*, 23; b) Kamlet, M. J.; Ablard, J. E. *J. Chem. Phys.* **1968**, *48*, 36; c) Kamlet, M. J.; Dickinson, C. *J. Chem. Phys.* **1968**, *48*, 43.

[45] a) Eremenko, L. T.; Nesterenko, D. A. *Chem. Phys. Reports.* **1997**, *16*, 1675; b) Astakhov, A. M.; Stepanov, R. S.; Babushkin, A. Y. *Combust. Explos. Shock Waves.* **1998**, *34*, 85, (Engl. Transl.).

[46] with K = 15.58, ρ [g cm^{-3}]; $\varphi = N\sqrt{M(-\Delta_E H)}$; N = moles of gases per g of explosives; M = average molar mass of formed gases; $\Delta_E H$ = calculated enthalpy of detonation (in cal g^{-1}); A = 1.01; B = 1.30.

[47] Mader, C. L.; "Detonation Properties of Condensed Explosives Computed Using the Becker-Kistiakowsky-Wilson Equation of State," *Los Alamos Scientific Laboratory* **1963**, Rept. LA-2900.

[48] Köhler, J.; Mayer, R. Explosivstoffe, 7. Aufl., Wiley-VCH, **1991**, Weinheim.

[49] WIWEB, private communications.

[50] Loebecke, A.; Pfeil, A.; Krause, H.; Sauer, J.; Holland U. *Prop. Explos. Pyrotech.* **1999**, *24*, 168.

[51] Schimdt, E. W., *Hydrazine and Its Derivatives, Vol. 2*, 2nd ed., Wiley, Chichester, New York, **2001**.

[52] Hiskey, M. A.; Hammer, A.; Holl, G.; Klapötke, T. M.; Polborn, K.; Stierstorfer, J.; Weigand J. J. *Chem. Matter.* **2005**, *17*, 3784.

[53] http://www.parrinst.com/.

[54] Standard Test Method for Arrhenius Kinetic Constants for Thermally Unstable Materials, ASTM Designation E698-99, 1999.

[55] Ozawa, T. Bull. *Chem. Chem. Soc. Jpn.* **1965**, *38*, 1881.

[56] Kissinger, H. E. *Anal. Chem.* **1957**, *29*, 1702.

[57] a) Sheldrick, G. M. *SHELXL-86*, *Program for Solution of Crystal Structures*; University of Göttingen: Göttingen, Germany, **1986**; b) Sheldrick, G. M. *SHELXL-97*, *Program for Solution of Crystal Structures*; University of Göttingen: Göttingen, Germany, **1997**.

[58] Copies of the data can be obtained free of charge on application to CCDC, 12 Union Road, Cambridge CB2 1EZ, UK (fax: (+44) 1223-336-033; e-mail: deposit@ccdc.cam.ac.uk).

[59] a) Barret, A. J.; Bates, L. R.; Jenkins, J. M.; White, J. R. *Govet. Rep. Announce (U.S.)* **1973**, *73(2)*, 70; b) Mayants, A. G.; Vladimirov, V. N.; Razumov, N. M.; Shlyapochnikov, V. A. *J. Org. Chem.* USSR (Engl. Transl.) **1991**, *27*, 2177; *Zh. Org. Khim.* **1991**, *11*, 2450.

[60] a) Spear, J. S.; Elischer, P. P. *Aust. J. Chem.* **1982**, *35*, 1; b) Mohan, V. K.; Tang, T. B. *J. Chem. Phys.* **1983**, *79(9)*, 4271; c) Chaudhri, M. M. *J. Mater. Sci. Lett.* **1984**, *3*, 565.

[61] Bassett, W. A.; Shen, A. H.; Bucknam, M.; Chou, I..-M. *Rev. Sci. Instr.* **1993**, *64*, 2340.

[62] a) Barnett, J. D.; Block, S.; Piermarini, G. J. *Rev. Sci. Instrum.* **1973**, *44*, 1; b) Piermarini, G. J.; Block, S. *Rev. Sci. Instrum.* **1975**, *46*, 973; c) Mao, H. K.; Bell, P. M.; Shaner, J. W.; Steinberg, D. J. *J. Appl. Phys.* **1978**, *49*, 3276.

[63] Bini, R.; Ballerini, R.; Pratesi, G.; Jodl, H. J. *Rev. Sci. Instrum.* **1997**, *68(8)*, 3154 and references therein.

[64] NATO Standardization STANAG 4147, Chemical Compatibility Ammunition Components with Explosives and Propellants, June **1992**.

[65] Wilker, S. 'Verträglichkeitsunteruchungen organischer Explosivstoffe mit Kontaktstoffen 1995-2000', WIWB Germany, Report Nr. 710/2411/00, 2000.

[66] Private communication with WIWEB.

C h a p t e r   I I I

N,*N*-BIS-(1(2)*H*-TETRAZOL-5-YL)-AMINE HYDRATE (**BTA**)

1 Introduction

Neutral as well as ionic azides can undergo cycloaddition with cyano groups yielding a huge variety of different tetrazole derivatives.[1] An interesting precursor for cycloaddition reactions with azide is the non-linear pseudohalide dicyanamide anion ($N(CN)_2^-$), which exhibits a rich variety of bonding modes for coordination in for example *3d*-complexes. Dicyanamide complexes have attracted much interest in recent years in the construction of supramolecular aggregates due to their intriguing network topologies and potential functions as new class of materials.[2]

The reaction of sodium dicyanamide with sodium azide under acid catalyzed condition yield the corresponding bis(tetrazolyl)amine as monohydrate (**BTA**).[3] In the continuous search of novel energetic materials with high nitrogen content for application, for example as low-smoke producing *pyrotechnic compositions*, *gas generators*, *propellants* and *primers* in primer charges (PC), high-energy-capacity transition metal complexes are of special interest and **BTA** might play an important role in future investigations as well applications.

1.1 Pyrotechnic composition and primers

A low-smoke pyrotechnic composition, for example, includes an high-nitrogen content (HNC), low carbon content energetic material, an oxidant and a colorant. The most promising high energy materials (HNC) suitable for low-smoke pyrotechnic composition may be derived from dihydrazino-*s*-tetrazine (**dht**, **29**) and derivatives, *N*,*N*-bis-(1(2)*H*-tetrazol-5-yl)-amine mono-hydrate (H_2**bta**, **30**) and 5,5'-bis-1*H*-tetrazole (H_2**bt**, **31**) (*Scheme 3.1*).[4]

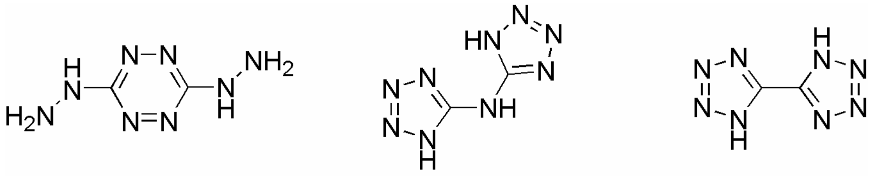

dht $\quad$ **H_2bta** $\quad$ **H_2bt**

Figure 3.1. Promising HNC high energy materials

In addition to the high energetic material, efforts have dealt with the search for replacement colorants to be used in low smoke pyrotechnics composition in view of previous colorants, such as cupric oxide, barium nitrate, strontium nitrate and the like. U.S. Patent No. 5,682,014 by Highsmith et al.[5] describes metal salts of *N*,*N*-bis-(1(2)*H*-tetrazol-5-yl)-amine (H_2**bta**, **30**) as non-azide fuels for gas-generant compositions and Hiskey et al.[4] introduced the metal salt as colorant in pyrotechnic compositions which can yield red, blue, green, yellow, purple, red-purple, and blue-green colors. Various metals salts can be used as colorants or a coloring agent to generate selected colors for pyrotechnic composition as each metal of the periodic table has well-known spectra associated with the burning of those materials.[6] An advantage of metal salts of high nitrogen materials is the low amount needed to be added to the pyrotechnic composition, which is in general less than 10 percent by weight to yield intense colors.

Furthermore, there is continued demand of new primer explosive systems (PC). Still, modern primary explosives (*Chapter I*) may be represented by lead azide as the main filling for detonators,[7] and by lead styphnate as the main filling for primers, usually associated with tetrazene as a sensitizer.[8] Recently, coordination compounds containing near stoichiometric fuel and oxidizer fractions have evinced great interest.[9] The extensive study on the relationship between structure of coordination compound and explosive properties has been reported by various research groups.[10] Nickel, copper and cobalt complexes appear suitable for detonator applications. For example, nickel hydrazinium nitrate (NHN)[11] may find wide ranging applications in conventional detonators, whereas bis-(5-nitrotetrazolato-*N*2)-tetraamine cobalt perchlorate (BNCP)[12] has emerged as an energy producing component for semi-conducting bridge (SCB) initiator applications. With respect to new PC's, BTA was investigated to see if it could serve as new HNC ligand system for new transition metal-based *primer explosives*.

Interestingly, characterization of H_2bta and its salts has not been reported yet. Therefore, a systematic investigation of the preparation and properties of **30** is important, and the recent results are going to be presented in this *Chapter*. One of the aims is to isolate and structurally characterize coordination polymers of certain metal salts exhibiting interesting frameworks with respect to the field of crystal engineering. As the amount of obtained crystal structure is beyond the scope of this work, only selected examples are going to be discussed.

1.2 Synthesis of **H_2bta** (**30**)

The first method of synthesizing *N,N-bis*-(1(2)*H*-tetrazol-5-yl)-amine (**30**) as its hydrate was described by William Norris et al.,[13] reacting sodium dicyanamide ($NaN(CN)_2$), sodium azide, and trimethylammonium chloride in water under refluxing condition. Due to several disadvantages, different synthetic routes have been published, and they all fall into three main types: (1) reaction of sodium dicyanamide with hydrazoic acid, in situ prepared from sodium azide and a corresponding weak acid like trimethylammonium chloride, boric acid, ammonium chloride and the like;[14] (2) reaction of sodium dicyanamide with sodium azide in the presence of a catalyst like zinc chloride, bromide or perchlorate, followed by an acid work-up;[15] and (3) reaction of **5-AT** with cyanogen bromide under base-catalyzed condition followed by a subsequent cycloaddition of azide under acid condition.

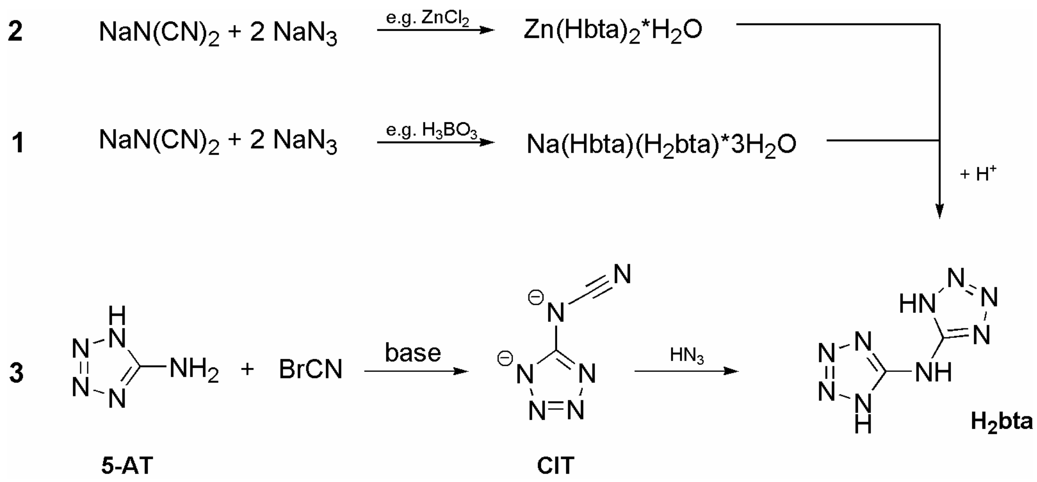

Scheme 3.1. Synthesis of **H_2bta** (**30**)

For reaction 1 and 2, the first reaction step yields certain metal complexes (*e.g.* Zn^{2+}, Na^{+}) as products which can be easily transformed to **30** by acidification. Treatment of **5-AT** under base condition with cyanogen bromide results in the formation of the very interesting and poorly described dianion of 5-cyanoiminotetrazolin (**CIT**, **33**), as sodium salt. Further treatment of the **CIT** salt with hydrazoic acid yields **30**. This procedure is not described in literature in that way, and since the chemistry, as well as the dianion itself, is very interesting, a detailed discussion will be given in the next chapter before coming back to the chemistry of **H_2bta**.

2 The Dianion of 5-Cyanoiminotetrazoline: $C_2N_6^{2-}$ (CIT)

2.1 Introduction

The most prominent binary carbon-nitrogen anion is the cyanide anion (CN^-). The salts of the hydrogen cyanide belong to the most important chemicals used in industrial, pharmaceutical and agricultural processes.[16] Among the binary carbon and nitrogen anions which have been reported, relatively few have alternating carbon-nitrogen connectivity,[17] although such structures are highly stable. Due to the expected alternating connectivity in *β*-carbon nitride (C_3N_4), alternating binary carbon-nitrogen anions may qualify as precursors for the synthesis of *β*-C_3N_4, a material predicted to be harder than diamond.[18] Moreover, non-alternating carbon-nitrogen anions obtained from the family of polycyanocarbons have been examined as coordination ligands to metals and as the basis for supramolecular frameworks.[19] The interest for practical applications of polycyanocarbons as electron acceptors or anions was also aroused for use as deeply colored dyes,[20] catalysts[21] and nonlinear optical materials.[22] Among them, formation of highly conductive charge transfer (CT) complexes and ferro- or antiferromagnetic CT complexes[23] have been most intensively investigated with respect to their properties as electron acceptors or anions by both chemists and physicists.[24]

Besides the carbon-nitrogen connectivity, there are other ways to systematically divide CN anions, such as the charge [singly charged ions, *e.g.* dicyan amide (**DCA**), NC-N-CN^-;[25] doubly charged ions, *e.g.* cyan amide (**CA**), NCN^{2-},[26] N,N',N''-tricyanoguanidinate (**TCG**), $C_4N_6^{2-}$,[17a] or triply charged ions, *e.g.* tricyanomelaminate (**TCMA**),[27] $(NC\text{-}NCN)_3^-$] or the carbon-nitrogen stoichiometry. Using the carbon-nitrogen stoichiometry as criterion, CN anions may be grouped into three classes: (i) nitrogen-rich (*e.g.* NC-N-CN^-, NCN^{2-}), (ii) carbon-rich CN anions (*e.g.* tricyanomethanide (**TCM**),[28] $C(CN)_3^-$) and (iii) CN anions with the same number of carbon and nitrogen atoms (*e.g.* cyanide, CN^-). Most of the nitrogen-rich CN anions are based on the tetrazole ring such as azidotetrazolate (**AzT**), CN_7^-,[29] cyanotetrazolate (**CT**),[30] $C_2N_5^-$, 5,5'-bistetrazolate (**BT**), $C_2N_8^{2-}$,[31] 5,5'-azotetrazolate (**ZT**), $C_2N_{10}^{2-}$,[32] and 3,6-bis(2*H*-tetrazol-5-yl)-1,2,4,5-tetrazinediide (**BTT**), $C_4N_{12}^{2-}$.[33] The nitrogen-rich anions are of special interest, as they are salts with high nitrogen content, having high heats of formation and showing in most cases remarkable insensitivities to friction, electrostatic discharge, and shock. These features can be in most cases attributed to the delocalized π-system of these anions.[34] The carbon-rich CN anions are mainly based on cyano – and polycyano groups. A compendium of selected anions is depicted in *Scheme 3.2*.

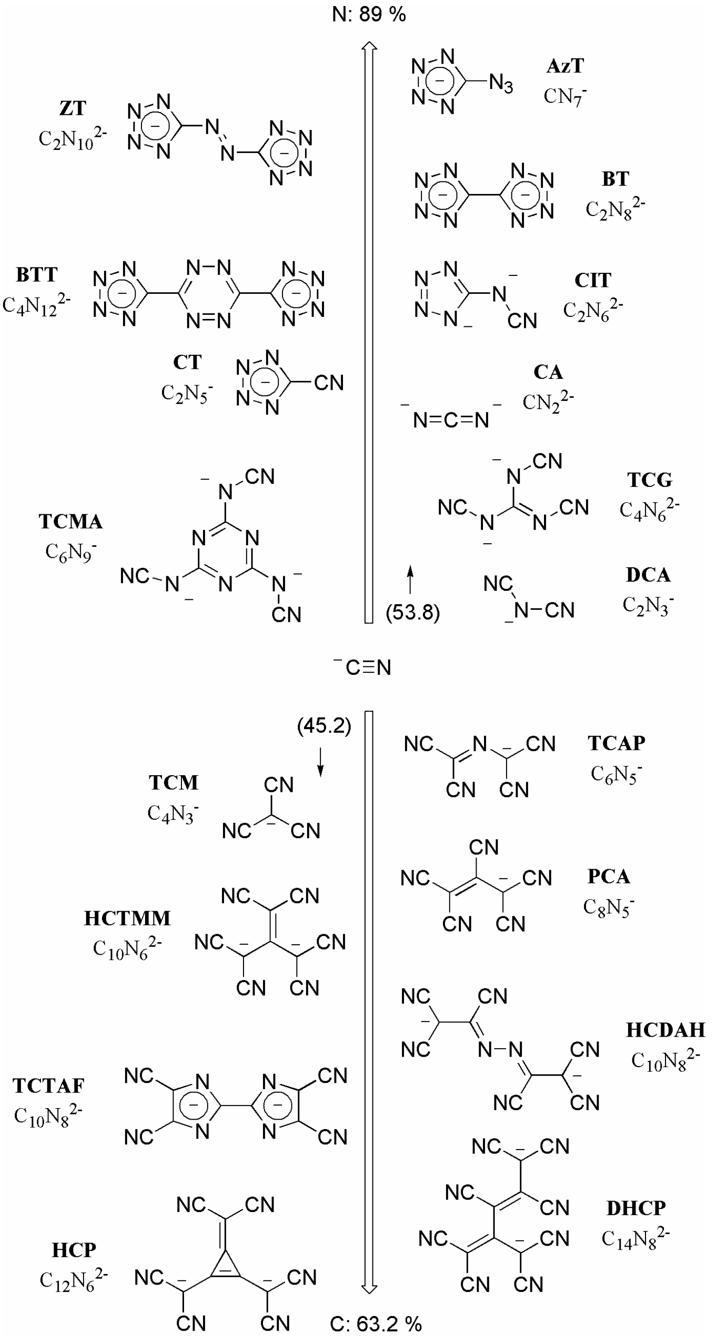

Figure 3.2. Selected carbon-nitrogen anions

Examples of polycyano organic anions are the tetracyano-2-azapropenide (**TCAP**), $C_6N_5^{2-}$, pentacyanoallylide (**PCA**), $C_8N_5^-$,[35] hexacyanotrimethylenemethanediide (**PCA**), $C_{10}N_6^{2-}$,[36] hexacyanodiazahexadienediide (**HCDAH**), $C_{10}N_8^{2-}$,[37] tetracyano-1,1',3,3'-tetraazafulvalenediide (**TCTAF**), $C_{10}N_8^{2-}$,[38] 2-dicyanomethyl-1,1,3,4,5,5-hexacyanopentadienediide (**DHCP**), $C_{14}N_8^{2-}$,[39] and tri(dicyanomethylene)cyclopropanediide (**HCP**), $C_{12}N_6^{2-}$.[36a]

A long forgotten and poorly characterized nitrogen-rich anion of this class represent the 5-cyaniminotetrazolinediide (**33**), $C_2N_6^{2-}$ - **CIT**,[3] which can be obtained by the reaction of aminotetrazole (**1**) with cyanogen bromide under base condition (Scheme 1).

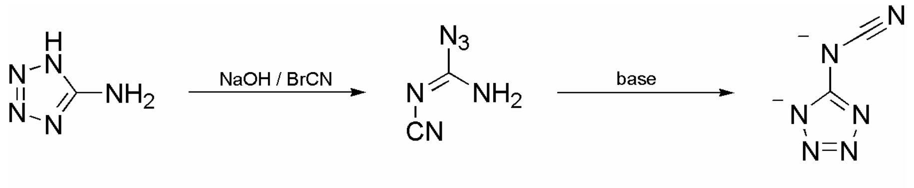

Scheme 3.2. Synthesis of **CIT** (**33**)

The azido-*N*-cyanoformamidine (cyanoguanyl azide) (**32**) which is formed as an intermediate can be isolated as long as no base is present. In general, the tetrazole ring may exist in equilibrium with the acyclic imidoyl azide form, and depending on the substituent at the imidoyl fragment present, both isomers can be observed. Electron withdrawing groups such as CN or NO_2 favor the open azide chain isomer, imidoyl azide, whereas electron donating groups (*e.g.* alkyl) or bases are required effecting the cyclization to the isomeric tetrazole.[3,40,41]

2.2 Results and Discussion

2.2.1 Synthesis and properties of **CIT** salts

The two step synthesis of 5-cyaniminotetrazoline salts (**CIT**) starts from amino-1*H*-tetrazolium monohydrate (**5-AT**), which after neutralization with sodium hydroxide, was reacted with cyanogen bromide to give azido-*N*-cyanoformamidine (**32**). **32** represents an easily accessible source for an NCN-N_3 unit. Treating a methanolic or ethanolic solution of **2** with bases (e.g. MOH, M = Li, Na, K, Cs; amines), immediate deprotonation and cyclization of **32** can be observed resulting in the formation of the stable 5-cyaniminotetrazolinediide salts (*Scheme 3.2*). Raman and IR spectroscopy are particularly suitable to identify **CIT** salts very fast with the help of the CN stretching mode at ca. 2150 and the missing N_3 stretching at 2190 cm^{-1} (for approximate assignment of all normal modes on the basis of DFT calculation, see Appendix A *Table A-1 – A-3*);

Pure alkali and ammonium CIT salts are stable at ambient temperature, and are neither heat nor shock sensitive. To determine the thermal properties of CIT salts, combined IR and DSC experiments were carried out. DSC experiments of the cesium CIT salt (**33**) revealed three interesting features: (i) an endothermic reversible change of the modification at ca. 253° (ΔH = 34.8 J/g for $\alpha \rightarrow \beta$ modification, *Figure 3.3*) which was supported by powder diffraction studies (*Figure 3.4*), (ii) melting at 335 °C (onset), and (iii) the decomposition of Cs_2CIT after melting in cesium azide and caesium dicyanamide. It is assumed that the presence of an over the entire dianion delocalised π-system probably accounts for the remarkable kinetic stability of CIT salts (see below).

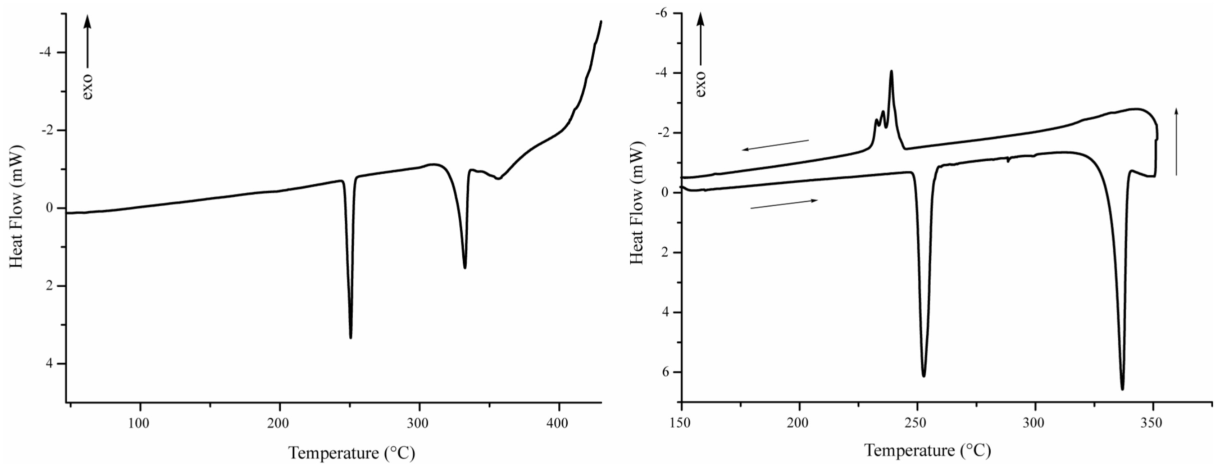

Figure 3.3. DSC experiments showing the decomposition of β-$Cs_2C_2N_6$ (left) and the non-reversibility after melting of β-$Cs_2C_2N_6$ (right).

2.2.2 DSC of Cs_2CIT (**34**)

The results of the different scanning calorimetry (DSC) experiments show that there are two endotherms (*Figure 3.3*, left), at 252 and 334 °C. The first endotherm is related to the transition of α-$Cs_2C_2N_6$ to the metastable β-$Cs_2C_2N_6$ modification, which is in accordance with the transformation that can be observed from the *in situ* data shown in *Figure 3.4*. The enthalpy of the strongly endothermic transformation was measured to be 34.8 J/g. The first transition was found to be reversible, which can be seen from the temperature-resolved *in situ* powder diffraction patterns in *Figure 3.4*. The second endotherm corresponds to the melting of β-$Cs_2C_2N_6$. This process is not reversible (*Figure 3.3*, right), which can be explained due to decomposition of **34** to CsN_3 (mp 310 °C) and $CsN(CN)_2$. Both compounds could be identified by their characteristic IR frequencies from a frozen-out sample of the melt. The cooling curve

(right) does not exhibit distinctive features which can be related to **34**, and therefore is indicative of an irreversible conversion of **34** to CsN_3 and $CsN(CN)_2$. The obtained melt starts to decompose in an exothermic reaction under formation of nitrogen above 395 °C.

2.2.3 In Situ X-ray Powder Diffraction of Cs_2CIT (**34**)

High-temperature *in situ* X-ray diffractometry was performed on a STOE Stadi P power diffractometer (Mo Kα_1 radiation, λ = 70.093 pm), with an integrated furnace and unsealed glass capillaries as sample containers from 180-260 °C and 260–180 °C in one run. The data collection was done with a 2θ range of 4.0 – 22.0° and a single scan collection of 8 min under isothermic conditions. The sample was heated to the starting temperature by applying a heating rate of 1 °C min^{-1}.

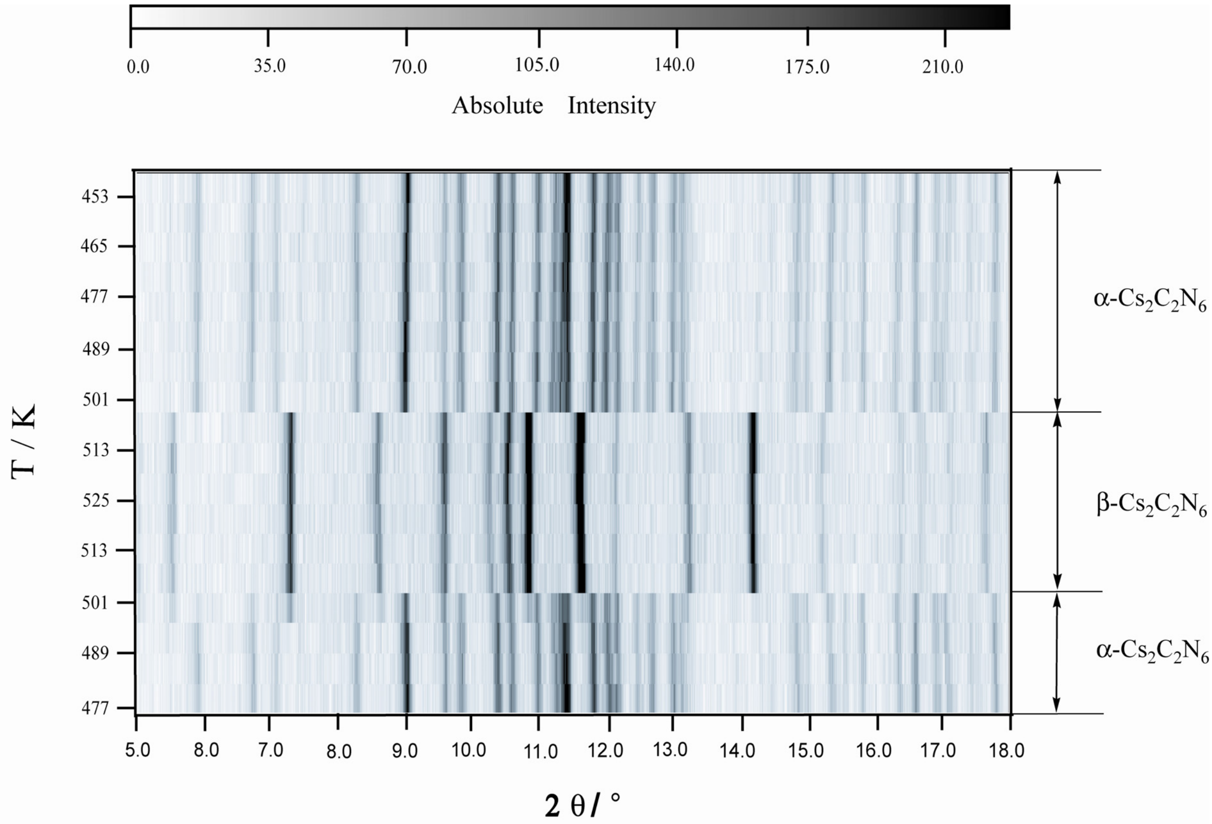

Figure 3.4. Temperature-dependent X-ray diffraction measurement from 180 °C (top) to 260 °C and 260 °C to 204 (bottom) °C between 4.0 and 22.0 in 2θ. To ensure a sufficient small time window for the detection off structural changes and to simultaneously maintain an acceptable data quality, the data acquisition time for a single scan was fixed to 8 min. A reversible phase transition between the α and β modification is observed. No overlap between of the different phases is observed.

The sequences of X-ray powder patterns collected from 160→260→204 °C, respectively, are shown in *Figure 3.4*. A prominent feature of the variable-temperature studies is the absence of a unique onset temperature for the observed phase transition, and there is no transitory regime observed, where no reflections are detected, indicate the non occurrence of an amorphous phase or intermediate glas transition, indicating also the reversibility of the first transition of α-$Cs_2C_2N_6$ → β-$Cs_2C_2N_6$ → α-$Cs_2C_2N_6$.

2.2.4 X-ray Crystal Structure of $(^{i}PrNH_3)_2$**CIT**•MeOH (**35**) and Cs_2CIT (**34**).

Figures 3.5 and *3.6* show the molecular units with the atom labeling scheme of **35** and **34**, respectively. Selected bond lengths and angles are presented in *Table 3.1*. **35** crystallizes in the triclinic space group *P*-1 with two formula units in the cell, and **5** in the monoclinic space group $P2_1$/n with 4 units in the cell.

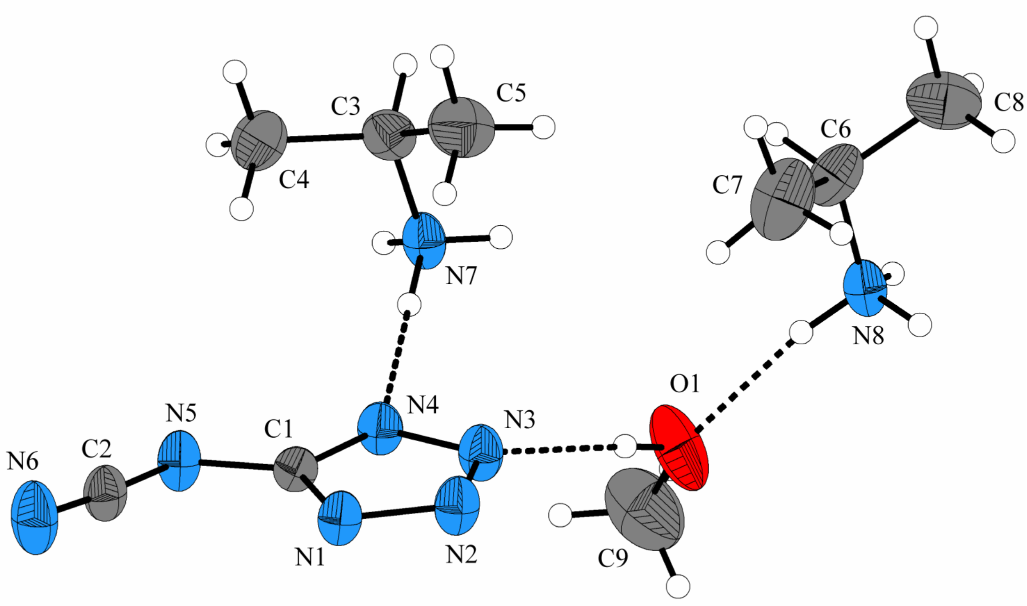

Figure 3.5. Formula unit and labeling scheme for **35** (ORTEP Plot, thermal ellipsoid represents 50% probability).

As shown in *Figure 3.4*, there are only small cation-anion interactions (hydrogen bridges) in the solid state structure of **35** (The bond distances and angles in the isopropylammonium and MeOH are as observed for many other salts with isopropylamine or MeOH as co-solvent and

therefore we abstain a discussion),[42] in contrast to the very complex bonding situation between anions and cations in **34**.

Table 3.1. Comparison of selected interatomic distance (Å) and bond angles (°) of the C_2N_6 frame in **34**, **35**, **36** and **37**.[a]

	34	**36**	**35**	**37**	**CIT**[b]	**CIT-SO$_3$**[b]
Bond Length						
C1–N1	1.337(2)	1.344(3)	1.338(4)	1.359(6)	1.358	1.352
N1–N2	1.348(2)	1.357(3)	1.362(4)	1.379(5)	1.355	1.359
N2–N3	1.301(2)	1.298(3)	1.309(4)	1.274(6)	1.321	1.294
N3–N4	1.348(2)	1.358(3)	1.357(4)	1.362(6)	1.358	1.366
C1–N4	1.331(2)	1.335(3)	1.337(4)	1.330(7)	1.357	1.379
C1–N5	1.368(2)	1.364(3)	1.388(4)	1.342(7)	1.387	1.344
C2–N5	1.301(2)	1.299(3)	1.302(4)	1.318(7)	1.293	1.306
C2–N6	1.159(2)	1.157(3)	1.174(4)	1.147(7)	1.197	1.186
Bond Angle						
N1–C1–N4	111.2(1)	109.8(2)	112.6(3)	106.9(5)	110.9	106.7
C1–N1–N2	104.8(1)	106.3(2)	104.0(2)	108.6(4)	104.9	106.4
N1–N2–N3	109.5(1)	108.2(2)	109.5(2)	105.8(4)	109.7	112.0
N2–N3–N4	109.6(1)	110.3(2)	109.8(2)	111.9(4)	109.7	106.5
N3–N4–C1	104.9(1)	105.4(2)	104.1(2)	106.8(4)	104.8	108.5
C1–N5–C2	116.1(1)	119.0(2)	116.8(3)	117.4(5)	123.6	121.0
N5–C2–N6	175.9(2)	173.3(2)	174.0(3)	173.2(7)	171.6	172.2

[a] for numbering see *Figure 3.7*; [b] theoretical gas phase data: B3LYP/aug-cc-pvTZ

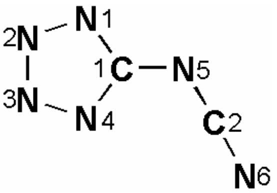

Figure 3.7. Molecular model and numbering scheme of the C_2N_6 frame in 5-cyanimino-tetrazolinediide.

The structure of **34** consists of an infinite three-dimensional network of repeating Cs_2CIT units. Each anion is bonded to twelve cesium cations while each Cs^+ has contacts to nine $N^{\delta-}$ atoms in six different CIT anions (*Figure 3.8*) with Cs-N bond distances of 3.131(2) to 3.586(3) Å. All Coulombic interactions (listed in *Table 3.2*) are either larger than the sum of the ionic radii of Cs^+ (1.92 Å, KZ = 9) and N^{3-} (1.32 Å)[43] or in the range, indicating that the structure is predominantly ionic. The sum of the calculated valency units for Cs_1^+ and Cs_2^+ accounts to

1.026 and 1.051, respectively, consistent with a single positive charge on both Cs^+ and a doubly negatively charged CIT ion (*Table 3.2*).

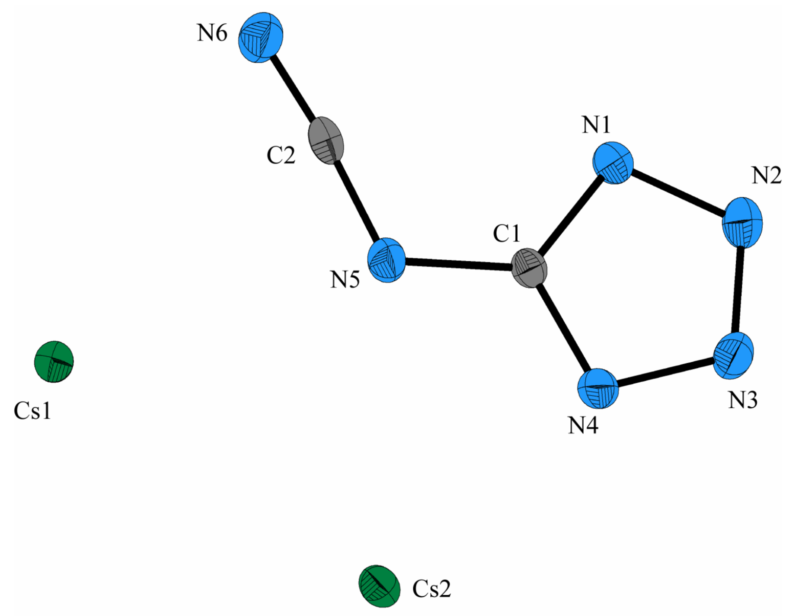

Figure 3.6. Formula unit and labeling scheme for **34** (ORTEP Plot, thermal ellipsoid represents 50% probability).

Table 3.2. Observed Cs-N contacts and calculated valency units in **34**

contact[a,b]	distance (Å)	valency units[c]	contact[a,b]	distance (Å)	valency units[c]
Cs1–N1^{ii}	3.403(3)	0.0969	Cs2–N1^{i}	3.481(3)	0.0836
Cs1–N2^{iii}	3.290(3)	0.1213	Cs2–N2^{iv}	3.302(3)	0.1184
Cs1–N2^{v}	3.505(3)	0.0799	Cs2–N3^{ii}	3.324(3)	0.1136
Cs1–N3^{vi}	3.320(3)	0.1143	Cs2–N4	3.178(3)	0.1525
Cs1–N3^{v}	3.233(3)	0.1362	Cs2–N4^{vi}	3.586(3)	0.0687
Cs1–N4^{vi}	3.131(2)	0.1679	Cs2–N5	3.483(3)	0.0832
Cs1–N5	3.330(3)	0.1120	Cs2–N5^{vi}	3.265(3)	0.1276
Cs1–N5^{ii}	3.571(3)	0.0706	Cs2–N6^{i}	3.154(3)	0.1606
Cs1–N6^{vii}	3.266(3)	0.1273	Cs2–N6^{vii}	3.208(3)	0.1433
sum of valency units		1.0264			1.0515

[a] Locations of contacts are shown in Figure 4. [b] Symmetry codes: (i) 1-x, 1-y, -z; (ii) 0.5-x, 0.5+y, 0.5-z; (iii) 1-x, 1-y, -z; (iv) -0.5+x, 0.5-y, -0.5+z; (v) x, 1+y, z; (vi) -x, 1-y, -z; (vii) -0.5+x, 1.5-y, -0.5+z. [c] Valency units were calculated using Brown's expression $s = (R/R_0)^{-N}$ where R is the observed contact distance; R_0 is the distance corresponding to a valency unit of 1, and N is a fitted constant. Values of R_0 for contacts to N and O differ by an average of 0.10 to 0.15 Å for other nuclei; R_0 for Cs–O is reported to be 2.24 Å, as no Cs–N contacts are given, R_0 was set to 2.39 Å. The value of N for Cs–O contacts is 6.6, and this value was used for the Cs–N contacts.

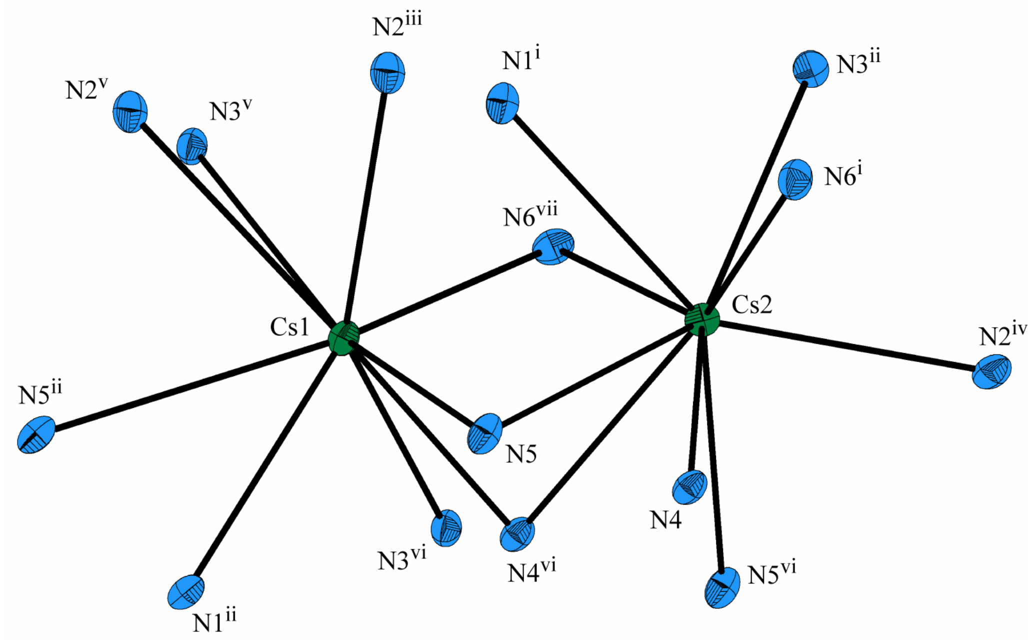

Figure 3.8. View of cesium coordination environment in Cs_2CIT

2.2.5 Structure and bonding of the CIT dianion.

In agreement with DFT calculations, the **CIT** anion (**33**) is almost planar in the solid state. The tetrazole ring in **34** and **35** is planar with the attached exocyclic nitrogen atom of the NCN moiety lying within the tetrazole plane (e.g. with a maximal deviation of 0.0034 Å in **35**). The cyanoimino moiety is slightly outside of the tetrazole plane (<N4–C1–C2–N6; **35**: 9.4(4)°, **34**: 5.4 (5)°). Similar to the situation found in covalent bound azides,[44] a trans bent geometry is found for the NCN group (<NCN, **35**: 175.9(2)°, **34**: 174.0(3)°). Actually, the **CIT** dianion is isoelectronic to the related azidotetrazolate monoanion (replacement of the middle N atom of the azido group by C^-), hence the hitherto unknown structure of azidotetrazolate can be expected to have similar features like those of **CIT**. As displayed in *Table 3.1*, the distances and angles of **CIT** in different salts are not significantly different. Thus it can be assumed that the geometry of the C_2N_6 dianion is little affected by coordination to a metal (X-ray data of **36**, below) or substitution at a ring nitrogen (X-ray data of **37**, below). The calculated gas phase geometry of **CIT** at B3LYP/aug-cc-pvTZ level of theory is similar to that found in the solid state and is given in *Table 3.1*.

As expected, for all **CIT** salts the N2–N3 bonds are significantly shorter than the N1–N2 and C1–N1 bonds (*Figure 3.7*, *e.g.* **34**: 1.309(4), 1.362(4), and 1.338(4) Å), which is comparable to the situation found in the structure of the cyano-tetrazolate.[30] The C2-N6 bond

length is significantly smaller than all other C–N or N–N bond lengths, indicating a stronger π-interaction along the cyano group of the NCN unit. The bond length found for the cyano group lies in a normal range (*e.g.* **35**: 1.159(2) Å; **34**: 1.174(4) for C2–N6; Table 2).[45] These relatively short N–N and C–N bond lengths, together with the planarity, indicate the presence of delocalization of π-bonds over the whole anionic species. MO and NBO calculations displayed the existence of a 10π-electron, 8-center bond unit (*Figures 3.9* and *3.10*).[46] In *Figure 3.9*, **A** and **B** are the energetically preferred Lewis representations of NNCM according to NBO analysis which is in agreement with the calculated Wiberg bond indices[47] (WBI) and the calculated partial charges (*Figure 3.9*). Investigation of the intramolecular donor-acceptor interactions utilizing the NBO partitioning scheme, clearly indicates a highly delocalized 10π-system according to resonance between Lewis representations **A** – **I**.

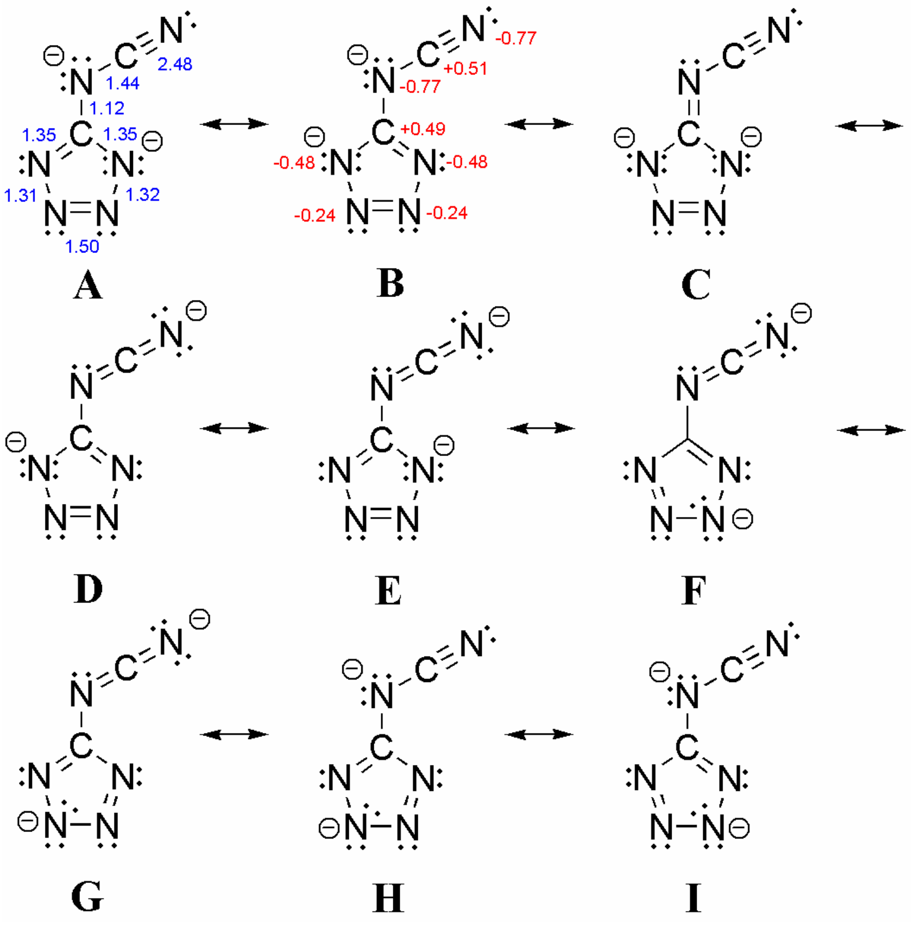

Figure 3.9. Nine possible Lewis representations according to NBO analysis along with WBI's (blue color) and NPA charges (red color).

The calculated WBIs indicate a stronger π-bond along the NCN moiety and the N_3-N_4 unit. The largest negative NPA net charge (NPA, natural population analysis) is found on the two N atoms of NCN unit. Summing the net charges of the NCN and the tetrazole moiety reveals for both units a negative charge close to -1 (NCN: -1.04; N_4C: -0.96*e*).

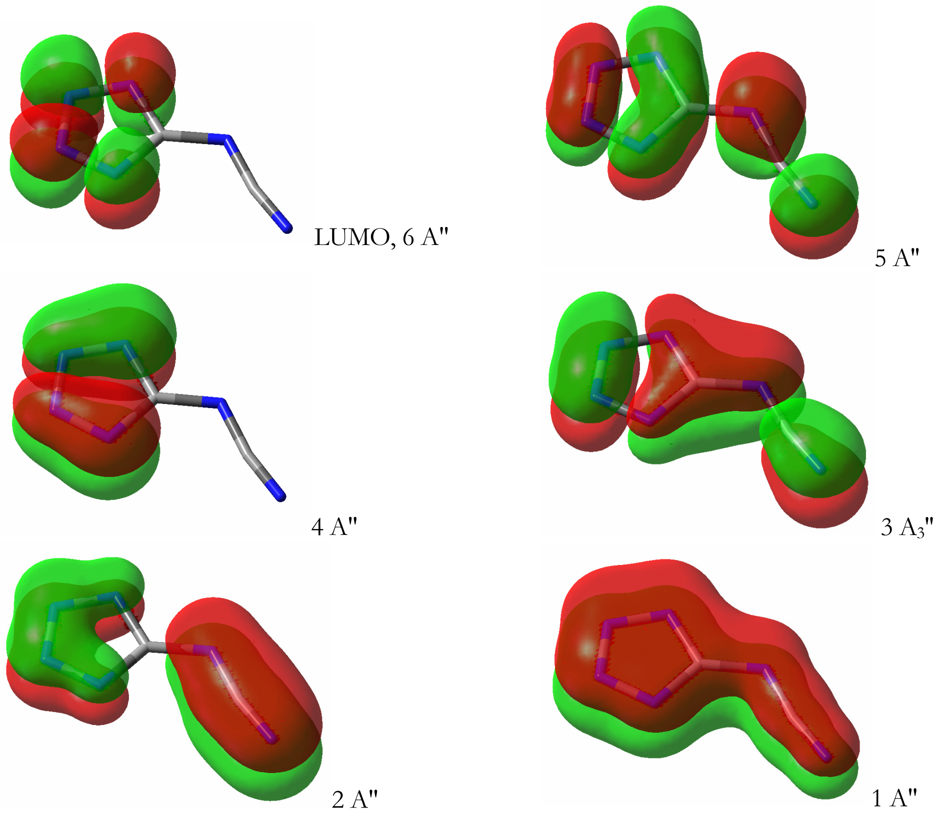

Figure 3.10. π-Type MOs (B3LYP/aug-cc-pvTZ) of **CIT** displaying the *10*π-8c-bond

2.2.6 Crystal structure of $[Pd(C_2N_6)(NH_3)_3]\cdot H_2O$ (**36**)

Complexes of CN-species with transition metals are well known and often exhibit interesting magnetic properties.[48] Due to the potential of being polydentate, several transition metal salts of CIT ($M(cit)(NH_3)_2$; M = Cu, Ni, Pd) were synthesized of which only the palladium complex will be introduced. These complexes are easily obtained from the reaction of the according transition metal(II)chlorides and **2** in ammonia solution.

The pale yellow palladium complex crystallizes in the monoclinic space group $P2_1/n$ with 4 units per cell. The structural data of **36** are presented in *Tables 3.1* and *3.3*, and the numbering scheme is depicted in *Figure 3.11*. The Pd atom lies in the center of a slightly distorted square-

planar arrangement composed of three NH_3 and one **CIT** ligand (coordination via N1 of the tetrazole ring), with N–Pd–N angles ranging from 89.58(9) to 90.22(9)° (mean deviation from the square plane is 0.0707 Å). All Pd-N distances are in the range of 2.008(2) to 2.046 (2) Å (*Table 3.3*) and lie well within the range of distances recorded previously.[49] The **CIT** ligand is not part of the square-plane as the tetrazole ring is twisted by 31.1° (N7–N9–N1–C1). The molecular parameters are comparable with those found in **35** and **34** (*Table 3.1*). It is interesting to note that the cyanoimino group is not involved in any bonding to the Pd metal.

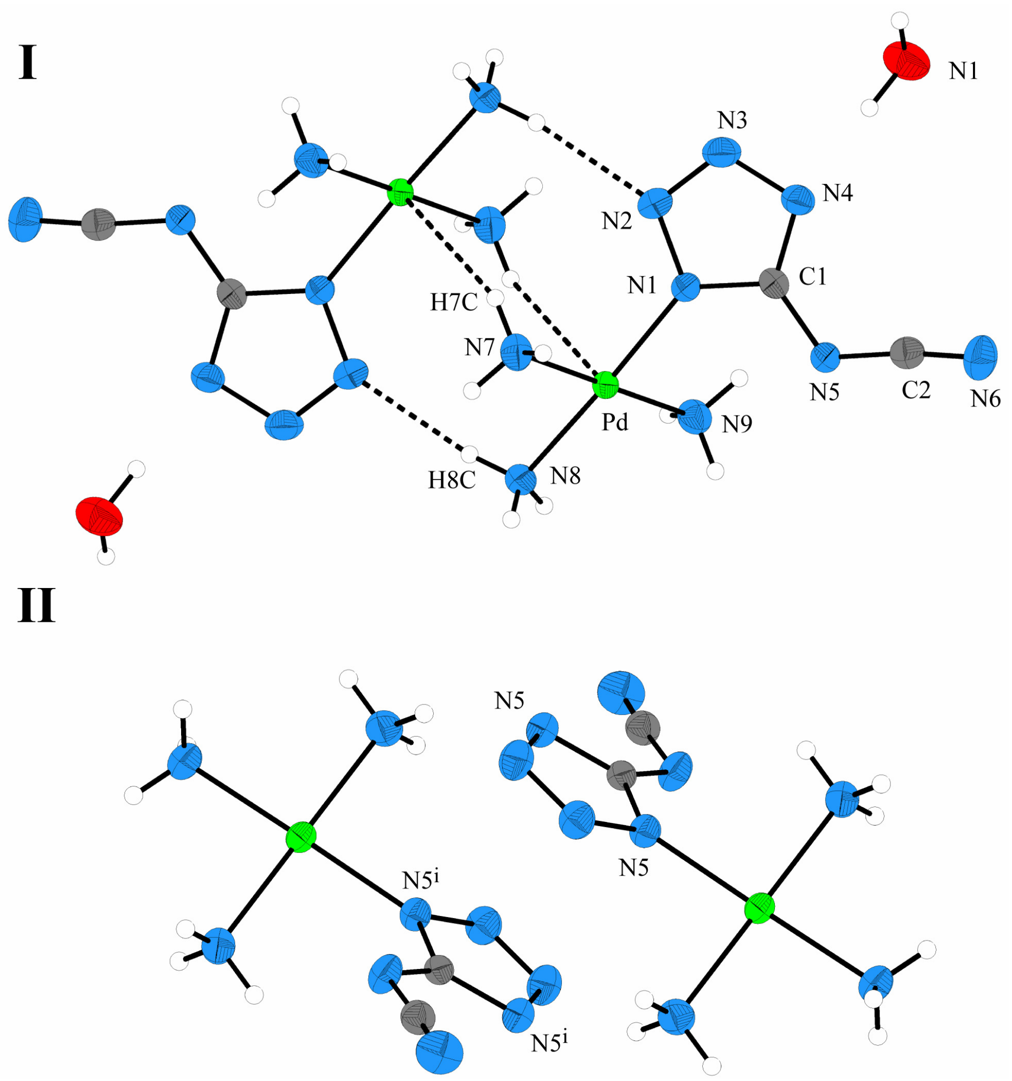

Figure 3.11. (**I**) The dimer $[Pd(C_2N_6)(NH_3)_3]{\bullet}H_2O$ (**36**), showing the atom-numbering scheme and displacement ellipsoid at 50% probability level; (II) Part of the crystal structure of **36**, showing the π-π-stacking interaction which links the dimers to chains along [010] axis. Atoms marked with ^{i} are at the symmetry position –x, –y, –z.

Table 3.3. Selected structural parameters (Å, °) of **36**

Pd–N1	2.008(2)	Pd–N8	2.043(2)
Pd–N7	2.046(2)	Pd–N9	2.043(2)
N1–Pd–N7	90.22(9)	N1–Pd–N8	176.90(8)
N7–Pd–N8	89.82(9)	N7–Pd–N9	179.67(9)
N8–Pd–N9	90.37(9)	Pd–N1–C1	132.5(2)
N9–Pd–N1	89.57(9)	Pd–N1–N2	120.9(2)

In the solid state, the complex is composed of dimers where the two complexes are related *via* an inversion centre. The long Pd–Pd^{i} distance of 4.2743(2) Å in the dimer excludes the possibility of the existence of a metal-metal interaction. A closer inspection of the molecular structure as shown in *Figure 3.11* reveals two agostic interactions (N7–H7C····Pd1^{i}; *d*(Pd···N7)^{i} = 3.536(3) Å; symmetry code: (i) -x, 1-y, -z) between the two Pd complex fragments forming the dimer. Apparently, these two interactions, together with an intermolecular hydrogen bond (N8–H8C····N2^{i}), can be regarded as the driving force for the dimerization.

Table 3.4. Hydrogen bond geometry (Å, °) of **36**

D–H····*A*	*D*–H	H····*A*	*D*····*A*	*D*–H····*A*
O1–H1A···N6^{i}	0.948(2)	2.072(3)	2.994(3)	164.0(2)
O1–H1B···N4	0.947(3)	2.037(4)	2.966(4)	166.3(2)
N7–H7A···O1^{ii}	0.89(2)	2.11(1)	2.989(3)	172.4(9)
N7–H7B···N4^{iii}	0.891(1)	2.154(6)	3.031(4)	157.4(5)
N8–H8B···N5^{iv}	0.891(1)	2.16(1)	3.031(4)	167.4(9)
N8–H8C···N2^{v}	0.890(9)	2.187(1)	3.066(3)	169.1(7)
N9–H9B···N6^{vi}	0.890(8)	2.302(6)	3.151(4)	159.4(5)

Symmetry codes: (i) -0.5+x, -0.5-y, -0.5+z; (ii) -0.5+x, 0.5-y, 0.5+z; (iii) -x, -y, -z; (iv) 0.5-x, 0.5+y, 0.5-z ; (v) –x, 1-y, -z ; (vi) x, 1+y, z.

Moreover, the dimers are linked by π-π-stacking interactions to chains along the [010] axis. The parallel tetrazole rings of the **CIT** ligands at (x, y, z) and (–x, –y, –z) have an interplanar stacking spacing of 3.307(2) Å. Additionally, several hydrogen bonds, including the water molecule, are found linking the dimers to a three dimensional network (*Table 3.4*).

2.2.7 The reaction of Cs_2CIT with SO_2.

A frozen mixture of $Cs_2C_2N_6$ (**35**) and SO_2 reacts on thawing and formation of a bright yellow solution which turns into a deep red solution within a few minutes. From this solution a gummy residue separates within 20 minutes from which a pale yellow solution was separated after one day. From this pale yellow solution, dicesium 5-cyaniminotetrazoline-1-sulfonatediide·SO_2, $Cs_2CITSO_3 \cdot SO_2$ (**37**) crystallized as pale yellow plates in an all over yield of 40% according eq [1]. Interestingly, the pale yellow crystals of **37** contain one SO_2 molecule (solvent) per formula unit and are surprisingly stable at room temperature even without SO_2 atmosphere. The loss of SO_2 starts only slowly from the surface of the crystals. It can be assumed that in the first reaction step SO_2 is attached to the N1 atom of the tetrazole ring followed by oxidation to SO_3 by SO_2 yielding the total reaction

$$2\ Cs_2C_2N_6 + 3\ SO_2 \xrightarrow{SO_2} 2\ Cs_2C_2N_6SO_3 + 1/8\ S_8 \qquad [1]$$

This reaction represents a typical disproportion reaction ($3\ SO_2 \rightarrow 2\ SO_3 + 1/8\ S_8$). The reaction of Cs_2CIT/SO_2 system is related to the known reaction of CsF with SO_2 resulting in $CsSO_3F$ and S_8.[50] Two more things are worth mentioning: (i) in contrast to the CsF/SO_2 reaction, no ultrasonic activation is needed for the spontaneous reaction of Cs_2CIT with SO_2,[50] and (ii) the related cesium cyano-tetrazolate was prepared in SO_2 without any reaction with the solvent SO_2.[30]

Unfortunately, the direct synthesis of **37** from CsN_3 and $CsN(CN)_2$ in SO_2 according *Scheme 3.3* did not yield the sulfonate **37**.

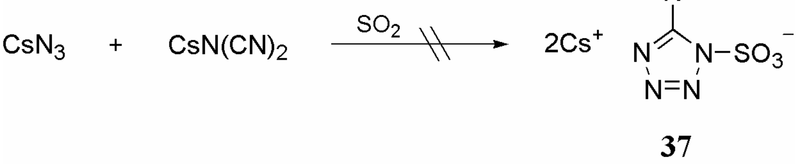

37

Scheme 3.3. Attempted synthesis of **37**

It is known that neutral as well as ionic azides can undergo cycloaddition with cyano groups, and W. Beck et al.[51] succeeded in the synthesis of bis(tetrazolate) dianions with complex metal azides. Also, the reaction of sodium dicyanamide with sodium azide under acid-catalyzed condition yields the corresponding bis(tetrazolate)amine.[3] It is also known that the reactivity of the 1,3-dipolar cycloaddition reaction of organic,[52] inorganic,[53] silyl,[54] and complexes as well as alkali metal azides with nitriles is greatly enhanced by electron-withdrawing groups bonded to the nitrile, and therefore there might be a chance for this reaction. Raman investigation of the obtained products (see experimental section) strongly supports the assumption that a condensation reaction took place, as no evidence for starting material (CsN_3 and $CsC(CN)_2$) was found. Unfortunately, also no evidence for the formation of the cesium **CIT** or **CITSO₃** was found. The reaction, which took place is still not understood and under further investigation.

2.2.8 Crystal Structure of $Cs_2CIT\text{-}SO_3 \cdot SO_2$ (**37**)

To ensure that the crystal was representative of the whole sample, its Raman spectrum was recorded, and no difference from the crushed sample was found. **37** crystallizes in the monoclinic space group $P2_1$ with two formula units in the unit cell. Bond lengths and angles are summarized in *Tables 3.1* and *3.5*. A view of the molecular arrangement can be depicted from *Figure 3.12*. Formally, **37** can be regarded as a donor-acceptor complex of CIT ($C_2N_6^{2-}$) and SO_3. However, upon "SO_3 complexation" the structural parameters of the CIT frame is not much affected (*Table 3.1*). The largest deviations are found for N2-N3 distance (**37**: 1.274(6) *vs.* **34**: 1.309(4) Å) and the C2-N6 (CN group, **37**: 1.147(7) vs. **34**: 1.174(4) Å), indicating a stronger localization of the π bonds in **37** along the N2-N3 and C2-N6 units. The S-N distance of 1.738(4) Å represents a typical single bond (*cf.* 1.791 Å in $SO_3(N_2O_2)^{2-}$,[55] and $\Sigma r_{cov}(SN)$ = 1.74 Å).[43] The length of the sulfonate S–O bonds are in good agreement with those of known sulfonate salts[55,56] and the sulfonate O atoms are approximately staggered with respect to the substituents on N1. The O–S–O angle in the sulfonate groups are increased due to the no longer balanced repulsion of the lone pairs, giving O–S–O angle greater than the tetrahedral angle of 109.47°. The SO_2 solvent molecule has regular bond lengths, and the O-S-O angle is comparable to those of the gas phase structure and therefore are not affected by the crystal lattice.[50,57]

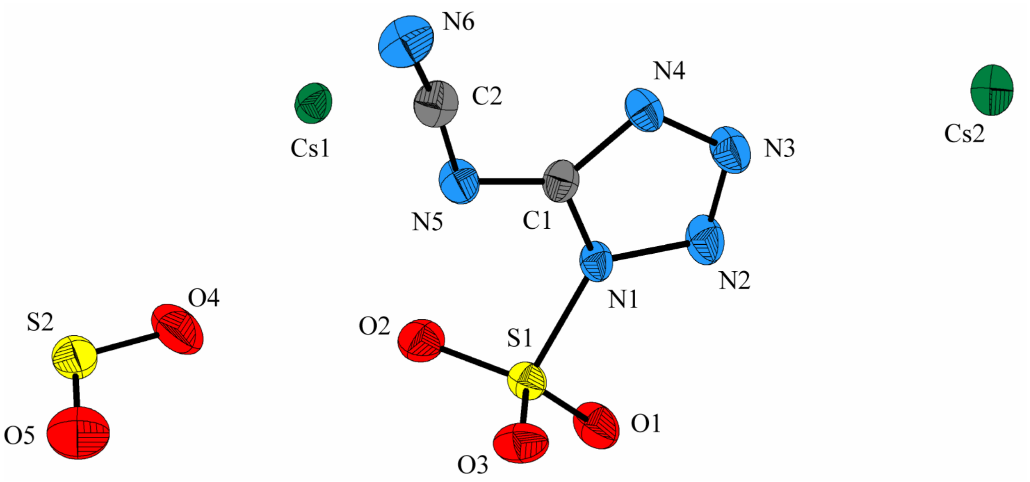

Figure 3.12. Formula unit and labeling scheme for **37** (ORTEP Plot, thermal ellipsoid represents 50% probability).

Table 3.5. Selected geometric parameters (Å, °) of **37**

N1–S1	1.738(4)	S1–O3	1.425(4)
S1–O1	1.434(4)	S2–O4	1.423(5)
S1–O2	1.437(4)	S2–O5	1.423(5)
O1–S1–O2	115.2(2)	N1–S1–O2	103.6(2)
O1–S1–O3	116.5(3)	N1–S1–O3	102.7(2)
O2–S1–O3	113.0(3)	O4–S2–O5	117.3(2)
N1–S1–O1	103.6(2)		

Both Cs^+ cations possess a coordination number of ten, which is quite common for cesium salts.[58] Cs1 has contacts to seven oxygen and three nitrogen atoms resulting from four dianions and two SO_2 molecules. Cs2 has contacts to five oxygen and five nitrogen atoms resulting from five dianions and three SO_2 molecules (*Figure 3.13*, *Table 3.6*). The SO_2 solvent molecule always coordinates to five different Cs cations. As shown by the investigation of the valency units, the Cs-N and Cs-O interactions are essentially ionic. The sum of the valency units to Cs^+ and the dianion is 1.9803, is consistent with a single positive charge on each Cs cation and two negative charges on the **CITSO$_3$** anion (*Table 3.6*).

Table 3.6. Observed Cs-N contacts and calculated valency units in **37**

contact[a,b]	distance (Å)	valency units[c]	Contact[a,b]	distance (Å)	valency units[c]
Cs1–O1^{i}	3.034(4)	0.1350	Cs2–O1^{iv}	3.390(4)	0.0649
Cs1–O2	3.146 (4)	0.1061	Cs2–O2^{iv}	3.147(3)	0.1061
Cs1–O2^{ii}	3.328(4)	0.0733	Cs2–O4^{iv} (SO_2)	3.277(5)	0.0812
Cs1–O3^{iii}	3.054(4)	0.1293	Cs2–O4^{viii} (SO_2)	3.743(5)	0.0337
Cs1–O3^{ii}	3.181(5)	0.0988	Cs2–O5^{ix} (SO_2)	3.406(5)	0.0629
Cs1–O4 (SO_2)	3.336(4)	0.0722	Cs2–N3	3.335(5)	0.1109
Cs1–O5^{ii} (SO_2)	3.537(4)	0.0491	Cs2–N3^{v}	3.435(5)	0.0913
Cs1–N2^{i}	3.306(4)	0.1175	Cs2–N4	3.503(5)	0.0802
Cs1–N5^{ii}	3.287(5)	0.1221	Cs2–N6^{vi}	3.127(5)	0.1697
Cs1–N5	3.315(5)	0.1154	Cs2–N6^{vii}	3.153(6)	0.1606
sum of valency units		1.0188			0.9615

[a] Locations of contacts are shown in Figure 10. [b] Symmetry codes for **7**: (i) -x, -0.5+y, -z; (ii) 1-x, -0.5+y, -z; (iii) x, -1+y, z; (iv) x, y, 1+z; (v) –x, 0.5+y, 1-z; (vi) -1+x, y, z; (vii) 1-x, 0.5+y, 1-z; (viii) –x, 0.5+y, -z; (ix) 1-x, y, z+1. [c] Valency units were calculated using Brown's expression $s = (R/R_0)^{-N}$ where R is the observed contact distance; R_0 is the distance corresponding to a valency unit of 1, and N is a fitted constant. Values of R_0 for contacts to N and O differ by an average of 0.10 to 0.15 Å for other nuclei; R_0 for Cs–O is reported to be 2.24 Å, as no Cs–N contacts are given, R_0 was set to 2.39 Å. The value of N for Cs–O contacts is 6.6, and this value was used for the Cs–N contacts.

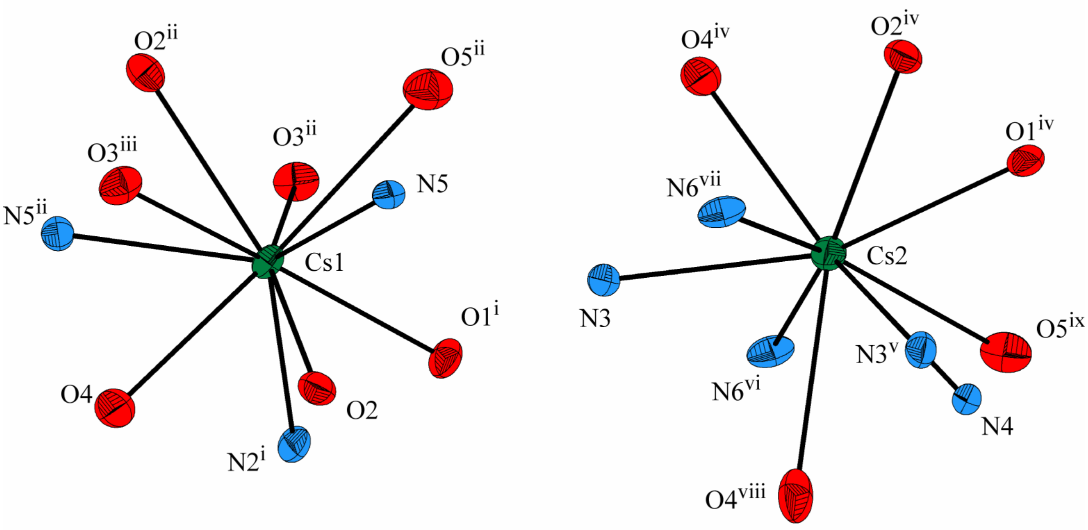

Figure 3.13. View of cesium coordination environment in $Cs_2CIT\text{-}SO_3{\cdot}SO_2$ (**37**)

2.2.9 CIT *versus* CITSO$_3$

The best Lewis representation, according to the NBO analysis along with the WBIs and partial charges, is displayed in *Figure 3.14*. The bond situation of the **CIT** subunit in **CITSO$_3$** corresponds to the best representation found for the **CIT** anion. Investigation of the donor-acceptor interaction displays similar delocalization effects as found for **CIT**, hence a similar resonance scheme as found for **CIT** (*Figure 3.9*) can be expected for **CITSO$_3$**. Interestingly, the

C2-N6 distance of the NCN and the N2-N4 distance decrease upon addition of SO_3, indicating a better localization of the triple bond along the CN group (WBI, **34**: 2.46 *vs.* **37**: 2.57) and a double bond along N2-N3 (WBI, **34**: 1.50 *vs.* **37**: 1.60). The S–N bond, as well as all S–O bonds, are highly polarized resulting in a large positive charge at S (+2.45*e*). Similar to the situation in the CIT anion, all N atoms attached to a carbon in the **CITSO₃** anion possess the largest negative charge, and for both species the most negatively charged N atom is the amido nitrogen followed by the terminal N atom of the NCN group. Upon addition, a considerable charge transfer occurs (q_{CT} = 0.49*e*). The tetrazole ring transfers 0.33*e* and the NCN moiety 0.16*e*, respectively, resulting in an overall negative charge for the **CIT** subunit of only 1.51*e*.

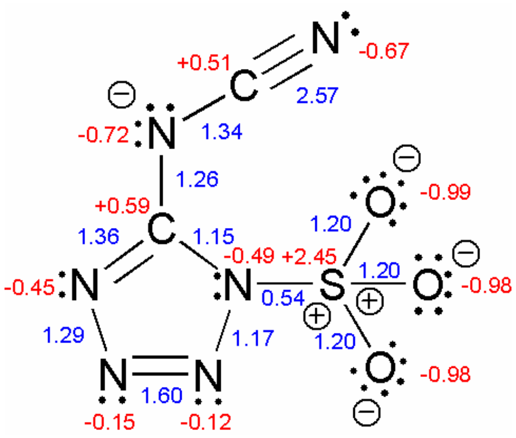

Figure 3.14. Best Lewis representation of **CITSO₃** according to NBO analysis along with WBI's (blue color) and NPA charges (red color).

2.3 Conclusions

An improved synthesis of **CIT** (CIT = $C_2N_6^{2-}$) salts and fully characterized a series of different **CIT** salts and complexes were reported for the first time. The **CIT** dianion represents a nitrogen-rich binary CN anion with surprisingly high thermal stability which decomposes in the case of the cesium salt (**34**) above 395 °C into cesium azide and cesium dicyan amide. The crystal structures of several **CIT** salts reveal the large coordination potential for **CIT** as ligand utilizing several mono- and bidentate modi. Surprisingly, Cs_2CIT reacts with liquid SO_2 in a disproportion reaction yielding a new anion, $C_2N_6SO_3^{2-}$ (**CITSO₃**). The easy access of **CIT** salts may qualify them as a useful educts for the preparation of new charge transfer, ferro- or antiferrormagnetic complexes, as well as basis for supramolecular frameworks, contacting organic radical cation salts and in material science as precursor for novel ternary $M_xC_yN_z$ or binary C_xN_y systems.

2.4 Experimental

Materials. All chemical reagents and solvents of analytical grade were obtained from Sigma-Aldrich Fine chemicals Inc. and used as supplied. Et_2O, MeOH and EtOH were dried according known procedures, freshly distilled and stored under nitrogen.

General Procedure. All reactions in liquid SO_2 were performed in two-bulb, two-valve Pyrex vessels incorporating 10 mL bulbs using techniques that have been described previously.[59] Solid reagents and crystals were manipulated in a Brown Drybox containing an internal circulating drying unit. The ^{1}H, ^{13}C and $^{14}N/^{15}N$ NMR spectra were recorded on a Jeol Eclipse 400 instrument. The spectra were measured in [d_6]-DMSO at 25°C. The chemical shifts are given relative to tetramethylsilane (^{1}H, ^{13}C) or nitromethane ($^{14}N/^{15}N$) as external standards. Coupling constants are given in Hz. Infrared (IR) spectra were recorded on a Perkin-Elmer Spektrum One FT-IR instrument as KBr pellets at 20°C. Raman spectra were recorded on a Perkin Elmer Spectrum 2000R NIR FT-Raman instrument equipped with a Nd:YAG laser (1064 nm). The intensities are reported in % relative to the most intense peak and given in parenthesis. Elemental analyses were performed with a Netsch Simultanous Thermal Analyser STA 429. Melting points were determined by differential scanning calorimeter (Perkin-Elmer Pyris 6 DSC, calibrated by standard pure Indium and Zinc). Measurements were performed at a heating rate of β = 10°C in closed Al-containers with a hole (1μm) on the top for gas release, and a 0.003*3/16-in. disk was used to optimize good thermal contact between the sample and the container with a nitrogen flow of 20 mL min^{-1}. The reference sample was an Al-container with air.

Synthesis of azido-*N*-cyanoformamidine (cyanoguanyl azide) (**32**). Amino-1*H*-tetrazolium monohydrate (25.95 g, 0.25 mol), suspension in 40 mL of water, was brought in solution and neutralized by adding a concentrated solution of sodium hydroxide (phenolphthalein as indicator). To the cooled solution (0°C) 75 ml acetone and cyanogen bromide (27.0 g, 0.25 mol) were added in small portions while agitating. The reaction mixture was stirred for 3 hours at 0°C and 2 hours at RT. After that, the solution was extracted with Et_2O (4 x 250 mL), and the ether solution was dried with anhydrous magnesium sulfate. Pure **2** (19,94 g, 72.5%) was obtained after evaporation and re-crystallization from Et_2O. m.p. 145 °C (dec.); IR (KBr, cm^{-1}): $\tilde{\nu}$ = 3355 (s), 3172 (s), 2707 (vw), 2659 (vw), 2456 (vw), 2187 (vs),

2161 (vs), 2131 (m, sh), 1646 (vs), 1562 (vs), 1497 (w), 1433 (vs), 1369 (m), 1243 (s), 1210 (s), 1191 (s), 1031 (m), 888 (m), 718 (w), 705 (w), 635 (m), 603 (m), 539 (w), 445 (w); Raman (200mW, 25 °C, cm^{-1}) $\tilde{\nu}$ = 3289 (2), 3178 (6), 2187 (100), 2166 (35), 2127 (10), 1673 (4), 1575 (15), 1564 (22), 1415 (40), 1373 (6), 1245 (9), 1191 (6), 1120 (2), 1027 (8), 894 (4), 720 (6), 609 (35), 561 (2), 485 (5), 442 (28), 227 (75), 191 (20), 159 (81), 115 (16); ^{1}H NMR ([d6]-DMSO, 25°C) δ: 8.53 (s, NH), 8.79 (s, NH); ^{13}C NMR ([d6]-DMSO, 25°C) δ: 114.2 (*C*N), 163.3 (C); ^{15}N NMR ([d6]-DMSO, 25°C) δ: -141.6 (*N*-NH_2), -147.5 (*C*N), -176.1 (N_β)[60], -267,8 (N_γ), -278.0 (N_α), -280.2 (N1-*N*H_2, $^1J_{NH}$ = 91.1 Hz); MS (DEI, 70 eV, >5%); *m/z* (%): 110 (48) [M^+], 81 (38), 68 (10), 67 (6), 66 (6), 54(12), 53 (32), 52 (5), 42 (100), 41 (23), 40 (10), 38 (6), 30 (55), 29 (21), 28 (36), 27 (18), 26 (7); $C_2H_2N_6$ (110.08): calc. C, 22.34; H, 2.07; N, 75.50 %; found: C, 22.37; H, 2.05; N, 75.54 %.

Isopropylammonium salt of 5-cyaniminotetrazoline, (^{i}PrNH$_3$)$_2$CIT•MeOH, (**35**). To a slurry of **32** (11,01 g, 0,1 mol) in 60 mL EtOH isopropylamine (12.41 g, 0.21 mol) was added at once, and the solution allowed to warm spontaneously. The azide dissolves with immediate precipitation of the salt **35**. The slurry was stirred for further 20 minutes and Et_2O (150 mL) was added. The white, hygroscopic powder was separated by filtration, washed with ether and dried. Yield 22.0 g (96 %) of **35**. X-ray-quality crystals of **35** • MeOH were grown from concentrated MeOH solution at RT in the course of 3 days. IR (KBr, cm^{-1}): $\tilde{\nu}$ = 3041 (m), 2990 (s), 2941 (s), 2832 (s), 2750 (s), 2655 (m), 2559 (m), 2554 (m), 2149 (vs), 1640 (m), 1532 (m), 1490 (vs), 1394 (m), 1383 (w), 1358 (m), 1244 (m), 1224 (m), 1199 (m), 1164 (m), 1130 (m), 1055 (w), 1038 (m), 954 (vw), 938 (vw), 801 (w), 760 (w), 571 (w), 478 (m); Raman (200mW, 25 °C, cm^{-1}) $\tilde{\nu}$ = 2984 (96), 2949 (95), 2933 (100), 2888 (69), 2749 (27), 2691 (16), 2562 (11), 2257 (7), 2148 (85), 1624 (9), 1501 (98), 1466 (49), 1400 (11), 1373 (19), 1360 (31), 1228 (30), 1201 (32), 1168 (16), 1132 (53), 1058 (82), 1019 (24), 957 (12), 940 (22), 804 (62), 763 (6), 570 (40), 482 (24), 442 (74), 426 (38), 378 (13), 349 (17), 208 (45), 171 (34), 136 (34); ^{1}H NMR ([d6]-DMSO, 25°C) δ: 1.09 (d, 6H, ^3J = 6.4 Hz), 3.17 (hept, 1H, ^3J = 6.4 Hz), 6.82 (s, 3H); ^{13}C NMR ([d6]-DMSO, 25°C) δ: 23.2 (CH_3), 43.1 (CH), 124.0 (CN), 163.2 (C); *m/z* (FAB^-, xenon, 6keV, glycerine matrix) 109 $[C_2N_6+H]^-$, 219 $[2(C_2N_6+H)+H]^-$; $C_8H_{20}N_8$ (228.30): calc. C, 42.09; H, 8.83; N, 49.08 %; found: C, 41.86; H, 8.92; N, 49.13 %.

Cesium salt of 5-cyaniminotetrazoline, Cs$_2$CIT, (**34**). **32** (6.85 g, 30 mmol) was dissolved in 80 mL MeOH, and a solution of CsOH*H_2O (10.08 g, 60 mmol) in 40 mL was added. The volatiles were removed under reduced pressure leaving a powdery white residue.

The residue was recrystallized from MeOH/Et_2O (10.9 g, 97 %). m.p. 335°C; IR (KBr, cm^{-1}): $\tilde{\nu}$ = 2379 (w), 2136 (vs), 1714 (w), 1639 (w), 1590 (w), 1526 (s), 1495 (vs), 1364 (s), 1261 (vw), 1217 (w), 1201 (w), 1190 (w), 1158 (vw), 1117 (w), 1042 (vw), 1003 (w), 791 (w), 763 (m), 704 (w), 626 (vw), 579 (m); Raman (200mW, 25 °C, cm^{-1}) $\tilde{\nu}$ = 2123 (38), 2115 (61), 1570 (7), 1521 (6), 1480 (26), 1469 (100), 1448 (8), 1358 (22), 1218 (12), 1183 (30), 1154 (8), 1104 (27), 1035 (68), 997 (7), 785 (13), 761 (7), 567 (25), 441 (33), 348 (19), 187 (39), 161 (10), 143 (7); ^{13}C NMR ([d6]-DMSO, 25°C) δ: 128.1 (CN), 166.6 (C); *m/z* (FAB^-, xenon, 6keV, NBA matrix) 109 $[C_2N_6+H]^-$; $C_2Cs_2N_6$ (373.87): calc. C, 6.43; Cs, 71.10; N, 22.48 %; found: C, 6.56; N, 22.23 %.

Triamine(CIT)palladium(II) monohydrate $[Pd(C_2N_6)(NH_3)_3]{\bullet}H_2O$ (**36**). To a solution of **32** (220 mg, 2 mmol) in 5 mL water and 2 mL conc. NH_3 a solution of tetraaminepalladium(II) chloride[61] (490.9 mg, 2 mmol) in 5 ml H_2O was added and heated for 10 minutes to 75°C. Pale yellow plates of **6** (406 mg, 72%) crystallized after one week from the pale yellow solution. IR (KBr, cm^{-1}): $\tilde{\nu}$ = 3444 (s), 3278 (s), 3164 (s), 3058 (s), 2923 (m), 285 (w), 2128 (vs), 1637 (w), 1577 (w), 1518 (s), 1380 (m), 1325 (vw), 1281 (m), 1265 (m), 1230 (m), 1115 (m), 861 (w), 837 (w), 786 (w), 748 (w), 569 (w), 501 (w), 478 (w); Raman (200mW, 25 °C, cm^{-1}) $\tilde{\nu}$ = 3279 (9), 3193 (10), 2123 (64), 1575 (5), 1514 (27), 1422 (3), 1377 (8), 1318 (10), 1297 (15), 1266 (22), 1230 (14), 1151 (5), 1116 (25), 1097 (28), 1003 (16), 851 (5), 788 (13), 751 (9), 573 (32), 509 (100), 487 (57), 364 (8), 257 (25), 219 (25), 154 (28); $C_2H_{11}N_9OPd$ (283.59): calc. C, 8.47; H, 3.91; N, 44.45%; found: C, 8.53; H, 3.82; N, 44.20%.

Dicesium 5-cyaniminotetrazoline-1-sulfonatediide·SO_2, $Cs_2CITSO_3{\cdot}SO_2$, (**37**). SO_2 (~ 10 mL) was condensed onto cooled (-196 °C) **34** (560 mg, 1.5 mmol), giving a bright yellow solution, which turned deep yellow, red and then brown after warming to RT. The reaction mixture was stirred for 1 day, and a clear, pale yellow solution containing a gummy residue was obtained. The solution was separated from the residue by filtration and reduced to half of its volume. After 1 week pale yellow crystals of **37** (312 mg, 40%) were obtained. IR (KBr, cm^{-1}): $\tilde{\nu}$ = 2342 (vw), 2153 (s), 1642 (sh, m), 1588 (sh, m), 1556 (vs), 1529 (vs), 1378 (m), 1358 (s), 1292 (vs), 1265 (vs), 1215 (sh, m), 1142 (m), 1125 (m), 1087 (s), 1042 (s), 742 (w), 629 (s), 608 (s), 559 (m), 476 (w); Raman (200mW, 25 °C, cm^{-1}) $\tilde{\nu}$ = 2166 (23), 1546 (13), 1477 (3), 1355 (4), 1303 (26), 1227 (13), 1144 (100), 1117 (8), 1086 (16), 1046 (47), 987 (7), 886 (3), 793 (10), 621 (6), 601 (7), 545 (17), 531 (7), 480 (20), 398 (7), 338 (24), 297 (30), 208 (25),

135 (20); ^{13}C NMR ([d6]-DMSO, 25°C) δ: 136.0 (CN), 164.1 (C); $C_2Cs_2N_6SO_3*xSO_2$ (x=1, 373.87): calc. C, 4.64; S,12.38; N, 16.22 %; found: C, 5.66; S, 9.30; N, 19.53 %.

Attempted direct Synthesis of $Cs_2CITSO_3·SO_2$, (37): In order to prepare **37** in a direct synthesis, SO_2 (~10 mL) was condensed at -196 °C onto freshly prepared CsN_3 (525 mg, 3 mmol)[62] and $CsN(CN)_2$ (597 mg, 3 mmol), giving a bright yellow solution at room temperature. Within minutes, the solution became orange/red and a dark red oil starts to separate. The reaction mixture was stirred at room temperature for 1 day, and the obtained clear yellow solution separated from the formed red residue by filtration. Concentration of the yellow solution by dynamic vacuum (gas phase IR: SO_2) yielded 0.135 g of a pale yellow product, soluble in MeOH. The Raman spectrum of the pale yellow solid, as well as of the red residue did not show any characteristic bands which could be assigned to **CIT**, **$CITSO_3$**, CsN_3 or $CsN(CN)_2$. The red residue (1.245 g) dissolves in water under release of SO_2, yielding a yellow solution. Both products are still under investigation.

X-ray Analyses. X-ray quality crystals of **35** and **36** were mounted in a Pyrex capillary and the X-ray crystallographic data collected on a Nonius Mach3 diffractometer with graphite-monochromated MoK_α radiation (λ = 0.71073 Å). The X-ray crystallographic data for **5** and **7** were collected on a Kappa CCD diffractometer using graphite-monochromated MoK_α radiation (λ = 0.71073 Å). Unit cell parameters of **4** and **6** were obtained from setting angles of a minimum of 25 carefully centered reflections having $2\theta > 20°$; the choice of the space groups was based on systematically absent reflections and confirmed by the successful solution and refinements of the structures. The structures were solved by direct methods (SHELXS-86 (**35**, **36**), SHELXS-97 (**34**), SIR97 (**37**))[63] and refined by means of full-matrix least-squares procedures using SHELXL-93 and SHELXL-97. Crystallographic data are summarized in *Appendix B*. Selected bond lengths and angles are available in *Table 3.1*, the numbering and the molecular model of the C_2N_6 frame in 5-cyaniminotetrazolinediide is given in *Figure 3.7.* All non-hydrogen atoms were refined anisotropically. In the case of **35** and **36** the hydrogen atoms were included at geometrically idealized positions and refined. They were assigned fixed isotropic temperature factors with the value of $-1.2B_{eq}$ of the atom to which they were bonded. Further information on the crystal-structure determinations (excluding structure factors) has been deposit with the Cambridge Crystallographic Data Centre as supplementary publication no. 267216(**35**), 267217(**36**), 267200(**37**) and 267201(**34**).[64]

3. H_2bta as HNC ligand system

As *N,N*-bis-(1(2)*H*-tetrazol-5-yl)-amine (H_2**bta**) is a bidentate chelating ligand with multi-proton donor sites, it is able to coordinate to a metal with three reversible types of protonated and deprotonated modes: neutral (H_2**bta**), mono-deprotonated (monoanion, H**bta**$^-$), and di-deprotonated (dianion, **bta**$^{2-}$) types (*Scheme 3.4*).

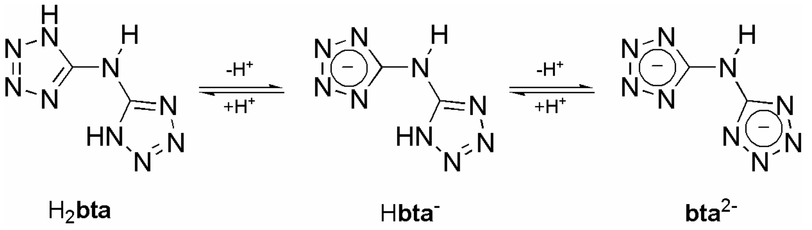

Scheme 3.4. H_2**bta** (**30**) with two reversible types of protonated and deprotonated mode

Moreover, H_2**bta** can be utilized as new bridging ligand for controlling the molecular architectures which, in combination with appropriate outer- and inner-sphere ligands, allows the variation of physicochemical and explosive properties within a wide range. H_2**bta** and its deprotonated modes might serve as ligand in a new generation of high-performance energetic materials with increased safety. As in comparison to azide based PCs, the azide group is disguised in a aminotetrazole moiety, known to be stabilized due to the extended 6π system.

3. 1 Alkali and alkaline earth metal salts

The procedure used to prepare BTA differs from the procedures described in literature, and a detailed description can be found in the experimental part. **BTA** is formed as a white amorphous powder, and all attempts to crystallize it without any additional coordinated solvents (like DMSO) failed so far. The structure of the parent H_2**bta** was obtained co-crystallized with the mono sodium salt in Na(Hbta)(H_2bta)*3H_2O (**38**). The synthesis for **38** can also be found in the experimental section, and a view of the subunit of the crystal structure of **38** is depicted in *Figure 3.15*; the structure is not going to be discussed in detail. **38** crystallizes in the orthorhombic crystal structure $P2_12_12_1$ with four molecular units in the unit cell. Sodium is coordinated in a distorted octahedral manner by two nitrogen atoms from one H_2**bta** and one H**bta**$^-$ molecule and four oxygen atoms donated from the water molecules. The H_2**bta** and one

H**bta**$^-$ molecule are connected thus to yield 1D stacks orientated along the [100] axis. These stacks are inter-linked by strong Crieg-like hydrogen bridges forming a complicated polymeric structure.

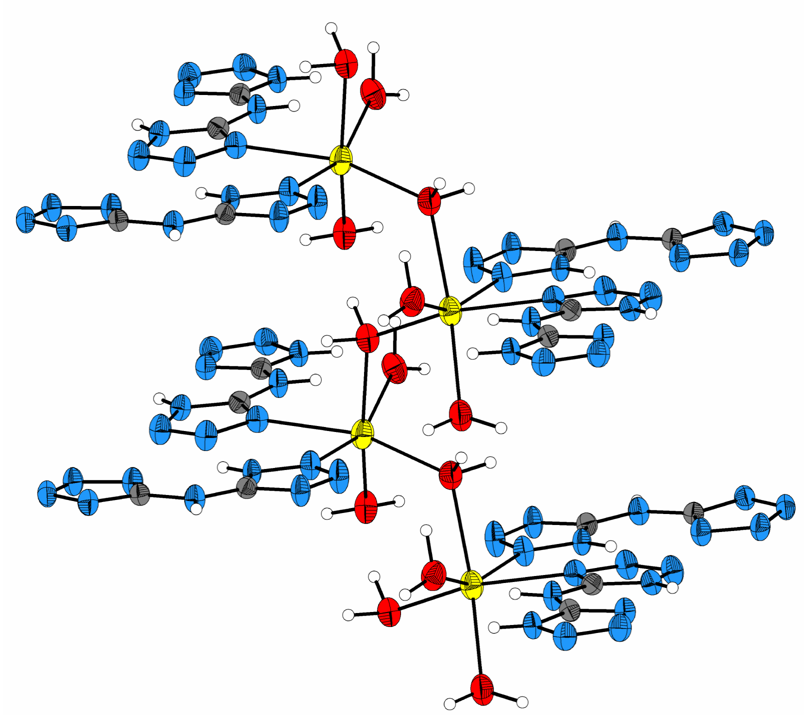

Figure 3.15. Subunit of the crystal structure in **38** along the [100] axis. (blue: nitrogen; gray: carbon; red: oxygen; white: hydrogen)

BTA is air stable and can be handled safely in hydrated from. It is not friction (> 360 N) and impact (> 40 J) sensitive and can be easily deprotonated with any hydroxide and carbonate of the alkaline or alkaline earth metals yielding, depending on the amount of added base, the corresponding mono-deprotonated (Cs^+(Hbta$^-$) (**39**) and the already mentioned mixed H_2bta/hbta$^-$ type in Na(Hbta)(H_2bta)*3H_2O (**38**)) or di-deprotonated ((M^+)$_2$(bta^{2-}) M^+ = Li (**40**), K (**41**), Na (**42**), Rb (**43**), Cs (**44**); M^{2+}bta^{2-} M = Ca (**45**), Ba (**46**)) salts. Crystals of **41** could not be obtained due to twinning problems.

3.1.1 Raman spectroscopy

The **bta** salts can be easily and rapidly identified by Raman and IR spectroscopy, especially for the deprotonated bta^{2-} (symmetry of the molecule C_{2v}). In the IR spectra three strong vibrations are observed at ~ 1688, 1630 and 1510 cm^{-1} which can be addressed to the ν_{asym} (C_{tet}–N–C_{tet}), ν_{asym} (C_{tet}–N–C_{tet} + N–H) and ν_{sym} (C_{tet}–N–C_{tet}), respectively. In the Raman

experiment only the ν_{sym} (C_{tet}–N–C_{tet}) vibrations (~ 1500 cm^{-1}) are observed as one of the strongest bands (*Figure 3.16*). Successively protonation (**bta**$^{2-}$ → H**bta**$^{-}$ → H_2**bta**) should lead in the case of the monodeprotonated species H**bta**$^{-}$ to a splitting of this mode (ν_{sym} C_{tet}–N–C_{tet}'), which is confirmed by the Raman spectrum of CsH**bat***H_2O (**39**) (*Figure 3.16*). In the case of the H_2**bta** (**30**), again only one vibration for the ν_{sym} (C_{tet}–N–C_{tet}) is observed, but shifted to higher wavenumber (1552 cm^{-1}, Figure *3.16*), since the vibration modes of the differently orientated tetrazole rings (Figure 3.15) are almost identical in energy. The Raman as well the IR spectra of the **bta** salts also contain a set of characteristic absorption bands: 3400-3000 cm^{-1} [ν(NH)], 1750-1550 cm^{-1} [δ(NH), ν_{asym} (C_{tet}–N–C_{tet})], 1550-1350 cm^{-1} [ν tetrazolate ring, δ(NH)], 1350-700 cm^{-1} [ν(NCN), ν(NN), ω(NNH_2), γ(CN), δ tetrazolate ring], <700 cm^{-1} [δ out of plane bend (N–H)].

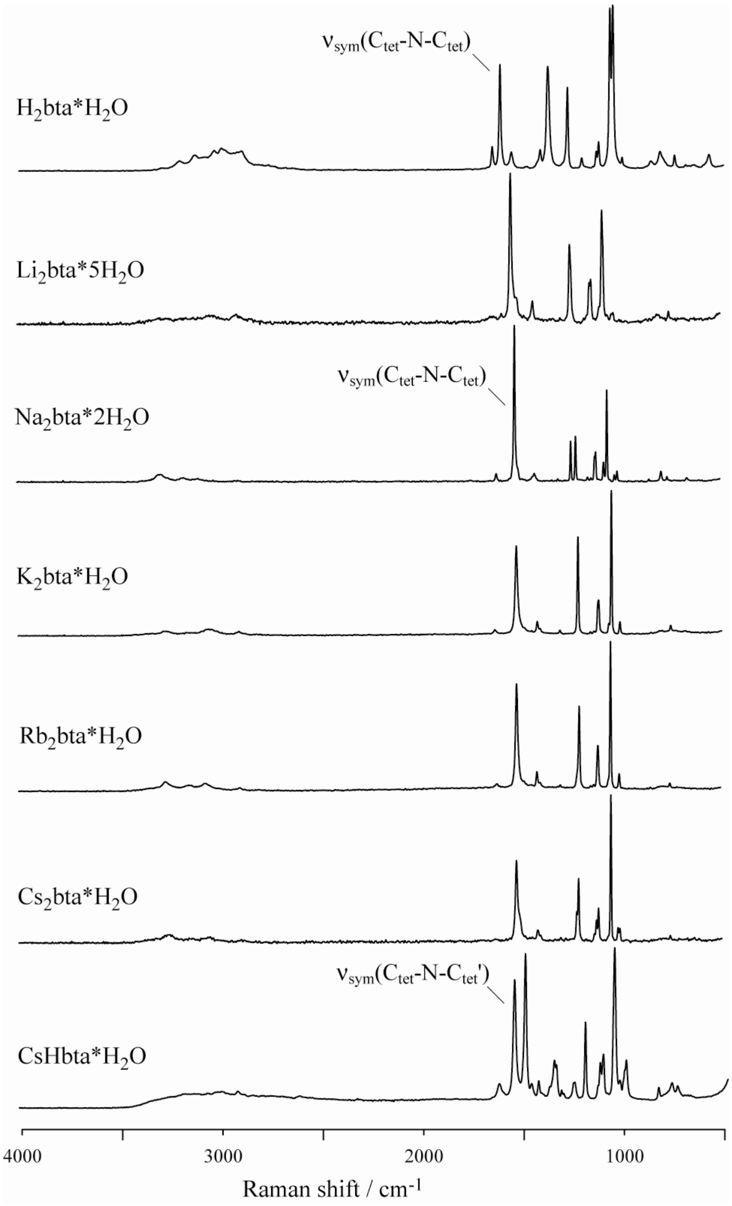

Figure 3.16. Raman spectra of alkaline **bta** salts

3.1.2 Crystal structure of $Li_2bta*5H_2O$(**40**)

Since the coordination pattern of the lithium salt **40** differs markedly from the others, a detailed discussion is given below. **40** crystallizes in the monoclinic space group $P2_1/n$ as pentahydrate which readily loses crystal water, stored on air. Weathered crystals of **40** ($Li_2(bta)*xH_2O$) showing an crystal water content of $2 < x < 2.5$. The asymmetric unit consists of two lithium cations, five water molecules and one bta ligand. The coordination environment of the Li^+ is shown in *Figure 3.17* (**A**). There are two differently coordinated Li^+ ions: The lithium atoms are coordinated distorted tetrahedral in which Li1 is connected to two nitrogen atoms (N2, N6; bta as bidentate ligand) and two water molecules, whereas Li2 is connected only to one nitrogen atom but three water molecules (N8; bta as monodentate ligand).

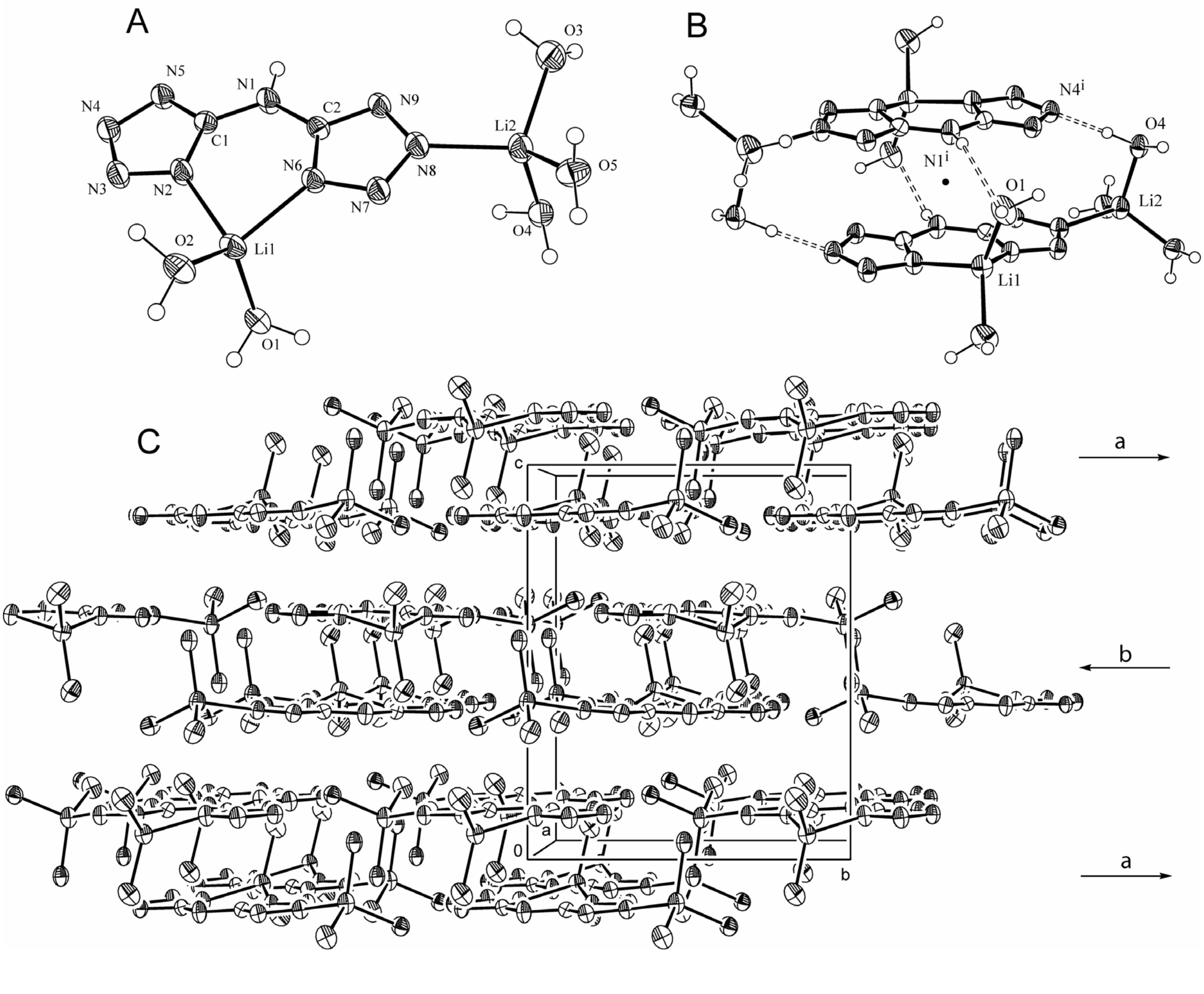

Figure 3.17. **A**: Coordination environment of the two Li^+ cations and numbering scheme of the molecular graph in **40** with 50% probability displacement ellipsoids; **B**: The dimeric subunit in **40** is related to the molecular graph by the symmetry operation 2-x, -y, -z. The dot indicates the inversion centre of this subunit; **C**: Packing diagram along the *a* axis, showing the layer sequence aba…; hydrogen atoms and hydrogen bonds are omit due to clarity.

The distances found for Li–N lies between 1.963(2) Å and 2.07(1) Å and for Li–O between 1.922(2) Å and 1.972(1) Å which is typical for tetrahedral coordinated Li^+ (*Table 3.7*).[65] The angular distribution around Li^+ is more uniform, ranging from 103.0(2) to 121.0(2)°. The smallest subunit of the crystal structure of **40** is an inversion symmetrically dimeric unit linked over two hydrogen bonds $N1^i$–$H1^i$····O1 and O4–H4A····$N4^i$ [symmetry code: (i) 2-x, -y, -z] together (*Figure 3.17*, **B**). These subunits are connected extensively by hydrogen bonds to sheet like layers forming rings to align along the *a* and *b* axis. In that way, channels running within the layers along that direction, which can be depicted from *Figure 3.17* (**C**). One layer, related to the next layer, is arranged in a reverse manner, and they are held together by only one type of hydrogen bond resulting from the interaction of two water molecules (O2–H2B····$O3^v$; symmetry code: (i) 2-x, 0.5+y, 0.5-z) coordinated to the lithium atoms (*Table 3.8*). The lateral packing of the layers arranged in an antiparallel manner (layer sequence is aba…) is simply a consequence of the centrosymmetric nature of the space group.

Table 3.7. Selected geometric parameters (Å, °) of **40** and **42**

Li_2(**bta**)*5H_2O (**40**)			
Li1–N2	2.026(5)	Li2–N2	2.052(5)
Li1–N6	2.07(1)	Li2–N2	1.96(2)
Li1–O1	1.939(8)	Li2–N2	1.972(4)
Li1–O2	1.95(2)	Li2–N2	1.922(6)
O1–Li1–N2	118.9(2)	O3–Li2–N8	107.0(2)
O1–Li1–N6	107.6(2)	O3–Li2–O4	116.3(2)
O1–Li1–O2	116.5(2)	O3–Li2–O5	103.0(2)
O2–Li1–N2	103.9(2)	O4–Li2–N8	105.8(2)
O2–Li1–N6	121.0(2)	O5–Li2–N8	117.5(2)
Na_2(**bta**)*2H_2O (**42**)			
Na1–$N5^i$	2.584(4)	Na1–$O1^{iv}$	2.365(6)
Na1–$N9^i$	2.572(5)	Na1–$O2^{iv}$	2.399(2)
Na1–$N6^{ii}$	2.510(4)		
Na1–$N8^{iii}$	2.584(4)		
O1–Na1–$N5^i$	94.57(2)	O2–Na1–$N5^i$	103.54(2)
O1–Na1–$N9^i$	151.41(3)	O2–Na1–$N9^i$	84.55(2)
O1–Na1–$N6^{ii}$	106.62(2)	O2–Na1–$N6^{ii}$	171.69(3)
O1–Na1–$N8^{iii}$	83.26(2)	O2–Na1–$N8^{iii}$	82.90(2)

Symmetry codes for Na_2(**bta**)*2H_2O **(42)**: (i) -1+x, 0.5-y, z; (ii) x, 0.5-y, z; (iii) 1-x,-y-z; (iv) x, -0.5-y, z.

3.1.3 Crystal structure of $Na_2(bta)*2H_2O$ (**42**)

The sodium salt crystallizes in the monoclinic space group $P2_1/m$ with four formula units in the unit cell. The numbering scheme and the coordination environment of the Na^+ can be depicted from *Figure 3.18*. The water molecules and **bta** anion, as well as the sodium cations, lie in special positions in space group $P2_1/m$, with $Z' = 0.5$. The Na^+ cations are positioned at (¼, n/2 + ½, ¼) and (¾, n/2 + ½, ¾) (n = zero or integer) forming a 1D metal-ligand chain with a shorter Na–Na distance of 3.220(1) [symmetry code: x, -0.5-y, z] and a longer Na–Na distance of 3.261(1) [symmetry code: x, 0.5-y, z] based on a reference sodium cation. Layers, consisting of water molecules and anions, lying on mirror planes which are found at y = (n/2 + ¼) (n = zero or integer).

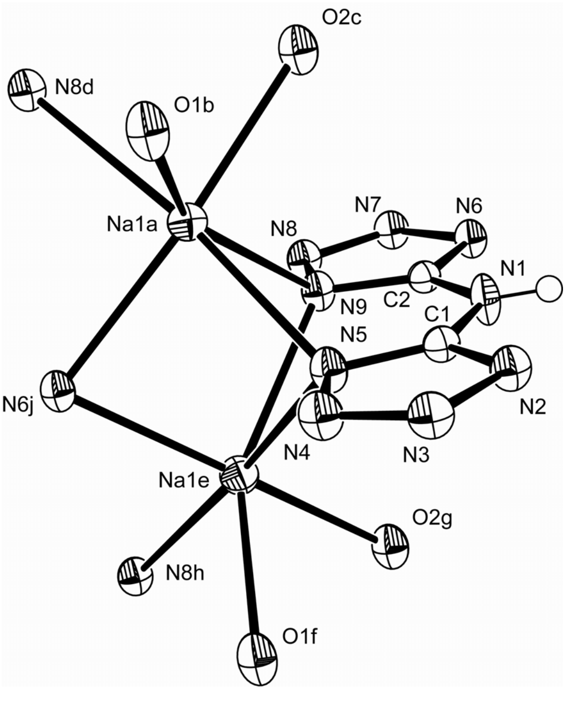

Figure 3.18. Part of the crystal structure of **42** showing the ionic components and the coordination geometry of Na. Displacement ellipsoids are drawn at the 50% probability level. Compared to the bta^{2-} anion as reference, atoms Na1a, O1a, O1b and N6j are at (1+x, y, z), N8d at (2-x, -0.5+y, -z), Na1e at (1+x, 0.5-y, z), O1f and O2g at (1+x, 1+y, z) and N8h at (2-x, 0.5+y, -z), respectively.

These layers are connected by the sodium cations. Each Na^+ is six-coordinated and approximately octahedral (*Table 3.8*, *Figure 3.18*). The coordination atoms (4N + 2O) around

the Na^+ lie in the anion at (1-x, -y, -z), (x, 0.5-y, z) and (-1+x, 0.5-y, z) (N donors), and at (x, -0.5-y, z) (O donors). These metal-ligand interactions thus generate a chain of confacial NaN_4O_2 octahedral running parallel to [010] (*Figure 3.19*), propagation of which by translation links all the ions and water molecules into a single-layered framework structure.

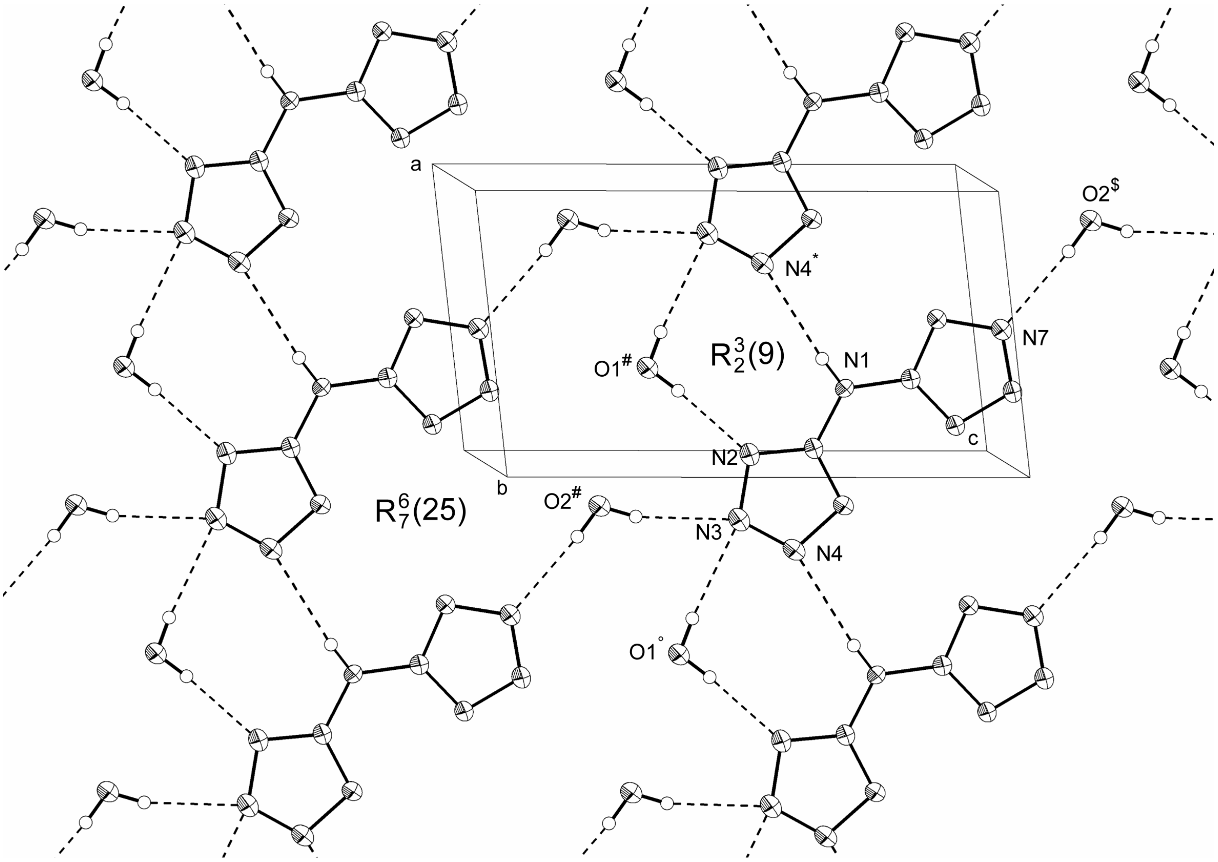

Figure 3.19. Part of the crystal structure of **42** showing the formation of the (010) sheet built from $R_7^6(25)$ and $R_3^3(9)$ rings. Atoms marked with an asterisk (*), hash (#), degree sign (°) or dollar sign ($) are at the symmetry positions (-1+x, y, z), (1-x, 0.5+y, 1-z), (2-x, 0.5+y, 1-z) and (-x, 0.5+y, -z), respectively.

In addition, the anions within each layer are linked over the water molecules into a continuous sheet by hydrogen bonds (*Table 3.8*, *Figure 3.19*). The water molecule O1 at (1-x, 0.5+y, 1-z) and (2-x, 0.5+y, 1-z) acts as hydrogen donor to N2 and N3 (O1–H1A····N2 and O1–H1B····N3) and together with the hydrogen bond N1–H1····$N4^{i}$ [symmetry code: (i) 1-x, y, z], chains parallel to [100] are generated. Adjacent [100] chains are linked by hydrogen bonds O2–H2A···$N3^{ii}$ and O2–H2B···$N7^{iv}$ [symmetry codes: (ii) 1-x, -0.5+y, 1-z and (iv) –x, -0.5+y, -z] over the second water molecule (*Table 3.8*). In this manner, the [100] chains are linked into (010) sheets built from $R_7^6(25)$ and $R_3^3(9)$ rings according the formalism of graph-set analysis of hydrogen-bond patterns.[66]

Table 3.8. Hydrogen bond geometry (Å, °) of **40** and **42**

D–H···*A*	*D*–H	H···*A*	*D*···*A*	*D*–H···*A*
Li_2(**bta**)*5H_2O (**40**)				
N1–H1···O1^{i}	0.860(3)	2.357(1)	3.14(1)	151.0(2)
O1–H1A···O5^{ii}	0.965(3)	1.914(9)	2.852(1)	163.3(2)
O1–H1B···N3^{iii}	0.921(7)	1.891(7)	2.79(1)	164.7(2)
O2–H2A···N9^{iv}	0.924(5)	1.874(7)	2.80(1)	174.9(2)
O2–H2B···O3^{v}	1.043(3)	2.008(4)	3.038(4)	169.0(2)
O3–H3A···O4^{vi}	0.906(8)	1.847(2)	2.74(2)	167.3(2)
O3–H3B···O2^{iv}	0.957(2)	2.225(3)	3.093(3)	150.3(2)
O4–H4A···N4^{i}	1.030(2)	1.747(3)	2.775(3)	175.7(2)
O4–H4B···N7^{ii}	0.943(5)	1.862(6)	2.79(1)	168.4(2)
O5–H5A···N6^{vii}	0.988(3)	2.262(2)	3.13(2)	146.2(2)
O5–H5B···N5^{viii}	0.913(4)	1.785(4)	2.692(6)	171.8(2)
Na_2(**bta**)*2H_2O (**42**)				
N1–H1···N4^{i}	0.76(3)	2.34(3)	3.10(1)	174(3)
O1–H1A···N2^{ii}	0.79(2)	1.99(2)	2.78(3)	175(2)
O1–H1B···N3^{iii}	0.79(2)	2.24(2)	3.02(3)	175(2)
O2–H2A···N3^{ii}	0.78(2)	2.14(2)	2.90(4)	165(2)
O2–H2B···N7^{iv}	0.77(2)	2.11(2)	2.89(2)	175(2)

Symmetry codes for Li_2(**bta**)*5H_2O (**40**): (i) 2-x, -y, -z; (ii) 2-x, -1-y, -z; (iii) 1-x, -y, -z; (iv) 1+x, y, z; (v) 2-x, 0.5+y, 0.5-z; (vi) 3-x, -1-y, -z ; (vii) 2-x, -0.5+y, 0.5-z ; (viii) x, -1+y, z. Symmetry codes for Na_2(**bta**)*2H_2O (**42**): (i) 1-x, y, z; (ii) 1-x, -0.5+y, 1-z ; (iii) 2-x, -0.5+y, 1-z; (iv) –x, -0.5+y, -z.

3.1.4 Crystal structure of **39**, **43** and **44**

Since the crystal structures of **39**, **43**, **44** and **46** are related to the crystal structure of **42**, and a detailed discussion would beyond the scope of this work, only a short description will be given. CsHbta*H_2O (**39**) crystallizes in the triclinic crystal system *P*-1 with two formula units in the unit cell. The before-mentioned formalism of graph-set analysis of hydrogen-bond patterns according to Etter[66] is a suitable tool to explain coordination polymers by means of repeating graph sets. The main graph sets in the structure of **39** is the $R_3^3(9)$ and the very common $R_2^2(8)$ (Figure 3.20). The $R_2^2(8)$ graph set represents the formation of a dimeric subunit of two bta molecules containing the inversion centre. The $R_3^3(9)$ has already been identified for **42** as liking unit of the **bta** moieties trough water molecules to strands, but here they serve also to the dimeric unit. Those units are linked through the cesium atoms and the $R_2^2(6)$ graph set to a 1D strand which is further linked by cesium atoms together with adjacent strands to a 2D overall sheet like structure (not shown in Figure 3.20).

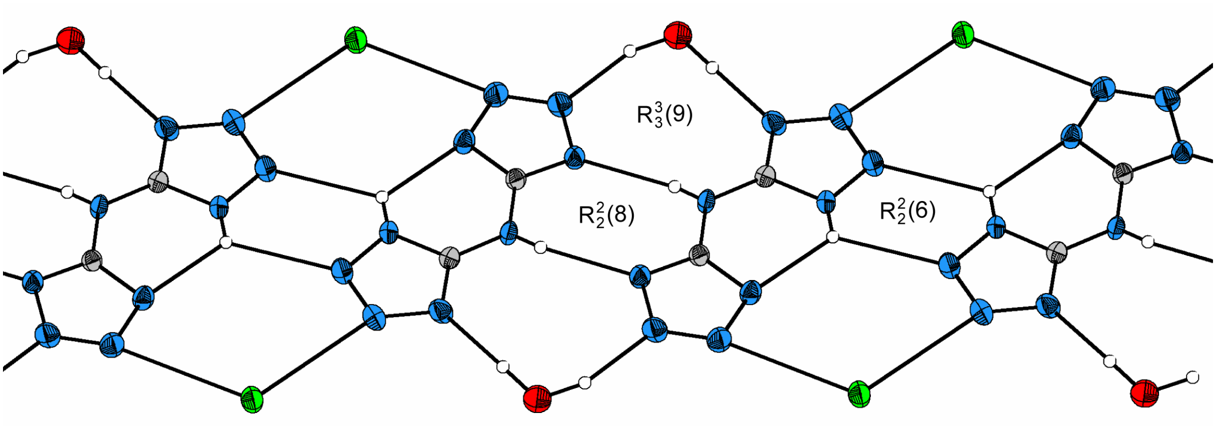

Figure 3.20. **A**: Main graphs sets in the 1D subunit of **39**. (blue: nitrogen; gray: carbon; red: oxygen; green: cesium; white: hydrogen).

Cs_2bta*H_2O (**44**) crystallizes in the orthorhombic space group *P*mc2_1 with two formula units in the unit cell. **44** forms also a 2D sheet like framework, but due to the lack of hydrogen donor atoms, however, only the formation of three types of hydrogen bonds are formed. *Figure 3.21* shows a few along the [100] axis, the same direction the 1D cesium chains running. The cesium atoms are located below and above these planes.

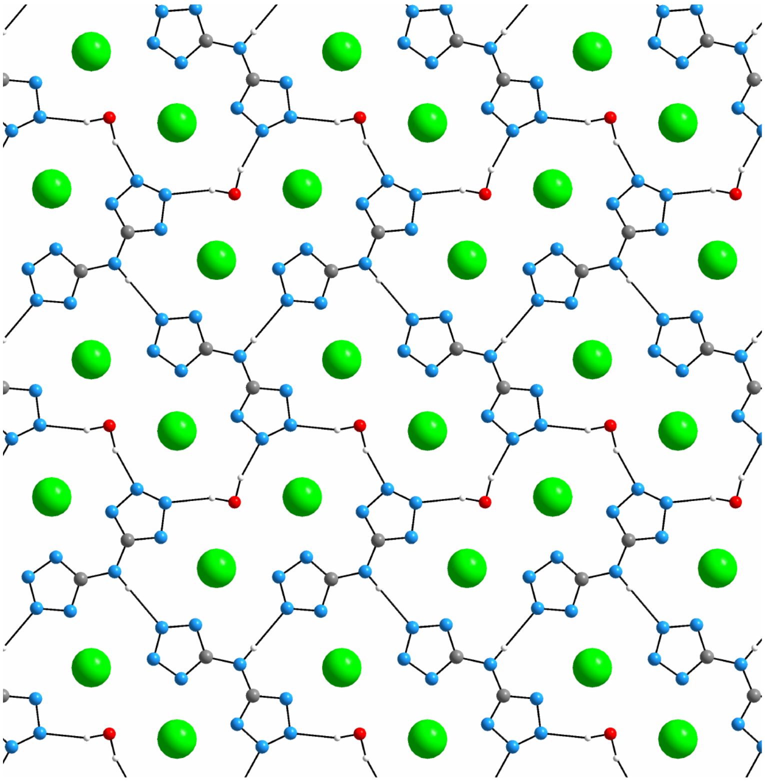

Figure 3.21. View along the [100] axis in **44**. Cesium atoms are located above and below these sheets forming 1D metal chains. (blue: nitrogen; gray: carbon; red: oxygen; green: cesium; white: hydrogen)

Rb_2bta*H_2O (**43**) crystallizes in the orthorhombic space group Pba$_2$ with four formula units in the unit cell. The crystal structure of Rb_2bta*H_2O (**43**) is comparable the structure of **44,** and due to the heavily disordered water molecules, a illustration is abstained.

3.1.5 Crystal structure of **45** and **46**

Ca**bta***5H_2O (**45**) crystallizes in the monoclinic space group *P*2/n with four formula units in the unit cell. The calcium salt of the bta dianion has an interesting feature. Calcium is seven coordinated, taking the form of a distorted overcapped octahedron in which four water molecules are directly linked to the metal, while the coordination is completed by two nitrogen atoms of an bta ligand (bidentate) and one nitrogen atom of a second bta ligand (monodentate). A closer inspection of this arrangement reveals the possibility of a second calcium atom to be coordinated which is related in symmetry to the first calcium atom by 0.5-x, y, 0.5-y. The same accounts for the second **bta** ligand, forming an overall dimeric structure which is the consequence of the two folded rotation axis this space group has as symmetry element. Atoms O1 and O4 are unique since they lie on the two folded rotation axis. The numbering scheme and the symmetry relation of **45** is depicted in Figure 3.22.

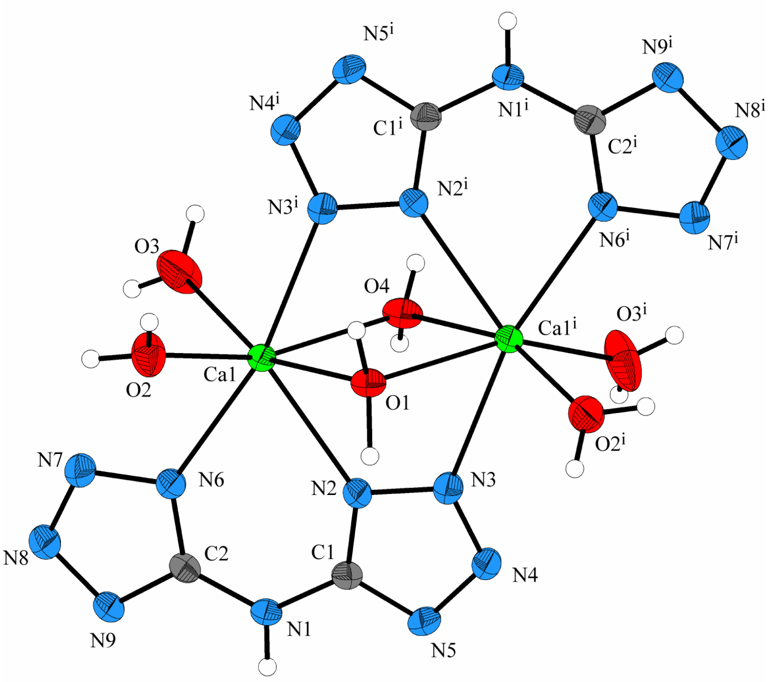

Figure 3.22. View of the dimeric unit in **45** showing the atom-numbering scheme and displacement ellipsoid at 50% probability level;. Atoms marked with ^{i} are at the symmetry position 0.5–x, y, 0.5–z.

The bta ring in **45** is essentially planar, and all observed bond length are as observed in other bta complexes (*e.g.* see this *Chapter*, 4) and therefore are not going to be discussed. The obtained Ca−O and Ca−N distances (ranging from Ca1−N3 2.491(2) to Ca1−N3 2.529(2) and for Ca1−O3 2.295(6) to Ca1−N3 2.551(3)) lie in the range normally obtained for the coordination of Ca^{2+} with other N or O donor systems.[67] These dimeric units are connected through several hydrogen bridges to an infinite three dimensional network.

The barium salt **46** crystallizes in the triclinic space group P-1 with two formula units in the unit cell. Moving from the comparable small calcium atom to the bigger barium atom leads to an almost identical arrangement of the cations and the bta ligands. Also, a dimeric subunit is formed with the difference that the half units are related *via* an inversion centre. Interestingly, since the coordination number of seven would difficult to be realized for Ba, in **46** a third bta ligand serves as addition N donor resulting in the formation of a chain like structure of the dimeric units together with an increasing of the coordination number to 9, typically for Ba structures. These chains are connected trough hydrogen bridges mediated by water molecules to an polymeric 3D structure. A view of the extended coordination mode by an additional bta ligand is depicted in *Figure 3.23*.

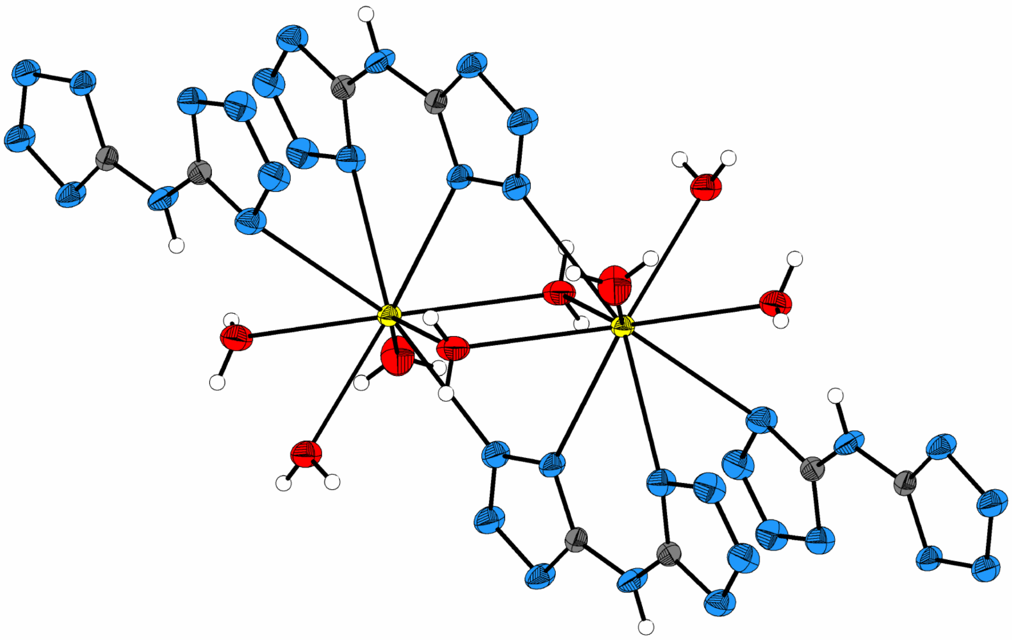

Figure 3.23. View of the extended dimeric unit in **46**. Displacement ellipsoid at 50% probability level. (blue: nitrogen; gray: carbon; red: oxygen; yellow: barium; white: hydrogen)

3.1.6 Experimental

H_2bta*H_2O (30):

Method 1: To a 500 ml three-neck reaction flask containing a refluxing suspension of sodium dicyanamide (8.9 g, 0.1 mol), sodium azide (13.0 g, 0.2 mol), 80 ml ethanol and 50 ml of water was added in the course of four hours 150 ml of 2M HCl. The reaction mixture was allowed to reflux for further 48 hours. After cooling to RT, 20 ml of conc. HCl was added and the white precipitate filtered off. The crude material was recrystallized from boiling water to give 15.22 g (89 % yield) of white, amorphous **30**.

Method 2: To a solution of aminotetrazole monohydrate (10.31 g, 0.1 mol) and sodium hydroxide (4.00 g, 0.1 mol) in 40 ml of water and 25 ml EtOH was added pulverized cyanogen bromide (10.59 g, 0.1 mol) in small portion at 0°C. After stirring the solution for 2 hours at 0 °C and 3 hours at RT, sodium azide (6.50 g, 0.1 mol) was added. In the course of 3 hours, 75 ml 2M HCl was added to the refluxing mixture and refluxing continued for further 48 hours. 1 (13.5 g, 79 % yield) was obtained according the work up procedure outlined in method 1. m.p. 263 (dec.) °C; IR (KBr, cm^{-1}): $\tilde{\nu}$ = 3456 (s), 3028 (s), 2932 (s), 2858 (s), 2671 (m), 2438 (m), 1796 (w), 1656 (vs), 1611 (s), 1556 (s), 1454 (m), 1352 (m), 1337 (m), 1282 (m), 1263 (m), 1154 (w), 1110 (m), 1072 (s), 1501 (s), 1036 (m), 1003 (m), 899 (m, br), 819 (m), 790 (m), 738 (m), 690 (m), 503 (m, br), 406 (w); Raman (200mW, 25 °C, cm^{-1}): $\tilde{\nu}$ = 3328 (11), 3120 (8, br), 1649 (9), 1618 (34), 1552 (54), 1480 (22), 1455 (17), 1370 (17), 1346 (15), 1267 (25), 1226 (26), 1151 (15), 1128 (15), 1073 (100), 1039 (42), 838 (7), 794 (17), 736 (9), 670 (7), 421 (22), 409 (48), 381 (9), 348 (20), 321 (48), 172 (100), 147 (46); ^{1}H NMR ([d6]-DMSO, 25°C) δ: 5.94 (s, br); ^{13}C NMR ([d6]-DMSO, 25°C) δ: 154.7 (C); ^{15}N NMR ([d6]-DMSO, 25°C) δ: -17.9 (N2), -123.8 (N1), -315.7 (NH); $C_2H_5N_9O$ (100.08): calcd. C, 14.3; H, 2.4; N, 83.3%; found: C, 14.1; H, 2.6; N, 83.1%.

Na(Hbta)(H_2bta)*3H_2O (38). According the above method 1, to a suspension of sodium dicyanamide (8.9 g, 0.1 mol), sodium azide (13.0 g, 02. mol), 80 ml ethanol and 50 ml water was added 75 ml 2M HCl and refluxed for further 48 hours. After cooling, rosettes of white needles crystallized slowly and the product was removed by filtration. The yield of the hydrated, acid sodium salt **38** was 3.44 g (18 % yield). Recrystallization from water gave colorless rods suitable for crystal structure determination. m.p. ~ 230 (dec.) °C; Raman

(200mW, 25 °C, cm^{-1}): $\tilde{\nu}$ = 3326 (10), 3201 (11), 1693 (11), 1617 (35), 1551 (44), 1479 (21), 1452 (27), 1370 (16), 1345 (32), 1298 (28), 1266 (27), 1225 (28), 1152 (21), 1138 (12), 1126 (16), 1093 (36), 1073 (98), 1054 (43), 1039 (43), 997 (26), 838 (10), 792 (19), 759 (36), 735 (13), 688 (9), 437 (24), 420 (26), 408 (52), 379 (12), 347 (21), 320 (58), 172 (100), 145 (50); $NaC_4H_5N_{18}*3H_2O$ (382.24): calcd. C, 12.6; H, 2.9; N, 66.0 %; found: C, 12.5; H, 2.8; N, 66.0 %.

General Procedure for the preparation of the alkali and alkaline earth metal bta salts. To *N,N*-bis-(1(2)*H*-tetrazol-5-yl)-amine monohydrate (**1**) in a sufficient amount of deionized water was added one (M^+(H**bta**$^-$), M^{2+}**bta**$^{2-}$) or two (M_2(bta)*xH_2O) equivalents of the corresponding metal hydroxide or metal carbonate. The resulting mixtures were stirred and heated to boiling - in the case of the carbonates, heating was continued until the gas evolution faded. Where necessary, the reaction mixture were filtered hot to remove insoluble impurities and than cooled (~ 5°C) with vigorous stirring to precipitate the salts. The products were collected and air-dried.

Li_2(bta)*5H_2O (40): colorless prisms; X-ray-quality crystals were grown from concentrated water solution at RT in the course of several weeks. m.p. 185-187 °C; IR (KBr, cm^{-1}): $\tilde{\nu}$ = 3498 (vs), 3414 (vs), 338 (vs), 4161 (s), 3141 (s), 2941 (m), 2780 (m), 1787 (w), 1656 (vs, sh), 1631 (vs), 1507 (s), 1477 (s), 1425 (m), 1322 (m), 1241 (m), 1141 (m), 1103 (w), 1057 (s), 1031 (w), 1002 (s), 921 (w), 850 (w), 789 (w), 751 (w), 734 (w), 721 (vw), 617 (m), 576 w), 490 (m); Raman (200mW, 25 °C, cm^{-1}): $\tilde{\nu}$ = 3398 (5), 3264 (6), 3123 (7), 2379 (4), 1622 (17), 1589 (50), 1511 (100), 1474 (19), 1432 (27), 1323 (7), 1297 (25), 1244 (66), 1148 (31), 1106 (29), 1090 (75), 1057 (26), 1034 (14), 999 (29), 851 (16), 792 (7), 751 (10), 739 (7), 409 (23), 375 (26), 314 (40), 225 (16), 210 (16), 185 (48), 161 (62), 129 (13); $Li_2C_2HN_9*xH_2O$ (x = 2: 201.00; X = 5: 255.05): (x = 2) calcd. C, 12.0; H, 2.5; N, 62.7%; found: C, 12.6; H, 2.3; N, 65.0%.

Na_2(bta)*2H_2O (42): colorless plates; X-ray-quality crystals were grown from concentrated water solution at RT in the course of several weeks. m.p. 350 °C (dec.); IR (KBr, cm^{-1}): $\tilde{\nu}$ = 3544 (s), 3274 (vs), 3154 (s), 3074 (s), 2896 (s), 2259 (w), 1696 (m), 1644 (s), 1608 (vs), 1518 (s), 1499 (vs), 1431 (m), 1305 (m), 1240 (m), 1234 (m), 1156 (w), 1141 (m), 1124 (m), 1024 (m), 1011 (w), 849 (m), 793 (s), 725 (m), 716 (m), 685 (s, 579 (s), 453 (w); Raman (200mW, 25 °C, cm^{-1}): $\tilde{\nu}$ = 3286 (5), 3171 (3), 1612 (6), 1522 (100), 1423 (6), 1306 (2), 1242 (26), 1218 (29), 1158 (3), 1141 (3), 1118 (19), 1078 (13), 1062 (59), 1024 (5), 1011 (7), 852 (2), 792 (7), 762 (4), 664 (3), 414 (10), 347 (13), 325 (13), 185 (16), 166 (14), 150 (7), 136 (14); ^{1}H NMR ([d6]-DMSO, 25°C) δ: 8.56 (s), 3.41 (H_2O); ^{13}C NMR ([d6]-DMSO, 25°C) δ: 161.6 (C); $Na_2C_2HN_9$*2H_2O (233.10): calcd. C, 10.3; H, 2.2; N, 54.1%; found: C, 10.3; H, 2.4; N, 53.5%.

K_2(bta)*H_2O (41): colorless rods; Although several recrystallizatisation attempts from both, concentrated aqueous solutions at RT and concentrated DMSO-water solutions at 60°C yielded beautiful colorless rods, a X-ray structure determination was not successful due to an unsolvable twin problem. m.p. 247 °C (dec.); IR (KBr, cm^{-1}): $\tilde{\nu}$ = 3443 (s), 3271 (s), 3148 (s), 3056 (vs), 2904 (s), 2809 (m), 2609 (w), 1688 (s), 1632 (vs), 1515 (vs), 1418 (m), 1404 (m), 1306 (s), 1218 (s), 1156 (m), 1139 (s), 1117 (m), 1113 (m), 1011 (m), 1007 (m), 856 (m), 809 (m), 750 (s), 731 (m), 677 (m); Raman (200mW, 25 °C, cm^{-1}): $\tilde{\nu}$ = 3280 (3), 3053 (5), 2903 (3), 1632 (4), 1525 (62), 1421 (10), 1308 (4), 1219 (69), 1116 (25), 1052 (100), 1010 (10), 757 (7), 405 (16), 350 (14), 308 (19), 156 (12); ^{1}H NMR ([d6]-DMSO, 25°C) δ: 8.56 (s), 3.41 (H_2O); ^{13}C NMR ([d6]-DMSO, 25°C) δ: 161.6 (C); $K_2C_2HN_9$*H_2O (247.30): calcd. C, 9.7; H, 1.2; N, 51.0%; found: C, 9.8; H, 1.2; N, 51.1%.

Rb_2(bta)*H_2O (43): colorless plates; X-ray-quality crystals were grown from concentrated DMSO-water solution at 60°C in the course of 4 days. m.p. 340 °C (dec.); IR (KBr, cm^{-1}): $\tilde{\nu}$ = 3443 (s), 3269 (s), 3146 (m), 3068 (m), 2899 (m), 1630 (vs), 1513 (vs), 1417 (m), 1303 (m), 1212 (m), 1153 (w), 1137 (m), 1119 (w), 1112 (w), 1010 (w), 855 (m), 750 (w), 699 (w), 686 (m); Raman (200mW, 25 °C, cm^{-1}): $\tilde{\nu}$ = 3270 (6), 3152 (4), 3069 (5), 2899 (3), 1617 (5), 1520 (72), 1419 (4), 1303 (4), 1208 (57), 1136 (5), 1115 (31), 1053 (100), 1009 (12), 855 (3), 758 (6), 400 (15), 346 (13), 308 (23), 179 (8); $Rb_2C_2H_3N_9O$ (340.04): calcd. C, 7.1; H, 0.9; N, 37.0%; found: C, 7.1; H, 1.0; N, 36.4%.

Cs_2(bta)*H_2O (44). colorless plates; X-ray-quality crystals were grown from concentrated DMSO-water solution at 60°C in the course of 2 days. m.p. 280 °C (dec.); IR (KBr, cm^{-1}): $\tilde{\nu}$ = 3444 (s), 3269 (s), 3158 (m), 3059 (m), 2901 (m), 1631 (vs), 1514 (vs), 1402 (m), 1305 (m, shoulder), 1217 (m), 1155 (w), 1138 (m), 1117 (w), 1112 (w), 1007 (w), 856 (m), 750 (w), 699 (w), 668 (w); Raman (200mW, 25 °C, cm^{-1}): $\tilde{\nu}$ = 3249 (6), 3148 (4), 3047 (5), 1617 (2), 1522 (56), 1416 (9), 1301 (4), 1221 (22), 1213 (44), 1114 (24), 1052 (100), 1016 (11), 1008 (10), 757 (5), 636 (4); 400 (17), 345 (13), 308 (21), 168 (9); ^{1}H NMR (D_2O, 25°C) δ: 7.33 (s), 3.41 (H_2O); ^{13}C NMR (D_2O, 25°C) δ: 162.8 (C); $Cs_2C_2H_3N_9O$ (434.92): calcd. C, 5.5; H, 0.7; N, 28.9%; found: C, 5.5; H, 0.7; N, 28.5%.

Cs(Hbta)*H_2O (39): colorless plates; X-ray-quality crystals were grown from concentrated DMSO-water solution at 60°C in the course of 3 days. m.p. 240 °C (dec.); IR (KBr, cm^{-1}): $\tilde{\nu}$ = 3424 (s), 3262 (s), 3060 (m), 2904 (m), 1631 (vs), 1514 (s), 1515 (s, shoulder), 1306 (m), 1236 (vw), 1218 (w), 1155 (vw), 1138 (w), 1122 (w), 1112 (vw), 1057 (vw), 1029 (m), 994 (w), 856 (vw), 793 (w), 749 (w), 657 (w); Raman (200mW, 25 °C, cm^{-1}): $\tilde{\nu}$ = 3002 (10), 2921 (11), 1629 (15), 1553 (80), 1500 (96), 1496 (15), 1434 (17), 1357 (30), 1347 (27), 1321 (11), 1256 (16), 1203 (54), 1131 (28), 1115 (34), 1059 (100); 1033 (17), 1001 (30), 842 (13), 776 (16), 749 (14), 406 (55), 381 (34), 348 (39), 312 (26), 161 (42), 147 (41); ^{1}H NMR ([d6]-DMSO, 25°C) δ: 8.28 (s, br); ^{13}C NMR ([d6]-DMSO, 25°C) δ: 156.8 (C); $Cs_2C_2H_3N_9O$ (303.02): calcd. C, 7.9; H, 1.3; N, 41.6%; found: C, 8.6; H, 1.0; N, 41.2%.

Cabta*5H_2O (45): colorless blocks; X-ray-quality crystals were grown from concentrated water solution at RT in the course of 5 days. m.p. 274 °C (dec.); IR (KBr, cm^{-1}): $\tilde{\nu}$ = 3450 - 3100 (vs, br), 1608 (vs), 1537 (s), 1504 (s), 1423 (m), 1303 (m), 1278 (w), 1260 (m), 1165 (w), 1140 (m), 1124 (w), 1085 (vw), 1026 (w), 852 (s), 795 (s), 748 (vs), 719 (vs); Raman (200mW, 25 °C, cm^{-1}): $\tilde{\nu}$ = 3212 (5), 1599 (5), 1532 (100), 1499 (9), 1426 (7), 1281 (21), 1262 (27), 1167 (4), 1139 (23), 1126 (21), 1085 (30), 1069 (45), 1027 (9), 1012 (7), 752 (6), 410 (23), 363 (12), 316 (17), 225 (13), 149 (9), 128 (11); $CaC_2H_3N_9O_5$ (281.24): calcd. C, 8.5; H, 3.9; N, 44.8%; found: C, 8.7; H, 3.9; N, 44.6%.

Babta*5H$_2$O (46): colorless blocks; X-ray-quality crystals were grown from concentrated water solution at RT in the course of 5 days. m.p. 295 °C (dec.); IR (KBr, cm^{-1}): $\tilde{\nu}$ = 3450 - 3100 (vs, br), 1626 (vs), 1520 (s), 1421 (s), 1415 (s, shoulder), 1305 (m), 1261 (m), 1247 (w), 1161 (w), 1140 (m), 1120 (w), 1072 (vw), 1011 (w), 859 (m), 793 (s), 747 (s), 635 (m, br), 496 (m, br); 404 (m); Raman (200mW, 25 °C, cm^{-1}): $\tilde{\nu}$ = 3176 (7), 1622 (5), 1539 (100), 1511 (30), 1422 (10), 1264 (38), 1251 (26), 1123 (44), 1075 (30), 1061 (75), 1011 (16), 759 (6), 756 (9), 403 (29), 360 (19), 329 (23), 205 (12), 159 (21), 143 (23), 115(16); $BaC_2H_3N_9O_5$ (377.49): calcd. C, 6.4; H, 2.7; N, 33.4 %; found: C, 6.5; H, 2.5; N, 34.7%.

3.2 H_2**bta** / $(NH_4)_2[Cu(NH_3)_6]$ System

3.2.1 Introduction

Cupric oxide is one of the most important additives used to a) catalyze decomposition reaction in gas generators in order to obtain cooler reaction gases b) as burning enhancer for AP based composite *propellants* and c) as coloring agent in *pyrotechnics*.[6,68] In this context the reaction of Cu^{2+} ions in aqueous ammonia solution with H_2**bta** was investigated. Depending on the reaction conditions three complexes were obtained: $Cu(bta)(NH_3)_2$ (**47**), $Cu(bta)(NH_3)_2*H_2O$ (**48**) and $(NH_4)_2Cu(bta)_2*2.5H_2O$ (**49**). The crystal structures of **47** and **48** are discussed with respect to the coordination mode of bta, which mediates in the case of **47** and **48** weak superexchange interactions between the adjacent magnetic transition metal Cu^{II} cations. This antiferromagnetic interactions result from 1D copper chains over a disguised azide end to end bridge. Interestingly, the structural arrangement of **47** completely changes in the present of crystal water. Azide-containing clusters and networks showing depending on the bridging mode a diverse array of magnetic properties: *e.g.* symmetric double end-on azide bridges typically mediate strong ferromagnetic exchange whereas symmetric end-to-end bridges antiferromagentic exchange interactions. Moreover, some physicochemical properties (e.g. heat of formation, friction and impact sensitivity, DSC) of these complexes with respect to high energetic materials are discussed.

3.2.2 Synthesis

Compounds **47**, **48** and **49** were synthesized by the direct combination of stoichiometric amounts (1:1, 1:1, 1:2, respectively) of $CuCl_2*2H_2O$ in water and **BTH** in diluted ammonia solution (in the case of **48**, conc. ammonia solution) under normal laboratory condition. **47** and **48** can be easily synthesized in high batches within a short time and are obtained as light blue (**47**) or black-blue (**48**) precipitate, respectively. From diluted solution, **47** crystallizes as blue, thin rods, suitable for X-ray structure determinations within two days and **49** crystallizes as black-blue thin needles, which turned out to be not suitable for a structure determination. In the case of **47**, X-ray quality crystals were obtained from conc. aqueous ammonia solution in an ammonia atmosphere within three weeks. In comparison to **47**, **49** crystallized as big, deep-blue coarse crystals, octahedral in shape which looses, stored on air, slowly crystal water.

3.2.3 Crystal structure of **47** and **48**

Selected bond length and angles of compounds **47** and **48** are included in *Table 3.9*. Only one labeled diagram is shown (*Figure 3.24*, (**47**)), since the molecular arrangement of **48** is similar in shape. In the molecular arrangement of **47** and **48**, each Cu^{II} ion is five-coordinated, with a distorted square-pyramidal geometry.

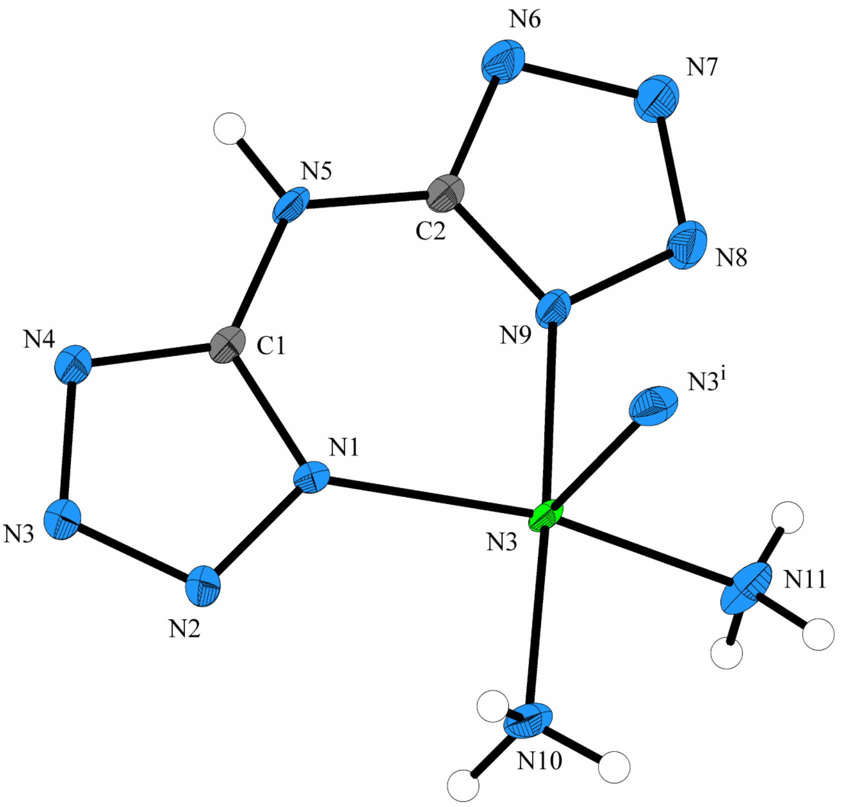

Figure 3.24. The coordination environment of the Cu^{II} ion in **47**, showing the atom numbering scheme. Displacement ellipsoid are drawn at the 50% probability level and H atoms are shown as spheres of arbitrary radii. [Symmetry code: i) -0.5-x, 0.5+y, 0.5-z.]

The basal plane is formed by the atoms N1 and N9 from one bidentate bta ligand, along with the atoms N10 and N11 from the two coordinated ammonia molecules, with a mean deviation of 0.2256 (**47**) and 0.0459 Å (**48**), respectively. The distortion from the square-pyramidal geometry is more pronounced in the case of **47** compared to **48**. With respect to the plane, in both cases the nitrogen atoms N1 and N11 lie below and N9 and N10 above this plane. A nitrogen molecule ($N3^{i}$) occupies the apical position (symmetry code: (**47**): i) -0.5-x, 0.5+y, 0.5-z; (**48**): i) x, 1.5-y, 0.5+z) with a rather long distance observed in **47** (2.319(2) Å) in contrast to **2** (2.269(2) Å). The Cu−N bond length to the nitrogen atoms of the bta ligand, ranging from 1.977(2) to 1.999(2) Å (*Table 2.9*), are slightly shorter than the Cu−N bond length to the

coordinated ammonia molecules (2.004(2) to 2.033(2) Å) and are similar to those observed in comparable copper complexes with e.g. tetrazole or ammonia ligands.[69] The copper atom is not in the basal plane, but is located 0.2064 (**47**) and 0.1884 (**48**) Å out of the mean basal plane towards $N3^{i}$. According to the valence-bond theory, if a Cu (d^9) ion is five-coordinated, there will be two probable coordination geometries around the metal ion, *viz.* trigonal-bipyramidal and square-pyramidal. In the former, the Cu ion adopts dsp^3 or sp^3d hybridization, and in the latter d^2sp^2 or sp^2d^2. These two configurations of a d^9 ion possess approximately equal energy, and they can interconvert. The angular structural index parameter τ of the coordination polyhedron for the Cu^{II} ions in **47** and **48** has been calculated according Addison *et al.*[70] The distortion value τ accounts in the case of **47** for 0.365 and for **48**, 0.0545, respectively. The τ value for both cases indicate that the coordination geometry around each Cu^{II} ion in **47** and **48** is a distorted square pyramid, being less distorted for the latter, and that the Cu (d^9) ions probably adopt sp^2d^2 hybrid orbitals to accept electrons from the ligands. This may be favorable to the paramagnetism and stability of **47** and **48**.

Table 3.9. Selected geometric parameters (Å, °) of **47** and **48**

	47	**48**		**47**	**48**
N5–C1	1.362(2)	1.377(3)	N1–N2	1.353(2)	1.362(3)
N5–C2	1.369(2)	1.375(3)	N8–N9	1.359(3)	1.364(2)
C1–N1	1.345(2)	1.334(3)	N2–N3	1.306(3)	1.296(3)
C2–N9	1.330(3)	1.337(3)	N7–N8	1.301(3)	1.301(3)
C1–N4	1.325(3)	1.324(3)	N3–N4	1.362(2)	1.361(3)
C2–N6	1.325(2)	1.329(3)	N6–N7	1.355(3)	1.363(3)
Cu–N1	1.999(2)	1.997(2)			
Cu–N9	1.977(2)	1.996(2)			
Cu–N10	2.005(2)	2.033(2)			
Cu–N11	2.007(2)	2.004(2)			
Cu–N3[a]	2.319(2)[i]	2.269(2)[i]			
N1–Cu–N9	85.56(7)	85.40(8)	N3[a]–Cu–N10	87.01(7)[i]	91.75(9)[i]
N1–Cu–N10	91.70(7)	89.63(9)	N3[a]–Cu–N11	99.87(9)[i]	97.95(8)[i]
N1–Cu–N11	154.82(9)	166.98(9)	Cu–N1–N2	125.1(1)	123.5(1)
N1–Cu–N3[a]	105.20(7)[i]	95.02(7)[i]	Cu–N1–C1	105.1(2)	131.1(2)
N9–Cu–N10	176.74(8)	170.25(8)	Cu[a]–N3–N2	119.3(1)[ii]	121.2(2)[ii]
N9–Cu–N11	91.32(8)	91.9(1)	Cu[a]–N3–N4	127.4(1)[ii]	126.7(1)[ii]
N3[a]–Cu–N9	92.01(7)[i]	97.03(8)[i]	Cu–N9–N8	124.4(1)	124.5(1)
N10–Cu–N11	91.92(8)	91.1(1)	Cu–N9–C2	129.9(2)	130.9(2)

[a] **47**: i) -0.5-x, 0.5+y, 0.5-z; ii) -0.5-x, -0.5+y, 0.5-z ; **48**: i) x, 1.5-y, 0.5+z; ii) x, 1.5-y, -0.5+z

The obvious deviation of the coordination around the Cu^{II} in **47** compared to **48** cannot be easily explained by the comparison of the molecular structures alone. A closer inspection of the crystal structure of **47** and **48** reveals a completely different picture of the molecular arrangements. In both complexes, each bta dianion acts as a tridentate ligand toward copper, connecting two Cu^{II} ions trough the N1, N9 and N3 nitrogen atoms, resulting in a one-dimensional zigzag chain. The Cu···Cu^{i} separation was found to be 6.1350(3) Å in **47** (*Figure 3.25*, **I**) and 6.116(1) Å in **48** (*Figure 3.26*, **I**), respectively (symmetry code: (**47**): i) -0.5-x, 0.5+y, 0.5-z; (**48**): i) x, 1.5-y, 0.5+z).

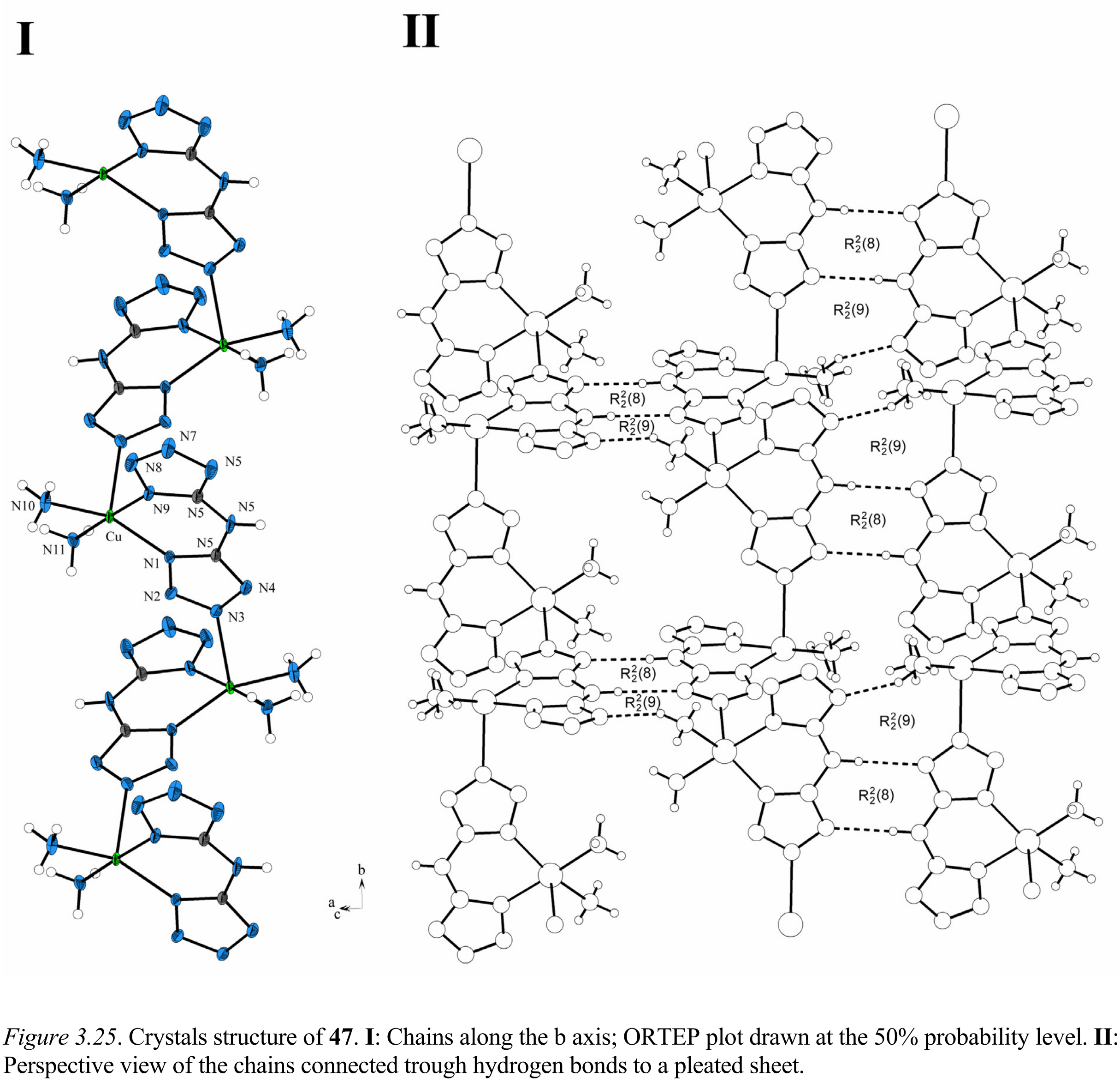

Figure 3.25. Crystals structure of **47**. **I**: Chains along the b axis; ORTEP plot drawn at the 50% probability level. **II**: Perspective view of the chains connected trough hydrogen bonds to a pleated sheet.

The folded chains in **47** are orientated in a one-dimensional zigzag pattern along the crystallographic *b* axis. These chains, orientated in an anti-parallel manner, are linked over two strong hydrogen bonds (N11–H1···N7^{ii} and N5–H7···N4^{v} [symmetry code: (ii) -0.5+x, 0.5-y;

(v) -1-x, -y, -z]) to a pleated sheet (*Figure 3.25*, **II**). The most important hydrogen-bonded ring motif of this sheet, in the formalism of graph-set analysis of hydrogen-bond patterns,[66] is identified as $R_2^2(9)$ and the very common $R_2^2(8)$. The sheet like structure in **47** reminds on the β-pleated sheet structure of proteins. The pleated sheets are connected to a 3D network by further hydrogen bonds (*Table 3.10*).

Table 3.10. Hydrogen bond geometry (Å, °) of **47** and **48**

D–H····*A*	*D*–H	H····*A*	*D*····*A*	*D*–H····*A*
47				
N10–H1····N7^{ii}	0.91(3)	2.30(3)	3.194(3)	167(2)
N10–H2····N8^{iii}	0.84(4)	2.33(3)	3.043(3)	142(3)
N11–H4····N8^{a}	0.78(3)	2.45(3)	2.982(3)	127(3)
N11–H5····N6^{iv}	0.92(4)	2.06(4)	2.927(3)	155(3)
N5–H7····N4^{v}	0.83(3)	2.14(3)	2.966(2)	177(2)
48				
N10–H1····N7^{ii}	0.88(3)	2.35(3)	3.191(3)	159(3)
N11–H4····N8^{iii}	0.90(4)	2.31(4)	3.203(3)	169(3)
N11–H5····N8^{a}	0.77(4)	2.52(4)	3.003(4)	122(3)
N5–H7····N6^{iv}	0.89(3)	2.05(3)	2.929(3)	172(2)
N10–H3····O1	0.92(4)	2.03(4)	2.939(3)	170(3)
O1–H1A····N4^{v}	0.71(4)	2.28(4)	2.970(3)	166(5)
O1–H1B····N7^{iii}	0.83(4)	2.21(4)	3.015(3)	163(3)

[a] intramolecular hydrogen bond;
Symmetry codes for **47**: i) -0.5-x, 0.5+y, 0.5-z; ii) -0.5+x, 0.5-y, 0.5+z; iii) 0.5-x, -0.5+y, 0.5-z; iv) 0.5+x, 0.5-y, 0.5+z; v) -1-x, -y, -z; **48**: i) x, 1.5-y, 0.5+z; ii) 2-x, -0.5+y, 0.5-z; iii) 2-x, 2-y, 1-z ; (iv) 3-x, 2-y, -z; (v) 1+x, 1.5-y, 0.5+z.

In contrast to **47**, the arrangement of the molecules in the crystal structure of **48** is different. Although **48** forms folded chains which are orientated in a one-dimensional zigzag pattern along the crystallographic *c* axis, these chains are not connected through hydrogen bonds to a pleated sheet. They are rather interlocking each other, forming fishbone-type sheets. The smallest subunit of two interlocking chains is depicted in *Figure 3.26* (**I**). If at all, this interaction between such a dimeric unit might result from a electrostatic interaction, since the distance between the Cu^{II}-$N3^{iii}$ of 3.285(3) [symmetry code: (iii) 2-x, 2-y, 1-z] is much longer than the sum of the van der Waals radii ($r_{A(Cu)} + r_{D(N)} = 2.95$ Å),[71] and therefore should rather be related to packing effects. One chain related to the next is counterrotated with respect to the running direction. The resulting fish-bone type sheets are connected through the water

molecule, ammonia and the NH-group to a 3D network (*Table 3.10*). Again, the hydrogen bond N5–H7····N6[iv] [symmetry code: (iv) 3-x, 2-y, -z] results in the occurrence of the well known $R_2^2(8)$ graph set (not depicted in *Figure 3.26*), yet resulting from the interaction of the layers compared to **47**.

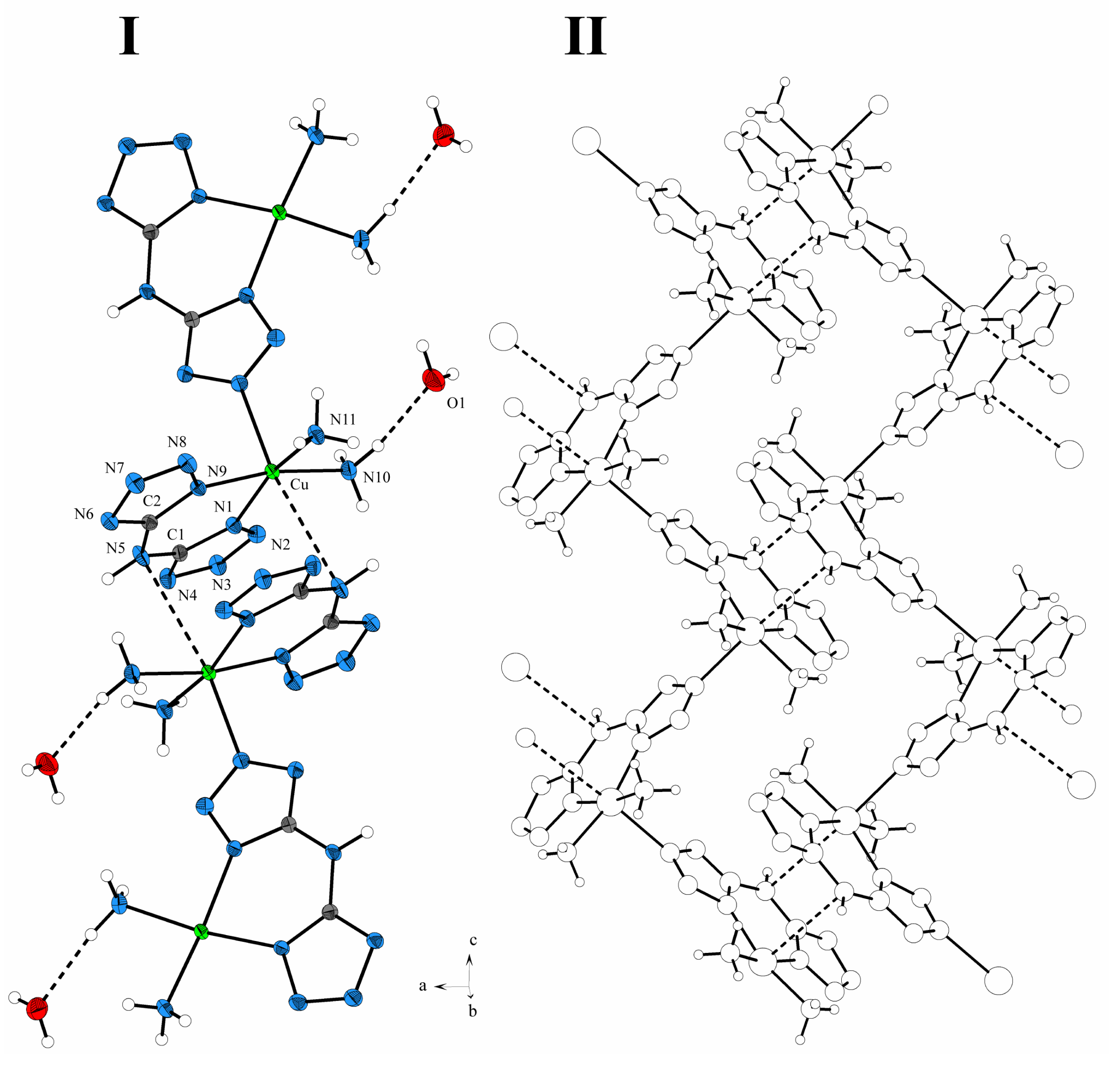

Figure 3.26. Crystals structure of **48**. **I**: Chains along the c axis; ORTEP plot drawn at the 50% probability level. **II**: Perspective view of the chains connected trough interlocking

In the case of **49**, a complete structure solution could not be performed due to unsolvable disorder of the crystal water molecules. Therefore a detailed discussion of the crystal structure is abstained. *Figure 3.27* shows the coordination sphere around the copper centre of the complex

49, indicating a distorted square pyramidal arrangement with almost equal Cu−N distances in the equatorial position (ranging from 1.962 to 1.982 Å), and in contrast to **47** and **48,** a very long apical Cu−N distance (2.864 Å *vs.* 2.319(2) and 2.269(2), *Table 3.9*) resulting in the formation of chain like stacks, orientated along the *b* axis. Since the apical distance is just slightly shorter then the sum of the van der Waals radii ($r_{A(Cu)} + r_{D(N)} = 2.95$ Å), this interaction should be seen as medium electrostatic interactions, giving rise to the assumption that the local symmetry at the copper center should be rather seen as a very distorted tetrahedron. This is in accordance with the EPR results (cubic environment with minor distortion) as well as the magnetic measurements, which indicates very weak superexchange between different copper centers.

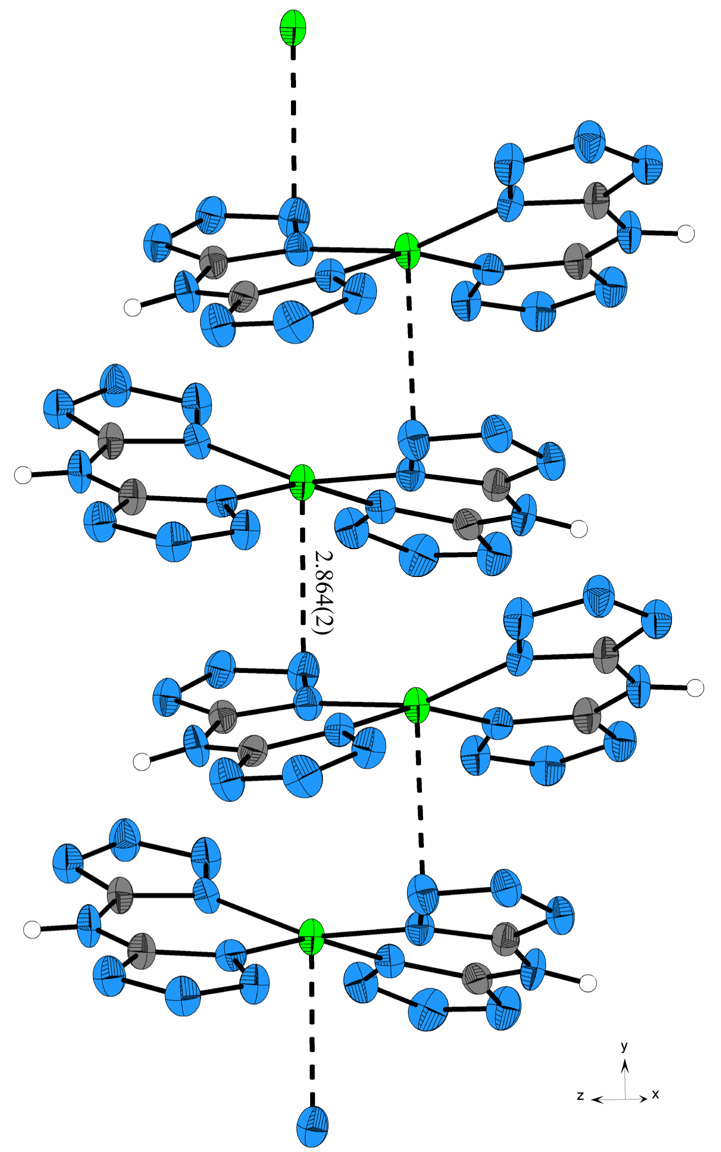

Figure 3.27. View of the chain like structure in **49**. Displacement ellipsoid at 50% probability level. (blue: nitrogen; gray: carbon; green: copper; white: hydrogen)

3.2.4 Magnetic properties of **47**, **48** and **49**

The magnetic susceptibility of the three complexes has been measured in the temperature range 300 – 2 K. The temperature dependence of $\chi_M T$ is shown in *Figure 3.28* for compound **47** and **48** and in *Figure 3.29* for compound **49**.

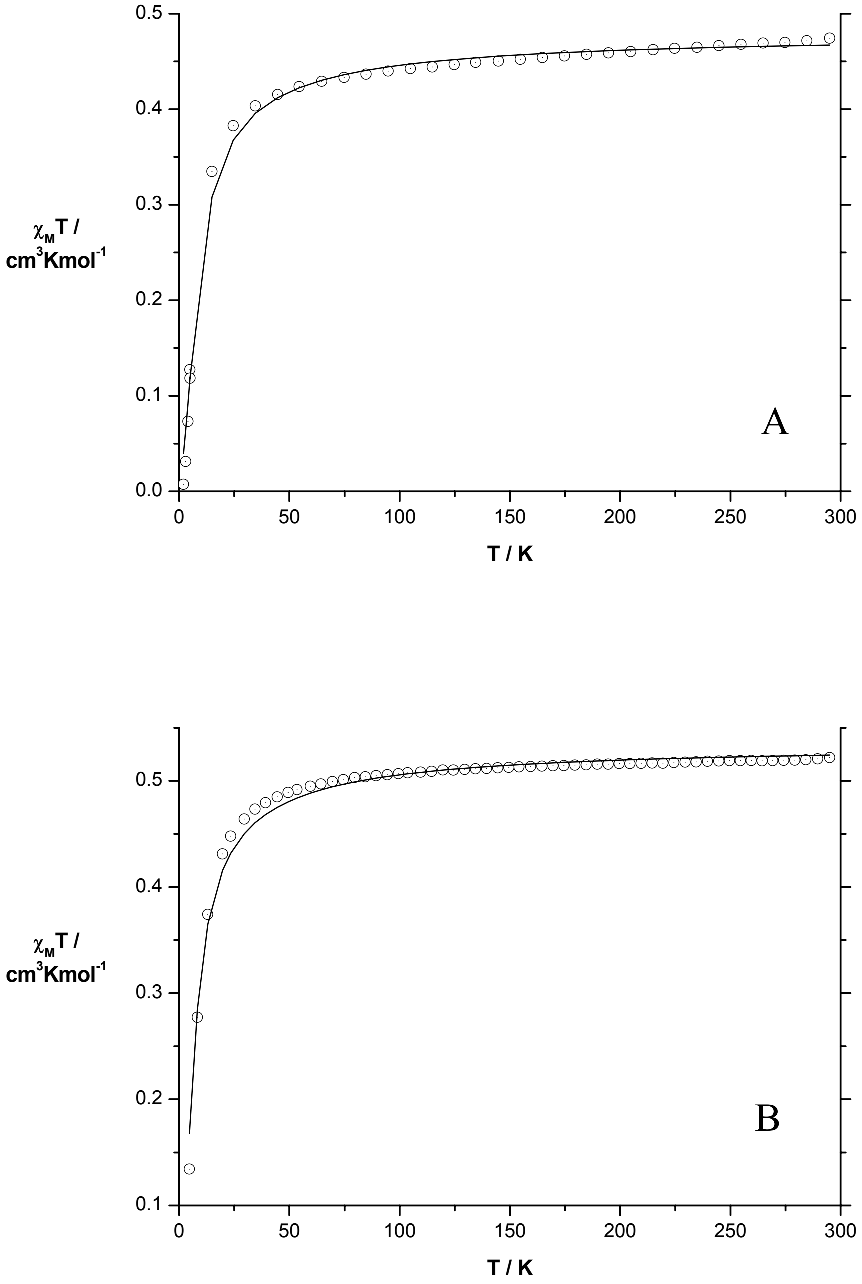

Figure 3.28. Plot of $\chi_M T$ vs. T for **47** (A) and **48** (B) under an applied magnetic field of 0.5 T. Solid lines represent the best fit of the date with the model described in the text

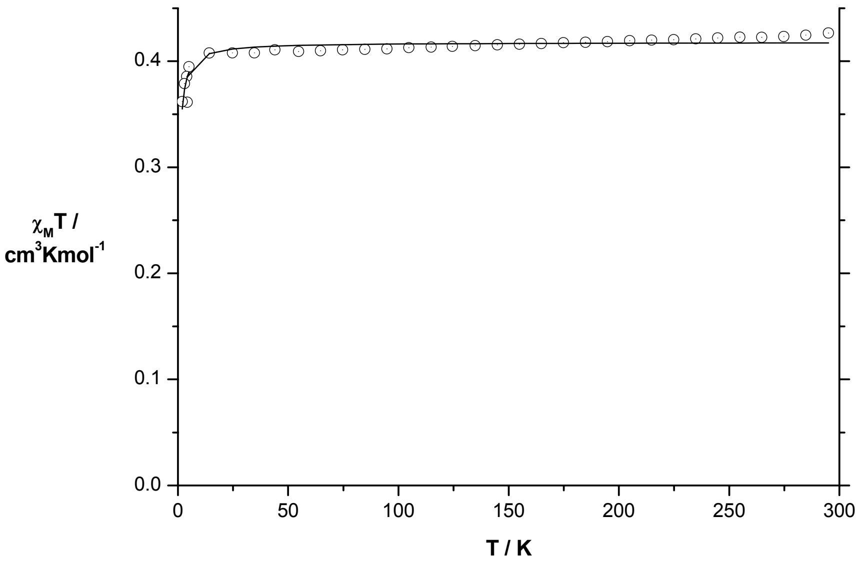

Figure 3.29. Plot of $\chi_M T$ vs. T for **49** under an applied magnetic field of 0.5 T. Solid lines represent the best fit of the date with the model described in the text.

The $\chi_M T$ product at room temperature is with 0.47 cm^3K/mol (**47**), 0.52 cm^3K/mol (**48**) and 0.43 cm^3K/mol (**49**) larger than the spin-only value of 0.37 expected for a single copper (II) ion (S = 1/2) assuming g = 2.00. Upon cooling $\chi_M T$ decreases significantly for compounds **47** and **48**, while the product is nearly constant in the case of compound **49**. The magnetic behavior of compound **47** and **48** is characteristic for antiferromagnetic-coupled copper centers. In order to estimate the magnitude of the antiferromagnetic coupling, the magnetic data were fitted using the equation for equally spaced copper(II) ions first applied by Bonner and Fisher[72] with the Hamiltonian in the form

$$H = -J\sum_{i=1}^{n-1} S_{Ai} S_{Ai+1}$$

The magnetic data of all three complexes were fitted leading to the parameters J = -7.82 ± 0.30; g = 2.26 ± 0.01 (compound **47**), J = -5.95 ± 0.13; g = 2.39 ± 0.01 (compound **48**) and J = -0.38 ± 0.03; g = 2.11 ± 0.01 (compound **49**). The antiferromagnetic coupling is rather weak in all three cases, especially for compound **49**, where the distances to the apical nitrogen atom are rather long. The reason for the weak interaction is that the magnetic orbitals, describing the single electron on the copper centers are mainly of $d_{x^2-y^2}$ type. The bta dianion connecting the cupper centers through N1, N9 and N3 nitrogen atoms belong to the basal plane of Cu (N1 and N9), but occupies an axial position of the square pyramidal coordination sphere on the neighboring Cu (N3). Consequently the interactions between the magnetic orbitals of the two copper centers are very weak leading to small coupling parameters. Similar observations were made for end-on azido-bridged copper complexes[73] and oxalato bridged systems.[74] An

explanation for the small differences in the coupling parameters of compound **47** and **48** cannot be found in the molecule structure of the two complexes.

The differences in the coordination environment of the copper centers are also reflected in the powder X-Band EPR spectra. The compounds **47** and **48** with the square pyramidal coordination environment exhibit spectra with a rhombic symmetry and clearly separated g values (g_1 = 2.184, g_2 = 2.094 and g_3 = 2.045; g_{iso} = 2.108 for compound **47**). In complex **49** with the very long apical Cu-N distances and the local symmetry close to a distorted tetrahedron a spectrum of a cubic system with small distortion (g_{iso} = 2.087) is obtained.

3.2.5 Thermal decomposition and thermodynamic aspects

The DSC thermograms of **1** and **3** for different heating rates (β = 2, 5, 10 and 15 °C min^{-1}) are presented in *Figure 3.30*. The decomposition undergoes in the case of **47** in two steps between 250 and 400 °C, and the final residue, estimated as copper, has the observed mass of 26.2 % as against the calculated value of 25.5 %. The second step can only be noticed as a weak exothermic effect between 300 and 400 °C in the DSC. Interestingly, the decomposition is comparable to an ammoniacal complex of copper oxalate and indicates that the first decomposition step might be determined as the deammoniation of **47**.[75]

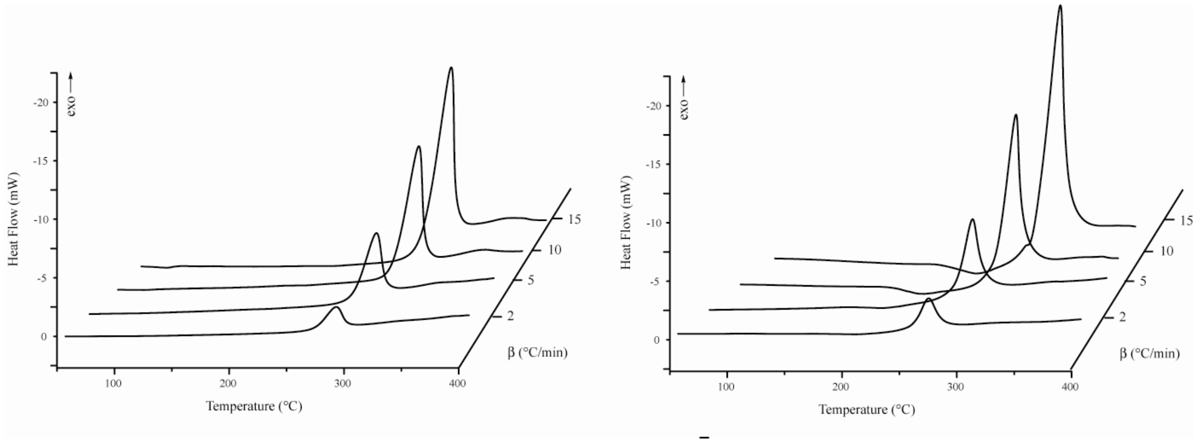

Figure 3.30. DSC thermographs of **47** (left) and **49** (right) (β = 2, 5, 10 and 20 °C/min)

In the case of **49**, the decomposition undergoes also in two steps, at which the first step corresponds to the loss of crystal water. This process is not well resolved in the DSC, since the release of water does not proceed stepwise. As indicated in the TGA experiment, the release of water occurs within a temperature range of 70 to 170 °C with a mass loss of 10.4 % (Calc.: 10.0 %). The second exotherm occurs in a sharp temperature range at 250 to 270 °C with a mass loss of 80.0 % (Calcd.: 75.8 %).[76]

Table 3.11 shows that with increased heating rates, the temperature of the exothermic maxima also increases. The kinetics of exothermic reactions are important in assessing the potential of materials and systems for thermal explosion, and the activation energy for compound **49** (56.46 ± 0.16 Kcal mol^{-1}) was estimated to be 9.5 Kcal mol^{-1} higher compared to **48** (46.90 ± 0.16 Kcal mol^{-1}) but still indicating a good thermal stability for both complexes.

Table 3.11. Physico-chemical properties of **47** and **49**

	47	**49**
Formula	$CuC_2H_7N_{11}$	$CuC_4H_{15}N_{20}O_{2.5}$
Molar Mass	248.70	446.84
N [%]	62.0	64.0
Ω [%][a]	-48.3	-47.5
β [°C]		
2	284.00	266.65
5	295.80	275.14
10	305.11	282.60
15	310.46	287.31
T_{int}[b]	250-300; 300-400	70-150; 250-270
$\Delta_{max}H$[c]	-434.5 J/g	-508.3 J/g
E_a [Kcal mol-1][d]	46.90 ± 0.16	56.46 ± 1.16
$-\Delta_C U_m$ [cal g^{-1}][e]	2233.8	1989.3
$-\Delta_C H_m°$ [Kcal mol^{-1}][f]	555.5	862.7
$\Delta_f H_m°$ [Kcal mol^{-1}][g]	+87.8	-29.2
$-\Delta_E H_m°$ [Kcal kg^{-1}][h]	398.2	236.5
Density [g cm^{-3}]	1.9882(2)	1.353[l]
Impact [J][i]	> 40	> 40
Friction [N][j]	> 360 (-)	> 360 (-)
Gas volume (25°C) [ml g^{-1}][k]	819	837

[a] Oxygen balance; [b] Range of decomposition by TGA (β = 5°C); [c] Heat of combustion from maximum exothermic step (DSC); [d] Activation energy according Ozawa ref. [77]; [e] Experimental constant volume combustion energy; [f] Experimental molar enthalpy of combustion; [g] Molar enthalpy of formation; [h] Calculated molar enthalpy of detonation, ICT Thermodynamic code see ref. [78]; [i,j] ref [79]; [k] Assuming only gaseous products, ICT Thermodynamic code see ref. [78]; [l] estimated from a structure determination.

For initial safety testing, the impact and friction sensitivity was tested according to BAM methods (see *Chapter I*, *3.3.2*) with the "BAM Fallhammer" and "BAM friction tester". Both compounds are insensitive toward impact (> 40 J) and friction (> 360 N) (*Table 3.11*).

The heats of combustion for the compounds **47** and **49** were determined experimentally, and the molar enthalpy of formation were calculated from a designed Hess thermochemical cycle according to reactions [1,2] and are summarized in *Table 3.11*.

47: $CuC_2H_7N_{11}$ (s) + 6 O_2 → CuO(s) + 2 CO_2 (g) + 3.5 H_2O (l) + 5.5 N_2 (g) [1]

49: $CuC_4H_{14}N_{20}O_2$ (s) + 7 O_2 → CuO(s) + 4 CO_2 (g) + 7 H_2O (l) + 10 N_2 (g) [2]

$$\Delta_f H_m^\circ = \Delta_f H_m^\circ(CuO,s) + x\Delta_f H_m^\circ(CO_2,g) + y\Delta_f H_m^\circ(H_2O,l) - \Delta_c H_m^\circ$$

The enthalpy criteria of energetic materials are governed by their molecular structure, and therefore, the move to heterocycles with a higher nitrogen content (e.g. from imidazole ($\Delta_f H_{cryst}^\circ$= 14.0 kcal/mol)[80], over 1,2,4-triazole ($\Delta_f H_{cryst}^\circ$= 26.1 kcal/mol) to tetrazole ($\Delta_f H_{cryst}^\circ$= 56.7 kcal/mol)[81]) the trend in the heats of formation is obvious. Therefore, bta as ligand also should lead to increased heats of formation. From the obtained heats of formation and the densities obtained from the crystal structure determinations, some thermochemical properties have been calculated using the ICT-Thermodynamic code and are depicted in *Table 3.11*.[78]

3.2.6 Conclusion

The H_2**bta** / $(NH_4)_2[Cu(NH_3)_6]$ system interesting which three representatives summarized in this *Chapter 3.2*. Depending on the reaction conditions $Cu(bta)(NH_3)_2$ (**47**), $Cu(bta)(NH_3)_2*H_2O$ (**48**) and $(NH_4)_2Cu(bta)_2*2.5H_2O$ (**49**) could be synthesized, and in the case of **47** and **49**, a scale up procedure is possible, since **47** and **48** are easily accessibly from cheap starting materials and riskless to handle. The complexes **47** and **49** are certainly of interest as additives in *pyrotechnics*, AP based *propellants* or other application as they show promising properties with respect to stability, sensitivity and energetic aspects. Furthermore, the crystal structures of **47** and **48** were discussed with respect to the coordination mode of bta, which mediates in the case of **47** and **48** weak superexchange interactions between the adjacent magnetic transition metal Cu^{II} cations, resulting from 1D copper chains over an disguised azide end to end bridge. The structural arrangement of **47** completely changes from a pleated layer-

like structure reminds on the β-pleated sheet structure of proteins to fishbone-type sheets in the case of **48**. These structural features have been discussed with respect to the occurrence of well known graph sets, already discussed in other motives found for bta complexes. It makes sense to compare azide-containing clusters and networks with the **bta** ligand since **bta** can be regarded as disguised azide. Depending on the bridging mode of the azide in such clusters and networks a diverse array of magnetic properties is observed: *e.g.* symmetric double end-on azide bridges typically mediate strong ferromagnetic exchange whereas symmetric end-to-end bridges antiferromagentic exchange interactions. The latter counts exactly for the **bta** ligand, as shown by the magnetic measurements performed on the investigated complexes.

3.2.7 Experimental

*CAUTION: Although the copper salts of **BTA** are kinetically stable compounds and turned out to be insensitive to friction (> 360 N) and impact (> 40 J), they are nonetheless energetic materials and appropriate safety precautions should be taken, especially when these compounds are prepared on a larger scale. Laboratories and personnel should be properly grounded, and safety equipment such as Kevlar® gloves, leather coat, face shield and ear plugs are necessary, especially when manipulating BTA salts in dehydrated form.*

All chemical reagents and solvents of analytical grade were obtained from Sigma-Aldrich Fine chemicals Inc. and used as supplied. Infrared (IR) spectra were recorded on a Perkin-Elmer Spektrum One FT-IR instrument as KBr pellets at 20°C. C, H and N determination were performed with a Netsch Simultanous Thermal Analyser STA 429.

[Cu(bta)(NH_3)$_2$] (**47**)**:** Single crystals suitable for X-ray analysis were obtained as follows: To a hot solution (70 °C) containing BTA*H_2O (342 mg, 2 mmol), 2.5 mL conc. NH_3 and 60 mL water was slowly added a solution of $CuCl_2$*$2H_2O$ (170.5 mg, 1 mol) in 5 mL water, producing a dark green solution. From this solution (kept in a 500 mL beaker), blue rod like single crystals suitable for the structure determination were grown within 2 days. The reaction can be smoothly up-scaled to 100 mmol, giving **47** in 95% yield as light blue

precipitate. After crystallization, the product was collected and washed with EtOH. m.p. > 250 °C (dec.); IR (KBr, cm^{-1}): $\tilde{\nu}$ = 3375 (m), 3325 (s), 3255 (m), 3134 (m), 3057 (m), 2919 (m), 2826 (m), 1627 (vs), 1546 (s), 1499 (s), 1464 (m), 1446 (m), 1327 (m), 1235 (s), 1160 (w), 1140 (w), 1123 (m), 1116 (m), 1093 (w), 1083 (w), 1017 (w), 853 (vw), 808 (w), 747 (s), 727 (s), 678 (m), 620 (w), 440 (vw), 416 (w); $CuC_2H_7N_{11}$ (248.70): calcd. C, 9.7; H, 2.8; N, 61.9 %; found: C, 9.8; H, 2.9; N, 61.7 %.

[Cu(bta)(NH_3)$_2$*H_2O] (**48**): Single crystals suitable for X-ray analysis were obtained as follows: To a refluxing solution containing BTA*H_2O (684 mg, 4 mmol), 20 mL conc. NH_3 and 10 mL water was slowly added a solution of $CuCl_2$*2H_2O (341 mg, 2 mol) in 10 mL water, producing a deep blue solution. After a few minutes **47** started to precipitate from this solution. The obtained mixture was refluxed for further 10 minutes and the precipitate filtered off. The obtained filtrate was kept in a closed flask from which in a approximately 3 weeks **48** crystallized as big, dark blue crystals, octahedral in shape (yield 15%). **48**, stored on air, loss slowly crystal water. IR (KBr, cm^{-1}): $\tilde{\nu}$ = 3375 (m), 3327 (s), 3271 (s), 3170 (w), 3053 (w), 2915 (w), 2823 (w), 1626 (vs), 1545 (s), 1499 (s), 1462 (w), 1445 (m), 1384 (vw), 1327 (w), 1237 (s), 1160 (w), 1123 (m), 1093 (w), 1017 (w), 853 (vw), 807 (w), 747 (m), 726 (m), 679 (w), 615 (w); $CuC_2H_9N_{11}O$ (266.71): calcd. C, 9.0; H, 3.4; N, 57.8 %; found: C, 9.1; H, 3.4; N, 57.7 %.

[(NH_4)$_2$Cu(bta)$_2$*2.5H_2O] (**49**): To a hot solution (70 °C) containing BTA*H_2O (3.420 g, 20 mmol), 10 mL conc. NH_3 and 50 mL water, a solution of $CuCl_2$*2H_2O (1.705 g, 10 mol) in 15 mL water was slowly added, producing a dark, black-green solution. This solution was stirred for further 30 minutes at 70 °C. After cooling, very fine blue-black needles of **3** crystallized and were collected and washed with EtOH (yield 84 %). > 250 °C (dec.); IR (KBr, cm^{-1}): $\tilde{\nu}$ = 3415 (s), 3313 (m), 3159 (m), 3034 (s), 2921 (s), 2807 (m), 1635 (s, shoulder), 1626 (vs), 1548 (s), 1502 (m), 1439 (vs, br), 1329 (m), 1257 (m), 1168 (w), 1124 (m), 1088 (w), 806 (m), 746 (m), 688 (m); $CuC_4H_{15}N_{20}O_{2.5}$ (446.84): calcd. C, 10.8; H, 3.4; N, 62.7 %; found: C, 11.0; H, 3.2; N, 62.8 %.

X-ray Structure Determination. Crystals were obtained as described above. The X-ray crystallographic data for **47** (CCDC 269320) were collected at 200 K on a STOE IPDS area detector, and for **48** (CCDC 269321) data were collected at 213 K on SIEMENS P4 diffractometer equipped with a Siemens CCD area detector using graphite-monochromated MoK_α radiation (λ = 0.71073 Å). The structures were solved by direct methods (SIR97 (**48**) and SHELXS-97 (**48**))[82] and refined by means of full-matrix least-squares procedures using SHELXL-97. For **48**, numerical absorption correction by SADABS and for **47**, XRed was used.[83] Crystallographic data are summarized in *Appendix B*. Selected bond lengths and angles are available in *Table 3.9*. All non-hydrogen atoms were refined anisotropically. The hydrogen atoms of compound **47** and **48** were located from difference electron-density map and refined isotropically.

Magnetic Measurements. Bulk magnetization measurements of pulverised samples were performed on a Quantum-Design-MPMSR-XL-SQUID-Magnetometer in a temperature range from 2 to 300 K. All measurements were carried out at two field strengths (0.2 and 0.5 T). Diamagnetic corrections were made using estimated values according to $\chi_{\text{dia}} \approx -0.5\times10^{-6}\, M_{\text{complex}}$.

EPR Measurements. EPR investigations were carried out on a ESP 300E (Bruker) instrument at room temperature on the solid.

DSC and TGA measurement were performed as described in *Chapter I, 3.3.1.*

3.3 H_2**bta** / CuX_2 ($X = Cl^-$, ClO_4^-) System

3.3.1 Introduction

Domestically-produced standard priming explosives (PEs) allow production of reliable priming charges (PCs) meeting the requirements of modern engineering, industry, and building. However, requirements to PCs continuously rise; PCs with elevated safety with respect to mechanical impact and static electricity are required. In addition, environmental safety requires elimination of toxic metal ions (see above) from PC formulation. It is impossible to accomplish the above task with standard PCs. As already discussed, **bta** serves in its different coordination mode as stable ligand, already discussed for the H_2**bta** / $(NH_4)_2[Cu(NH_3)_6]$ system (*this Chapter, 3.2*). Since the occurrence of energetic oxygen rich cations is comparable few, counterions such as nitrate (NO_3^-), dinitramide ($N(NO_2)_2^-$) or the perchlorate (ClO_4^-) anion are required in combination with the **bta** ligand system. In such systems, of course, the **bta** needs to coordinate in its protonated form (H_2**bta**). The following *Chapter* discusses the H_2**bta** / CuX_2 ($X = Cl^-$, ClO_4^-) system, and it will be derived that H_2**bta** might serve as ligand in new High-Energy-Capacity Copper(II) **bta** salts suitable for safe non-toxic PC formulations, as possibly photosensitive compounds utilized in laser detonators as well as colorants in pyrotechnic formulations.

3.3.2 Synthesis

The reaction of $CuCl_2$ in hydrochloric acid and H_2bta strongly depends on the reaction conditions, like temperature, reaction time and concentration of the acid. The reaction of 1 eq. H_2**bta** and 1 eq $CuCl_2$ does not necessarily lead to the formation of the corresponding 1:1 product.

$$CuCl_2{*}2H_2O + H_2bta{*}H_2O \xrightarrow[45°C,\ 5\ min.]{conc.\ HCl} [CuCl_2(H_2\mathbf{bta})(H_2O)]\ {*}3H_2O \qquad \mathbf{50}$$

$$CuCl_2{*}2H_2O + 2H_2bta{*}H_2O \xrightarrow[refux,\ 2\ min.]{conc.\ HCl} [CuCl(H_2\mathbf{bta})_2]Cl \qquad \mathbf{51}$$

$$CuCl_2{*}2H_2O + 2H_2bta{*}H_2O \xrightarrow[RT,\ 2\ d]{conc.\ HCl} [CuCl_2(H_2\mathbf{bta})_2]\ {*}2H_2O \qquad \mathbf{52}$$

$$CuCl_2{*}2H_2O + 2H_2bta{*}H_2O \xrightarrow[75°C,\ 4\ h]{35\ \%\ HClO_4} [Cu(H_2\mathbf{bta})(ClO_4)_2]\ {*}H_2O \qquad \mathbf{53}$$

Scheme 3.5. H_2**bta** / CuX_2 ($X = Cl^-$, ClO_4^-) System

All reactions were conducted in conc. hydrochloric acid or 35% perchloric acid (in the case of **53**) and obtained according to *Scheme 3.5*. The complexes are crystalline, typically blue-colored compounds and not soluble in water without decomposition. They were characterized by means of IR spectroscopy, elemental analysis and X-ray structure determination. The following chapter gives a short discussion of the molecular structures of **50**, **51**, **52** and **53**.

3.3.3 Molecular structure of [$CuCl_2$(H_2**bta**)(H_2O)]*2H_2O (**50**)

Aquadichloro(bis(1*H*-tetrazolyl-5yl)-amino-κ^{2}N,N')copper(II) dihydrate (**50**) crystallizes in the triclinic space group *P*-1 with two formula units in the unit cell. The asymmetric unit of (**50**) consists of one [$CuCl_2$(H_2**bta**)(H_2O)] unit and two solvent water molecules. The oxygen atom O3 of the solvent water is disordered with a site occupation factor (SOF) ratio of 0.58 : 0.42. The Cu(II) ion is coordinated in a slightly distorted square-pyramidal mode to two N of the H_2**bta** ligand, one chloro and one water molecule in the basal plane, with a second chloro ligand in the apical position (*Figure 3.31*, β = N9−Cu−Cl1; α = O1−Cu−N1 → τ = 0.03)[70].

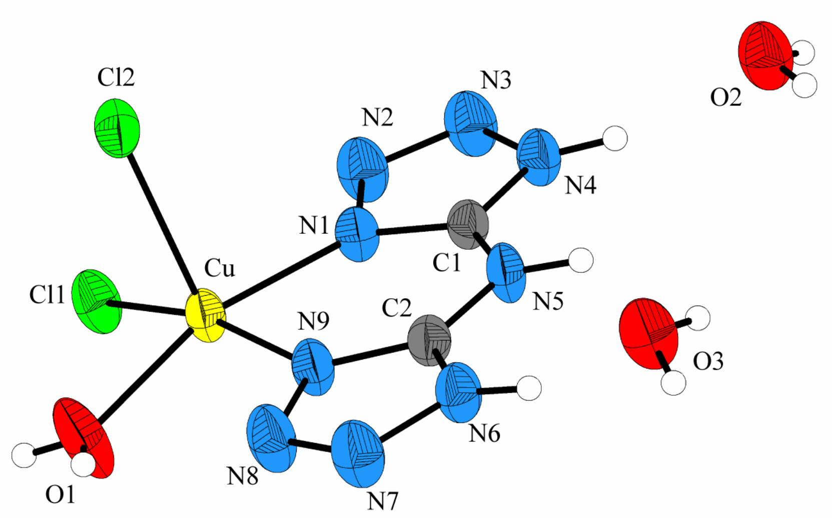

Figure 3.31. The coordination environment of the Cu^{II} ion in **50**, showing the atom-labeling scheme. Displacement ellipsoid are drawn at the 50% probability level and H atoms are shown as spheres of arbitrary radii. For clarity only one position of O3 is depicted. Selected bond length [Å]: Cu−N1 2.005(2), Cu−N9 1.969(2), Cu−O1 1.987(2), Cu−Cl1 2.244(7), Cu−Cl2 2.5619(7); Selected bond angle [°]: N9−Cu−Cl1 165.86(6), O1−Cu−N1 164.86(8), N9−Cu−O1 87.21(7), N9−Cu−N1 85.50(7), O1−Cu−Cl1 88.69(5), N1−Cu−Cl1 94.97(5), N9−Cu−Cl2 94.80(6), O1−Cu−Cl2 96.98(7); N1−Cu−Cl2 97.74(5)

As a result of the intermolecular interaction of the apical chloro ligand of the monomer with the hydrogen atom of the secondary amine of another bta ligand (N5−H···Cl2^{i} 3.063(2) [symmetry code: (i) 1-x, y, z]), a ladder-type chain is formed. The intermolecular hydrogen bonds stabilize the extended structure to a 3D network in which one of the water molecules (O3) of crystallization links three monomers to one another, acting as hydrogen-bond donor to two chloro ligands of two monomers (Cl2^{i}, Cl1^{ii}, [symmetry codes: (i) 1-x, y, z; (ii) -1+x, 1+y, z]), whereas the other water molecule (O2) links symmetry-related chains over a comparable weak hydrogen bond (O2−H···N3^{iii} 3.176(2) [symmetry code: (iii) -x, -1-y, 1-z]). A subunit of this arrangement can be depicted in *Figure 3.32*. These chains are further connected through the aqua ligand (O1) as well as the second chloro (Cl1) ligand to an infinite 3D network.

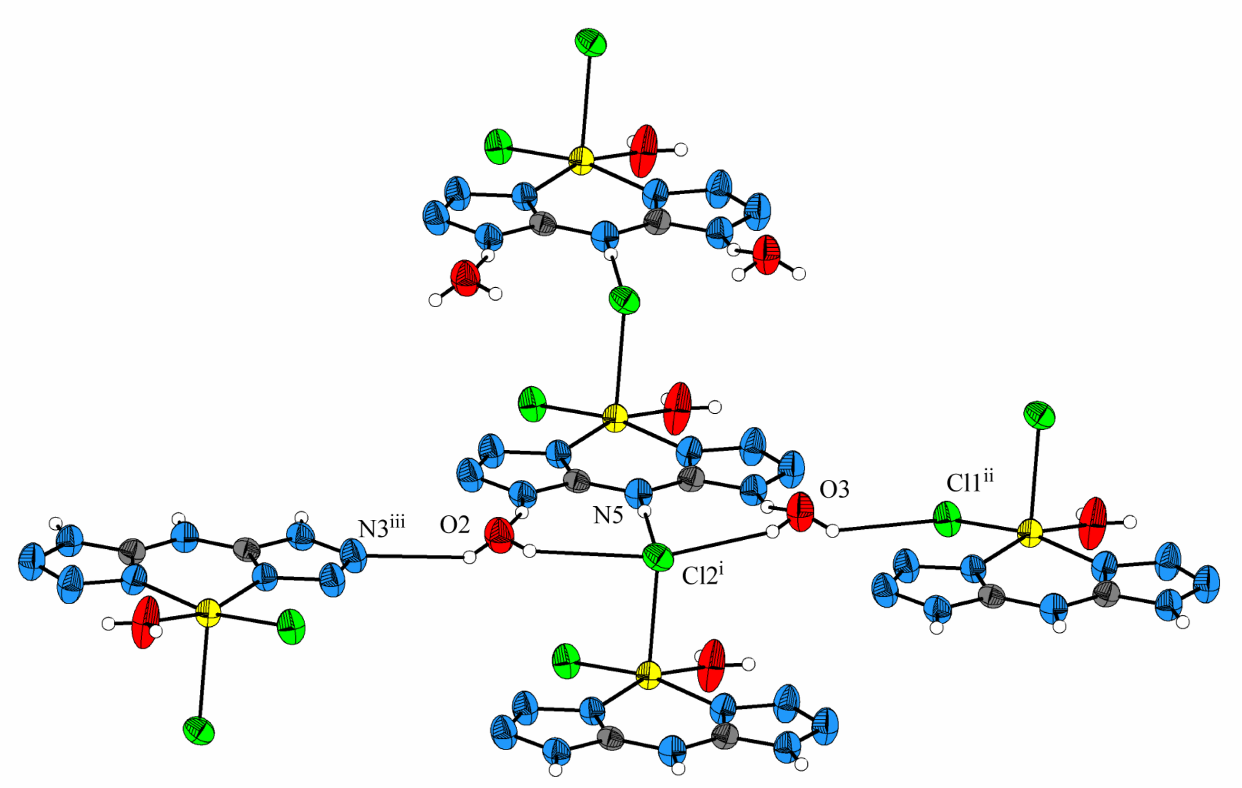

Figure 3.32. The hydrogen-bonding system in **50**. Displacement ellipsoid are drawn at the 50% probability level and H atoms are shown as spheres of arbitrary radii. [symmetry codes: (i) 1-x, y, z; (ii) -1+x, 1+y, z; (iii) –x, -1-y, 1-z]

3.3.4 Molecular structure of [CuCl(H_2**bta**)$_2$]Cl (**51**)

Chlorobis(bis(1*H*-tetrazolyl-5yl)-amino-κ^{2}N,N')copper(II) chlorid (**51**) crystallizes in the triclinic space group *P*-1with two formula units in the unit cell. The most important geometric parameters can be depicted from the legend of *Figure 3.33*. In this complex, similar to **50**,

copper is also five coordinated by four nitrogen atoms (N1, N9, N10 and N18) and one chloro ligand (Cl1). The Cu(II) ion displays again a distorted square-pyramidal coordination, being linked to three nitrogen atoms (N1, N9, N18) and one chloro ligand (Cl1) in the basal plane, and another nitrogen atom (N10) in the apical site (*Figure 3.33*, β = N9−Cu−N18; α = N1−Cu−Cl1 → τ = 0.24)[70]. The Cu−N bond length in the basal plane ranges 1.995(2) − 2.010(2) Å, which is typical and also found in complexes with e.g. 1,10-phenantroline as ligand system.[84] The basal Cu−Cl1 bond distance (2.2525(7) Å) is similar within experimental error, to those reported in related complexes.[85] The bond distance found for the apical Cu−N accounts for 2.260(2) Å. The mean plane in the molecule is the six-membered H_2**bta** chelate ring defined by atoms N1, C1, N5, C2, N9 and Cu which is planar with negligible distortion (average r.m.s. deviation form the six-atom plane is 0.0084 Å). The plane defined by N1, N9, N18 and Cl1, deviates from planarity (average r.m.s. deviation form the six-atom plane is 0.2463 Å), since the chloro ligand lies under this plane with a distance out of this least square plane of 0.8126 Å.

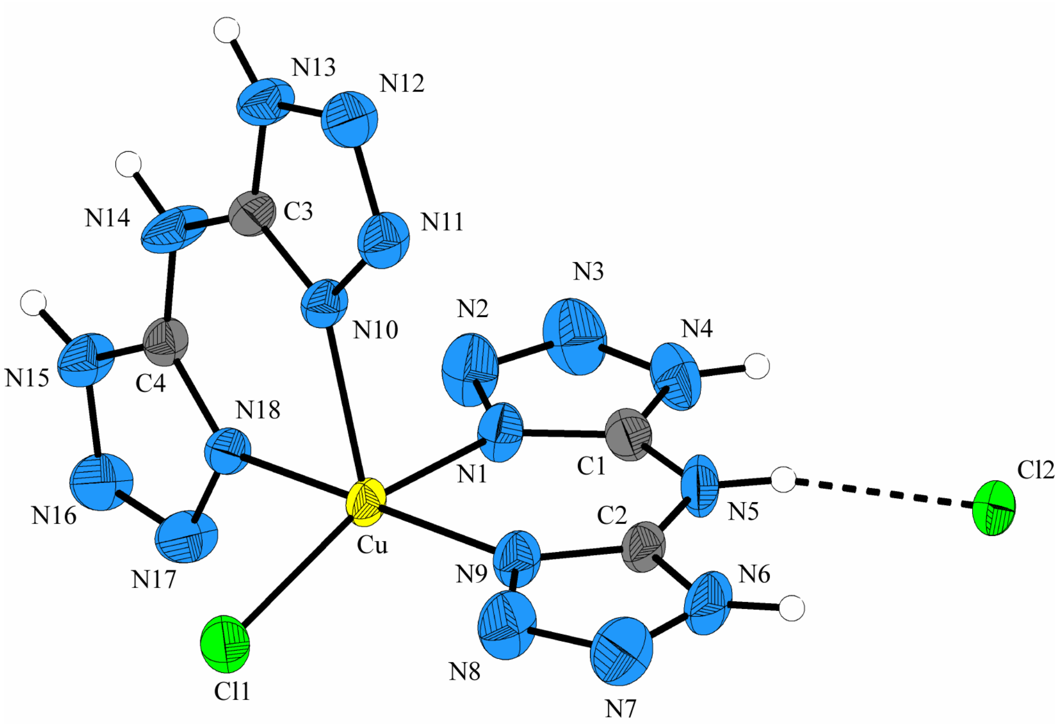

Figure 3.33. The coordination environment of the Cu^{II} ion in **51**, showing the atom-labeling scheme. Displacement ellipsoid are drawn at the 50% probability level and H atoms are shown as spheres of arbitrary radii. For clarity only one position of O3 is depicted. Selected bond length [Å]: Cu−N1 2.010(2), Cu−N9 1.996(2), Cu−N18 1.995(2), Cu−Cl1 2.2525(7), Cu−N10 2.260(2); Selected bond angle [°]: N9−Cu−N18 173.21(8), N1−Cu−Cl1 158.79(7), N18−Cu−N1 89.00(8), N18−Cu−N1 85.63(8), N18−Cu−Cl1 88.88(6), N9−Cu−Cl1 94.62(6), N18−Cu−N10 83.03(8), N9−Cu−N10 101.37(8); N1−Cu−N10 92.95(8)

3.3.5 Molecular structure of [$CuCl_2$(H_2**bta**)$_2$]*2H_2O (**52**)

Dichlorobis(bis(1*H*-tetrazolyl-5yl)-amino-κ^{2}N,N')copper(II) dihydrate (**51**) crystallizes in the monoclinic space group *P*2$_1$/n with two formula units in the unit cell. The Cu atom in **52** lies on an inversion center, and thus the coordinated N atoms of the bta ligands form a perfect plane including the Cu^{2+} cation. The Cu atom has an elongated octahedral coordination, as shown in *Figure 3.34*. The nitrogen atoms of the H_2bta coordinates in the equatorial plane, whereas the axial position are occupied by Cl atoms. The Cu−N and the Cu−Cl bond distances are 2.003(3) / 2.016(3) and 2.822(6) Å, respectively, which are similar to the values found in analogous complexes in which Cl atoms adopt an axial position in a distorted octahedron around the Cu(II) atom and is typical for an Jahn-Teller distortion.[86]

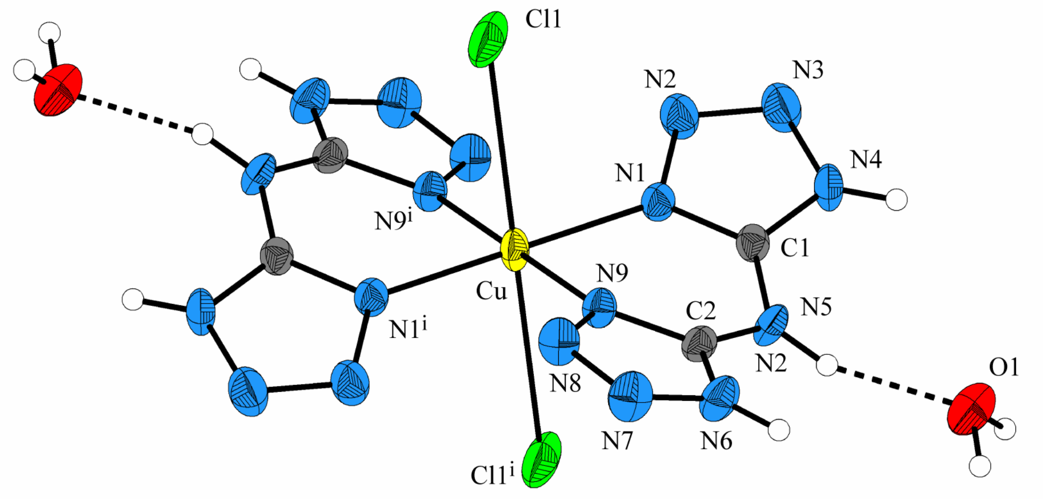

Figure 3.34. The coordination environment of the Cu^{II} ion in **52**, showing the atom-labeling scheme. Displacement ellipsoid are drawn at the 50% probability level and H atoms are shown as spheres of arbitrary radii. For clarity only one position of O3 is depicted. Selected bond length [Å]: Cu−N1 2.003(3), Cu−N9 2.016(3), Cu−Cl1 2.822(6), Selected bond angle [°]: N1−Cu−N9 84.61(1), N1−Cu−Cl1 87.52(3), N9−Cu−Cl1 96.59(3). [Symmetry code: (i) 1-x, -y, 2-x.]

3.3.5 Molecular structure of [Cu(H_2**bta**)$_2$](ClO_4)$_2$*H_2O (**53**)

Bis(bis(1*H*-tetrazolyl-5yl)-amino-κ^{2}N,N')copper(II) perchlorate monohydrate (**52**) crystallizes in the triclinic space group *P*-1with two formula units in the unit cell. In contrast to the other discussed copper salts the coordination sphere around the copper centre of the complex **53** indicates a distorted square pyramidal arrangement with almost equal Cu−N distances in the equatorial position (*Figure 3.35*). A detailed discussion is abstained.

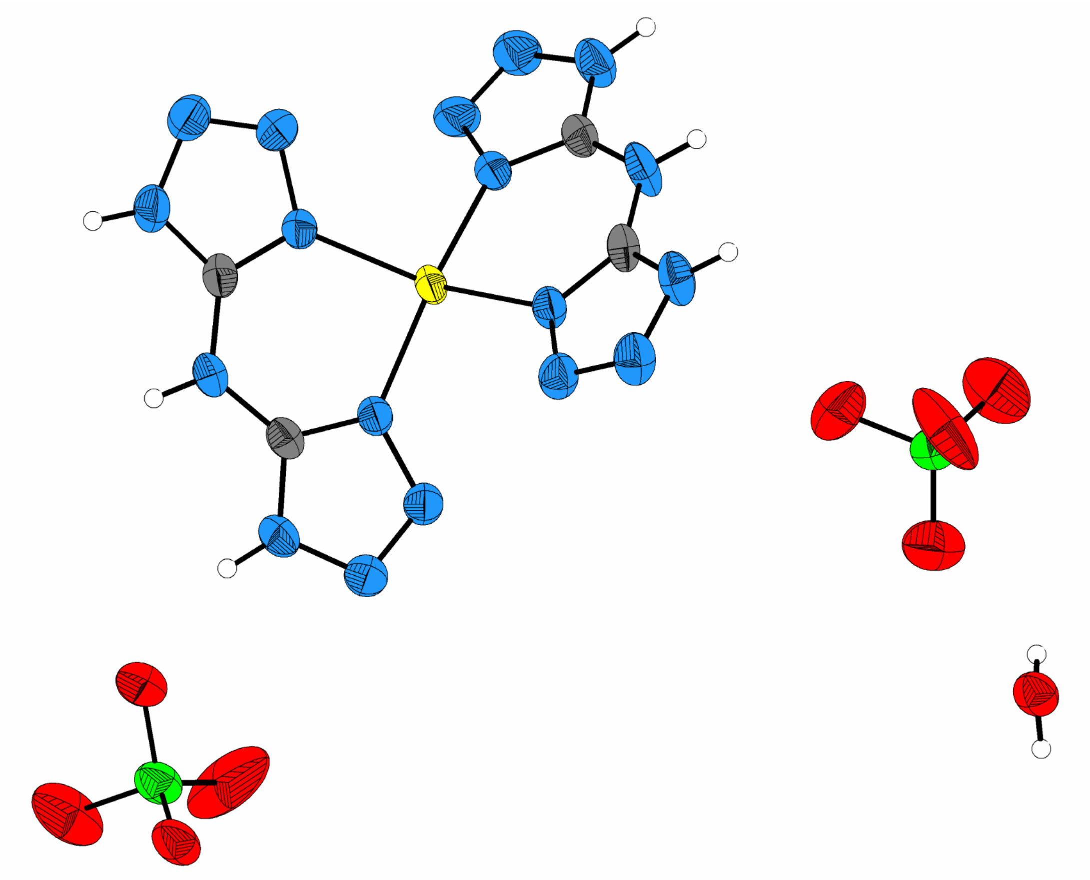

Figure 3.35. View of the molecular structure of **53**. Displacement ellipsoid at 50% probability level. (blue: nitrogen; gray: carbon; green: copper; red: oxygen; yellow: chlorine, white: hydrogen)

3.3.7 Discussion

The IR spectra of the investigated salts contain the expected absorptions bands, already discussed for the alkaline bta salts and the protonated mode of the ligand (this *Chapter*, *3.3.1*). Interestingly, the spectra of the investigated protonated copper complexes are very similar to the spectra of H_2bta*H_2O (**30**) as it monohydrate (*Figure 3.36*), indicating that the spectra are dominated by the absorption bands of the ligand. The IR spectra of compounds **50-53** contain for the ligand and the water molecules a set of characteristic absorption bands: 3500-3100 cm^{-1} [ν (H_2O), ν (N–H)], 3000-2850 [ν(N–H), overones], ~1700 [ν_{asym} (C_{tet}–N–C_{tet})], 1680-1550 [ν_{asym} (C_{tet}–N–C_{tet} + N–H)], 1550-1350 [ν_{asym} (C_{tet}–N–C_{tet}), ν tetrazole ring, ν (N5–H)] 1350-700 [ν (N1–C–N4), ν (N–N), ν (CN), tetrazole ring, δ(H_2O)], <700 [δ (out of plane bend . N–H)]. The ν (NH) absorption bands in the IR spectra of crystalline compounds have a very complex shape. Crystalline samples show in the region 2800-3500 several main absorption peaks which can be partly assigned to N–H bonds. Due to the formation of intermolecular

hydrogen bonds in the crystalline network, a red shift of stretching modes establishes that the heteromolecular hydrogen-bond interaction between the N–H (donor) groups of the bta ligand are strong.

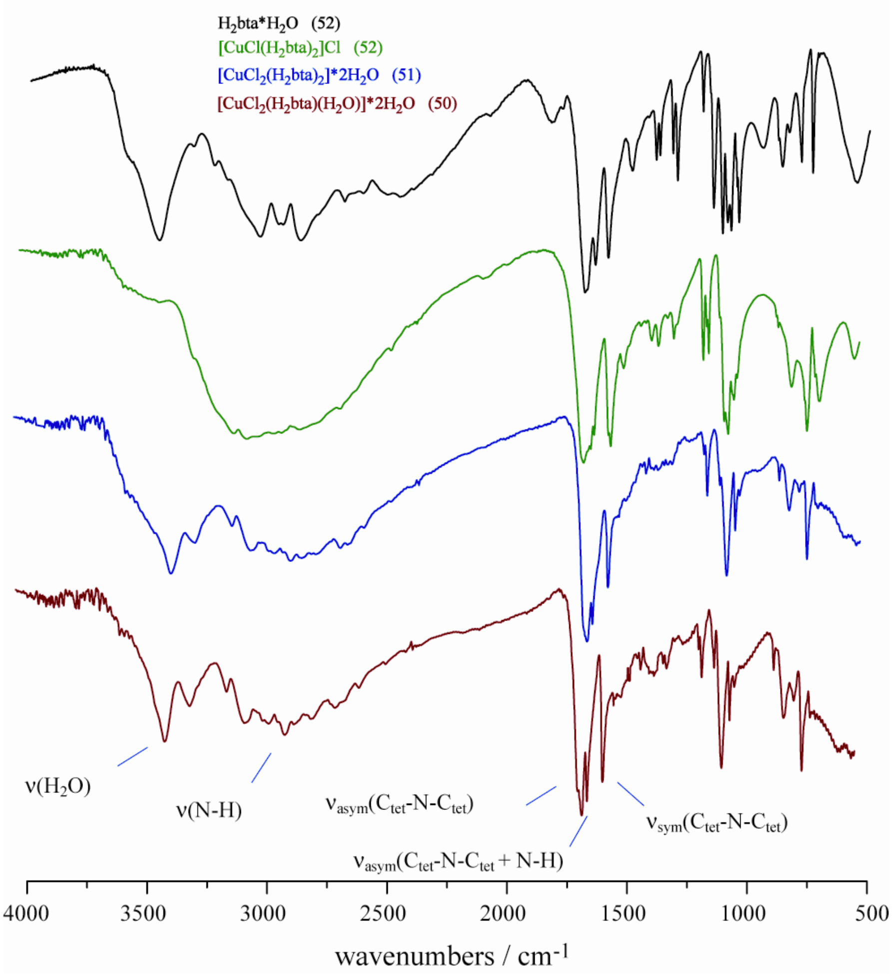

Figure 3.36. IR spectra of **50**, **51**, **52** and **30**

Raman investigations of colored transition metal complexes fail in most cases, since the samples tend to show fluorescence. The attempt to record a Raman spectra of chlorobis(bis(1*H*-tetrazolyl-5yl)-amino-κ^2N,N')copper(II) chlorid (**51**), resulted in the immediate explosion of the sample. In the case of **50** and **52** no reaction was observed, and **53** has not been tested yet. This observation is quite interesting, since modern concepts of the initiation of explosives with pulsed-laser radiation is based on the ignition at centers formed upon hypothesis of radiation absorption by optical microheterogeneities in separate crystals.[87] This is also in accordance with the observation during these experiments. Depending on how the crystallization of **51** was

performed, it is possible to obtain different modification of the same substance. Interestingly only one type of crystal explodes in the Raman experiment. Sensitivity test of **51** reveals for all batches, however, a very good stability toward heat (decomposes in the DSC experiment above 250°C), friction (160 N) and impact (no initiation with the test drop hammer). In *Figure 3.37* the results of the Raman experiment (Laser: Nd/YAG 1054 nm), performed with different laser power, is depicted. In all cases the first scan leads to explosion.

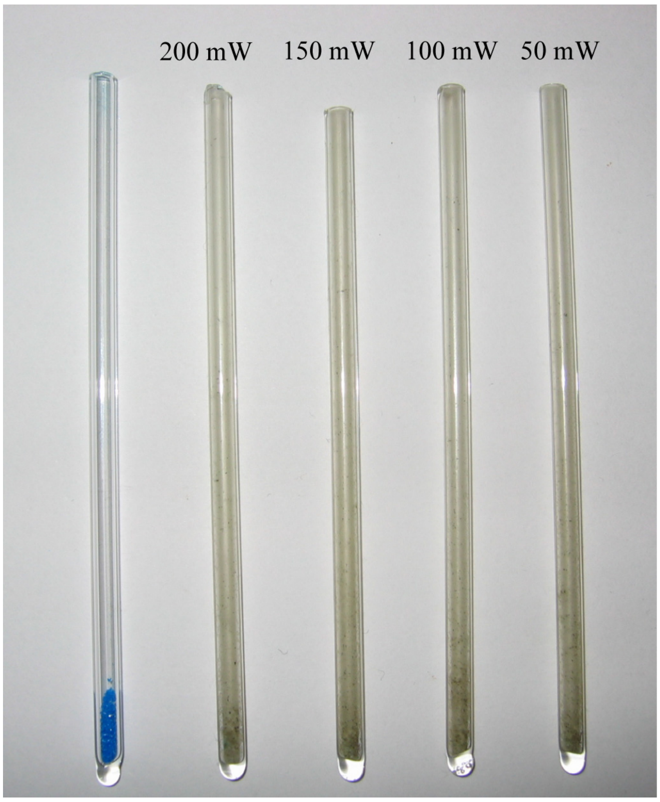

Figure 3.37. Raman experiment of **52**

These are just preliminary results since these compounds are still being investigated. Especially the perchlorate **53** is of interest as it shows a good oxygen to fuel proportion (Ω = -5.5 %) and first DSC investigations show a thermal stability of this compound up to 230 °C. It also was found that some of the investigated copper salts (e.g. **50** and **51**) can be used to replace basic copper hydroxide or copper carbonate, originally used as blue colorant in “Bengalic Fire”, yielding brighter colors with an enhanced burning rate. A detailed description of this experiment is beyond the scope of the work.

3.3.7 Experimental

*CAUTION: Perchlorates are energetic materials and tend to explode under certain condition, appropriate safety precautions should be taken, especially when this compound is prepared on a larger scale. Laboratories and personnel should be properly grounded and safety equipment such as Kevlar® gloves, leather coat, face shield and ear plugs are necessary when manipulating **53**.*

[$CuCl_2(H_2bta)(H_2O)$]*$2H_2O$ (50): Single crystals suitable for X-ray analysis were obtained as follows: To a warm (45 °C) solution of BTA*H_2O (342 mg, 2 mmol) in 20 mL conc. HCl was added a solution of $CuCl_2$*$2H_2O$ (341 mg, 2 mol) in 10 mL conc. HCl, producing a gree-blue solution. This solution was warmed for 5 minutes at 45°C and left for crystallization. After ~ 2 weeks **50** was obtained as blue-green crystals suitable for X-ray structure determination (yield 65%). **50**, stored on air, loss crystal water. $CuC_2H_9Cl_2N_9O_3$ (341.60): calcd. C, 7.0; H, 2.7; N, 36.9 %; found: C, 7.3; H, 2.4; N, 37.2 %.

[$CuCl(H_2bta)_2$]Cl (51): Single crystals suitable for X-ray analysis were obtained as follows: To a refluxing solution of BTA*H_2O (342 mg, 2 mmol) in 10 mL conc. HCl was added a solution of $CuCl_2$*$2H_2O$ (170 mg, 1 mol) in 3 mL conc. HCl, producing a blue solution. This solution was refluxed for further 2 minutes and the heat immediately removed. After ~ 10 minutes **51** was obtained as fine blue crystals suitable for X-ray structure determination (yield 75%). $CuC_4H_6Cl_2N_{18}$ (440.66): calcd. C, 10.9; H, 1.4; N, 57.2; Cl, 16.1 %; found: C, 11.0; H, 1.4; N, 57.3; Cl, 16.2 %.

[$CuCl_2(H_2bta)_2$]*$2H_2O$ (52): Single crystals suitable for X-ray analysis were obtained as follows: To a solution of BTA*H_2O (342 mg, 2 mmol) in 20 mL conc. HCl was added a solution of $CuCl_2$*$2H_2O$ (170 mg, 1 mol) in 6 mL conc. HCl, producing a blue-green solution. From this solution, **52** was obtained as big, coarse blue crystals after two days (yield 75%). If the concentration of the BTA and copper salt is to high, **51** mixed with **52** is obtained. $CuC_4H_6Cl_2N_{18}$ (476.69): calcd. C, 10.8; H, 2.1; N, 52.9, Cl, 14.9 %; found: C, 10.1; H, 2.2; N, 52.6; Cl, 14.6 %.

$[Cu(H_2bta)_2](ClO_4)_2*H_2O$ (53): Single crystals suitable for X-ray analysis were obtained as follows: To a hot solution (75 °C) of BTA*H_2O (342 mg, 2 mmol) in 15 mL water and 15 ml conc. perchloric acid was added a solution of $Cu(ClO_4)_2*6H_2O$ (370.5 mg, 1 mol) in 5 mL water producing a blue solution. This solution was heated for 4 h. Note: Take care, that the solution gets not dry **and** that no product start to crystallize during heating (extreme risk of explosion). From this solution, **52** was obtained as big, coarse blue plates after ~ 1 week (yield 64%). $CuC_4H_6Cl_2N_{18}$ (586.67): calcd. C, 8.2; H, 1.4; N, 43.0, Cl, 12.1 %; found: C, 8.3; H, 1.4; N, 43.3 %.

3.4 Conclusion

Although only preliminary results are presented, copper BTA salts might play an important role in the development of safe non-toxic PC formulations, as possibly photosensitive compounds utilized in laser detonators (e.g. **51**) as well as colorants in pyrotechnic formulations. Since the starting materials are cheap and the preparation is straight forward, BTA has a high potential as ingredient in explosive or propellant formulations too. Basic copper salts like **48** are predestined to serves as stabilizer in TLP or other explosive formulation because of the capability to catch protons. Interesting system could also be derived from complexes which prefer to have a octahedral coordination like Co^{3+}. First investigations in this direction have already started and *Figure 3.38* depicts the structural arrangement of $[Co(H_2bta)_2(hbta)]Cl_2$ (**54**). This structure contains the first octahedral coordinated cobalt with 27 nitrogen atoms in its coordination sphere. The next step is the exchange of the Cl by ClO_4!

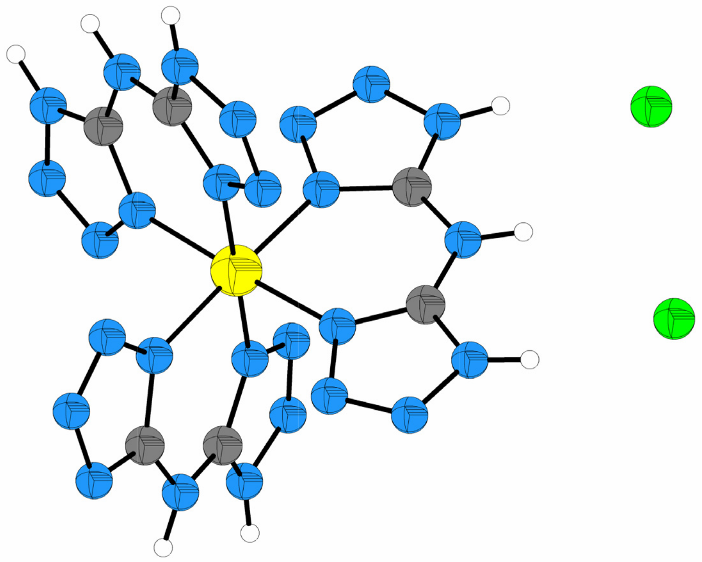

Figure 3.38. Molecular arrangement of 54. (blue: nitrogen; gray: carbon; green: chlorine; yellow: cobalt, white: hydrogen)

4. References

[1] Butler, R. N. In *Comprehensive Heterocyclic Chemistry*; Katritzky, A. R., Rees, C. W., Scriven, E. F. V., Eds.; Pergamon: Oxford, U.K., **1996**; Vol. 4.

[2] a) Eddaoudi, M.; Kim, J.; Rosi, N.; Vodak, D.; Wachter, J.; O'Keeffe, M.; Yaghi, O. M. Science **2002**, *295*, 469; b) Li, H.; Eddaoudi, M.; O'Keeffe, M.; Yaghi, O. M. Nature **1999**, *402*, 276; c) Batten, S. R.; Jensen, P.; Moubaraki, B.; Murray, K. S.; Robson, R. *Chem. Commun.* **1998**, 439.

[3] Norris, W. P., Henry, R. A. *J. Am. Chem. Soc.* **1963**, *29*, 650.

[4] a) Hiskey, M. A.; Chavez, D. E.; Naud, D. L. Unites State Patent 6,214,139, **2001**; b) Hiskey, M. A.; Chavez, D. E.; Naud, D. L. Unites State Patent 6,458,227, **2003**; c) Hiskey M. A. *et. al*, Unites State Patent 5,917,146, **2000**.

[5] Highsmith, T. K.; Blau, R. J.; Lund, G. K. Unites State Patent 5,682,014, **1995**.

[6] a) Shimizu, T. *Fireworks − Art, Science and Technique*, Maruzen Co Ltd., Tokyo, J, **1981**; b) Lancaster, R.; Shimizu, T.; Butler, R. E. A.; Hall, R. G. *Fireworks − Principle and Practise*, Chemical Publishing Company Inc., New York, USA, **1974**.

[7] Köhler, J.; Meyer, R., 'Explosivstoffe', Wiley-VCH, D-Weinheim, D, 9. Auflage, **1998**.

[8] Akhavan, J. *The Chemistry of Explosives*, RCS Paperbacks, Cambridge, **1998**.

[9] a) Leontjev, V. G.; Shesttakov, E. K. *Proceedings of International Pyrotechnoology Seminar*, **1995**, 520; b) Patil, K. C.; Vernekar Pai, V. R. *Synth. React. Inorg. Met. Org. Chem.* **1982**, *12*, 383; c) Zhilin, A. Yu; Ilyshin, M. A.; Tselinskii, I. V.; Kozlov, A. S.; Kuz'mina, N. E. *Russ. J. Appl. Chem.* **2002**, *75(11)*, 1849; d) Smirnov, A. V.; Ilyushin, M. A.; Tselinskii, I. V. *Russ. J. Appl. Chem.* **2004**, *77(5)*, 794.

[10] a) Tomlinson, W. R.; Ottoson, K. G.; Audriete, L.F. *J. Am. Chem. Soc.* **1949**, *71*, 375; b) Joyner, T. B. *Can. J. Chem.* **1969**, *74*, 2729; c) Sinditskii, S. V.; Serushkin, V.V. *Def. Sci. J.* **1996**, *46*, 371.

[11] Zh, S.; Wu, Y.; Zhang, W.; Mu, J. *Propellants, Explosives Pyrotech.* **1996**, *22(6)*, 317.

[12] a) Parry, M.; Dickson, P. M.; Field, J. E. *19th International Annual Conference ICT*, Karlsruhe **1988**, 44/1; b) Liebarger, M. L. *Ind. Eng. Chem. Prod. Res. Dev.* **1985**, *24*, 438.

[13] Norris, W. P.; Henry, R. A. *J. Org. Chem.* **1964**, *29(3)*, 650.

[14] Highsmith, T. K.; Hajik, R. M.; Wardle, R. B.; Lund, G. K.; Blau, R. J. Unites State Patent 5,468,866, **1995**.

[15] Mareček, P.; Dudek, K.; Liška F. New Trends in Research of Energetic Materials, Proceedings of the Seminar, 7th, Pardubice, Czech Republic, Arp. 20-22, **2004**, *2*, 566.

[16] Holleman Wiberg, *Lehrbuch der Anorganischen Chemie*, 101. Aufl., Walter de Gruyter, **1995**.

[17] a) Subrayan, R. P.; Francis, A. H. ; Kampf, J. W.; Rasmussen, P. G. *Chem. Mat.* **1995**, *7*, 2213; b) Ciganek, E.; Linn, W. J.; Webster, 0. W. In *The Chemistry of the Cyano Group;* Rappoport, Z., Ed.; Interscience Publishers: London, 1970, 423; c) Webster, O. W. In *Kirk-Othmer Encyclopedia of Chemical Technology,* 4th ed.; Howe-Grant, M., Ed., **1993**, Vol. 7, 809.

[18] Liu, A.; Cohen, M. L. *Science* **1989**, *245*, 841.

[19] a) Kaim, W.; Moscheroshc, M. *Coord. Chem. Rev.* **1994**, *129*, 157; b) Dunbar, K. R. *Angew. Chem., Int. Ed. Engl.* **1996**, *35*, 1659; c) Duclos, S.; Conan, F.; Triki, S.; Le Mest, Y.; Gonzalez, M. L.; Pala, J. S. *Polyhedron* **1999**, *18*, 1935; d) Triki, S.; Pala, J. S.; Decoster, M.; Molinie, P.; Toupet, L. *Angew. Chem., Int. Ed.* **1999**, *38*, 113.

[20] a) Dhar, D. N. Chem. Rev. **1967**, *67*, 611; (b) Fatiadi, A. J. *Synthesis* **1986**, 249; c) Roland, J. R.; McKusick, B. C. *J. Am. Chem. Soc.* **1961**, *83*, 1652.

[21] a) Miura; T., Masaki, Y. *Tetrahedron* **1995**, *51*, 10477; (b) Masaki, Y.; Miura, T. Ochiai, M. *Bull. Chem. Soc. Jpn.* **1996**, *69*, 195.

[22] (a) Nicoud, J. F.; Twieg, R. J. *Nonlinear Optical Properties of Organic Molecules and Crystals*, ed. Chemla, D. S.; Zyss, J. Academic Press, Orlando, Tokyo, **1987**, vol. 1, p. 227; (b) Matsuoka, M.; Kitao, T.; Nakatsu, K. *Nonlinear Optics of Organics and Semiconductors*, ed. Kobayashi, T.; Springer-Verlag, Berlin, Tokyo, **1989**, p. 228.

[23] a) Miller, J. S.; Epstein, A. J.; Reiff, W. M. *Acc. Chem. Res.* **1988**, *21*, 114; b) Miller, J. S.; Epstein, A. J.; Reiff, W. M. *Chem. Rev.* **1988**, *88*, 201; c) Miller, J. S.; Epstein, A. J. *Angew. Chem., Int. Ed. Engl.* **1994**, *33*, 385; d) Miller, J. S.; Epstein, A. J. *Chem. Commun.* **1998**, 1319.

[24] Geiser, U.; Schlueter, J. A. *Chem. Rev.* **2004**, *104*, 5203.

[25] Jürgens, B.; Irran, E.; Schnick W. *J. Solid State Chem.* **2001**, *157*, 241.

[26] a) Becker, M.; Jansen, M.; Lieb, A.; Milius, W.; Schnick, W. *Z. Anorg.Allg. Chem.* **1998**, *624* (1), 113; b) Liu, X.; Müller, P.; Kroll, P.; Dronskowski, R. *Inorg.Chem.* **2002**, *41(16)*, 4259; c) Riedel, R.; Kroke, E.; Greiner, A.; Gabriel, A. O.; Ruwisch, L.; Nicolich, J. *Chem. Mater.* **1998**, *10*, 2964.

[27] a) Madelung, W.; Kern, E. *Liebigs Ann. Chem.* **1922**, *427*, 26; b) Jürgens, B., Irran, E.; Schneider, J.; Schnick, W**.** *Inorg. Chem.* **2000,** *39,* 665; c) Irran, E.; Jürgens, B.; Schnick W. *Solid State Sci.* **2002**, *4*, 1305; d) Irran, E.; Jürgens, B.; Schnick W. *Chem. Eur. J.* **2001**, *7*, 5372.

[28] a) Witt, J. R.; Britton, D. *Acta Cryst. Sec. B* **1971**, *27*, 1835; b) Jäger, L.; Kretschmann, M.; Köhler, H. *Z. Anorg. Allg. Chem.* **1992**, *611*, 68; c) Köhler, H.; Jeschke, M.; Nefedov, V. I. *Z. Anorg. Allg. Chem.* **1987**, *552*, 210; d) Andersen, P.; Klewe, B.; Thom, E. *Acta Chem. Scand.* **1967**, *21(6)*, 1530.

[29] a) Marsh, F. D. *J. Org. Chem.* **1972**, *37(19)*, 2966; b) Lieber, E.; Levering, *J. Am. Chem. Soc.* **1951**, *73(3)*, 1313; c) Hammerl, A.; Klapötke, T. M.; Nöth, H.; Warchhold; M. *Propellants Explos. Pyrotech.* **2003**, *28*, 165; d) Hammerl, A.; Klapötke, T. M.; Mayer, P.; Weigand, J. J. *Propellants Explos. Pyrotech.* **2005**, *30(1)*, 17; e) Hammerl, A.; Klapötke, T. M. *Inorg. Chem.,* **2002**, *41*, 906.

[30] a) Arp, H. P. H.; Decken, A.; Passmore, J.; Wood, D. J. *Inorg. Chem.* **2000**, *39*, 1840; b) Graeber, E. J.; Morosin, B. *Acta Crystallogr.* **1983**, *C39*, 567.

[31] a) Reed, R.; Brady, V. L.; Hirtner, J. M. *Proceedings of the 18th International Pyrotechnics Seminar*, July 13-17, **1992**, 939; b) Akutsu, Y.; Tamura, M. *J. Energetic Mater.* **1993**, *16*, 205.

[32] see *Chapter II* and refernces therein.

[33] a) Lifschitz, J. *Chem. Ber.* **1915**, *48*, 410; b) Curtius, T. Darapsky, A.; Müller, E. *Chem. Ber.* **1915**, *48*, 1614; c) Lifschitz, J. *Chem. Ber.* **1916**, *49*, 489; d) Lifschitz, J.; Donath, W. F. *Recl. Trav. Chim. Pays-Bas* **1918**, *37*, 270.

[34] Klapötke, T. M.; Mayer, P.; Schulz, A.; Weigand, J. J. *Prop. Explos. Pyrotech.* **2004**, *29(6)*, 325.

[35] Sekizaki, S.; Yamochi, H.; Saito, G. *Synth. Met.* **2003**, *135*, 631.

[36] a) Horiuchi, S.; Yamochi, H.; Saito, G.; Sakaguchi, K.-i.; Kusunoki, M. *J. Am. Chem. Soc.* **1996**, *118*, 8604; b) Yamochi, H.; Nakamura, T.; Saito, G.; Kikuchi, T.; Sato, S.; Nozawa, K.; Kinoshita, M.; Sugano, T.; Wudl, F. *Synth. Met.* **1991**, *42,* 1741.

[37] Yamochi, H.; Tsutsumi, K.; Kawasaki, T.; Saito, G. *Synth. Met.***1999**, *103*, 2004.

[38] Prasanna, S.; Radhakrishnan, T. P. *Synth. Met.* **1996**, *78*, 127.

[39] Yamochi, H.; Konsha, A.; Saito, G.; Matsumoto, K.; Kusunoki,M.; Sakaguchi, K.-i. *Mol. Cryst. Liq. Cryst.* **2000**, *350*, 265.

[40] Kessenich, E.; Polborn, K.; Schulz, A. *Inorg. Chem*. **2001**, *40*, 1102.

[41] Butler, R. N. *Comp. Heterocycl. Chem.* 1st ed.; **1984**; Vol. 5, p 791 and references therein.

[42] (a) Hosomi, H.; Ito, Y.; Ohba, S. *Acta Cryst.* **1998**, *C54*, 142-145; (b) Zhang, X.-L.; Li, Z.-X. *Acta Cryst.* **2005**, *E61*, o266.

[43] Holleman Wiberg, *Lehrbuch der Anorganischen Chemie*, 101. Aufl., Walter de Gruyter, 1995, Appendix IV, p-1838.

[44] Schulz, A.; Klapötke, T. M. *Inorg. Chem.* **1996**, *35*, 4791.

[45] Potočňák, Dunja-Jurčo, M.; Mikloš, D.; Jäger, L. *Acta Cryst.* **1996**, *C52*, 1653.

[46] a) E. D. Glendening, A. E. Reed, J. E. Carpenter, F. Weinhold, *NBO Version 3.1;* b) A. E. Reed, L. A. Curtiss, F. Weinhold, *Chem. Rev.* **1988**, *88*, 899.

[47] Wiberg, K. *Tetrahedron* **1968,** *24*, 1083.

[48] a) Miller, J. S.; Epstein, A. J.; Reiff, W. M. *Acc. Chem. Res.* **1988**, *21*, 114; b) Miller, J. S.; Epstein, A. J.; Reiff, W. M. *Science* **1988**, *240*, 40; c) Miller, J. S.; Epstein, A. J.; Reiff, W. M. *Chem. Rev.* **1988**, *88*, 201; d) Miller, J. S.; Epstein, A. J. *New Aspects of Organic Chemistry;* Yoshida, Z., Shiba, T., Ohsiro, Y., Eds.; VCH Publishers: New York, 1989; Vol. 237; e) Miller, J. S.; Epstein, A. J. *Angew. Chem., Int. Ed. Engl.* **1994**, *33*, 3, 385; *Angew. Chem.* **1994**, *106,* 399; f) Miller, J. S.; Epstein, A. J. *Adv. Chem. Ser.* **1995**, *245*, 161; g) Gadet, V.; Mallah, T.; Castro, I.; Verdaguer, M. *J. Am. Chem. Soc.* **1992**, *114*, 9213; h) Mallah, T.; Ferlay, S.; Auberger, C.; Helary, C.; L'Hermite, F. Ouahes, F.; Vaissermann, J.; Verdaguer, M.; Veillet, P. *Mol. Cryst., Liq. Cryst.* **1995**, *273*, 141; i) Ferlay, S.; Mallah, T.; Ouahes, R.; Veillet, P.; Verdaguer, M. *Nature* **1995**, *378*, 701; j) Entley, W. R.; Girolami, G. S. *Science* **1995**, *268*, 397; k) Entley, W. R.; Girolami, G. S. *Inorg. Chem.* **1994**, *33*, 5165; l) Entley, W. R.; Treadway, C. R.; Girolami, G. S. *Mol. Cryst., Liq. Cryst.* **1995**, *273*, 153; m) Manson, J. L.; Kmety, C. R.; Huang, Q.; Lynn, J. W.; Bendele, G. B.; Pagola, S.; Stephens, P. W.; n) Liable-Sands, L. M.; Rheingold,A. L.; Epstein, A. J.; Miller, J. S. *Chem. Mater.* **1998,** *10,* 2552.

[49] a) Penavić, M. *Acta Cryst.* **1986**, *C42*, 1283-1284; b) Kirik, S. D.; Solovyov, L. A.; Blokhin, A. I.; Yakimov, I. S.; Blokhina, M. L. *Acta Cryst.* **1996**, *B52*, 900.

[50] Kornath, A.; Neumann, F. *Inorg. Chem.* **1997**, *36*, 2708 and references therein.

[51] Beck, W.; Fehlhammer, W. P. Angew. Chem. 1967, 79, 146 and references therein.

[52] a) Lazukina, L. A.; Khuzar, V. P. *Zh. Org. Khim.* **1979**, *15*, 2216; b) Melnikov, A. A.; Sokolova, M. M.; Pervozvanskaya, M. A.; Melnikov, V. V. *Zh. Org. Khim.* **1979**, *15*, 1861.

[53] Finnegan, W. G.; Henry, R. A.; Lofquist, R. *J. Am. Chem. Soc.* **1958**, *80*, 3908.

[54] Washburne, S. S.; Peterson, W. R., Jr. *J. Organomet. Chem.* **1970**, *21*, 427.

[55] Jeffrey, G. A.; Stadler, H. P. *J. Chem. Soc.* **1951**, 1467.

[56] a) De Ridder, D. J. A.; Goubitz, K.; Fontijn, M.; Capková P.; Dova, E.; Schenk H. *Acta Cryst.* **2001**, *B57*, 780; b) Wei, C. H.; Hingerty, B. E. *Acta Cryst.* **1981**, *B37*, 1992.

[57] Allavena, M; Rysnik, R.; White D.; Calder, V.; Mann, D. E. *J. Chem. Phys.* **1969**, *50*, 3399.

[58] Huheey, J. H. *Inorganic Chemistry: Principles of Structure and Reactivity*, 3rd ed.; Harper and Row: New York, **1963**, pp 509.

[59] Tornieprth-Oetting, I. C.; Klapötke, T. M., in: *Inorganic Experiments*, Woollins, J. D. (ed.), VCH, Weinheim, **1994**, 217.

[60] Connectivity for the azide group: R- $N_\alpha N_\beta N_\gamma$

[61] Chernyaev, I. I., Handbock on Synthesis of Complex Compounds of Platinum Metal, Moscow **1964**, Nauca.

[62] Gerken, M.; Schneider, S.; Schroer, T.; Haiges, R.; Christe, K. O. *Z. Anorg. Allg. Chem.* **2002**, *628*, 909.

[63] a) Sheldrick, G. M. *SHELXL-86*, *Program for Solution of Crystal Structures*; University of Göttingen: Göttingen, Germany, 1986; b) Sheldrick, G. M. *SHELXL-97*, *Program for Solution of Crystal Structures*; University of Göttingen: Göttingen, Germany, 1997.

[64] Copies of the data can be obtained free of charge on application to CCDC, 12 Union Road, Cambridge CB2 1EZ, UK (fax: (+44) 1223-336-033; e-mail: deposit@ccdc.cam.ac.uk).

[65] Olsher, U. *Chem. Rev.* **1991**, *91*, 137.

[66] a) Etter, M. C. *Acc. Chem. Res.* **1990**, *23*, 120; b) Etter, M. C.; MacDonald, J. C. *Acta Cryst.* **1990**, *B46*, 256.

[67] Salido, M. L. G.; Mascarós, P.A.; Valero, M. D. G.; Low, J. N.; Gallagher, J. F.; Glidewell, C. *Acta Cryst.* **2004**, *B60*, 46.

[68] Gore, G. M.; Nazare, A. N.; Divekar, C. N.; Hait, S. K.; Asthana, S. N. *J. Energetic Mater.* **2004**, *22(3)*, 151 and references therin.

[69] a) Lyakhov, A. S.; Gaponik, P. N.; Degtyarik, M. M.; Ivashkevich, L. S. *Acta Cryst* **2003**, *C59*, m204; b) Mills, A. M.; Flinzner, K.; Stassen, A. F.; Haasnoot, J. G.; Spek, A. L. *Acta Cryst* **2002**, *C58*, m243; d) Ivashkevich, L. S.; Lyakhov, A. S.; Gaponik, P. N.; Bogatikov, A. N.; Govorova, A. A. *Acta Cryst* **2001**, *E57*, m335; d) Gökaugac, G.; Tatar, L.; Kisakürek, D.; Ülkü, D. *Acta Cryst* **1999**, *C55*, 1413; e) Tatar, L.; Gökagac, G.; Ülkü, D. *Acta Cryst* **2000**, *E56*, m335.

[70] a) Addison, A. W. ; Rao, T. N. ; Reedijk, J.; Rijn, J. van *J. Chem.Soc. Dalton Trans.* **1984**, 1349; b) The largest bond angles around the Cu(II) center (β: N(9)−Cu−N(10)=176.74(8)° (**47**) *vs.* N(9)−Cu−N(10)=170.25(8)° (**48**)) is larger than the second-largest one (α: N(1)−Cu−N(11)=154.82(7)° (**47**) *vs.* N(1)−Cu−N(11)=166.98(8)° (**48**)). The value of the differences between the longest and shortest Cu-N bond distances of the basal atoms apply for ΔCu-N is 0.030 Å (**47**) and 0.036 Å (**48**), respectively. Since the angular structural index parameter, $\tau = (\beta - \alpha)/60$, is evaluated by the two largest angles ($\alpha < \beta$) in the five-coordinate geometry, the value of τ indicates a regular square based pyramidal stereochemistry ($\tau = 0.0$) or a regular trigonal bipyramidal stereochemistry ($\tau = 1.0$).

[71] Bondi, A. *J. Phys. Chem.* **1964**, *68(3)*, 441.

[72] a) Kahn, O. *Molecular Magnetism VHC*, **1993**; b) Bonner, J. C.; Fisher, M. E. *Phys. Rev.* **1964**, *135*, 640.

[73] Koner, S.; Saha, S.; Mallah, T.; Okamoto, K.-I. *Inorg. Chem.* **2004**, *43*, 840.

[74] Julve, M.; Verdaguer, M.; Gleizes, A.; Philoche-Levisalles, M.; Kahn, O. *Inorg. Chem.* **1984**, *23*, 3808.

[75] Prasad, R. *Thermochim. Acta* **2003**, *406*, 99.

[76] This discrepancy might be explained by the strong explosion process of the compound during the second steps which leads to the loss of material in the crucible.

[77] Ozawa, T. Bull. *Chem. Chem. Soc. Jpn.* **1965**, *38*, 1881.

[78] *ICT – Thermdynamic Code*, Version 1.0, Frauenhofer-Institut für Chemische Technologie (ICT). Pfinztal/Berghausen, Germany 1988-2000.

[79] [i] Insensitive > 40 J, less sensitive ≥ 35 J, sensitive ≥ 4, very sensitive ≤ 3 J; [j] Insensitive > 360 N, less sensitive = 360 N, sensitive < 360 N a. > 80 N, very sensitive ≤ 80 N, extreme sensitive ≤ 10 N; According to the UN Recommendations on the Transport of Dangerous Goods (+) indicates: not safe for transport.

[80] West, R. C.; Selby, S. M. *Handbook of Chemistry and Physics*, 48th ed.; The Chemical Rubber Co.; Cleveland, OH, **1967-1968**; pp D22-D51.

[81] Ostrovskii, V. A.; Pevzner, M. S.; Kofman, T. P.; Tselinskii, I. V. *Targets Heterocycl. Syst.* **1999**, *3*, 467.

[82] a) Altomare, A.; Burla, M. C. M; Camalli, M.; Cascarano, G. L.; Giacovazzo, C.; Guagliardi, A.; Moliterni, A. G. G.; Polidori, G.; Spagna, R. *J. Appl. Crystallogr.* **1999**, *32*, 115-119; b) Sheldrick, G. M. *SHELXL-97*, *Program for Solution of Crystal Structures*; University of Göttingen: Göttingen, Germany, **1997**

[83] a) SMART rev. V4.C50, Brucker Germany; b) XRed, rev. 1.09, Darmstad Germany.

[84] a) Nakai, H. Deguchi, Y. *Bull. Chem. Soc. Jap.* **1975**, *48*, 2557; b) Heldal, H. E.; Sletten, J. Acta CHem. Scand. 1997, 51, 122.

[85] Johansson, A.; Håkansson, M. *Acta Cryst.* **2004**, *E60*, m1068.

[86] Prins, R.; Biagini-Cingi, M.; De Graff, R. A. G.; Haasnoot, J.;Manotti-Lanfredi, A.-M., Rabu, P.; Reedijk, P.; Ugozzli, E. *Inorg. Chim. Acta* **1996**, 248, 35.

[87] Ilyshin, M. A.; Tselinskii, I. V.; Chernai, A. V. *Ross. Khim. Zh.* **1997**, *41(4)*, 81.

Chapter IV

*1,5-DIAMINO-1H-TETRAZOLE (**DAT**)*

1 Introduction

1.2 **DAT**

Aminotetrazoles have the highest content of nitrogen among the organic substances (e.g. 82.3 wt.% for 5-amino-*1H*-tetrazole **14** (**5-AT**) and 84.0 wt.% for 1,5-diamino-*1H*-tetrazole **55** (**DAT**), and in spite of their large positive enthalpies of formation[1], they exhibit surprisingly high thermal stabilities (*Figure 4.1*).[2]

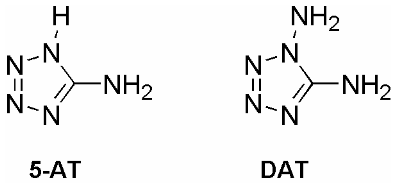

Figure 4.1. Aminotetrazoles

Therefore, aminotetrazoles and certain derivatives are prospective materials for the generation of gases, as blowing agents, solid propellants and other combustible and thermally decomposing systems as already discussed for **5-AT** in *Chapter I.* Interestingly, **55** and it's derivatives had never been considered as gas-generating agents, and only little work has been done using **55** as a valuable intermediate in the preparation of high-energy-density materials (HEDMs)[3] or other useful tetrazole containing compounds.[4] The reason for this might be the difficult accessibility of **55**. So far only three synthetic methods for the preparation of **55** have been described. Based on the reaction of **14** as the sodium salt with hydroxylamine-*O*-sulfonic acid (HOSA), **55** is formed in a low yield (8,5%) together with the 2,5-diamino-2*H*-tetrazole isomer **56** (*Scheme 3.1*).[5]

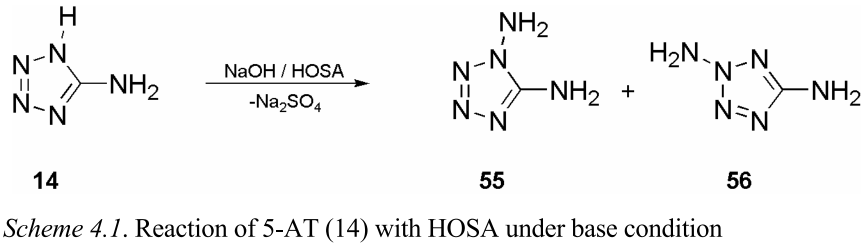

Scheme 4.1. Reaction of 5-AT (14) with HOSA under base condition

Gaponik et al.[4a] improved the 1933 reported synthesis of Stolle et al.[6] who synthesized **55** by reacting thiosemicarbazide (**57**) with lead(II) oxide and sodium azide in a CO_2 atmosphere in ethanol as solvent. **14** is converted into the corresponding carbodiimide (**58)** with lead(II) oxide, which reacts with *in situ* formed HN_3 under ring closing to yield **56** (*Scheme 4.2*). Unfortunately, this reaction leads to the formation of large amounts of lead azide as the side-product, which makes this synthesis problematic for an industrial scale.

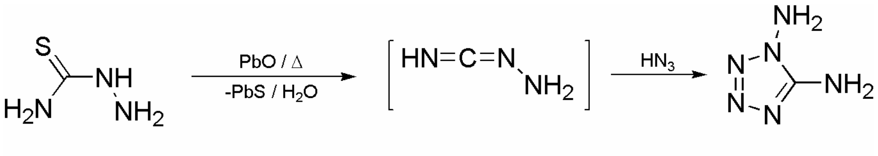

Scheme 4.2. Synthesis of DAT (**55**) according Gaponik et al.

Since the tetrazole derivatives represent fuels, appropriate oxidizers are important in order to realize corresponding propellant formulations. The parent aminotetrazoles can be protonated, and therefore salts with energetic oxygen rich cations, such as nitrate (NO_3^-), dinitramide ($N(NO_2)_2^-$) or the perchlorate (ClO_4^-) anion are sought.[7]

1.2 Energetic salts

Nitrate, dinitramide, perchlorate and azide salts of nitrogen rich cations have received major attention for a number of reasons: a high oxygen balance (nitrate, dinitramide and perchlorate salts), a high heat of formation $\Delta_fH°$, the release of large amounts of gases (e.g. N_2) as favored explosion products and high values of the density ρ. At present, the search for high energy compounds is mainly directed towards molecular crystals made from neutral molecules. The reason for this is that ionic crystals normally have poor values of $\Delta_fH°_{solid}$ (solid state formation enthalpy may be estimated as $\Delta_fH°_{solid} = \Delta_fH°(gas)-E_{coh}-RT$) coming from high contribution of crystal cohesive energy (E_{coh}). This contribution is comparably small for molecular crystals of covalent compounds, typically lower than 0.12 kcal/g,[8] but for ionic crystals, E_{coh} is typically one order of magnitude larger owing to the long-range electrostatic interactions between ions (e.g. low $\Delta_fH°_{solid}$(AN, ammonium nitrate) = -1.09 kcal/g due to significant cohesion of the crystal E_{coh}(AN) = 2.08 kcal/g). To minimize the contribution of E_{coh}, it is important to combine anions (e.g. nitrate, perchlorate or dinitramide anions for good oxidation abilities) with large cations in order to

increase the distance between charged groups. Calculations on ethane and $H_3C\text{-}NH_3^+$ suggest a very high contribution of the ammonium group $–NH_3^+$ to $\Delta_fH°$ (~145 kcal/mol).[9] Thus, some ionic crystals might provide valuable energetic constituents of propellants provided their cohesive energy is not too large. For example, the best known of the highly energetic nitrate and dinitramide salts are the oxidizers ammonium nitrate (**AN**) and ammonium dinitramide (**ADN**).[10] In the case of nitrogen rich anions, hydrazinium azide[11] and its organic derivatives[12] were extensively investigated, which are in most cases unfortunately volatile and hygroscopic and also have relatively low densities.

1.3 Crystal building units

To understand the interplay of cations and anions within a network and predict important values like densities, E_{coh} and $\Delta_fH°$, an algorithm is necessary for a predictable and controllable long-range molecular organization.[13] Basically, the crystal structure of the material is a result of iterative self-assembling of the constituent molecular, co-molecular (bimolecular)[14] or ion pair subunits, considered as fundamental crystal building units. However, the prediction of solid-state structure of crystals is commonly frustrated by the complexity and lack of directionality of intermolecular forces. The packing control in three dimensions is elusive, owing to the numerous possible intermolecular interactions and multiplicity of structural possibilities. Therefore it is important to have a closer look into the structural aspects which account for the interplay between such factors, as directional demands of the interactions and geometrical dictates the close-packing. In this context, it is also of interest to investigate known and new salts of aminotetrazoles especially with nitrate, dinitramide[15] and azide as counter ions especially focused in the formation of robust hydrogen-bonded multidimensional networks within these salts. The dimensionality and general structural feature of a multidimensional network depends on the modules which serve as 'topological directors' and strongly depends on the symmetry of the ions. A search in the Cambridge Structural Database (CSD) revealed that the crystal structure of guanidinium nitrate [$HGN^+NO_3^-$] consists of hydrogen-bonded polar layers, stacked in the third dimension by van der Waals interactions (*Figure 4.2*, **I**).[16] The hydrogen bonded ring motif, in the formalism of graph-set analysis of hydrogen-bond patterns,[17] which are found for [$HGN^+NO_3^-$] are the $R_6^3(12)$ and the very common $R_2^2(8)$. The latter was also observed in other structures *e.g.* discussed in *Chapter II* (2.2.2) and *Chapter III* (3.1.3,4 and 3.2.3).

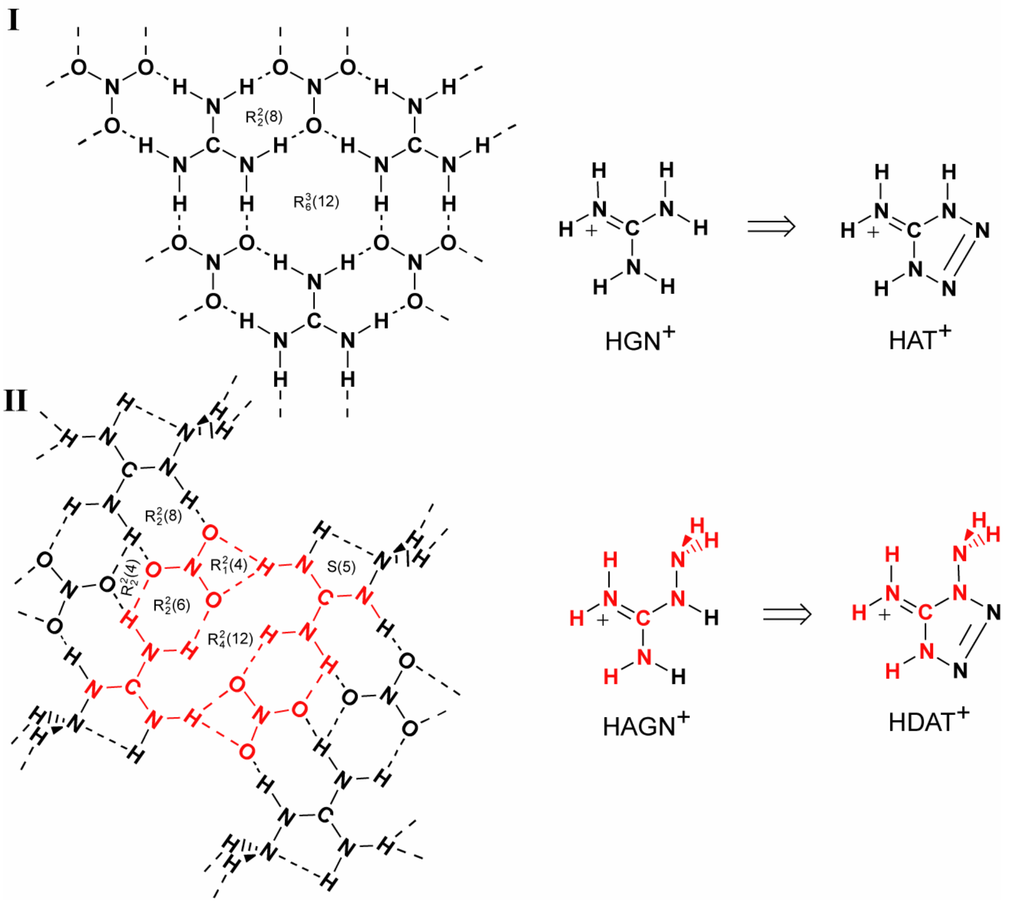

Figure 4.2. Scheme of the 2D organization pattern of [$HGN^+NO_3^-$] **I** and [$HAGN^+NO_3^-$] **II** through intermolecular hydrogen bonds.

As the bond pattern strongly depends on the symmetry of the cations, lowering symmetry by a formal introduction of an amino group should modify the hydrogen-bond connectivity pattern. In the case of aminoguanidinium nitrate [$HAGN^+NO_3^-$],[18] the terminal NH_2 group is positioned in such a fashion that the hydrogen atoms appear above and below the plane of the rest of the molecule, and the lone pair is directed towards the hydrogen atom of one of the C=NH_2 moieties forming an intramolecular bond with the motifs $S(5)$. The nitrate and aminoguanidinium moieties are approximately coplanar. Within the same plane the nitrate groups are linked through hydrogen bonds to the N atoms by hydrogen bonded ring motifs $R_1^2(4)$, $R_2^2(4)$, $R_2^2(6)$, $R_2^2(8)$ and $R_4^2(12)$ (Figure 1, **II**). Above and below this plane, the groups are bonded intermolecularly through the H atoms of the terminal amino group. In comparison to the above mentioned salts, and in order to gain further details of topological similarities of diaminotetrazolium salts, a closer inspection of the two- and three-dimensional hydrogen-bonded networks are going to be discussed for the new synthesized energetic salts.

2. $HDAT^+$ / $MeDAT^+$ salts

Aminotetrazoles are heterocycles, rich in electron pairs. The reaction with weak or strong acids leads with **14** (R = H, discussed elsewhere)[19] and **55** (R = NH_2) only with strong acids (X^- = Cl, Br, I, NO_3, ClO_4, SO_4, picrate)[4a,20] to the formation of the corresponding salts (*Scheme 4.3*).

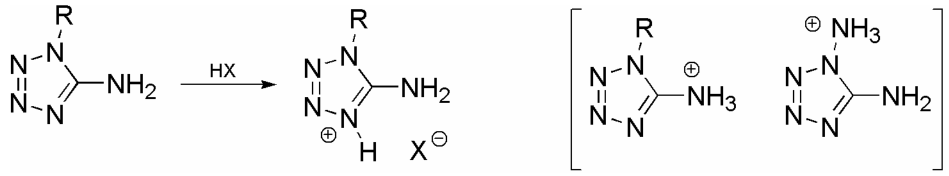

Scheme 4.3. Protonation of **5-AT** and **DAT**

Protonation of **14** and **55** can proceed both on the nitrogen atoms of the tetrazole ring and on the amino group(s). It was determined to proceed unambiguously at the N4 atom of the ring (*Scheme 4.3*).[21] Nothing is known in the literature about the corresponding azide or dinitramide salts concerning the isolation of such salts.

The protonation of **55** with HNO_3 (**59a**) and $HClO_4$ (**59b**) as well as the quaternization with MeI and subsequently metathesis of the iodide with corresponding silver salts and a new derivative of **55**, the 1-amino-4-methyl-5-imino-4,5-dihydro-1*H*-tetrazole **60** as its iodide, azide, nitrate and dinitramide salt (**61a-d**) were investigated during this thesis (*Figure 4.3*). Also a new and improved synthesis of **55** was developed in order to make **55** accessible on a larger scale.

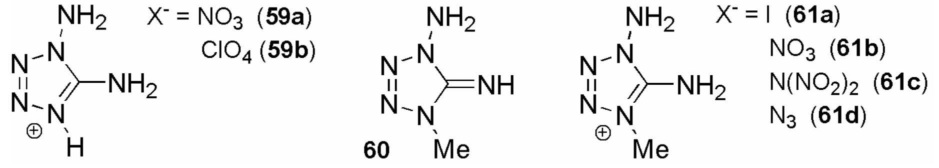

Figure 4.3. Reaction products of **DAT**

2.1 Synthesis

The synthesis strategy for **55** is based on the studies of Lieber et al. who treated diaminoguanidine nitrate (**AGN**, **12**) with one and two molar portions of nitrous acid in a buffered acetic acid media.[22] According to Lieber, the treatment of **12** with two moles of nitrous acid (MNO_2 (M = Na, K) in acetic solution), yielded the corresponding alkali metal salt of tetrazolyl azide (**62**) as the only isolable product.[23]

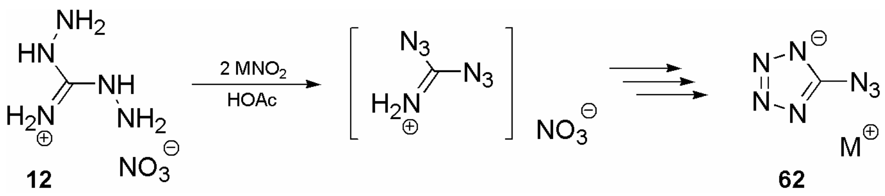

Scheme 4.4. Synthesis of the metal salt of azidotetrazole

The reaction with one equivalent of nitrous acid in acetic acid media resulted mainly in the recovery of **12** (80 to 95%) and in the isolation of a small quantity of the corresponding metal salt of tetrazolyl azide **62** (*Scheme 4.4*). It is known, that the reaction of nitrous acid with aminoguanidine is strongly dependent on the reaction conditions, and aminoguanidine reacts with nitrous acid in three ways: if the reaction is carried out in strong mineral acids, it leads to the formation of guanyl azide; in aqueous solution alone 1-guanyl-4-nitroso-aminoguanyltetrazene is formed, whereas in a solution of acetic acid ditetrazolyltriazene is obtained.[24] In general, the reaction between HNO_2 and a hydrazine moiety can yield the corresponding azide or result in the degradation of the hydrazine to the corresponding amine depending on the p*H*.[25]

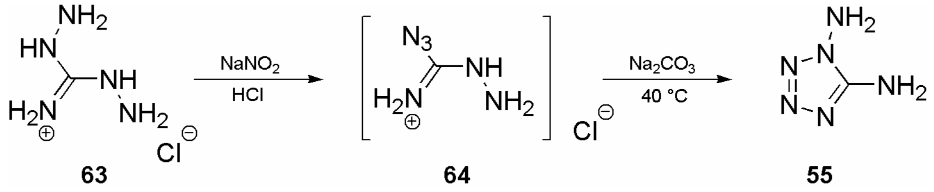

Scheme 4.5. Improved synthesis of **55**

Based on that, reaction conditions were modified and diaminoguanidinium chloride (**AGCl**, **63**) in hydrochloric acid used as starting material. After the diazotation, the reaction mixture was carefully brought to p*H* 8 with sodium carbonate to deprotonate the intermediately-formed amino substituted azido guanyl chloride **64**. **64** cyclizes under this reaction condition and **55** is formed in an overall yield of 58% (*Scheme 4.5*).

The preparation of **59a** and **59b** was easily archived by the reaction of **55** with the corresponding acids (see experimental section, **59a** 93%, **59b** 97% yield). All attempts to prepare a corresponding $HDAT^+N_3^-$ were unsuccessful due to the low acidity of HN_3. It is known from other authors, that in high-nitrogen heterocyclic rings having amino groups attached to the ring there is an electronic interaction between the amino groups and the ring system. As a consequence, a significant reduction of the basicity of the lone pair of the amino group is observed (e.g. 4-amino-1,2,4-triazole has a pK_a of 2.25,[26] 1*H*-1,2,4-triazole has a pK_a of 10.04,[27] while 1*H*-1,2,3-triazole has pK_a of 8.2[26]).

The 1,5-diamino-4-methyl-1*H*-tetrazolium iodide (**61a**) was prepared via the quaternization of **55** with iodomethane. Due to the formal exchange of the proton at N4 by a methyl group, a lower acidity and hence a higher stability of the corresponding azide (**61d**) was expected. The reaction of **55** with MeI is regiospecific when performed in refluxing acetonitrile using an excess of MeI. It yields **61a** in an overall yield of 86%. The reaction of **55** with one equivalent MeI in refluxing EtOH yields a mixture of isomers which could not easily be separated. By metathesis of **61a** with corresponding silver salts the nitrate (**61b**, X = NO_3, 93%), dinitramide (**61c**, X = $N(NO_2)_2$, 85%) and azide (**61d**, X = N_3, 90%) were obtained (*Scheme 4.6*). All salts were formed in good to excellent yields in high purity and could be re-crystallized from concentrated alcoholic solutions layered with diethyl ether. Compared to the low melting salts of 1,2,4- and 1,2,3-triazole systems introduced by Drake *et al.*[28], two of our new salts can also be classified as ionic liquids,[29] **59b** (mp 97 °C) and **61c** (mp 85 °C), the melting points of the others lies in average 40 °C higher (Table 6).

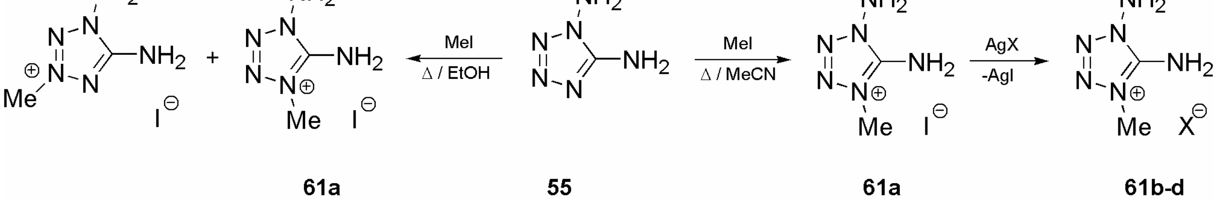

61a **55** **61a** **61b-d**

Scheme 4.6. Synthesis of **61a-d**

2.2 IR spectroscopy

Vibrational spectroscopy was useful in qualitative analysis of all the salts especially to evaluate the formation of the hydrogen bond network. In all spectra, the bands of the respective energetic anions (N_3^-, ClO_4^-, NO_3^- and $N(NO_2)_2^-$) were obvious, and as these bands usually have characteristic fingerprints in both the infrared and the Raman spectra, they could be identified easily. The nitrate anion, NO_3^- usually has a strong stretch at 1345 cm^{-1} in the infrared and a strong band around 1043–1050 cm^{-1} in the Raman spectrum.[30] The perchlorate anion, ClO_4^-, has a strong broad stretch centered around 1119 cm^{-1} in the infrared spectra, and strong bands at 958 cm^{-1} and 459 cm^{-1} in the Raman spectrum.[31] The dinitramine anion, $N(NO_2)_2^-$, has strong stretches in the infrared spectrum at around 1530, 1445, 1345, 1183 and 1025 cm^{-1} and strong bands in the Raman at 1335 and 830 cm^{-1}.[32] For the azide anion, N_3^-, characteristic bands at 2092 cm^{-1} and 1369 cm^{-1} can be observed in the infrared and Raman spectra.[33] The IR and Raman spectra of compounds **59a-b** and **61a-d** contain for the cations a set of characteristic absorption bands: 3400-3100 cm^{-1} [ν(N–H)], 3000-2850 [ν(C–H), **61a-d**], ~1715 [ν(C1=N5)], 1680-1550 [δ(N6H_2), δ(N5H_2)], 1550-1350 [ν, tetrazole ring, $\delta_{as}(CH_3)$ **61a-d**, δ(N4–H)], ~1380 [δ(CH_3) **61a-d**] 1350-700 [ν(N1–C1–N4), ν(N–N), ω(N1–N6H_2) **59a-b** a. **61a-d**, γ(CN), δ tetrazole ring], <700 [δ, out of plane bend N–H), ω(N5H_2). The ν(NH) absorption bands in the IR spectra of crystalline compounds **59a-b** and **61a-d** have a complex shape depending on the mode of sample preparation. Crystalline samples show in the region 3100-3400 several main absorption peaks which can be assigned to N–H bonds. Due to the formation of intermolecular hydrogen bonds in the crystalline network, a red shift of stretching modes establishes that the heteromolecular hydrogen-bond interaction between the N–H (donor) groups of the tetrazole moieties and the anion (acceptor) are strong (an increase from 25 cm^{-1} to 40 cm^{-1} in the NH_2 asymmetric stretching area was observed). In the case of the $MeDAT^+$ salts these bands coalesce into mainly two broad bands having a complex shape (*Figure 4.4*). In order to elucidate the nature of these bands, the spectra of compounds **59a-b** and **61a-d** were recorded in MeCN solutions. *Figure 4.4* shows as example the obtained spectra in solution of the $MeDAT^+$ salts **61a-d**. With the help of DFT calculation (*Table 4.1*), it was possible to assign the stretching motions. The positions of the absorption maxima and their intensity ratio changes significantly, indicating the strong contribution of intermolecular hydrogen bonds. In solution the obtained spectra of **61a-d** are identical. The bands at 3342(ν_1), 3213(ν_4), 3172(ν_3) and 3142(ν_5) cm^{-1} have been assigned to ν_{asym}(N5H_2), ν_{asym}(N6H_2), ν_{sym}(N5H_2) and ν_{sym}(N6H_2), respectively and the band at 3262 (ν_{ob}) cm^{-1} to the binary overtone of the ν (N6H_2) (ν_6).

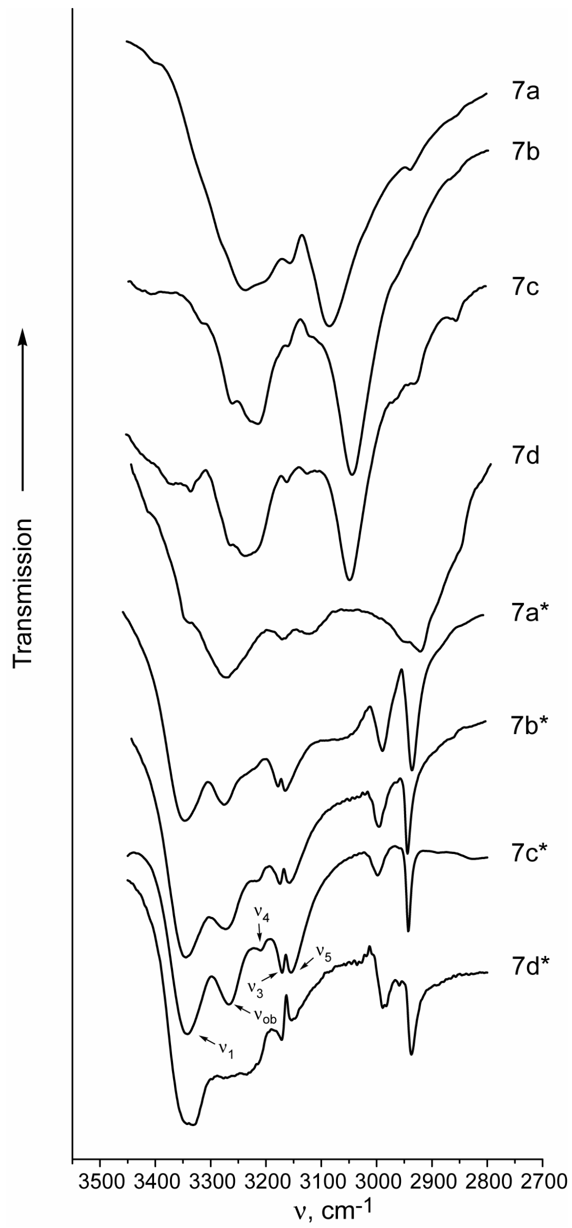

Figure 4.4. IR spectra of **61a-d** recorded in KBr and in CH_3CN solution (*).

The bands observed in the spectra of crystalline samples but absent in the spectra of dilute solutions should be attributed to N–H bonds involved in intermolecular hydrogen bonding and those not involved in intramolecular N–H bonding. Comparing the IR and Raman data of **55** with the corresponding protonated or methylated salts (e.g. **59a** and **61b**), some interesting results can be derived. *Table 4.1* gives the obtained values of these derivatives in solution (IR) and in the solid state (Raman) compared to the calculated values. The scaled calculated frequencies agree well with the experimental data. In the case of protonation (methylation) a new band can be found at ~1715 cm^{-1} (**59a**) or 1699 cm^{-1} (**61a**). It can be assigned to the strongly coupled mode (ν_7) between the ν (C1–N5) (ν_8) and ν ($N6H_2$) (ν_6) and appears at significantly higher wavenumber. The

spectroscopic results are in accordance with a shortening of the C1–N5 bond and with a shorter bond length observed in the DAT salts (e.g. 1.302 (4) Å, **59a**) as compared to the parent compound **55** (1.334 (4) Å).[34] These spectroscopic results are in excellent correlation with the crystallographic data (*Table 4.3*).

Table 4.1. Calculated and experimental IR and Raman data of **55**, **59a** and **61a**

No.	approx. assignment[b]	DAT[a]	calcd[c]	IR/Raman int./act.[d]	DAT^{+a}	calcd[c]	IR/Raman int./act.[d]	MeDAT^{+a}	calcd[c]	IR/Raman int./act.[d]
ν_1	$\nu_{asym}(N5H_2)$	3324/3324	3711 (3325)	67.6/40.6	3345/3363	3697 (3313)	177.5/36.8	3335/3312	3707 (3321)	143.3/28.6
ν_2	$\nu(N4H)$	-	-	-	3321/3363	3625 (3248)	206.1/79.4	-	-	-
ν_3	$\nu_{sym}(N5H_2)$	3154/3193	3589 (3216)	49.2/131.8	3155/-	3561 (3191)	198.5/84.6	3216/3208	3571 (3200)	176.9/91.8
ν_4	$\nu_{asym}(N6H_2)$	3237/3243	3576 (3204)	21.3/66.3	3255/3274	3586 (3213)	65.1/50.7	3256/-	3586 (3213)	60.5/55.1
ν_5	$\nu_{sym}(N6H_2)$	3154/3154	3486 (3123)	4.4/160.2	3094/-	3488 (3125)	51.9/134.2	3105/-	3488 (3125)	48.8/151.2
ν_6	$\delta(N6H_2)$	1656/1670	1713 (1669)	154.9/8.2	1617	1686 (1643)	50.6/8.8	1614/1634	1684 (1641)	63.2/11.4
ν_7	$\nu(C1\text{-}N5)$ + $\delta_{sym}(N6H_2)$	1632/1623	1660 (1618)	176.1/16.0	1719	1766 (1675)	436.2/3.8	1699/1705	1755 (1710)	360.0/5.4
ν_8	$\delta(N5H_2)$	-/1547	1589 (1548)	7.5/9.3	1565	1612 (1571)	19.9/4.9	1584/1607	1607 (1566)	30.1/4.7

[a] Observed IR (in solution) and Raman spectra (in the solid state), freq in cm^{-1}. [b] The assignments are tentative due to interference form intermolecular hydrogen bonds and lattice vibrations. [c] Frequencies (cm^{-1}) calculated at B3LYP/6-31+G(d); the frequencies involving mainly stretching motions of N-H groups were scaled by an empirical factor of 0.8961, in the case of bending vibrations of the NH_2 groups a scaling factor of 0.9745 were used to maximize their agreement with the observed values; scaled values are given in parentheses. [d] Calculated infrared intensities [km/mole] and Raman activities [$Å^4$/amu] obtained from the B3LYP/6-31+G(d) calculations.

2.3 ^{15}N Chemical Shifts and ^{1}H-^{15}N Coupling Constants

In the case of **55**, the assignment of the resonances was straightforward. The ^{15}N peaks of the amino substituents are well separated from those of the tetrazole ring. The nitrogen with the bonded amino group (N1) is the one with the most pyrrole-like character, and its NMR signal is expected to appear at highest field compared to the signals of the other nitrogen atoms.[35] The $^{15}N\{^1H\}$-NMR spectrum of DAT shows six signals for the six different nitrogen atoms. The signals of the NH_2 groups appear as expected at high field and are strong and positive[36] when the spectrum is recorded with broadband decoupling. This is due to the strong positive NOE, resulting from the directly bonded protons. With increasing nitrogen-proton distance the NOE changes its sign and causes a decrease of signal intensity. The dependency of signal intensity on the NOE can thus be nicely used to assign the ^{15}N-signals in the tetrazole ring (*Figure 4.5*) and to differentiate between di- and three coordinated nitrogen atoms, as well as between the substituted and non-substituted nitrogen atoms.

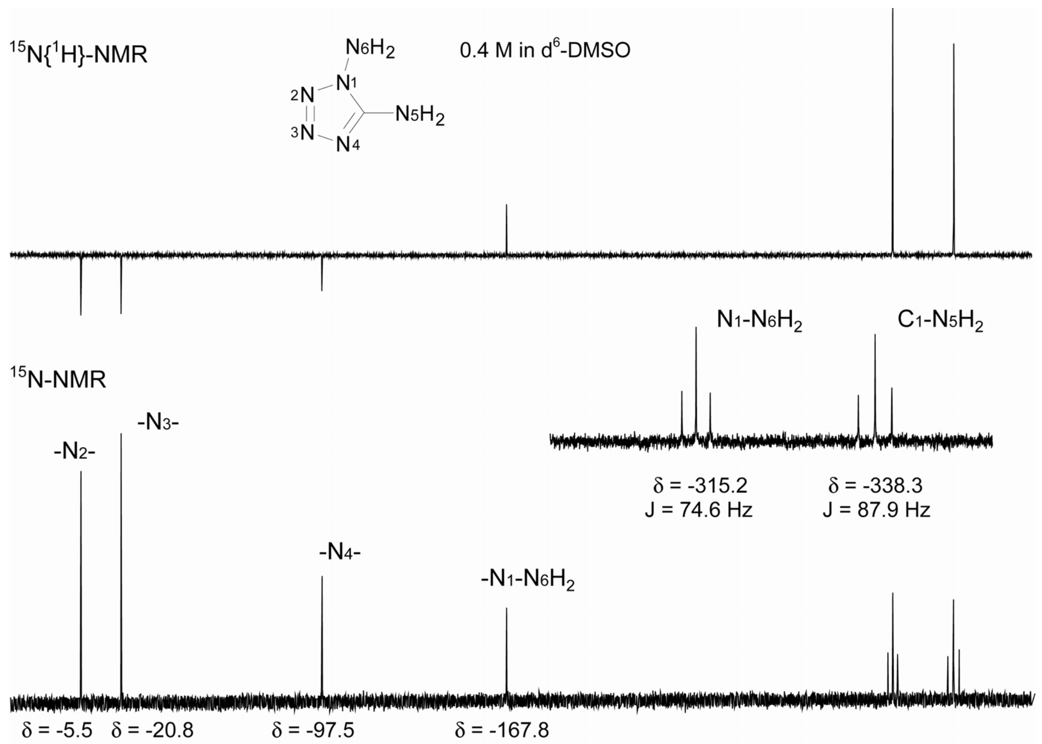

Figure 4.5. Proton broadband decoupled (top) and coupled (bottom) ^{15}N NMR spectra of **55** recorded in d6-DMSO

The assignment of the peaks between the three 2-coordinated nitrogen atoms can be achieved mainly by the fact that N4 has one nitrogen and one carbon as nearest neighbors, whereas N2 and N3 are surrounded by nitrogen atoms. Therefore, the signals of N2 and N3 appear at lowest field owing to electronegativity effects. This is consistent with the trends observed for other comparable ^{15}N chemical shifts.[37] The assignment of the peaks N2 and N3 can be achieved due to the α-effect of the NH_2-group at N1. The electronegativity effect at N3 is lower than at N2, resulting in a low field NMR-signal for N2. In the proton coupled ^{15}N NMR, where due to the pulse delay (3 s) the NOE is negligible small, all ^{15}N NMR signals are positive. The $^{1}J(^{1}H–^{15}N)$ couplings for the signals of the NH_2-groups are clearly observed, yielding triplets with coupling constant of 74.6 Hz (N6) and 87.9 Hz (N5), respectively.

The ^{15}N NMR chemical shift data of the neutral and protonated compounds are presented in *Table 4.2*. The ^{15}N protonation (methylation for **61a** and **61d**) induced shift (PIS) shows that in [d6]-DMSO (CD_3OD) the protonated form displaces in all cases the same type of cations: protonation takes place at N4 of the ring. The greatest PIS effect was observed for N4 and is negative. In the case of the methylated derivative **61a,d**, an upfiled shift of -89.2 ppm is observed. Protonation (methylation) of the azoles increases the electron demand of the ring favoring the perpendicular conformation of the amino group (N5) attached to the carbon atom (C1) of the tetrazole moiety. In this way the amino lone pair can best interact with the azolium ring. The “PIS”

effect for N5 is in all cases positive. This observation is in agreement with other relevant studies, the two most significant reported the use of ^{15}N NMR spectroscopy for the determination of the protonation site of *C*-aminopyrazoles[38] and *C*-amino-1,2,4-triazoles.[39] Due to fast proton exchange on the NMR time scale only in the case of **55** and **61a**, $J(^{1}H–^{15}N)$ couplings could be observed.

Table 4.2. ^{15}N and ^{13}C NMR chemical shifts (ppm) and coupling constants (*J*, Hz) for the compounds studied.

compounds [a]	N1	N2	N3	N4	N5	N6	C1[d]
5-AT[b]	-137.1	-13.1	-13.1	**-137.1**	-338.9	-	157.2[b]
HATNO$_3$[b,e]	-165.2 [-28.1]	-24.5 [11.4]	-24.5 [-11.4]	**-165.2** **[-28.1]**	-329.1 [9.8]	-	152.4[b]
55[b]	-167.0 ^{2}J 2.3 Hz	-5.5	-20.8	**-97.5**	-338.3 ^{1}J 87.9 Hz	-315.2 ^{1}J 74.6 Hz	155.0[b]
59a[c]	-164.9 [2.1]	-21.9 [-16.4]	-33.1 [-12.3]	**-170.4** **[-72.9]**	-333.3 [5.0]	-319.6 [-4.4]	152.8[b]; 151.2[c]
59b[c]	-169.4 [-2.4]	-20.5 [-15.0]	-36.6 [-15.8]	**-177.5** **[-80.0]**	-329.6 [8.7]	-317.9 [-2.7]	149.7[c]
61a[b]	-167.9 [-0.9] ^{2}J 1.7 Hz	-24.0 [-18.5]	-35.3 [-14.5] ^{3}J 1.9 Hz	**-186.0** **[-88.5]** ^{2}J 2.0 Hz	-319.0 [19.3]	-307.3 [7.9] ^{1}J 76.1 Hz	148.1[b]
61d[b]	-167.9 [-0.9] ^{2}J 1.8 Hz	-24.3 [-18.8]	-35.9 [-15.1]	**-186.7** **[-89.2]** ^{2}J 2.0 Hz	-316.8 [21.5]	-308.8 [6.4] ^{1}J 76.8 Hz	147.5[c]

PIS effect in parentheses; [a] all shifts were measured with respect to CH_3NO_2 internal standard; negative shifts are upfield from CH_3NO_2.[b] [d6]-DMSO. [c] CD_3OD; [d] ^{13}C NMR shift; [e] 5-amino-1*H*-tetrazolium nitrate.

2.4 ^{1}H and ^{13}C NMR spectra

In the ^{1}H NMR spectrum, for the resonance of the N–H bound protons only one signal was observed in the case of the protonated DAT derivatives **59a** and **59b**. Compared to the starting DAT **55,** it is shifted upfield due to fast proton exchange. For the methylated derivatives for the iodide **61a** and the azide **61d,** two singlets could be observed, whereas in the case of the nitrate **61b** and dinitramide **61c** only one singlet was detected. Upon alkylation or protonation there is a slight up-filed shift observed for the ^{13}C-NMR resonances (*Table 4.2*). This effect has been observed in several other nitrogen heterocycles upon protonation or alkylation of the heterocyclic ring system.[40]

The position of the nucleophilic attack during the quaternization of **55** with MeI resulting in **61a** was first determined by a ^{1}H-HMBC NMR spectrum was performed. The methylation of the tetrazole ring at the 4-position results undoubtedly from the *^{1}H-HMBC* NMR spectrum (*Figure 4.6*;

^{1}H-HMBC: ^{1}H-^{13}C heteronuclear multiple bond correlation experiment). In this method, the ^{13}C-satellites in the ^1H-NMR spectrum are observed, which reduces acquisition time considerably, due to the higher sensitivity of ^1H compared to that of ^{13}C. The spectrum shown is also field gradient enhanced and was recorded using 8 Hz for the long range $^{13}C,^1H$-coupling.

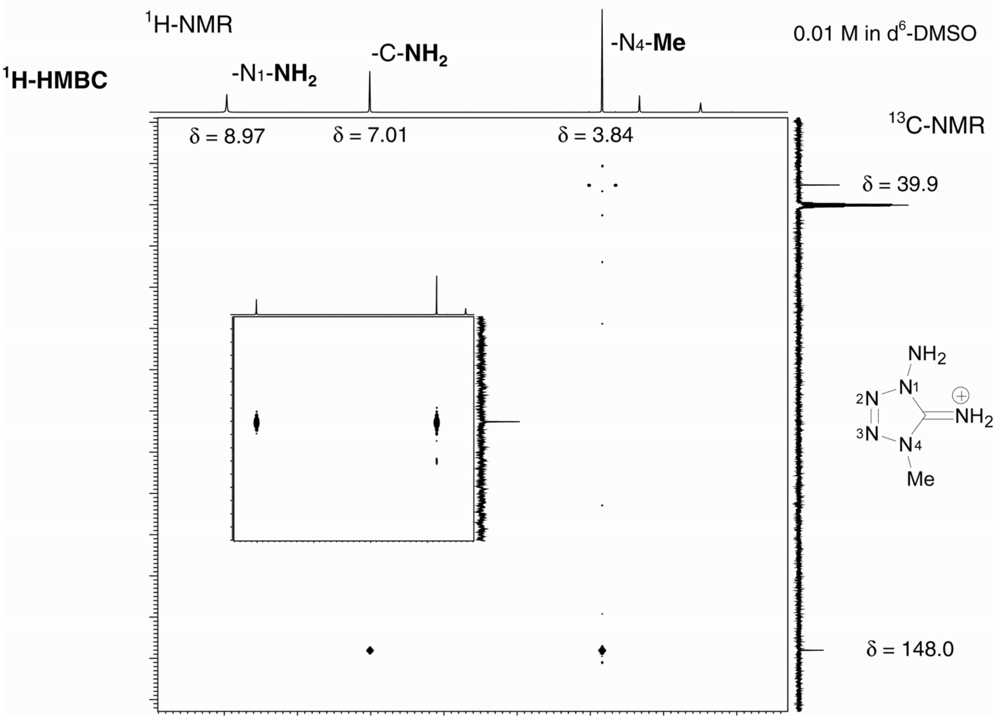

Figure 4.6. ^1H-HMBC NMR spectrum of **61a**

The cross peaks between the signal of the ring carbon atom (δ = 148.0 ppm) and the N-Me group (δ = 3.84 ppm) as well as the C-NH_2 (δ = 7.01 ppm) group results from a $^{13}C,^1H$-coupling over 3 and 2 bonds, respectively. In the case of 2- or 3-methylation, no cross peak should be observed, because the $^{13}C,^1H$-coupling constants of over four bonds is known to be much smaller.[41]

With the particular pulse sequence employed also cross peaks due to $^1J(^{13}C,^1H)$ are observed. A value for $^1J(^{13}C,^1H)$ of 140 Hz was used during the experiment. The two cross peaks between the N-Me ^1H-signal and the Me-^{13}C-signal correspond to the ^{13}C-sattelits in the ^1H-NMR spectrum; from their separation the $^1J(^{13}C,^1H)$ coupling constant can be evaluated (144.8 Hz).

2.5 Molecular structure of **59a**, **59b**, **61b** and **61d**

Figures 4.7 and *4.8* display the molecular units of **59a** and **59b** with atom labeling scheme. Selected bond lengths and angles are presented in *Table 4.3*. In accordance with other X-ray structure determinations, in **59a** and **59b** the $DATH^+$ cations have also the structure in which the N4 atom is protonated (*Scheme 4.3*). Both salts have as common features the molecular structure of the $DATH^+$ moiety and its relative disposition with respect to the nitrate or perchlorate anion.

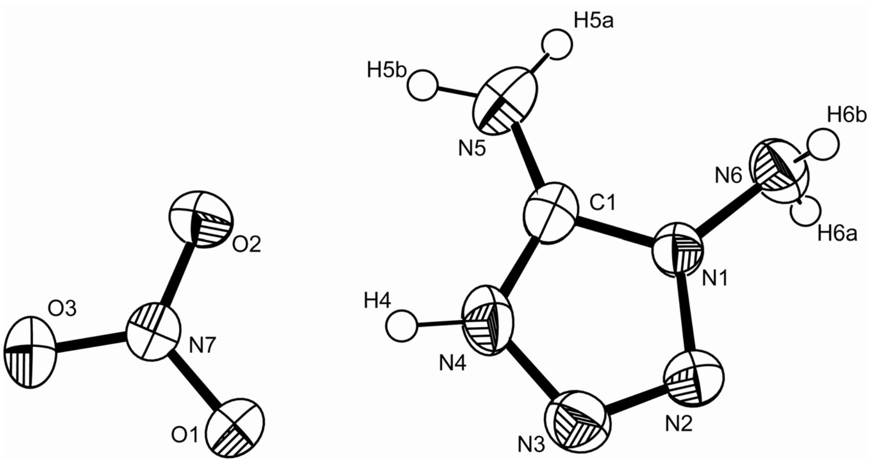

Figure 4.7. Formula unit and labeling scheme for **59a** (ORTEP Plot, thermal ellipsoid represents 50% probability).

The $DATH^+$ cations are not different, within the limits of accuracy.[21] The tetrazole ring is planar with the attached exocyclic nitrogen atoms lying within this plane (maximal deviation is 0.046 Å for **59a** and 0.074 Å for **59b** of N6 from this plane). The amino group attached to N1 is pyramidal and adopts a staggered conformation with respect to N2, similar to that observed for the unprotonated **55**.[34] This observation is consistent with a theoretical study concerning the hybridization and conformation of amino groups in *N*-aminoazoles of Foces-Foces *et al.* They found that sp^3 hybridization of the amino groups is favored over sp^2, and that the amino lone pair adopts an eclipsed position with respect to the ring in monocyclic *N*-amino-azoles, including 1-amino-1*H*-tetrazoles.[42] The amino group attached to C1 is planar and lies in the plane of the tetrazole moiety (sum of angles 360°) indicating a strong interaction of the nitrogen lone pair with the π system of the tetrazole ring. This is consistent with the observation of a shorter C1–N5 bond found for the salts compared to the parent compound **55** (*Table 4.3*). Interestingly for unprotonated amino-*C*-azoles e.g. 4-aminopyrazoles two polymorphic forms are reported,[43] The main difference consists in the conformation of the NH_2 group with respect to the pyrazole ring: an almost eclipsed

and a twisted form is found. For **55** and for DATH$^+$ cation, a strong π-delocalization in the N1–C5–N4 fragment is found.

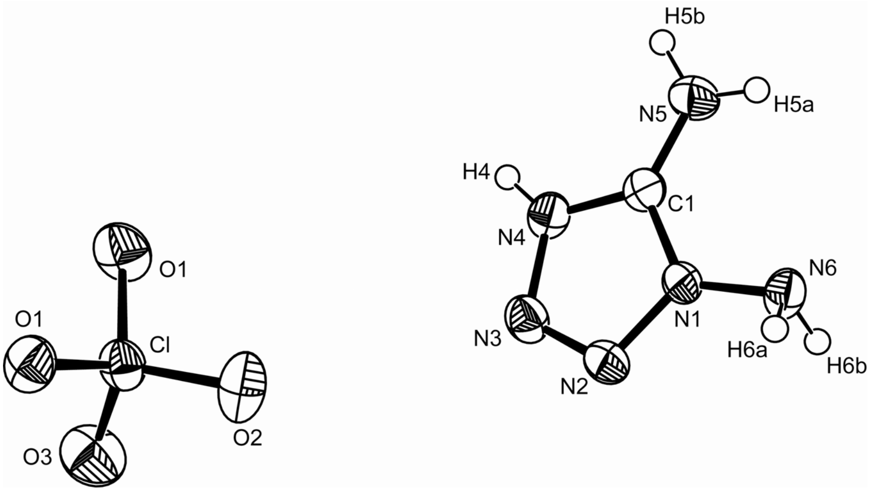

Figure 4.8. Formula unit and labeling scheme for **59b** (ORTEP Plot, thermal ellipsoid represents 50% probability).

The bond distances indicate discrete single and double bonds for the rest of the ring (Table 2). A closer inspection of the exocyclic bond lengths of the amino groups to the bonded atoms (C1–N5: 1.302(4) Å (**59a**) and 1.304 Å (**59b**); N1-N6: 1.385(2) Å (**59a)** and 1.387(2) Å (**59a)**) compared to the experimental N–N and C–N distances in HN=NH and H_2N-NH_2 (1.252 Å and 1.449 Å, respectively) and H_2C=NH and CH_3-NH_2 (1.273 Å and 1.471 Å, respectively) further supports this observation[44] and displays

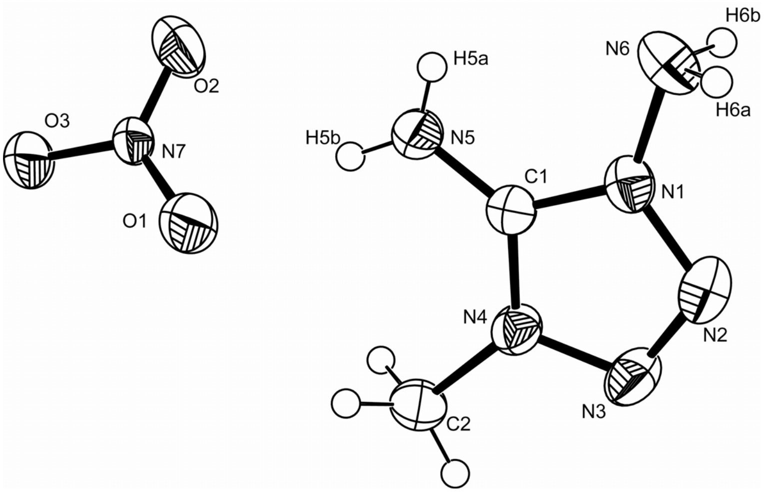

Figure 4.9. Formula unit and labeling scheme for **59b** (ORTEP Plot, thermal ellipsoid represents 50% probability).

the “hydrazinic” character of the amino group in the 1-position compared to the “aniline-like” character of the 5-amino group. The bond distances and angles in the perchlorate and nitrate anion are as observed for many other salts of nitrous or perchloric acids with amines and are omitted in *Table 4.3*.[45]

Table 4.3. Comparison of Selected Interatomic Distance (Å) and Selected Bond Angles (deg) of **55**, **59a**, **59b** and **61a-d**.

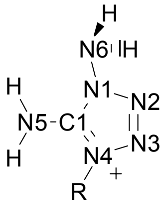

	55[a]	**59a**	**59b**	**61a**	**61b**	**61c**	**61d**
	-	**R = H**	**R = H**	**R = C2**	**R = C2**	**R = C2**	**R = C2**
Bond Length							
N1-C1	1.345(1)	1.323(9)	1.340(3)	1.355(1)	1.340(4)	1.335(3)	1.328(6)
N1-N2	1.363(1)	1.366(2)	1.368(2)	1.383(9)	1.364(4)	1.361(3)	1.373(6)
N2-N3	1.279(1)	1.260(4)	1.272(3)	1.234(9)	1.280(4)	1.274(3)	1.275(6)
N3-N4	1.367(1)	1.354(8)	1.361(3)	1.386(8)	1.354(4)	1.361(3)	1.362(6)
N1-N6	1.383(1)	1.385(2)	1.387(2)	1.378(9)	1.388(3)	1.402(3)	1.390(5)
C1-N4	1.327(1)	1.336(3)	1.333(3)	1.339(8)	1.341(3)	1.336(3)	1.321(6)
C1-N5	1.334(1)	1.302(4)	1.304(3)	1.32(1)	1.299(4)	1.315(3)	1.321(7)
N4-R	-	-	-	1.42(1)	1.458(4)	1.445(3)	1.470(6)
Bond Angle							
C1-N1-N2	108.84(8)	110.4(2)	110.4(2)	108.3(7)	110.4(2)	110.1(2)	109.8(4)
N2-N1-N6	125.13(8)	124.5(1)	126.0(2)	125.7(6)	126.1(2)	124.3(2)	125.7(4)
N5-C1-N1	123.87(9)	130.3(2)	127.1(2)	125.7(6)	127.3(3)	127.3(2)	126.0(5)
C1-N4-N3	105.56(8)	110.0(2)	110.6(2)	108.2(7)	110.0(2)	110.0(2)	110.2(4)
N3-N2-N1	105.79(8)	107.2(1)	107.4(2)	108.6(6)	107.1(2)	107.8(2)	107.2(4)
C1-N1-N6	126.02(9)	125.1(1)	123.5(2)	125.8(6)	123.4(3)	125.6(2)	124.4(4)
N5-C1-N4	128.17(8)	130.3(2)	129.2(2)	129.1(7)	128.7(3)	128.5(2)	129.2(5)
N4-C1-N1	107.90(8)	103.7(1)	103.7(2)	105.2(9)	103.9(2)	104.2(2)	104.9(5)
N2-N3-N4	111.92(9)	108.7(1)	108.0(2)	109.6(6)	108.5(2)	107.9(2)	107.9(4)
C1-N4-R	-		-	128.5(7)	128.2(3)	127.7(2)	128.8(4)

[a] from ref [34]

In *Figures 4.9* and *4.10* the molecular units of **61b** and **61d** are displayed. In the salts the formal exchange of the proton at N4 by a methyl group shows only slightly differences in the molecular parameters found for $MeDAT^{+}$ cation as compared to $HDAT^{+}$ cation. Selected bond lengths and angles are contained in *Table 4.3*. The above discussion for **59a** and **59b** also accounts for the $MeDAT^{+}$ salts as the methyl group hardly influences the molecular parameters. In all salts the bond distances and angles in the five-membered ring reflect the effect of protonation giving rise to an almost symmetrical ring with respect to an axis through C1 and the midpoint of the N2–N3

bond. The small differences in the bond length and angles within the cations of the salts might be the result of packing effects in the crystals.

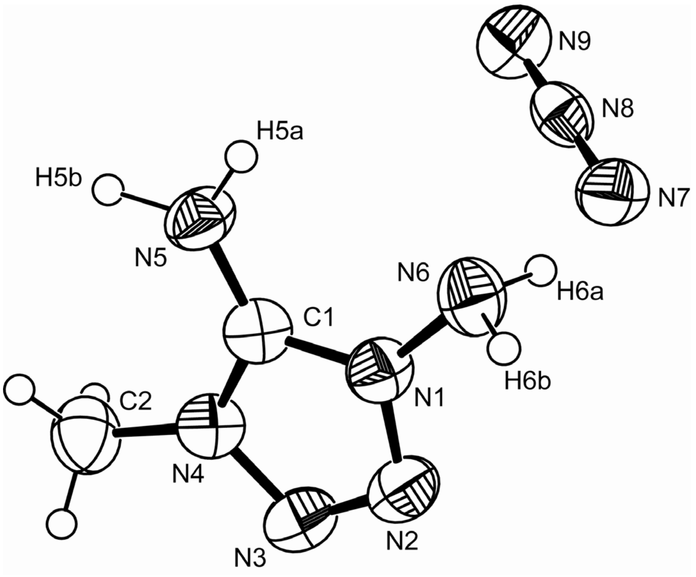

Figure 4.10. Formula unit and labeling scheme for **59d** (ORTEP Plot, thermal ellipsoid represents 50% probability).

2.6 Crystal structure of **59a**, **59b**, **61b** and **61d**

59a crystallizes in the monoclinic space group *C*2/c with eight formula units per unit cell. The nitrate **61b** crystallizes in the orthorhombic space group *F*dd2 with sixteen formula units per unit cell. The X-ray analysis for this two compounds confirmed that the ratio of acid to base is 1:1, and the ions are connected through several kinds of hydrogen bonds (*Table 4.4*). Analysis of the crystal packing of **59a** and **61b** showed the existence of numerous hydrogen bonds, such as strong (e.g. N4–H4····O1, 2.721(4) Å for **59a**; N5–H5b····O1 2.853(4) Å for **61b**; *Table 4.4*) and medium N–H····O contacts which are well within the sum of the van der Waals radii ($r_{A(O)} + r_{D(N)} = 3.10$ Å).[46] Also, the N–H–O angles of e.g. 151(2)° (N4–H4–O1) (**59a)** and 173(4)° (N4–H4–O1) (**51b**) are indicative of a strongly directional rather than purely electrostatic interaction. The hydrogen atom H4 on N4 in **59a** forms two intermolecular N4–H4····O1 and N4–H4····O2 hydrogen bonds with the two oxygen atoms (O1, O2) of the nitrate anion, yielding cation/anion pairs as depicted in Figure 4.11. The resulting graph set is characterized as $R_1^2(4)$, and together with the graph set $R_2^2(6)$, this module can be seen as the first order network. The cations are linked over hydrogen bonds N5–H5b····O2^{i} and N6–H6b····O1^{ii} [symmetry code: (i) 2-x, -y, 1-z; (ii) x, 1-y, -0,5+z] to infinitive chains which are characterized as $C_2^2(8)$ graph set.

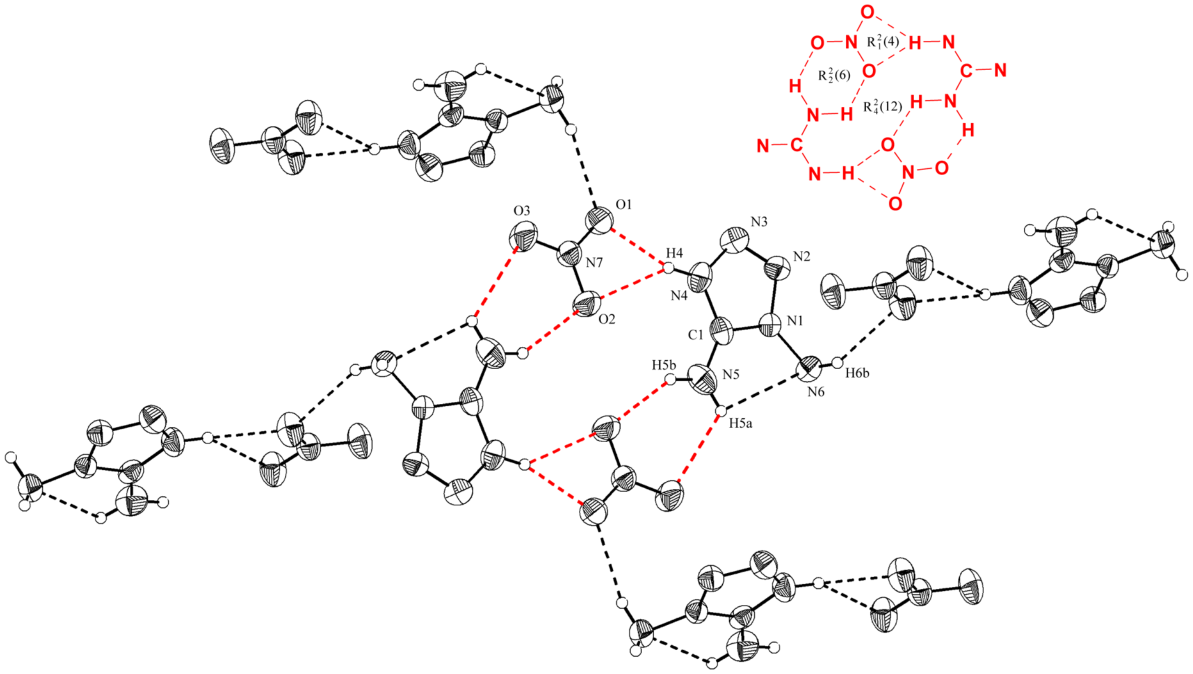

Figure 4.11. Surrounding of the NO_3^- anion in the structure of **59a** with hydrogen bonds to the cations marked as dotted lines (ORTEP Plot, thermal ellipsoid represents 50% probability). Only strong hydrogen bonds are displayed

Together with the repeating module $R_1^2(4)/R_2^2(6)$, a three-dimensional supramolecular network with a planar dimeric molecular unit as main module is formed ($R_4^2(12)$ graph set as the center of this unit contains the inversion centre). This unit is already identified in diaminoguanidinium nitrate as the main two-dimensional building block (*Figure 4.2*, **II**). These planar units are connected through N6–H6a····O1^{ii} [symmetry code: (ii) x, 1-y, -0,5+z] in such a way that the planes are orientated almost perpendicular to the original unit. All contacts used for the discussion of graph-set analysis of hydrogen-bond patterns are shorter than the sum of the van der Waals radii ($r_{A(O)} + r_{D(N)}$ = 3.10 Å). There are also electrostatic interactions, which are longer than the sum of the van der Waals radii and involve weak hydrogen bond interactions (e.g. N5–H5a····O3 3.361(2) Å and N6–H6a····O2 3201(3) Å). They also contribute to the three-dimensional network. There is no evidence of any aromatic π–π stacking interactions. Examination of the structure with *PLATON* [47] shows that there are no solvent-accessible voids in the crystal structure of **59a**.

Table 4.4. Hydrogen bond geometry (Å, °) of **59a**, **59b**, **61b** and **61d**

D–H···*A*	*D*–H	H···*A*	*D*···*A*	*D*–H···*A*
59a				
N4–H4···O1	0.860(5)	1.937(2)	2.721(4)	151(2)
N4–H4···O2	0.860(5)	2.32(2)	3.06(2)	144.0(2)
N5–H5a···N6^{a}	0.860(3)	2.64(2)	2.894(2)	98.5(2)
N5–H5a···O3^{i}	0.860(3)	2.66(1)	3.057(8)	109.2(2)
N5–H5b···O2^{i}	0.860(6)	2.16(1)	2.93(2)	148.3(2)
N6–H6b···O1^{ii}	0.873(4)	2.226(3)	3.014(5)	150.1(2)
59b				
N5–H5a···N6^{a}	0.852(2)	2.649(1)	2.896(2)	98.17(1)
N5–H5a···O2^{iii}	0.852(2)	2.146(2)	2.944(4)	155.68(1)
N5–H5b···O2^{iv}	0.882(1)	2.460(3)	3.075(4)	127.28(1)
N5–H5b···O1^{v}	0.882(1)	2.210(4)	3.046(5)	157.99(1)
N4–H4···O4^{vi}	0.786(2)	2.059(6)	2.817(8)	162.14(2)
61b				
N5–H5b···O1	0.83(4)	2.03(4)	2.853(4)	173(4)
N5–H5a···N6^{a}	0.77(4)	2.57(4)	2.895(4)	108(4)
N5–H5a···O2^{vii}	0.77(4)	2.24(4)	2.905(4)	145(5)
N6–H6b···O3^{viii}	0.87(4)	2.25(4)	3.039(3)	151(4)
N6–H6a···O2^{ix}	0.95(4)	2.18(4)	3.036(4)	149(3)
61d				
N5–H5a···N6^{a}	0.94(6)	2.65(6)	2.892(7)	95(4)
N6–H6a···N7	1.04(6)	2.03(6)	3.029(7)	161(5)
N6–H6b···N7^{x}	0.96(7)	2.11(7)	2.973(6)	149(6)
N5–H5a···N7^{xi}	0.94(6)	2.00(6)	2.892(6)	159(5)
N5–H5b···N9^{xii}	1.01(5)	1.82(6)	2.830(6)	171(5)

[a] intramolecular hydrogen bond;
Symmetry codes for **59a**: (i) 2-x, -y, 1-z; (ii) x, 1-y, -0.5+z.; **59b**: (iii) 0.5-x, -0.5+y, 0.5-z; (iv) 0.5+x, -0.5-y, -0.5+z; (v) -0.5+x, -0.5-y, 0.5+z; (vi) 1-x, -y, 1-z. ; **61b**: (vii) -x, -y, z; (viii) 0.25-x, -0.25+y, 0.75+z; (ix) -x, -y, 1+z.; **61d**: (x) –x, 1-y, 0.5+z; (xi) x, y, -1+z; (xii) 0.5+x, 1.5-y, -1+z.

The formal exchange of the hydrogen atom at N4 by a methyl group leads to a different arrangement of the ions in the case of **61b**. The motif changes completely, and the formation of planar dimeric units is no longer observed. As expected and shown by calculations of the crystal densities of energetic materials, the introduction of a methyl group leads to lower densities due to bigger voids or unfilled space (ρ(**59a**) = 1.73 g cm^{-3}; ρ(**7b**)) = 1.51 g cm^{-3}).[48] The replacement of the hydrogen atom in **61b** by a methyl group leads also to the formation of a three dimensional hydrogen bond network. However, the mismatching of donor and acceptor sites placed on both counter ions, compared to [HAGN^{+}NO$_3^{-}$] (*Figure 4.2*, **I**) and **51b**, leads to a significantly modified crystal organization and the appearance of only two ring graph sets ($R_1^2(4)$, $R_4^4(12)$, *Figure 4.12*).

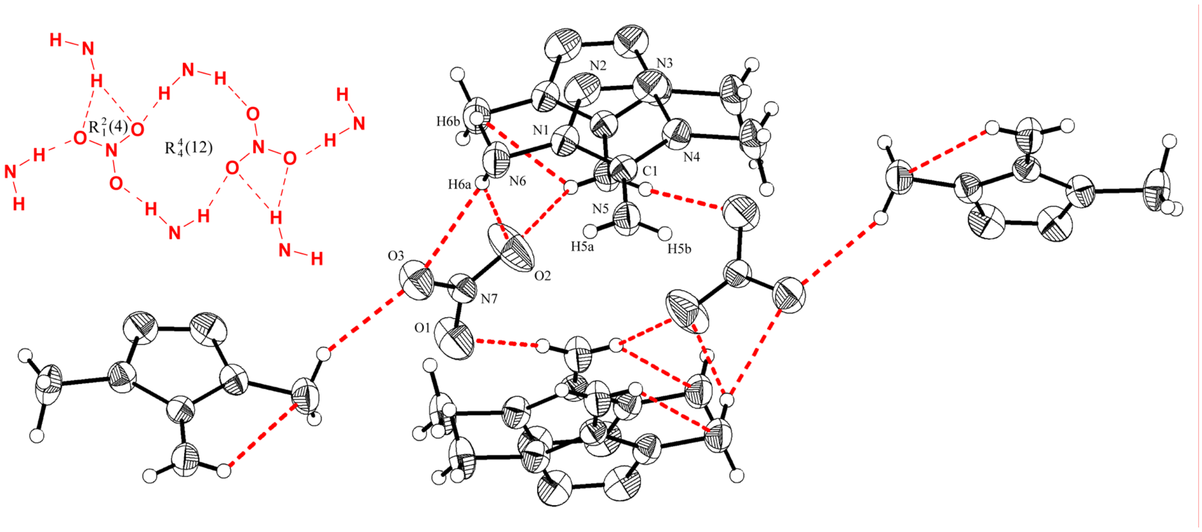

Figure 4.12. Surrounding of the NO_3^- anion in the structure of **61b** with hydrogen bonds to the cations marked as dotted lines (ORTEP Plot, thermal ellipsoid represents 50% probability). Only strong hydrogen bonds are displayed.

59b crystallizes in the monoclinic space group $P2_1/n$ with four formula units per unit cell. Compared to **59a** the exchange of the counter ion by the perchlorate ion leads in the case of **59b** also to the formation of dimeric subunits ($R_4^2(8)$ graph set as the center of this unit contains the inversion centre), but due to the symmetry of the perchlorate anion (T_d) these units lie not in one plane (*Figure 4.13*). Interestingly, the main graph set subunit of **59a** ($R_4^2(12)$) is reduced in **59b** to $R_4^2(8)$ which can be understood by the formal decrease of the bond angle at the central atom of the anion from 120° in the NO_3^- anion to 109° in the perchlorate anion.

Within the crystal structure of **59b** only O1, O2 and O4 of the perchlorate anion are involved in the hydrogen bond interaction, the shortest O3 interaction of O3 (O3–N4) accounts for 3.321(2) Å without any hydrogen bond interaction. Therefore due to the formal symmetry change of the ClO_4 moiety (tetrahedral) compared to the NO_3 anion (planar) the reduction of the symmetry leads to a modified crystal organization and the observation of a new graph set ($R_4^2(8)$).

The X-ray crystal structure of **61d** (orthorhombic, space group $Pna2_1$, *Figure 4.14*) reveals that the azide anion links the cations over four strong hydrogen bridges (*Table 4.4*) in such a way, that N7 forms three hydrogen bridges (N6–H6a····N7, N6–H6b····N7^{x} and N5–H5a····N7^{xi} [symmetry code: (x) –x, 1-y, 0.5+z; (xi) x, y, -1+z]) whereas N9 only one (N5–H5b····N9^{xii} [symmetry code: (xii) 0.5+x, 1.5-y, -1+z]).

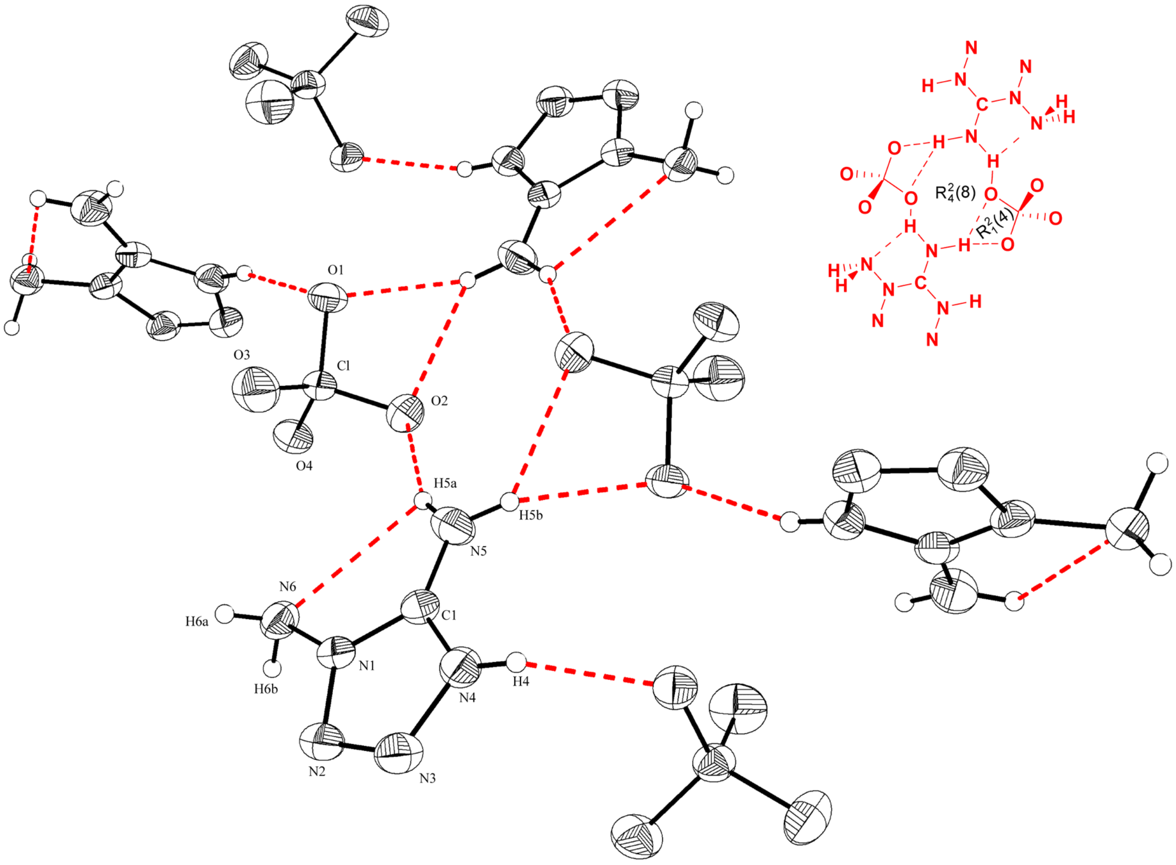

Figure 4.13. Surrounding of the ClO_4^- anion in the structure of **59b** with hydrogen bonds to the cations marked as dotted lines (ORTEP Plot, thermal ellipsoid represents 50% probability). Only strong hydrogen bonds are displayed.

The different coordination pattern of the terminal nitrogen atoms of the azide group explains the observed difference in the N7–N8 (1.184(5) Å) and N8–N9 (1.170(5) Å) bond length. The observed distances for NH···N hydrogen bonds agree well with the distances found in other ionic azide compounds.[11,12] A rather unusual graph set ($R_4^2(11)$) is found for **61d**. These motifs are connected in such a fashion trough a two folded axis, that infinitive chains are formed. Together with the hydrogen bond between N5–H5b···N9^{xii} this chains are connected to a three dimensional network.

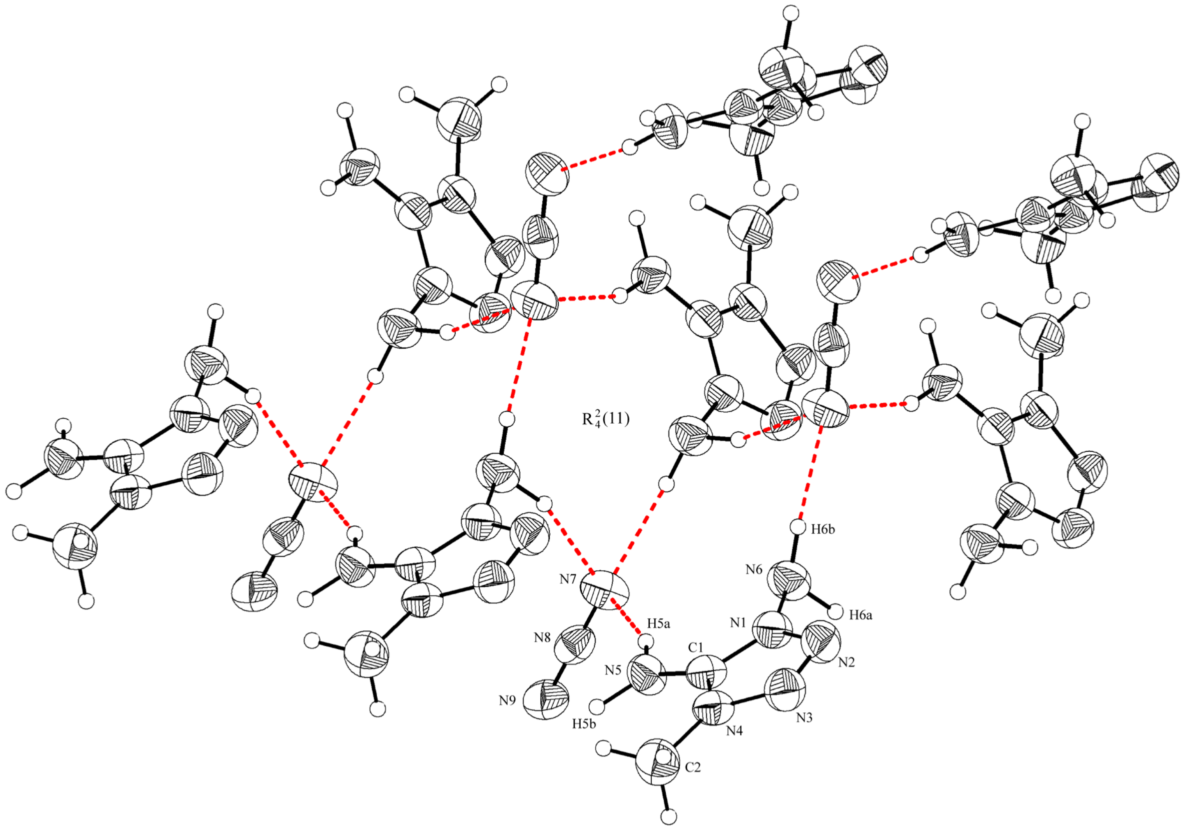

Figure 4.14. Surrounding of the N_3^- anion in the structure of **61d** with hydrogen bonds to the cations marked as dotted lines (ORTEP Plot, thermal ellipsoid represents 50% probability). Only strong hydrogen bonds are displayed. The intramolecular hydrogen bond is omitted for clarity.

2.7 MeDATN(NO_2)$_2$ (**61c**)

The ability of the dinitramide (DN) anion to form stable oxygen-rich salts with high densities with a variety of cations[49] makes DN a promising candidate in the development of new tetrazole based oxidizers. Such salts would be expected to possess both a high nitrogen *and* a high oxygen content. The combination of the oxygen-rich anion (DN) with a nitrogen-rich cation forms a class of energetic materials, whose energy is derived from their very high positive heat of formation (directly attributed to the large number of inherently energetic N-N, N-O and N-C bonds) as well as the combustion of the carbon atoms. Therefore, the 1,5-diamino-4-methyl-1*H*-tetrazolium dinitramide (**61c**) is of special interest, and the X-ray determination with respect to an so far not observed intriguing interaction of one nitro group with the tetrazolium cation ($MeDAT^+$) utilizing the theory of atoms in molecules (AIM)[50] is discussed in the following Chapter.

2.7.1 Crystal structure of **61c**

61c crystallizes in the orthorhombic space group $P2_12_12_1$ with four formula units in the unit cell (numbering scheme of **61c** is depicted in *Figure 4.15*, *Table 4.3*) as racemic twin. The structure contains one crystallographically independent cation and one anion. As the methyl group hardly influences the molecular parameter of the tetrazole moiety (MeDAT, see above), a detailed discussion is abstained. The overall geometry of the dinitramide ion is similar to that observed for other comparable dinitramide salts, like guanidinium and biguanidinium salts.[49c,d] The two N–N bond lengths are asymmetric (N7–N8 1.350(3) Å; N8–N9 1.391(3) Å; *cf.* a typical N=N double bond (1.245 Å); N–N single bond (1.454 Å))[51] and a NNN angles of 115.4(2)° was observed. The nitro groups are twisted out of the central NNN plane (O3-N9-N7-O1 -24.5(2)°). Hence, the local symmetry of the anion is C_1. As known also form others [49a-d] the metrical parameters of the DN ion are easily and strongly influenced by the environment.

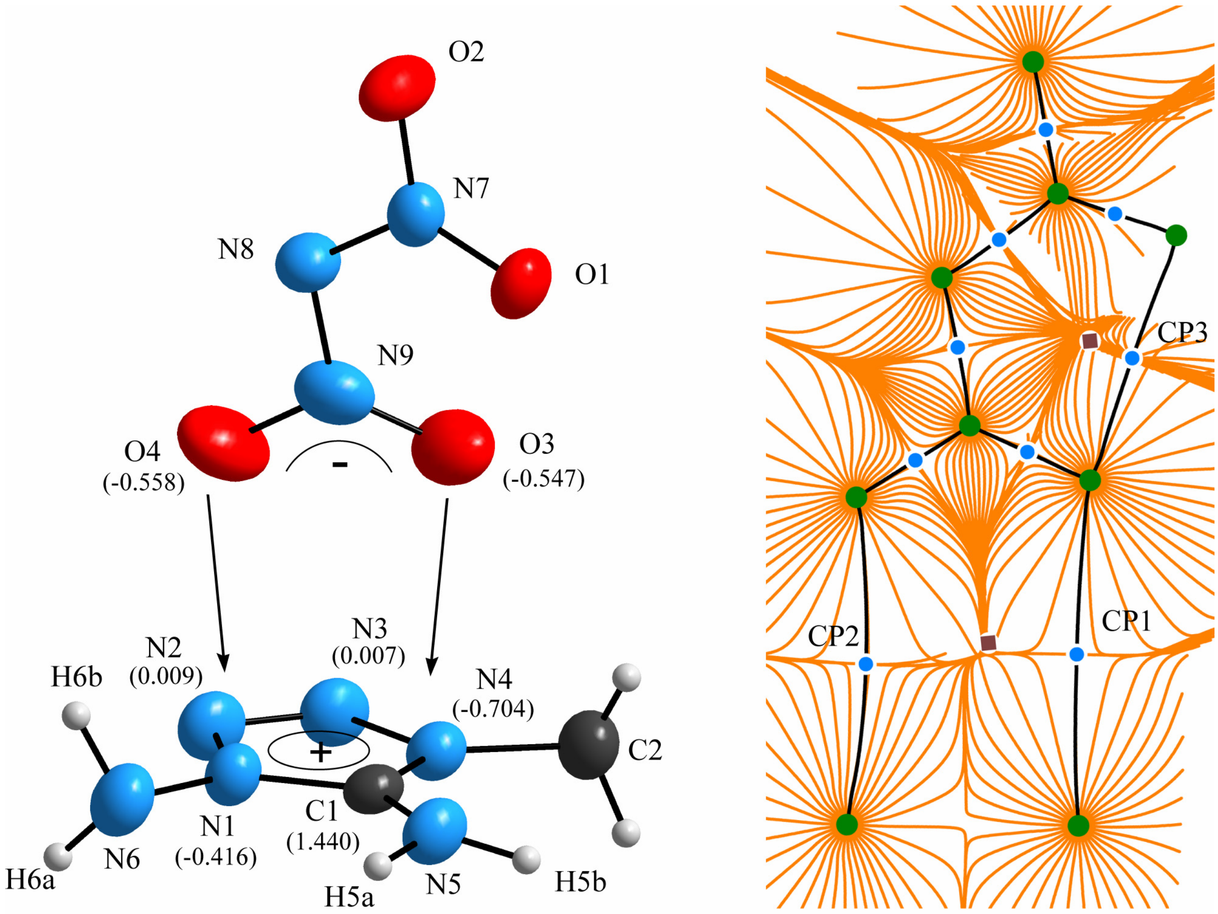

Figure 4.15. Left: Formula unit and labeling scheme used for **61c** (Thermal ellipsoid represents 50% probability, structural parameter are given in *Table 4.3*). Selected AIM charges in parenthesis. Right: the gradient lines of the electron density and the projection of the molecular graph onto the N2-N4-O3 plane. The bond CP's are shown as green circles and the ring CP's are shown as brown rectangles.

In *Figure 4.16* the view along the *a*-axis is displayed showing the zigzag strand composed of alternating MeDAT and DN ions. Each strand is further connected by strong hydrogen bonds (N5–H5a····O1^{i} and N5–H5a····O2^{i} [symmetry code: (i) -1+x, y, z]) forming a three-dimensional network (*Table 4.4*). In turn, these strands are formed by two different type of interactions: (1) a strong hydrogen bond between N5–H5b····O2^{ii} (symmetry code: (ii) -0.5+x, 0.5-y, 1-z) and (2) a closed-shell interaction between the O atoms of one nitro group (O3-N9-O4) with the tetrazole moiety (*Table 4.4*).

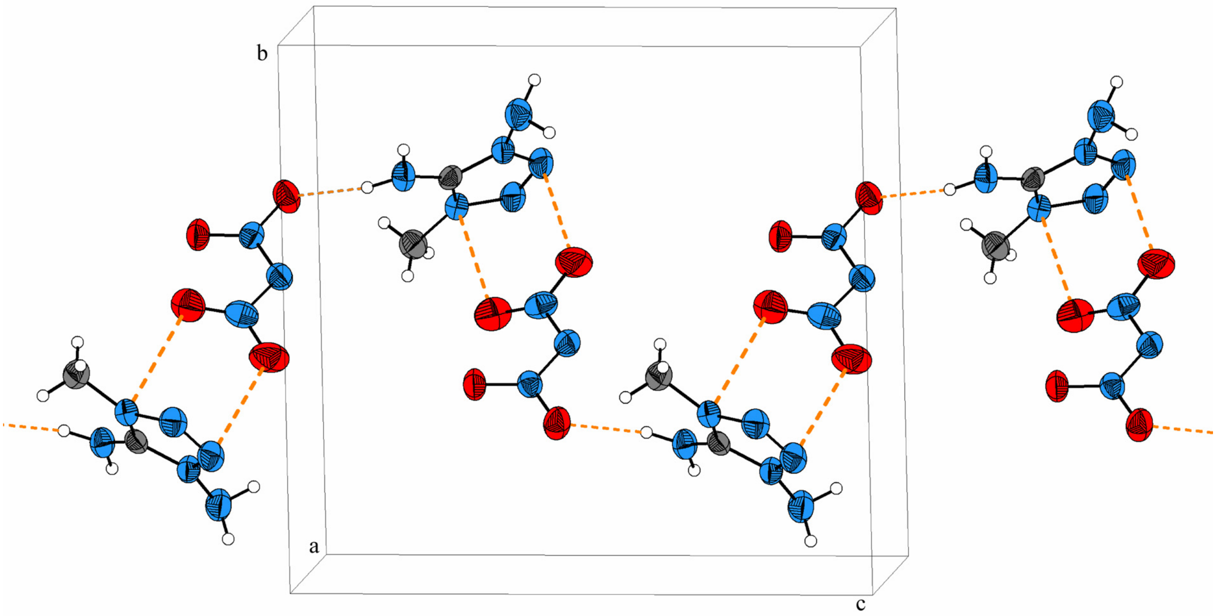

Figure 4.16. View of the strand formed by alternating cations (MeDAT) and anions (DN) displayed along the *a*-axis in **61c**. Short contacts between the cations and anions are shown by dotted (····, N5–H5b····O2) and dashed (- - - , O(dinitramide) and tetrazole moiety) lines, respectively. (ORTEP Plot, thermal ellipsoid represents 50% probability).

Table 4.4. Hydrogen bond geometry (Å, °) and selected distances of DN to the tetrazole moiety in **61c**.

D–H····*A*	*D*–H	H····*A*	*D*····*A*	*D*–H····*A*
7c				
N5–H5a····N6^{a}	0.91(2)	2.69(3)	2.998(3)	98(2)
N5–H5a····O1^{i}	0.91(2)	2.23(1)	3.093(3)	160(3)
N5–H5a····O2^{i}	0.91(2)	2.51(3)	2.965(3)	111(2)
N5–H5b····O2^{ii}	0.89(1)	2.05(1)	2.921(3)	167(2)
N1····O4^{iii}			3.086(3)	
N2····O4^{iii}			3.020(3)	
N4····O3^{iii}			3.187(3)	
C1····O3^{iii}			3.278(3)	

a) intramolecular hydrogen bond; Symmetry codes for **61c**: (i) -1+x, y, z ; (ii) –0.5+x, 0.5-y, 1-z ; (iii) 1-x, 0.5+y, 1.5-z

The interionic distances for the O4 and O3 contacts with the tetrazole ring are in the range of 3.020(3) to 3.278(3) Å. For closed-shell interactions, there is a somewhat arbitrary dividing line between what is or is not an interaction when only the sum of the van der Waals radii are applied as criterion. Since the MeDAT is a non-spherical ion which is also able to form hydrogen bonds, it is hard to compare the anion-cation interactions with those in alkali DN salts which are observed in the range of 2.810(2) ($K^+[N_3O_4]^-$) to 3.534(6) Å ($Cs^+[N_3O_4]^-$).[49b]

2.7.2 Closed-shell interaction in **61c**

What is the nature of bonding between the dinitramide anion and the tetrazolyl cation in **61a**? Although further extensive hydrogen bonding could be possible, the anion and cation adopt an almost perpendicular arrangement (<(N2-N4-O3) = 91.64(9) °) with fairly short O3•••N4 and O4•••N2 contacts (*d*(O3-N4) = 3.18(3), *d*(O4-N2) = 3.020(3) Å). Selected AIM[50] charges are given in *Figure 4.15*,[52] and it is noted that all oxygen atoms carry a negative charge as expected whereas the nitrogen atoms of the tetrazole ring possess net charges which are also negative or close to zero (*Figure 4.15*, *Appendix A Table A-5*). The positive charge of the cation locates mainly at the two carbon and the hydrogen atoms of the amino groups. The negatively charged oxygen atoms of the dinitramide anion (q_{O3} = -0.55, q_{O4}= -0.56*e*), however, are directed towards N2 and N4 (q_{N2} = 0.01, q_{N4} = -0.70*e*). In agreement with the larger negative charge on N4, the O4•••N2 distance is slightly longer (0.16 Å). Moreover, there is only a very small degree of charge transfer from the dinitramide anion to the tetrazolium cation (q_{ct} = 0.02*e*).[52]

The theory of Atoms in Molecules[50] was used to analyze the chemical bonding in **61c**. This theory describes a molecule in terms of electron density, $\rho(\mathbf{r})$, its gradient vector field, $\nabla\rho(\mathbf{r})$, Laplacian, $\nabla^2\rho(\mathbf{r})$, and bond critical points, CP.[50,53] The type of interaction is characterized by the sign and magnitude of the Laplacian of $\rho(\mathbf{r}_b)$ at the bond critical point. If electronic charge is concentrated in the bond CP ($\nabla^2\rho(\mathbf{r}_b) < 0$)) this type of interaction is referred to as shared interactions.[50] Interactions which are dominated by contraction of charge away from the interatomic surface towards each nuclei ($\nabla^2\rho(\mathbf{r}_b) > 0$) are called close-shell interactions. For closed-shell interaction, $\rho(\mathbf{r}_b)$ is relatively low in value and the value of the $\nabla^2\rho(\mathbf{r}_b)$ is positive. The sign of the Laplacian is determined by the positive curvature of $\rho(\mathbf{r}_b)$ along the interaction line, as the exclusion principle leads to relative depletion of charge in the interatomic surface. In **61c**, every expected covalent bond has been characterized by a negative Laplacian at the bond CP (*Appendix A Table A-7*). In addition to the expected bond path network, three (3,-1)[54] unusual bond CP's have

been found on the O3•••N4 (CP1), O4•••N2 (CP2) and O1•••O3 (CP3) lines (*Figure 4.15*). The origin of the latter bond CP (CP3) has been described recently by Pinkerton *et al.* as a bonding closed-shell type interaction between the negatively charged oxygen atoms belonging to different nitro groups.[55] CP1 and CP2 are associated with an interaction between the atoms which are linked by these bond CP's.

Table 4.5. Bond Critical Points in **61c***

	$\rho(\mathbf{r}_b)$	$\nabla^2\rho(\mathbf{r}_b)$	λ_1	λ_2	λ_3	$\lvert\lambda_1\rvert/\lambda_3$	$G(\mathbf{r}_b)$	$V(\mathbf{r}_b)$	$G(\mathbf{r}_b)/\rho(\mathbf{r}_b)$
CP1	0.008338	0.0296	-0.00651	-0.00142	0.03758	0.173	0.00645	-0.00549	0.77
CP2	0.006762	0.0218	-0.00536	-0.00359	0.03077	0.174	0.00471	-0.00396	0.70
CP3	0.021239	0.0893	-0.01876	-0.01843	0.12651	0.148	0.02027	-0.01822	0.95

* All quantities in atomic units, CP is a (3,–1) critical point, ρ is electron density, $\nabla^2\rho$ is the Laplacian of ρ, $\lambda_{1,2,3}$ are eigenvalues of Hessian of ρ, G is the kinetic and V the potential energy density; B3LYP/6-311+G(3d,2p) density; X-ray structural data used.

A ring CP inside the O4-N2-N4-O3-N9 space was also found, thus the Poincaré-Hopf rule is satisfied.[50] The calculated positive Laplacian of the electron density ($\nabla^2\rho(\mathbf{r}_b)$) and the relatively low value of $\rho(\mathbf{r}_b)$ at both bond critical points (CP1 and CP2) indicate that the O3•••N4 (CP1), O4•••N2 (CP2) contacts are dominated by bonding closed-shell interaction.[56] The high values of the ratio $G(\mathbf{r}_b)/\rho(\mathbf{r}_b)$ at the bond CP's (0.77, and 0.70) and the ratio of the eigenvalues $\lvert\lambda_1\rvert/\lambda_3 << 1$ support this conclusion (*Table 4.5*).[57] Additional information about chemical bond type is available from the total electronic energy density $E^e(\mathbf{r}_b) = G(\mathbf{r}_b) + V(\mathbf{r}_b)$. Closed-shell interactions are dominated by the kinetic energy density $G(\mathbf{r}_b)$ in the region of the bond CP, $G(\mathbf{r}_b)$ being slightly greater than potential energy density $\lvert V(\mathbf{r}_b)\rvert$ and the energy density ($E^e(\mathbf{r}_b) > 0$) close to zero (*Table 4.5*).

2.8 Thermodynamic aspects

2.8.1 Heats of formation and detonation

The heats of combustion for compounds **59b**, **61b**, **61c** and **61d** were determined experimentally and are summarized in *Table 4.6.* The enthalpy of formation for the salts **59b**, **61b**, **61c** and **61d** was calculated by following the Born-Haber energy cycles[7c,58] (*Scheme 4.7*) according to reaction [1]-[4]. The reaction enthalpies ($\Delta_R H$) for reactions [5] and [6] were calculated using the parameterized *ab initio* molecular orbital methods Gaussian-2 (G2)[59] and Gaussian-3 (G3).[60]

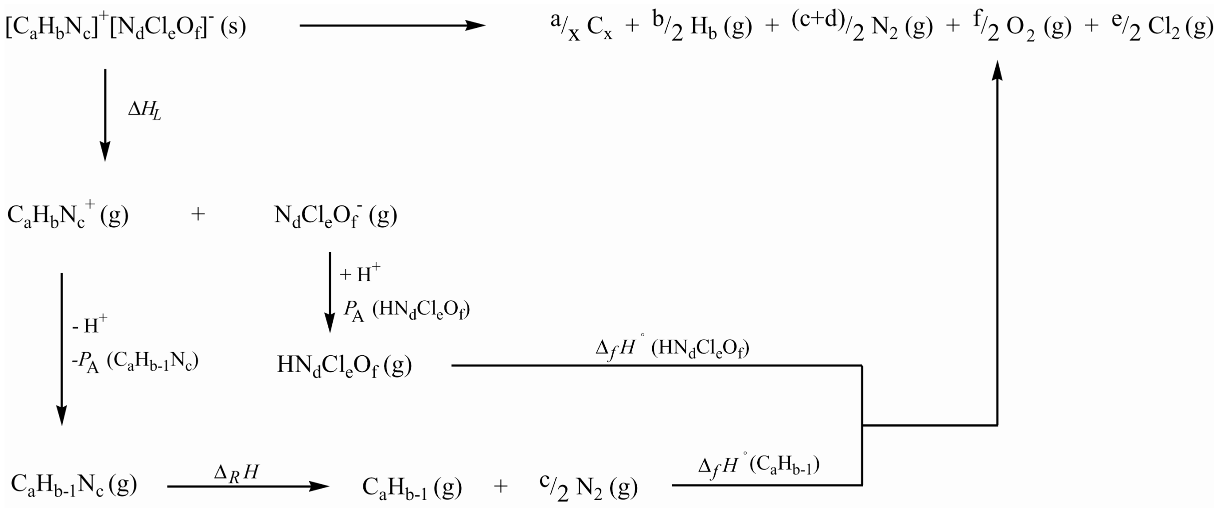

Scheme 4.7. General Born-Haber energy cycle for the reactions [1]-[4]. For encoding compounds **59a**, **59b** and **61b-d** see *Table 4.6.*

From the computed G2 and G3 enthalpies (*Appendix A Table A-8*) the reaction enthalpy $\Delta_R H$ for reaction [5] was calculated to be -125.4 (G2) and -125.0 (G3) kcal mol^{-1} and for [6], -341.1 (G2) and -335.4 (G3) kcal mol^{-1}, respectively.

$[CH_5N_6]^+[ClO_4]^-$ (s) → 1/x C_x (g) + 5/2 H_2 (g) + 3 N_2 (g) + 2 O_2 (g) + 1/2 Cl_2 (g) [1]

$[C_2H_7N_6]^+[N_3]^-$ (s) → 2/x C_x (g) + 7/2 H_2 (g) + 9/2 N_2 (g) [2]

$[C_2H_7N_6]^+[NO_3]^-$ (s) → 2/x C_x (g) + 7/2 H_2 (g) + 7/2 N_2 (g) + 3/2 O_2 (g) [3]

$[C_2H_7N_6]^+[N(NO_2)_2]^-$ (s) → 2/x C_x (g) + 7/2 H_2 (g) + 9/2 N_2 (g) + 2 O_2 (g) [4]

$C_2H_6N_7$ (g) → C_2H_6 (g) + 3N_2 (g) [5]

CH_4N_6 (g) + $HClO_4$ (g) → CO_2 (g) + 3N_2 (g) + 2 H_2O (g) + HCl (g) [6]

Table 4.6. Thermochemical Results of the Synthesized Salts **59a**, **59b** and **61b-d**.

	abcdef[a]	Ω^b [%]	ρ^c [g/cm^3]	$\Delta_f H^{\circ\, d}$	$\Delta_c H^{\circ}_{calc.}$ [e]	$\Delta_E H^{\circ}_{calc.}$ [f]	$\Delta_c U_{exp.}$ [g]	$\Delta_c H^{\circ}_{exp.}$ [h]	T_m [i]	T_d [i]
2a[j]	156103	-14.7	1.727	+60.7	-1993	-1245	-311	-1888	138	168
2b	156014	-5.5	1.902	+45.9 (+40.4)	-1036	-928	-199	-972	97	192
7b	276103	-40.6	1.506	+41.7 (+41.2)	-2645	-1039	-439	-2456	121	181
7c	276304	-25.3	1.719	+92.1 (+91.1)	-2346	-1179	-478	-2135	85	184
7d	276300	-76.4	1.417	+161.6 (+161.5)	-3744	-1028	-570	-3594	135	137

[a] Encoded formula. [b] Oxygen balance. [c] Calculated density from X-ray structure. [d] Calculated molar enthalpy of formation in kcal mol^{-1} using G2 (G3) method. [e] Calculated molar enthalpy of combustion in cal g^{-1}. [f] Calculated molar enthalpy of detonation in cal g^{-1}. [g] Experimental constant volume combustion energy in kcal mol^{-1}. [h] Experimental molar enthalpy of combustion in cal g^{-1}. [i] From DSC experiment (β = 10°C min^{-1}), T_m (melting point), T_d (peak maximum temperature of the decomposition step), °C. [j] From Ref [7c].

The corresponding lattice enthalpies, ΔH_L for salts M_pX_q, were derived from U_{POT} using the relationship provided by Jenkins et al. (eq. 1):

$$\Delta H_L = U_{POT} + [p(n_M/2-2) + q(n_X/2-2]RT \qquad \text{(eq. 1)}$$

where n_M and n_X depend on the nature of the ions, M^{p+} and X^{q-}, and are equal to 3 for monoatomic ions, 5 for linear polyatomic ions, and 6 for nonlinear polyatomic ions.[61] The equation for lattice potential energies U_{POT} (eq. 2) has the form

$$U_{POT}[kJmol^{-1}] = 2I[\alpha(V_m)^{-\frac{1}{3}} + \beta] \qquad \text{(eq. 2)}$$

where α = 117.3 and β = 51.9 according to the stoichiometry of the salts **59b**, **61b**, **61c** and **61d** (M_pX_q; $p = p = 1$; I = ½(pq^2-qp^2) = 1). V_m is the molecular volume (V_m = V/Z). With the calculated enthalpies of reaction [5] and [6] and the experimentally known enthalpies of formation for HNO_3 (g), HN_3 (g), $HN(NO_2)_2$ (g, calcd.),[62] C_2H_6 (g), CH_4 (g), and N_2 (g) ($\Delta_f H°$ (exp.); *Appendix A Table A-8*) and proton affinities (P_A; *Appendix A Table A-8*), also calculated with G2 and G3 methods, it was possible to calculate the standard enthalpies of formation for the salts **59b**, **61b**, **61c** and **61d**. Using the so obtained values for the enthalpies of formation and the literature values for the enthalpy of formation of H_2O (l) ($\Delta_f H°(H_2O)$ = -68.1 kcal mol^{-1})[63,64], CO_2 (g) ($\Delta_f H°(CO_2)$ = -94.2 kcal mol^{-1})[65], and HCl (g) ($\Delta_f H°$(HCl) = -22.3 kcal mol^{-1})[64], it was also possible to calculate the enthalpies of the (oxygen) combustion of the salts **59b**, **61b**, **61c** and **61d** according reaction [7]-[10].

$[CH_5N_6]^+[ClO_4]^-$ (s) → CO_2 (g) + 2 H_2O (l) + 3 N_2 (g) + HCl (g) [7]

$[C_2H_7N_6]^+[N_3]^-$ (s) + 15/4 O_2 → 2 CO_2 (g) + 7/2 H_2O (l) + 9/2 N_2 (g) [8]

$[C_2H_7N_6]^+[NO_3]^-$ (s) + 9/4 O_2 → 2 CO_2 (g) + 7/2 H_2O (l) + 7/2 N_2 (g) [9]

$[C_2H_7N_6]^+[N(NO_2)_2]^-$ (s) + 7/4 O_2 → 2 CO_2 (g) + 7/2 H_2O (l) + 9/2 N_2 (g) [10]

Table A-8 (Appendix A) summarizes the thermochemical data needed for the calculations of the heats of formation of compounds **59b**, **61b**, **61c** and **61d**. *Table 4.6* shows a comparison of the experimentally determined and calculated heats of combustion (on the basis of the Born-Haber energy cycles, see *Scheme 4.7*) for the salts **59b**, **61b**, **61c** and **61d**. Typical experimental results (averaged over three measurements each) of the constant volume combustion energy ($\Delta_c U$) of the new salts are given in *Table 4.6*. The standard molar enthalpy of combustion ($\Delta_c H^\circ$) was derived from $\Delta_c H^\circ = \Delta_c U + \Delta nRT$ ($\Delta n = \sum n_i$ (products, g) $- \sum n_i$ (reactants, g); $\sum n_i$ is the total molar amount of gases in products or reactants). The obtained values are in reasonable agreement with the experimentally determined values with a deviation of less than 9 %, e.g. in the case of **61d**, $\Delta_c H^\circ_{calc.}$ and $\Delta_f H^\circ$ were calculated to be -3744 kcal g^{-1} and 161.6 kcal mol^{-1}, respectively which is in good agreement with the experimental obtained value of -3594 kcal g^{-1} ($\Delta_c H^\circ_{exp.}$).

To determine the decomposition products and to assess more quantitatively the expected detonation properties of the salts **59b**, **61b**, **61c** and **61d**, the Kistiakowsky-Wilson Rule for salts **59b** and **61c** (reaction [11] and [12]) and the modified K-W rule for **7b** and **7d** (reaction [13] and [14], Ω lower then -40%)[66] were used to derive together with the experimentally known enthalpies of formation of H_2O (g) ($\Delta_f H°(H_2O)$ = -57.8 kcal mol^{-1})[63,64], CO (g) ($\Delta_f H°(CO)$ = -26.5 kcal mol^{-1})[65] and HCl (g) ($\Delta_f H°(HCl)$ = -22.3 kcal mol^{-1})[64] the enthalpies of detonation ($\Delta_E H^\circ_{calc.}$) for the salts **59b**, **61b**, **61c** and **61d** (see *Table 4.6*).

$[CH_5N_6]^+[ClO_4]^-$ (s) → CO_2 (g) + 2 H_2O (g) + 3 N_2 (g) + HCl (g) [11]

$[C_2H_7N_6]^+[N(NO_2)_2]^-$ (s) → 2 CO (g) + 2 H_2O (g) + 9/2 N_2 (g) + 3/2 H_2 (g) [12]

$[C_2H_7N_6]^+[NO_3]^-$ (s) → 1/x C_x + CO (g) + 2 H_2O (g) + 7/2 N_2 (g) + 3/2 H_2 (g) [13]

$[C_2H_7N_6]^+[N_3]^-$ (s) → 2/x C_x + 9/2 N_2 (g) + 7/2 H_2 (g) [14]

2.8.2 Detonation pressures and velocities

The expected detonation pressures (*P*) and detonation velocities (*D*) were calculated using the semi-empirical equations suggested by Kamlet and Jacobs (Eqs. (3) and (4), Table 7).[67,68]

$$P[10^8 Pa] = K\rho^2\varphi \qquad [3]$$

$$D[mm\mu s^{-1}] = A\varphi^{1/2}(1 + B\rho) \qquad [4]$$

For the compounds **59b**, **61b**, **61c** and **61d** the calculated detonation pressures lie in the range of *P* = 20.8 GPa (**61d**, comparable to TNT,[69] *P* = 20.6 GPa) to P = 33.6 GPa (**61c**, comparable to RDX,[69] *P* = 34.4 GPa). Detonation velocities are in the range of *D* = 7405 m s^{-1} (**61d**, comparable to nitroglycerin,[70] *D* = 7610 m s^{-1}) to *D* = 8827 m s^{-1} (**61c**, comparable to RDX,[70] *D* = 8750 m s^{-1}). In the case of the chloride free salts they correlate well with the increase of density (**61d** (1.417) < **61b** (1.506) < **61c** (1.719) ≈ **59a** (1.727)).

2.8.3 Sensitivity test

Impact testing was carried out on a "BAM Fallhammer" in accordance to the BAM Method (*Chapter I, 2.2.3*).[71] From *Table 4.7*, it is obvious that there is a range in impact sensitivities, from insensitive for the nitrate **61b** (>40 J) to the less sensitive azide **61d** (15 J) compared to **59a** (9 J), **59b** (7 J) and **61c** (7 J). However, in all cases the salts are less sensitive to impact than the highly used dry explosives RDX (5 J), Tetryl (4 J) or the more sensitive PETN (3 J).[72] Interestingly, the friction sensitivity of the compounds is much higher than expected (*Table 4.7*).

Table 4.7. Explosive Properties and Initial Safety Testing of the synthesized Salts **59a**, **59b** and **61b-d**.

	P [GPa]	*D* [m s^{-1}]	Impact[a] [kg cm]; (Nm)	Friction[b,c]
2a	33.3	8774	90 (9 J)	192 N (-)
2b	32.2	8383	70 (7 J)	60 N (+)
7b	23.4	7682	> 200 (>40 J)	120 N (-)
7c	33.6	8827	70 (7 J)	24 N (+)
7d	20.8	7405	150 (15 J)	192 N (-)

[a] Insensitive > 40 J, less sensitive ≥ 35 J, sensitive ≥ 4, very sensitive ≤ 3 J. [b] Insensitive > 360 N, less sensitive = 360 N, sensitive < 360 N a. > 80 N, very sensitive ≤ 80 N, extreme sensitive ≤ 10 N. [c] According to the UN Recommendations on the Transport of Dangerous Goods (+) indicates: not safe for transport, ref 73a.

In the case of the nitrates **59a** and **61b** and unexpectedly the azide **61d**, the friction sensitivity - determined with the BAM friction tester (*Chapter I, 2.2.3*) - lies in the sensitivity range of common secondary explosives like RDX (dry, 120 N) or nitrocellulose (dry, 240 N). But the highly energetic salt **59b** (60 N) should be handled with extreme care, as its friction sensitivity reaches values comparable to the very sensitive PETN (dry, 60N). The dinitramide salt **61c** posses the highest friction sensitivity with a value of 24 N which is still lower than the very sensitive lead azide (10 N).

2.8.4 Koenen test of **59c**

HDATNO$_3$ (**59c**) is a compound with a slightly negative oxygen balance (-14.7 %) and good density of 1.727 g cm^{-3}. *Figure 4.17* and *4.18* displace the results of the Koenen tests without additional oxidizer using two different orifice plates (Figure *4.17* (d = 2mm) and *4.18* (d = 6 mm)). In both cases, the test was accompanied with a strong detonation leading in the case of d = 2 mm to the occurrence of G type fragmentation and in the case of d = 6 mm to F.

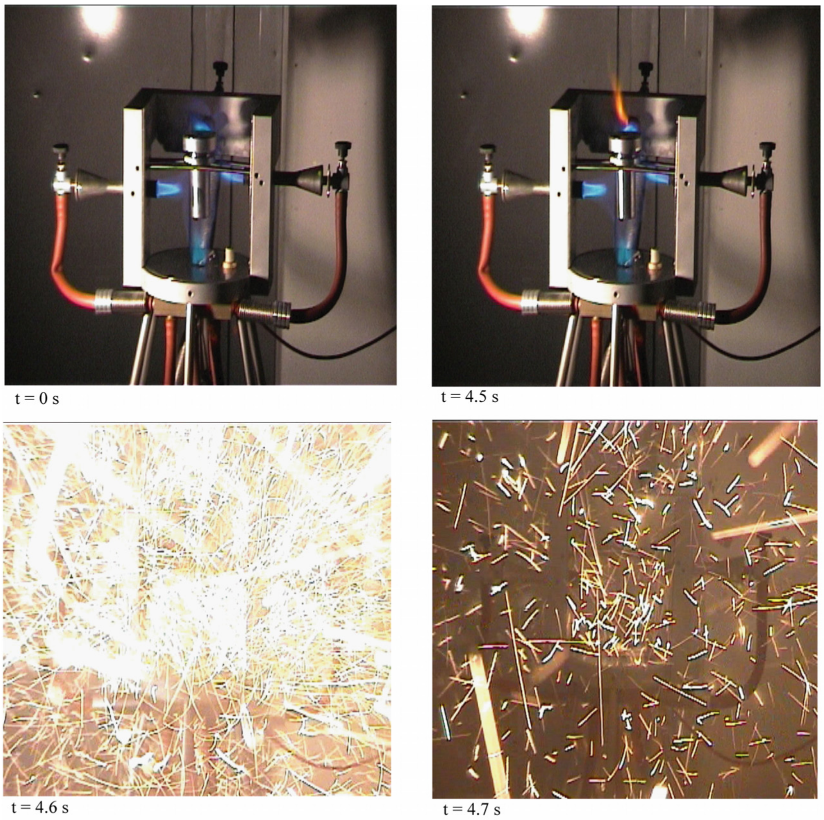

m = 8 g

d = 2 mm

Type of Fragments : G

(Thimble is desdroyed in a lot of littel pieces)

Figure 4.17. Koenen test of **59c** (d = 2mm)

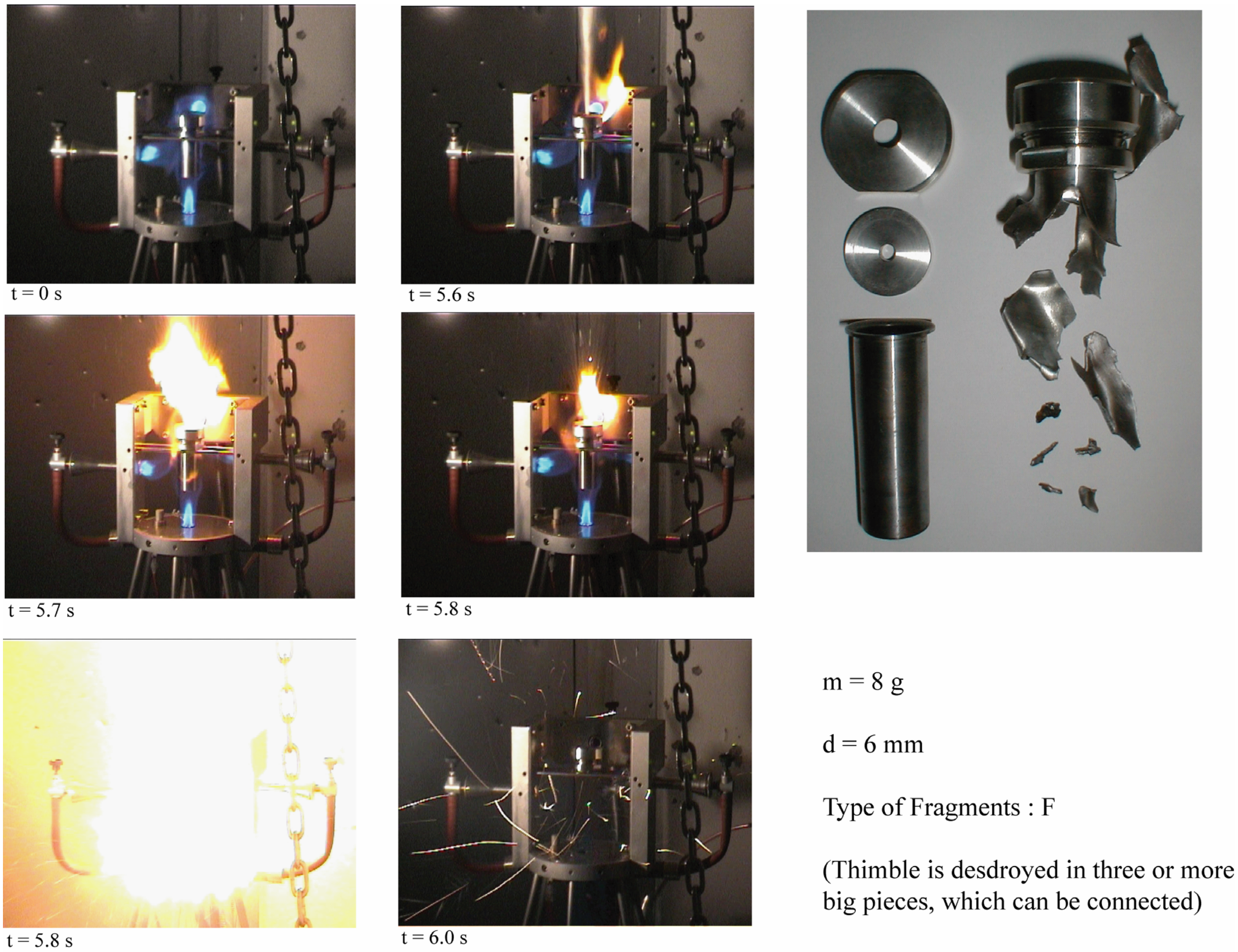

Figure 4.18. Koenen test of **59c** (d = 6 mm)

As it can be depicted from *Figure 4.17*, the detonation occurred after ~ 4.5 second without visible occurrence of the formation of gases. Whereas in the case of the second test, illustrated in the second picture (*Figure 4.18, left*), the formation of huge amount of gases can be seen which are approximately ignite after 5.7 seconds before the detonation occurs.

2.9 Thermal behavior

The thermal decomposition of the highly energetic 1,5-diamino-4-methyl-1*H*-tetrazolium nitrate (**61b**), 1,5-diamino-4-methyl-1*H*-tetrazolium dinitramide (**61c**) and 1,5-diamino-4-methyl-1*H*-tetrazolium azide (**61d**) are interesting with respect to the their thermal behavior investigated by thermogravimetric analysis (TGA) and differential scanning calorimetry (DSC) and the results are going to presented in the following *Chapters*. Moreover, the explosion and decomposition

products were determined by means of IR spectroscopy, and mass spectrometry and reasonable decomposition pathways are discussed.

Table 4.8. Properties of the salts **61b**, **61c** and **61d** related to the DSC and TGA measurements

	T_m[a]	$\Delta_m H$[b]	T_d.[c]	T_{int}[d]	$\Delta_{max} H$[e]	purity[f]	Mass loss[g]
61b	121	122	181	185 – 250	2085	> 99%	33% (150-195°C) 58% (195-275°C)
61c	85 (T_g 82 °C)[h]	118	184	150 – 230	2823	> 98%	90% (150-250°C)
61d	133 (133)[i]	181[j] (171)[k]	137	137 – 310	916	> 98%	34% (105-160°C) 36% (160-185°C) 19% (185-310°C)

[a] Melting point (onset) from DSC experiment (β = 10°C min^{-1}), °C. [b] Enthalpy of melting J g^{-1}. [c] Decomposition temperature (onset) from DSC experiment (β = 10°C min^{-1}), °C. [d] Range of decomposition, °C. [e] Heat of combustion from maximum exothermic step, J g^{-1}. [f] According the ASTM protocol E 928 – 96. [g] from TGA experiment (β = 10°C min^{-1}). [h] Onset of phase transition. [h] Melting point (onset) from DSC experiment (β = 10°C min^{-1}) in closed Al-container °C. [j] Indicating a marked degree of sublimation around the melting temperature together with the start of the decomposition. [k] Enthalpy of melting J g^{-1} determined in closed Al-container.

2.9.1 DSC and TGA

DSC and TGA were used to evaluate the relative thermal stabilities of **61b**, **61c** and **61d** and are measured under comparable condition (Al-containers with a hole (1 μm) on the top for gas release for DSC measurements). *Figure 4.19-4.21* shows the obtained DSC and TGA thermographs of these salts. All three compounds have relatively low melting points (**61a**, mp 121°C (onset); **61d**, 135°C (onset)), with the lowest for the dinitramide salt (**61c**, 85°C (onset)) and start to decompose in the range of 175 – 250°C (**2b**), 150 – 230°C (**2c**) and 137 – 310°C (**2d**). The enthalpy of melting, $\Delta_m H$, were found to be 122 (**2b**), 118 (**2c**) and 181 (**2d**) J g^{-1} (*Table 4.8*).

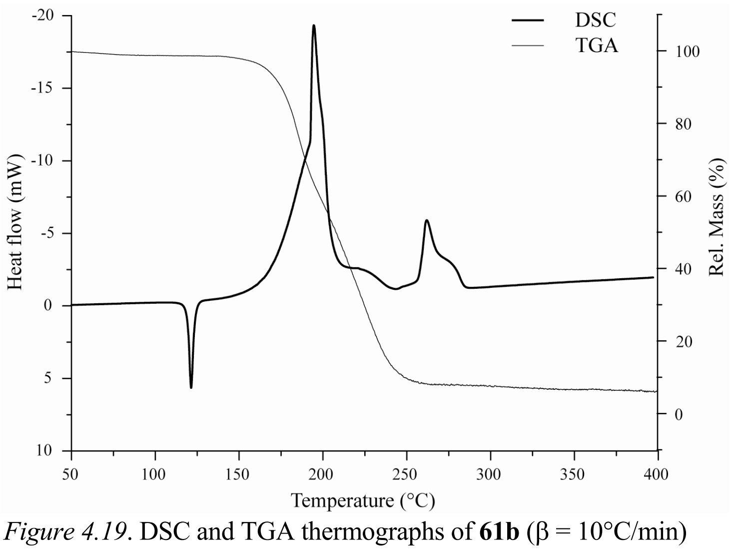

Figure 4.19. DSC and TGA thermographs of **61b** (β = 10°C/min)

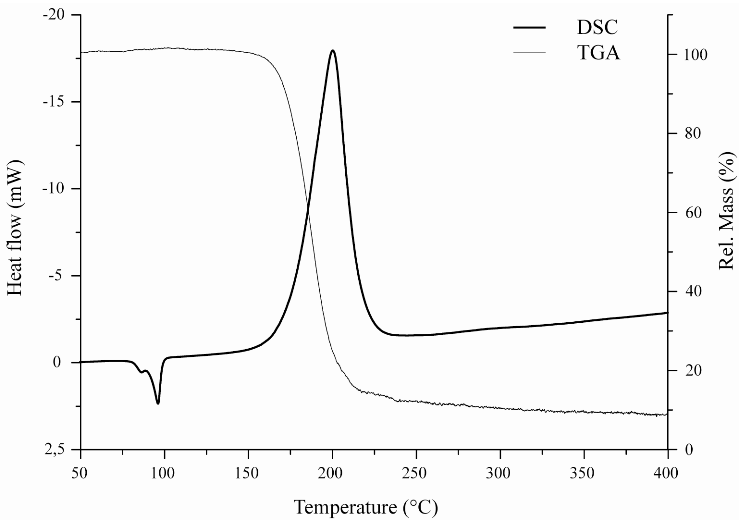

Figure 4.20. DSC and TGA thermographs of **61c** (β = 10°C/min)

61b shows three main signals which can be related to the melting, first endothermic signal, the main decomposition reaction (second exothermic signal) and third exothermic signal, which corresponds to condensation reaction of the residual fragments of the exothermic step. In the case of the azide **61d,** two endothermic steps indicate a marked degree of sublimation around the melting temperature together with the start of the decomposition. Repeating the experiment with a closed Al-container with the same heating rate resulted in the coalescence of the two endothermic signals into one signal. The main decomposition step of **61d** is found in the region of 160 – 220 °C and, comparable to **61b**, the weak exothermic region (275 – 325°C) also corresponds to condensation reactions of residual fragments of the decomposition step.

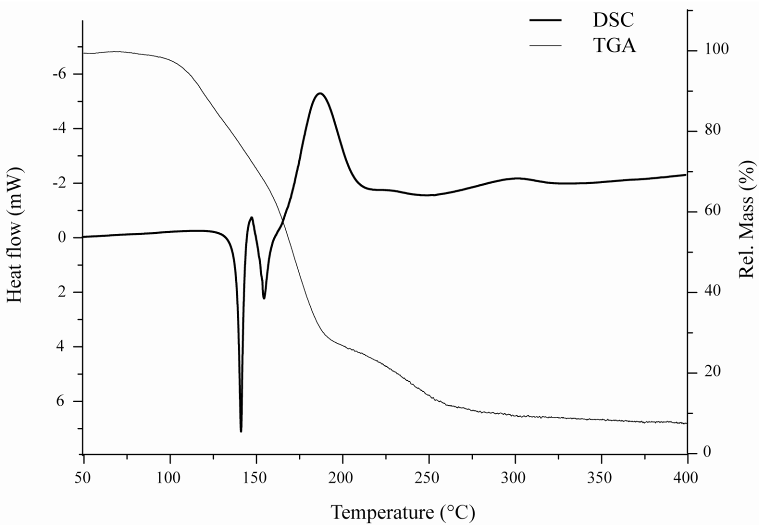

Figure 4.21. DSC and TGA thermographs of **61d** (β = 10°C/min)

The DSC curves of the investigated **61c** is divided into three parts, the first one corresponds to a phase transition region which appears as one small endothermic reaction (T_g = 82 °C), the second part shortly after, is related to the melting region of **61c** as a endothermic peak. The third exothermic peak corresponds to the decomposition reaction. The purities of the compounds were determined to be higher than 98% by the evaluation of the corresponding melting peaks with the van't Hoff equation according ASTM protocol E 928 – 96.[73]

All three salts do not decompose residual free in the temperature range of 50 – 400°C, as the mass loss in all case was determined by TGA to be ~ 90% (*Table 4.8*). The reason for this is found in the formation of condensation products with higher molecular mass, e.g. melam, melem or melom.[74] These products decompose at higher temperatures (> 500°C) to volatile substances like cyanamide, hydrogen cyanide and ammonia.[75] According to the mass loss derived from the TGA experiment, the dinitramide salt (**61c**) decomposes in one single step, whereas for **61b,** two decomposition steps are determined and in the case of **61d** three (*Table 4.8*). A closer inspection of the decomposition products of these salts reveals in all cases comparable decomposition pathways.

Table 4.9. Maximum exothermic responses of **61b-d** as a function of scan speed.

S. no.	β (°C/min)	T_p (°C)	E_a(kcal mol^{-1}) Ozawa [28]	E_a (kcal mol^{-1})[a] Kissinger [29]
2b				
1	2	176.55	31.08 ±0.88	31.09 ±0.82
2	5	186.58		
3	10	195.56		
4	20	205.48		
5	40	216.09		
2c				
1	2	177.12	32.89 ±1.08	32.91 ±1.01
2	5	186.44		
3	10	195.23		
4	20	204.03		
5	40	214.64		
2d				
1	10	185.14	25.65 ±1.00	25.72 ±0.90
2	15	190.93		
3	20	194.85		
4	30	201.13		
5	50	211.04		

[a] Refined Kissinger activation energy according ASTM E 698 – 99 [76].

2.9.2 Activation Energy

Differential scanning calorimetric studies have been carried out at five different heating rates (*Table 4.9*) to calculate the energy of activation by following the methods according the ASTM protocol.[76] It is observed that the temperature of decomposition increases with the increased heating rate of heating of the sample. The calculated activation energy values are in the case of **61b** and **61c** comparable and have been found to be 31.1 kcal mol^{-1} (**61b**, Ozawa) and 32.9 kcal mol^{-1} (**61c**, Ozawa), respectively. Compared to this, the activation energy of **61d** was estimated to be 26.7 kcal mol^{-1} (Ozawa). The activation energy values suggest that **61c** is more thermally unstable than **61b** and **61c** indicating a different decomposition pathway, when compared in terms of calculated activation energies. The refined values of the activation energy obtained according the Kissinger method show an excellent correlation (*Table 4.9*).

Table 4.10. Observed mass (*m/z*) in the decomposition experiments of **61d**

m/z	**61b**	**61c**	**61d**	
126	x	x	x	$(H_2NCN)_3$
81	x	x		$(HCN)_3$
69	x	x	x	1,2,4-Triazole
57	x	x	x	MeN_3, H_2NNCNH
56		x		
54	x			$(HCN)_2$
46	x			$MeONO_2$*
44	x	x		CO_2, N_2O
43			x	HN_3
42			x	H_2NCN
32	x			CH_3OH
30	x	x		NO, H_2CO
29			x	
28	x	x	x	CO, N_2
27	x		x	HCN
18	x	x		H_2O
17	x	x		NH_3
15			x	
14	x	x	x	

* mass peak not observed

2.9.3 Decomposition experiments

Possible decomposition scheme for **61d**

The typical products detected during the decomposition of the azide **61d** (by means of IR and mass spectrometry) are HN_3 (*m/z* 43), NH_4N_3, HCN (m/z *27*), NH_3 (*m/z* 17), MeN_3 (*m/z* 57), N_2

(*m/z* 28) and traces of 1,2,4-triazole (*m/z* 69) (*Table 4.10*). Two distinctive temperature regimes have been identified for the decomposition of **61d**. As it is typical for ammonium salts of hydrazoic acid, the release of HN_3 starts at comparably low temperature and in the case of **61d**, the appearance of HN_3 in the IR spectra was already observed at about 60°C (*Figure 4.22*). This is not consistent with the TGA experiment where this temperature was determined to be ~ 105°C. One explanation for this observation is that the thermodynamic conditions for both experiments are different with respect to pressure. The IR experiment was carried out by thermal heating with a pressure of 5 µbar, whereas the TGA experiments had nitrogen as purge gas (20 mL min^{-1}). The mass loss of the first step was determined to be ~ 34% which is in excellent agreement with the reaction process shown in Scheme 1 for the first step, the release of HN_3.

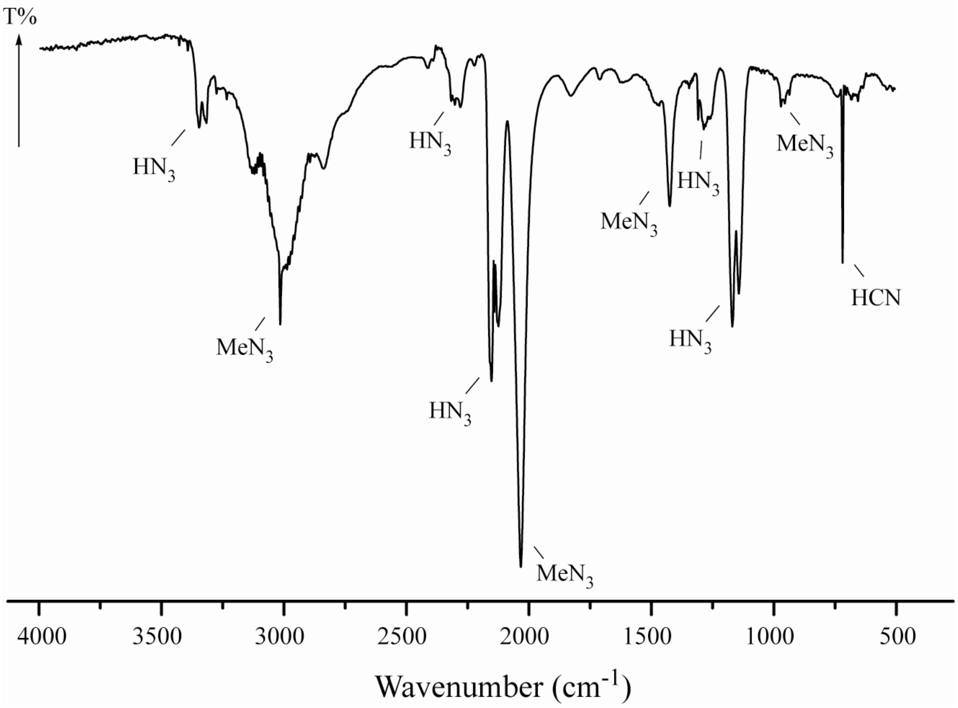

Figure 4.22. Gas phase IR spectrum of the decomposition products of **61d**

The 1-amino-4-methyl-5-imino-4,5-dihydro-1*H*-tetrazole (**60**) which remains after the evolution of the HN_3 decomposes under thermal stress to methyl azide (**62**) and the aminocyanamide (**63**), and this process also coincidences well with the observed mass loss of 36% (*Table 4.9*, *Scheme 4.8*, **I**) for the second step. In accordance with the observation of Levchik et al.[77] the trimerization product of **63**, 2,6,6-trihydrazino-*1,3,5*-triazine (**64**), was not detected as it is unstable at high temperatures and partially decomposes under ring-narrowing with the formation of 1,2,4-triazole (**65**).[78]

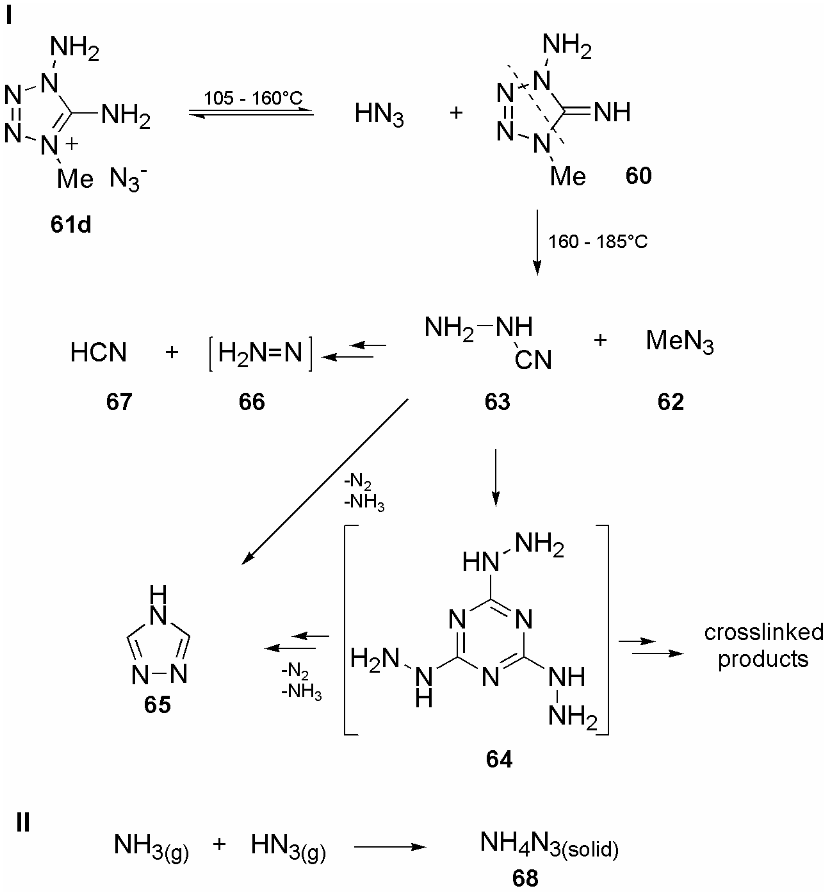

Scheme 4.8. Possible decomposition pathway of **61d**.

In the small amount of solid residue of the decomposition experiments, triazine structures crosslinked by -NH- could be identified by means of IR spectroscopy. The thermal decomposition residues after the third stage of weight loss (~ 10%) have IR spectra similar to those of the products of thermal decomposition of 5-aminotetrazole, showing characteristic absorptions (3400-3100, 1670-1350, 810 and 780 cm^{-1}) of condensed crosslinked melamine derivatives.[79] The other possible decomposition route of **63** is the decomposition to HCN (**67**) under the formation of the corresponding unstable nitrene (**66**). **67** was also identified in the IR spectrum of the explosion products of **61d** (*Figure 4.22*).

The TGA results are also in very good agreement with stepwise decomposition determined by IR spectroscopy. The identification of the decomposition gases allows the evaluation of the chemical processes during the thermal degradation of **61d**. *Figures 4.23* show those decomposition gases detected by IR spectroscopy and released during heating of **61d** from 30 to 190°C. Ammonium azide (**68**) is produced from the recombination of ammonia NH_3 and HN_3, which is subsequently produced during the decomposition of **61d** and illustrates the descent of the

intensities of the bands of HN_3 in the IR spectra (*Scheme 4.8*, **II**, *Figure 4.23*) at temperatures higher than 150°C. **68** was identified in the obtained sublimate. The mechanism for the decomposition of **60** becomes predominant as indicated by the increasing band around 2050 cm^{-1} which belongs to MeN_3 (**62**) (*Figure 4.23*). The vibrational frequencies of the experimentally observed IR-active gases are summarized in *Table 4.11*.

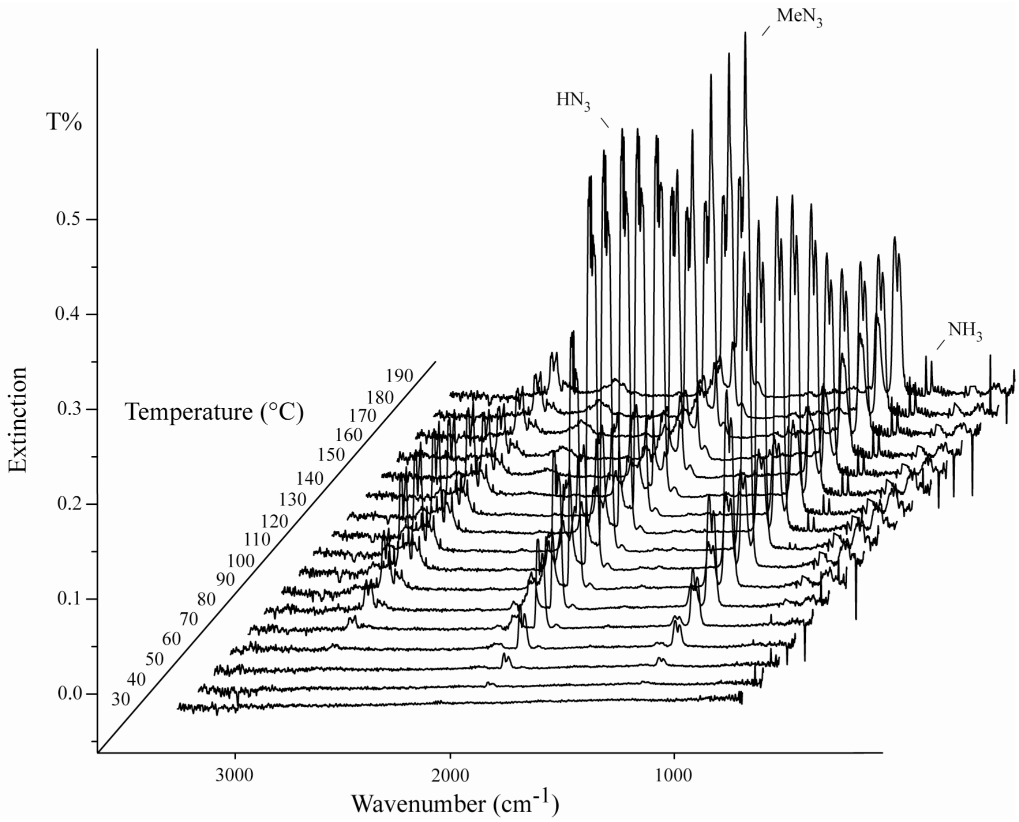

Figure 4.23. Infrared spectroscopic evolved gas analysis of **61d**

Table 4.11. Vibrational frequencies (cm^{-1}) of the experimentally observed molecules in the gas phase

Species	Frequencies	ref
HN_3	3336 (m), 2140 (vs), 1264 (m), 1151 (vs), 607 (w), 607 (vw)	[80]
MeN_3	2940 (m), 2818 (w), 2539 (vw), 2198 (s), 2104 (vs), 1466 (vw), 1450 (vw), 1284 (s), 920 (w), 676 (w)	[81]
NH_3	3336 (m), 1626 (s), 968 (vs), 933 (vs)	[82]
HCN	3311 (s), 2097 (w), 712 (vs)	[80]
$MeONO_2$	2959 (m), 2917 (m), 1678 (vs), 1661 (vs), 1442 (m), 1430 (m), 1296 (s), 1287 (s), 1278 (s), 1017 (s), 862 (s), 855 (s), 853 (s), 844 (s) 758 (m), 658 (m)	[83]
N_2O	3891 (w), 3480 (m), 2809 (w), 2591 (m), 2488 (m), 2457 (vs), 2217 (vs), 1890 (w), 1302 (vs), 1275 (vs), 1183 (m), 1155 (m), 694 (w), 588 (w)	[84]
CO_2	3716 (w), 3609 (w), 2326 (vs), 741 (m), 667 (vs)	[85]
CO	2179 (vs), 2114 (vs)	[85]
H_2O	3657 (s), 1595 (s)	[80]

Possible decomposition scheme for **61b**

The thermal decomposition of **61b** under reduced pressure in the temperature of 140 to 300°C is shown in *Figure 4.24*. **61b** melts at 121°C, and the melt is stable up to 190°C where shortly after, in accordance to the DSC experiment, decomposition occurs and a broad exothermic peak in the DSC, and a sudden rise of gaseous products in the IR spectra indicates a spontaneous decomposition. In comparison to AN, **61b** shows a comparable decomposition region of ~ 185 – 250 °C (AN 210°C and 260°C) which leads in contrast to AN to the formation of $MeONO_2$ (**70**) (*m/z* 46, no mass peak observed) and only as a minor process to the formation of HNO_3 (**69**, *m/z* 63)[86] (*Scheme 4.9*).

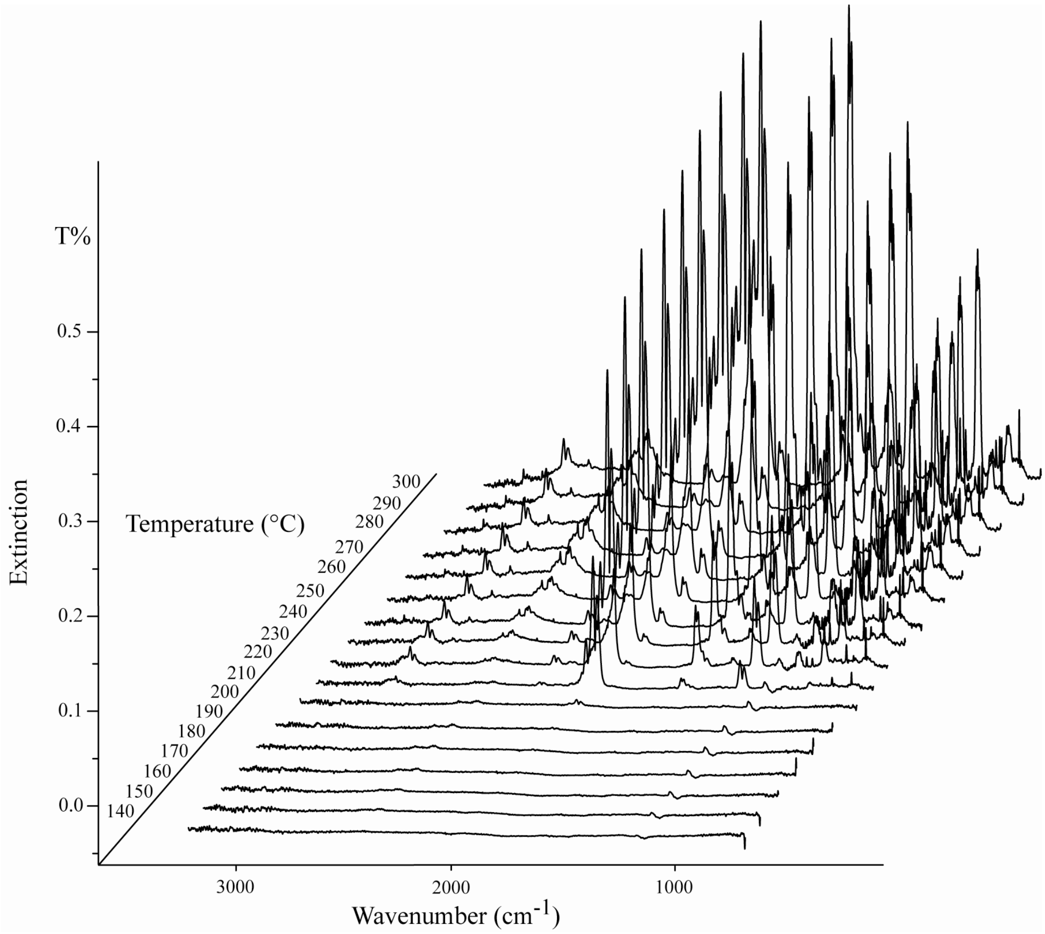

Figure 4.24. Infrared spectroscopic evolved gas analysis of **61b**

Compared to **61d** and AN, in the case of **61b** the main processes involve a methyl group transfer to **55** and methyl nitrate (**70**) and not a proton transfer to **69** (HN_3 in the case of **61d**) and **60** (*Scheme 4.9*, **I**). The main process observed is the formation of **70** (*m/z* 46, no mass peak observed), which was found to be the major product (*Figure 4.25*) in the IR spectra of the explosion products as well as in the spectra of the decomposition experiments and could also be identified in the mass spectrometry experiments (*Figure 4.26*). Interestingly, under this reaction

condition, the decomposition pathway discussed in [74], which involves the imino form of DAT (**55**), undergoes not the decomposition with the evolution of HN_3 (this was found in the case of **61d**), but rather eliminates nitrogen from DAT (**55**) (*Scheme 4.9*, **II**).

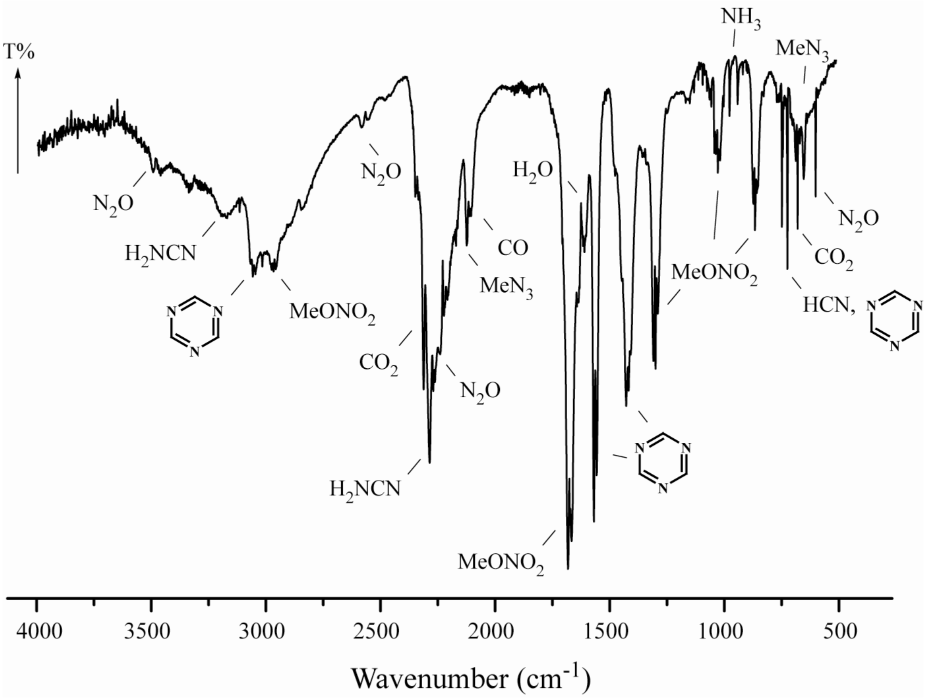

Figure 4.25. Gas phase IR spectrum of the decomposition products of **61b**

The resulting unstable nitrene (**71**) decomposes to HCN, NH_3 and N_2 according *Scheme 4.9* and in a minor process to cyanamide which is less stable and dimerizes to dicyandiamide that reacts through an intermediate to melamine (**72**).[87]

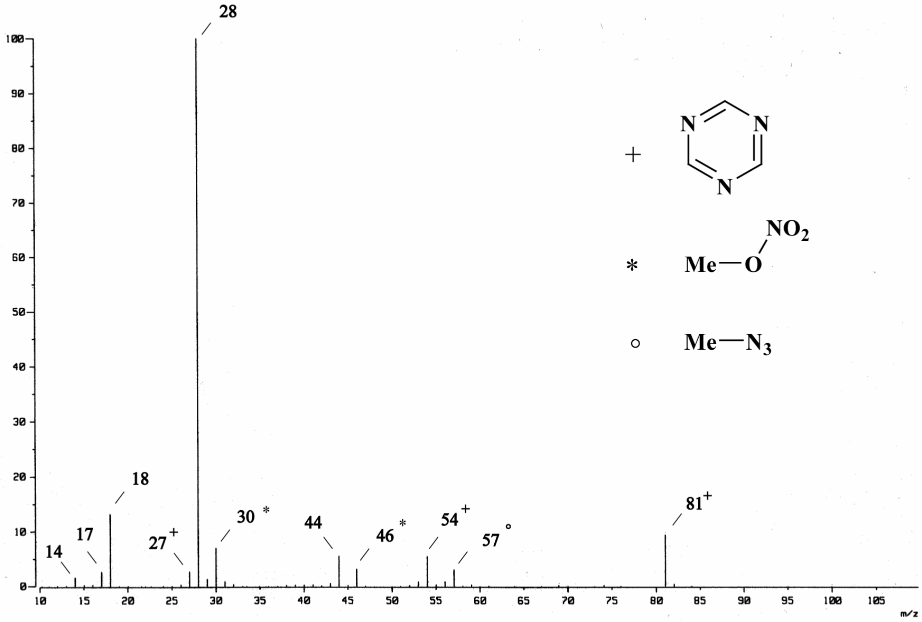

Figure 4.26. Mass spectrum of the decomposition products of **61b**

Cyanamide as gaseous product was also identified in the IR spectrum (*Figure 4.25*) but in the gas phase cyanamide decomposes to NH_3, N_2 and HCN and was therefore not detected in the mass spectrum due to the hot ionic source.

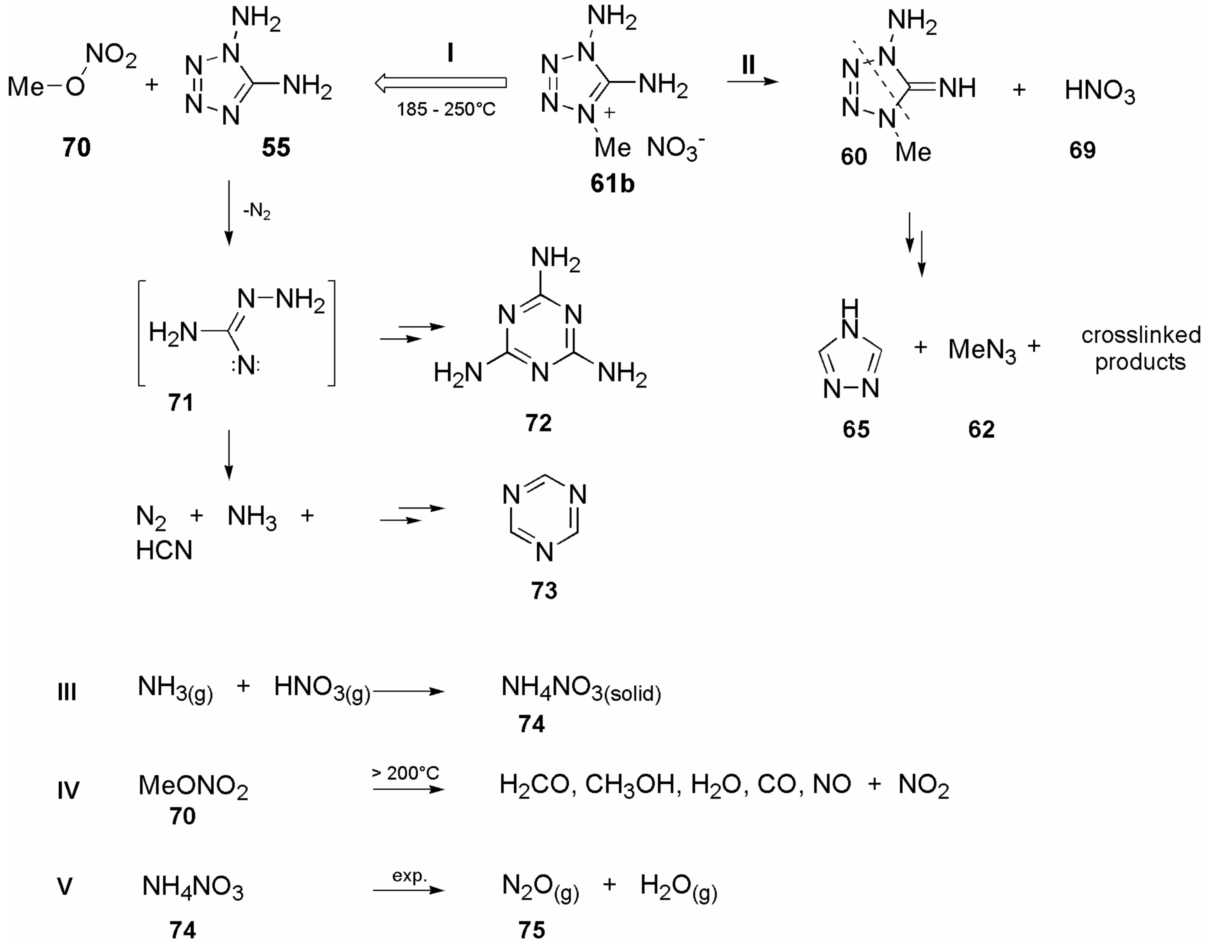

Scheme 4.9. Possible decomposition pathway of **61b**

The hydrogen cyanide undergoes *in situ* cyclotrimerization to the 1,3,5-triazine (**73**) (*m/z* 81, *Figure 4.26*), which is known to proceed under harsh condition [88] and was also identified in the IR as well as mass spectrum (*Figure 4.25* and *4.26*). In the case of **61b** only small amount of MeN_3 indicate the partly decomposition of **55** according to *Scheme 4.9* (**II**) resulting from a proton transfer. Nitric acid and MeN_3 were found as components in the mass spectra of the residual explosion products in small quantities.

The 1,2,4-Triazole (**65**), 1-amino-4-methyl-5-imino-4,5-dihydro-1*H*-tetrazole (**60**), 1,5-diamino-1*H*-tetrazole (**55**), 1,3,5-triazine (**73**) and melamine (**72**) could be identified by means of ^{13}C NMR spectroscopy (*Figure 4.27*) and were found in the residue of the decomposition experiments. Ammonium nitrate (**74**), resulting from the recombination of HNO_3 and NH_3, was

identified as one component of the obtained sublimate (*Scheme 4.9*, **III**) and explains the low concentration of ammonia. The thermal decomposition of **70** above 200°C leads to the formation of CH_2O (*m/z* 30), CH_3OH (*m/z* 32), H_2O (*m/z* 18), CO (*m/z* 28), NO (*m/z* 30) and NO_2 (*m/z* 46) (Scheme 4.7, **IV**).[89] The thermal decomposition of AN during explosion processes leads to the formation of N_2O (**75**) (*m/z* 44) and H_2O (*m/z* 16) and explains the occurrence of **75** in the IR spectrum (*Scheme 4.9*, **V**).

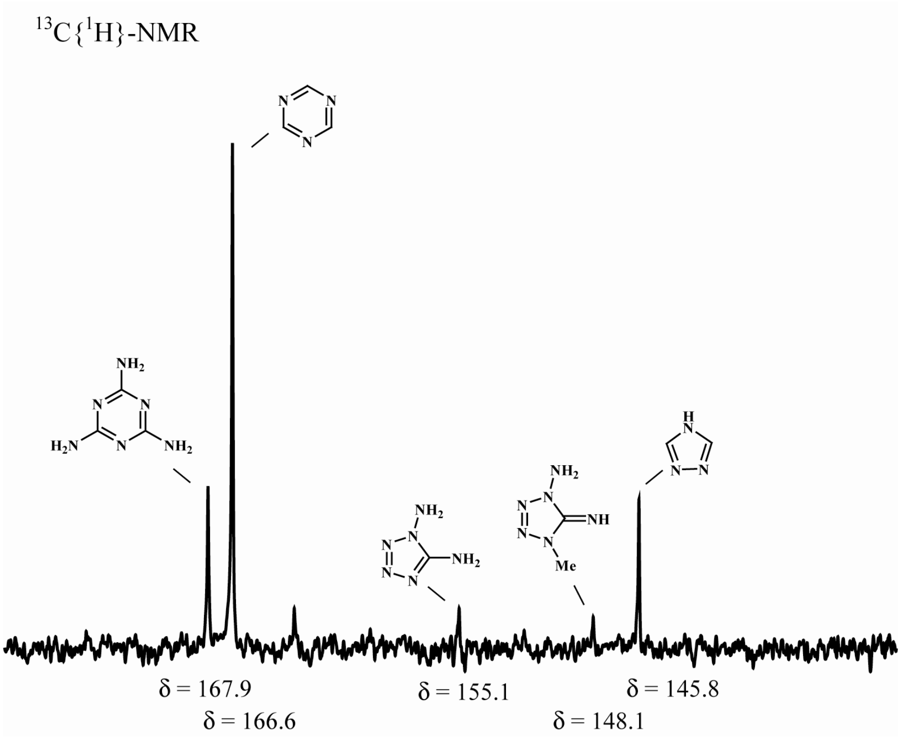

Figure 4.27. ^{13}C-NMR spectra of decomposition products of **61b** recorded in [d6]-DMSO

Possible decomposition scheme for **61c**

Compared to **61b**, **61c** (melting point 85°C) shows a relatively stable melt up to ~ 150°C where shortly after, also in accordance with the DSC experiment, decomposition occurs, and a broad exothermic peak in the DSC and a sudden rise of gaseous products in the IR spectra indicates a spontaneous decomposition in one step. The thermal decomposition of **61c** under reduced pressure in the temperature range from 40 to 220°C is depicted in *Figure 4.28*. Typical products observed during the decomposition of **61c** are N_2O (**75**) as the main product, MeN_3 (**62**), $MeONO_2$ (**70**), 1,3,5-triazine (**73**), HCN (**67**), NH_3 and H_2O (*Figure 4.29*, Table 4).

The thermal decomposition is initiated by a proton transfer to subsequently produce dinitraminic acid HN_3O_4 (**76**) in the melt. According to [90], **76** decomposes under formation of N_2O

(**75**) and HNO_3 which produces **61b** from the recombination of **55** and HNO_3. This reaction process is shown in *Scheme 4.10* (**I**) and explains the obtained decomposition products which are similar to those of **61b**. No evidence, whether from the explosion experiments or the decomposition experiments, was found for the formation of DAT (**55**) (*Scheme 4.10*, **II**) and methyldinitramide (**77**).

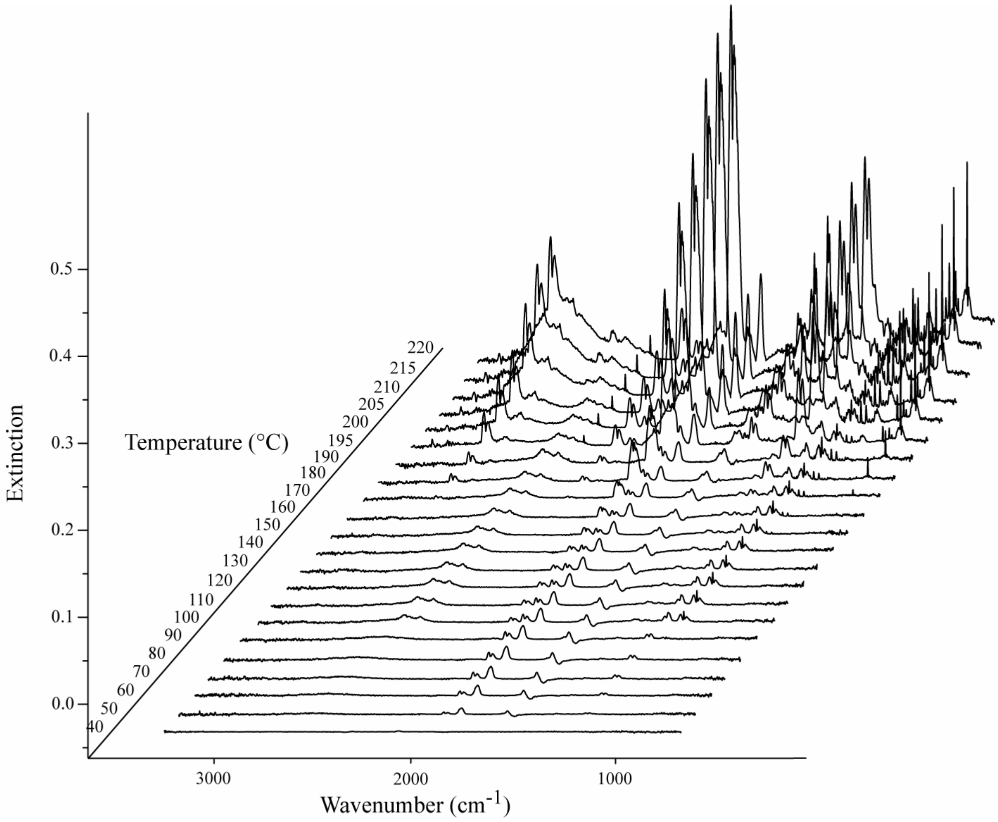

Figure 4.28. Infrared spectroscopic evolved gas analysis of **61c**

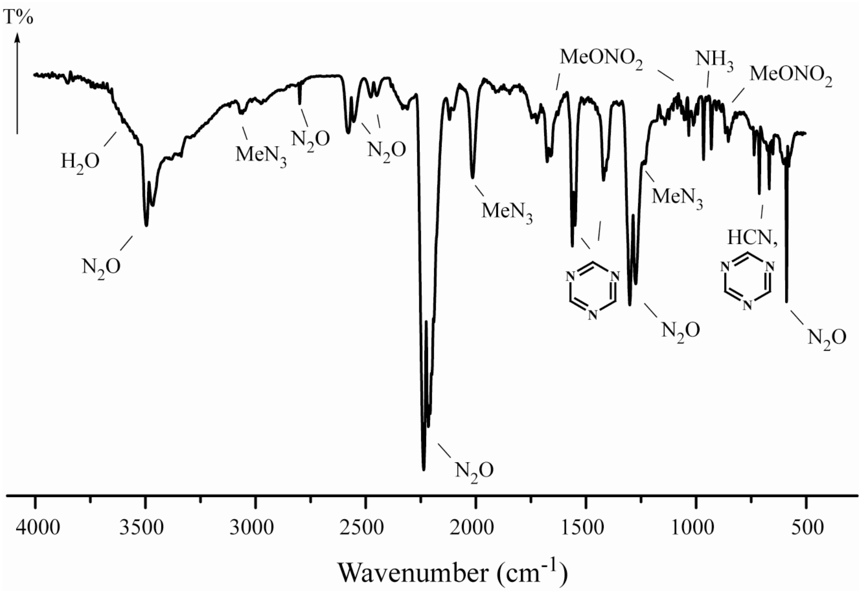

Figure 3.29. Gas phase IR spetrum of the decomposition products of **61c**

Interestingly, during the decomposition of **61c**, the formation of NO_2 was not observed which exclude the favored mechanism of decomposition of HN_3O_4 (**76**) to NO_2 (**78**) and $HNNO_2$ (**79**) according [91] at higher temperatures (*Scheme 4.10*, **III**).

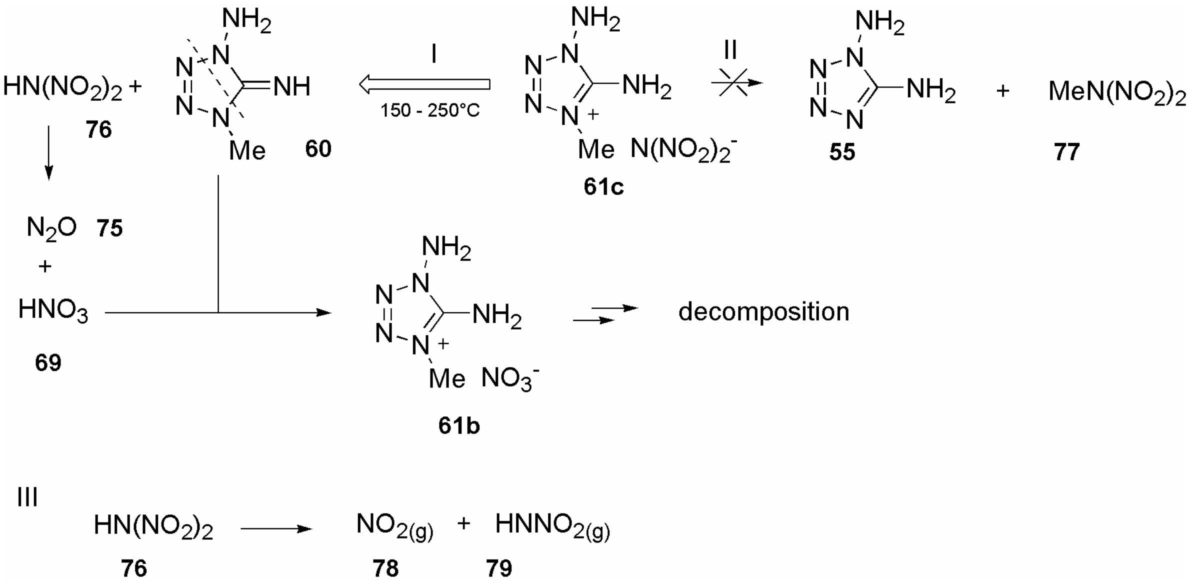

Scheme 4.10. Possible decomposition pathway of **61c**

2.10 Conclusion

The new synthesis of DAT (**55**) provides a new and easier approach to the highly energetic salts **59a**, **59b** and **61b-c**. All new salts exhibit good to reasonable physical properties, like high densities (> 1.50 g cm^{-3}), good thermal stabilities, and distinctive melting points around 100 °C. Depending on their properties, these salts can be seen as new examples of secondary explosives (**59a**, **61b**, ~ **61d**) or as primary explosives (**61c** and **61d**). All compounds show calculated detonation velocities and detonation pressure comparable to those of high explosives such as PETN, RDX or HMX. The molar enthalpies of formation of the new salts were calculated from the combustion energy obtained from corresponding oxygen bomb calorimetric measurements and show in all cases high combustion energies and high molar enthalpies of formation. From a closer inspection of the crystal structure, the intermolecular hydrogen bonding plays an important role for the crystal packing, and together with the formalism of graph-set analysis of hydrogen-bond patterns, interesting results could be derived. The novel salts **61b**, **61c** and **61d** of 1-amino-4-methyl-5-imino-4,5-dihydro-1*H*-tetrazole (**60**) are new energetic materials with high nitrogen

content. **61c** is very sensitive to friction but shows a reasonable stability toward impact. According the UN guideline ST/SG/AC.10/11, **61c** is not safe for transport but prilling of **61c** might increase the stability toward friction. The predicted detonation performance is higher than those found for RDX and the oxygen balance is in a reasonable limit. Therefore, **61c** might find application in liquid monopropellants, similar to HAN [92] and ADN [93] monopropellants. **61b** and **61c** are quite promising new materials, too, which might find application also as a supplement in monopropellants (**61b**) or as a new promising material for gas generating mixtures (**61b**, **61c** and **61d**). Mass spectrometry and IR spectroscopy were used to identify the gaseous products. The decomposition appears in the cases of **61c** and **61d** to be initiated by a proton transfer to form the corresponding acid HN_3 and HN_3O_4, whereas in the case of **61b,** a methyl group transfer to $MeONO_2$ is observed as initial process. The gaseous products after the exothermic decomposition are comparable and are in agreement of the proposed decomposition pathways. The decomposition temperatures of **61b** and **61c** are significantly higher than that of **61d** and were supported by evaluation the values of the activation energy according to the method of Ozawa and Kissinger. All three compounds showing distinctive decomposition pathways which lead in the case of **61b** and **61c** to the same products and in the case of **61d** predominately to the formation of HN_3 and MeN_3. In all cases the major gaseous decomposition products are still highly endothermic compounds.

2.11 Experimental

*CAUTION: Silver azide, silver dinitramide, aminotetrazoles and their derivatives are energetic materials and tend to explode under certain conditions. Appropriate safety precautions should be taken, especially when these compounds are prepared on a larger scale. Laboratories and personnel should be properly grounded, and safety equipment such as Kevlar® gloves, leather coat, face shield and ear plugs are necessary, especially in the case of **61c** a. **61d**.*

All chemical reagents and solvents of analytical grade were obtained from Sigma-Aldrich Fine chemicals Inc. and used as supplied. MeCN, MeOH and EtOH were dried according known procedures, freshly distilled and stored under nitrogen. Silver azide and silver dinitramide[29] were prepared according to known procedures. The ^{1}H, ^{13}C and $^{14}N/^{15}N$ NMR spectra were recorded on a JEOl Eclipse 400 instrument. The spectra were measured in [d_6]-DMSO or CD_3OD at 25°C. The chemical shifts are given relative to tetramethylsilane (^{1}H, ^{13}C) or nitromethane ($^{14}N/^{15}N$) as

external standards. Coupling constants are given in Hz. Infrared (IR) spectra were recorded on a Perkin-Elmer Spektrum One FT-IR instrument as KBr pellets at 20°C. Raman spectra were recorded on a Perkin Elmer Spectrum 2000R NIR FT-Raman instrument equipped with a Nd:YAG laser (1064 nm). The intensities are reported in % relative to the most intense peak and given in parenthesis. Elemental analyses were performed with a Netsch Simultanous Thermal Analyser STA 429. Melting points were determined by differential scanning calorimeter (Perkin-Elmer Pyris 6 DSC, calibrated by standard pure Indium and Zinc). Measurements were performed at a heating rate of β = 10°C in closed Al-containers with a hole (1 μm) on the top for gas release with a nitrogen flow of 20 mL min^{-1}. The reference sample was an Al-container with air.

Synthesis of 1,5-Diamino-1*H*-tetrazole (**55**). A solution of diaminoguanidinium chloride (1.507 g, 12 mmol) in 20 mL of water and 0,5 mL conc. HCl (37 %) was cooled to 0°C (some solid reprecipitated). A solution of sodium nitrite (830 mg, 12 mmol) in 5 mL water was added slowly keeping the temperature at 0-2°C. The solution obtained was allowed to stand in ice-water for 30 minutes. It was then brought to p*H* 8 with solid sodium carbonate and stirred for 20 minutes at 40°C and subsequently evaporated to dryness under vacuum (water aspirator) in a stream of pure nitrogen. The residue was extracted with hot EtOH (3 x 15 mL) leaving after evaporation pure 1,5-diamino-1*H*-tetrazole which was recrystallized from water (700 mg, 7 mmol, 58 %); m.p. 185-187 °C; IR (KBr, cm^{-1}): $\tilde{\nu}$ = 3324 (vs), 3237 (s), 3154 (s), 1656 (vs), 1632 (sh), 1576 (m), 1329 (s), 1134 (vw), 1109 (m), 1076 (m), 1001 (m), 932 (m), 788 (vw), 745 (w), 699 (w), 686 (m), 626 (sh), 603 (m), 487 (vw); Raman (200mW, 25 °C, cm^{-1}): $\tilde{\nu}$ = 3323 (12), 3244 (11), 3154 (9), 1670 (9), 1623 (5), 1547 (19), 1496 (5), 1329 (14), 1307 (18), 1133 (3), 1106 (14), 1978 (11), 1001 (5), 951 (4), 792 (100), 698 (15), 323 (24), 231 (13), 140 (18); ^{1}H NMR ([d6]-DMSO) δ: 6.35 (s, NH_2), 6.40 (s, NH_2); ^{13}C NMR ([d6]-DMSO, 25°C) δ: 155.0; ^{15}N NMR ([d6]-DMSO, 25°C) δ: -5.5 (N3), -20.8 (N2), -97.5 (N4), -167,8 (*N*1-NH_2), -315.2 (N1-*N*H_2, $^{1}J_{NH}$ = 74.6 Hz), -338.3 (C-*N*H_2, $^{1}J_{NH}$ = 87.9 Hz); MS (DEI, 70 eV, >5%); *m*/*z* (%): 101 (1) [M^+ + 1], 100 (9) [M^+], 75 (2), 56 (2), 44 (6), 43 (100), 42 (11), 41 (3), 32 (4), 31 (3), 30 (23), 29 (16), 28 (24), 27 (11), 26 (1), 18 (5), 17 (5), 16 (5), 13 (1); CH_4N_6 (100.08): calcd. C, 12.0; H, 4.0; N, 84.0 %; found: C, 12.1; H, 3.9; N, 83.7 %.

Synthesis of 1,5-Diamino-1*H*-tetrazolium nitrate (59a). (Method 1) **55** (1000.8 mg, 10 mmol) and 1.4 mL of conc. HNO_3 (65 %) were gently heated to give a clear solution. Upon careful addition of Et_2O (20 mL) to this solution, the product separated as white precipitate. The precipitate was filtered and washed several times with Et_2O to give **59a** (1.50 g, 9.2 mmol, 92 %). Recrystallisation from EtOH/H_2O yielded **59a** as colorless plates. (Method 2)[9] **2** (20g, 0.2 mol) was dissolved at 70 °C in a solution of 35 mL conc. HNO_3 (65 %) and 20 mL H_2O. After cooling to room temperature, the solution was left at 5 °C for crystallization. After filtration the product was washed with cold EtOH and dried *in vacuo* over P_4O_{10} (30.5 g, 18.7 mmol , 93%); m.p. 138-139 °C; IR (KBr, cm^{-1}): $\tilde{\nu}$ = 3425 (s), 3341 (s), 3146 (w), 2961 (w), 2841 (w), 2806 (vw), 2659 (w), 2472 (vw), 2346 (vw), 1726 (s), 1649 (vw), 1609 (w), 1494 (m), 1436 (w), 1384 (vs, $NO3^-$), 1305 (s), 1107 (m, 1039 (s), 976 (m), 841 (m), 728 (w), 710 (m), 660 (vw), 475 (m); Raman (200mW, 25 °C, cm^{-1}): $\tilde{\nu}$ = 3342 (6), 2997 (1), 1735 (1), 1567 (13), 1488 (7), 1465 (8), 1400 (4), 1342 (9), 1092 (7), 1057 (30), 1042 (100, NO_3^-), 745 (57), 730 (9), 718 (9), 401 (13), 151 (18), 136 (11), 119 (9); ^1H NMR (CD_3OD) δ: 5.14 (s, -NH, NH_2); ^{13}C NMR (CD_3OD, 25°C) δ: 151.2; ^{14}N NMR (CD_3OD, 25°C) δ: -11.6 (NO_3^-), -27.0 (N3, N2, $\Delta\nu_{1/2}$ = 1503 Hz), -164 (*N*1-NH_2, *N*4-H, $\Delta\nu_{1/2}$ = 1271 Hz), -343 (N1-*N*H_2, C-*N*H_2 $\Delta\nu_{1/2}$ = 1329 Hz); ^{15}N NMR (CD_3OD, 25°C) δ: -11.6 (NO_3^-), -21.9 (N3), -33.1 (N2), -164,8 (*N*1-NH_2), -170.4 (N*4*-H), -319.6 (N1-*N*H_2), 333.3 (C-*N*H_2); *m/z* (FAB^+, xenon, 6keV, m-NBA matrix) 101 $[DAT+H]^+$; *m/z* (DEI) 100 [(M -HNO_3) (9)], 45 (21), 44 (5), 43 (100), 42 (11), 41 (4), 30 (22), 29 (15), 28 (25), 27 (9); $CH_5N_7O_3$ (163.10): calcd. C, 7.4; H, 3.1; N, 60.1 %; found: C, 7.3; H, 3.1; N, 59.8 %.

Synthesis of 1,5-Diamino-1*H*-tetrazolium perchlorate (59b). (Method 1) DAT **55** (1000.8 mg, 10 mmol) and 502 μL of $HClO_4$ (70 %) were gently heated to give a clear solution. This solution was washed five times with Et_2O (10 mL). The resulting aqueous phase was overlayered with Et_2O (20 mL) and left for crystallization. After 1 week the perchlorate **59b** starts to crystallize as large colorless plate (1.90 g, 9.5 mmol, 95 %). (Method 2) A Schlenk flask was loaded with **55** (1000.8 mg, 10 mmol) and dry methanol (15 mL) was added via a syringe. Concentrated perchloric acid (837 mg, 10 mmol, 70%) was carefully added. The colorless homogenous reaction mixture was stirred for one hour at ambient temperature. Excellent crystals were formed from concentrated methanol solution layered with diethyl ether (1.85 g, 9.3 mmol, 93 %). m.p. 97-98 °C; (KBr, cm^{-1}): $\tilde{\nu}$ = 3416 (s), 3319 (s), 3151 (s), 3094 (s), 1718 (vs), 1616 (m), 1563 (w), 1509 (vw), 1338 (m), 1290 (m), 1145 (vs), 1109 (vs), 1090 (vs), 1013 (m), 941 (m), 781 (vw), 756 (m), 703 (m), 688 (m), 653 (m), 636 (s), 627 (s), 572 (m); Raman (200mW, 25 °C, cm^-

[1]): $\tilde{\nu}$ = 3295 (4), 3219 (3), 1725 (4), 1637 (6), 1585 (3), 1512 (6), 1445 (7), 1316 (19), 1134 (8), 1076 (7), 1036 (7), 1004 (6), 926 (100), 785 (64), 689 (9), 626 (18), 462 (27) 456 (27), 305 (22), 257 (7), 141 (15); ^{1}H NMR (CD_3OD, 25°C) δ: 5.21 (s, -NH, NH_2); ^{13}C NMR (CD_3OD, 25°C) δ: 149.7; ^{14}N NMR (CD_3OD, 25°C) δ: -30 (N3, N2, $\Delta\nu_{1/2}$ = 1936 Hz), -179 (*N*1-NH_2, *N*4-H, $\Delta\nu_{1/2}$ = 1329 Hz), -346 (N1-*N*H_2, C-*N*H_2, $\Delta\nu_{1/2}$ = 1214 Hz); ^{15}N NMR (CD_3OD, 25°C) δ: -20.5 (N3), -36.6 (N2), -169.4 (*N*1-NH_2), -177.5 (N*4*-H), -317.9 (N1-*N*H_2), 329.6 (C-*N*H_2); ^{35}Cl NMR (CD_3OD) δ: 1.01 (s, ClO_4^-); *m/z* (FAB^+, xenon, 6keV, m-NBA matrix) 101 $[DAT+H]^+$; $CH_5N_6ClO_4$ (200.54): calcd. C, 5.6; H, 2.5; N, 41.9 %; found: C, 5.9; H, 2.8; N, 41.5 %.

Synthesis of 1,5-Diamino-4-methyl-1*H*-tetrazolium iodide (61a). To a solution of **55** (1.50 g, 15 mmol) in 50 mL of MeCN was added an excess of MeI (6.4 mL, 90 mmol) and refluxed for 14h. The color of the reaction mixture turned from colorless to deep red. Colorless crystals start to separate from the cold solution after 5 days (750 mg, 20 %). Another crop of the product was obtained by evaporation of the mother liquor *in vacuo* to half of its volume (2,4 g, 66 %); Total yield (86 %). (KBr, cm^{-1}): $\tilde{\nu}$ = 3215 (s), 3068 (s), 1702 (vs), 1613 (m), 1571 (w), 1445 (w), 1426 (w), 1392 (m), 1368 (w), 1245 (w), 1197 (w), 1117 (w), 1031 (m), 1001 (w), 913 (vw), 787 (w), 773 (w), 707 (vw), 671 (vw), 634 (w), 606 (w), 586 (m), 528 (w); Raman (200mW, 25 °C, cm^{-1}) $\tilde{\nu}$ = 3243 (19), 3168 (20), 3020 (7), 2940 (25), 1700 (6), 1613 (6), 1572 (7), 1524 (6), 1445 (5), 1424 (5), 1390 (11), 1369 (24), 1190 (5), 1116 (6), 1025 (13), 998 (4), 788 (64), 602 (15), 545 (5), 412 (6), 308 (9), 292 (11), 275 (7), 182 (11) ; ^{1}H NMR ([d6]-DMSO, 25°C) δ: 3.84 (s, CH_3), 7.01 (s, C-NH_2), 8.97 (s, N-NH_2) ; ^{13}C NMR ([d6]-DMSO, 25°C) δ: 39.9 (CH_3), 148.0 (C); ^{15}N NMR ([d6]-DMSO, 25°C) δ: -24.2 (N3), -35.5 (N2), -167,8 (*N*1-NH_2), -215.6 (N*4*-Me), -309.1 (N1-*N*H_2), 320.0 (C-*N*H_2); *m/z* (FAB^+, xenon, 6keV, m-NBA matrix): 115 $[MeDAT]^+$; $C_2H_7IN_6$ (242.02): calc. C, 9.9; H, 2.9; N, 34.7 %; found: C, 9.8; H, 2.9; N, 34.8 %.

Synthesis of 1,5-Diamino-4-methyl-1*H*-tetrazolium nitrate (61b). To a solution of **61a** (1.21 g, 5 mmol) in 15 mL of MeOH/MeCN (1:1) was added $AgNO_3$ (0.85 g, 5 mmol) and stirred for 30 min in the dark. After removal of AgI the solvents were evaporated *in vacuo* and the residue recrystallized from MeOH/Et_2O (728 mg, 4.7 mmol, 93 %). m.p. 121-122 °C; IR (KBr, cm^{-1}): $\tilde{\nu}$ = 3406 (vw), 3256 (w), 3216 (m), 3045 (s), 1699 (vs), 1614 (m), 1584 (vw), 1384 (vs; - NO_3^-), 1356 (vw), 1261 (w), 1198 (w), 1115 (w), 1036 (m), 1006 (w), 911 (m), 832 (w), 787 (vw), 774 (m), 670

(w), 635 (w), 605 (w), 579 (m), 525 (w); Raman (200mW, 25 °C, cm^{-1}) $\tilde{\nu}$ = 3312 (5), 3208 (5), 3046 (4), 2965 (12), 1705 (2), 1634 (4), 1607 (3), 1531 (5), 1459 (5), 1376 (19), 1250 (2), 1122 (4), 1049 (100), 985 (3), 871 (1), 793 (69), 721 (7), 609 (17), 326 (10), 304 (6), 193 (7), 131 (7); ^{1}H NMR (CD_3OD, 25°C) δ: 3.92 (s, CH_3), 4.87 (s, C-NH_2, N-NH_2); ^{13}C NMR (CD_3OD, 25°C) δ: 33.6 (CH_3), 148.1 (C); ^{14}N NMR (CD_3OD, 25°C) δ: -33.0 (N2,N3, $\Delta\nu_{1/2}$ = 1600 Hz), -190.6 (*N*1-NH_2, $\Delta\nu_{1/2}$ = 1480 Hz) -334.0 (N1-*N*H_2, C-*N*H_2 $\Delta\nu_{1/2}$ = 910 Hz); *m/z* (FAB^+, xenon, 6keV, m-NBA matrix): 115 $[MeDAT]^+$; *m/z* (FAB^-, xenon, 6keV, m-NBA matrix): 62 $[NO_3]^-$; $C_2H_7N_7O_3$ (177.15): calcd. C, 13.6; H, 4.0; N, 55.4 %; found: C, 13.4; H, 3.8; N, 55.1 %.

Synthesis of 1,5-Diamino-4-methyl-1*H*-tetrazolium dinitramide (61c). To a solution of **61a** (1.21 g, 5 mmol) in 20 mL of MeCN under N_2 was added a solution of $AgN(NO_2)_2$ in 15 mL of MeCN (1070 mg, 5 mmol).[94] After 1 hour the precipitated AgI was removed by filtration and the solution concentrated to half of its volume. The solution was layered with Et_2O and kept in the refrigerator. Crystals deposit in the course of one week (940 mg, 4.3 mmol, 85%). m.p. 85-86°C; IR (KBr, cm^{-1}): $\tilde{\nu}$ = 3335 (s), 3282 (s), 3245 (s), 3198 (s), 3141 (s), 1709 (vs), 1632 (m), 1592 (w), 1526 (vs), 1422 (vs), 1374 (m), 1322 (m), 1170 (vs, br), 1018 (vs), 961 (m), 944 (m), 819 (m), 791 (m), 780 (m), 764 (m), 738 (m), 705 (m), 665 (vw), 603 (m), 581 (m), 523 (w); Raman (200mW, 25 °C, cm^{-1}) $\tilde{\nu}$ = 3334 (9), 3284 (11), 3227 (10), 3047 (4), 2966 (12), 1708 (5), 1633 (7), 1589 (6), 1526 (9), 1402 (14), 1375 (23), 1322 (65), 1252 (4), 1165 (6), 1123 (7), 1049 (35), 1018 (12), 946 (10), 822 (36), 792 (100), 764 (8), 721 (3), 602 (20), 483 (21), 456 (7), 302 (22), 276 (12), 132 (21); ^{1}H NMR (CD_3OD, 25°C) δ: 3.91 (s, CH_3), 4.82 (s, C-NH_2, N-NH_2); ^{13}C NMR (CD_3OD, 25°C) δ: 34.9 (CH_3), 149.3 (C); ^{14}N NMR (CD_3OD, 25°C) δ: -12.4 (N(*N*$O_2)_2^-$, $\Delta\nu_{1/2}$ = 60 Hz), -60.4 (N3, N2, $\Delta\nu_{1/2}$ = 850 Hz), -189.9 (*N*1-NH_2, *N*4-Me, *N*$(NO_2)_2^-$, $\Delta\nu_{1/2}$ = 1120 Hz), -334.0 (N1-*N*H_2, C-*N*H_2 $\Delta\nu_{1/2}$ = 950 Hz); *m/z* (FAB^+, xenon, 6keV, m-NBA matrix): 115 $[MeDAT]^+$; *m/z* (FAB^-, xenon, 6keV, m-NBA matrix): 106 $[N(NO_2)_2]^-$; $C_2H_7N_9O_4$ (221.14): calc. C, 10.9; H, 3.2; N, 57.0 %; found: C, 11.1; H, 3.3; N, 56.4 %.

Synthesis of 1,5-Diamino-4-methyl-1*H*-tetrazolium azide (61d). To a solution of **61a** (1.21 g, 5 mmol) in 30 mL of H_2O was added an excess of AgN_3 (1.125g, 7,5 mmol) and stirred for 24h in the dark. After removing the excess AgN_3 and AgI the water was evaporated *in vacuo* and the residue recrystallized from EtOH/Et_2O (616 mg, 4 mmol, 90 %). m.p. 135-137 °C (decomp.);

IR (KBr, cm^{-1}): $\tilde{\nu}$ = 3264 (s, br), 3118 (s, br), 2939 (s, br), 2036 (vs), 1705 (vs), 1626 (s), 1454 (w), 1422 (w), 1395 (m), 1372 (w), 1345 (w), 1245 (w), 1191 (w), 1120 (w), 1033 (w), 1004 (w), 911 (vw), 792 (m), 734 (vw), 683 (s), 628 (m), 601 (w), 534 (w), 467 (w); Raman (200mW, 25 °C, cm^{-1}) $\tilde{\nu}$ = 3251 (11), 3173 (15), 3012 (9), 2950 (24), 1708 (15), 1604 (17), 1525 (16), 1426 (16), 1395 (21), 1375 (33), 1340 (33), 1250 (17), 1194 (11), 1122 (14), 1031 (14), 871 (1), 793 (100), 630 (11), 606 (28), 343 (27), 306 (14), 280 (14), 180 (64) ; ^{1}H NMR ([d6]-DMSO, 25°C) δ: 3.77 (s, CH_3), 4.81 (s, C-NH_2), 6.82 (s, N-NH_2); ^{13}C NMR ([d6]-DMSO, 25°C) δ: 33.8 (CH_3), 147.5 (C); ^{14}N NMR ([d6]-DMSO, 25°C) δ: -133.2 (N_β, $\Delta\nu_{1/2}$ = 120 Hz), -277.6 (N_α, $\Delta\nu_{1/2}$ = 320 Hz); ^{15}N NMR (CD_3OD, 25°C) δ: -23.5 (N3), -34.7 (N2), -134.4 (N_β), -169,2 (*N*1-NH_2), -187.4 (N*4*-H), -282.8 (N_α -323.7 (N1-*N*H_2), 331.2 (C-*N*H_2); *m/z* (FAB$^+$, xenon, 6keV, m-NBA matrix): 115 [MeDAT]$^+$; *m/z* (FAB$^-$, xenon, 6keV, m-NBA matrix): 42 [N3]$^-$; $C_2H_7N_9$ (157.17): calc. C, 15.2; H, 4.5; N, 80.2 %; found: C, 15.0; H, 4.5; N, 80.1 %.

X-ray Analyses. Crystals were obtained as described above. X-ray quality crystals of **59a** (CCDC 261253) were mounted in a Pyrex capillary and the X-ray crystallographic data collected on a Nonius Mach3 diffractometer with graphite-monochromated MoK_α radiation (λ = 0.71073 Å). The X-ray crystallographic data for **59b** (CCDC 261252), **61a** (CCDC 261254) and **61b** (CCDC 261255) were collected on a SIEMENS P4 diffractometer equipped with a Siemens CCD area detector, and for **61d** (CCDC 261459), data were collected on a Nonius Kappa CCD diffractometer using graphite-monochromated MoK_α radiation (λ = 0.71073 Å). Unit cell parameters for **59a** were obtained from setting angles of a minimum of 25 carefully centered reflections having $2\theta > 20°$; the choice of the space group was based on systematically absent reflections and confirmed by the successful solution and refinements of the structures. The structures were solved by direct methods (SHELXS-86, SHELXS-97)[95] and refined by means of full-matrix least-squares procedures using SHELXL-93 and SHELXL-97. Empirical absorption correction by Psi-scans was used for **59b**. In the case of **59b**, **61a** and **61b** numerical absorption correction by SADABS and for **61d** XRed was used. Crystallographic data are summarized in *Appendix B*. Selected bond lengths and angles are available in *Table 4.3*. All non-hydrogen atoms were refined anisotropically. In the case of **59a** the hydrogen atoms were included at geometrically idealized positions and refined. They were assigned fixed isotropic temperature factors with the value of $1.2B_{eq}$ of the atom to which they were bonded. The hydrogen atoms of compound **59b**, **61a**, **61b** and **61d** were located from difference electron-density map and refined isotropically. In the case of **61a** and **61d** the hydrogen atoms of the methyl group were inserted in idealized position and were refined riding on the atom to which they were bonded (fixed isotropic temperature factors with the value of $1.2B_{eq}$).

3. References

[1] Kozyro, A. A.; Simirsky, V. V.; Krasulin, A. P.; Sevruk, V. M.; Kabo, G. J.; Frenkel, M. L.; Gaponik, P. N.; Grigotiev, Yu. V. *Zhurn. Fiz. Khim.* **1990**, *64*, 656 (in Russian).

[2] a) Levchik, S. V.; Balabanovich, A. I.; Ivashkevich, O. A.; Lesnikovich, A. I.; Gaponik, P. N. Costa, L. *Thermochim. Acta* **1992**, *207*, 115; b) Levchik, S. V.; Balabanovich, A. I.; Ivashkevich, O. A.; Lesnikovich, A. I.; Gaponik, P. N. Costa, L. *Thermochim. Acta* **1993**, *255*, 53; c) Lesnikovich, A. I.; Ivashkevich, O. A.; Levchik, S. V.; Balabanovich, A. I.; Gaponik, P. N.; Kulak, A. A. *Thermochim. Acta* **2002**, *388*, 233; d) Gao, A.; Oyumi, Y.; Brill, T. B. *Combust. Flame* **1991**, *83*, 345; e) Levchik, S. V.; Balabanovich, A. I.; Ivashkevich, O. A.; Gaponik, P. N.; Costa, L. *Polym. Degrad. Stability* **1995**, *47*, 333.

[3] a) Sinditskii, V. P.; Fogelzang, A. E. *Russ. Khim. Zh.* **1997**, *4*, 74; b) Gaponik, P. N.; Karavai, V. P. *Khim. Geterotsikl. Soedin.* **1984**, 1388.

[4] a) Gaponik, P. N.; Karavai, V. P. *Khim. Geterotsikl. Soedin.* **1984**, 1388; b) Willer, R. L.; Henry, R. A. *J. Org. Chem.* **1988**, *53(22)*, 5371.

[5] Raap, R. *Can. J. Chem* **1969**, *47(19)*, 3677.

[6] Stollé, R.; Netz, H.; Kramer, O.; Rothschild, S.; Erbe, E.; Schick, O. *J. Prak. Chem.* **1933**, *138*, 1.

[7] a) Hammerl, A.; Holl, G.; Kaiser, M.; Klapötke, T. M.; Mayer, P.; Nöth, H.; Piotrowski, H.; Suter, M. *Z. Naturforsch.* **2001**, *56 b*, 857; b) Hammerl, A.; Holl, G.; Klapötke, T. M.; Mayer, P.; Nöth, H.; Piotrowski, H.; Warchhold, M. *Eur. J. Inorg. Chem.* **2002**, *4*, 834; c) Geith, J; Klapötke, T. M.; Weigand, J.; Holl, G. *Prop. Explos. Pyrotech.* **2004**, *29(1)*, 3.

[8] Mathieu, D.; Bougrat, P. *Chem. Phys. Lett.* **1999**, *303*, 601.

[9] a) Rousseau, E.; Mathieu, D. *J. Comput. Chem.* **2000**, *21*, 367; b) Audoux, J.; Beaucamp, S.; Mathieu, D.; Poullain, D. *35th Int. Annual Conference of ICT* **2004**, *Karlsruhe*, pp. 33/1.

[10] a) Tartakovsky, V. A.; Luk'yanov, O. A. *25th Int. Annual Conference of ICT* **1994**, *Karlsruhe*, pp. 13/1; b) VanSteen, H. H.; Kodde, A. M. *Prop. Explos. Pyrotech.* **1990**, *15(2)*, 58; c) Patil, D. G.; Jain, Brill, T. B. *Prop. Explos. Pyrotech.* **1992**, *17(3)*, 99; d) van Niekerk, A. P.; Brower, K. R. *Prop. Explos. Pyrotech.* **1995**, *20(5)*, 273.

[11] a) Klapötke, T. M.; White, P. S.; Tornieporth-Oetting, I. C.; *Polyhydron* **1996**, *15*, 2597; b) Holfter, H.; Klapötke, T. M.; Schulz, A. *Eur. J. Solid State* **1996**, *33*, 855.

[12] a) Habereder, T.; Hammerl, A.; Holl, G.; Klapötke, T. M.; Knizek, J.; Nöth, H. *Eur. J. Inorg. Chem.* **1999**, *5*, 849; b) Habereder, T.; Hammerl, A.; Holl, G.; Klapötke, T. M.; Mayer, P.; Nöth, H. *31th Int. Annual Conference of ICT* **2000**, *Karlsruhe*, pp. 150/1; c) Hammerl, A.; Holl, G.; Hübler, K.; Klapötke, T. M.; Mayer, P. *Eur. J. Inorg. Chem.* **2001**, 755; d) Hammerl, A.; Holl, G.; Kaiser, M.; Klapötke, T.M.; Mayer, P.; Nöth, H.; Warchhold, M. *Z. Anorg. Allg. Chem.* **2001**, *627*, 1471; e) Hammerl, A.; Holl, G.; Kaiser, M.; Klapötke, T.M.; Kränzle, R.; Vogt, M. *Z. Anorg. Allg. Chem.* **2002**, *628*, 322.

[13] Desiraju, G. R. *Crystal Engineering: The Design of Organic Solids* **1989**, Amsterdam, Elsevier.

[14] Alle, F. H.; Raithby, P. R.; Schields, G. S.; Taylor, R. *Chem. Commun.* **1998**, 1043.

[15] Klapötke, T. M.; Mayer, P.; Schulz, A.; Weigand, J. J. *J. Am. Chem. Soc.* **2005**, *127*, 2032.

[16] Katrusiak, A. *Acta Cryst.* **1994**, *C50*, 1161.

[17] a) Etter, M. C. *Acc. Chem. Res.* **1990**, *23*, 120; b) Etter, M. C.; MacDonald, J. C. *Acta Cryst.* **1990**, *B46*, 256.

[18] Akella, A.; Keszler, D. *Acta Cryst.* **1994**, *C50*, 1974.

[19] Denver, M. v.; Heeb, G.; Klapötke, T. M.; Kramer, G.; Spieß, G.; Welch, J. M. *Prop. Explos. Pyrotech.* **2005**, *30(3)*, 191.

[20] Drake, G.; Hawkins, T.; *AFRL/PRSP AFOSR Ionic Liquids Workshop*. March **2004**. Tampa, Fl.

[21] Matulis, V. E.; Lyakhov, A. S.; Gaponik, P. N.; Voitekhovich, S. V.; Ivashkevich, O. A. *J. Mol. Struc.* **2003**, *649*, 309.

[22] Lieber E.; Levering, D. R. *J. Am. Chem. Soc.* **1951**, *73*, 1313.

[23] a) Hammerl, A.; Klapötke, T. M.; Nöth, H.; Warchold, M. *Prop. Explos. Pyrotech.* **2003**, *28(4)*, 174; b) Hammerl, A.; Klapötke, T. M.; Mayer, P.; Weigand, J. J. *Prop. Explos. Pyrotech.* **2005**, *30(1)*, 17.

[24] Lieber, E.; Smith, G. B. L. *Chem. Rev.* **1939**, *25*, 213.

[25] Perrott, J. R.; Stedman, G.; Uysal, N. *Dalton Trans.* **1976**, *20*, 2058.

[26] Milcent, R.; Redeuilh, C.; *J. Heterocycl. Chem.* **1980**, *17*, 1691.

[27] Haussen, L. D.; Baca, E. J.; Scheiner, P.; *J. Heterocycl. Chem.* **1970**, *7*, 991.

[28] Drake, G.; Hawkins, T.; Brand, A.; Hall, L.; Mckay, M. *Prop. Explos. Pyrotech.* **2003**, *28(4)*, 174.

[29] a) Welton, T. *Chem. Rev.* **1999**, *99*, 2071; b) Wasserscheid, P.; Keim, W.; *Angew. Chem.* **2000**, *112*, 3926; c) Wilkes, J. S.; *Green Chem.* **2002**, *4*, 73.

[30] a) Williamson, K.; Li, P.; Devlin, J. P. *J. Chem. Phys.* **1968**, *48*, 3891; b) Fernandes, J. R.; Ganguly, S.; Rao, C. N. R. *Spectrochim. Acta.* **1979**, *35A*, 1013.

[31] a) Cohn, H. *J. Chem. Soc.* **1952**, 4282; b) Redlich, P.; Holt, J.; Biegeleisen, T. *J. Am. Chem. Soc.* **1944**, *66*, 13; c) Grothe, H.; Willner, H. *Angew. Chem.*, **1996**, *108*, 816.

[32] Christe, K. O. ; Wilson, W. W.; Petrie, M. A.; Michels, H. H.; Bottaro, J. C.; Gilardi, R. *Inorg. Chem.* **1996**, *35*, 5068.

[33] Müller, U. *Structur and Bonding.* **1974**, *14*, 141.

[34] Lyakhov, A. S.; Gaponik, P. N.; Voitekhovich, S. V. *Acta Cryst.* **2001**, *C57*, 185.

[35] a) Markgraf, J. H.; Sadighi, J. P. *Heterocycles* **1995**, *40(2)*, 583; b) Claramunt, R. M.; Sanz, D.; López, C.; Jiménez, J. A.; Jimeno, M. L.; Elgueor, J.; Fruchier, A. *Magn. Reson. Chem.* **1997**, *35(1)*, 35.

[36] a) A. M Orendt, J. Michl. J. Reiter, *Magn. Reson. Chem.* **1989**, *27*, 1; b) N. Naulet, D. Tomé, G. J. Martin, *Magn. Reson. Chem.* **1983**, *21(9)*, 564.

[37] Stefaniak, L; Roberts, J. D.; Witanowski, M; Webb, G. A. *Org. Magn. Reson.* **1984**, *22*, 209.

[38] Garrone, A.; Fruttero, R.; Tironi, C.; Gasco, A. *J. Chem. Soc., Perkin Trans. 2* **1989**, 1941.

[39] Fritz, H. *Bull. Soc. Chim. Belg.* **1984**, *93*, 559.

[40] Sveshnikov, N. N.; Nelson, J. H. *Magn. Reson. Chem.* **1997**, *35(3)*, 209.

[41] Kalinowski, H.-O.; Berger, S.; Braun, S. *^{13}C-NMR-Spektroskopie*, Georg Thieme Verlag Stuttgart, New York, **1984**.

[42] a) Foces-Foces, C.; Cano, F. H.; Claramunt, R. M.; Sanz, D.; Catalan, J.; Fabero, F.; Fruchier, A.; Elguero, J. *J. Chem. Soc. Perkin Trans. 2.* **1990**, 237; b) Claramunt, R. M.; Sanz, D.; Catalán, J; Fabero, F.; Garcia, N. A.; Foces-Foces, C.; Llamas-Saiz, A. L.; Elguero, J. *J. Chem. Soc. Perkin Trans. 2.* **1993**, 1687.

[43] Infantes; L. Foces-Foces, C.; Cabildo, P.; Claramunt, R. M.; Mó, O.; Yáñez, M.; Elguero, J. *Heterocycles.* **1998**, *49*, 157.

[44] Harmony, M. D.; Laurie, V. W.; Kuczkowski, R. L.; Schwedeman, R. H.; Ramsay, D. A.; Lovas, F. L.; Lafferty, W. J.; Maki, A. G. *J. Phys. Che,. Ref. Data 8* **1979**, 619.

[45] a) Asath Bahadur, S.; Rajaram, R. K.; Nethaji, M. *Acta Cryst.* **1991**, *C47*, 1420, b) Wojtczak, A.; Jaskólski, M.; Kosturkiewicz, Z. *Acta Cryst.* **1988**, *C44*, 1779; c) a) Alfonso, M.; Wang, Y.; Stoeckli-Evans, H. *Acta Cryst.* **2001**, *C57*, 1184; d) Shao, S.-C.; Zhu, D.-R.; Zhu, X.-H.; You, X.-Z.; Shanmuga Sundara Raj, S.; Fun, H.-K. *Acta Cryst.* **1999**, *C55*, 1412.

[46] Bondi, A. *J. Phys. Chem*. **1964**, **68,** 441.

[47] Spek, A. L. *J. Appl. Cryst.* **2003**, *36*, 7.

[48] a) Piacenza, G.; Legsai, G.; Blaive, B.; Gallo, R. *J. Phys. Org. Chem.* **1996**, *9*, 427; b) Immirzi, A.; Perini, B. *Acta Cryst.* **1977**, *A33*, 136; c) Ammon, L.; Mitchel, S. *Prop. Explos. Pyrotech.* **1998**, *23(4)*, 260.

[49] a) Bottaro, J. C.; Penwell, P. E.; Schmitt, R. J. *J. Am. Chem. Soc.* **1997**, *119(40)*, 9405; b) Gilardi, R.; Flippen-Anderson, J.; Georg, C.; Butcher, R. J. *J. Am. Chem. Soc.* **1997**, *119(40)*, 9411; c) Sitzmann, M. E.; Gilardi, R.; Butcher, R. J.; Koppes, W. M.; Stern, A. G.; Trasher, J. S.; Trivedi, N. J.; Yang, Z.-Y. *Inorg. Chem.* **2000**, *39(4)*, 843; d) Martin, A.; Pinkerton, A. A.; Gilardi, R. D.; Bottaro, J. C. *Acta Crystallogr.* **1997**, *B53*, 504.

[50] Bader, R. F. W. *Atoms in Molecules: A Quantum Theory*; The international Series of Monographs of Chemistry; Oxford University Press, **1990**.

[51] N-N values and N=N values from: *International Tables for X-ray Crystallography*; Kluwer Academic Publisher: Dordrecht, **1992**; Volume C.

[52] For NPA charges see *Appendix A Table A-5*. NPA charges give a similar picture and exactly the same amount of charge transfer.

[53] Bader, R. F. W. *Chem. Rev.* **1991**, *91*, 893.

[54] For nomenclature definitions of critical points see ref. 50.

[55] Zhurova, E.A.; Tsirelson, V. G.; Stash, A. I. Pinkerton, A. *J. Am. Chem. Soc.* **2002**, *124*, 4574 and references therein.

[56] Bianchi, R.; Gervasio, G.; Marabello, D. *Inorg. Chem.* **2000**, *39*, 2360.

[57] Bader, R. F. W.; Essen, H. *J. Chem. Phys.* **1984**, *80*, 1943.

[58] Klapötke, T. M.; Rienacker, C. M.; Zewen, H. *Z. Anorg. Allg. Chem.* **2002**, *628*, 2372.

[59] a) Curtis, L. A.; Head-Gordon, M.; Fox, D. J.; Ragahavachari, K.; Pople, J. A. *J. Chem. Phys.* **1989**, *90*, 5622; b) Curtiss, L. A.; Ragahavachari, K.; Trucks, G. W.; Pople, J. A. *ibid.* **1991**, *94*, 7221; c) Curtiss, L. A.; Ragahavachari, K.; Redfern, P. C.; Pople, J. A. *ibid.* **1998**, *109*, 42.

[60] Curtiss, L. A.; Ragahavachari, K.; Redfern, P. C.; Pople, J. A. *J. Chem. Phys.* **1998**, *109*, 7764.

[61] Jenkins, H. D. B.; Tudeal, D.; Glasser, L. *Inorg. Chem.* **2002**, *41(9)*, 2364.

[62] Michels, H. H.; Montgomery, Jr. J. A. *J. Phys. Chem.* **1993**, *97*, 6602.

[63] *NIST Chemistry WebBook*, NIST Standard Reference Database Number 69 – March, 2003 Release, www version://webbook.nist.gov/chemistry/.

[64] Cox, J. D.; Wagman, D. D.; Medvedev, V. A. *CODATA Key Values for Thermodynamics*, *Hemisphere Publishing Corp.*, New York, **1984**, p. 1.

[65] Chase, M.W., Jr., NIST-JANAF Themochemical Tables, Fourth Edition*, J. Phys. Chem. Ref. Data, Monograph 9,* **1998**, 1.

[66] Akhavan, J. *The Chemistry of Explosives*, RCS Paperbacks, Cambridge, **1998**.

[67] a) Kamlet, M. J.; Jacobs, S. J. *J. Chem. Phys.* **1968**, *48*, 23; b) Kamlet, M. J.; Ablard, J. E. *J. Chem. Phys.* **1968**, *48*, 36; c) Kamlet, M. J.; Dickinson, C. *J. Chem. Phys.* **1968**, *48*, 43; d) Eremenko, L. T.; Nesterenko, D. A. *Chem. Phys. Reports.* **1997**, *16*, 1675; e) Astakhov, A. M.; Stepanov, R. S.; Babushkin, A. Y. *Combust. Explos. Shock Waves.* **1998**, *34*, 85, (Engl. Transl.).

[68] with K = 15.58, ρ [g cm^{-3}]; $\varphi = N\sqrt{M(-\Delta_E H)}$; N = moles of gases per g of explosives; M = average molar mass of formed gases; $\Delta_E H$ = calculated enthalpy of detonation (in cal g^{-1}); A = 1.01; B = 1.30.

[69] Mader, C. L.; "Detonation Properties of Condensed Explosives Computed Using the Becker-Kistiakowsky-Wilson Equation of State," *Los Alamos Scientific Laboratory* **1963**, Rept. LA-2900.

[70] Köhler, J.; Mayer, R. Explosivstoffe, 7. Aufl., Wiley-VCH, **1991**, Weinheim.

[71] a) Test methods according to the UN Recommendations on the Transport of Dangerous Goods, Manual of Tests and Criteria, fourth revised edition, United Nations Publication, New York and Geneva, **2003**, ISBN 92-1-139087-7, Sales No. E.03.VIII.2.; b) 13.4.2 Test 3(a)(ii) BAM Fallhammer.

[72] WIWEB, private communications.

[73] Standard Test Methods for Mol Percent Impurity by DSC. *ASTM designation E928-96*, **2003**.

[74] Stoner, C. E.; Brill, T.B. *Combust. Flame* **1991**, *83*, 302.

[75] Costa, L.; Camino, G. *J. Therm. Anal.* **1988**, *34*, 423.

[76] Standard Test Methods for Arrhenius Kinetic Constants for Thermally Unstable Materials. *ASTM designation E698-99*, **1999**.

[77] Levchick, S. V.; Balabanovich, A. I.; Ivashkevich, O. A.; Lesnikovich, A. I.; Gaponik, P.N.; Costa, L. *Thermochim. Acta* **1993**, *225*, 53.

[78] a) Behringer, H.; Fischer, H. J. *Chem. Ber.* **1962**, *95*, 2546; b) Sapssov, A.; Golovinsky, E.; Demirov, C. *Chem. Ber.* **1999**, *99*, 3734.

[79] a) Levchick, S. V.; Balabanovich, A. I.; Ivashkevich, O. A.; Lesnikovich, A. I.; Gaponik, P. N.; Costa, L. *Thermochim. Acta* 1992, *207*, 115; b) Juergens, B.; Irran, E.; Senker, J.; Kroll, P.; Muller, H.; Schnick, W. *J. Am. Chem. Soc.* **2003**, *125(34)*, 10288.

[80] Shimanouchi, T. *Tables of Molecular Vibrational Frequencies Consolidated* Volume II, J. Phys. Chem. Ref. Data **1972**, *6(3)*, 993.

[81] Milligan, D. E.; Jacox, M. E. *J. Chem. Phys.* **1975**, *56*, 333.

[82] Shimanouchi, T. *Tables of Molecular Vibrational Frequencies Consolidated* Volume I, National Bureau of Standards 1, **1972**.

[83] Brand, C. D.; Cawthon, T. M. *J. Am. Chem. Soc.* **1955**, *77*, 319.

[84] a) Nakamoto, K. *Infrared and Raman Spectra of Inorganic and Coodination Compounds*, 4th ed.; Wiley & Sons: New York, Chichester, Brisbane, Toronto, Singapore, **1986**.

[85] Mecke, R.; Langenbucher, F. Infrared Spectra, Heyden & Son, **1965**, London, Serial No. 6.

[86] a) Kestila, E.; Haju, M. E. E.; Valkonen, J. *Thermochim. Acta* **1993**, *214*, 67; b) Oyumi, Y.; Brill, T. B. *J. Phys. Chem.* **1985**, *89*, 4325.

[87] Gmelin, L. *Gmelins Handbuch der anorgnischen Chemie*, 8. Aufl. Verlag Chemie, Weinheim, **1971**, Syst.Nr. 14, Teil D1, 347.

[88] Low, M. J. D.; Ramamurthy, P. *J. Res. Inst. Catal.* **1968**, *16(2)*, 535.

[89] Jain, S. R.; Rao, M. V.; Verneker, V. R. *Prop. Explos. Pyrotech.* **1979**, *3*, 761.

[90] Mishra, I. B.; Russell, T. P. *Thermochim. Acta* **2002**, *384*, 47.

[91] Brill, T. B.; Brush, P. J.; Patil, D. J. *Combust. Flame* **1993**, *92*, 178.

[92] Meinhardt, D.; Brewster, G.; Christofferson, S.; Wucherer, E. J. AIAA 98-4006, *34*th AIAA/ASME/SAE/ASEE Joint Propulsion Conference, 13 – 15 July, Cleveland, OH, USA, **1998**.

[93] Anflo, K.; Grönland, T. A.; Wingborg, N. AIAA 2000-3162, *36*th AIAA/ASME/SAE/ASEE Joint Propulsion Conference, 16 – 19 July, Huntsville, AL, USA, **2000**.

[94] How-Ghee, A.; Fraenk, W.; Karaghiosoff, K.; Klapötke, T. M.; Mayer, P.; Nöth, H.; Sprott, J.; Warchhold, M. *Z. Anorg. Allg. Chem.* **2002**, *628*, 2894.

[95] a) Sheldrick, G. M. *SHELXL-86*, *Program for Solution of Crystal Structures*; University of Göttingen: Göttingen, Germany, **1986**; b) Sheldrick, G. M. *SHELXL-97*, *Program for Solution of Crystal Structures*; University of Göttingen: Göttingen, Germany, **1997**; c) Gabe, E. J.; Le Page, Y.; Charland, J.-P.; Lee, F. L.; White, P. S. *J. Appl. Crystallogr.* **1989**, 22, 384; d) XRed, rev. 1.09, Darmstad Germany.

Chapter V

1,4-BIS-[TETRAZOL-5-YL]-1,4-DIMETHYL-2-TETRAZENES

1 Introduction

Although the great strength of the nitrogen-nitrogen triple bond relative to the corresponding double and single bonds (226 *vs.* 100 and 38 Kcal, respectively) strongly militate against the stability of molecules containing catenated nitrogen systems, a substantial number of such structures are in fact known. These range from 3-nitrogen systems such as the azide anion (N_3^-) and 1,3-disubstituted triazenes (RN=N-NHR) through 4-, 5-, 6-, and 7- to 8- and, in one instance, 10-nitrogen chains.[1] Whereas the higher parent "hydro-nitrogens" (H_xN_y) are generally unknown, or, at best, dangerously explosive, their substituted analogues frequently enjoy much greater stability, particularly when aryl substituents are present (*Chapter I, 3*). Among these systems, the linkage of four nitrogen atoms is of special interest as for example many 2-Tetrazenes show unexpected stability. There are five possibilities for the linkage of four di- and/or three-coordinated N-atoms to a chain (*Figure 5.1*). The weakest link in a chain always determines the overall strength, so it is imperative to search for target compounds devoid of any isolated N−N single bonds that cannot gain partial multiple bond character trough resonance with neighboring bonds. Therefore the saturated four-membered chain (*Figure 5.1*, **I**) and the 1-tetrazene (**III**) were excluded as base structure of the synthetic target molecules. Note: Tetrazene (*Chapter I, 1.2*) contains motive **II** (*Figure 5.1*) as base structure. **IV** and **V** has also been excluded.

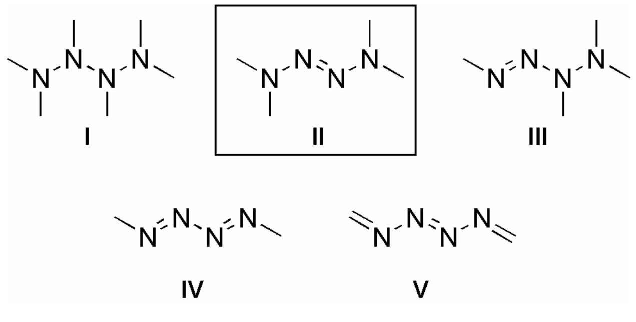

Figure 5.1. Five possibilities for the linkage of four di- and/or three-coordinated N-atoms

2-Tetrazenes were described for the first time in 1878 by E. Fischer,[2] and since then have attracted considerable attention as a source of aminyl radicals and their products.[3,4] The parent

compound, N_4H_4, was generated in 1975 from 1,1,4,4-tetrakis(trimethylsilyl)-2-tetrazene by N. Wiberg *et al.*[5] It is isoelectronic with the butadiene dianion, thus representing an electron-rich compound. The electronic structure of the planar conformation has three occupied π MOs, of which the highest (HOMO) is antibonding. Therefore, the thermodynamically stability of N_4H_4 is closely related to the shape of the π MO's.[6,7] 2-Tetrazenes are expected to show interesting molecular and intramolecular hydrogen bonding, which makes them useful building blocks in (supra)molecular structures and nitrogen-rich polymers.

1.1 Synthesis

Tetrazenes can be prepared by the two methods shown in *Scheme 5.2*. (**A**) Building of nitrogen chains, and (**B**) exchange of substituents (mutual transformation of tetrazenes).

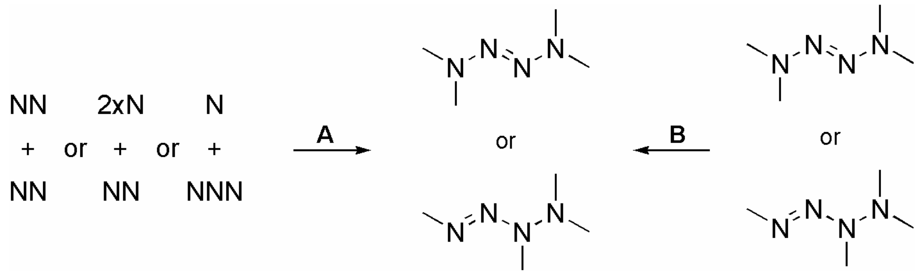

Scheme 5.1. Preparation of tetrazenes

1.1.1 A: Building of Nitrogen Chains

Organic tetrazenes can be formed by the oxidation of 1,1-disubstituted hydrazines (from two "N2"-fragments) by various oxidizing agents: Angeli's salt (Na_2ONNO_2),[8] benzeneselenic acid,[9,10] quinones,[11],[12] Br_2, I_2,[13,14] *t*-BuOCl,[15] HgO, MnO_2,[16,17] $KMnO_4$,[18] $KBrO_3$,[19] $Pb(OAc)_4$ etc.[20]

Tetrazene formation from inorganic diazenes is a general reaction to yield the corresponding silyl derivative **83**. Thus, besides $Me_3Si\text{-}N{=}N\text{-}SiMe_3$ (**82**), other silyldiazenes such as $Me_3Si\text{-}N{=}N\text{-}H$, $Me_3Si\text{-}N{=}N\text{-}SiF_3$ and $Me_2Si(N{=}N\text{-}SiMe_3)_2$ also react by dimerization of the azo system (*Scheme 5.2*).[21] The direct oxidation of the *N,N*-bis(trimethylsilyl)hydrazine (**80**) does not yield the corresponding 2-tetrazene **83**. **80** has to be first transformed to the

corresponding lithium derivative **81**. Oxidation of **81** to the corresponding diazene **82** with subsequently cyclization yields **83**.

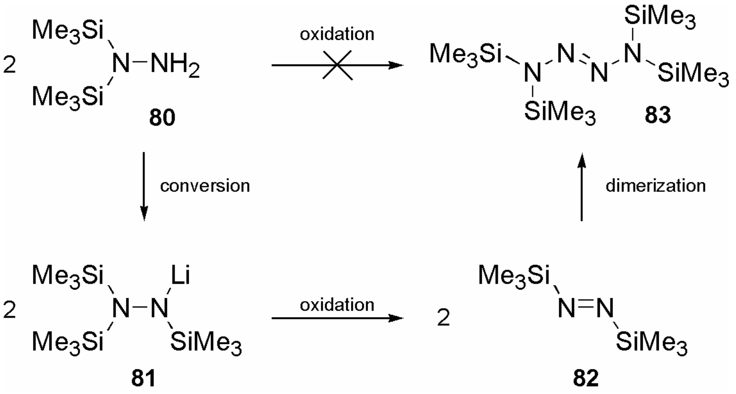

Scheme 5.2. Preparation of tetrakis(trimethylsilyl)-2-tetrazene

Another route to tetrazenes (examples given in *Scheme 4.3*) is the formation of a tetrazene adducts which are obtained from the free ligand and an appropriate metal halide. These tetrazadiene complexes are usually prepared by the treatment of suitable transition metal complexes with organic azides[22] or diazonium salts[23] and can be converted to the 2-tetrazene by adding an appropriate electrophile.

$$Co(C_5H_5)(CO)_2 + 2PhN_3 \longrightarrow Co(C_5H_5)(PhNNNNPh) + N_2 + 2CO$$

$$IrCl(CO)(PPh_3)_2 + 2ArN_2^+ + 2e^- \longrightarrow Ir(ArNNNNAr)(CO)(PPh_3)_2 + Cl^-$$

Scheme 5.3. Tetrazadiene complexes

Beyond these possibilities to form the tetrazenes, it is possible to generate the tetrazenes from two "N1" and one "N2" fragments (*Scheme 5.4*, I) and from one "N3" and one "N1" fragments (*Scheme 5.4*, II).[24,25]

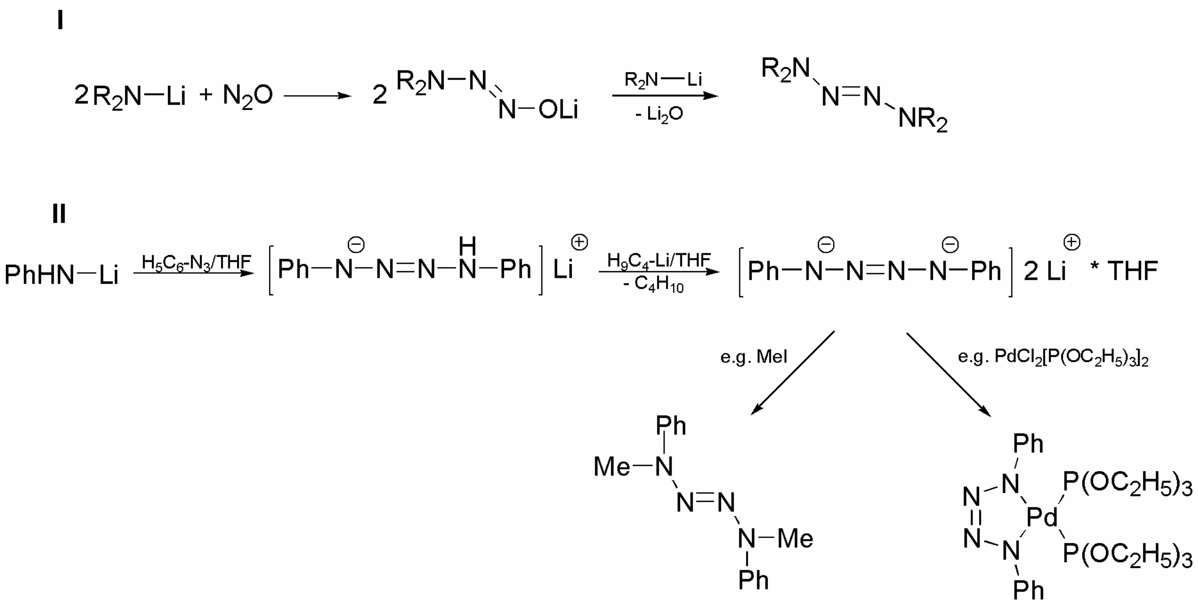

Scheme 5.4. From two "N1" and one "N2" or one "N3" and one "N1" fragment

The latter two synthetic routes are very useful to obtain 2-tetrazenes with different substitution pattern, depending on the electrophiles and amines being used.

1.1.2 **B**: Exchange of substituents

Using partially substituted or unsubstituted tetrazenes, e. g. $(R_3E)_{4-n}N_4H_n$ ($n < 4$; E = C, Si, Ge, Sn; R = (H), Alkyl, Aryl), which can be obtained from the protolysis of the corresponding tetrazenes, other tetrazenes are formed by silylation, germylation, stannylation or nucleophilic reaction with corresponding aryl-, alkyhalids (Scheme 5.5). By carrying out this reaction, it is in many cases advantageous to transform the tetrazenes $(R_3E)_{4-n}N_4H_n$ to tetrazinides $(R_3E)_{4-n}N_4H_{n-m}Li_m$, which react at low temperatures with corresponding reactand *e. g.* dimethyl sulfate Me_2SO_4 or halides like R'_3EX (E = Si, Ge, Sn; X = halogen)[26].

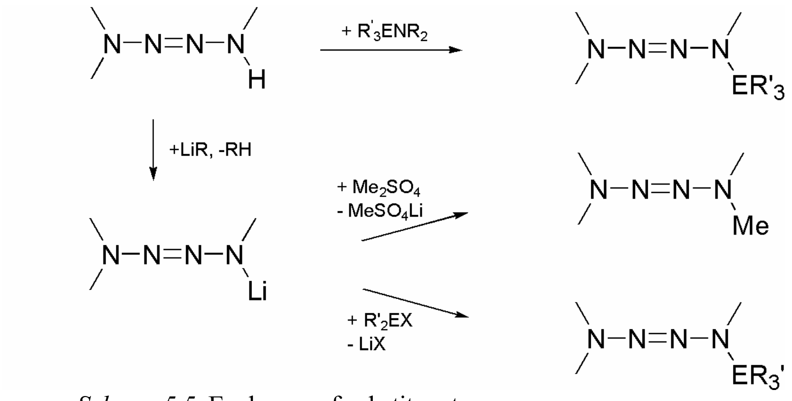

Scheme 5.5. Exchange of substituents

1.2 Stability of 2-tetrazenes

Investigation on thermolysis and photolysis of Group IV derivatives of 2-tetrazenes show that these compounds decompose by free radical mechanism according to Eqs. [1] and [2] (Thermolysis Pathways I and II) as well as by non-free radical pathways [3] and [4] (Thermolysis Pathways III and IV; *Scheme 5.6*). The formed radicals abstracts instantly hydrogen from the chemical environment or react with reactant tetrazene or their thermolysis products. An isomerization of the tetrazene according to a 1,3-migration, photolytic transformation of trans- to cis-2-tetrazene and rotation of the azo-bound amino groups about the N-N single bond can proceed before or run parallel to the thermolysis or photolysis. The activation energies of these thermolysis reactions are often in a comparable range, so that the different reactions proceed side by side. The percentage share of the competing decompositions of the total thermolysis can be changed significantly by changing the reaction conditions.[21a,27]

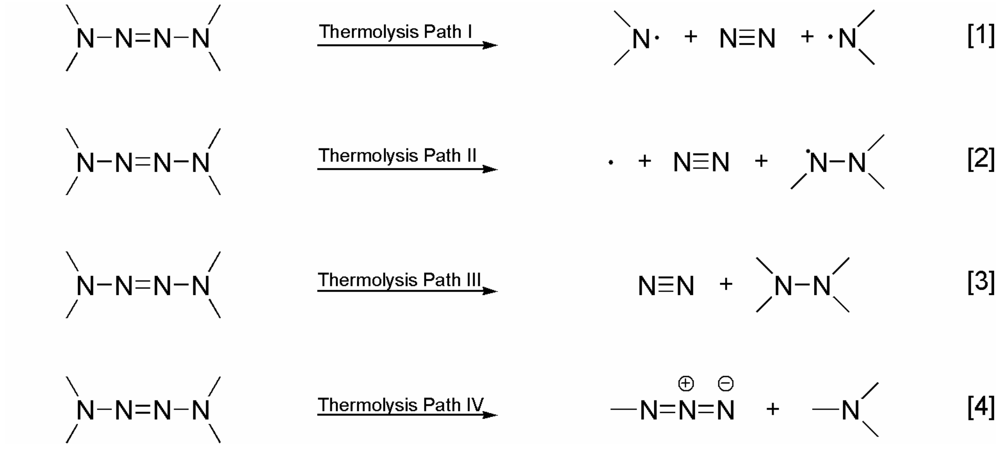

Scheme 5.6. Decomposition pathways of 2-tetrazenes

1.3 1,4-Bis-[1-methyltetrazolyl-5-yl]-1,4-dimethyl-2-tetrazene (**84**)

During the diploma thesis, the permethylated example **84b** of the hitherto unknown 1,4-bis-[tetrazolyl-5-yl]-2-tetrazene (**85**) (*Figure 5.2*) was synthesized.[28]

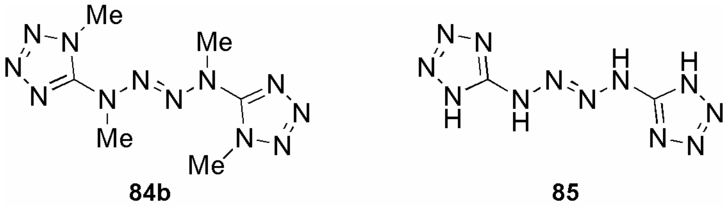

Figure 5.2. 1,4-bis-[tetrazolyl-5-yl]-2-tetrazenes

1,4-bis-[1-methyltetrazol-5-yl)-1,4-dimethyl-2-tetrazene **84b** can be understood as a stable hexamere of diazomethane ($C_6N_{12}H_{12}$ = 6*CH_2N_2) (*Figure 5.2*). It could be derived from a one pot reaction using 1-methyl-5-(methylamino)-1*H*-tetrazole **86** as starting material[29]. In the first step, **86** is converted to the *N*-nitrosoamino-1*H*-tetrazole **87**, which is then reduced by Zn/CH_3COOH to give the corresponding 1,1-substituted hydrazine derivative **88b**. A following *in situ* oxidation, with the help of bromine in concentrated acetic acid (*Scheme 5.7*), gives the desired compound **84b**. Re-crystallization from acetone/chloroform gave colorless rods suitable for single crystal X-ray structure determination.

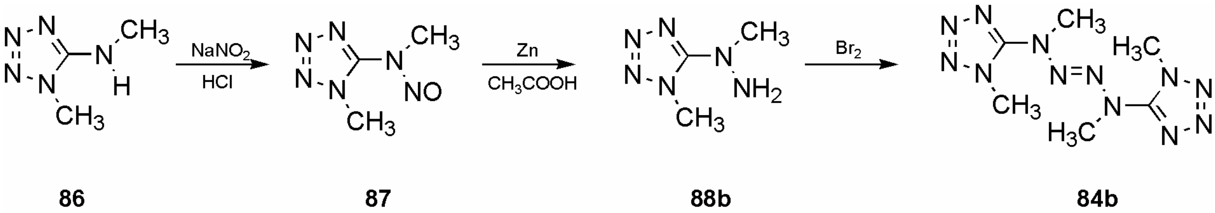

Scheme 5.7. One-pot synthesis of **84**

84b is surprisingly stable and melts without decomposition at 159.8 - 159.9 °C. **84b** is neither sensitive to friction (state force > 360 N), impact (drop hammer test; state energy > 30 Nm) nor heat.[30] Above 180°C, **84b** deflagrates smokeless upon releasing large amounts of N_2. Moreover, **84b** is moderately soluble in several common organic solvents (*e.g.* chloroform, dichlormethane, benzene, acetone and DMSO) upon heating.

Introducing different substituents might result in new compounds, being suitable as phlegmatizers, monomers for energetic polymers or plasticizer, gas generators or *primers*.[31] New strategies to synthesize corresponding 1-substituted (R = H) and 1,1-substituted hydrazine

derivatives are required (**88a-d**). This project only concentrated on the modification of the substituents of the tetrazole moiety (*Figure 5.8*). The preparation of the parent compound (**84a**) and the introduction of the corresponding allyl **(84c)** and *cyclo*-hexyl **(84d)** groups in 4-bis-[1-tetrazol-5-yl)-1,4-dimethyl-2-tetrazene were focused and the isolation of the yet not characterized methyl substituted hydrazine derivative (**88b**) (*Scheme 5.8*).

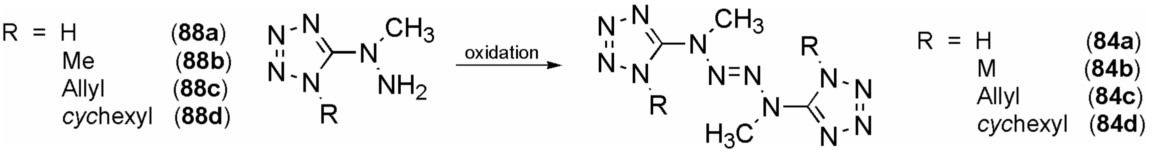

Scheme 5.8. Synthetic targets

2. Substituted hydrazine derivatives

During the investigation of **84b** it turned out that the reduction of a corresponding *N*-nitrosoaminotetrazoles to the hydrazine derivatives is not suitable to gain high yields of the corresponding substituted hydrazine derivatives, and therefore other routs are required.

2.1 Cyanohydrazines

88a was obtained in high yields (72%) by the reaction of 1-cyano-1-methyl-hydrazine (**89**) which *in situ* formed hydrazoic acid in alcoholic solution. The required cyanohydrazine **96** was obtained according a modified procedure of Ryckmans et al.[32] **96** was obtained as a colorless oil in a reasonable yield (60%) with sufficient purity by the reaction of MMH (**95**) with BrCN in DCM and Na_2CO_3 as base. From *Scheme 5.9* the reaction sequence can be depicted. **96 c**an be easily identified by means of Raman spectroscopy by its characteristic stretching vibration of the CN group at 2208 cm^{-1}.

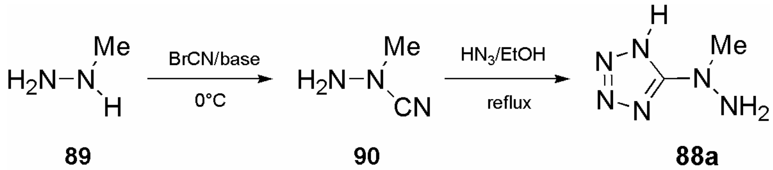

Scheme 5.9. Synthesis of **88a**

The reaction of **90** with HN_3 gave the desired *N*-methyl-*N*-(1(2)*H*-tetrazol-5-yl)-hydrazine **88a** as monohydrate in moderate yield (less than 40% based on MMH). The reason for the low yield was found on the one hand by the loss of product during the separation procedure of the hydrazine derivative **90** and on the other hand on the insufficient amount of HN_3 which was generated *in situ* by the reaction of conc. HCl and NaN_3. As HN_3 is very volatile, significant quantities of hydrazoic acid was lost while heating the reaction mixture at temperatures greater than 65°C through the condenser. Therefore, the procedure was changed in a way that, that the isolation of the hydrazine was not necessary and the loss of HN_3 negligible. The MMH was reacted with cyanogen bromide in EtOH instead of DCM. After formation of the hydrazine, the inorganic salts were simply removed by filtration and the alcohol solution treated with excess of HN_3 under reflux. The tetrazole **88a** is obtained as a pure crystalline solid by concentrating and chilling the reaction mixture with a good overall yield of 72% (based on MMH).

For the substituted tetrazole derivatives **88b**, **88c** and **88d**, in principle, alkylation reaction of **88a** in form of an alkaline salt should lead to the corresponding tetrazoles on heating with appropriate alkyl halides (*e.g.* MeI, EtI, allyliodide). As already discussed in *Chapter II* (1.1), the reaction of tetrazolates with alkyl halides results in the formation of a mixture of the 5-substituted-1*N* (**88b-d**) and 2-*N*-alkyl-tetrazoles (**91-b**) (*Scheme 5.10*).

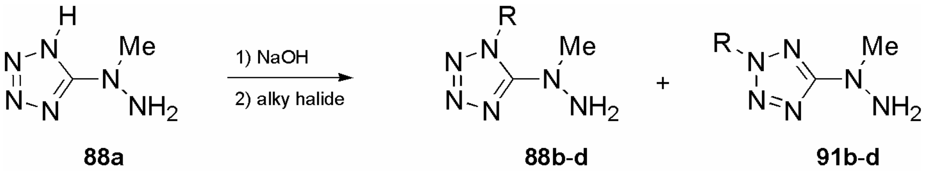

Scheme 5.10. Alkylation of **88a**

2.2 Thiosemicarbazides

Since the use of huge amounts of hydrazoic acid is a hazard which needs to be avoided, and since the cyanohydrazines are not suitable for the preparation of the 1,1-substituted hydrazine **88b-d**, a different method was needed. During the diploma thesis aminotetrazoles were prepared from corresponding thioureas.[28] Thiosemicarbazides are amino substituted thioureas, and therefore it was expected that the reaction analogous to that of the aminotetrazoles might yield the corresponding hydrazine derivatives. This was tested for the *N*-methyl-*N*-(1(2)*H*-tetrazol-5-yl)-hydrazine **88a**. Following the reaction sequence *Scheme 5.11* the hydrazine derivative **88a** could be obtained starting from the 2-methyl-thiosemicarbazid **92a**

in 62 % yield. The thiosemicarbazide **92a** was converted with MeI to the 2,*S*-dimethylisothiosemicarabzide hydriodide (**93a**) followed by the treatment of the salt **93a** with NaN_3 in boiling EtOH. It is known that isothiorhonium salts can react with an azide source to the corresponding tetrazoles.[33,34]

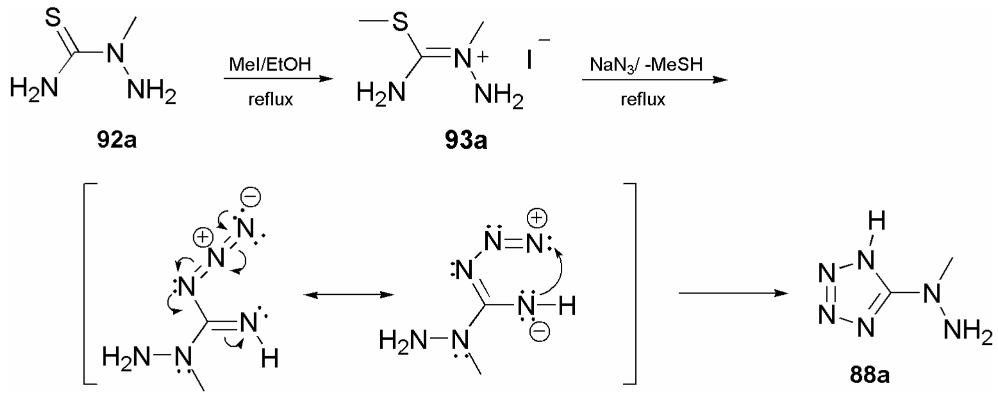

Scheme 5.11. Synthesis of **88a** from 2-methyl-thiosemicarbazide

Different methods are known for the preparation of substituted thiosemicarbazides. One way uses an *N*-substituted carbamothioic chloride **94** and the monosubstituted hydrazine **89** yielding **92b** (*Scheme 5.12*, I).[35] Another method uses a substituted isothiocyanate **95** and **89** yielding **96** (*Scheme 5.12*, II).[36] The usage of a MMH (**89**), CS_2, an alkylating agent (yields **97** as intermediate) and the corresponding amine **98** (*Scheme 5.12*, III),[37] leads, similar to the reaction of the substituted isothiocyanate **95** with *e.g.* an aryl substituted hydrazine **99** (*Scheme 5.12*, IV)[70], to the formation of the undesired 1,4 substituted thiosemicarbazides **100** and **101**.

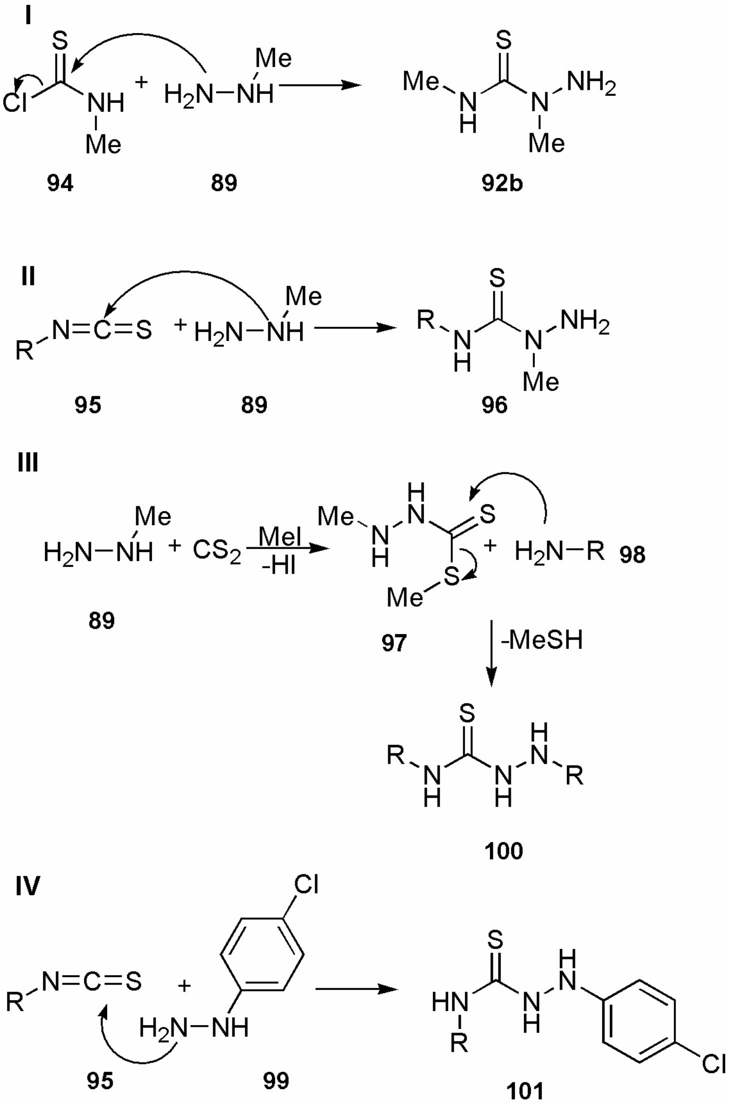

Scheme 5.12. Preparation of substituted thiosemicarbazide

To avoid undesired side reactions, resulting from a possible Dimroth rearrangement-like imidoyl azide-tetrazole ring-chain isomerism of the generated tetrazolylhydrazines (**102**) (*Scheme 5.13*, I), which is part of the thermal behavior of substituted 1,5-diaminotetrazoles (**103**),[38] only 2-methylsubstituted thiosemicarbazides were used. With the substitution at the 2-position, the possibility of the rearrangement is blocked, leading to a fully regiospecific reaction to the desired substituted 5-hydrazinotetrazoles (**88a-d**) (*Scheme 5.13,* II).

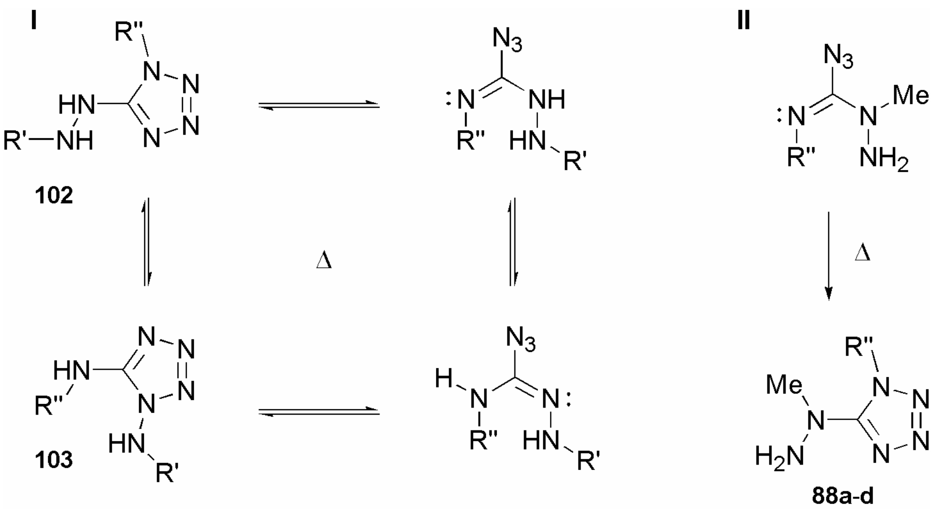

Scheme 5.13. Imidoyl azide-tetrazole ring-chain isomerism

For the preparation of the thiosemicarbazides **92b-c**, a modified procedure of Scovill et al. was used (*Scheme 5.14*).[36,39] **92a** is commercially available. To a cold ethereal solution of the corresponding isothiocyanate was added an ethereal solution of MMH. The products separated as fine white precipitates giving 89% to 97% yield (**92b** (92 %), **92c** (97 %), **92d** (89 %)). The colorless solids was purified by washing with cold Et_2O; no further purification was required. In all cases, the 2,4-substituted products were obtained, which can be explained by the α-effect of the hydrazine resulting in the regioselective reaction (*Scheme 5.14*).

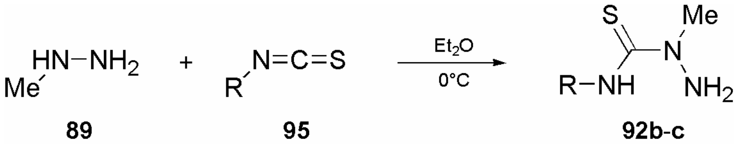

Scheme 5.14. Preparation of 1,3-substituted thiosemicarbazides

In the next step, the thiosemicarbazides **92a-d** were transformed to the *S*-methyl-isothiorhonium hydriodides **93a-d** with MeI in refluxing ethanol. The obtained salts were not isolated. After the required reaction time of 4-6 hours (monitored by ^{1}H NMR) the ethanol solution of isothiorhonium hydriodides **93a-d** were cooled to 40 °C and treated with sodium azide (1.5 eq). Note: The cooling is recommended before adding the sodium azide, since it was observed that especially in the case of the methyl substituted derivative **93b**, an extremely exothermic reaction can suddenly occur. After adding the azide, the reaction mixtures were

refluxed for 24 hours yielding a ~ 90 % yield of the products in solution (determined by means of NMR spectroscopy).

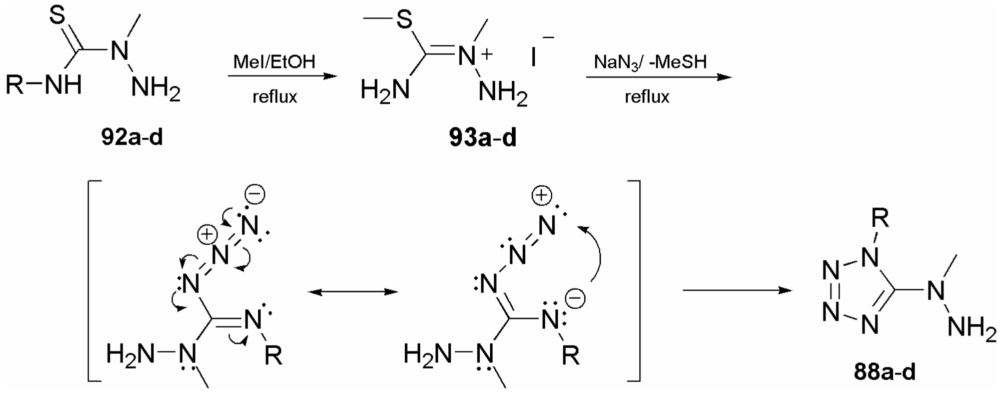

Scheme 5.15. Preparation of the substituted hydrazine derivatives **88a-d**

The purification of the products by means of extraction or recrystallization turned out to be problematic. The only suitable purification methods are the column chromatography on silica gel and for **88b** and **88d**, sublimation. Although yields were determined to be higher than 90 % in solution, only pure product in the range of 45 – 77 % were obtained (*Table 5.1*). The obtained yield for **88a** is much lower compared to the method using the cyanohydrazines.

Table 5.1. Yields and mobile phase for the purification of **88a-d**

R	product	yield [%]	mobile phase		R_f
H	**88a**	45 (72)[a]	EtOH / Et_2O	1 : 8	0.36
Me	**88b**	54	EtOH / Et_2O	1 : 10	0.31
Allyl	**88c**	77	DCM / AcOEt	1 : 1	0.33
cyc-hexyl	**88d**	56	Et_2O / AcOEt	1 : 1	0.33

[a] obtained from the cyanohydrazine method

2.2.1 Possible mechanism of hydrazine decomposition

The highly decreased yields of **88a-d** might be explained by the instability of the hydrazine derivatives towards oxygen and light, which explains also that the first attempts to isolate e.g. **88b** by Butler and Scott were unsuccessful.[40,41,42] *Scheme 5.16* reveals a possible

decomposition pathway initiated by oxidation with oxygen to the corresponding hydroperoxide. The radical degradation leads over several steps to the diazene **I** and the substituted 1-(1*H*-tetrazol-5-yl)-2-hydroperoxy-1-methylhydrazine **II**.

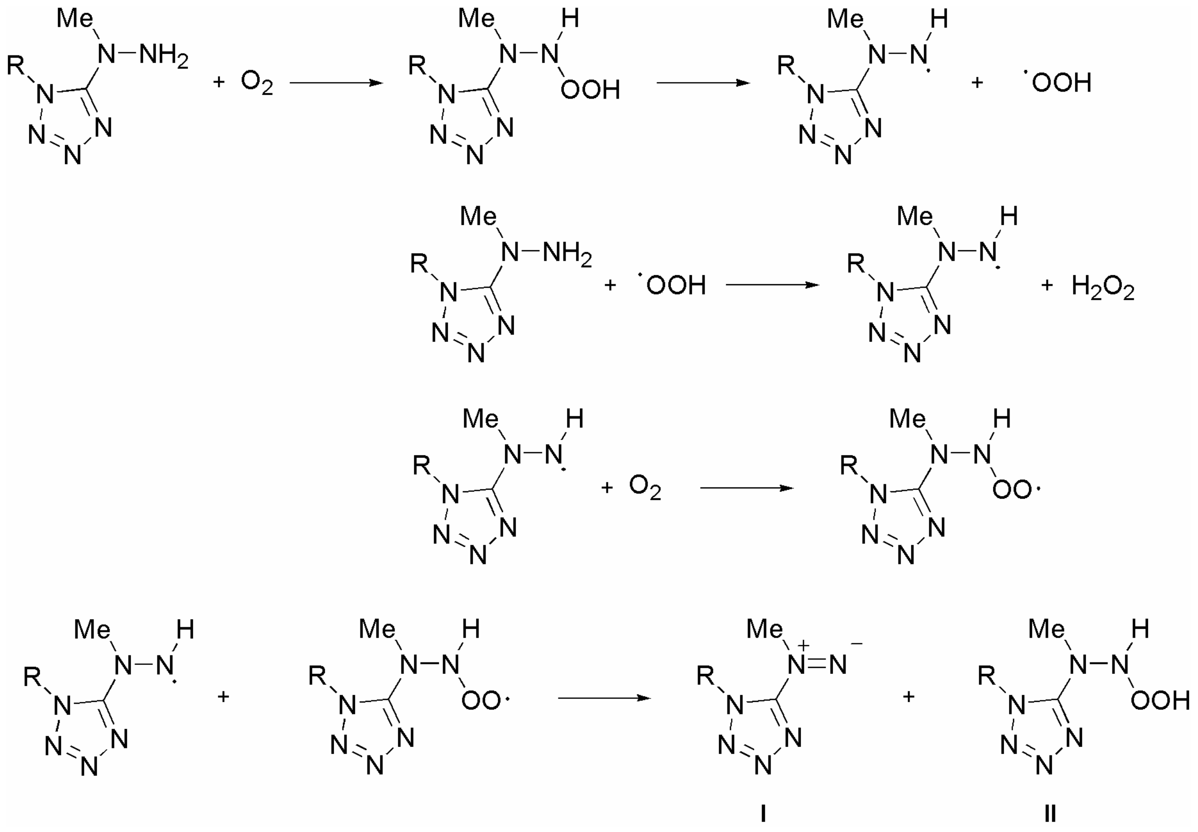

Scheme 5.16. Oxygen induced formation of diazene **I** and hydroperoxide **II**

Different studies have shown, that hydrazines tend to be easily oxidized in presence of elemental oxygen, leading to various products. Considering the great loss of product, using the column chromatography for purification, it is obvious that a reaction that degradates the hydrazine derivatives, might have happened. Note: The proposed decomposition schemes are based on the observation of several by products which could be assigned by means of NMR experiments during the work up procedure, especially for **88a** and **b**, but should only give an idea what might have happened also based on observation from others mentioned in literature. In the case of **88a** and **88b**, the corresponding aminotetrazoles (Scheme 5.18, **V**) were obtained (both are also verified by a crystal structure determination, see below). For **88b**, the corresponding nitroso derivative (Scheme 5.19, **VI**) could be doubtless identified (*Chapter VI*, I). Beyond the formation of the hydrazones (Scheme 5.17, **III**), the corresponding tetrazoles

(Scheme 5.17, **IV**), and evidence of the formation of the tetrazenes (Scheme 5.18, **84a-d**) were observed. Possible reactions to form these side products are given in *Scheme 5.17 – 5.19*. The major gaseous products of the oxidation of the hydrazines were ammonia, nitrogen and methane. Taking a look at the appearing intermediates of these reactions, the tetrazolylmethyldiazene **I** plays an important role, resulting from the radical reaction of oxygen with the hydrazine derivative shown in *Scheme 5.16*. Transferring the known oxidation of the unsymmetrical dimethylhydrazine[43,44] to our system, the formed species given in *Scheme 5.16* could be obtained. By assuming the formation of the tetrazolylmethyldiazene **I**, the formation of numerous products can be understood following the paths given in *Scheme 5.17*. Besides the formation of the hydrazones (**III**) and the tetrazoles (**IV**) can be explained referring to the work of Sisler et al. (*Scheme 5.17*).[45]

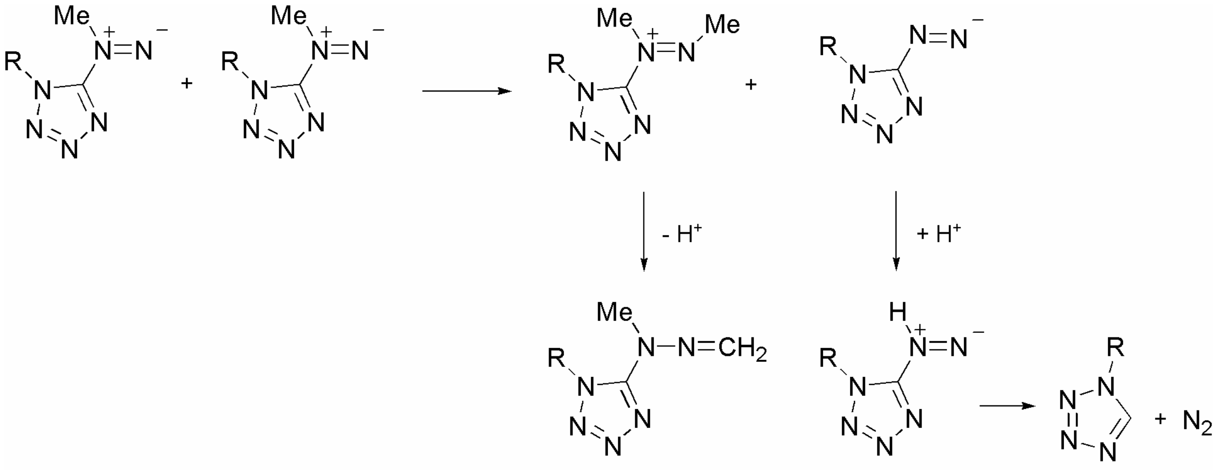

III **IV**

Scheme 5.17. Methyl group transfer of diazene **I** yielding **III** and **IV**

A very important side reaction is the possible dimerization of the formed diazenes **I** to the corresponding tetrazenes and the following possible degradation to the aminotetrazoles (*Scheme 3.18*, **V**). That has already been observed by Rademacher et al., investigating aryl substituted 2-tetrazenes.[46]

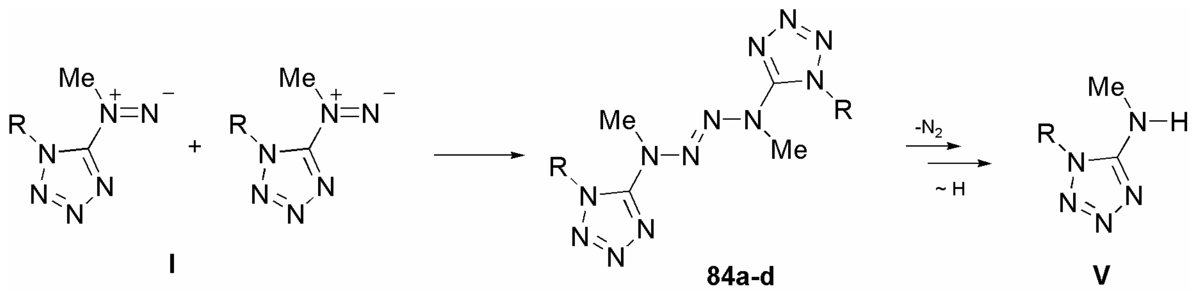

Scheme 5.18. Dimerization of diazene **I**

Another important reaction is the formation of *N*-nitrosoamines (*Scheme 5.19*, **VI**) and water, resulting from the decomposition of **II** which was reported by Urry.[43] A possible base-catalyzed mechanism is outlined in *Scheme 5.19*. As also discussed by others, the formation of the *N*-nitrosoamines (**VI**) in the case of alkylsubstituted hydrazines is very likely and can have extreme differences in the magnitude of the yields. It has to be taken great care when manipulating these compounds since this class of compounds are known be highly carcinogenic and mutagenic. Therefore, the products should be handled cooled and if possible under inert atmosphere

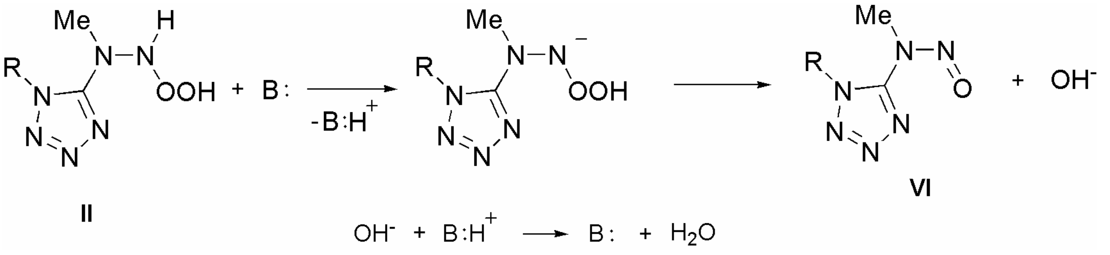

Scheme 5.19. Formation of nitrosoamines **VI**

2.2.2 Properties of 88a-d

The compound **88a** forms colorless crystals, moderately soluble in water and alcohols like MeOH and EtOH. **88a** has a high solubility in DMF and DMSO. Recrystallization from absolute EtOH provides this compound without crystal water. Suitable single crystals for X-ray structure determination were obtained by recrystallization from water and EtOH. **88a** is an air stable not explosive compound, which decomposes smokeless without explosion at temperatures above 185°C.

Although compound **88b** was meant to be stable only in solution, it was possible to isolate it for the first time and perform a full characterization by means of spectroscopic methods as

well as single X-ray crystal structure determination. The compound **88b** forms colorless crystals and is moderately soluble in water, alcohols like MeOH and EtOH, DCM and Et_2O. **88b** is soluble in DMF and DMSO. Suitable single crystals for single X-ray crystal structure determination were obtained by recrystallization from DCM. **88b** is a stable, not explosive compound, which melts at about 82 – 83 °C and can be purified by means of sublimation.

The cyclohexyl derivative **88d** and the allyl derivative **88c** were also obtained in moderate yields. **88c** was obtained as colorless oil, which turned slowly red when exposed to air and light. Both compounds could also be identified doubtless by means of spectroscopic methods. **88c** is poorly soluble in Et_2O, moderately soluble in EtOH, acetonitrile, water and very well soluble in DCM and DMSO, insoluble in *n*-heptane. **88d** is moderately soluble in Et_2O, and alcohols like EtOH and MeOH, and very good soluble in DCM and DMSO. **88d** is not explosive and melts from 128 – 130 °C and starts to sublimate without decomposition at ~ 200 °C.

2.2.4 Mass spectrometry of **88b**

Since the mass spectra of **88a** and **88b** are comparable only the spectrum of **88b** is going to be discussed in more detail. Enforcement of a DEI^+ with compound **88b** and MeOH as solvent leads to the mass spectrum depicted in *Figure 5.3,* which contains a strong molecular peak at *m/z* 128 and a clear $[M+1]^+$-peak, as it is usually for N-alkyl substituted tetrazoles. The fragmentation pattern of **88b** is very complex. The main processes of this fragmentation can be depicted from *Scheme 5.20*. The peak with the highest intensity is the peak *m/z* 57, resulting from the formation of MeN_3 (cleavage d, retro 1,3-dipolar cycloaddition). Surprisingly, the fragmentation pathway of the loss of N_2 (cleavage c) is for the methyl substituted derivative **88b** only of minor importance. The relatively weak peaks of *m/z* 85 and 84, compared with the strong peak at *m/z* 57, are evidence for the existence of this path. The cleavage of MeN_3 (d) leads in several steps to the peaks at *m/z* 71, 56, 55, 46, 43 and 42. The α-cleavage of the methyl group or hydrazine moiety is responsible for the peaks at *m/z* 113 and *m/z* 83. The fragmentation of the tetrazole moiety, obtained from the α-cleavage, leads to the peaks at *m/z* 83 and *m/z* 55 that are most probably daughter ions of this reaction. The peak at *m/z* 113 results either from the loss of the methyl group from the tetrazole or hydrazine moiety. The fragmentation paths b and c play only a minor role whereas path a (cleavage of N_3 radical) is

not observed. Summarizing the observation it can be driven that the most important fragmentation pathway is: $H_2NNMe\text{-}CN_4Me$ → MeN_3 (*m/z* 57) → MeN_2 (*m/z* 43), and $H_2NNMe\text{-}CN_4Me$ → CH_3N_3 (*m/z* 57) → CH_2N_2 (*m/z* 45), H_2N_2 (*m/z* 30), HN_2 (*m/z* 29), N_2 (*m/z* 28). In all cases, the formed cations are stabilized either by locating the positive charge on the nitrogen atom or by a delocalized π-system.

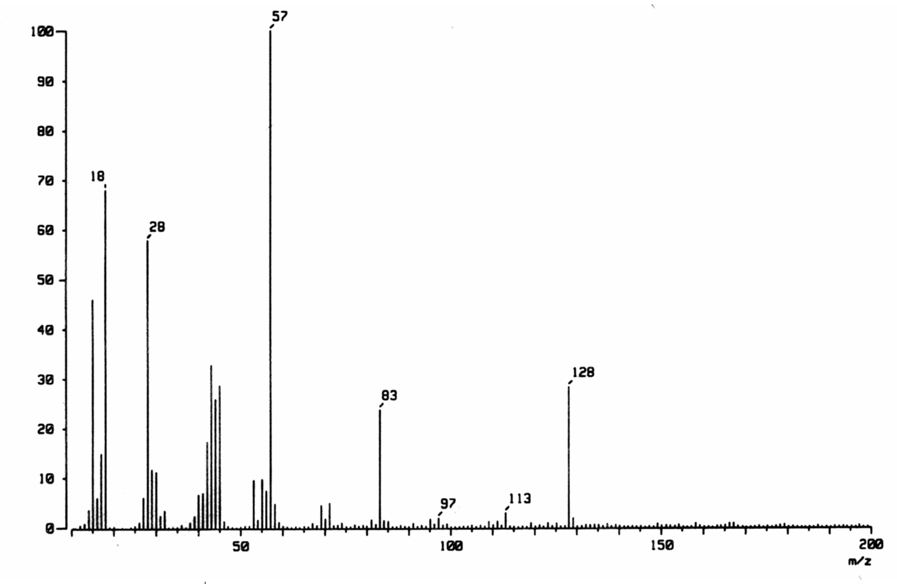

Figure 5.3. DEI$^+$ mass spectrum of **88b**

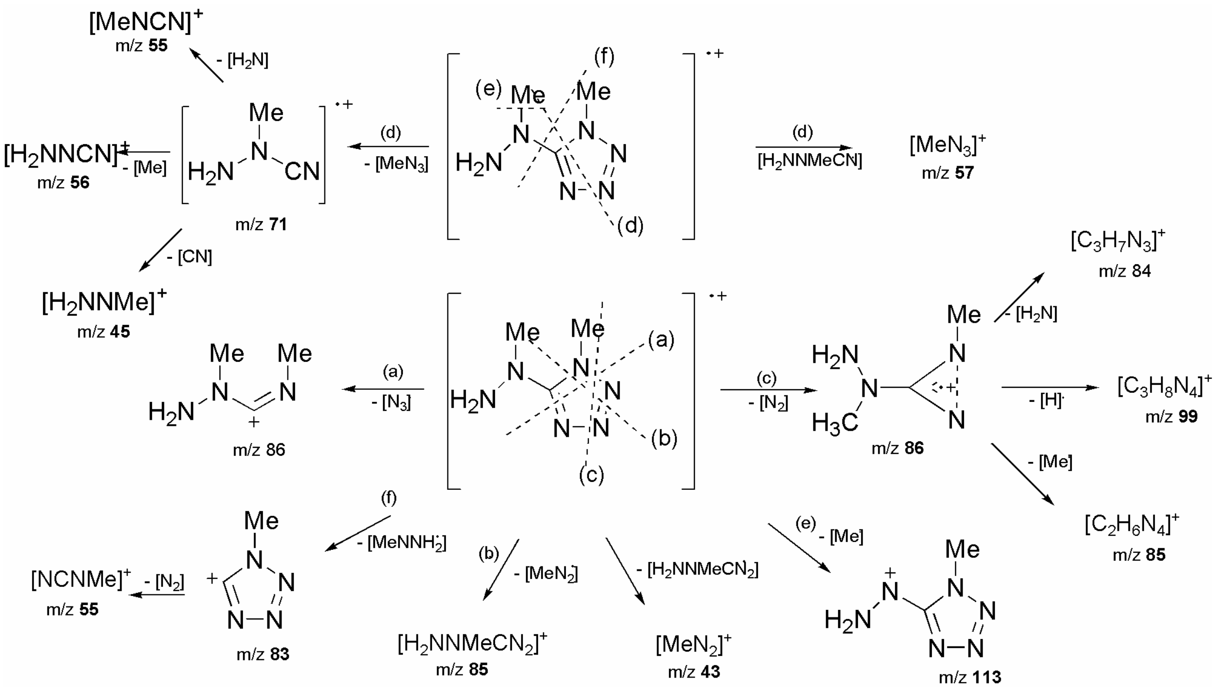

Scheme 5.20. Proposed fragmentation path of **88**

2.2.5 Raman and IR spectroscopy

The Raman and the IR data are in good agreement with other 1,1-substituted hydrazine derivatives. The highest vibration frequencies are due to N-H stretching vibrations and hydrogen bridges toward the water molecule (**88a**) and intermolecular interactions for **88b-d**. The symmetric and anti-symmetric N-H stretching vibrations are clearly resolved in the IR and also in the Raman spectra in region between 3173 – 3314 cm^{-1}. The stretching vibration of the CH-group is found in the region around 2930 cm^{-1} and was found to be more complex in the case of the ally and *cylco*-hexyl substituted compound **88c** and **88d**. The deformation mode for the water molecule is found at 1410 cm^{-1} as a very sharp and strong band (**88a**). As it is already known from other tetrazoles and the *ab initio* calculations of their spectra most of the modes are extensively mixed, and it is difficult to address them to a specific band. The C-N and N-N stretching and the C-H deformation modes are found in the region between 1700 and 1000 cm^{-1}. Below this value the bands belong to the deformation modes of the ring and the out-of plane bends of the NH group.

2.2.4 Crystal structure determination of **88a** and **88b**

Figure 5.4 shows the molecular structure of **88a**. It crystallizes in the monoclinic space group $P2_1/c$ with four formula units in the unit cell. All observed bond length and angles of the hydrazine moiety as well as the tetrazole unit are in excellent agreement with those reported in literature and are compared with compound **88b** in *Table 5.2*.

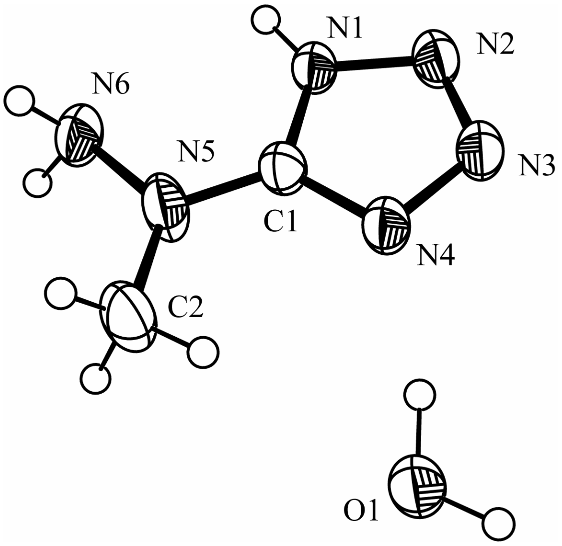

Figure 5.4. Formula unit and labeling scheme for **88a** (ORTEP Plot, thermal ellipsoid represents 50% probability).

Figure 5.5 shows the molecular structure of **88b**. **88b** crystallizes in the orthorhombic space group *P*bca with eight formula units in the unit cell. All observed bond distances and angles of the hydrazine moiety as well as the tetrazole unit are in excellent agreement with those reported in literature[47] and are comparable to the unsubstituted derivative **88a** (R = H). *Table 5.2* shows a comparison of selected bond lengths and bond angles. There are no differences found in the structural parameters of the tetrazole moiety, whereas in the case of **88a** a shortening of the bonds compared to **88b** in the hydrazine moiety is observed (*Table 5.2*).

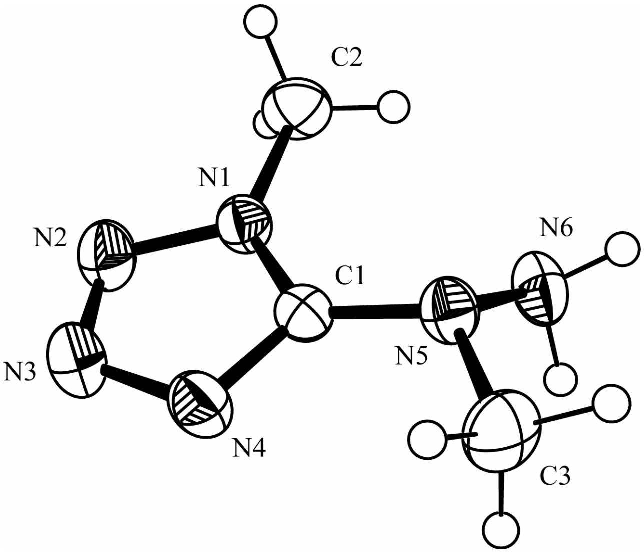

Figure 5.5. Formula unit and labeling scheme for **88b** (ORTEP Plot, thermal ellipsoid represents 50% probability).

Table 5.2. Comparison of selected interatomic distance (Å) and selected bond angles (deg) of **88a** and **88b**

	88a	**88b**		**88a**	**88b**
Å					
N1-C1	1.333(2)	1.342(2)	**N5-C1**	1.337(2)	1.371(2)
N1-N2	1.345(2)	1.355(2)	**N5-N6**	1.394(2)	1.432(2)
N2-N3	1.280(2)	1.288(2)	**N1-C2**	-	1.458(2)
N3-N4	1.368(2)	1.365(2)	**N5-C3**	1.440(2)	1.461(2)
N4-C1	1.323(2)	1.324(2)			
°					
C1-N1-N2	108.4(1)	108.0(1)	**C1-N5-C3**	122.5(1)	115.7(1)
N3-N2-N1	106.6(1)	106.8(1)	**N6-N5-C3**	121.3(1)	115.4(1)
N2-N3-N4	111.2(1)	110.9(1)	**N4-C1-N1**	108.8(1)	108.7(1)
C1-N4-N3	104.9(1)	105.6(1)	**N4-C1-N5**	126.7(2)	125.9(1)
C1-N5-N6	115.9(2)	113.2(1)	**N1-C1-N5**	124.5(2)	126.1(1)

This observation can be best explained by the occurrence of an intramolecular hydrogen bridge in the case of **88a** (N1–H1····N6 2.704(4) Å; N1–H1–N6 94.5(1)°) leading to an almost planar structure of the molecule including the hydrazine moiety within this plane (torsion angle N3–N2–N5–N6 -177.7 (1) ° (**88a**) *vs.* N3–N2–N5–N6 141.91 ° (**88b**)). This arrangement in **88a** is rather unusual since the lowest energy conformation in hydrazines is usually found to be gauche. But in the case of **88a** the conformation of the two amino groups is different with respect to their orientation; they are almost rotated by 90° (94.2(1)°). This leads for the lone pair at the N5 nitrogen atom to a better conjugation with the π system of the tetrazole ring. In accordance with this, the observed N5–C1 bond as well as the N5–N6 bond is significantly shortened compared to those bonds in **88b** (N5-C1 1.337(2) (**88a**) *vs.* 1.371(2) (**88b**); N5-N6 1.394(2) (**88a**) *vs.* 1.432(2) (**88b**)). The obtained bond lengths found in the hydrazine moiety of **88b** are typical for unstrained hydrazines.

The crystal arrangement of compound **88a** is composed of hydrogen bridges between the tetrazole and the water molecule, leading to the formation of chains as depicted in *Figure 5.6*. Within the chain, the tetrazole rings of all molecules lie approximately on a plane. *Figure 5.6* shows a view of the unit cell of **88a** along the [100] axis. The chains are oriented parallel to the [010] axis. Within the chain the molecule are arranged in such way, that the planes of the molecules form a zigzag pattern (N1-H1···O1^{i} 2.826(5); O1^{i}-H1b···N4^{i} 2.89(2), symmetry code: (i) 1-x, 0,5+y, 1.5-z).

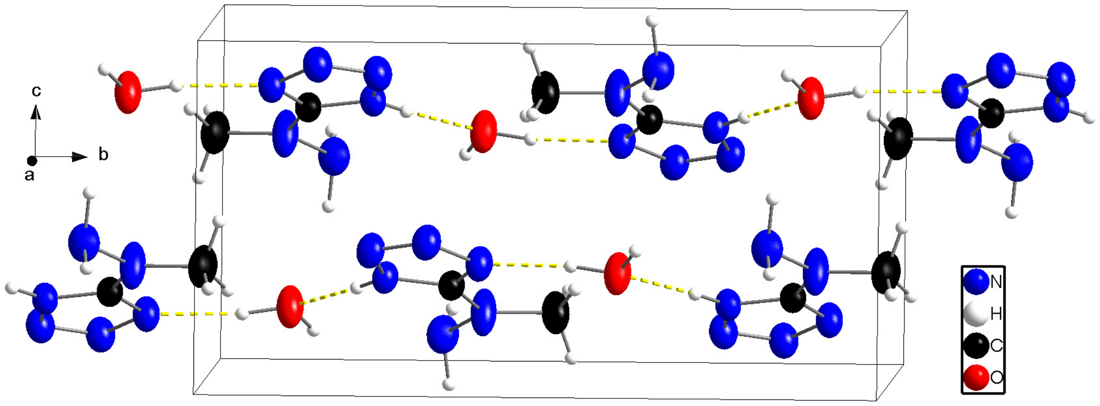

Figure 5.6. Crystal arrangement of **88a** viewed along the [100] axis (ORTEP Plot, thermal ellipsoid represents 50% probability).

In the case of **88b** also a chain-like structure is found in the crystal structure (*Figure 5.7*), resulting from a weak hydrogen bond (N6-H7···N4^i 3.117(2); symmetry code: (i) -0.5-x, y, 0.5-z). These chains are orientated parallel to [100] axis. Between those chains no interactions were observed.

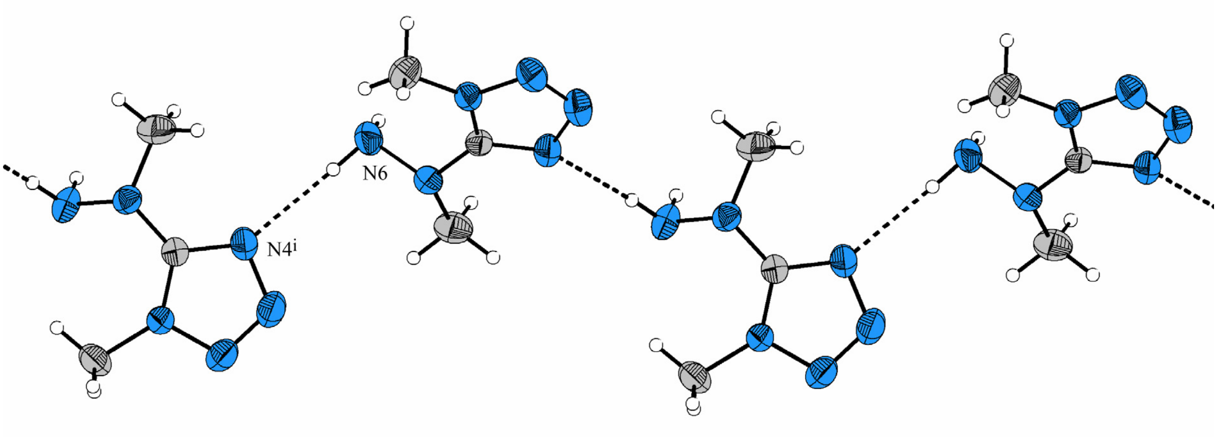

Figure 5.7. Crystal arrangement of **88b** viewed along the [010] axis (ORTEP Plot, thermal ellipsoid represents 50% probability).

3. Oxidation of hydrazine derivatives 88a-d

As already mentioned, different oxidations methods are used to transform 1,1-substituted hydrazine to the corresponding 2-tetrazenes. During this work many oxidation methods have been tried to convert the compound **88a** into the desired tetrazene **84a** (*Scheme 5.21*). The oxidation was carried out with bromine,[48] HgO,[49,50] $KBrO_3$, NaOCl,[51] $KMnO_4$,[52] Benzochinon[53] and $Pb(OAc)_4$[54] in different medias.

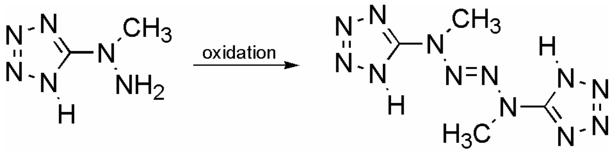

88a **84a**

Scheme 5.21. Oxidation of **88a** to **84a**

Table 5.3 summarizes the used methods and the obtained yields of the tetrazene **84a**. In all cases, the compound **88a** was obtained only in small amounts, and the range of yields never

did overstep 33%. In almost every case the tetrazene precipitated out from the reaction solution as an amorphous colorless powder. **88a** is poorly soluble in hot MeOH and EtOH, almost insoluble in H_2O but shows reasonable solubility in DMSO and DMF. **84a** is not very friction (192 N) or heat sensitive, but it detonates during the drop hammer test. Above 207 °C it decomposes smokeless.

The polarity of the solvent is important for the oxidation reaction and depends on the substituents of the hydrazines. In fact, aryl groups need aprotic solvents such as chloroform or diglyme, while with alkyl groups better yields are obtained in water or alcohols.[55] Due to the poor solubility of **88a** in organic solvent most of the oxidation reaction has been performed in acidic medium like acid/water, base or in some cases alcohols were used. According to Anderson et al.,[48] the hydrazine derivative was dissolved in either HCl (2M) or TFA/H_2O (1:1) at 0°C. To this solution was added bromine drop by drop until the color of bromine persisted for more than 5 minutes. The product precipitated from the reaction solution as a white colorless powder. It was isolated by filtration and washed with water until bromine free. In that way, yield between 8 and 15% of the compound **84a** was obtained.

Table 5.3. Oxidations methods

Method	**84a [%]**
Br_2/HCl	15%
Br_2/TFA	8%
HgO/pyridine	33%
HgO/MeOH	-
HgO/KOH	13%[a]
NaOCl/NaOH	-
NaOCl/6n HCl	14%
NaOCl/AcOH	14%
$KMnO_4$/KOH	-
$KMnO_4$/acetone	-
$KBrO_3$/HCl conc.	20%
$Pb(OAc)_4$/pyridine	-
Benzochinon/MeOH	-

[a] as potassium salt

Higher yields were obtained using a modified method from Bellamy et al.[50] It was found out that the oxidation with HgO in alcohols did not form the corresponding tetrazene **84a**. Although Rademacher et al.[49] was very successful with this method, **88a** did not react in this media, and therefore it was decided to change to base.[56] Starting from the corresponding potassium salt of the hydrazine derivative, the potassium salt (**104**) of the tetrazene **84a** was obtained in an all over yield of 14% (*Scheme 5.22*).

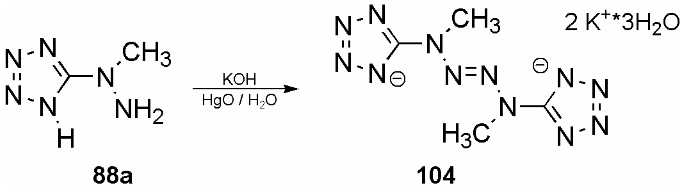

Scheme 5.22. Oxidation of **88a** to **104**

The potassium salt **104** crystallized as trihydrate from the reaction solution after 4 months. The structure is going to be discussed in a later *Chapter*. The highest yield was obtained (33 %) when using pyridine as solvent. In this case, the product was isolated by acidification with HCl of the Hg/HgO free aqueous pyridine solution. The product precipitated in form of an orange product. Hypochlorite as oxidation agent according Wieland et al.[51] did only succeed when performing the reaction in acidic media (yield 14%). In basic media no product could be isolated. Therefore the reaction was performed in 6N HCl or acetic acid. In both cases the product precipitated from the reaction medium and was isolated as already mentioned above. Using NaOH solution as reaction media, the corresponding sodium salt was not obtained. Acidification of the solution did not lead to the precipitation of the tetrazene **88a**. For the oxidation of the hydrazine **88a**, potassium bromate in conc. HCl was also an efficient oxidant and yielded the corresponding tetrazene **84a** in 20%. Oxidation of **88a** using the systems $KMnO_4$/KOH or acetone, $Pb(OAc)_4$/pyridine or benzochinon/MeOH did not lead to the formation of **84a** but to some interesting side products. In the case of benzochinon oxidation, a crystalline orange product precipitated from the reaction mixture but could not be identified yet.

In the case of **88b-c**, only three different methods were tempted for the oxidation to the corresponding tetrazenes **84b-c**. According Rademacher et al.[49] the oxidation of the hydrazines **88b-d** in alcohol with HgO did not lead to any product. Only starting material could be recovered.

Also, attempts using benzeneseleni acid, PhSeOOH, as oxidation reagent fails, although according to Back et al.,[57] the oxidation of hydrazines to the tetrazenes should be quite successful accompanied with good yields. A great advantage of the benzeneselenic acid would have been the use as a catalyst with hydrogen peroxide as oxidation.[58] Similar to the oxidation of **88a** with Br_2, the *in situ* oxidation with bromine in an ice-cooled acetic acid/water solution turned out to be also suitable to oxidize the corresponding hydrazines **88b-d**. The desired tetrazenes **84b-d** were obtained in moderate yields ranging from 13% (**84c**) to 49% (**84b**). The reaction needs to be carried out in acetic acid/water. Using DCM as example for a non-aqueous solvent leads only to the formation of the corresponding hydrazine hydrochlorids. The reaction was performed similar to the before-mentioned synthesis but using a diluted aqueous solution of bromine. During the addition of the bromine, the temperature had been kept at 0°C by using an ice bath.

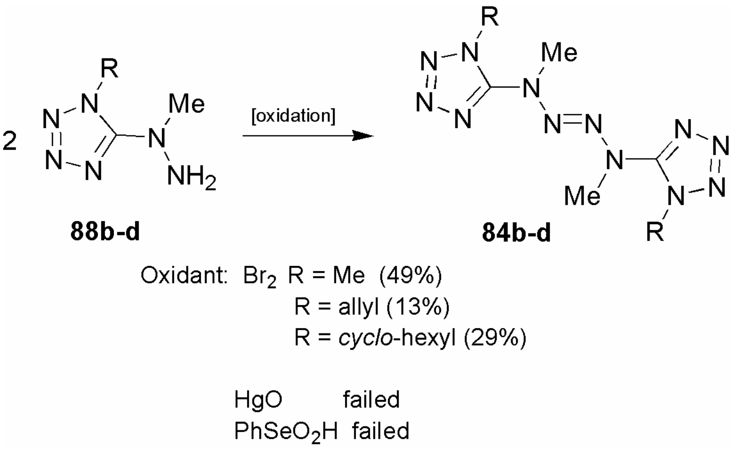

Scheme 5.23. Oxidation of **88b-d** to **84b-d**

In the case of **84c** and **84d** the products precipitated from the reaction mixture as an amorphous colorless or light brown powder. **84c** and **84d** were separated by filtration and washed until bromine free. For the methyl derivative **84b** the product started to crystallize within one day, and after standing for another week fine thin needles were obtained. All compounds are insoluble in water and only poorly soluble in alcohols. The allyl (**84c)** and the cyclohexyl derivatives (**84d**) show a higher solubility in for example DCM and $CHCl_3$ compared to **84b**. Single crystals of **84d** suitable for X-ray structure determination were obtained by recrystallization from $CHCl_3$. All three products show a good solubility in DMSO and DMF. They are not friction, heat or impact sensitive and can be stored on air and light. In the case of the methyl substituted derivative (**84b**) the synthesis was improved. The reaction

steps were minimized from eight to three with an increased overall yield of 26% compared to former 4%.

The low yields of the 2-tetrazenes might be explained by a degradation of 2-tetrazenes in acidic media. In acid solution, the decomposition proceeds over ionic intermediates, leading to the formation of N_2, nitrenium- and ammonium-ions as well as to the amino-radical cation (*Scheme 5.24*). In all cases, the formation of the corresponding *N*-methyl-5-aminotetrazolium bromides **105a-d** and aminotetrazolium bromides **106a-d** again was identified by means of spectroscopic methods. In some cases the molecular arrangements were also determined by crystal structure determination.

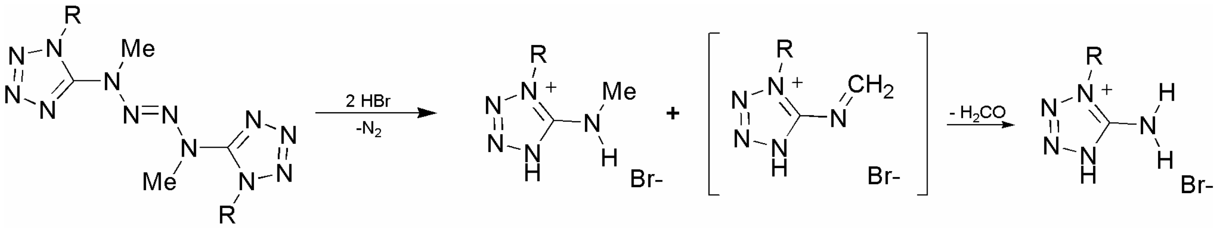

84a-d **105a-d** **106a-d**

Scheme 5.24. Acid catalyzed decomposition of **88a-d**

The example depicted in *Figure 3.7* shows the molecular structure of **105a**. The bromide forms air stable, not hygroscopic colorless prisms, which crystallizes in the monoclinic space group $P2_1$/n.

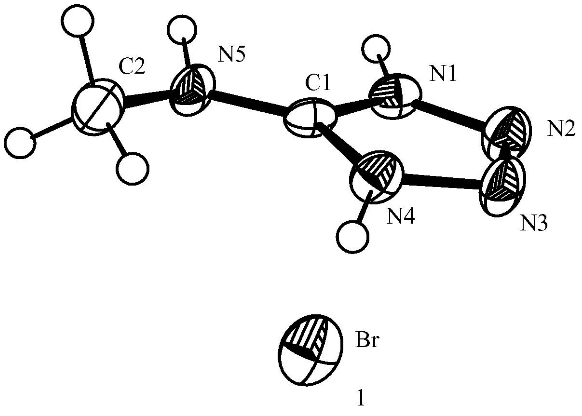

Figure 5.8. Molecular structure of **105a** viewed (ORTEP Plot, thermal ellipsoid represents 50% probability)

3.1 Characterization of **88a-d**

84a-d have been fully characterized and unequivocally identified by Raman and IR spectroscopy, high mass resolution spectrometry and NMR techniques. For **84d** and **84a** (as potassium salts **104**) it was possible to confirm the structures by X-Ray structure determination.

3.1.1 Raman and IR spectroscopy

Raman and IR spectroscopy are particularly suitable to identify **84a-d** quickly. Due to C_i symmetry of the molecules in the solid state the $N_{acyclic}$=$N_{acyclic}$ stretching mode between the central N atoms appears at 1492 cm^{-1} (**84b**), 1495 cm^{-1} (**84c**) and 1486 cm^{-1} (**84d**) only in the Raman spectrum, respectively, and represents the largest peak (*Figure 5.9*).

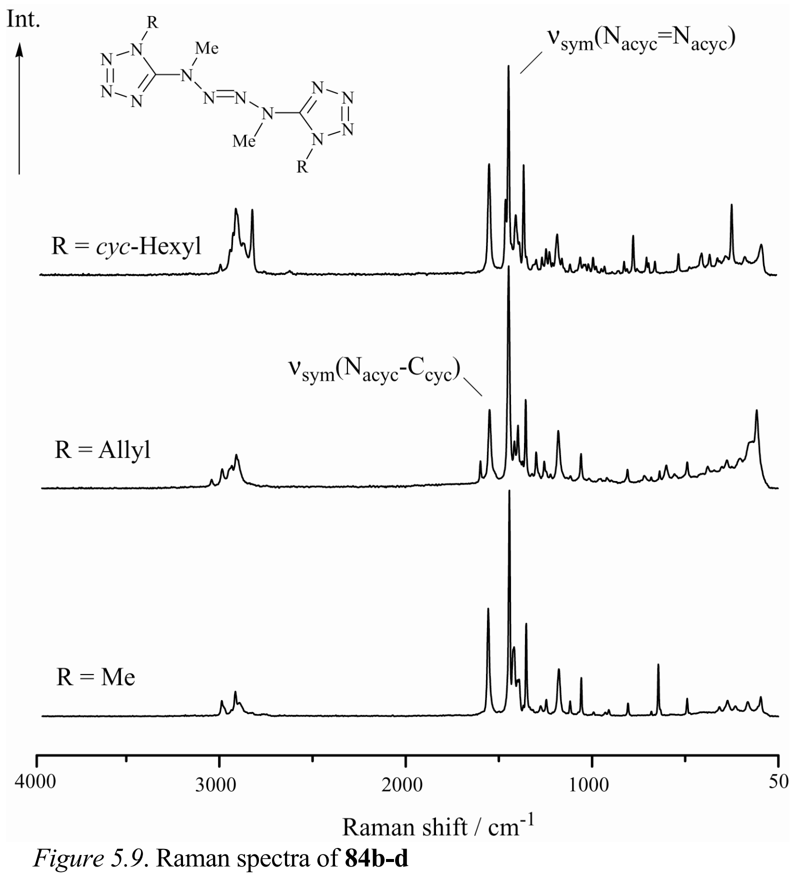

Figure 5.9. Raman spectra of **84b-d**

Whereas the $\nu_{as}(N_{acyclic}-C_{tetrazole})$ is found only in the IR spectrum with the highest intensity at 1565 cm^{-1} (**84b**), 1560 cm^{-1} (**84c**) and 1560 cm-1 (**84d**) (*cf.* $\nu_s(N_{acyclic}-C_{tetrazole})$ = 1606 cm^{-1}, 1597 cm^{-1} and 1591 cm^{-1} in the Raman spectrum).

3.1.2 Mass spectrometry of **84b**

Figure 5.9 shows the mass spectrum of **84b** recorded in DEI+ mode. This compound also gives a molecule peak at *m/z* 252. The main fragmentation path of **84b** is the α fragmentation at the azo group leading to *m/z* 140. The loss of nitrogen (*m/z* 28) leads to fragment *m/z* 112 (*Scheme 5.25*).

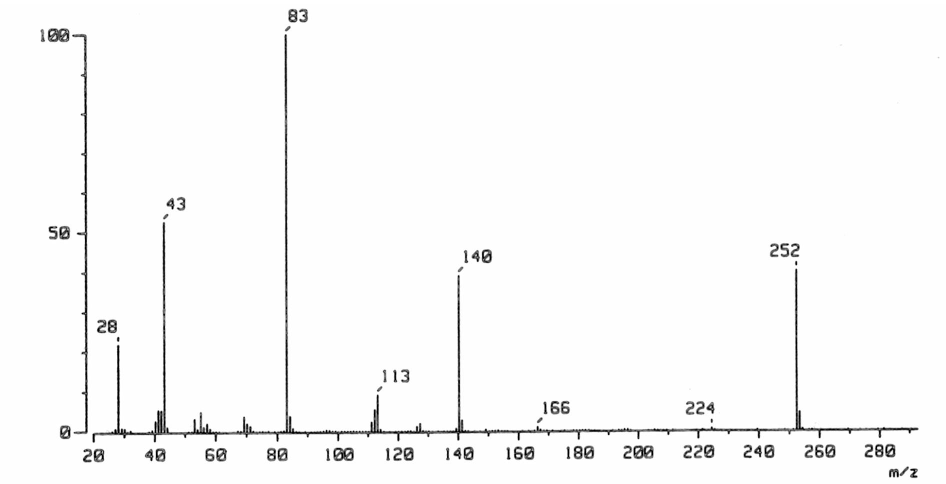

Figure 5.9. DEI^{+} mass spectrum of **84b**

The asymmetrical breakdown of the tetrazene unit (*Scheme 5.25*) is accompanied by an isomerization of the trans-2-tetrazene to the cis-2-tetrazene. The resonance stabilized radicals are then formed by hydrogen atom transfer over a six-membered transition state.

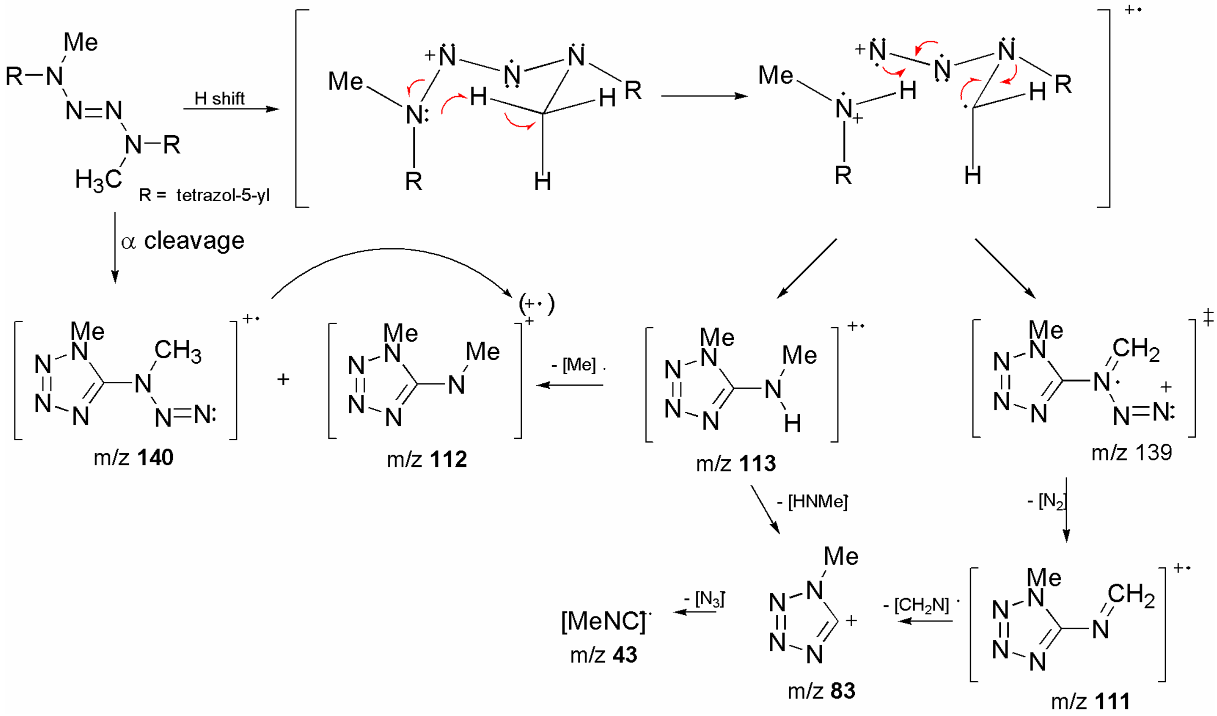

Scheme 5.25. Possible fragmentation pathway of **84b**

This mechanism is in good accordance with the observed decomposition pathways of the tetrazenes in solution and yields the same products. The further fragmentations of these radical cations follow the rules for 5-substituted aminotetrazoles and will not be discussed here in detail.[59] The peaks at *m/z* 83 and *m/z* 43 are most probably daughter ions of the fragmentation of the tetrazole moiety to methylisonitrile by a cycloreversion (MeNC + N_3).

3.1.3 Mass spectrometry of **84d**

Analyzing the spectra of **84d** some differences are observed compared to the spectrum of **84b**. The spectrum given in *Figure 5.10* also clearly shows the mass peak at *m/z* 388. Again the above mentioned fragmentations account, leading to the observation of *m/z* 208 and *m/z* 180 for the alpha cleavage. The isomerization and proton transfer accounts for *m/z* 209, 178, 151, 109 and 83. The peaks at *m/z* 151, 109 and *m/z* 83 are typical for the fragmentation of the tetrazole moiety forming cyclohexylisonitril by a cycloreversion. The peaks lower than *m/z* 100 correspond basically to the fragmentation of the cyclohexyl substituent. Interestingly, the peak at *m/z* 360 indicates the loss of the nitrogen from one of the tetrazole rings (*Scheme 3.14*). This process does not play an important role for **84a** and **84b**, but for **84d** the cyclohexyl groups seem to stabilize the corresponding cation very well. The loss of nitrogen leads to *m/z* 360.

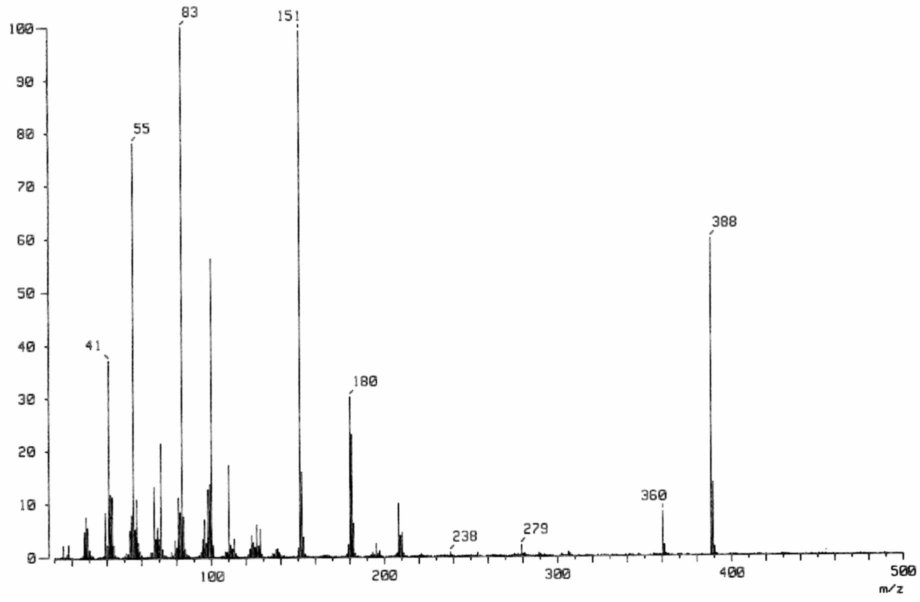

Figure 5.10. DEI$^+$ mass spectrum of **84d**

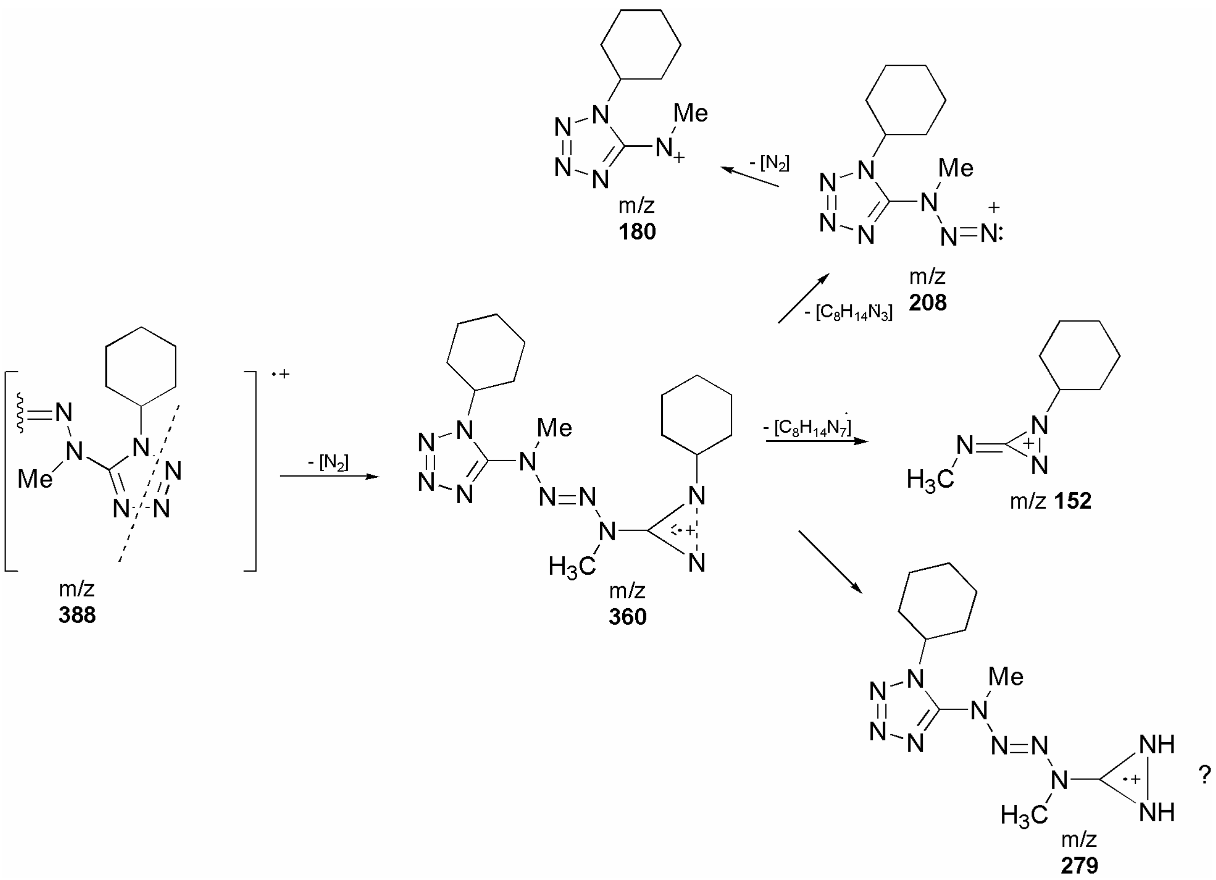

Scheme 5.26. Possible fragmentation pathway of **84b**

The alpha cleavage at the azo group leads to the fragments *m/z* 152 and *m/z* 208. Curious is *m/z* 279 which might result from the formation of a diaziridine which is speculative and should just be seen as a possibility. The latter process would result from proton transfer and degradation of the cyclohexyl group.

3.2 Molecular structure of **84d** and **104**

84d crystallizes in the monoclinic space group $P2_1/n$ with two formula units in the unit cell. Selected bond length and bond angels are summarized in *Table 5.4* and are compared to **84b** (R=Me) and the potassium salt **104** (R = K). *Figure 5.11* depicts the molecular arrangement of **84d**. Being in agreement with former computation and structure determination,[28] the molecule adopts a nonplanar molecular structure (C_i symmetry) with two tetrazolyl substituents and an almost planar N4 chain (sum of the bond angles for all four N atoms is close to 360°), that is, however, in contrast to the structural features of the unsubstituted parent molecule N_4H_4 (2-tetrazene)[60,61] (see *Table 5.4*). Both tetrazolyl carbon atoms lie in the N4 plane, whereas both

tetrazole rings are twisted out of this plane (e.g. dihedral angle N4-C1-N5-N6: 153.2(3)°) which might result from the bulky *cyclo*-hexyl substituents. In comparison to the methyl derivative **84b**, where a good delocalization of the π system over the whole molecule was found, in the case of 84d the delocalization of the π electron density over the entire molecule is not possible.

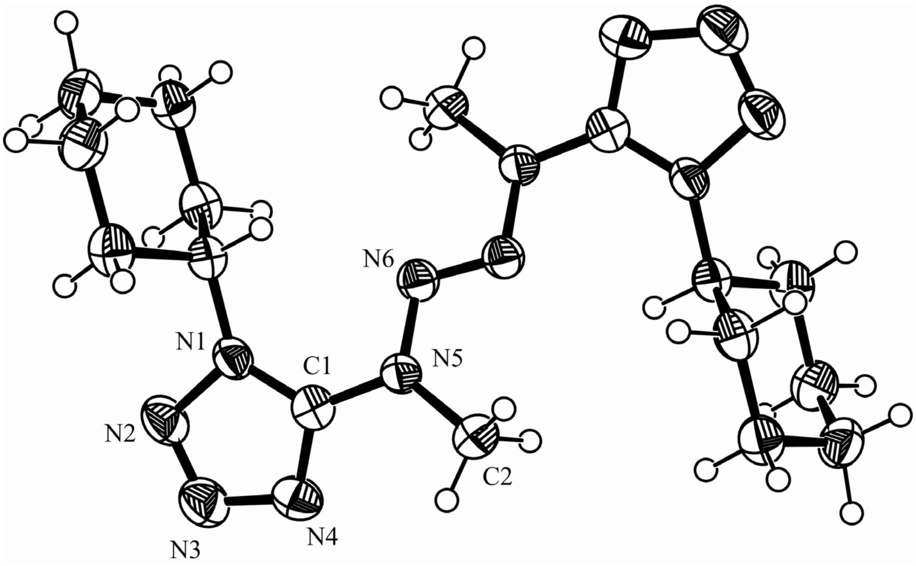

Figure 5.11. ORTEP plot of the molecule structure of compound **84d** with thermal ellipsoid at 50% probability level. Cyclohexyl group not labeled due to clarity. Inversion centre lies in the middle of the molecule.

Moreover, there are significant differences between **88d** and N_4H_4 with respect to the bond length. The bond length between the N atoms of the azo group (N6-N6') increases considerably from 1.205 Å in N_4H_4 to 1.27(2) Å in **88d**. On the other hand, the bond lengths of the formal N-N single bonds decrease from 1.429 Å (N_4H_4) to 1.379(5) Å (N5-N6), indicating a stronger delocalization of the azo π bond along the N4 moiety within **88d**, which is also in accordance with the observed structural parameters found in **84b** and **104** (*Table 5.4*). The influence of the *cyclo*-hexyl groups on the structural parameter of the tetrazole ring is not going to be discussed here in detail, as the observed bond lengths and bond angles within the tetrazole ring are in good agreement, compared to **84b** and **104**. The bond distances and angles within the *cyclo*-hexyl group are typical and agree well with those found in the literature.[62] Within the crystal there are no significant intermolecular interactions observed. *Figure 5.12* shows stacks formed by the molecules, which are arranged along the [100] axis.

Table 5.4. Selected structural parameters of different tetrazenes

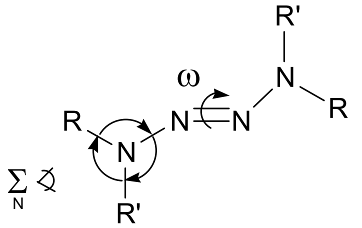

NRR’	Ref.	$d_{N=N}$	d_{N-N}	$\sum_N ∢$	∢NNN	ω
NH_2	[63]	1.21	1.43	~ 330	109	~ 0
$N[Si(CH_3)_3]_2$	[64]	1.27	1.39	360	112	2
$N(CH_2CH_2)_2O$	[65]	1.25	1.39	349	113	0
$N(C(CH_3)(C_6H_4Cl)$	[66]	1.25	1.38	351	114	0
$N(Si(CH_3)_3)(C_6H_5)$	[67]	1.25	1.39	358	112	16
$N(C_2H_4OH)(C_6H_5)$	[68]	1.254(1)	1.364(1)	358.6(5)	112.6(1)	0.9(2)
84b	[28]	1.261(2)	1.367(2)	359.8(4)	111.2(2)	0
104		1.254(4)	1.37(1)	360.0(1)	111.05(1)	0
84d		1.27(2)	1.379(5)	360.0(2)	110.6(2)	0

NN-bond length d_{NN} [Å], angle sum $\sum_N ∢$ **[°]**, angle ∢NNN **[°],** torsion angle ω [°] (ω = 0° correspond to the LP of the R_2N-moiety perpendicular to the N_4-plane)

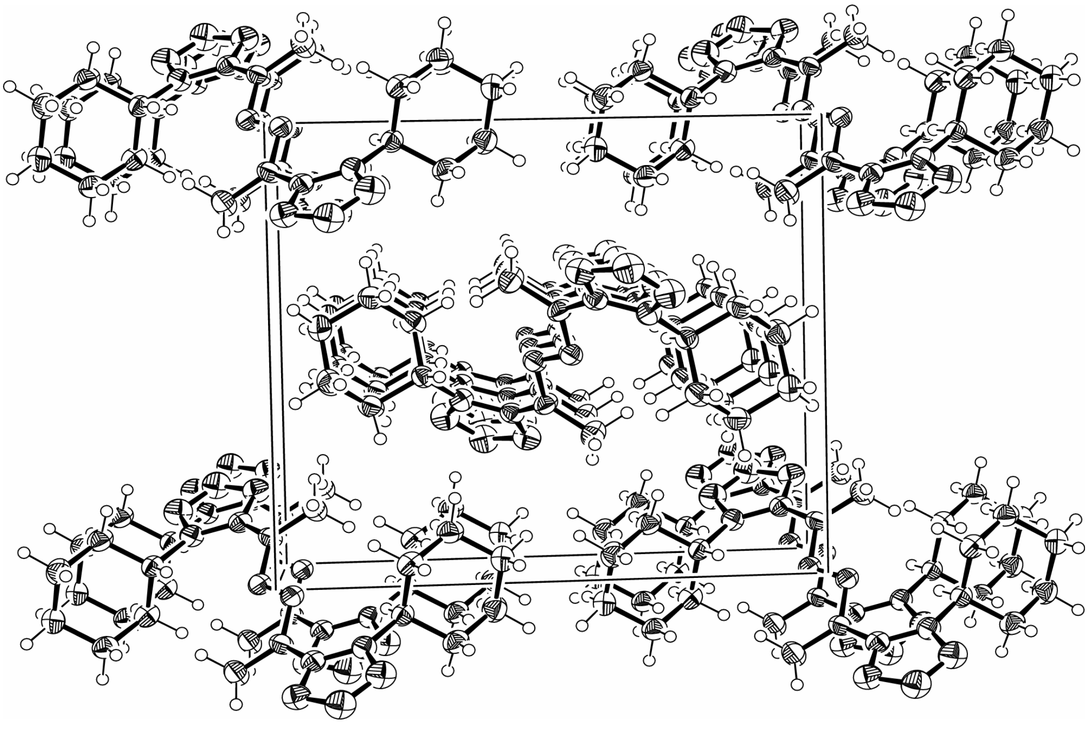

Figure 5.12. View of the crystal structure of **84d** along the [100] axis. ORTEP Plot, thermal ellipsoid represents 50% probability)

104 crystallizes in the centro-symmetric monoclinic space group *C*2/c with four formula units in the unit cell (*Figure 5.13*). Crystallographic details, as well as selected bond length and bond angles are summarized in *Table 5.4*.

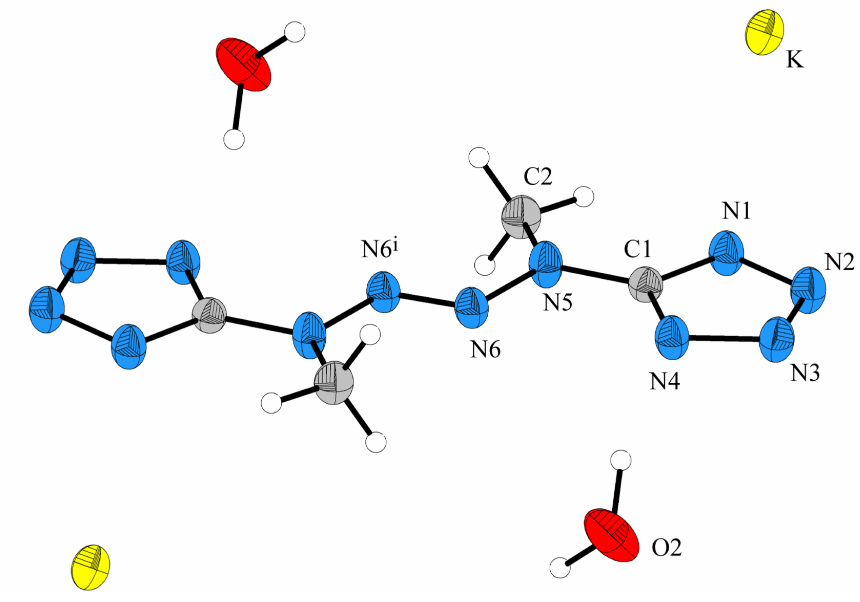

Figure 5.13. View of the molecular arrangement of **104**, showing the atom-labeling scheme. Displacement ellipsoid are drawn at the 50% probability level and H atoms are shown as spheres of arbitrary radii. The third water molecule is omitted due to clarity. [Symmetry code: (i) -x, -y, 1-x.]

Compared to the **84b**, **104** does not show obvious structure changes: The bond distance between the N atoms of the azo group (N=N **84b** 1.261(1); **104** 1.257(5) Å) is slightly shortened and the formal N-N single bond (N-N **84b** 1.367(2); **104** 1.381(1) Å) lengthened. In both compounds, the amino group atoms are in a planar environment as indicated by the sum of bond angles for which values of around 360° are found. The four nitrogen atoms of the 2-tetrazene unit and the directly bonded C atoms of the tetrazole ring are arranged in one plane. In contrast to **84b**, where the tetrazole moieties are slightly rotated out of this plane (N4-C1-N5-N6: 170.09(1)°), for **104** a value of 175.99(3)° is found. Also for **104** the C1-N5 bond length (1.381(7) Å) is much shorter than CN bond length found in azidoamidinium salt and other amino substituted tetrazoles (*Chapter VI*, I). This indicates also a strong π interaction of the tetrazole units with the tetrazene moiety, leading to a delocalized π-system over the whole molecule. The four nitrogen atoms of the 2-tetrazene units and the tetrazolate moieties show essentially coplanar arrangements.

4. Decomposition experiments of 84a and 84b

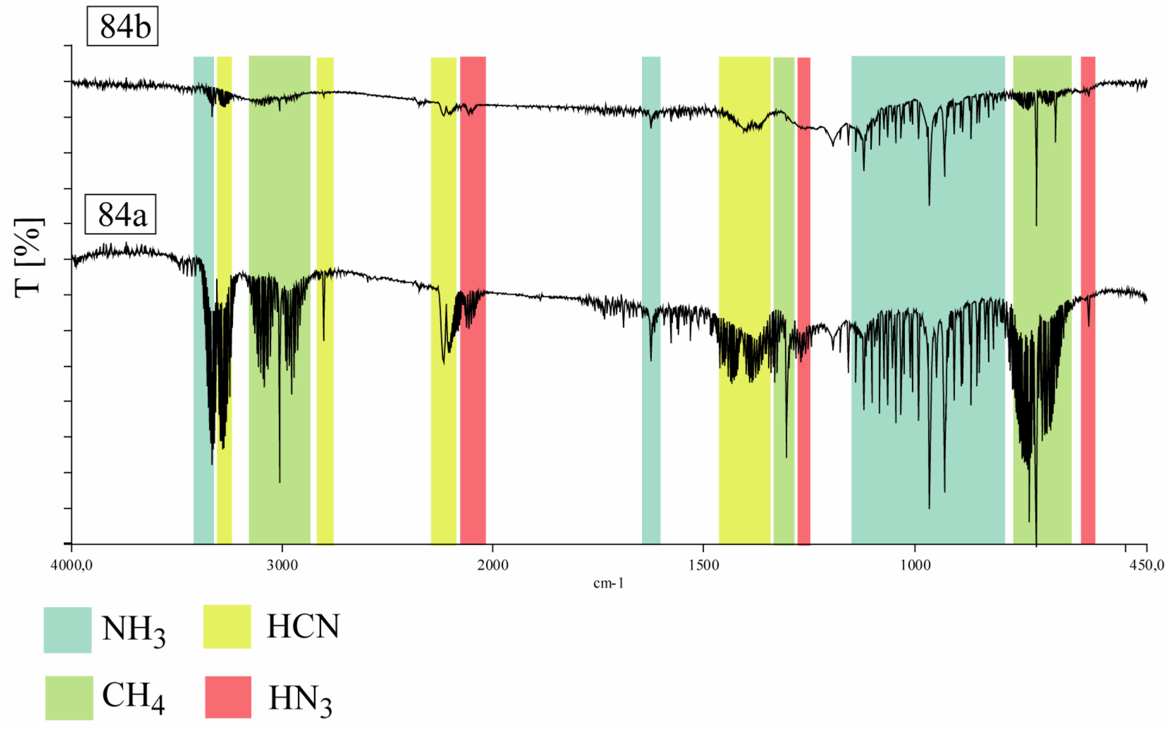

Figure 5.14. IR spectra of evolved gases from pyrolysis experiments of **88a** and **88b**

In order to determine the explosion gases of **84a** and **84b**, combined IR and MS pyrolysis experiments were carried out. *Figure 5.14* shows the gaseous products obtained after the explosion of **84a** and **84b**. The pyrolysis was supported by mass spectrometry, and for **84a** as only gaseous products ammonia, methane, hydrogen cyanide and traces of hydrazoic acid was observed. Compared to **84a** these products are only found as traces in the case of **84b**, indicating a different decomposition pathway.

In order to determine the stepwise decomposition of **84b**, the IR and MS pyrolysis experiments were analyzed more closely. The most important gaseous product observed were molecular nitrogen. N,N'-dimethylcarbodiimide (MeNCNMe, **107**) was also found as decomposition product. Therefore, it is assumed that thermal stressing results in breaking the N5−N6 bonds which generates one equivalent molecular nitrogen and two equivalents of a 1-methyl-(N-methyl)iminotetrazolyl radical (**108**). Under this condition, **108** opens yielding the azide form which decomposes under release of N3 radicals and **107**. Recombination of two N3 radicals gives three equivalents of N2 leading to the overall Equation [1] with an energy release of $\Delta_{calc.}G_{298}$=-927.6 kJ mol^{-1}.[69]

$C_6N_{12}H_{21}$ (**84b**) → $4N_2$ + 2MeNCNMe (**107**) [1]

5. Conclusion

A new synthesis was introduced for the preparation of several alkyl substituted hydrazinotetrazoles yielding the products in a range of 54 to 77 % yield. Especially, **88a**, **88b** and **88c** are interesting. **88a** and **88b** could be used as additives in propellant formulation or as propellants themselves with an appropriate oxidizer, since they can be seen as a solid version of MMH (N: 60.8 %), DMH (N: 46.6 %) and UDMH (N: 46.6 %) but with higher nitrogen content (**88a** (N: 73.7 %), **88b** (N: 65.6 %)). Both compounds show remarkable stabilities and are easily obtained as colorless crystalline products from the reported procedures. Since **88b** has an allyl group as substituents, polymerization reaction might be of interest yielding new energetic polymers. Corresponding investigations with Prof. Langhals are currently underway.

The reduction of the eight-step-reaction for the preparation of the **84b** was reduced to a three step synthesis. The obtained overall yield of 26% exceeds the former synthesis, which yielded 4%. Moreover, a general synthesis for the preparation of substituted (R = H, Me, allyl, cyclohexyl) 1,4-bis-(1R-1*H*-tetrazol-5-yl)-1,4-dimethyl-2-tetrazene was developed. Two products could be confirmed by means of single X-ray crystal determination (**84d**, **104**). Although the yields of the tetrazenes are still not satisfactory, the interest in these compounds is quite high. For example, the exchange of the methyl group in **84b** to hydrogen in **84a** completely changes the decomposition behavior, resulting also in a higher impact sensitivity of **84a** compared to **84b**.

84a-d represents easily accessible new highly energetic density materials which may qualify as environmentally-friendly energetic sources and or as leading candidates for alternative energy storage media once the problem with the last oxidation step is solved. Moreover, the compounds are expected to show distinctive decomposition pathway (e.g. **84a** and **b**) to molecular nitrogen and other still endothermic compounds like ammonia, methane and HN_3. The properties of theses compounds might be tuned by the introduction of certain substituents. Hence, in combination with appropriate oxidizer this class of compounds could be utilized as a new gas generator or propellant which gives off exclusively non toxic gases in a propulsion process might serve as additive or phlegmatizers in *explosives* formulation.

6. Experimental

*CAUTION: Although the tetrazole and 2-tetrazene derivatives are kinetically stable compounds and most time insensitive to electrostatic discharge, friction and impact, they are nonetheless energetic materials and appropriate safety precautions should be taken, especially when compound **88a** is prepared on a larger scale. Laboratories and personnel should be properly grounded.*

1-Cyano-1-methyl-hydrazine (90): To a pre-cooled (0°C) solution of BrCN (4.5g, 42,5 mmol) in 100 mL of dichloromethane, a mixture of MMH (2.0g, 42,5 mmol), sodium carbonate (2.5g, 21,3 mmol) and water (20 cm^3) was added dropwise under vigorous stirring. The mixture was stirred until no further evolution of CO_2 was observed. The two layers were separated and the aqueous phase extracted three times with methylene chloride. The organic phases were joined together and dried over magnesium sulphate. The solvent was removed under reduced pressure, affording 2.11g (70%) of an oil. Raman (200 mW, liquid) $\tilde{\nu}$ [cm^{-1}]: 3334 (10), 3275 (21), 3205 (17), 2982 (7), 2942 (10), 2905 (11), 2813 (11), 2208 (68), 1615 (4), 1443 (11), 1421 (10), 1330 (3), 1162 (4), 1077 (4), 761 (100), 702 (9), 631 (3), 533 (5), 401 (13), 287 (10), 225 (36); ^1H NMR ($CDCl_3$) δ: 3.14 (s, Me), 4.31 (br, NH_2); ^{13}C NMR ($CDCl_3$) δ: 44.4 (*C*H_3), 117.7 (*C*N).

2,4-Dimethylthiosemicarbazide (92b): Methylisothiocyanate (36.5 g, 0.5 mol), dissolved in 100 mL diethylether, was added drop wise to an ice-cooled solution of methylhydrazine (23.0 g, 0.5 mol) in 100 mL diethylether over 1 h and stirred for another 2 h. The precipitated colorless solid was separated by filtration and washed with cold diethylether (54.6 g, 0.46 mol, 91.8 %). The obtained data are consistent with the published data.

4-Allyl-2-methylthiosemicarbazide (92c): A solution of methylhydrazine (19.3 g, 0.42 mol) and 50 mL diethylether was slowly added to a cooled (ice bath) solution of allylisothiocyanate (40.0 g, 0.40 mol) in 200 mL diethylether. After the addition of MMH the slurry was stirred for further 2 h. The product was separated by filtration and washed several times with cold diethylether (56.2 g, 0.39 mol, 96.9 %). IR (KBr, cm^{-1}): $\tilde{\nu}$ = 3320 (s), 3259 (s),

3173 (m), 3076 (w), 3012 (w), 2975 (w), 2921 (w), 2057 (vw), 1849 (vw), 1641 (m), 1623 (m), 1523 (vs), 1449 (w), 1412 (w), 1370 (s), 1321 (m), 1260 (s), 1154 (w), 1086 (m), 1020 (w), 996 (m), 951 (w), 924 (s), 910 (m), 885 (vs), 698 (m), 671 (m), 641 (m), 609 (w), 531 (vw), 474 (vw), 445 (vw); Raman (200 mW, 25° C, cm^{-1}): $\tilde{\nu}$ = 3332 (30), 3246 (20), 3175 (45), 3077 (23), 3013 (35), 2980 (35), 2956 (27), 2925 (37), 1644 (100), 1619 (31), 1517 (13), 1426 (51), 1413 (43), 1370 (23), 1289 (77), 1264 (30), 1222 (23), 1157 (7), 1090 (8), 1025 (13), 1004 (12), 951 (27), 923 (20), 888 (20), 688 (57), 644 (36), 471 (30), 374 (50), 283 (13), 245 (20), 162 (43), 141 (43); ^{1}H-NMR ([d6]-DMSO) δ: 3.43 (s, 3H, CH_3), 4.07 (t, J = 5.68 Hz, 2H, NCH_2), 4.87 (s, 2H, NH_2), 5.02 (d, J_{cis} = 10.3 Hz, 1H), 5.09 (d, J_{trans} = 17.2 Hz, 1H), 5.85 (ddt, J = 5.40 Hz, 10.3 Hz, 17.3 Hz, 1H), 8.12 (t, J = 5.1, 1H, NH); ^{13}C-NMR ([d6]-DMSO) δ: 43.1 (CH$_3$), 47.1 (NCH$_2$), 115.7 (CH$_2$CH), 136.2 (CHCH$_2$), 181.6 (CS).

4-Cyclohexyl-2-methylthiosemicarbazide (**92d**)**:** To a solution of cyclohexyl-isothiocyanate (26.00 g, 0.186 mol) in 50 mL diethylether was added a a solution of methylhydrazine (8.56 g, 0.186 mol) in 50 mL diethylether drop wise. Stirring was continued for 2 h at room temperature. After filtration and washing with Et_2O, **92d** was obtained as colorless solid (30.7 g, 0.165 mol, 88.7 %); IR (KBr, cm^{-1}): $\tilde{\nu}$ = 3321 (s), 3258 (m), 3171 (m), 3145 (m), 2933 (vs), 2849 (s), 2655 (vw), 2229 (vw), 2074 (vw), 1420 (s), 1627 (m), 1525 (vs), 1467 (w), 1446 (m), 1408 (w), 1388 (m), 1368 (s), 1343 (m), 1325 (m), 1257 (w), 1245 (w), 1217 (vw), 1187 (vw), 1156 (w), 1105 (w), 1098 (w), 1079(m), 1049 (vw), 1020 (w), 973 (m), 902 (m), 885 (s), 843 (vw), 800 (vw), 783 (vw), 760 (vw), 737 (vw), 712 (vw), 669 (m), 607 (w), 582 (w), 529 (vw), 489 (vw), 467 (vw), 453 (vw), 427 (vw), 408 (vw); Raman (200 mW, 25 °C, cm^{-1}): $\tilde{\nu}$ = 3322 (17), 3256 (31), 3148 (25), 2939 (75), 2900 (31), 2851 (100), 2658 (11), 1642 (15), 1627 (15), 1442 (70), 1413 (23), 1348 (39), 1297 (19), 1258 (57), 1248 (38), 1215 (15), 1191 (15), 1157 (11), 1075 (21), 1051 (28), 1029 (61), 975 (23), 887 (15), 845 (39), 801 (73), 716 (72), 583 (8), 529 (43), 489 (37), 455 (34), 335 (40), 238 (23), 201 (27); ^{1}H-NMR ($CDCl_3$): δ = 1.12 – 1.97 (m, 10H), 3.57 (s, 3H, CH_3), 3.73 (s, 2H, NH_2), 4.09 (m, 1H, CH) 7.66 (br. s, 1H, NH);^{13}C-NMR ($CDCl_3$): δ = 24.9 (C), 25.6 (C), 33.1 (C), 43.6 (CH$_3$), 53.4 (C), 180.6 (CS).

***N*-Methyl-*N*-(1(2)*H*-tetrazol-5-yl)-hydrazine monohydrate (88a):** A solution of MMH (23.02 g, 0,5 mol) in Ethanol (160 mL) was added dropwise to a cooled (0°C) and vigorously stirred solution of BrCN (52.96 g, 0,50 mol) in Ethanol (240 mL), H_2O (4 mL) and Na_2CO_3 (26.5 g, 0,25 mol). After the addition (ca. 1,5 h) the reaction mixture was allowed to warm up to R.T., and stirring continued until the evolution of CO_2 was finished. The insoluble salts were removed by filtration. To this clear solution, NaN_3 (65g, 1 mol) and a mixture of conc. HCl (80 mL) in H_2O (200 mL) **(CAUTION, evolution of HN_3, Fumehood!!!)** was added. The reaction mixture was heated under reflux for 48h and solution concentrated *in vacuo* **(HN_3 !!!)** to 1/3 of it's volume. During this process the product precipitates as colorless crystals. Recrystallisation from water/ethanol gave the monohydrate **88a** suitable for single crystal X-ray structure determination. Yield 47.78 g (362 mmol, 72 %); m.p. 185 °C (decomposition); $\tilde{\nu}$ (KBr)[cm^{-1}]: 3429 (m, -NH), 3314 (s), 3212 (m), 3173 (m), 2936 (m), 2779 (m), 2648 (m), 1674 (vs), 1597 (vs), 1461 (w), 1427 (w), 1411 (m), 1364 (vw), 1341 (vw), 1279 (m, 1248 (m), 1181 (m), 1112 (w), 1027 (vs), 996 (m), 906 (s), 8881 (shoulder), 734 (s), 681 (m), 621 (vw); Raman (200 mW) $\tilde{\nu}$ [cm^{-1}]: 3314 (37), 3273 (22), 3214 (59), 3027 (16), 2940 (41), 2815 (20), 1679 (58), 1595 (22), 1460 (29), 1429 (48), 1409 (50), 1367 (13), 1320 (18), 1281 (88), 1252 (31), 1184 (29), 1110 (41), 1063 (100), 1027 (73), 996 (32), 916 (56), 735 (14), 683 (14), 636 (88), 541 (56), 529 (41), 389 (68), 331 (18), 172 (65); ^{1}H NMR ([d6]-DMSO]) δ: 3.14 (s, -NH, NH_2 due to fast proton exchange); ^{13}C NMR ([d6]-DMSO]) δ: 42.4 (CH_3), 161.9 (C); ^{15}N NMR ([d6]-DMSO]) δ: -10.1 (N2, N3, broad), -138.5 (N1, N4, broad), -296.7 (-NMe-*N*H_2), -311.6 (-*N*Me-NH_2); *m/z* (EI) 114 [(M) (100)], 111 (7), 99 (23), 97 (10), 86 (10), 81 (6), 71 (11), 69 (11), 57 (27), 56 (12), 55 (14), 46 (9), 45 (26), 44 (36), 43 (86), 42 (57), 41 (22), 40 (13), 30 (31), 29 (35), 28 (49), 27 (8), 18 (11), 17 (8), 16 (8), 15 (51); $C_2H_8N_6O$ (132.11): Calc. C, 18.2; H, 6.1; N, 63.6%; Found: C, 18.6; H, 5.7; N, 63.6%.

***N*-Methyl-*N*-(1-methyl-1*H*-tetrazol-5-yl)-hydrazine (88b):** To a solution of 2,4-dimethylthiosemicarbazide **92b** (4.76 g, 40 mmol) in 50 mL ethanol was added methyliodide (5.68 g, 40 mmol) and refluxed for 4 h (monitored by ^{1}H NMR). After cooling the reaction mixture below 40°C, sodium azide (3.9 g, 60 mmol) was added and the reaction mixture refluxed for about 18 h (monitored by TLC or ^{13}C-NMR) under nitrogen. After removing the solvents the oily residue was dissolved in dichloromethane to precipitate most of the sodium iodide. NaI was removed by filtration. The clear solution was concentrated and the product

purified by column chromatography (EtOH/Et_2O 1:10) on silica gel (2.78 g, 22 mmol, 54 %). IR (KBr, cm^{-1}): $\tilde{\nu}$ = 3309 (s), 3179 (m), 3009 (w), 2976 (m), 2916 (w), 2870 (w), 2790 (vw), 2529 (vw), 2272 (vw), 2179 (vw), 1947 (vw), 1646 (vs), 1557 (vs), 1472 (s), 1452 (s), 1405 (m), 1337 (w), 1316 (w), 1266 (m), 1204 (m), 1127 (m), 1100 (s), 1039 (s), 967 (w), 907 (s), 802 (w), 746 (s), 717 (s), 693 (w), 624 (m), 525 (w), 459 (w); Raman (200 mW, 25 °C, cm^{-1}): $\tilde{\nu}$ = 3302 (12), 3224 (17), 3183 (15), 3011 (17), 2977 (35), 2913 (19), 2871 (12), 2792 (10), 1648 (15), 1552 (17), 1475 (19), 1456 (19), 1408 (19), 1393 (12), 1318 (10), 1271 (38), 1202 (6), 1130 (7), 1101 (22), 1045 (13), 968 (6), 905 (3), 729 (100), 624 (27), 521 (13), 463 (7), 394 (19), 325 (17), 206 (15); ^{1}H-NMR ([d6]-DMSO, 270 MHz): 3.11 (s, 3H, CH_3), 3.96 (s, 3H, CH_3), 4.83 (s, 2H, NH_2); ^{13}C-NMR ([d6]-DMSO) δ: 36.8 (CH_3), 44.3 (CH_3), 159.6 (*C*); *m/z* (DEI): 128 [M (28)], 113 (3), 97 (2), 83 (24), 57 (100), 43 (33), 28 (58), 18 (68), 15 (46); $C_3H_8N_6$ (128.0810 found M^+ 128.0807); $C_3H_8N_6$ (128.14): calcd. C, 28.1; H, 6.3; N, 65.6 %; found: C, 27.9; H, 6.2; N, 65.5 %.

***N*-(1-Allyl-1*H*-tetrazol-5-yl)-*N*-methylhydrazine (88c):** Methyliodide (2.86 g, 20 mmol) was added to a solution of 4-allyl-2-methylthiosemicarbazide **92c** (2.90 g, 20 mmol) in 30 mL ethanol and refluxed for 4 h (monitored by ^{1}H NMR). The solution was cooled below 40°C and sodium azide (1.95 g, 30 mmol) was added. The reaction mixture was refluxed under nitrogen until all starting material was consumed (reaction should be monitored by TLC or ^{13}C-NMR, ca. 60 hours). After removal of the solvent, the residue was dissolved in dichloromethane to precipitate most of the sodium iodide and azide. After filtration, the DCM was removed *in vacuo* and the oily residue was purified by column chromatography (DMC:EtOAc 1:1) on silica gel to give pure **40b** as a colorless oil (2.37 g, 15 mmol, 77.0 %). Raman (200 mW, 25° C, cm^{-1}): $\tilde{\nu}$ = 3765 (3), 3336 (14), 3283 (9), 3232 (20), 3092 (15), 3023 (30), 2991 (32), 2951 (27), 2872 (14), 2802 (14), 1647 (100), 1557 (20), 1450 (21), 1413 (36), 1340 (27), 1292 (53), 1283 (53), 1259 (50), 1103 (31), 996 (12), 940 (14), 769 (32), 764 (34), 741 (15), 692 (15), 633 (56), 521 (12), 401 (30), 320 (19), 299 (19), 147 (50); ^{1}H-NMR ($CDCl_3$) δ: 3.20 (s, 3H, CH_3), 3.98 (s, 2H, NH_2), 5.05 (m, 2H, CH_2), 5.15 (d, 2H, NCH_2), 5.90 (m, 1H, C*H*); ^{13}C-NMR ($CDCl_3$) δ: 44.9 (CH_3), 50.7 (CH_2), 118.4 (CH_2), 131.8 (*C*H), 158.4 (*C*); *m/z* (DEI): 154 [M (16)], 109 (6), 99 (3), 83 (7), 45 (23), 41 (100), 28 (16), 15 (17); $C_5H_{10}N_6$ (154.0967 found M^+ 154.0970); calculated: C, 39.0; H, 6.5; N, 54.5 %; found: C, 39.2; H, 6.5; N, 54.1 %.

***N*-(1-Cyclohexyl-1*H*-tetrazol-5-yl)-*N*-methylhydrazine (88d):** 4-Cyclohexyl-2-methyl thiosemicarbazide **92d** (19.5 g, 104 mmol) was dissolved in 150 mL ethanol and methyliodide (14.5 g, 102 mmol) was added. After refluxing for 4 h (monitored by ^{1}H NMR), the solution was cooled below 40°C and sodium azide (9.75 g, 150 mmol) was added. The reaction mixture was refluxed under nitrogen until all starting material was consumed (monitored by TLC or ^{13}C-NMR, ca. 80 hours). After removal of the solvent, the residue was dissolved in dichloromethane to precipitate most of the sodium iodide and azide. After filtration, the DCM was removed *in vacuo* and the oily reddish residue was purified by column chromatography (Et_2O/AcOEt 1:1) on silica gel to give pure **88d** as a colorless solid (11.23 g, 58 mmol, 56.5 %). IR (KBr, cm^{-1}): $\tilde{\nu}$ = 3337 (vs), 3229 (w), 2998 (w), 2937 (vs), 2925 (vs), 2853 (vs), 2792 (w), 2661 (vw), 2169 (vw), 1636 (s), 1547 (vs), 1454 (vs), 1447 (vs), 1436 (s), 1412 (m), 1396 (w), 1342 (m), 1310 (w), 1253 (m), 1216 (m), 1168 (m), 1141 (w), 1127 (m), 1105 (m), 1096 (m), 1053 (w), 1019 (w), 1005 (m), 893 (s), 851 (w), 818 (w), 261 (w), 747 (s), 707 (vw), 629 (w). 583 (w), 510 (vw), 483 (vw), 467 (w); Raman (200 mW, 25 °C, cm^{-1}): $\tilde{\nu}$ = 3335 (21), 3233 (28), 3000 (16), 2941 (100), 2926 (96), 2896 (45), 2855 (81), 2794 (14), 2661 (7), 1639 (15), 1535 (19), 1447 (73), 1412 (20), 1336 (18), 1304 (22), 1274 (58), 1256 (35), 1197 (11), 1166 (10), 1144 (10), 1109 (23), 1078 (15), 1051 (21), 1029 (33), 1004 (21), 897 (10), 855 (11), 820 (63), 791 (9), 763 (53), 630 (38), 587 (33), 469 (13), 444 (21), 419 (12), 330 (20), 289 (37), 236 (16), 194 (20), 124 (19); ^{1}H-NMR ([d6]-DMSO) δ: 1.19 – 2.02 (m, 10H) 3.10 (s, 3H, CH_3), 4.86 (s, 2H, NH_2), 4.97 (m, 1H, N*H*); ^{13}C-NMR ([d6]-DMSO) δ: 25.4 (*C*), 25.6 (*C*H_3), 39.5 (*C*), 44.8 (*C*), 158.9 (*C*); *m/z* (DEI): 196 [M^+ (32)], 114 (76), 83 (85), 55 (100), 43 (72); $C_8H_{16}N_6$ (196.1436 found M^+ 196.1439); calculated: C, 49.0; H, 8.2; N, 42.8 %; found: C, 48.8; H 8.1; N, 42.6 %.

1,4-*bis*-(1(2)*H*-Tetrazol-5-yl)-1,4-dimethyl-2-tetrazene (84a):

I Oxidation with bromine

<u>in HCl:</u> A solution of **88a** (6.6g, 50 mmol) in 25 mL 2M HCl (25 mL) and water (25 mL) was cooled to 0 °C. To this solution Bromine was added drop wise until the orange color persisted. The reaction mixture was stirred for 1h at 0 °C and then the white precipitate separated by filtration and washed with cold water until bromine free (0.827g, 3.7 mmol, 15 %). The so obtained product was pure enough for further use and characterization; m.p. 200-207°C

(decomposition); $\tilde{\nu}$ (KBr)[cm^{-1}]: 3438 (w, -NH), 2942 (m, Me), 2773 (m), 2671 (m), 1602 (vs), 1583 (vs), 1454 (w), 1436 (m), 1426(m), 1405 (s), 1283 (w, 1243 (vw), 1157 (s), 1118 (w), 1091 (w), 1049 (m), 1031 (m), 996 (m), 980 (s), 867 (w), 724 (w), 686 (w), 655 (m), 567 (vw); Raman (200 mW) $\tilde{\nu}$ [cm^{-1}]: 3041 (2), 2995 (1), 2950 (6), 1624 (31), 1493 (100), 1453 (6), 1425 (15), 1399 (23), 1390 (17), 1291 (5), 1236 (8), 1200 (11), 1123 (4), 1082 (13), 1048 (5), 998 (3), 960 (9), 840 (2), 727 (1), 521 (13), 400 (3), 324 (5), 198 (9), 155 (8); ^{1}H NMR ([d6]-DMSO]) δ: 3.64 (s, Me); ^{13}C NMR ([d6]-DMSO]) δ: 34.5 (CH_3), 156.9 (C); *m/z* (DEI) 224 [(M) (15)], 126 (8), 99 (31), 97 (6), 81 (8), 79 (8), 71 (45), 69 (6), 57 (7), 56 (5), 55 (9), 43 (15), 42 (74), 41 (53), 40 (28), 39 (10), 38 (7), 29 (30), 28 (100), 27 (10); $C_4H_6N_{12}$ (224.0995 found M^+ 224.0980): Calc. C, 21.4; H, 3.6; N, 75.0%; Found: C, 20.9; H, 4.0; N, 74.3%.

in F_3CCOOH: **88a** (4.567g, 40 mmol) was dissolved in 50 mL CF_3COOH and 50 mL H_2O and cooled to 0°C. To this solution bromine was added drop wise until the reaction mixture shows the characteristic orange-brown color of bromine. The reaction mixture was kept 12h at 0°C and the precipitate separated by filtration and washed with water until bromine free. By this method 350 mg (1,6 mmol, 8 %) of the tetrazene **84a** was obtained.

II Oxidation with HgO

in pyridine: HgO (2.85g, 13mmol) was added slowly (ca. 1h) to a stirred solution of **88a** (1g, 8.8 mmol) in pyridine (15 mL) at 0°C. After the addition of HgO the reaction mixture was stirred for further 6h. After filtration, H_2O (20 mL) was added to the filtrate and the pH of the solution was adjusted to 1 by slowly adding conc. HCl (cooling required). The separated tetrazene **84a** was filtered, washed with water and dried yielding 325 mg (1,5 mmol, 33%).

in MeOH: The oxidation of **88a** (1g, 8.8 mmol) with HgO (4,75g, 22 mmol) in MeOH (25 mL) at 0°C does not yield the tetrazene **84a**. During the addition of HgO the evolution of a gas was observed that was very likely to be N_2. The by-products of this reaction where not determined.

III Oxidation with NaOCl

<u>in HCl:</u> 88a (5g, 44mmol) was dissolved in 6 M HCl (100 mL) and cooled to 0°C. NaOCl solution in water (13%, 24 mL, 44 mmol) was added dropwise over 2 h. The mixture was kept stirring for further 30 min at 0°C. The precipitate was filtered, washed with water and EtOH. After drying 700 mg (3.1 mmol, 14 %) of tetrazene **84a** was obtained.

<u>in CH_3COOH:</u> NaOCl solution (13%, 2,4 mL, 4,4 mmol) was added slowly to a solution of **88a** (500 mg, 4.4 mmol) in water (10 mL) at 0°C. After the addition the reaction mixture was cooled for further 2 h and the precipitate filtered. After washing with water, EtOH and Et_2O, 60 mg (0.3 mmol, 14%) of compound **84a** was obtained.

IV Oxidation with $KBrO_3$

A solution of **88a** (1g, 8.8mmol) in conc. HCl (5mL) was cooled to 0°C and a solution of $KBrO_3$ (0.49g, 2.9 mmol) in 5 mL was added in small portion very slowly. After the orange color of bromine persisted the addition of $KBrO_3$ was stopped and the reaction mixture stirred for further 30 min at 0°C. The tetrazene **84a** was separated by filtration, washed with water and EtOH yielding 200 mg (0.89mmol, 20%) of product.

1,4-*bis*-(1-Methyl-1*H*-tetrazol-5-yl)-1,4-dimethyl-2-tetrazene (84b): 1-Methyl-1-(1-methyl-1*H*-tetrazol-5-yl)hydrazine **88b** (1.02 g, 8 mmol) was dissolved in 20 mL of a 1 : 5 mixture of acetic acid and water. To this solution, a saturated solution of bromine in water was added drop wise at 0°C until the brown color of the bromine solution persisted longer than 2 minutes. During this addition, the product separates continuously. The suspension was kept at the fridge overnight and the product separated by filtration (493 mg, 1.95 mmol, 49%). m.p. 159.8 - 159.9 °C; IR (KBr): $\tilde{\nu}$ = 3026 (vw), 1622 (m), 1568 (m), 1468 (s), 1411 (m), 1396 (w), 1382 (vw), 1319 (vw), 1274 (vw), 1217 (w), 1117 (s), 1101 (m), 1039 (vw), 1006 (w), 962 (vw,), 730 (w), 716 (w), 681 (vw), 656 (m), 468 (vw) cm^{-1}; Raman (200 mW; 25 °C): $\tilde{\nu}$ = 3035 (5), 2963 (8), 1606 (46), 1492 (100), 1467 (31), 1440 (16), 1402 (40), 1324 (4), 1294 (7), 1227

(20), 1166 (6), 1107 (17), 1040 (1), 959 (3), 856 (6), 730 (2), 693 (26), 538 (8), 365 (4), 322 (7), 279 (4), 213 (6), 143 (11) cm^{-1}; ^{1}H NMR ([d6]-DMSO): δ: 3.63 (s, 3H, CH_3), 4.13 (s, 3H, CH_3); ^{13}C-NMR ([d6]-DMSO): δ: 35.7 (CH_3), 39.8 (CH_3), 154.9 (*C*); MS (70 eV): *m/z* (DEI) 252 (40) [M^+], 140 (39), 113 (9), 112 (6), 83 (100) [$MeCN_5^+$], 55 (5), 43 (53), 42 (5) [N_3^+], 41 (6), 28 (22) [N_2^+]; $C_6H_{12}N_{12}$ (252.1290 found M^+ 252.1308); calculated. C, 28.6; H, 4.8; N, 66.6%; Found: C, 28.5; H, 5.0; N, 66.8%.

1,4-*bis*-(1-Allyl-1*H*-tetrazol-5-yl)-1,4-dimethyl-2-tetrazene (88c): 1-(1-Allyl-1*H*-tetrazol-5-yl)-1-methylhydrazine **88c** (0.5 g, 3.2 mmol) was dissolved in 10 mL of a 1 : 5 mixture of acetic acid and water and cooled in an ice-bath to 0°C. To this solution, a saturated solution of bromine in water was added drop wise at 0°C until the brown color of the bromine solution persisted longer than 2 minutes. During this addition, the product separates continuously as a beige powder. The solvent was removed by filtration to and the obtained product was dried on air (60 mg, 0.20 mmol, 12.5 %). IR (KBr, cm^{-1}): $\tilde{\nu}$ = 2936 (vw), 1685 (vw), 1643 (vw), 1629 (vw), 1618 (vw), 1560 (vs), 1468 (w), 1442 (w), 1418 (w), 1407 (w), 1345 (vw), 1331 (vw), 1276 (vw), 1262 (vw), 1219 (vw), 1169 (vw), 1123 (m), 1056 (w), 1006 (m), 961 (vw), 775 (vw), 726 (vw), 684 (vw), 657 (w); Raman (200 mW, 25 °C, cm^{-1}): $\tilde{\nu}$ = 3089 (5), 3032 (9), 2980 (10), 2956 (15), 1646 (14), 1597 (35), 1495 (100), 1464 (21), 1445 (28), 1403 (38), 1347 (17), 1304 (12), 1228 (21), 1106 (15), 857 (7), 767 (5), 727 (4), 685 (7), 649 (9), 603 (6), 536 (11), 426 (9), 349 (9), 323 (14), 251 (14), 163 (37); ^{1}H-NMR ($CDCl_3$) δ: 3.68 (s, 3H, CH_3), 5.05 (d, 1H, J_{trans} = 16 Hz, CH_{2trans}), 5.14 (d, 4H, *J* = 5 Hz, CH_2), 5.31 (d, 1H, J_{cic} = 11.6 Hz, CH_{2cis}), 5.99 (ddt, 2H, *J* = 5 Hz, 10.5 Hz, 17.2 Hz, C*H*); ^{13}C-NMR ($CDCl_3$) δ: 35.8 (CH_3), 51.1 (CH_2), 119.0 (CH_2), 130.55 (*C*H), 154.14 (*C*); *m/z* (DEI) 305 (4) [M+1], 304 (25) [M^+], 220 (7), 218 (8), 166 (14), 139 (23), 138 (21), 121 (5), 118 (5), 109 (55), 95 (4), 82 (14), 81 (6), 69 (6), 68 (10), 57 (10), 56 (5), 55 (23), 54 (9), 53 (12), 43 (14), 42 (22), 41 (100), 40 (6), 39 (31), 28 (16), 27 (7), 18 (7), 15 (8); $C_{10}H_{16}N_{12}$ (304.1621 found M^+ 304.1627).

1,4-*bis*-[1-Cyclohexyl-1*H*-tetrazol-5-yl)-1,4-dimethyl-2-tetrazene (84d): 1-(1-Cyclo hexyl-1*H*-tetrazol-5-yl)-1-methylhydrazine **88d** (1 g, 5.1 mmol) was dissolved in 10 mL a 1:5 mixture of acetic acid and water and cooled in an ice-bath to 0°C. To this solution, a saturated solution of bromine in water was added drop wise at 0°C until the brown color of the bromine solution persisted longer than 2 minutes. The product precipitated instantly as a beige powder

and was separated by filtration and dried on air (0.28 g, 0.72 mmol, 28.8 %). IR (KBr, cm^{-1}): $\tilde{\nu}$ = 2940 (w), 2925 (w), 2861 (w), 1560 (vs), 1472 (vw), 1437 (w), 1410 (w), 1387 (vw), 1342 (vw), 1296 (vw), 1261 (vw), 1211 (vw), 1195 (vw),1166 (w), 1138 (m), 1096 (vw), 1064 (w), 1018 (w), 901 (vw), 819 (vw), 802 (vw), 758 (vw), 735 (vw), 654 (w), 585 (w), 516 (w); Raman (200 mW, 25 °C, cm^{-1}): $\tilde{\nu}$ = 3032 (5), 2949 (32), 2861 (32), 1591 (53), 1502 (37), 1486 (100), 1448 (31), 1405 (53), 1338 (9), 1307 (10), 1285 (14), 1267 (13), 1225 (21), 1200 (10), 1156 (7), 1102 (10), 1058 (8), 1033 (10), 971 (6), 866 (9), 818 (21), 746 (9), 701 (7), 575 (12), 450 (13), 407 (12), 366 (9), 289 (32), 219 (9), 130 (16); ^{1}H-NMR ($CDCl_3$) δ: 1.30 – 2,03 (m, 10H), 2.11 (s, 3H, CH_3), 3.62 (s, 3H, NH_2), 4.53 (m, 1H, N*H*Hex); ^{13}C-NMR ($CDCl_3$) δ: 24.9 (*C*), 25.7 (*C*), 32.9 (*C*H_3), 36.0 (*C*), 59.4 (*C*), 153.9 (*C*); *m/z* (DEI): 181 (44), 110 (64), 71 (88), 55 (100), 41 (56), 42 (21), 28 (16), 15 (18); *m/z* (DEI) 389 (14) [M+1], 388 (60) [M^+], 360 (8), 210 (4), 208 (10), 182 (6), 181 (23), 280 (30), 152 (16), 151 (99), 128 (5), 126 (6), 123 (4), 110 (17), 100 (56), 99 (14), 98 (13), 96 (7), 84 (8), 83 (100), 82 (8), 81 (11), 71 (71), 69 (6), 67 (13), 57 (11), 56 (5), 55 (78), 54 (7), 53 (5), 43 (11), 42 (12), 41 (37), 39 (8), 29 (6), 28 (8), 27 (8); $C_{16}H_{28}N_{12}$ (388.2560 found M^+ 388.2602).

7. References

[1] Benson, F. A. *The High Nitrogen Compounds*, Wiley, New York, **1984**.

[2] Fischer, E. *Liebigs Ann. Chem.* **1878**, *190*, 67.

[3] Danen, W. C.; Neugebauer, F. A. *Angew. Chem., Int. Ed. Engl.* **1975**, *14*, 783.

[4] Esker, J. E.; Newcomb, M. *Advan. Heterocycl. Chem.* **1993**, *58*, 1.

[5] Wiberg, N.; Bachhuber, H.; Bayer, H. *Angew. Chem., Int. Ed. Engl.* **1975**, *14*, 177.

[6] Bischhof, R.; Gleiter, R.; Dach, R.; Enders, D.; Seebach, D. *Tetrahedron* **1975**, *31*, 1415.

[7] Bock, H.; Göbel, I.; Näther, C.; Solouki, B.; John, A. *Chem. Ber.* **1994**, *127*, 2197.

[8] Lemal, D. M.; Rave, T. W. *J. Am. Chem. Soc* **1965**, *87*, 393.

[9] Back, T. G. *J. Chem. Soc., Chem. Commun.* **1981**, 530.

[10] Back, T. G.; Kerr, R. G. *Can. J. Chem.* **1982**, *60*, 2711.

[11] Hinman, R. L.; Hamm, K. L. *J. Am. Chem. Soc.* **1959**, *81*, 3294.

[12] Nelsen, S. F.; Heath, D. H. *J. Am. Chem. Soc.* **1969**, *91*, 6452.

[13] Roberts, J. R.; Ingold, K. U. *J. Am. Chem. Soc.* **1969**, *95*, 3228 .

[14] Forgione, P. S.; Spargue, G. S.; Troffkin, H. J. *J. Am. Chem. Soc.* **1966**, *88*, 1079.

[15] Overberger, C. G.; Marks, B. S.; Byrd, N. R. *J. Am. Chem. Soc.* **1955**, *77*, 4104.

[16] Overberger, C. G.; Palmer, L. C.; Marks, B. S.; Byrd, N. R. *J. Am. Chem. Soc.* **1955**, *77*, 4100.

[17] Bhatnagar, I.; George, M. V. *J. Org. Chem.* **1968**, *33*, 2407.

[18] Hammond, G. S.; Seidel, B.; Pincock, R. E. *J. Org. Chem.* **1959**, *28*, 3275.

[19] Forgione, P. S.; Spargue, G. S.; Troffkin, H. J. *J. Am. Chem. Soc.* **1966**, *88*, 1079.

[20] Jones, D. W. *J. Chem. Soc. Perkin Trans. I* **1976**, 1150.

[21] a) Wiber, N.; *Adv. Organomet. Chem.* **1984**, *23*, 131; b) Wiberg, N.; Vasisht, S. K.; Bayer, H.; Meyers, R. *Chem. Ber.* **1979**, *112*, 2718; c) Wiberg, N.; Uhlenbrock, W. *Chem. Ber.* **1972**, *105*, 63; d) Wiberg, N.; Vasisht, S. K.; Fischer, G. *Angew. Chem., Int. Ed. Engl.* **1976**, *15*, 236.

[22] Otsuka, V; Nakamura, A. *Inorg. Chem.* **1968**, *7*, 2542.

[23] Gilchrist, A. B.; Sutton, D. *Can. J. Chem.* **1974**, *52*, 3387.

[24] Meier, R. *Chem. Ber.* **1953**, *86*, 1483.

[25] Lee, S. W.; Miller, G. A.; Campana, C. F.; Maciejewski, M. L.; Trogler, W. *J. Am. Chem. Soc.* **1987**, *109*, 5050.

[26] Wiberg, N.; Bayer, H.; Vasisht, S. K. *Chem. Ber.* **1981**, *114*, 2658.

[27] a) Child, R. G.; Morton, G.; Pidacks, C.; Tomcufcik, A. S. *Nature* **1964**, 391. b) Michejda, C. J.; Hoss, W. P. *J. Am. Chem. Soc.*, **1970**, *92*, 6298.

[28] a) Weigand, J. J. *1,4-Bis(1'-methyltetrazolyl)-1,4-dimethyl-2-tetrazene and other nitrogen rich high energy density materials* Diploma thesis, Ludwig-Maximilian University, **2002**.; b) T. M. Klapötke, P. Mayer, A. Schulz, J. J. Weigand *Prop. Explos. Pyrotech.* **2004**, *29(6)*, 273.

[29] Percival, D. F.; Herbst, R. M.; *J. Org. Chem.* **1957**, *22*, 925.

[30] Klapötke, T. M.; Rienäcker, C. M. *Prop. Explos. Pyrotech.* **2001**, *26(1)*, 43

[31] R. Reed, B. Y. S. Lee, R. A. Henry, Unites State Patent 4,358,327 **1982**.

[32] Ryckmans, T.; Viehe, H.-G.; Feneau-Dupont, J.; Tinant, B.; Declercq, J.-P. *Tetrahedron* **1997**, *53(5)*, 1729.

[33] Garbrecht, W. L.; Herbst, R. M. *J. Org. Chem.* **1953**, *18*, 1022.

[34] Henry, R. A.; Boschan, R. H. *J. Am. Chem. Soc.* **1954**, *76*, 1949.

[35] Sasse, K. Deutsches Patent Nr. 1 670 956, **1971**.

[36] Holmberg, B.; Psilanderheim, B. *J. Prakt. Chem.* **1910**, *82*, 440.

[37] Gibbs, C. G. Unites State Patent 4,331,497 **1980.**

[38] Moderhack, D.; Goos, K. H.; Preu, L. *Chem. Ber.*, **1990**, 1575.

[39] Scovill, J. P. *Phosphorus, Sulfur, and Silicon.* **1991**, *60*, 15.

[40] Stief, L. J.; DeCarlo, V. J. *J. Phys. Chem.*, **1966**, 4638.

[41] Wieland, H. Chem. *Ber.* **1920**, *53B*, 1313.

[42] Butler, R. N.; Scott, F. L. *J. Org. Chem.* **1966**, 3182.

[43] Urry, W. H.; Olsen, A. L.; Bens, E. M.; Kruse, H. W.; Ikoku, C.; Gaibel, Z. *Autoxidation of 1,1-Dimethylhydrazine* U.S. Naval Ordinance Test Station Technical Publication 3903; **1965**.

[44] Loper, G. L. *Proceedings of the Conference on Environmental Chemistry of Hydrazine Fuels*. **1977**, 129-159.

[45] Sisler, H. H.; Mathur, M. A. *paper presented in part at the Proceeding of the Conference on Environmental Chemistry of Hydrazines Fuels*, Tyndall AFB, **1977**.

[46] Porath, B.; Rademacher, P.; Boese, R.; Bläser, D. *Z. Naturforsch.* **2002**, *57b*, 365.

[47] A. Hammerl, „Hochernergetische, Stickstoffreiche Verbindungen“, *PhD thesis, Ludwig-Maximilians-Universität*, **2001**.

[48] Anderson, S.; Glover, E. E.; Vaughan, K. D. *J.C.S. Perkin I*, **1975**, 1232.

[49] Porath, B.; Rademacher, P.; Boese, R.; Bläser, D. *Z. Naturforsch.* **2002**, 57, 365.

[50] Bellamy, A. J.; Maclean, L. *J.C.S. Perkin I* **1979**, 204.

[51] Wieland, H.; Wecker, E. *Chem. Berichte* **1910**, 3260.

[52] Fehlauer, A.; Grosz, K.; Slopianka, M.; Sucrow, W.; Lockley, W. J. S.; Lwowski, W. *Chem. Ber.* **1976**, *109*, 253.

[53] Thesing, J.; Willersinn, H. *Chem. Berichte* **1956**, 1195.

[54] Milcent, R., Guevrekian-Soghomoniantz, M.; Barbier, G. *J. Heterocyclic Chem.***1984**, *23*, 1986.

[55] Nelsen, S. F.; Heath, D. H. *J. Am. Chem. Soc.* **1969**, *91*, 6452.

[56] Porath, B.; Münzenberg, B. R.; Heymans, P.; Rademacher, P.; Boese, R.; Bläser, D.; Latz, R. *Eur. J. Org. Chem.* **1998**, 1431.

[57] Back, T. G. *Chem. Commun.* **1981**, 530.

[58] Farina, M.; Barbosa, N. B. V.; Nogueira, C. W.; Folmer, V.; Zeni, G.; Andrade, L.-H.; Braga, A. L.; Rocha, J. B. T. *Brazillian Journal of Medical and Biological Research*, **2002**, *35*, 623.

[59] Mishia, J. B. *Decomposition of tetrazoles*, *CPIA Publication*, **1981**, 399.

[60] Wiberg, N.; Bachhuber, H.; Bayer, H. *Angew. Chem., Int. Ed. Engl.* **1975**, *14*, 177.

[61] Kroner, J.; Wiberg, N.; Bayer, H. *Angew. Chem., Int. Ed. Engl.* **1975**, *14*, 203.

[62] Smith, H. W.; Mastropaolo, D.; Camerman, A.; Camerman, N. *J. Chem. Cryst.* **1994**, *24*, 239.

[63] Veith, M.; Schlemmer, G. *Z. Anorg. Allg. Chem.* **1982**, *42*, 2511.

[64] Veith, M. *Acta Cryst.* **1975**, *B31*, 678.

[65] Day, R. O.; Michejda, C. J.; Kingsbury, C. A.; Day, V. W.; McOmie, J. F. W. *J. Chem. Soc., Chem. Commun.* **1974**, 66.

[66] Nelsen, S. F.; Landis, R. T.; Calabrese, J. C. *J. Org. Chem.* **1977**, *42*, 4192.

[67] Miller, G. A.; Lee, S. W.; Trogler, W. C. *Organometallics* **1989**, *8*, 738.

[68] Porath, B.; Münzenberg, R.; Heymanns, P.; Rademacher, P.; Boese, R.; Bläser, D.; Latz, R. *Eur. J. Org. Chem.* **1998**, 1431.

[69] Geometries and frequencies were calculated utilizing the B3LYP/6-311+G(3df,2p) level of theory. Thermodynamical data were derived from B3LYP/6-311+G(3df,2p) level utilizing the thermochemical corrections of the B3LYP/6-31G(d,p) level. Inspection of the conformational space showed that a C_2 symmetry structure represents the global minimum for **84b** which is only separated by less than 0.2 kcal/mol from the C_i and < 3 kcal/mol from several planar C_{2h} symmetry structures.

C h a p t e r   V I

NITRAMINES

1. N-Nitroso- and N-Nitraminotetrazoles

An ideal explosive is powerful, safe and easy to handle, can be stockpiled for long periods in any climate and is hard to detonate except under precisely specified conditions. The history of high explosives goes back to 1885, were the first high explosive, 2,4,6-trinitrophenol (picric acid),[1] was put into service in France. Due to some disadvantages – high melting point, reaction with metals as well its sensitivity – of this compound, it was substituted by another high explosive, fulfilling the expectations of the producers: 2,4,6-trinitrolouene (TNT)[2]; this compound is still used today in explosive mixtures.

The next generation of explosives with higher performance are the nitramine compounds hexahydro-1,3,5-trinitro-*S*-triazine (RDX)[3] followed by octahydro-1,3,5,7-tetranitro-1,3,5,7-tetrazine (HMX)[4] (*Figure 6.1*). In the pure state these compounds are too sensitive and can only be used with insensitive additives or in mixtures with e.g. TNT. Since the search of new energetic compounds with increased performance is progressing relatively slowly, the trends and development of 'New Products' has rather to be seen in the manufacturing of blended and polymer-bounded explosives meeting the desired demands such as easy processing and handling together with keeping a high security level is the state-of-the-art. Currently, much effort is made in order to increase the safety of the explosive products on handling and in case of fire or other unwanted external influences like impact, falling and being fired upon. With respect to this, nitramines are of special interest and are going to be discussed in the following *Chapters*.

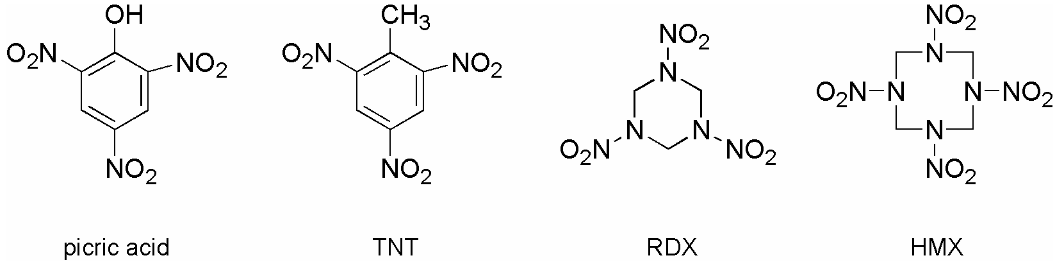

Figure 6.1. Secondary explosives

In continuation of the work described in the previous *Chapters* on compounds with a high nitrogen content the investigating of the chemistry of aminotetrazole derivatives with respect to their use as components in propellants and explosives[5,6] is of special interest since they can be readily converted to corresponding *N*-nitroso- and *N*-nitraminotetrazoles. They are of interest, since they have two energetic sites: the nitroso/nitramino and the tetrazole moiety. Particularly *N*-nitraminotetrazoles are of interest, as they might be used as modifiers for the combustion rates in rocket propellants, as cool gas generators or other or as additives in special *explosives* and were investigated e.g. by Willer et al.[7]

Not much attention has been given to energetic materials based on nitraminotetrazoles, and important data, like NMR and crystal structures are missing for compounds already described in literature.[8] Therefore it is important to reinvestigate the chemistry of certain nitraminotetrazoles, especially with respect to NMR, crystal structure and rotational barriers around the N−N bond and compare different synthetic routes. The synthesis in all cases is based on the conversion of the easily accessible *N*-aminotetrazoles,[9] either by the direct nitration with nitrating agents (e.g. acetic anhydride/HNO_3) or by dehydration of the corresponding nitrates with conc. sulfuric acid.[10] The direct conversion of easily accessible *N*-nitrosaminotetrazoles to the corresponding nitramines by the action of peroxytrifluoroacetic acid, yielding the corresponding pure secondary nitramines, was also investigated. *N*-nitrosamines exhibit strong carcinogenic and mutagenic properties and are potential $NO^{\cdot}/NO^{+}$ donors[11] through homolytic and heterolytic cleavage of the N−NO bond, respectively. For *N*-nitrosaminotetrazoles similar properties should be expected. This class of compounds is only little investigated, however.[12] In the following *Chapters* the synthesis, multinuclear NMR data and molecular structures in the crystal of *N*-nitrosaminotetrazoles (**111a**, **111c**) are reported. The NMR data and molecular structures of the new nitroso compounds are compared to those of the corresponding *N*-nitraminotetrazoles (**112a-c**).

1.1 Synthesis and properties of *N*-Nitroso- and *N*-Nitraminotetrazoles

The nitroso- (**111a,c**) and nitraminotetrazoles (**112a-c**) are prepared starting from the corresponding substituted 5-aminotetrazoles. The syntheses of the 5-aminotetrazoles belong to one of the following four main reaction types: (1) amino group or ring functionalization of 5-aminotetrazoles,[13,14] which often results in mixtures of isomers;[15,16] (2) substitution of a leaving group in the tetrazole 5-position with amines;[17] (3) various azide-mediated tetrazole ring

formation reactions (e.g. from cabodiimides,[18] cyanamides[19] or α-chloroformamidines[20]); and (4) reaction of aminoguanidine derivatives with sodium nitrite under acid condition.[21,18] The latter reaction is the most convenient for the synthesis of the corresponding symmetric substituted 1-methyl-5-(methylamino)-1*H*-tetrazole (**109a**), 1-isopropyl-5-(isopropylamino)-1*H*-tetrazole (**109b**) and 5,6-dihydro-7*H*-imidazolo[1,2-*d*]tetrazole (**109c**). **109a-c** were obtained according known procedures from the substituted *S*-methyl-isothiouronium hydriodides (**107a-c**), which were first converted to the corresponding guanidinium derivatives (**108a-c**) with anhydrous hydrazine.

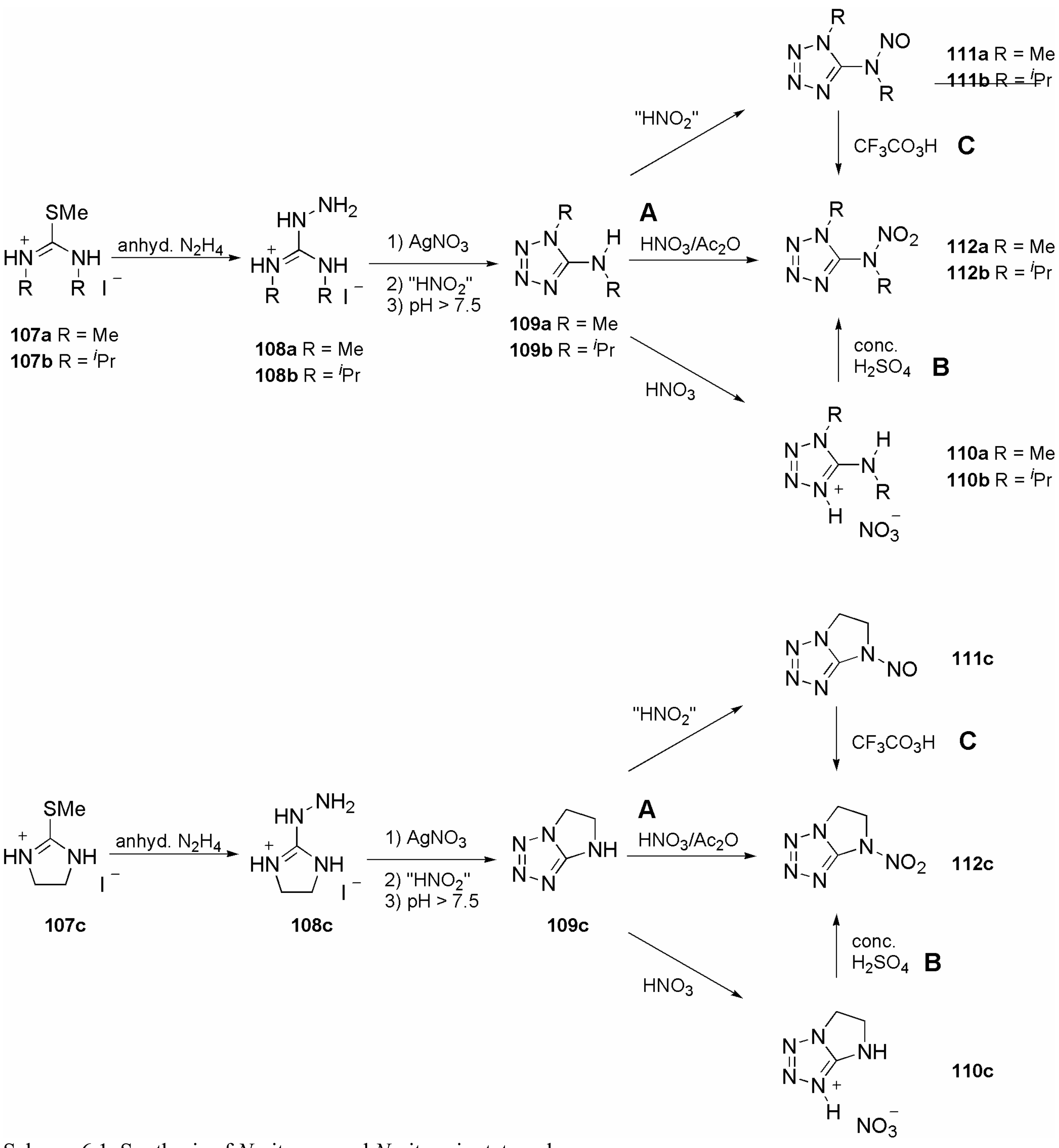

Scheme 6.1. Synthesis of *N*-nitroso- and *N*-nitraminotetrazoles

108a-c were then reacted with nitrous acid followed by a base workup to yield the 5-aminotetrazoles in good overall yields (**109a** (82%), **109b** (71%), **109c** (75%), *Scheme 6.1*). The 5-aminotetrazoles (**109a-c**) could all be directly converted to the corresponding nitraminotetrazoles (**112a-c**) using the nitration system acetic anhydride/nitric acid (*Scheme 6.1*, **A**) or *via* the corresponding nitrates (**110a-c**), as described by Garrison and Herbst[22] for the nitration of **109a** (*Scheme 6.1*, **B**). The obtained yield for **112c**, by direct nitration differs from that mentioned in ref [23] by 7%, and in the case of the methyl substituted derivative (**112a**) a higher yield was obtained compared to Garrison and Herbst (*Table 6.1*).[22] It is known from literature, that peroxytrifluoroacetic acid (CF_3CO_3H) has been found to be a unique reagent for the oxidation of nitrosamines[24], and so far it seems that this reagent has never been used for the oxidation of nitrosaminotetrazoles. The corresponding nitrosoamines were obtained according known procedures only for **111a** and **111c**.[22] In the case of **109b** the reaction with nitrous acid resulted in the formation of a complex mixture of products from which it was not possible to isolate **111b**. **111a** and **111c** were converted to **112a** and **112c** by CF_3CO_3H in DCM in excellent yields (82 % and 80 %, respectively, *Scheme 6.1*, **C**).

Table 6.1. Synthesis of the 5-aminotetrazole derivatives **109a-c**, **111a**, **111c** and **112a-c**

	comp	yield [%]				mp (lit. mp) [°C]
			method A	method B	method C	
1	**109a**	82[a]				175.0-175.5
2	**109b**	71[a]				163.5-164.0
3	**109c**	75[a]				175.0-175.5
4	**111a**	84[b]				46.0-47.0 (46-47[22])
5	**111b**	-				–
6	**111c**	94[b]				110.0-110.5 (–)
7	**112a**		64[c]	81 (75[22])[b]	82[d]	58.0-58.5 (58[22])
8	**112b**		66[c]	75[b]	–	56.0-57.0 (–)
9	**112c**		68[c] (75[23])	64[b]	80[d]	150.0 dec. (160[23])

[a] based on the corresponding thiourea derivative. [b] based on the corresponding 5-aminotetrazoles. [c] based on the corresponding nitrate. [d] based on the corresponding 5-nitrosoaminotetrazole.

1.2 Molecular Structures

Selected data on the molecular geometry of the compounds **111a,c**, **112a-c** as well as the corresponding 5-aminotetrazoles **109a,c** are given in *Table 6.2* (N−X: **109a,c** (X = H); **111a,c** (X = NO); **112a-c** (X = NO_2). The molecular structures of **109a,c**, **111a,c** and **112a-c** in the crystal are shown in *Figures 6.3*, *6.4* and *6.5*, respectively. Compounds **109a** and **112a** (*Figure 6.3*) crystallize in the orthorhombic space group *P*bca with eight formula units in the unit cell;

109c (*Figure 6.2*) and **112b** (*Figure 6.5*) in the monoclinic space group $P2_1/n$ with four formula units in the unit cell.

Table 6.2. Comparison of selected interatomic distances (Å), bond angles (°) and torsion angles (°) in **111a**,**c**, **112a**-**c** and **109a**,**c**[a]

	109a	**111a**	**112a**	**109c**	**111c**	**112c**	**112b**
Bond Length [Å]							
C1−N1	1.343(2)	1.329(3)	1.336(3)	1.325(2)	1.319(2)	1.276(4)	1.338(2)
N1−N2	1.362(2)	1.356(2)	1.341(3)	1.348(2)	1.348(2)	1.375(4)	1.341(2)
N2−N3	1.291(2)	1.284(3)	1.299(3)	1.288(2)	1.299(2)	1.317(4)	1.303(2)
N3−N4	1.374(2)	1.360(3)	1.359(3)	1.379(2)	1.384(2)	1.335(4)	1.358(2)
N4−C1	1.330(2)	1.310(3)	1.308(3)	1.316(2)	1.312(2)	1.339(4)	1.315(2)
C1−N5	1.338(2)	1.385(2)	1.391(3)	1.343(2)	1.378(2)	1.370(4)	1.397(2)
N1−C2	1.451(2)	1.454(3)	1.457(3)	1.453(2)	1.459(2)	1.435(4)	1.480(2)
N5−C3	1.451(2)	1.447(3)	1.460(3)	1.474(2)	1.486(2)	1.491(4)	1.486(2)
N5−X							
N5−N6		1.335(3)	1.390(3)		1.331(2)	1.354(4)	1.376(2)
N6−O1		1.227(2)	1.221(3)		1.223(2)	1.191(4)	1.214(2)
N6−O2			1.220(3)			1.205(4)	1.225(2)
Bond Angle [°]							
N4−C1−N5	126.6(1)	122.0(2)	125.9(2)	138.9(1)	139.4(1)	139.4(3)	126.5(1)
N4−C1−N1	108.7(1)	110.2(2)	110.2(2)	109.7(1)	111.4(1)	111.1(1)	109.9(1)
N1−C1−N5	124.7(2)	127.8(2)	123.7(2)	111.3(1)	109.2(1)	109.5(1)	123.6(1)
N3−N2−N1	106.2(1)	106.3(2)	106.9(2)	105.4(1)	105.3(1)	102.1(3)	106.6(1)
N2−N3−N4	111.3(1)	111.6(2)	110.7(2)	111.8(2)	112.0(1)	114.2(3)	111.0(1)
C1−N4−N3	105.3(1)	104.6(2)	104.9(2)	104.0(1)	102.9(1)	102.7(3)	104.9(1)
C1−N1−C2	129.5(2)	133.9(2)	130.1(2)	113.1(1)	115.1(1)	115.6(3)	130.5(1)
N2−N1−C2	122.1(2)	118.7(2)	122.5(2)	137.0(1)	136.3(1)	134.5(3)	121.8(1)
C1−N5−C3	120.3(2)	119.9(2)	120.6(2)	107.4(1)	110.1(1)	110.0(3)	123.0(1)
N5−X							
C1−N5−N6		117.1(2)	116.2(2)		121.7(1)	125.0(3)	115.6(1)
C3−N5−N6		123.0(2)	118.0(2)		127.1(1)	124.4(3)	119.5(1)
N5−N6−O1		113.5(2)	115.8(2)		112.7(1)	114.9(3)	117.7(1)
N5−N6−O2			117.2(2)			115.8(3)	116.3(1)
O1−N6−O2			127.0(2)			129.3(4)	126.0(1)
Torsion Angle [°]							
O1−N6−N5−C3		-1.4(3)			6.3(2)		
O1−N6−N5−C1		179.2(2)			172.8(1)		
N1−C1−N5−C3		3.8(3)			1.3(2)		

[a] for numbering see *Figure 6.2*

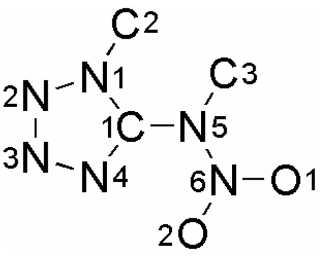

Figure 6.2. Connectivity and numbering scheme for the substituted tetrazole moiety in **109a**,**c**, **111a**,**c** and **112a**-**c**.

For **111a** (*Figure 6.3*), **111c** (*Figure 6.4*) and **112a** (*Figure 6.3*) the structures were solved in the monoclinic space group $P2_1/c$ with four units in the unit cell. Comparing all investigated compounds with respect to the tetrazole moiety and the exocyclic atoms N5 and C2 (i.e. the lengths of the N−C and N−N bonds as well as the corresponding bond angles) the tetrazole rings are approximately planar within the limits of accuracy (maximal deviation is 0.060(1) Å for **109c** and 0.042(2) Å for **112a** from this plane; *Appendix B*). The geometrical parameters found compare well to those observed for other tetrazole derivatives.[25] The interatomic distances in the tetrazole rings are not equal, ranging from 1.284(3) to 1.384(2) Å. The amino groups in the aminotetrazoles **109a** and **109c** are planar in accord with a sp^2 hybridization of the nitrogen atom. The angle sums around N5 are 356° (**109a**) and 351° (**109c**), respectively (*Table 6.2*). Moreover, the C1−N5 bond lengths in **109a** and **109c** compared to those in the nitrosamines and nitramines are closer to those typical for C=N double bonds. In the case of the substitution of the proton by a nitroso or nitro group, an elongation of the C1−N5 bond is found, with a maximum of 1.397(2) Å for **112b**. Depending on the nature of the substituent at N5, different features in the molecular structures of the investigated compounds were observed.

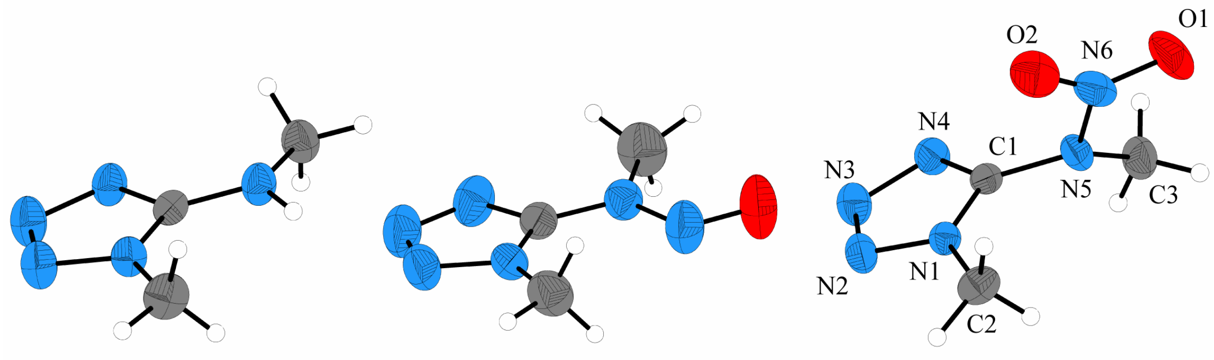

109a 111a 112a

Figure 6.3. Molecular structures and labeling scheme for **109a**, **111a** and **112a** (ORTEP Plot, thermal ellipsoids represent 50% probability).

The formal exchange of the proton in **109a** and **109c** by a nitroso group leads to the *N*-nitrosamines **111a** (*Figure 6.3*) and **111c** (*Figure 6.4*). The nitrosamine moiety in **111a** and **111c** lies almost in the plane of the tetrazole ring; the dihedral angle between the tetrazole plane and the −N(NO)− plane is 3.8° for **111a** and 7.2° for **111c**. The relevant torsion angles are given in *Table 6.2*. It is known that nitroso groups exhibit orientational disorder in the solid state,[26] which often leads to situations in which both isomers, Z (cisoid with respect to C−N) and E (transoid with respect to C−N), occupy the same site in the crystal. However, the crystal structure of **3a** and **3c** reveals that the *N*-nitrosamine moiety is ordered and adopts the E

conformation (Figure 3 and 4). No residual electron density peaks were found in the nearest vicinity of this group in both compounds, indicating that the crystal indeed consists solely of the E rotamere. Compared to reported values of *N*-methyl-*N*-nitrosoanilines, the observed bond lengths differ dramatically.[27] The bond distance C1−N5 in **111a** (1.385(2) Å) and **111c** (1.378(2) Å) is much shorter than corresponding C−N bonds in nitrosoanilines, which are typically longer than 1.43Å. The N5−N6 bond is much longer (1.335(3) Å (**111a**) and 1.331(2) Å (**111c**) *vs.* ~1.30 Å in *N*-methy-*N*-nitrosoanilines) and the N6−O1 bond (1.227(2) (**111a**) and 1.223(2) (**111c**) Å) was found to be shortened by ~ 0.04 Å with respect to the corresponding bond length in nitrosoanilines. An explanation might be the better π-conjugation of the terazole moiety with the lone pair at the N5 compared to anilines, which results in a shortening of the C1−N5 bond together with an elongation of the N5−N6 bond (see below, NBO anaysis). Bond lengths and angles of the tetrazole fragments for both compounds agree well with the geometry of similar molecules bearing substituents inducing sp^2 hybridization at the amino nitrogen atom N5.

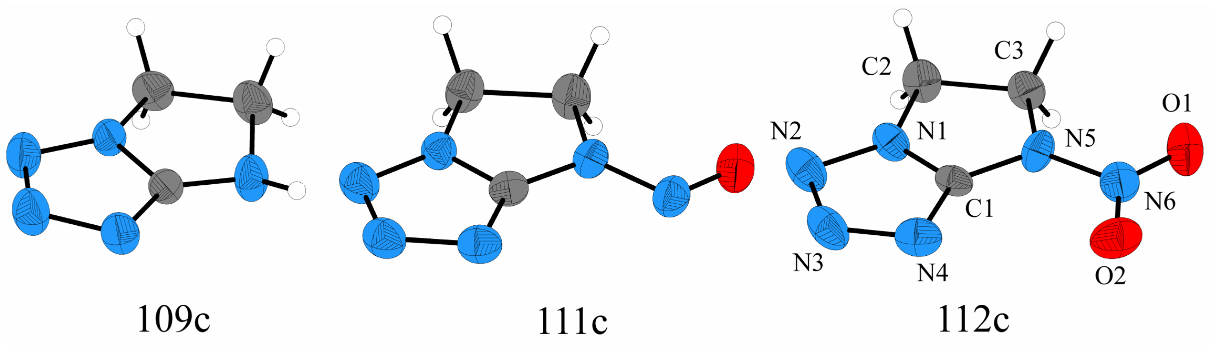

Figure 6.4. Molecular structures and labeling scheme for **109c**, **111c** and **112c** (ORTEP Plot, thermal ellipsoids represent 50% probability)

Selected bond length and bond angles of **112a** (*Figure 6.3*), **112b** (*Figure 6.5*) and **112c** (*Figure 6.4*) are contained in *Table 6.2*. For all three compounds the tetrazole ring and the arrangement around the nitrogen atoms of the nitramine moiety is planar within the limits of accuracy of the structure determination. The bond length and angles of the nitramine group for **112a-c** are comparable to those already reported.[28] In all three cases the lone pair on N5 is stereochemically inactive, which makes the bond angles about N5 essentially trigonal planar (angle sums around N5: 352.6(2) (**112a**), 358.1(1) (**112b**) and 359.4(3) (**112c**), respectively). This is found to be typical for unstrained nitramine units.[28] For **112c** some differences with respect to certain structural parameters are observed. Compared to the nitramine moiety in **112a**

and **112b** which is almost perpendicular to the plane of the tetrazole ring (torsion angle N1−C1−N5−N6 -78.5(2) (**112a)** and -90.3(2) ° (**112b**)) the nitramine moiety in **112c** lies in the same plane as the tetrazole ring (N1−C1−N5−N6 -176.28(1), indicating a possible interaction between the π-system of the tetrazole ring and the nitramine unit. The π-electron delocalization in **112c** is reflected e.g. in the bond distance C1−N5 (1.370(4) Å) which was found to be shortened by ~0.03 Å compared to **112a** (1.391(3) Å) and **112b** (1.397(2) Å). This is also supported by the results of an NBO analysis (see below). In accordance with that the N5−N6 bond was found to be unusually shortened in the case of **112c** (1.354(4) Å) compared to **112a** (1.390(3) Å) and **112b** (1.376(2) Å). The differences of the non-bridged structures such as **6a** and **112b** compared to **112c** can be best explained by repulsive interaction of the sp^2-type lone pair at N4 and the electron density localized at O2 of the nitro groups. This interaction leads to the orthogonal structure in **112a** and **112b** since the O2 atom of the nitro group tries to be as distant as possible from N4. Consequently a large N4−O2 distance is found in **112a** (3.510(1) Å) and **112b** (3.329(1) Å, compared to a fairly short distance in **112c** (2.880(2) Å).

Since densities of explosives are important for predicting explosive properties, a semi-empirical computer program invented by Willer et al., China Lake, was used to predict the densities of compounds **112a-c**. The predicted densities are 1.53 (**112a**), 1.27 (**112b**) and 1.71 (**112c**) g cm^{-3}. These agree remarkably well with the measured densities by X-ray crystallography (*Appendix B*, 1.522, 1.305 and 1.690 g cm^{-3}, respectively) and also illustrate that cyclic compounds are much more dense than acyclic compounds.[54]

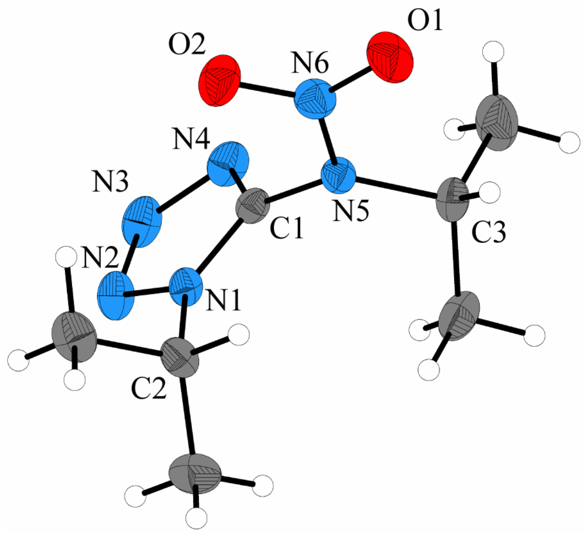

Figure 6.5. Molecular structure and labeling scheme **112b** (ORTEP plot, thermal ellipsoids represent 50% probability).

1.3 NBO analysis

A striking feature of the structure of all investigated tetrazolyl substituted nitroso- and nitramines is the almost planar environment of the nitrogen atom N5 (angle sums around N5 ranging from 352.6(2) to 360.0(2)°, *Table 6.2*). As shown by NBO analysis,[29] in all investigated species the lone pair at the nitrogen atom N5 is localized in a pure p-type atomic orbital. As a consequence the p-type lone pair at the nitrogen atom N5 (notation: p-LP(N5)) can be further delocalized resulting in intramolecular interactions (non-covalent effects). The best Lewis representation according to NBO is given in *Figure 6.6* (**A**) and displays two double bonds between C1-N4 and N2-N3 of the tetrazolyl ring.

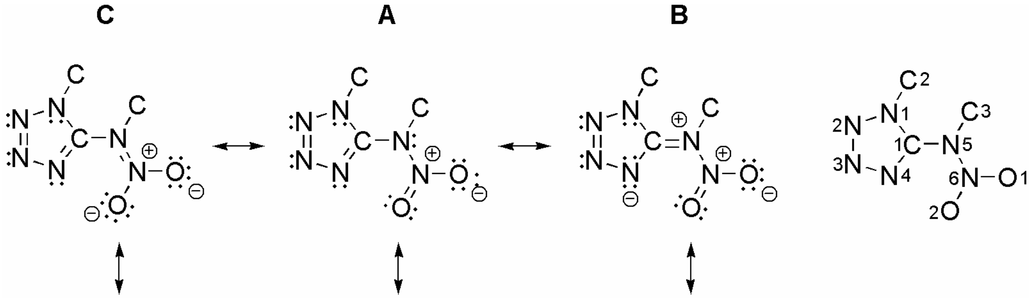

Figure 6.6. Lewis representation of the donor-acceptor interaction of p-LP(N5) with π^*(C1–N4) (**B**) and π^*(O1-N6) (**C**), respectively

This finding is supported by the calculated Wiberg bond indices (*Table 6.3*). Investigation of the non-covalent effects reveales two main possibilities for delocalization: into the tetrazolyl ring (**B**) and into the NO- or NO_2-group (**C**). For the planar systems (**111a**, **111c**, **112c**) there are two significant interactions of the nitrogen lone pair (p-LP(N5)) with the two unoccupied, localized antibonding π^*(C1–N4) (**B**) and π^*(O1-N6) (**C**) orbitals, which is described by the resonance between the Lewis representations **A**, **B** and **C** (*Figure 6.6*, *Table 6.4*). Moreover, delocalization into the NO- (**111a**, **111c**) and NO_2-group (**112c**) is always slightly favored over the ring delocalization as indicated by the sum of the intramolecular donor-acceptor energies (*Table 6.4*, e.g. in **111a** Σ_{NO}(54.2 kcal mol^{-1}) > Σ_{ring}(51.2 kcal mol^{-1})). For the two non-planar species (**112a** and **112b**) the sum of the intramolecular donor-acceptor energies into the tetrazole moiety is as expected much smaller (*Table 6.4*, e.g. in **112a** Σ_{NO2}(51.2 kcal mol^{-1}) > Σ_{ring}(28.3 kcal mol^{-1})). A comparison of the planar structures of **111a** and **111c**, shows in the case of **111c** an unfavorable charge distribution. This is displayed by the electrostatic potential (ESP) mapped on the electronic density surface (*Appendix A Figure A-3*) where a negatively charged tetrazole ring system is located next to the negatively charged nitroso group. In the case

of **111a** due to the different arrangement of the nitramine moiety, which is rotated by 180° compared to **111c**, such a repulsive interaction is not observed (*Appendix A Figure A-4*).

Table 6.3. Comparison of selected calculated Wiberg bond indices (WBI) from the NBO analysis of **111a**,**c** and **112a**-**c**.[a]

	111a	112a	111c	112c	112b
Bond Length [Å]					
C1−N1	1.22	1.21	1.19	1.07	1.22
N1−N2	1.18	1.23	1.18	0.87	1.23
N2−N3	1.63	1.59	1.63	1.10	1.58
N3−N4	1.30	1.32	1.28	1.01	1.33
N4−C1	1.46	1.50	1.49	1.41	1.49
C1−N5	1.05	1.00	1.04	0.92	0.98
N1−C2	0.93	0.92	0.93	0.76	0.89
N5−C3	0.92	0.93	0.91	0.73	0.89
N5−N6	1.26	1.02	1.25	0.84	1.04
N6−O1	1.71	1.48	1.73	1.13	1.47
N6−O2		1.48		1.14	1.48

[a] for numbering see *Figure 6.7*

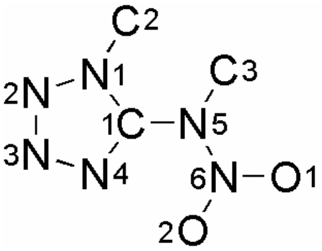

Figure 6.7. Connectivity and numbering scheme for the substituted tetrazole moiety in **111a**,**c**, **112a**-**c**.

Therefore it can be concluded that the significant interaction of the nitrogen lone pair (p-LP(N5)) with the two unoccupied, localized antibonding π*(C1–N4) (**B**) and π*(O1-N6) (**C**) orbitals, which describes the resonance between the Lewis representations **A**, **B** and **C,** is the driving force for the planarization of these systems.

Table 6.4. Summary of the NBO Analysis of **111a**,**c** and **112a**-**c** (p-LP(N5) → σ/π*(XY) Donor-Acceptor Interactions in Kcal mol^{-1})[a]

	111a	**111c**	**112a**	**112b**	**112c**
p-LP(N5) → π^*(C1-N4)	47.9	48.5	7.7	0.8	47.4
p-LP(N5) → σ^*(O1-N6)	50.4	54.8	40.1	43.6	45.2
$\Sigma_{NO/NO2}$[a]	54.2	57.9	51.2	52.0	52.0
Σ_{ring}[a]	51.2	50.9	28.3	22.9	50.3

[a] the experimental data have been used in the NBO algorithm.

Interestingly, by oxidation of the nitroso group to the nitro group (**112a** and **112b**) these non-bridges structures, as already discussed before, are no longer planar since the lone pair on

N4 and the electron density localized on the corresponding oxygen atom try to be as distant as possible from each other (Mullican and NBO charges on N4 and O2, *Appendix A Table A-9*). This situation is also nicely displayed by the corresponding ESP's mapped onto the electron density surface (*Appendix A Figure A-5 − A-7*). In the case of **111c**, from the electrostatic point of view the bridging ethylene unit forces this molecule in the unfavorable coplanar structure.

1.4 ^{15}N Chemical Shifts and ^{1}H-^{15}N Coupling Constants

The ^{15}N NMR shifts and the values of the ^{15}N,^{1}H coupling constants are presented in *Table 6.5*. For all compounds the proton coupled as well as the proton decoupled NMR spectra (with full NOE) were recorded. The assignments are based on the analysis of the ^{15}N,^{1}H NMR coupling patterns in the proton decoupled NMR spectra and, where necessary, on the comparison with literature data.[30] In previous reports the assignments were associated with the assumption that in tetrazoles N-1 and N-4 in general resonate at lower frequency whereas N-2 and N-3 resonate at higher frequency, and that alkyl substitution results in a significant shift of the pyrrole-type nitrogen resonance to lower frequency.[31] In accordance with this, it was found that the ^{15}N NMR chemical shifts correlate well with the electron densities at the nitrogen atoms (see above) and together with the ^{15}N,^{1}H NMR coupling patterns the assignment of the ^{15}N NMR signals to the nitrogen atoms of the tetrazole moiety was straightforward.

Table 6.5. ^{15}N and ^{13}C NMR chemical shifts (ppm) and ^{15}N,^{1}H coupling constants (*J*, Hz) of the compounds studied.

	N-1	N-2	N-3	N-4	N-5	X(N-6)	C-1
109a[a]	-186.8	-21.8	1.8	-94.9	-341.3	−	155.7[b]
	^{2}J(N1CH$_3$) = 1.5	^{3}J(N2CH$_3$) = 1.5		^{3}J(N4CH$_3$) = 2.4	^{1}J(NH) = 91.5	(H)	
109b[a]	-164.6	-28.8	2.5	-94.7	-312.5	−	153.5[b]
	^{2}J(N1CH) = 2.6	^{3}J(N2CH) = 2.2			^{1}J(NH) = 86.8	(H)	
109c[a]	-163.3	-29.2	21.0	-104.1	-349.2	−	165.8[a]
		^{3}J(N2CH$_2$) = 1.8		^{3}J(N4CH$_2$) = 2.2	^{1}J(NH) = 89.3	(H)	
111a[a]	-168.0	-9.1	4.7	-72.8	-139.7	172.7	153.3[b]
	^{2}J(N1CH$_3$) = 2.0	^{3}J(N2CH$_3$) = 1.7			^{2}J(N5CH$_3$) = 1.5	(NO)[c]	
111c[a]	-153.5	-23.5	24.9	-92.8	-144.6	167.4	158.3[b]
	^{2}J(N1CH$_2$) = 1.9					(NO)	
112a[a]	-153.2	-5.9	10.2	-58.9	-219.6	-34.9	147.8[b]
	^{2}J(N1CH$_3$) = 1.3			^{3}J(N4CH$_3$) = 2.2		(NO$_2$)	
112b[a]	-129.2	-10.1	13.3	-56.5	-202.2	-36.5	147.0[b]
	^{2}J(N1CH) = 2.2	^{3}J(N2CH) = 2.1				(NO$_2$)	
112c[a]	-156.8	-24.5	26.1	-83.2	-203.5	-42.0	158.6[b]
	^{2}J(N1CH$_2$) = 1.1					(NO$_2$)	

[a][d6]-DMSO; [b] [d6]-acetone; all shifts are given with respect to CH_3NO_2 (^{15}N) and TMS (^{13}C) as external standard; in the case of ^{15}N NMR negative shifts are upfield from CH_3NO_2; [c] Coupling of protons α to the nitroso group to the nitroso nitrogen atom and are less then 1.0 Hz, for **111a** (^{3}J(^{15}N-H) = 0.9 Hz) - **111c** (^{3}J(^{15}N-H) = 0.8 Hz);

The signal of the nitrogen atom (N-5) of the amino substituent for the aminotetrazoles **109a-c** could be assigned due to its chemical shift, well separated from the ^{15}N NMR signals of the nitrogen atoms of the tetrazole moiety, as well as its splitting to a doublet in the proton coupled ^{15}N NMR spectrum. The observed values for the one bond coupling constant are typical for $^{1}J(^{15}N,^{1}H)$ of three-coordinate nitrogen and range from 86.8 to 91.5 Hz (*Table 6.5*).[32] For all the compounds **109a-c**, **111a**, **111c** and **112a-c** it was found that the ^{15}N NMR chemical shifts of the nitrogen atoms of the tetrazole ring become more negative in the order N-3 < N-2 < N-4 < N-1. A more detailed insight into the electron charge distribution throughout the investigated compounds can be obtained from hybrid density functional theory (B3LYP). The optimized (B3LYP/6-31G(d,p))[33] geometries of the compounds have been used to calculate the electron charge distribution. The results summarized in *Table A-9* (Mullican and NBO charges, *Appendix A*), predict a general shift of electron charge towards the nitrosamino (**111a** and **111c**) and nitramino (**112a-c**) group and simultaneously an extreme differentiation of electron density throughout the tetrazole moiety. From these results using the Mulliken populations the atoms of the tetrazole moiety show the highest electron density of the two coordinated nitrogen atoms at N4. For N2 and N3 the Mulliken population shows similar values, which are higher for N3 compared to N2. However, as the Mulliken population analyses are known to be basis set dependent, also the results from a natural population analysis were included. They also give similar values for N2 and N3, but now the values for N2 are slightly higher.[34] In addition, the nitrosamino as well the nitramino group carries an overall negative net charge, resulting in a substantial separation of charges between the tetrazole *versus* nitrosamino or nitramino moiety (Σq(tetrazole) = ~ +0.20−0.25e *vs.* Σq(nitrosamino/nitramino) = ~ -0.20−0.25e; *Appendix A Table A-9*).

In accordance to the aminotetrazoles discussed previously, the ^{15}N NMR signal of the amino nitrogen (N5) of the nitrosaminotetrazoles **111a** and **111c** also appears upfield from the nitromethane reference, while the signal of the nitroso nitrogen (N6) is found far at low field. In the case of the nitrosotetrazoles **111a** and **111c**, the ^{15}N chemical shift of the N=O nitrogen atom appears downfield relative to that of aliphatic nitrosamines in a range characteristic for aromatic nitrosamines, which also indicates extensive electron delocalization within the tetrazole moiety (NBO analyses).[35] Comparing the investigated nitrosamines (**5a** and **5c**) there is a remarkable upfield shift of 5.3 ppm from **5a** (172.7 ppm) to **5c** (167.4 ppm) which can be attributed to the different extent of crossconjugation into the tetrazole moiety, also observed in the NBO analysis.[36,37]

The nitraminotetrazoles **112a-c** in a given solvent ([d6]-DMSO) are good examples for the so called β-effect of alkyl groups. It has already been observed that nitrogen magnetic shielding decreases significantly in the following sequence of alkyl substitution at nitrogen for a given group X (X = tetrazole moiety).[38]

$CH_3N(X) > RCH_2N(X) > R_2CHN(X) > R_3CN(X)$

R is an alkyl group, and X represents any atom or group of atoms. This is called the β-effect as each step involves the introduction of a carbon atom at the β-position with respect to the nitrogen atom concerned, and produces a deshielding effect Δσ = 6 to 12 ppm. In the present case, the replacement of the methyl group in **112a** by the isopropyl (**112b**) or ethylene bridge (**112c**), respectively, produces a β-effect and a concomitant deshielding of the amino nitrogen (N5), Δσ = about 17 ppm, just within the range expected. In the case of the nitrogen atom (N6) of the nitro group the signals are observed at the expected region (δ = -20 to -45 ppm).[39] In the case of the **112c** a pronounced upfield shift for N6 (as well as N4) is observed (**112c** (N6, -42.0 ppm) *vs.* e.g. **112a** (N6, -34.9 ppm)) which can be attributed to the intramolecular donor-acceptor interaction of the π-system (see NBO analyses) of the tetrazole moiety with the nitramine unit (*Table 6.4*).

1.5 ^{1}H and ^{13}C NMR spectra

In the ^{1}H NMR spectra of **109a-c** only one signal is observed for the N−H protons in the region (5.5 to 7.0 ppm), typical for secondary amines. The ^{1}H and ^{13}C NMR data of the alkyl groups are as expected. As becomes evident from *Table 6.5*, the formal exchange of the proton at N5 by a nitroso (**111a**,**c**) or nitro (**112a-c**) group leads to an upfield shift for the corresponding ^{13}C NMR resonance. In the case of **111a** and **111c** only the E isomer was observed, indicating a restricted rotation along the N5−N6 bond (see below). In the case of **109b** and **112b** a dynamic behavior in solution is observed, which can be attributed to the rotation of the isopropyl groups. The ^{1}H and ^{13}C{^{1}H} NMR spectra of the nitramine **112b** (*Figure 6.8*) are temperature dependent. They indicate, that rotation of the isopropyl groups became slow on the NMR time scale at low temperatures. At -65 °C four doublets are observed in the ^{1}H NMR spectrum corresponding to four different methyl groups. Accordingly four signals are observed in the ^{13}C NMR spectrum in the methyl region. Raising the temperature results in the pairwise coalescence of the ^{1}H and ^{13}C NMR signals of the methyl groups. In

addition to the dynamic behavior, the ^{1}H spectra show an interesting temperature dependence of the chemical shifts of the CH-protons of the ^{i}Pr groups. This temperature dependence is different for the two different CH-protons and causes their signals to overlap at low temperature.

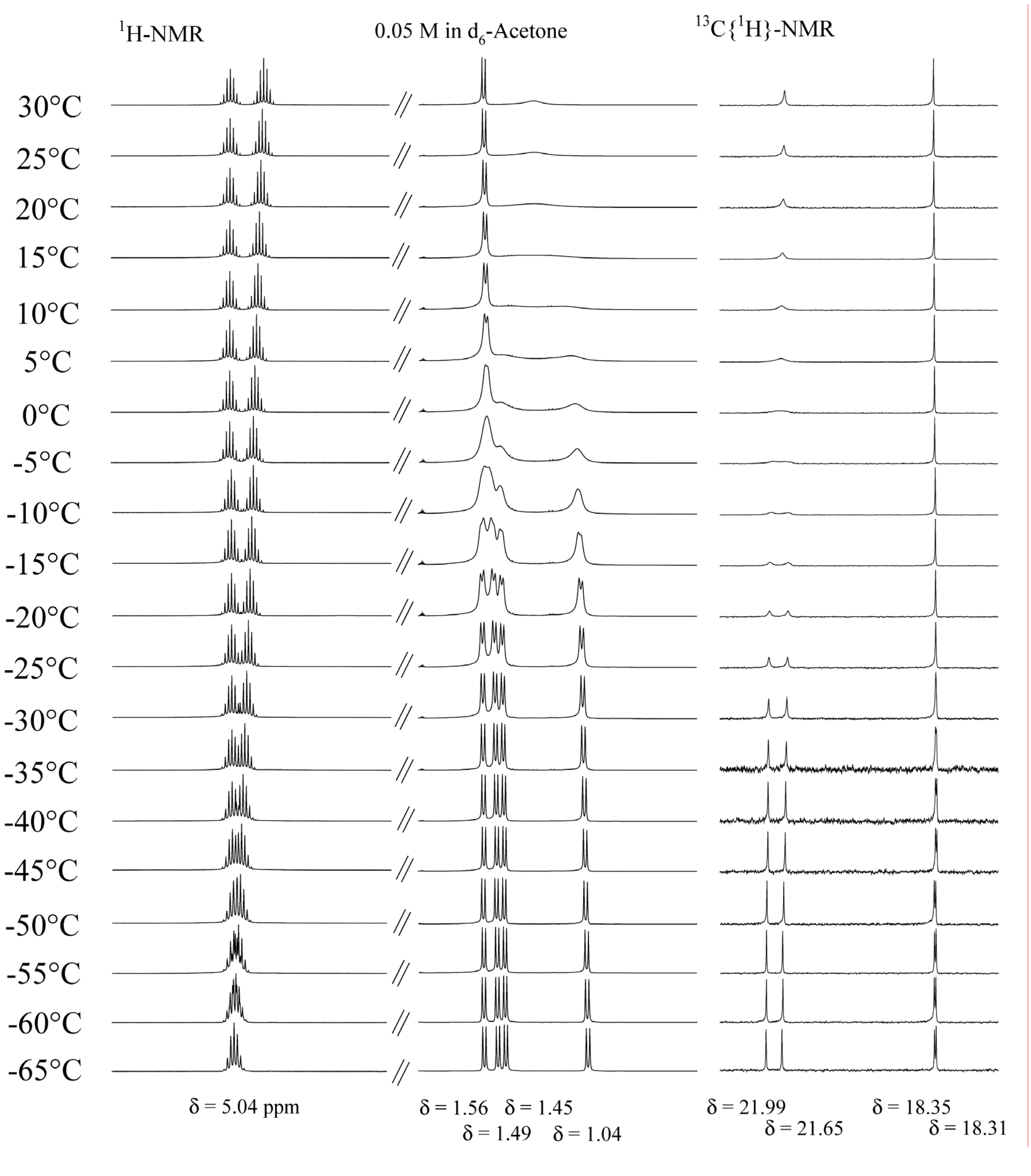

Figure 6.8. Temperature depended ^{1}H and ^{13}C{^{1}H} NMR spectra of **112b**

1.6 Raman and IR spectroscopy

In contrast to alkyl substituted *N*-nitroso compounds, which exhibit a characteristicly weak band at 1445-1490 cm^{-1} (N=O stretching) in the IR and Raman spectra,[40] the corresponding band in the Raman and IR spectra is found at higher wavenumbers (~1584 cm^{-1}). According to the results of a frequency analysis (B3LYP/6-31G(d,p)), the ν(N=O) mode is coupled in the case of **111a** with the ν(C1-N5) mode and for the bridged compound **111c** with the ν(C1-N4) mode. They are split into two characteristic bands, a strong band at ~1580 cm^{-1} and a medium band at ~1530 cm^{-1}, respectively. In the case of **112a-c**, the *N*−NO_2 groups give rise to the strong absorption in the 1285-1299 ($\nu_{sym}(NO_2)$) and 1560-1595 ($\nu_{asym}(NO_2)$) cm^{-1} regions and to a weak band at 945-970 (ν(N−N)) cm^{-1}.[41] The IR and Raman spectra of compounds **109a,c**, **111a,c** and **112a-c** contain further characteristic absorption bands: 3250-3100 cm^{-1} [ν(N–H) **109a,c**], 3000-2850 [ν(C–H), **109a,c**, **111a,c** and **112a-c**], 1680-1550 [ν(N6H) **109a,c**], 1550-1350 [ν,.tetrazole ring, $\nu_{as}(CH_3, CH_2, CH)$, ν(N4–H)], ~1380 [ν(CH_3 CH_2, CH)] 1350-700 [ν(N1–C1–N4), ν(N–N), ν(N6H), ν(CN), ν, tetrazole ring], <700 [ν,.out of plane bend N–H), ν(N6H)].

1.7 N,N Rotational Barriers

The isomerization process which interchanges the alkyl groups e.g. in Me_2NNO requires roughly 23 kcal mol^{-1}.[42] The mechanism is thought to involve rotation about the N−N bond rather than inversion of the nitroso nitrogen; calculations predict the latter to require activation energies which are four times as large as those of the rotation about the N−N bond.[43] *N*-nitroso compounds generally exhibit planar structures, because rotational barriers along the N−NO bond[44] are of similar magnitude compared to those of amides.[45] This can be understood in terms of a resonance structure (*Figure 6.9*), which displays partial double bond character of the N−N(O) bond, in a manner similar to the N−C(O) bond in amides.

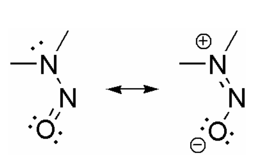

Figure 6.9. Resonance in *N*-nitrosamines

A series of different types of nitrosamines have been investigated with respect to their rotational barriers. From these investigations, rotational barriers of monocyclic five-membered *N*-nitrosamines as well as other monocyclic *N*-nitrosamines are estimated to be larger than 20-21kcal mol^{-1}.[46]

Rotational barriers with respect to the N−NO bonds were calculated with the Gaussian 98 program (*Table 6.6*).[33] The geometry optimizations were carried out at the B3LYP level of theory including the 6-31G(d,p) and 6-311+G(3df,2p) basis sets, using procedures implemented in the Gaussian molecular orbital packages. The calculated total energies for each ground state structure as well as transition states (*Figure 6.10*) are given in *Tables A-10 − A-12* (*Appendix A*). Vibrational frequencies calculations were performed on all stationary points at the B3LYP level. Transition state structures were characterized by a single imaginary frequency, whereas the corresponding isomers (for **111a,c** iso1 and iso2; for **112a** and **112c** only one ground state structure) had none. Two transitional rotational conformations of *N*-nitrosoamines were calculated for **111a** and **111c**, *s-cis* (*sp*_**ts**) and *s-trans* (*ap*_**ts**) conformations (NO bond syn-periplanar (*sp*_**ts**) or anti-periplanar (*ap*_**ts**) with respect to the nitrogen lone pair, *Figure 6.10*). In both cases, the *sp*_**ts** conformation was favored over the *ap*_**ts** conformation (*Table 6.6*).

Table 6.6. Potential Energy Barriers[a] (Kcal mol^{-1}) for the Rotation about the N−N Bond in **111a**,**c** a. **112a**,**c**.

compound theoret level	*syn* rotation about N−N bond (*sp*_**ts**)[a]	*anti* rotation about N−N bond (*ap*_**ts**)[a]	compound theoret level	rotation about N−N bond (**ts**)[a]
111a			**112a**	
B3LYP/6-31G(d,p)	21.4 (21.2)	25.2 (23.3)	B3LYP/6-31G(d,p)	12.8 (11.0)
B3LYP/6-311+G(3df,2p)	21.1	23.9	B3LYP/6-311+G(3df,2p)	10.8
111c			**112c**	
B3LYP/6-31G(d,p)	18.0 (18.0)	21.2 (21.3)	B3LYP/6-31G(d,p)	9.2 (9.4)
B3LYP/6-311+G(3df,2p)	17.3	21.3	B3LYP/6-311+G(3df,2p)	8.5

[a] uncorrected values in kcal mol^{-1}; in parenthesis Gibbs free energy: $\Delta G^{\ddagger}$(298 K; kcal mol^{-1}).

This conformational preference can be interpreted in terms of repulsive interactions of the vicinal nitrogen lone pair of electrons of the amine and NO group in the *s-trans* rotated conformer. Rotational barriers about the N−NO bonds were evaluated on the basis of the most stable ground minimum structure of the nitrosamines **111a** and **111c**, and the values are shown in *Table 6.6*. The rotational barrier of the *N*-nitrosaminotetrazoles **111a** and **111c** was evaluated computationally to be 21.2 kcal mol^{-1} (**111a**) and 18.0 kcal mol^{-1} (**111c**) (B3LYP/6-31G(d,p)). These values compare well with those of the barriers of monocyclic nitrosamines.

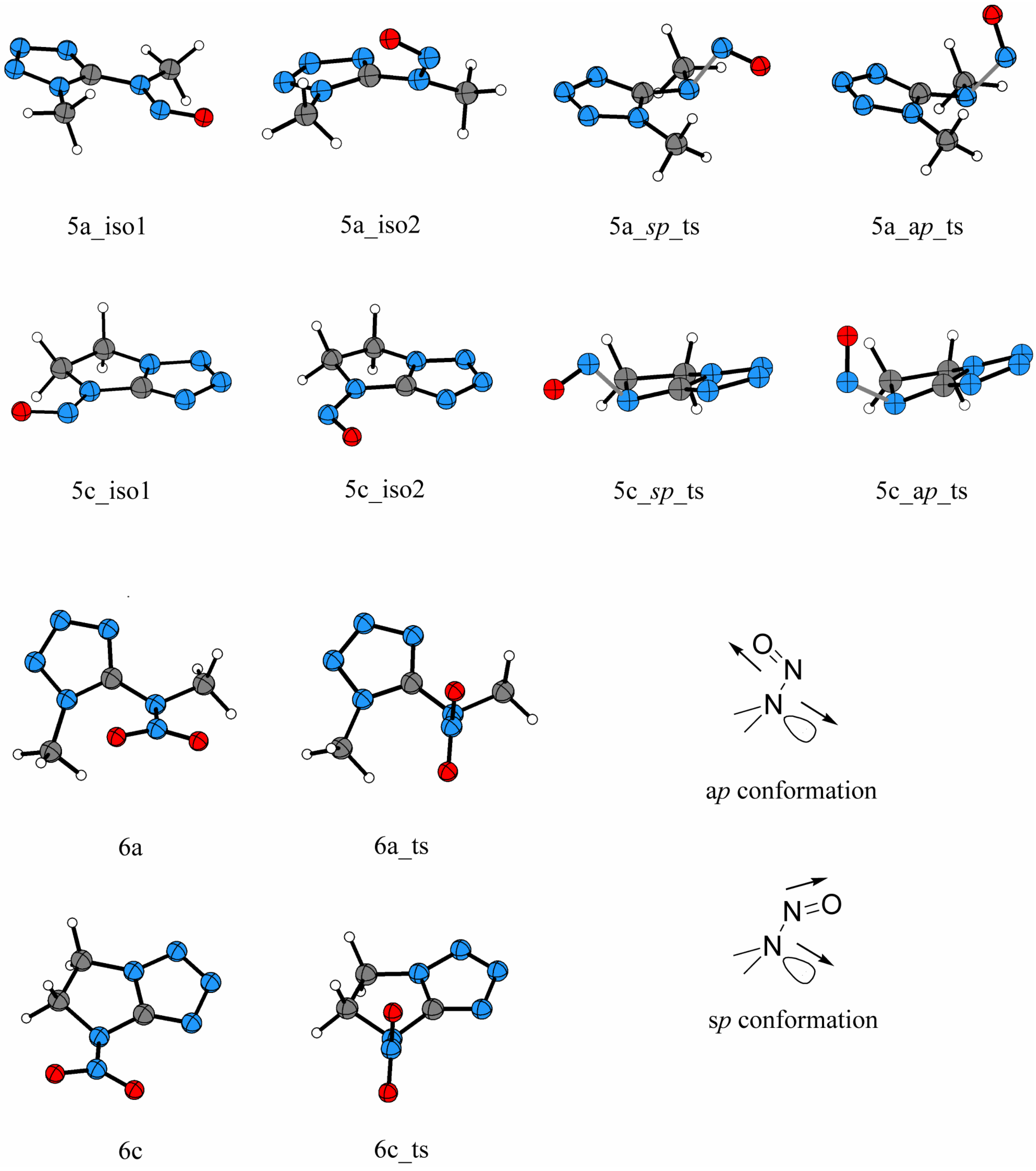

Figure 6.10. Optimized structures and transition states of *N*-nitrosoaminotetrazoles **111a**, **111c** and *N*-nitramino-tetrazoles **112a** and **112c**.

In the case of the *N*-nitraminotetrazoles **112a** and **112c**, the corresponding rotational barriers about the N−NO_2 bonds were also evaluated on the basis of the most stable ground minimum structures (*Figure 6.10*), and the values are shown in *Table 6.6*. The barrier of

internal rotation around the N−N bond in *e.g.* the *N,N*-dimethylnitramine molecule was determined experimentally to 9 kcal mol^{-1} [47] and estimated theoretically to 4 − 13 kcal mol^{-1}.[48] The rotation of the NO_2 group by 90°, i.e., perpendicular to the C1−N5−C3 plane, increases the N−N bond length and the arrangement of the C−N and N−N bonds around the amide nitrogen atom becomes tetrahedral.[47] In the case of **112a** and **112c** rotational barriers of comparable magnitude where obtained with values of 11.0 and 9.4 kcal mol^{-1}, respectively.

Interestingly, the computed barriers apparently seem to correlate with the observed bond angles C1−N5−C3, indicating that the low rotational barrier of the N−NO as well as at the N−NO_2 bond of the investigated compounds is due to angle strain at the amino nitrogen atom (e.g. **110a** 119.9(2)° *vs.* **110c** 110.1(1)° and **112a** 120.6(2)° *vs.* **112c** 110.0(3)°).

1.8 Thermochemistry

The heats of combustion for the compounds **112a** and **112c** were determined experimentally, and the molar enthalpies of formation were calculated from a designed Hess thermochemical cycle according to reactions [1,2]. Typical experimental results (averaged over three measurements each) of the combustion energy at constant volume ($\Delta_c U$) for the compounds are given in *Table 6.7*. The standard molar enthalpy of combustion ($\Delta_c H^\circ$) was derived from $\Delta_c H^\circ = \Delta_c U + \Delta nRT$ ($\Delta n = \sum n_i$ (products, g) $- \sum n_i$ (reactants, g); $\sum n_i$ is the total molar amount of gases in products or reactants).

6a: $C_3H_6N_6O_2$ (s) + 3.5 O_2 → 3 CO_2 (g) + 3 H_2O (l) + 3 N_2 (g) [**1**]

6c: $C_3H_4N_6O_2$ (s) + 3 O_2 → 3 CO_2 (g) + 2 H_2O (l) + 3 N_2 (g) [**2**]

$$\Delta_f H_m^\circ = x\Delta_f H_m^\circ(CO_2, g) + y\Delta_f H_m^\circ(H_2O, l) - \Delta_c H_m^\circ$$

6a: $C_3H_6N_6O_2$ (s) → 5/3C + CO + 1/3CO_2 + 8/3H_2 + 1/3 H_2O + 3 N_2 [**3**]

6c: $C_3H_4N_6O_2$ (s) → 5/3C + CO + 1/3CO_2 + 5/3H_2 + 1/3 H_2O + 3 N_2 [**4**]

The enthalpies of detonation ($\Delta_E H_m^\circ$) for **112a** and **112c** were calculated with the ICT Thermodynamic code.[49] To assess more quantitatively the expected detonation properties of **6a**

and **112c**, the modified Kistiakowsky-Wilson Rule[50] (reactions [3] and [4], Ω lower then -40%) was used to calculate the expected detonation pressures (*P*) and detonation velocities (*D*) as well as the semi-empirical equations suggested by Kamlet and Jacobs (Eqs. [5] and [6], *Table 6.7*).[51,52] The values thus obtained reach in the case of **112c** those of TNT with respect to the detonation pressure (22.0 GPa *vs.* TNT,[53] *P* = 20.6 GPa) and those of nitroglycerin with respect to the detonation velocity (7181 m s^{-1} *vs.* nitroglycerin,[1] *D* = 7610 m s^{-1}). Both compounds show a high gas yield, calculated with the ICT Thermodynamic code.

$$P[10^8 Pa] = K\rho^2\varphi \qquad [\mathbf{5}]$$

$$D[mm\mu s^{-1}] = A\varphi^{1/2}(1 + B\rho) \qquad [\mathbf{6}]$$

Table 6.7. Thermochemical properties of **112a** and **112c**

	112a	**112c**
Formula	$C_3H_6N_6O_2$	$C_3H_4N_6O_2$
Molar Mass	158.12	156.10
N [%]	53.2	53.8
Ω [%][a]	-70.8	61.5
$-\Delta_C U_m$ [cal/g][b]	3119	3247
$-\Delta_C H_m°$ [kcal mol^{-1}][c]	489.9	503.9
$\Delta_f H_m°$ [kcal mol^{-1}][d]	+2.8	+85.2
$-\Delta_E H_m°$ [kcal kg^{-1}][e]	549	1035
Density [g cm^{-3}][f]	1.522	1.690
Density [g cm^{-3}] calcd.[g]	1.53	1.71
P [GPa][h]	14.3	22.0
D [m s^{-1}][h]	5988	7181
Gas volume (25°C) [ml g^{-1}][i]	1010	934

[a] Oxygen balance; [b] Experimental combustion energy at constant volume; [c] Experimental molar enthalpy of combustion; [d] Molar enthalpy of formation; [e] Calculated molar enthalpy of detonation, ICT Thermodynamic code see ref. [49]; [f] from crystal structure determination; [g] calcd. See ref [54]; [h] calculated from semi-empirical equations suggested by Kamlet and Jacobs see ref. [51,52]; [i] Assuming only gaseous products, ICT Thermodynamic code see ref. [49].

1.9 Conclusion

Since experimental data and crystallographic parameters as well as rotational barriers of *N*-nitroso as well as *N*-nitraminotetrazole are rare in literature, simple examples with low carbon and hydrogen content with respect to those parameters were investigated. A detailed discussion of the ^{15}N NMR data and structural parameters is given, and the intriguing bond situation is discussed in terms of natural bond analysis (NBO). The NBO analysis indicates for the nitrosotetrazoles **111a** and **111c** two significant interactions of the nitrogen lone pair (p-LP(N5)) with the two unoccupied, localized antibonding π*(C1–N4) and π*(O1-N6) orbitals. In the case of the none bridged nitro derivatives **112a** and **112b** the interaction with the antibonding π*(C1–N4) is no longer observed due to the rotation of the tetrazole moiety out of the nitramine plane. As the nitroso group is somewhat related to the structural features of amides, the special conformational behavior of the *N*-nitrosaminotetrazoles **111a** and **111c** is characterized by calculated high rotational barriers. They are found in the range typical for aromatic *N*-nitrosamines and are almost double in magnitude compared to those of the corresponding nitro derivatives **112a** and **112c**. For **112a** and **112c**, the heat of formation was determined experimentally with bomb calorimetry resulting in positive values for both compounds. The heat of combustion estimated semi-empirically with the help of the thermochemical ICT code was used to calculated the gas yield, indicating in both cases high amounts of produced gases (1010 (**112a**) and 934 (**112c**) ml $g^{-}1$).

1.10 Experimental

CAUTION: Although aminotetrazoles are kinetically stable and in most cases are insensitive to electrostatic discharge, friction, and impact, they are nonetheless energetic materials and appropriate safety precautions should be taken, especially in the case of the N-nitrosamino- as well as the N-nitraminotetrazoles. Laboratories and personnel should be properly grounded, and safety equipment such as Kevlar® gloves, leather coat, face shield and ear plugs are necessary when compounds ***112a*** *and* ***112c*** *are synthesized on a larger scale. Moreover, since N-nitrosamines are known to have strong carcinogenic and mutagenic properties, special care has to be taken when manipulating* ***111a*** *and* ***111c***.

The amino-1*H*-tetrazoles were prepared according to previously published procedures.[12,16] A detailed description of the procedure for **108a-c**, **109a-c** and the corresponding nitrates **110a-c** can be found in [55].

General Procedure for the Preparation of 5-Nitrosoaminotetrazoles 111a and 111c: The nitrosoamines **111a** and **111c** were prepared following published procedures[22]: To a cooled solution of the respective amino-1*H*-tetrazole (25 mmol) in 50 mL of 2M HCl was slowly added a solution of sodium nitrite (1.73 g, 25 mmol) in 20 mL of water. During the addition the temperature was maintained between 0 and 5 °C. The resulting mixture was stirred at 5-10 °C for 30 minutes and then brought to pH 8 with anhydrous potassium carbonate. In the case of **11a**, the aqueous solution was extracted with DCM (3 x 100 mL) and the combined organic extracts washed with water (2 x 70 mL) and dried over $MgSO_4$. After removing the solvent *in vacuo* the yellow residue was recrystallized from water/EtOH yielding light sensitive pale-yellow plates (84 %). In the case of **5c**, the crude product separated during the addition of the potassium carbonate. Recrystallization from water/EtOH yielded pale-yellow needles (94 %).

1-Methyl-5-(methylnitrosoamino)-1*H*-tetrazole (11a): m.p. 46-47 °C; $\tilde{\nu}$ (KBr) [cm^{-1}]: 3040 (vw, $-CH_3$), 2954 (vw, $-CH_3$), 1626 (w), 1576 (vs, $\tilde{\nu}_{asym.}$ *NO*), 1512 (m), 1464 (m), 1446 (vs), 1455 (vs), 1415 (m), 1391 (m), 1318 (vw), 1277 (m, $\tilde{\nu}$ -N-N=N-$^+$), 1225 (s, $\tilde{\nu}_{sym.}$ *NO*), 1208 (m, $\tilde{\nu}$ *tetrazole*), 1125 (s, $\tilde{\nu}$ *tetrazole*), 1097 (s, $\tilde{\nu}$ *tetrazole*), 1037 (w, $\tilde{\nu}$ *tetrazole*), 973 (m), 946 (s, $\tilde{\nu}$ $-CH_3$*N*-*N*O), 814 (s), 730 (m), 701 (s), 691 (m), 519 (w), 462 (vw); Raman (200 mW) $\tilde{\nu}$ [cm^{-1}]: 3041 (11), 2966 (25), 1580 (100, $\tilde{\nu}_{asym.}$ *NO*), 1511 (48), 1456 (11), 1418 (6), 1393 (13), 1318 (7, $\tilde{\nu}$ -N-N=N-), 1278 (16, $\tilde{\nu}_{sym}$ NO_2), 1097 (7, $\tilde{\nu}$ *tetrazole*), 1041 (2, $\tilde{\nu}$ *tetrazole*), 947 (11, $\tilde{\nu}$ $-CH_3$*N*-*N*O), 815 (9), 731 (4), 702 (37), 521 (6), 464 (23), 286 (4), 357 (8), 326 (7), 231 (6), 199 (13); ^{1}H NMR ($CDCl_3$) δ: 3.58 (s, 3H, $-CH_3$), 4.21 (s, 3H, CH_3); ^{13}C NMR ([d6]Acetone) δ: 32.1 (CH_3), 37.4 (CH_3), 153.3 (C); ^{14}N NMR ($CDCl_3$) δ: 170 (N-*N*O, $\Delta\nu_{1/2}$ = 1101 Hz), -6 (N2, N3 $\Delta\nu_{1/2}$ = 1009 Hz), -75 (N4, $\Delta\nu_{1/2}$ = 550 Hz), -141 (-*N*Me-NO, ..$\Delta\nu_{1/2}$ = 459 Hz), -173 (N1, $\Delta\nu_{1/2}$ = 367 Hz); *m/z* (EI) 143 [(M + H^+) (15)], 127 (36), 126 (10), 113 (12), 83 (5), 71 (4), 70 (5), 69 (8), 52 (5), 43 (100), 42 (5), 41 (11), 40 (8), 30 (10), 28 (12), 15 (25); $C_3H_6N_6O$ (142.12): Calcd. C, 25.4; H, 4.3; N, 59.1 %; Found: C, 25.5; H, 4.3; N, 59.5 %.

7-nitroso-5,6-dihydro-7*H*-imidazolo[1,2-*d*]tetrazole (111c): m.p. 110-110.5 °C (dec.); $\tilde{\nu}$ (KBr)[cm^{-1}]: 3028 (vw, -CH_2), 1585 (vs, $\tilde{\nu}_{asym.}$ *NO*), 1536 (m), 1473 (vs), 1455 (vs), 1430 (m), 1358 (ms, 1315 (w), 1280 (vw), 1264 (s, $\tilde{\nu}$ -N-N=N-$^+$), 1240 (s, $\tilde{\nu}_{sym.}$ *NO*), 1192 (s, $\tilde{\nu}$ *tetrazole*), 1157 (vs, $\tilde{\nu}$ *tetrazole*), 961 (m, $\tilde{\nu}$ -CH_3*N*-*N*O), 803 (s), 763 (m), 726 (m), 687 (vw), 604 (w), 516 (vw), 367 (vw), 337 (vw); Raman (200 mW) $\tilde{\nu}$ [cm^{-1}]: 3028 (17), 2987 (20), 2961 (22), 1584 (100, $\tilde{\nu}_{asym.}$ *NO*), 1538 (27), 1481 (22), 1468 (21), 1456 (37), 1357 (2), 1316 (13, $\tilde{\nu}$ -N-N=N-), 1263 (15, $\tilde{\nu}_{sym}$ *NO_2*), 1235 (8), 1206 (7, $\tilde{\nu}$ *tetrazole*), 1187 (6, $\tilde{\nu}$ *tetrazole*), 1158 (6, $\tilde{\nu}$ *tetrazole*), 1045 (14, $\tilde{\nu}$ *tetrazole*), 963 (5, $\tilde{\nu}$ *tetrazole)*, 933 (5, $\tilde{\nu}$ -CH_3*N*-*N*O), 802 (4), 764 (31), 729 (3), 605 (21), 518 (32), 409 (23), 365 (8), 349 (16), 207 (19), 126 (8); ^1H NMR ([d_6]DMSO) AA'BB'-spectrum (δ_A= 4.64, δ_B= 4.72, N = 31 Hz, CH_2); ^{13}C NMR ([d_6]Acetone) δ: 43.0 (CH_2), 53.9 (CH_2), 158.3 (C); *m/z* (EI) 140 [(M^+) (100)], 109 (5), 96 (25), 67 (9), 55 (60), 54 (27), 53 (44), 44 (5), 41 (5), 40 (7), 30 (51), 28 (90), 27 (15); $C_3H_4N_6O$ (140.10): Calcd. C, 25.7; H, 2.9; N, 60.0 %; Found: C, 25.6; H, 3.3; N, 59.7 %.

General Procedures for the Preparation of 5-Nitraminotetrazoles (112a-c): Method A: **112a-c:** The amino-1*H*-tetrazoles **109a-c** were transformed according to known procedures (for details see supporting information) to the corresponding amino-1*H*-tetrazolium nitrates.[22] The nitrate (20 mmol) was slowly added with stirring to cooled (~ -8 °C) conc. sulfuric acid (4.5 mL). During the addition of the nitrate the temperature of the reaction mixture should not exceed 0°C. After the addition the reaction mixture was stirred for further 10 minutes, quickly heated to 25 °C and poured onto 30 g of ice. The white crystalline solid was separated by filteration and washed with water until it became acid free and was recrystallized from an appropriate (see below) solvent. A second crop of product was obtained by extracting the aqueous solution with Et_2O followed by the workup procedures described above. Method B: **112a-c:** The method described in [23] was used: To cooled acetic anhydride (5 g; ice-bath), 5 g 100% nitric acid was added dropwise over 10 minutes. After 20 minutes, 25 mmol of the respective amino-1*H*-tetrazole was added in small portions over 10 minutes. The solution was stirred for further 20 minutes and then quenched on 25 g of crushed ice. The crude product was collected, washed until it became acid free and recrystallized from an appropriate (see below) solvent. Method C: **112a** and **112c**: To a well stirred suspension of 0.41 mL (15 mmol) of 90% hydrogen peroxide in 10 mL DCM (cooling with an ice-bath recommended) was added 2.60 mL (18 mmol) of trifluoroacetic anhydride in one portion. After 5 minutes the solution was

allowed to warm to room temperature and 10 mmol of the corresponding nitrosamine in 5 mL of DCM was added drop-wise over a 30-minute period. During this addition an exothermic reaction occurred which caused the solution to boil. After the addition was completed the mixture was heated under reflux for one hour. The DCM solution was then washed with water (3 x 15 ml) and dried over $MgSO_4$. The solvent was removed by distillation under reduced pressure and the residue was recrystallized from an appropriate (see below) solvent.

1-Methyl-5-(methylnitramino)-1*H*-tetrazole (**112a**)**:** Recrystallization from benzene / pentane. m.p. 58-58.5 °C; $\tilde{\nu}$ (KBr) [cm^{-1}]: 3038 (vw), 2961 (vw, $-CH_3$), 2925 (vw, $-CH_3$), 2854 (vw, $-CH_3$), 1576 (vs, $\tilde{\nu}_{asym}$ *NO2*), 1545 (m), 1487 (m), 1461 (m), 1430 (m), 1384 (w), 1314 (m, $\tilde{\nu}$ -N-N=N-$^+$), 1294 (s, $\tilde{\nu}_{sym}$ *NO2*), 1269 (m), 1214 (m, $\tilde{\nu}$ *tetrazole*), 1181 (m, $\tilde{\nu}$ *tetrazole*), 1127 (m, $\tilde{\nu}$ *tetrazole*), 1093 (m, $\tilde{\nu}$ *tetrazole*), 1049 (w), 989 (w), 949 (m, $\tilde{\nu}$ -CH_3*N*-*N*O_2), 786 (m), 761 (m), 748 (w), 606 (m); Raman (200 mW) $\tilde{\nu}$ [cm^{-1}]: 3038 (33), 3025 (34), 2962 (99), 2829 (9), 1551 (100, $\tilde{\nu}_{asym}$ *NO2*), 1488 (14), 1440 (25), 1418 (23), 1315 (27, $\tilde{\nu}$ -N-N=N-$^+$), 1291 (33, $\tilde{\nu}_{sym}$ *NO2*), 1270 (45, $\tilde{\nu}$ *tetrazole*), 1216 (26, $\tilde{\nu}$ *tetrazole*), 1153 (7, $\tilde{\nu}$ *tetrazole*), 1096 (15), 1051 (8), 991 (10), 951 (38, $\tilde{\nu}$ -CH_3*N*-*N*O_2), 787 (70), 699 (63), 607 (32), 490 (40), 451 (27), 402 (22), 321 (15), 280 (24), 254 (20), 142 (74); ^{1}H NMR ([d_6]Acetone) δ: 3.82 (s, 3H, CH_3), 4.10 (s, 3H, CH_3); ^{13}C NMR ([d_6]Acetone) δ: 29.8 (CH_3), 35.7 (CH_3), 147.8 (C); ^{14}N NMR ([d_6]Acetone) δ: 10 (N2, $\Delta\nu_{1/2}$ = 578 Hz), -4 (N3, $\Delta\nu_{1/2}$ = 616 Hz), -35 (-CH_3N-*NO_2*, $\Delta\nu_{1/2}$ = 23 Hz), -58 (N4, $\Delta\nu_{1/2}$ = 374 Hz), -155 (N1, $\Delta\nu_{1/2}$ = 181 Hz), -219 (-CH_3*N*-NO_2, $\Delta\nu_{1/2}$ = 919 Hz); *m/z* (CI, *i-Buten*) 159 [(M + H^+) (100)]; $C_3H_6N_6O_2$ (158.12): Calcd. C, 22.8; H, 3.8; N, 53.2 %; Found: C, 22.8; H, 3.9; N, 53.4 %.

1-Isopropyl-5-(isopropylnitramino)-1*H*-tetrazole (**112b**)**:** Recrystallization from EtOH / water. m.p. 56-57 °C; $\tilde{\nu}$ (KBr) [cm^{-1}]: 2994 (vw, -*i*Pr), 2971 (vw, -*i*Pr), 2883 (vw, -*i*Pr), 2847 (vw, -*i*Pr), 1567 (vs, $\tilde{\nu}_{asym}$ *NO2*), 1469 (w), 1461 (w), 1448 (vw), 1426 (m), 1401 (vw), 1391 (w), 1385 (vw), 1375 (vw), 1350 (vw), 1321 (m, $\tilde{\nu}$ -N-N=N-$^+$), 1288 (s, $\tilde{\nu}_{sym}$ *NO2*), 1254 (vw), 1243 (vw), 1182 (w, $\tilde{\nu}$ *tetrazole*), 1164 (w, $\tilde{\nu}$ *tetrazole*), 1137 (vw, $\tilde{\nu}$ *tetrazole*), 1125 (m, $\tilde{\nu}$ *tetrazole*), 1091 (w, $\tilde{\nu}$ *tetrazole*), 1062 (w, $\tilde{\nu}$ *tetrazole*), 994 (vw), 970 (w, $\tilde{\nu}$ -CH_3*N*-*N*O_2), 946 (vw), 934 (vw), 885 (vw), 792 (w), 760 (w), 736 (vw), 726 (vw), 668 (vw), 643 (vw), 589

(vw), 555; Raman (200 mW) $\tilde{\nu}$ [cm^{-1}]: 2999 (100), 2990 (84), 2974 (80), 2946 (93), 2929 (69), 2875 (28), 2773 (6), 2733 (11), 1576 (12), 1522 (83, $\tilde{\nu}_{asym}$ *NO2*), 1457 (53), 1398 (29), 1322 (21), 1285 (40, $\tilde{\nu}$ -N-N=N-$^{+}$), 1253 (41, $\tilde{\nu}_{sym}$ *NO2*), 1183 (17, $\tilde{\nu}$ *tetrazole*), 1138 (29, $\tilde{\nu}$ *tetrazole*), 1092 (39, $\tilde{\nu}$ *tetrazole*), 1068 (29, $\tilde{\nu}$ *tetrazole*), 1048 (12), 994 (12), 948 (24, $\tilde{\nu}$ -CH_3*N*-*N*O_2), 888 (45), 795 (60), 767 (12), 735 (10), 646 (42), 588 (19), 564 (19), 477 (41), 439 (49), 377 (17), 349 (34), 317 (24), 295 (24), 152 (84), 119 (44); *The compound shows in solution dynamic behavior.* ^{1}H NMR ([d$_6$]Acetone, 25 °C) δ: 1.31 (s, 6H, CH(C*H*$_3$)$_2$), 1.58 (d, 6H, ^3J 6.6 Hz, -CH(C*H*$_3$)$_2$), 4.9 (septett, 1H, ^3J 6.6 Hz, -C*H*(CH_3)$_2$), 5.07 (septett, 1H, ^3J 6.6 Hz, -C*H*(CH_3)$_2$); ([d$_6$]Acetone, -65 °C) δ: 1.03 (d, 3H, ^3J 7.0 Hz, -CH_3), 1.45 (d, 3H, ^3J 6.4 Hz, -CH_3), 1.49 (d, 3H, ^3J 6.6 Hz, -CH_3), 1.56 (d, 3H, ^3J 6.6 Hz, -CH_3), 5.05 (septett, 2H, ^3J 6.6 Hz, -C*H*(CH_3)$_2$); ^{13}C NMR ([d$_6$]Acetone, 25 °C) δ: 18.6 (CH_3), 21.1 (CH_3), 51.3 (CH), 55.5 (CH), 147.0 (C); ([d$_6$]Acetone, -65 °C) δ: 18.3 (CH_3), 18.3 (CH_3), 21.6 (CH_3), 22.0 (CH_3), 50.8 (CH), 54.9 (CH), 146.9 (C); ^{14}N NMR ([d$_6$]Acetone, 25°C) δ: 13 (N2, $\Delta\nu_{1/2}$ = 666 Hz), -11 (N3, $\Delta\nu_{1/2}$ = 571 Hz), -36 (-*i*PrN-*NO$_2$*, $\Delta\nu_{1/2}$ = 24 Hz), -56 (N4, $\Delta\nu_{1/2}$ = 435 Hz), -130 (N1, $\Delta\nu_{1/2}$ = 201 Hz), -200 (-*i*Pr*N*-NO_2, $\Delta\nu_{1/2}$ = 989 Hz); *m/z* (CI, *i-Buten*) 215 [(M + H$^+$) (18)], 210 (15), 196 (15), 170 (100), 169 (18); *m/z* (DEI) 169 (37), 154 (12), 127 (24), 126 (10), 110 (9), 111 (36), 99 (10), 86 (39), 85 (11), 14 (84), 80 (29), 69 (14), 64 (15), 58 (22), 57 (16), 48 (19), 43 (100), 42 (21), 41 (30), 39 (9); $C_7H_{14}N_6O_2$ (214.23): Calcd. C, 39.3; H, 6.6; N, 39.2 %; Found: C, 39.2; H, 6.6; N, 39.4 %.

7-Nitro-5,6-dihydro-7*H*-imidazolo[1,2-*d*]tetrazole (112c): Recrystallization from acetone/water. m.p. 150 °C (dec.); $\tilde{\nu}$ (KBr) [cm^{-1}]: 3035 (vw, -CH_2), 3017 (vw, -CH_2), 1592 (vs, $\tilde{\nu}_{asym}$ *NO2*), 1550 (s, $\tilde{\nu}$ (C=N)), 1515 (m), 1472 (m), 1359 (s), 1335 (vs, $\tilde{\nu}$ -N-N=N-$^{+}$), 1299 (s, $\tilde{\nu}_{sym}$ *NO2*), 1276 (m), 1235 (m), 1204 (m, $\tilde{\nu}$ *tetrazole*), 1186 (m, $\tilde{\nu}$ *tetrazole*), 1138 (w, $\tilde{\nu}$ *tetrazole*), 1108 (vw, $\tilde{\nu}$ *tetrazole*), 1041 (vw, $\tilde{\nu}$ *tetrazole*), 956 (w, $\tilde{\nu}$ -CH_3*N*-*N*O_2), 800 (w), 763 (w), 747 (w), 715 (m), 683 (m), 527 (vw); Raman (200 mW) $\tilde{\nu}$ [cm^{-1}]: 3035 (45), 3018 (33), 2995 (52), 2976 (60), 2933 (12), 2902 (14), 1582 (59), 1552 (100, $\tilde{\nu}_{asym}$ *NO2*), 1495 (10), 1471 (37), 1457 (25), 1378 (9), 1363 (18), 1291 (48, $\tilde{\nu}$ -N-N=N-$^{+}$), 1268 (30), 1235 (60, $\tilde{\nu}_{sym}$ *NO2*), 1207 (26), 1140 (17, $\tilde{\nu}$ *tetrazole*), 1109 (10, $\tilde{\nu}$ *tetrazole*), 1042 (60, $\tilde{\nu}$ *tetrazole*), 957 (12, $\tilde{\nu}$ *tetrazole*), 935 (21, $\tilde{\nu}$ -CH_3*N*-*N*O_2), 801 (90), 763 (8), 719 (7), 683 (23), 527 (31), 441 (29), 402 (42), 326 (22), 213 (29), 122 (21); ^{1}H NMR ([d$_6$]Acetone) AA'BB'-spectrum (δ_A=

4.85, δ_B= 5.36, N = 29 Hz, CH_2); ^{13}C NMR ([d_6]Acetone) δ: 42.9 (CH_2), 58.2 (CH_2), 158.6 (C); ^{14}N NMR ([d6]Acetone) δ: 30 (N3, $\Delta\nu_{1/2}$ = 238 Hz), -25 (N2, $\Delta\nu_{1/2}$ = 262 Hz), -42 (-RN-*NO₂*, $\Delta\nu_{1/2}$ = 24 Hz), -82 (N4, $\Delta\nu_{1/2}$ = 190 Hz), -158 (N1, $\Delta\nu_{1/2}$ = 142 Hz), -206 (-*RN*-NO_2, $\Delta\nu_{1/2}$ = 476 Hz); *m/z* (DEI) [(M^+) (34)], 111 (30), 98 (11), 55 (70), 54 (100), 53 (59), 52 (30), 46 (45), 40 (13), 30 (53); $C_3H_4N_6O_2$ (156.10): Calcd: C, 23.1; H, 2.6; N, 53.8%; Found: C, 22.7; H, 2.7; N, 53.6%.

2. Mono- and Dinitrobiuret

In the continuing search for new energetic materials to improve explosives and propellants, it is of interest to successfully utilize the formulations of monocyclic nitramines like hexahydro-1,2,5-trinitro-*S*-triazine (RDX), octahydro-1,3,5,7-tetranitro-1,3,5,7-tetrazine (HMX) and nitroaromatics like 2,4,6-trinitro toluene (TNT). However, owing to the number of accidents involving initiation of munitions by impact/shock, there is a need for the development of conciliatory materials having characteristics of insensitivity close to 1,3,5-triamino-2,4,6-trinitrobenzene (TATB) and commensurate detonation performance. A member of the azaheterocyclic nitramine urea class, 2-oxo-1,3,5-trinitro-1,3,5-triazacyclohexane (Keto-RDX or K-6)[56] exceeds the performance area of TNT or PETN, but a level higher than HMX cannot be achieved.[57] As the presence of nitrourea moiety in a cyclic structure ensures high densities,[58] new azaheterocyclic nitramines are sought to meet the requirements of increased stability and insensitivity, coupled with high performance. *Scheme 6.2* shows the synthetic route to Keto-RDX starting from dinitrourea (DNU) and an alcohol.

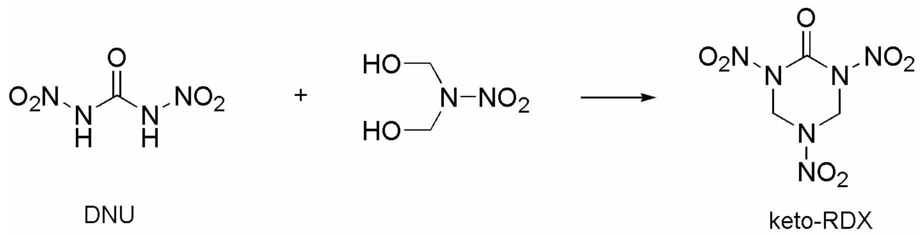

Scheme 6.2. Condensation of DNU with an alcohol to keto-RDX (K-6)

Several mono- and dinitroureas have been synthesised as energetic materials and have attractive densities and predicted performance. Most prominent examples are mono- and dinitroureas, and the explosives based on these base structures have in the most cases high densities (> 1.90 g cm^{-3}). This can be attributed to the inherently high density of the urea frame work. The development of a simple procedure for the preparation of *N,N'*-dinitrourea has opened a new way to *N*-nitroamines starting from urea.[59] The availability of *N,N'*-dinitrourea salts for example makes it possible to synthesize new compounds on their base structure.[60]

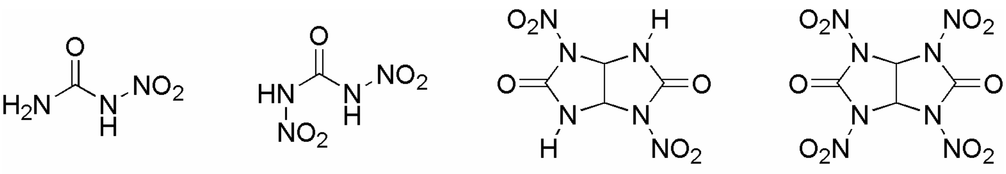

MNU DNU DNGU TNGU

Figure 6.11. Examples of nitroureas

However, the dinitrurea explosives suffer from hydrolytic lability, restricting their use; but the mono-nitrourea compounds are fairly stable to hydrolysis and are relatively insensitive to shock. The earliest and best known examples of mono- and dinitroureas were 1,4,4,6-tetranitroglycouril (TNGU) and 1,4-dinitroglycouril (DNGU) synthesized by Boileau et al.[61] Both TNGU and DNGU (*Figure 6.11*) were found to have a high crystal densities (2.04 and 1.98 g cm^{-3}). A comparison of DNGU and TNGU, with respect to their stability and sensitivity, is indicative of the general trend between mono- and dinitrourea explosives. TNGU is unstable in water while DNGU decomposed only slowly on treatment with boiling water. DNGU has a significant higher drop hammer value than TGNU and better thermal stability. DNGU has been, in fact, investigated as an insensitive energetic material that was proposed to be an alternative to RDX and TNT.[62] Pagoria and coworkers synthesized a number of cyclic nitrourea explosives based on RDX and HMX with some attractive densities and the most interesting is certainly K-6.[63]

Compared to the structurally similar RDX, Keto-RDX shows, depending on the crystal shape, comparable physical properties, but in the BAM impact testing all K-6 samples except one coarse crystal fraction revealed a pronounced sensitivity of 2.0 Nm, which approaches primary explosive behavior.[64] It is to expect that energetic materials based on the cyclic nitramine structure of RDX and HMX might have a higher performance, if the elemental composition is only marginally modified, yielding good energy capability, thermal stability, as well as a method of preparation from readily available cheap starting materials.[63] In this context, compared to nitrourea [65] the chemistry of the corresponding biuret derivatives mononitrobiuret (MNB) and 1,5-dinitrobiuret (DNB) as synthetic equivalents for the preparation of azaheterocyclic nitramine urea class derivatives has never been achieved (*Figure 6.12*).

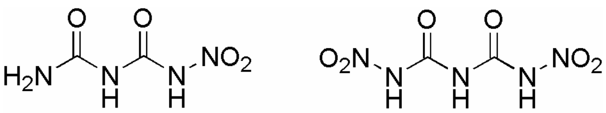

MNB (**113**) DNB (**114**)

Figure 6.12. **MNB** and **DNB**

2.1 Synthesis of **MNB** and **DNB**

Mononitrobiuret (**113**) was readily prepared by nitration of biuret 1 with HNO_3/H_2SO_4. Dinitrobiuret (**114**) was obtained by the treatment of **113** with 100 % HNO3 according a modified procedure of Thiele et al (*Scheme 6.3*).[66] For the entire reaction sequence (*Scheme 6.3*), an overall yield of 46% was obtained starting from biuret (**115**). Both **MNB** and **DNB** were characterized by IR, Raman, ^1H, ^{13}C, $^{14,15}N$ NMR spectroscopy and single crystal X-ray diffraction. **MNB** is an air stable white solid which starts to decompose without melting at 153 °C. It is soluble in common polar solvents and is not friction, impact or heat sensitive. **DNB** is also an air stable white microcrystalline solid, but in contrast to **MNB**, is very friction, impact and heat sensitive. It will explode when heated above 127 °C, *therefore appropiate saftey precaution should be taken when manipulating **DNB***. In the solid state, **DNB** is indefinitely stable. It is soluble in most organic solvents. The stability of the solution is dependend on the basisity of the solvent. For example, it readily decomposes in aqueous solution to N_2O, CO_2 and H_2O (see below).

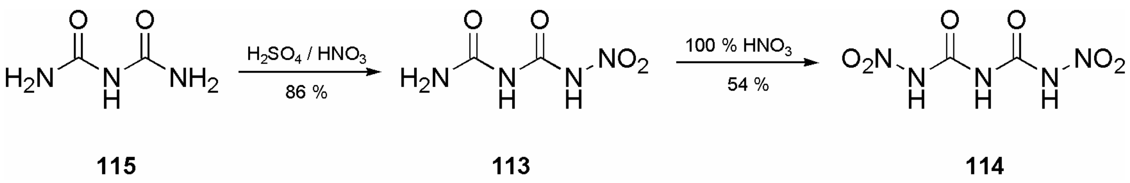

Scheme 6.3. Synthesis of MNB and DNB

2.2 Raman and IR spectroscopy of **MNB** and **DNB**

The IR and Raman spectra of **113** and **114** are comparable. The assignment of most of the modes is complicated owing to the strong dependence of their band position upon strong interaction of **MNB** and **DNB** with the molecules in the solid state.[67,68] This is particularly evident when comparing the gas phase IR and Raman data[69,70] with the results obtained in the solid state.[71] The approximate assignment of the normal modes is based on the infrared band contours, group frequencies, infrared intensities, Raman activities, and ab initio predictions, which are supported by a normal coordinate analysis.

Table A-12 and A-13 (*Appendix A*) displays the calculated and observed frequencies for **MNB** and **DNB** along with the qualitative description of the atoms or groups that dominate the motion in each case. The IR spectra of **MNB** and **DNB** themselves are not well characterized

but the vibrational spectra of the akin biuret-hydrate and metal complexes of biuret have been recorded and discussed in a few papers.[72,73] By comparing the spectra of **MNB** and **DNB** it is possible to assign the stretching vibration at 3433 cm^{-1} (ν_1) to the NH_2 group of **MNB** and the band at 3291 cm^{-1} (ν_2, **MNB**; ν_1, **DNB**) to the stretching vibration of the -CO-*NH*-CO- group of both compounds. The band at 3146 cm^{-1} (ν_3, **MNB**) and 3210 cm^{-1} (ν_2, **DNB**) are attributed to the stretching vibration of the –*NH*-NO_2 group. The bands at 3071, 2969 and 2805 cm^{-1} are a result of combinations or overtones of some modes rather than of vibrations of fundamental modes and are not listed in *Table A-13 and A-14*. The IR spectrum of **MNB** [**DNB**] shows four [four] bands between 1800 and 1550 cm^{-1}, two [one] C=O stretching at 1739 and 1714 cm^{-1} (ν_5, ν_6) [1764 cm^{-1} (ν_3)] and one NH_2 scissors (bending) at 1572 cm^{-1} (ν_8) for **MNB**. The splitting of the C=O band for **DNB** is not observed. The asymmetric stretching vibration of the NO_2 group can be found at 1630 cm^{-1} (ν_7) for **MNB**, whereas in the case of **DNB** a splitting of this band into two bands (1630 (ν_6), 1618 cm^{-1} (ν_7)) is observed due to the C_2 symmetry of the molecule. The symmetric stretching vibration of the NO_2 group in **MNB** is found at 1366 cm^{-1} (ν_{12}), whereas for DNB two bands at 1336 and 1318 cm^{-1} (ν_{11}, ν_{12}) which are strongly coupled with other modes are found. Two in plane bends of the NH group for **MNB** can be found at 1490 (ν_9) and 1383 cm^{-1} (ν_{10}), and in the case of **DNB** the expected three in plane bends are found at 1568, 1484 and 1464 cm^{-1} (ν_8, ν_9 and ν_{10}). The bands at 1395, 1206 and 951 cm^{-1} (ν_{10}, ν_{13} and ν_{15}) [1393, 1275, 1143 and 1061 cm^{-1} (ν_{11}, ν_{13}, ν_{14} and ν_{15})] can in most cases only partly attributed to C-N stretching vibrations due to combination with N-H bending, NH_2 rocking and NO_2 stretching vibrations. Mainly one [two] modes, ν_{16} [ν_{16}, ν_{17}], is associated with the N-NO_2 stretching at 1006 cm^{-1} [1048 and 995 cm^{-1}]. The bands below 900 cm^{-1} of **MNB** and **DNB** are assigned to out-of-plane bend, skeletal in and out-of-plane deformations, and our assignment of the corresponding modes (ν_{17}- ν_{36} of **MNB** and ν_{18}- ν_{42} of **DNB**) also agree with this propositions.

2.3 NMR spectroscopy of **MNB** and **DNB**

Comparison of the ^1H-, ^{13}C- and ^{15}N-NMR data of mono- and dinitrobiuret with those of biuret reveals the influence of the nitro groups (*Table 6.8*). In DMSO proton exchange is slow on the NMR time scale and distinct signals are observed for the different amino protons. Introduction of a nitro group causes a shift of the ^1H NMR signal of the adjacent NH proton to lower field. In contrast, the ^{13}C NMR signal of the corresponding carbonyl group is shifted to

higher field. For **MNB** separate signals are observed for the two amino protons, indicating that rotation of the NH_2 group is slow on the NMR time scale. Nitro substitution at the amino groups causes a low field shift of the ^{15}N NMR signal of the corresponding amino nitrogen atom, which is found at δ = -181.8 (**MNB**) and δ = -182.7 (**DNB**) in a range typical for $\delta^{15}N$ of the amino group in nitramines.[74] There is no effect of nitro substitution on $\delta^{15}N$ of the central NH unit in the biuret framework (-254.8 to -259.4).

In the nitramine units of **MNB** and **DNB** the presence of the electron withdrawing nitro group causes an increase of the acidity and hence of the mobility of the adjacent NH proton. This becomes clearly evident in the ^{1}H-coupled ^{15}N NMR spectra. They show well resolved multiplets for the NH_2 and the central NH moiety, while only a broad singlet is observed for the NO_2-bonded NH unit (*Figure 6.13*). The proton decoupled ^{15}N NMR spectra display clearly the different NOE effect, experienced by the nitrogen nuclei in NH_2, NH and NO_2 groups, which can be quite helpful for the assignment of the signals. For the NH_2 groups strong positive NMR signals are observed. The signals are much weaker for the NH moieties and become even negative for the NO_2 groups. In the case of **MNB** the intensity of the signal of the NO_2 bonded nitrogen atom is lowered to such a extend by proton irradiation, that the signal almost vanishes, while it is clearly observable in the proton coupled ^{15}N NMR spectrum. This demonstrates how dangerous it is to rely exclusively on proton decoupled NMR spectra when monitoring half spin nuclei with a negative magnetogyric ratio.

Table 6.8. NMR data of biuret, **MNB** and **DNB**

		115	113	114
δ^1H^a	NH_2	6.79	7.27, 7.08	
	–CO–NH–CO–	8.69	9.32	9.19
	–NHNO$_2$		13.16	10.96
$\delta^{13}C$	–CONH2	156.3	153.8	
	–CO–NHNO$_2$		148.8	145.5
$\delta^{15}N$	NH_2	-297.8	-294.2	
	$^1J_{NH}$	89.6	89.3	
	–CO–NH–CO–	-259.4	-254.8	-256.9
	$^1J_{NH}$	89.7	90.4	90.4
	–CO–NHNO$_2$		-181.8	-182.7
	NO_2		-41.5	-44.5

[a] All shifts were referenced with respect to tetramethylsilane (^1H, ^{13}C) and nitromethane (^{14}N, ^{15}N) as external standards. Negative shifts are upfield from CH_3NO_2.

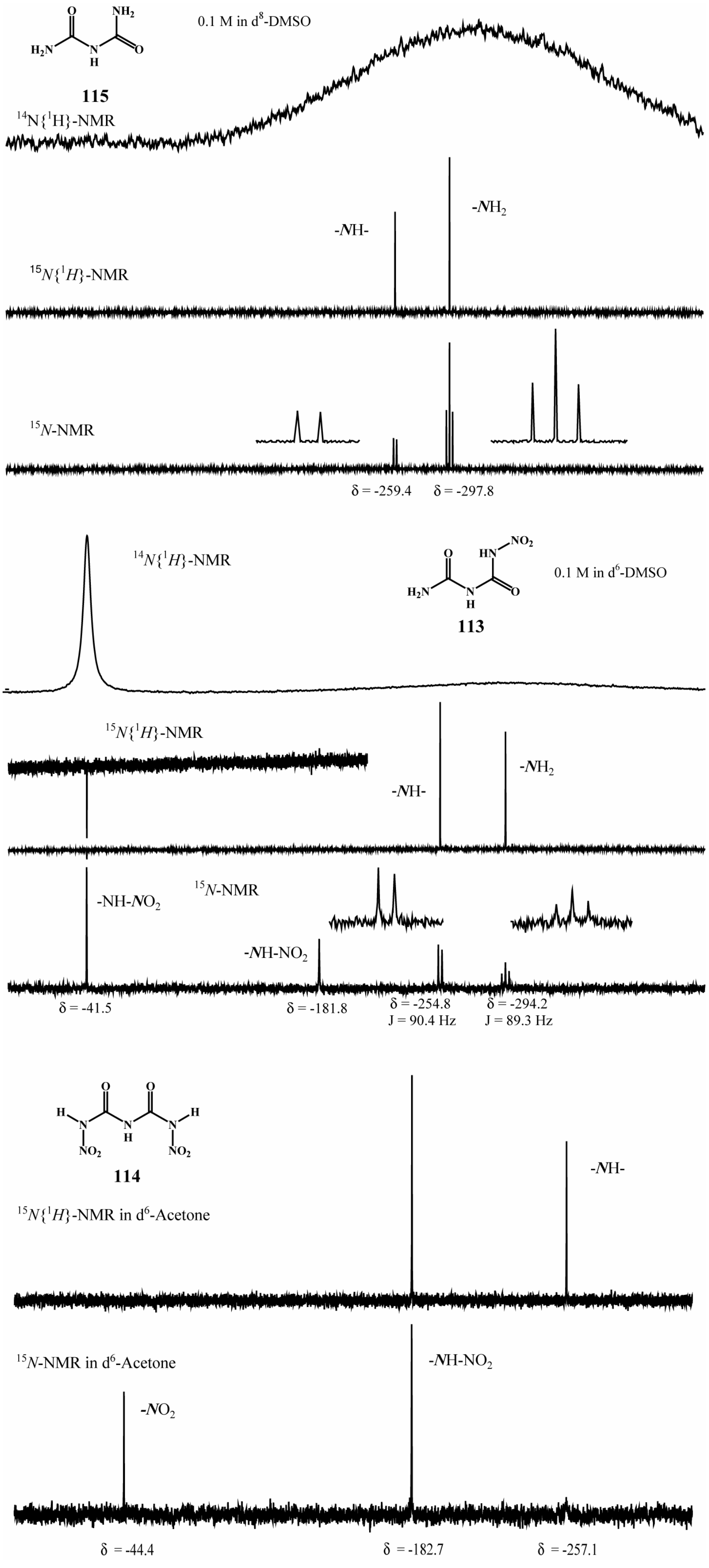

Figure 6.13. ^{14,15}N NMR spectra of biuret, MNB and DNB

2.4 Molecular structure of **MNB** and **DNB**

MNB crystallizes in the monoclinic space group C_1 with eight formula units in the unit cell. The two crystallographically different molecules display nearly identical bond length and angles. Following the described synthesis above, **DNB** is obtained without crystal water. The water free **DNB** crystallizes in the orthorhombic space group $P2_12_12_1$ with two formula units in the unit cell. Careful recrystallization of **DBN** from aqueous methanol afforded **DNB** as monohydrate which, in contrast to the water free compound crystallizes in the monoclinic space group *I*2/a. *Table 6.8* shows selected bond length of biuret, **MNB**, **DNB*H₂O** and **DNB** and a view of the molecular arrangement of **MNB**, **DNB*H₂O** and **DNB** is depicted in Figures 14 – 16.

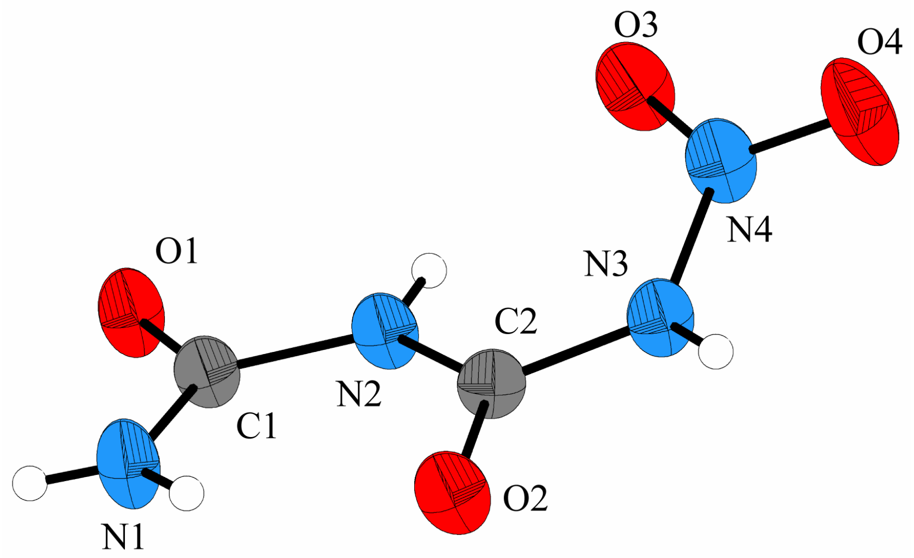

Figure 6.14. Formula unit and labeling scheme for **MNB** (ORTEP Plot, thermal ellipsoid represents 50% probability). For clarity only one molecule of the asymmetric unit is depicted.

In the case of biuret, **MNB** and **DNB*H₂O**, the biuret framework is planar within the limits of accuracy of the structure determination. The bond lengths and angles of the nitramine group in **MNB** and **MNB*H₂O** are comparable to those already reported for nitramines.[75] Compared to the nitramine moieties in DNB*H_2O, which lie in the plane of the biuret framework (torsion angle O2−C2−N3−N4 176.9(2)°), the nitramine moiety in **MNB** is slightly rotated out of this plane (O2−C2−N3−N4 157.7(3)°). The small deviation from planarity, observed for N3 (angle sum 352°) in **MNB** is in contrast to the planarity (sp^2 hybridization) of N3 (N1) in **DNB*H₂O**. The bond distance C2-N3 (C1−N1) in **MNB** and **DNB*H₂O** (1.387(4)

and 1.403(2) Å, respectively) is shorter than a C−N single bond (1.47 Å) and C-N bond distances normally found for nitramines, which are typically longer than 1.42 Å.[28]

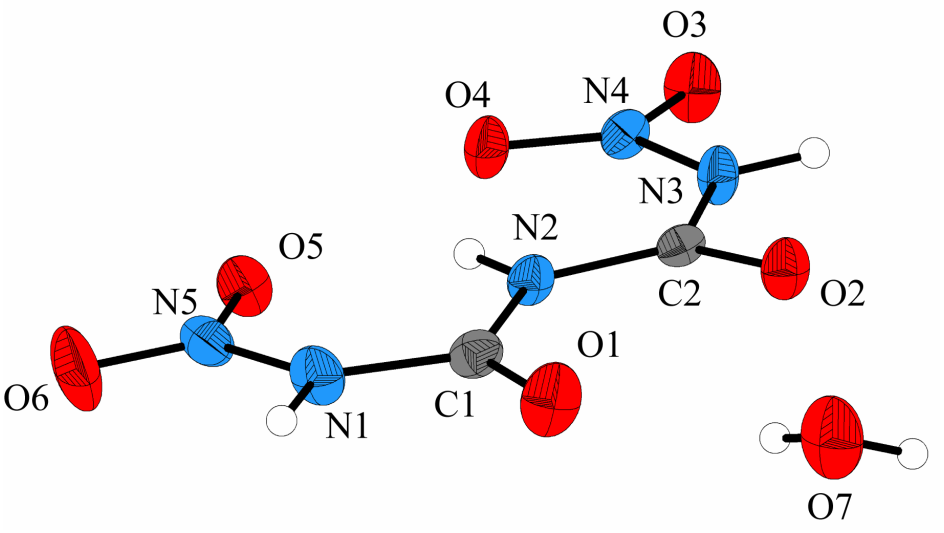

Figure 6.15. Formula unit and labeling scheme for **DNB*H_2O** (ORTEP Plot, thermal ellipsoid represents 50% probability).

Table 6.8. Selected bond length of **MNB, DNB*H_2O and DNB**

Å	Biuret[a]	MNB	DNB*H_2O	DNB	typical bond length[b]
N1−C1	1.33(2)	1.319(4)	1.396(3)	1.380(4)	C−N 1.47
N2−C1	1.39(1)	1.404(4)	1.381(2)	1.381(4)	C=N 1.28
N2−C2	1.39(9)	1.360(3)	1.355(2)	1.389(3)	
N3−C2	1.36(1)	1.387(4)	1.403(2)	1.380(4)	C−O 1.43
N3−N4		1.382(3)	1.371(2)	1.384(4)	C=N 1.20
N1−N5			1.365(2)	1.381(4)	
					N−O 1.44
C1−O1	1.25(5)	1.237(3)	1.200(2)	1.208(4)	N=O 1.20
C2−O2	1.24(6)	1.221(3)	1.210(2)	1.207(4)	
N4−O3		1.214(4)	1.217(2)	1.211(3)	
N4−O4		1.220(3)	1.218(2)	1.206(3)	
N5−O5			1.229(2)	1.216(4)	
N5−O6			1.214(2)	1.210(3)	

A from ref. [76]; b see ref. [77]

In contrast to **DNB*H2O**, the molecular arrangement in **DNB** is completely different. Both nitraminogroups are rotated by approximately 180° yielding an C_{2v} symmetry of the molecule. The corresponding bonds are almost identical (Table 6.8), and the slightly deviation might be explained by packing effects within the crystal. Interestingly, in comparison to the

structural arrangement in **DNB*H_2O**, the nitramine groups are also rotated out of the biuret base structure (torsion angle O2−C2−N3−N4 7.4(6)°) but showing a better delocalization of the π system over the whole molecule. This is indicated by the shorter, almost identical two bond length N2−C2 (**DNB*H_2O** (1.355(2) Å) *vs.* **DNB** (1.389(3)Å)) and N2−C1 (**DNB*H_2O** (1.381(2) Å) *vs.* **DNB** (1.381(4)Å)) for **DNB**, whereas those bonds in **DNB*H_2O** showing a high degree of asymmetry. The latter finding might be explained by the strong hydrogen bridge in DNB*H_2O (O7–H7B····O1, 2.818(2) Å).

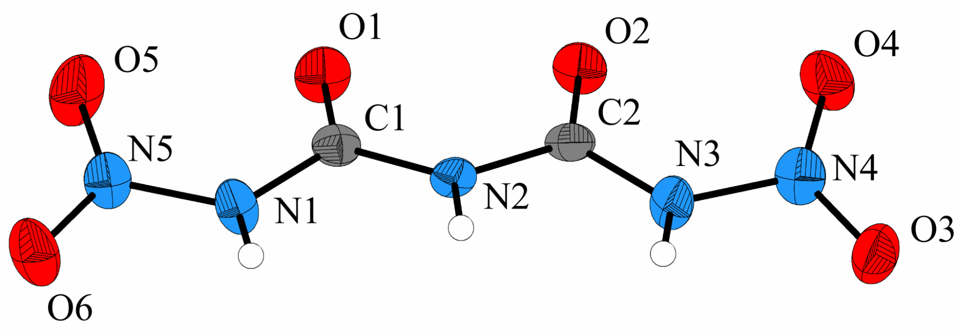

Figure 6.16. Formula unit and labeling scheme for **DNB** (ORTEP Plot, thermal ellipsoid represents 50% probability).

2.5 Reaction of **DNB** with base

2.5.1 Synthesis of **DNB** salts

Treatment of **DNB** with base yields depending on the concentration of the added base, the salts of the mono and doubly deprotonated **DNB**, respectively. Thus the monopotassium dinitrobiuretate (**116**) precipitates in form of a waterfree, white powder when a methanolic solution of DNB is treated with a methanolic solution of KOH at temperatures below 5 °C.

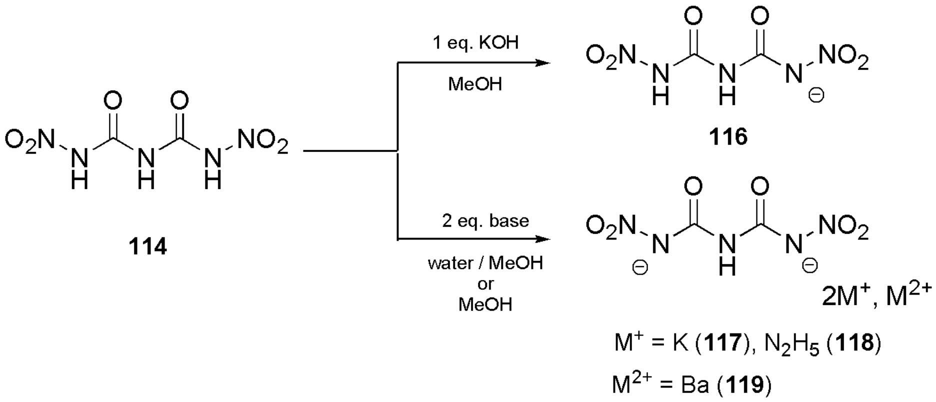

Scheme 6.4. Preparation of mono or doubly deprotonated **DNB** salts

The corresponding salts of doubly deprotonated **DNB** are obtained by the treatment of cold aqueous (for e.g. the Ba-salt, alcoholic) solutions of **DNB** with two equivalents of a base (e.g. hydrazine hydrate (**118**), KOH (**117**), $Ba(EtO)_2$ (**119**)). The obtained products are salted out by adding methanol. Careful recrystallization from aqueous alcoholic solutions yields the salt as colorless needles in yields higher than 60% (*Scheme 6.4*). *Figure 6.17* depicts the IR spectra of **116** and **117**.

2.5.2 IR spectroscopy

With the help of the already discussed IR and Raman spectra of **DNB** and **MNB**, the assignment of the frequency modes is straight forward. Interestingly, **117** crystallizes as monohydrate.

Table 6.9. IR frequencies and modes in **116** and **117**

	116 (cm^{-1})	**117** (cm^{-1})	Assignment
#		824, 1384, 1650, 3487	γ(H_2O), δ(H_2O), ν(H_2O)
*	763, 1728	765, 1702, 1716, 1738	π(C=O), ν(CO)
+	1234, 1285, 1677, 3158, 3229	1189, 3239	δ(N-H), ν(N-H)
°	1312, 1469, 1580	1315, 1499	ν(NO_2), ν(N-NO_2)

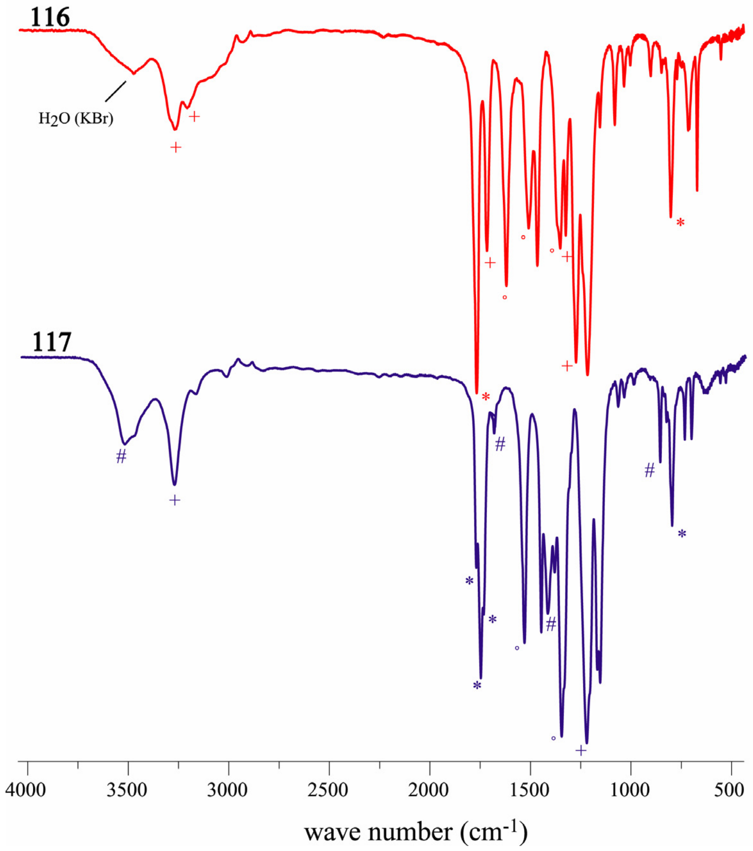

Figure 6.17. IR spectra of **116** and **117**

The stretching vibration of the coordinated water appears, as expected, at 3487 cm^{-1}. The other modes agree also and are depicted in *Table 6.9*. The stretching vibrations of the C=O for both compounds appears also as expected in the region around 1720 to 1740 cm^{-1} and are slightly shifted towards lower wavenumbers combared to the parent **DNB**. The symmetric and asymmetric stretching vibration appears for the nitramide at higher wavenumber (**116** $\nu_{asym}(NO_2)$ 1580 cm^{-1}), whereas deprotonation leads to an significant shift toward lower wavenumbers (**116** $\nu_{asym}(NO_2)$ 1469 cm^{-1} and **117** $\nu_{asym}(NO_2)$ 1499 cm^{-1}). The stretching vibrations for the N–H mode appears in the case of **117** as one sharp signal, whereas in the case of **116** several modes are obtained. *Table 6.9* depicts a more detailed assignment of the observed modes of the IR experiment.

2.5.3 Molecular structure of dipotassium dinitrobiuretate (**117**)

Figure 6.18 display the molecular arrangement of the dipotassium salt of DNB. Interestingly, the molecular framework is the same compared to the water-free DNB but the nitramide moieties are rotated out of the biuret base structure. The potassium salt crystallizes in the triclinic space group *P*-1 with two formula units in the unit cell. A detailed discussion is abstained.

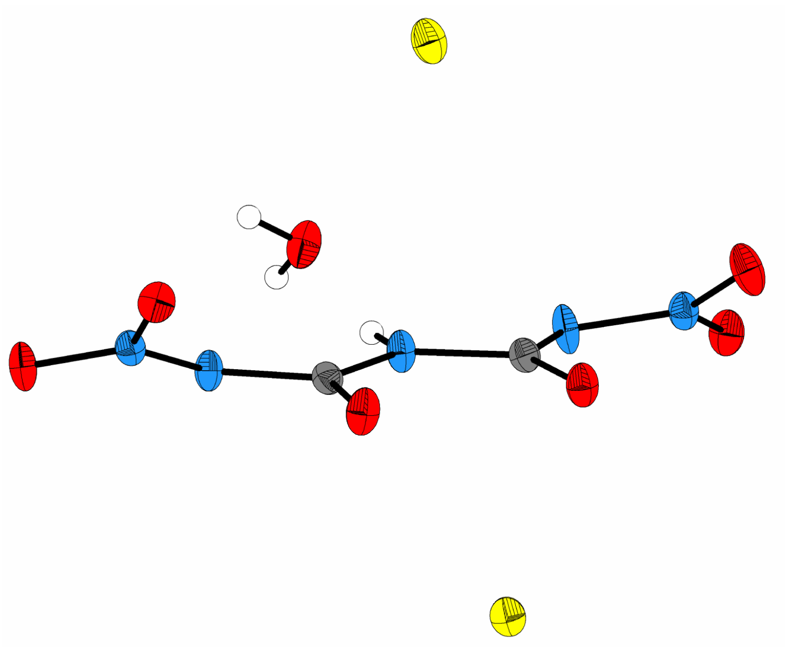

Figure 6.18. View of the molecular structure of **117**. Displacement ellipsoid at 50% probability level. (blue: nitrogen; gray: carbon; red: oxygen; yellow: potassium, white: hydrogen)

2.5.4 ^{1}H and ^{13}C NMR of **DNB** and **DNB** salts

With the help of NMR spectroscopy it is possible to determine the deprotonation mode of the corresponding DNB species in solution (for simplification: DNB (parent) DNB^- (mono deprotonated) and DNB^{2-} (double deprotonated); *Table 6.10*). DNB is a fairly strong dibasic acid which is capable of undergoing stepwise ionization with formation of acid and neutral salts. This can be monitored by means of ^{1}H and ^{13}C NMR since in the case of the deprotonation of the **DNB** an upfield shift, as to expect since the acidity decreases, for the NH protons is observed, whereas in the ^{13}C NMR experiment an downfield shift of the carbonyl signal (*Table 6.10*).

Table 6.10. ^{1}H and ^{13}C NMR of **DNB** and deprotonated species

^{1}H / ^{13}C-NMR

		DNB	DNB^-	DNB^{2-}
δ ^{1}H	–CO-N*H*-CO-	10.64 (s, 1H)	9.80 (s, 1H)	9.54 (s, 1H)
	–N*H*NO2	14.72 (s, 2H)	14.59 (s, 1H)	-
δ ^{13}C	–*C*O–	147.0	153.7	158.6

All shifts were referenced with respect to tetramethylsilane (^{1}H, ^{13}C). [d6]-DMSO was used as solvent.

3. Decomposition of **DNB** in solution

In the solid state **DNB** and its salts are fairly stable. In solution, especially water or highly basic solvents like DMSO, **DNB** and its salts decomposes very fast under the formation of exclusively N_2O, ammonia, CO_2 and water. In solvents like acetone, **DNB** is relatively stable and ^{15}N NMR spectra can be recorded. The first step of the decomposition of **DNB** in solution ([d6]-DMSO) follows a similar acid-catalyzed pathway as proposed by Cox et al.[78] The initial step is the isomerization of **DNB** to the *aci*-nitro form **120**. The mechanism for this step is outlined in *Scheme 6.5*. The protonation of the *aci*-nitro form represents the rate determining step, which proceeds by a water mediated proton transfer from the nitrogen atom to one oxygen atom of the nitro group. Release of N_2O (**121**) and (H_2O) **122** forms an intermediate carbamine acid derivative **123** which decomposes immediately to nitrourea (**124**) and CO_2 (**125**). This transformation can be nicely monitored by the upfield shift of the acidic protons and the increase of the peak intensity at 11.16 ppm in the ^{1}H NMR spectra. Nitrourea itself is under this conditions also not stable and decomposes in contrast to the mechanism proposed by

Dewhurst[79] not to isocyanic acid, but following the same pathway as outlined above to ammonia (**126**) and CO_2. During this process the pH of the solution increases as the amount of **DNB** decreases. This leads to the formation of ammonium carbamate (**128**), which has a higher stability in neutral as well basic media. Due to the continuing decomposition of nitrourea (**124**) and the increasing amount of ammonia in solution, the proton exchange of NH_3 and water becomes fast on the NMR time scale, resulting in one broad signal (*Figure 6.19*). Also the decomposition pathway of nitrourea (**124**) changes from an acid to a base catalyzed mechanism, which is indicated by the observation of nitramine (**129**) as ammonium salt **130**. As final decomposition products, only traces of the corresponding ammonium salt of DNB and ammonium carbamate (**128**) are observed indicating an almost complete decomposition in solution. The whole process can be nicely monitored not only by ^{1}H but also by ^{13}C and ^{14}N NMR spectroscopy and are also depicted in *Figure 6.19*.

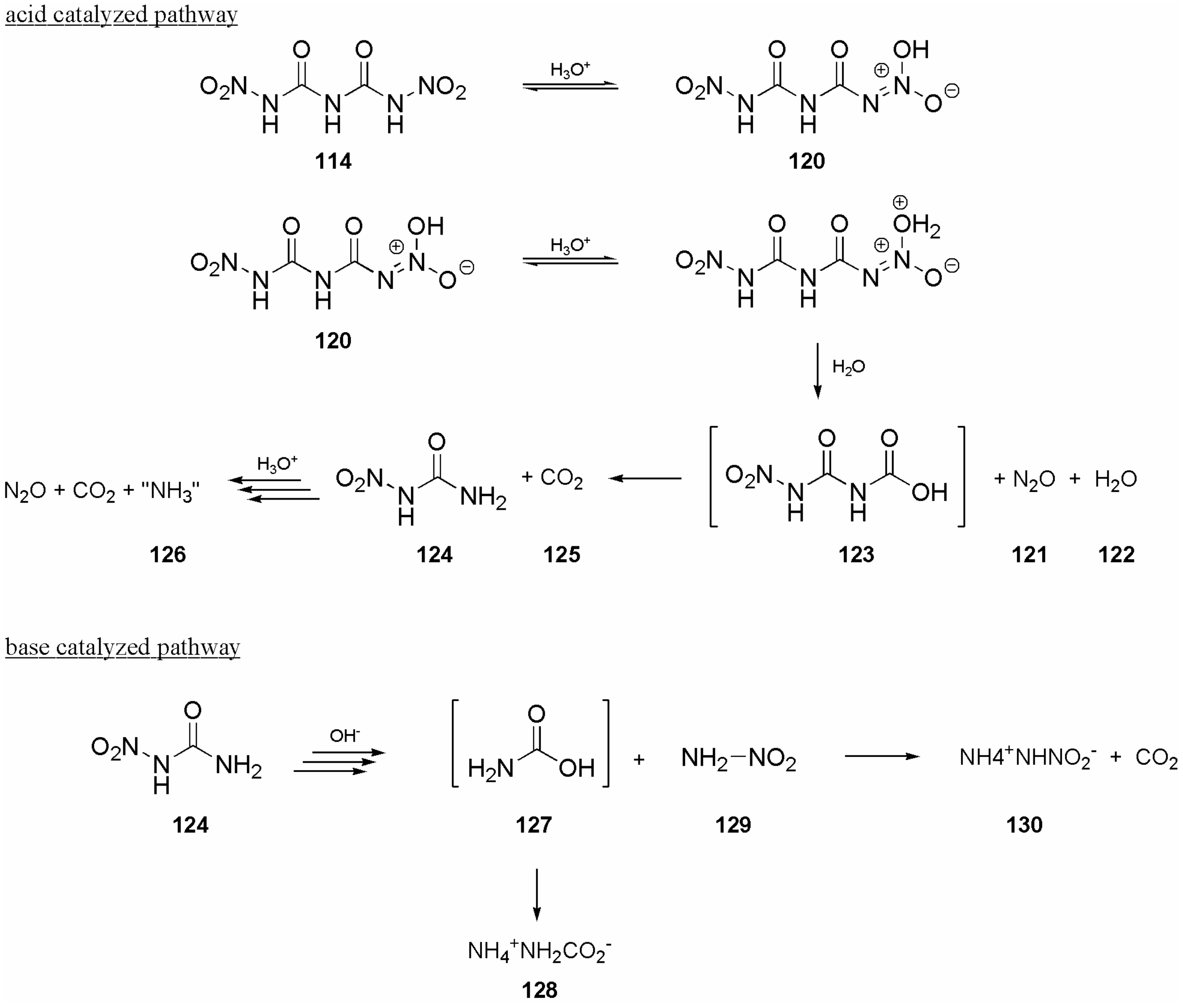

Scheme 6.5. Possible decomposition pathway of DNB monitored in [d6]-DMSO solution.

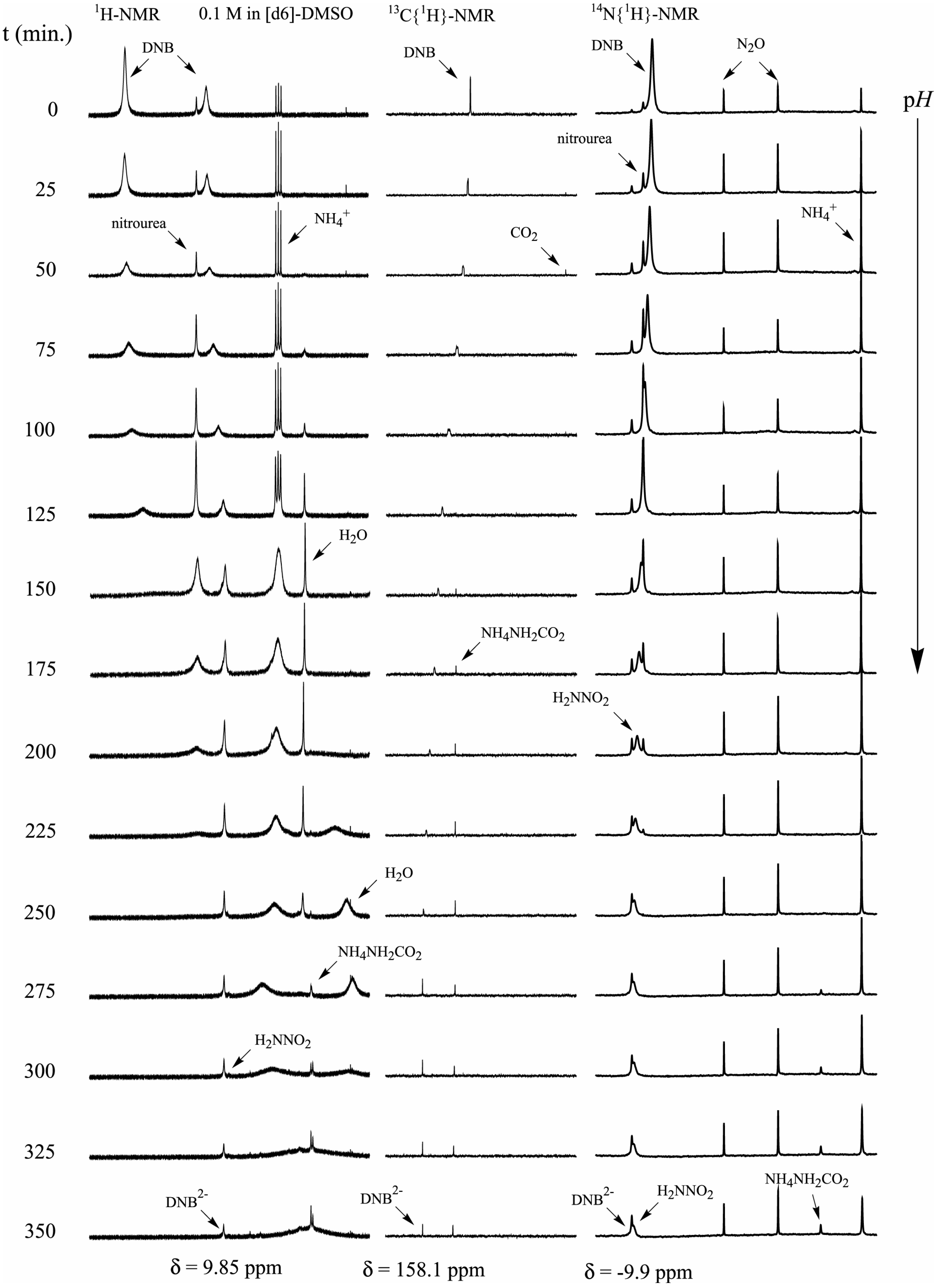

Figure 6.19. Decomposition of **DNB** in [d6]-DMSO solution monitored by ^{1}H, ^{13}C and ^{14}N spectroscopy. Intensities are not scaled, especially the last spectra (t > 250 min.) are not displayed with the real absolute intensity.

2.7 Thermochemistry of **MNB** and **DNB**

2.7.1 Thermal behavior

Figure 6.20 displays characteristic DSC thermographs of **MNB** at different heating rates. **MNB** decomposes without melting. The thermographs show, depending on the heating rate, up to five thermal effects (heating rate 20°C/min). The first decomposition step (~154 – 164°C) is exothermic followed by two or three weak endothermic signals at 210 – 240°C. In the last endothermic reaction at above 350°C complete degradation takes place (*Figure 6.21*).

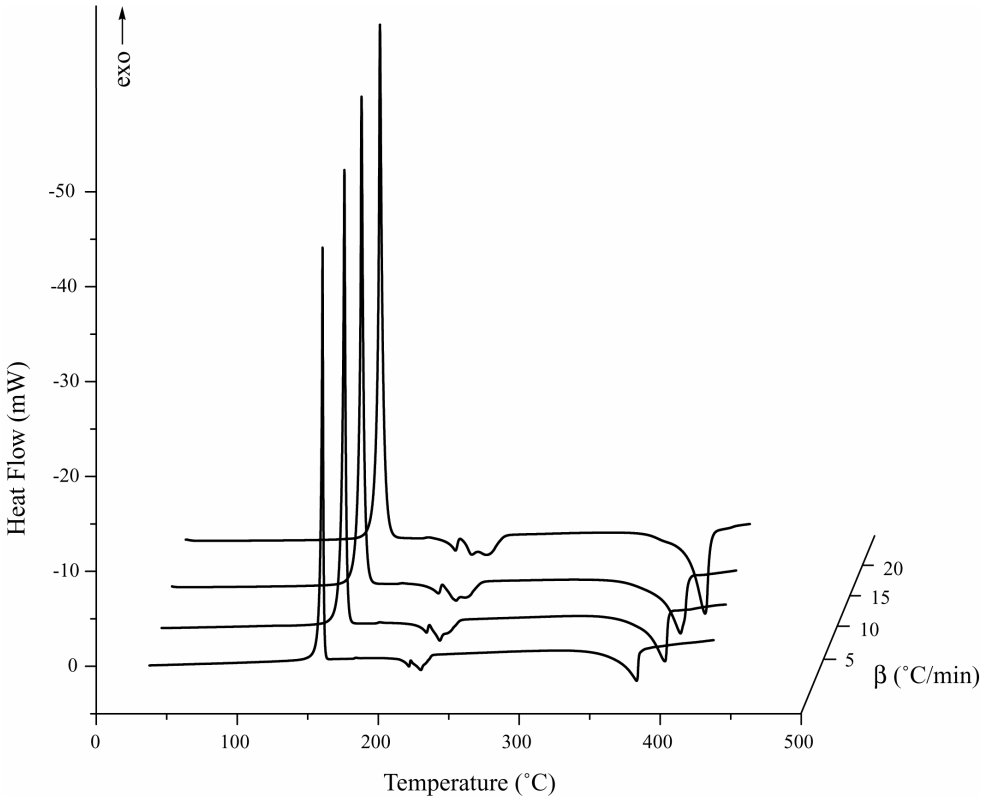

Figure 6.20. DSC thermographs of **MNB** (β = 5, 10, 15 and 20°C/min)

TGA measurements of MNB show a complete, residue-free thermal decomposition in three steps (*Figure 6.21*). The three decomposition steps can be observed by Differential Thermo-Gravimetric (DTGA) measurements at a heating rate of 10°C/min. The first step (at 154 - 164°C) with a 59.5% weight loss corresponds to the formation of nitramide, water, dinitrogen monoxide and urea (sublimate). These products have been identified in the gas phase (by IR, mass spectrometry). As residual products of the first decomposition step a mixture of

biuret (9%), triuret (71%), tetrauret (7%) and cyanuric acid (13%) were identified (*Figure 6.22*, *Table 6.11*).

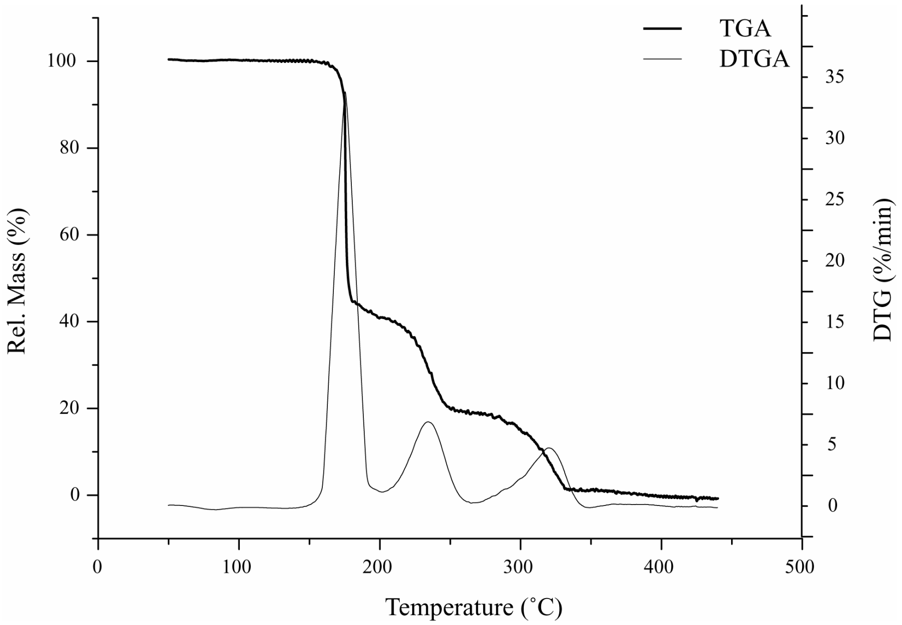

Figure 6.21. TGA and DTGA thermograph of **MNB** (β = 10°C/min, nitrogen atmosphere)

The second step (210 – 260°C) with 23.0% weight loss corresponds to the decomposition of the urea derivatives by forming cyanuric acid and HNCO. The third step (> 350°C) with 16.5% weight loss corresponds to the depolymerization of cyanuric acid with the release of HNCO.[80] The thermograph of MNB (heating rate of 5°C/min) clearly shows three decomposition steps with a peak at 163°C for the first exothermic step.

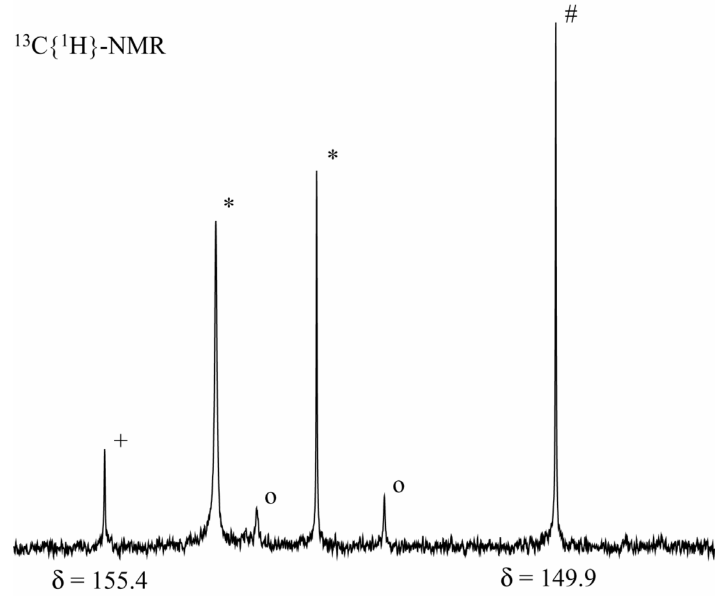

Figure 6.22. ^{13}C-NMR spectra of decomposition products of **MNB**. For description the *Table 6.11*

The energy evolved during the exothermic decomposition is 958 kJ/g. The data obtained at different heating rates are summarized in *Table 6.12*.

Table 6.11. Residual products after the first decomposition step of **MNB** (154-164°C).

assignment		+ biuret [81]	* triuret [82]	o tetrauret [82]	# cyanuric acid [81]
δ^1H	NH_2	6.79 (s, 4H)	7.20/6.96 (s, 4H)	7.37/7.01 (s, 4H)	
	-CO-N*H*-CO-	8.69 (s, 1H)	9.66 (s, 2H)	9.71 (s, 2H), 10.61 (s, 1H)	11.10 (s, 3H)
$\delta^{13}C$	-*C*O-NH-		152.8	152.0	149.9
	-*C*O-NH_2	155.4	154.1	153.6	

It is seen from *Table 6.12* that as the heating rate increases, the temperature of the exothermic maxima also increases. The energy of activation for the first decomposition step, as estimated by the method of Ozawa[83] and Kissinger[84], are 212 and 215 kJ/mol respectively, i.e. in close agreement.[85] It should be noted that increased heating rates cause an exothermic peak to shift, in a way not necessarily related to the activation energy (e.g. melting). This depends among other things on the response of the instrument, the sample size, contact area and position of the sample on the DSC pan, as well as for energetic materials their ratio of area/volume which must be taken into account. Therefore the sample size was kept small to minimize temperature gradients within the sample and a 0.003*3/16-in. disk was used to optimize good thermal contact between the sample and container (according ASTM E 698 – 99).

Table 6.12. Maximum exothermic responses of **MNB** and **DNB** as a function of scan speed.

S. no.	β (°C/min)	T_p (°C)	E_a(kJ/mol) Ozawa [23]	E_a (kJ/mol) Kissinger [24]
MNB				
1	5	163.23	212	215
2	10	168.34		
3	15	171.41		
4	20	172.79		
5	25	175.35		
DNB				
1	15	128.92	148	149
2	20	130.83		
3	25	133.70		
4	30	134.94		
5	40	137.29		

Also the volatility of the compounds used was taken into account by testing the samples using a sealed hermetic container to prevent interferences from vaporization and weight loss of unreacted material. It was found that the use of a hermetic container or a high-pressure cell was not necessary for **MNB**, but was for **DNB** to make a good estimate of the activation energy. We assume that the rate constant follows the Arrhenius law and that the exothermic reaction can be considered as a single step; certainly the conversion at the maximum rate is independent of the heating rate, when this is linear.

Figure 6.23 shows characteristic DSC spectra of **DNB** with different heating rates. **DNB** decomposes without melting. The thermographs show, depending on the heating rate, three thermal effects; in the case of fast heating rates (above 10°C/min) only one single exothermic signal is observed.

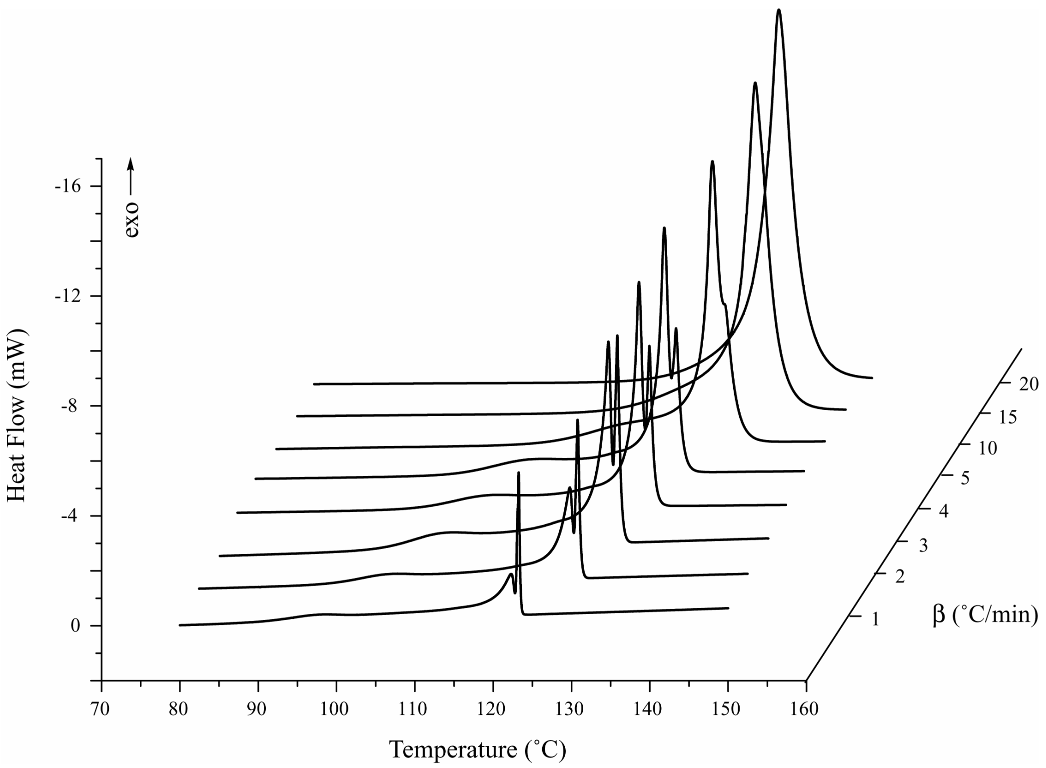

Figure 6.23. DSC thermographs of DNB (β = 1, 2, 3, 4, 5, 10, 15 and 20°C/min).

The DSC curves of **DNB** show clearly that the decomposition of **DNB** does not occur in a single step; the reactions of **DNB** between 120 and 130°C are not clearly resolved, indicating simultaneous or consecutive reactions steps. The energy evolved during decomposition is 1130

kJ/g. **DNB** has a lower thermal stability than MNB. As seen from Fig. 5, **DNB** shows three different activated reactions, which cannot be separated when the heating rate is higher than 10°C/min. To evaluate the stability of **DNB**, the activation energy was estimated using the standard test method for the rate constant for thermally unstable materials[85] at heating rates higher than 10°C/min and following the methods of Ozawa[83] and Kissinger[84] (*Table 6.12*).

Figure 6.24 shows the TGA (heating rate 1°C/min) and DTGA curve of **DNB**. The DTGA curve shows a sharp exotherm with a maximum at 123°C. The TGA curve reveals a characteristic, one-step mass decrement before the main spontaneous decomposition. The weight loss starts at 90°C and the rate of loss is constant and slow between 95 and 117°C. However, a sudden mass loss is observed immediately after 117°C and ends at 124°C. The total weight loss at 90 – 124°C was found to be 100% within experimental error.

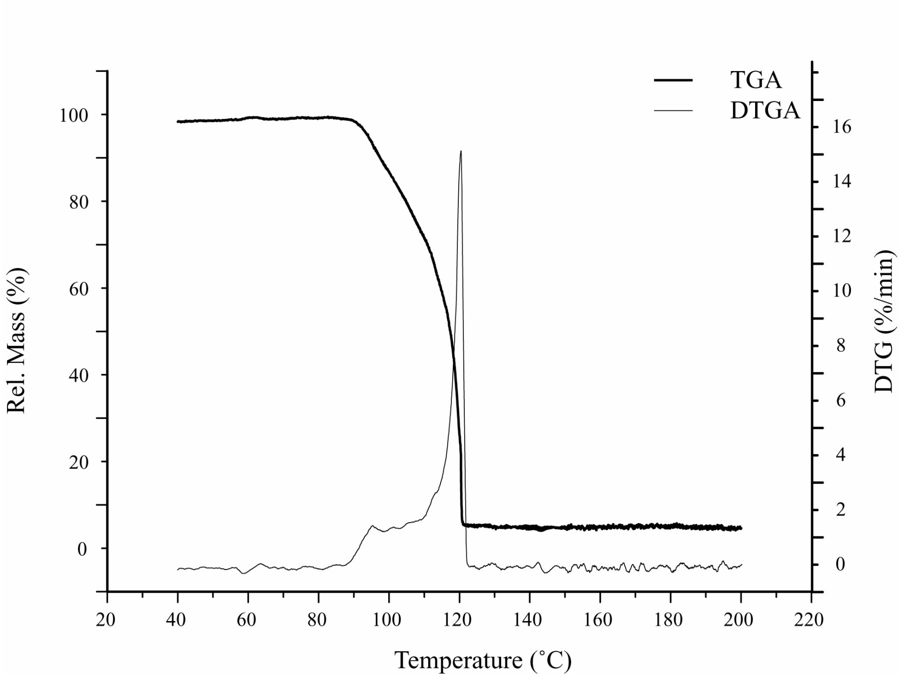

Figure 6.24. TG and DTG thermograph of **DNB** (β = 1°C/min, nitrogen atmosphere)

2.7.2 IR spectroscopy

The identification of the decomposition gases allows the evaluation of the chemical processes during the thermal degradation of **MNB** and **DNB**. *Figures 6.25* and *6.26* show those decomposition gases detected by IR spectroscopy and released during heating for the exothermic step of **MNB** (160 – 192°C) and **DNB** (98 – 130°C).

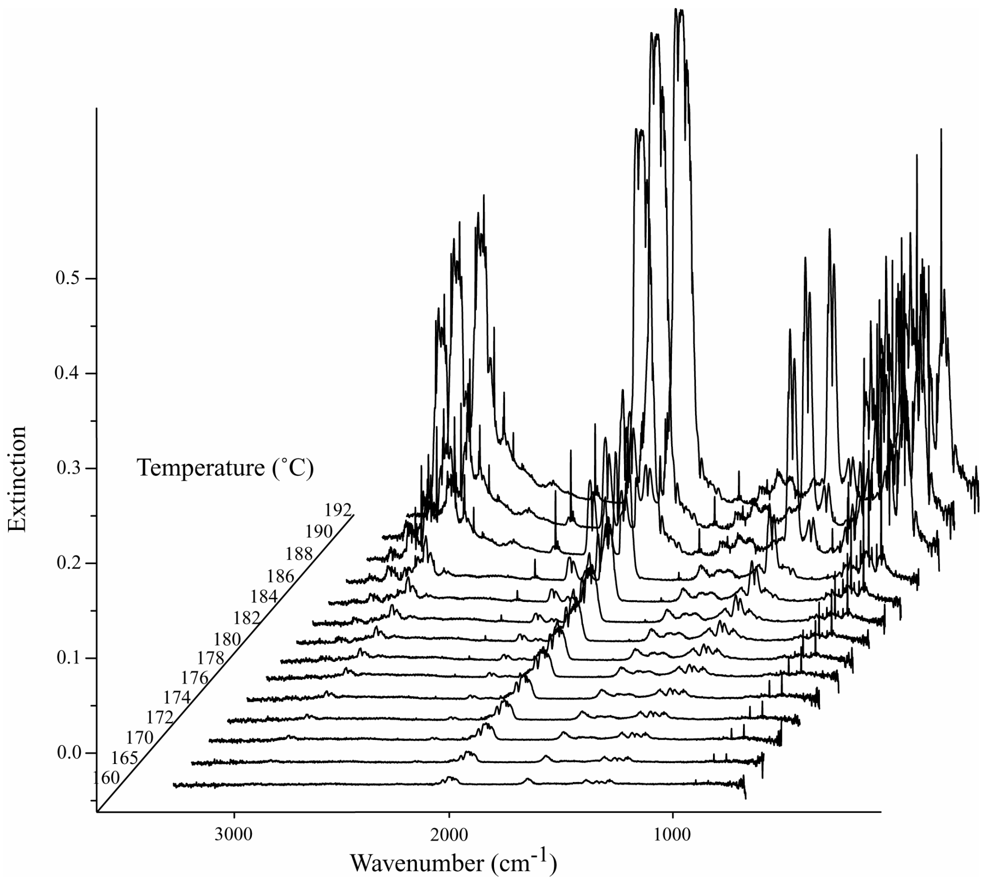

Figure 6.25. Infrared spectroscopic evolved gas analysis of **MNB**

The vibrational frequencies of the experimentally observed IR-active gases are summarized in *Table 6.13*. In both cases thermal decomposition reaction yields HNCO, N_2O, CO_2 and H_2O as gaseous products. The formation of gaseous products starts in the case of MNB slowly between 160 and 186°C (*Figure 6.25*). A sudden rise is observed shortly above 186°C, indicating a spontaneous decomposition. Continuing the heating of **MNB** up to 350°C shows only the formation of HNCO. No other decomposition gases could be detected after the first decomposition step. In the case of **DNB** (*Figure 6.26*) a regular rise in the formation of gaseous products is observed. This is not consistent with the TGA/DSC data. One explanation for this observation is that the thermodynamic conditions for both experiments are different with respect to pressure. The IR experiment was carried out by thermal heating with a pressure of 5 μbar, whereas the TGA/DSC experiments had nitrogen as purge gas (20 cc/min). It is known that **DNB** is labile in a vacuum, especially when heated. Heating a 200 mg sample of **DNB** at 60°C (5 μbar) for ~ 15 min gave a violent decomposition, resulting in a complete destruction of the glass vessel used. The exothermic decomposition of **MNB** and **DNB** leads to almost identical gas phase spectra (*Figure 6.27*), which are confirmed by mass spectrometry.

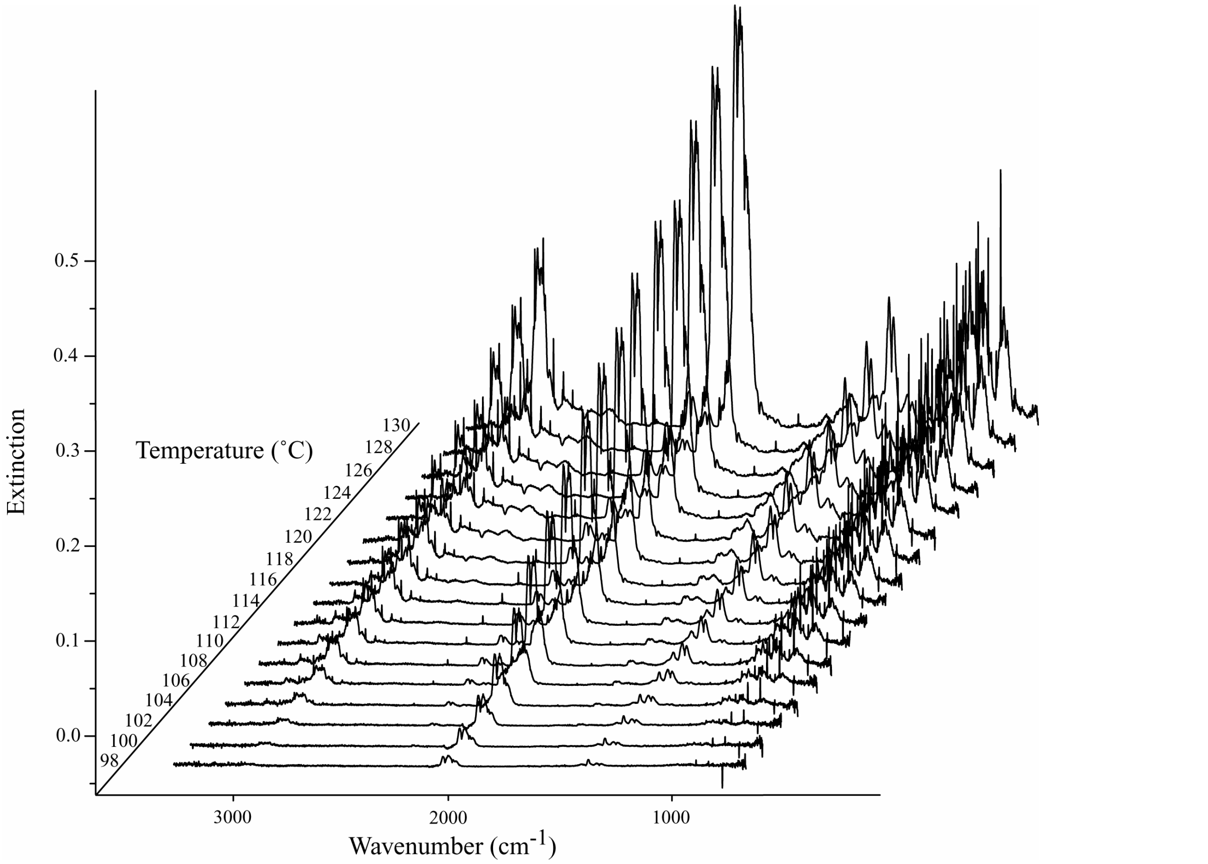

Figure 6.26. Infrared spectroscopic evolved gas analysis of **DNB**

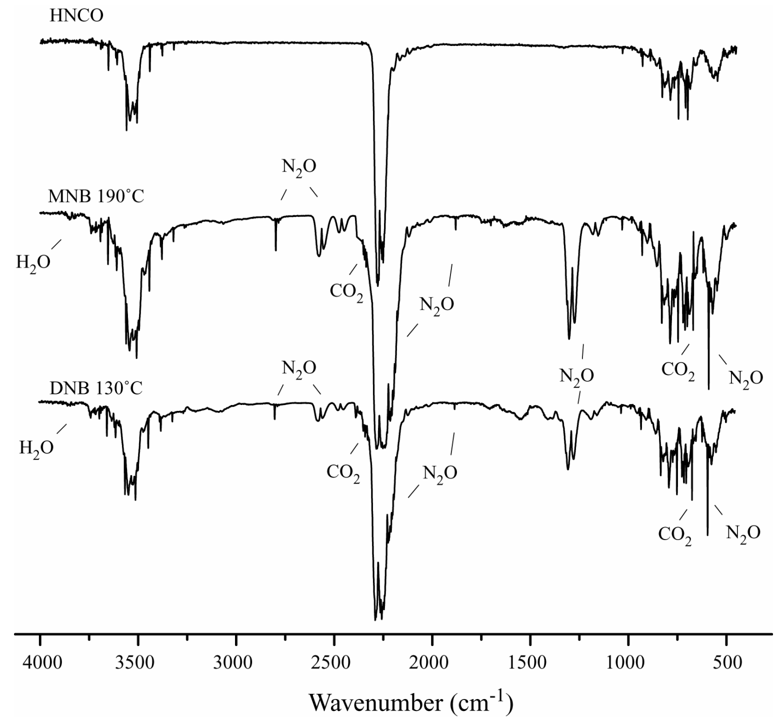

Figure 6.27. IR spectra of HNCO and decomposition gases of MNB (190°C) and DNB (130°C)

*Table 6.13.*Vibrational frequencies (cm^{-1}) of the experimentally observed molecules

Species	Frequencies	ref
HNCO	3538 (s), 2279 (vs), 2253 (vs), 1327 (w), 777 (w), 657 (w), 577 (w)	[86]
N_2O	3891 (w), 3480 (m), 2809 (w), 2591 (m), 2488 (m), 2457 (vs), 2217 (vs), 1890 (w), 1302 (vs), 1275 (vs), 1183 (m), 1155 (m), 694 (w), 588 (w)	[87]
CO_2	3716 (w), 3609 (w), 2326 (vs), 741 (m), 667 (vs)	[88]
H_2O	3657 (s), 1595 (s)	[89]

2.7.3 Mass spectrometry

In the MS experiments the following decomposition gases were detected by their characteristic mass fragments (see *Figure 6.28* and *6.29*): water (m/z = 17 and 18), dinitrogen monoxide (m/z = 14, 16, 28, 30 and 44), carbon dioxide (m/z = 12, 16, 28, 22 and 44) and isocyanic acid (m/z = 15, 28, 29, 42 and 43). For MNB the ion with m/z = 86 coincides with the fragmentation of MNB by mass spectrometric induced S_Ni reaction[90], yielding the nitramide ion peak (m/z = 62) and the dimeric isocyanic acid (m/z = 86). The peak at m/z = 70 results from an α-cleavage of an NH_2 radical of the dimeric isocyanic acid (m/z = 86). The ion m/z = 60 (from urea) accounts for the reaction of ammonia with isocyanic acid (*Scheme 6.6*)

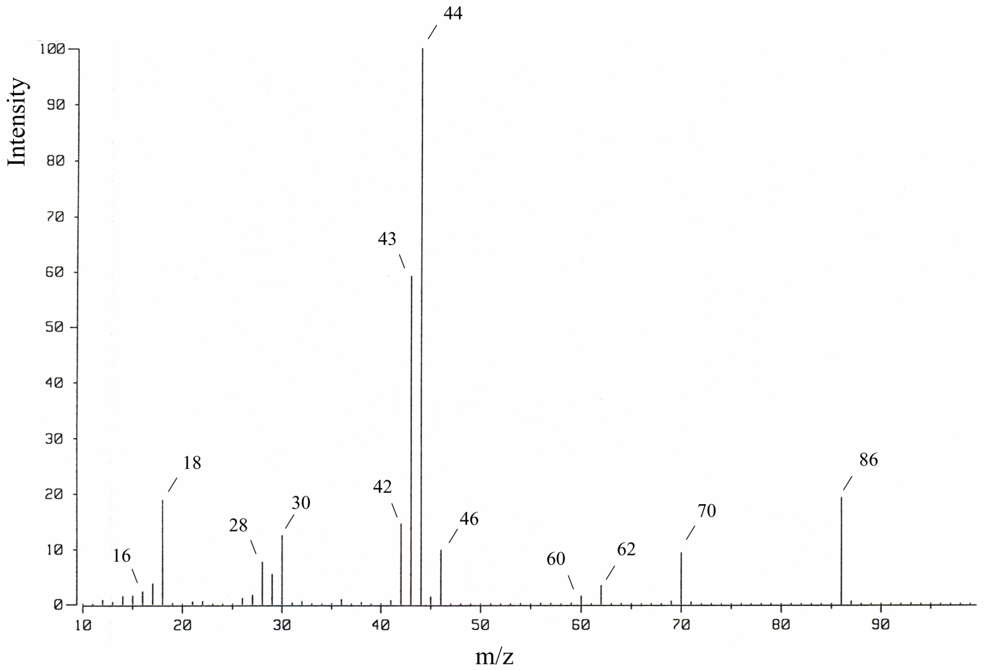

Figure 6.28. EI-mass spectrum (70 eV) of the decomposition gases of **MNB**

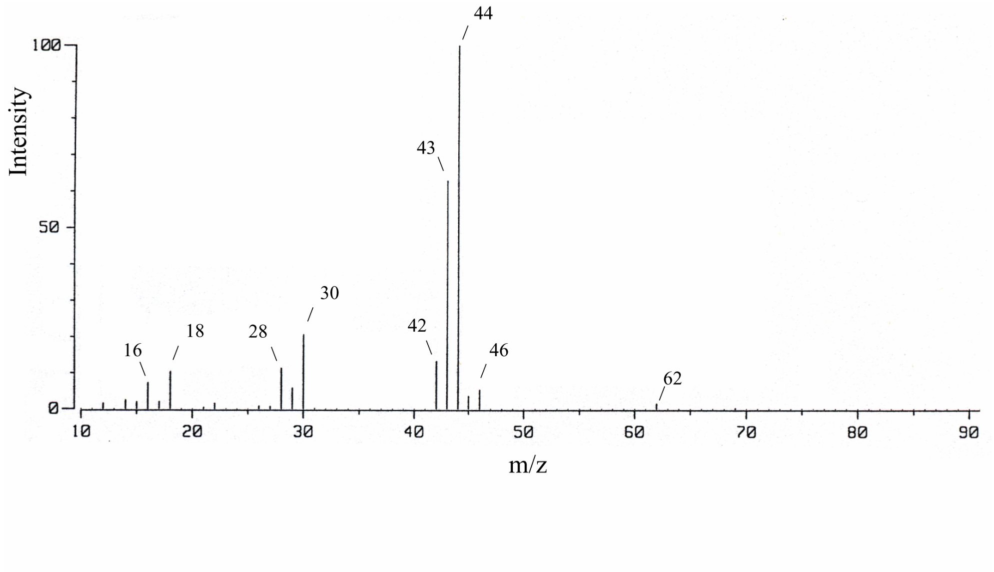

Figure 6.29. EI-mass spectrum (70 eV) of the decomposition gases of **DNB**

and explains the absence of ammonia in the IR spectra. Also the fragmentation of DNB starts with the mass spectroscopic induced S_Ni-reaction [90] yielding the nitramide ion peak (m/z = 62). Ions with mass higher than m/z 62 are not found in the spectrum of DNB. The remaining peaks can be attributed to the decomposition products already discussed.

2.7.4 Discussion

The thermal decomposition of **MNB** and **DNB** is initiated by an intramolecular S_Ni-reaction of the nitramide unit forming nitramide (I) and the corresponding unstable intermediate derivatives (II and III). Nitramide decomposes in the gas phase to N_2O and water (IV), which reacts with gaseous isocyanic acid (V) to ammonia (VI) and carbon dioxide (VII). The intermediate of the decomposition of **DNB** leads directly to isocyanic acid, dinitrogen oxide and carbon dioxide, whereas in the case of **MNB** this intermediate decomposes to two molecules isocyanic acid (*Scheme 6.7*). The theoretical mass loss for the first exothermic decomposition step of MNB (60%) coincides well with the experimentally determined value (59.5%). The initial step leads for both MNB and DNB to the formation of N_2O, CO_2, H_2O and HNCO. Due to the higher decomposition temperature of MNB during the decomposition step, the residue components HNCO (V) and NH_3 (VI) react in the gas phase reaction to urea (VIII). This leads at higher temperature to a series of condensation products, such as biuret (IX), triuret (X),

tetrauret (XI) and cyanuric acid (XII).[91] This result is consistent with the observation of several endothermic effects at 210 – 260 °C, as determined by DSC and the final complete residue-free decomposition above 350 °C.[92] Urea, biuret and cyanuric acid were found in the sublimate after pyrolysis. In the case of DNB very small amounts of sublimate were obtained when the pyrolysis was carried out with a heating rate less than 3°C/min. This sublimate was identified as urea by mass spectrometry, but due to the low decomposition temperature, condensation products similar to those found after decomposition of MNB could not be observed.

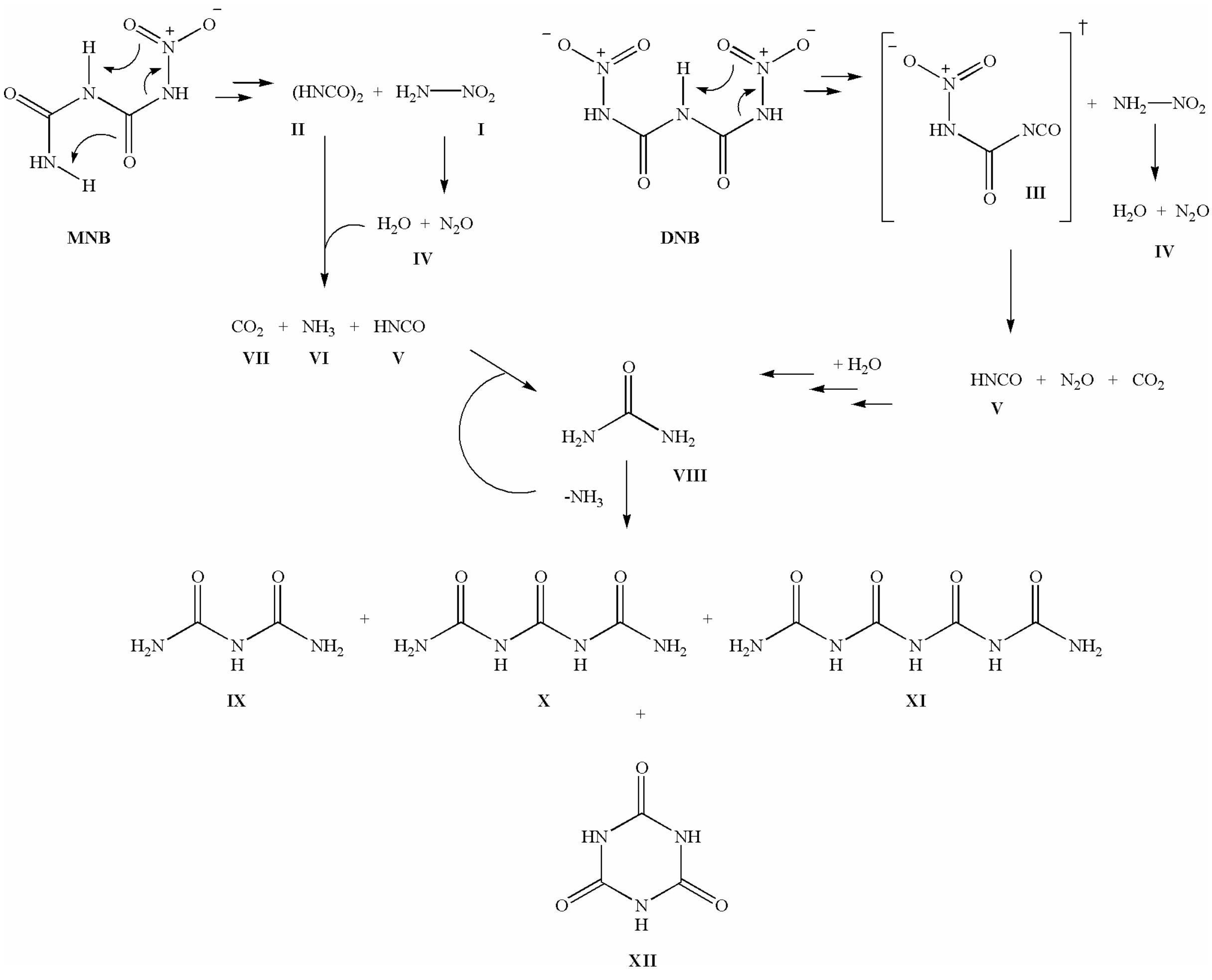

Scheme 6.6. Possible decomposition pathway of **MNB** and **DNB**

2.7 Explosive properties

The heat of combustion ($\Delta H_{com.}$) of DNB was determined experimentally using oxygen bomb calorimetry. The standard heat of formation ($\Delta H_f°$) was obtained on the basis of quantum chemical computations at the electron correlated ab initio MP2 level of theory using a correlated consistent double-zeta basis set (cc-pV-DZ).[5c] The detonation velocity (*VOD*) and and detonation pressure of DNB were calculated using the empirical equations by Kamlet and Jacobs (*Chapter V*, 2.8.2). *Table 6.14* shows a comparison of obtained values with those of well known explosives. The explosive properties of DNB indicate that it is comparable with PETN. In contrast to PETN, RDX and HMX, DNB has a positive oxygen balances and therefore a further oxidizer in an explosive formulation is not needed.

Table 6.14. Comparison of DNB with explsoives

	Oxygen balance (%)	$\Delta H_{com.}$ (kJ/kg)	ΔH°_{f} (kJ/kg)	VOD (m/s)
DNB	+20.6	5195	-353	8660
PETN	-26.5	5231	-2069	8300
RDX	-21.6	5625	300	8750
HMX	-21.6	5601	254	9100

In order to classify **DNB** as explosive, the “Koenen test” was applied. *Figure 6.30* depicts the outcome of this experiment. For all tests the thimble was destroyed in three or more big pieces (8 g, 8 mm; classified as F) or destroyed into little pieces (8 g, 6 mm; classified as G). So far, an proper valuation of the sensitivity of **DNB** can not be given as no test with port diameter greater than 10 mm has been applied, but **DNB** is expected to lie between the classification of an sensitive to very sensitive explosive.

Steel sleeve test of DNB (8 g, 6 mm)

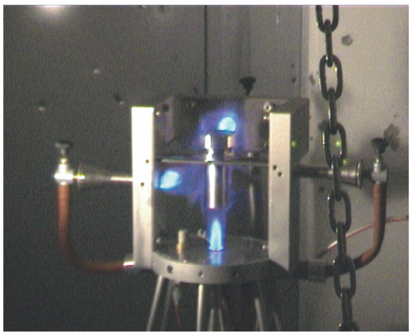

t = 0 s

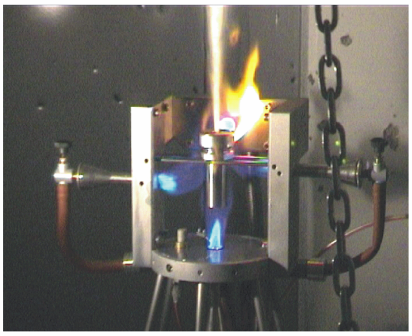

t = 5.0 s

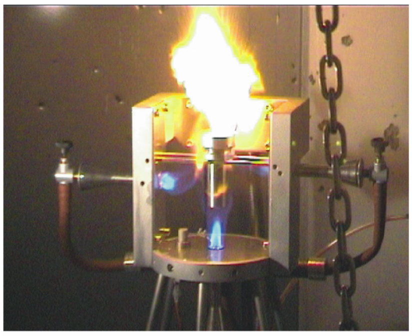

t = 5.5 s

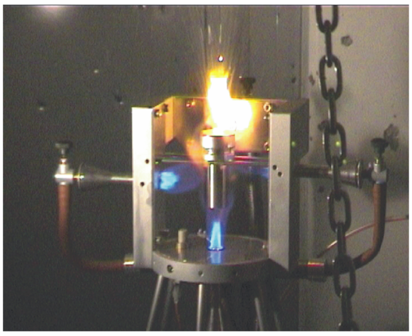

t = 5.8 s

t = 5.9 s

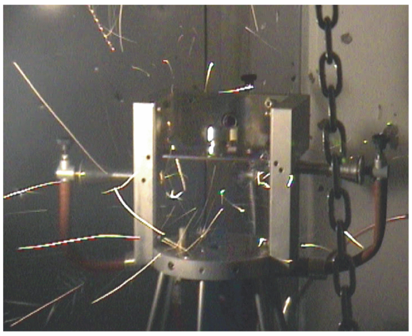

t = 6.0 s

before test after test

DNB (8 g, 6 mm)

Figure 6.30. Koenen test with **DNB**

2.9 Conclusion

MNB and **DNB** are energetic materials showing a distinctive thermal behavior. Unfortunately, the thermal stability of **DNB** is not very promising for use as a propellant or explosive, because the decomposition starts at an onset temperature of 90°C and takes place in three steps. **DNB** decomposes spontaneously with an onset temperature of 132°C for a heating rate of 20°C/min. Only the decomposition gases N_2O, CO_2 and HNCO were generated. **MNB**

shows better thermal stability and decomposition starts at an onset temperature at 157°C for a heating rate of 5°C/min. **MNB** decomposes in several steps forming urea, biuret, triuret, tetrauret and cyanuric acid. But, compared to the properties of DNU, both **MNB** and **DNB** are promising materials, which might be used as synthetic equivalents for the preparation of other new azaheterocyclic nitramines.[93]

2.10 Experimental

CAUTION: DNB is an energetic material and appropriate safety precautions should be taken, especially when this compound is prepared on a larger scale. Laboratories and personnel should be properly grounded, and safety equipment such as Kevlar® gloves, leather coat, face shield and ear plugs are necessary when manipulating DNB.

DSC and TGA experiments: DSC measurements were carried out as follows. Samples (**MNB** ~ 1 mg, **DNB** ~ 0.4 mg) were analyzed in closed Al-containers with a hole (1µm) on the top for gas release with a nitrogen flow of 20 mL/min. The reference sample was an Al-container with air. Experiments were carried out from 30 °C-170 °C (**DNB**) and 30 °C-445 °C (**MNB**). The sample and the reference pan were heated in a differential scanning calorimeter (Perkin-Elmer Pyris 6 DSC, calibrated by standard pure Indium and Zinc) at different heating rates of 1, 2, 3, 4, 5, 10, 15, 20 and 25 °C for **DNB** and 5, 10, 15, 20 and 25 °C min^{-1} for **MNB**. **MNB** and **DNB** were subjected to TGA analysis in a nitrogen atmosphere in open Al_2O_3 crucibles (sample weight ~ 1 mg) at two heating rates (1, 10 °C min^{-1} **DNB**) and 10°C min^{-1} for **MNB** with a thermogravimetric analyzer (Setaram DTA-TGA 92) in the temperature range from 30 °C-170 °C (**DNB**) and 30 °C-445 °C (**MNB**). For the removal of moisture, all samples were dried *in vacuo* for 24 h at 40°C.

Thermal decomposition experiments: In order to analyse the gases from the stepwise decomposition of the compounds, a specially equipped IR-cell was loaded with the compounds (~ 2 mg) and evacuated. The sample holder of the IR cell was heated at a rate of 1 °C min^{-1} (CARBOLITE 900 °C Tube Furnace type MTF 9/15) and the reaction products were allowed to expand continuously into the gas cell. During this heating IR-spectra were recorded

continuously as a function of the heating rate using a Perkin-Elmer Spektrum One FT-IR instrument. In the case of MNB the IR cell was evacuated between the exothermic/endothermic steps, which had been determined by DSC. To record the mass spectra, a sample (~ 1mg) of the corresponding compound was heated at a heating rate of 1 °C min^{-1} (CARBOLITE 900 °C Tube Furnace type MTF 9/15) in a one side closed glass tube (length: 500 mm; diameter: 5 mm) connected to the reservoir of the mass spectrometer (JEOL MStation JMS 700). In this case, the spectra were also recorded as a function of the heating rate. For **MNB** as well as **DNB** the residual decomposition products (e.g. sublimate and residue after the first and second decomposition step of **MNB**) were identified by means of mass spectrometry (EI and DEI mode) and NMR (^{1}H, ^{13}C) techniques. The ^{1}H and ^{13}C spectra were recorded on a JEOL Eclipse 400 instrument in [d6]-DMSO, and chemical shifts were referenced to TMS. Reference data for urea, biuret and cyanuric acid were obtained from authentic samples (Aldrich) and in the case of triuret and tetrauret from [82].

Mononitrobiuret (113): Mononitrobiurte was obtained according to literature procedure [**Fehler! Textmarke nicht definiert.**]. m.p. 153 °C (dec.). IR $\tilde{\nu}$ (KBr)[cm^{-1}]: 3433(s), 3291(s), 3146(w), 3071(w), 2969(m), 2805(m), 1739(vs), 1630(vs), 1572(s), 1490(m), 1431(m), 1383(m), 1335(s), 1200(s), 1117(w), 1072(w), 1015(w), 956(w), 826(w), 777(w), 756(m), 717(w), 654(w), 598(m), 556(m), 502(w). Raman (200 mW) $\tilde{\nu}$ [cm^{-1}]: 3292(22), 1714(32), 1631(25), 1551(10), 1552(10), 1426(18), 1352(77), 1194(6), 1119(14), 1073(6), 1011(10), 961(100), 770(13), 758(13), 729(8), 498(21), 435(20), 380(30), 302(25), 176(16), 142(19). ^{1}H NMR ([d6]-DMSO): δ = 13.16 (s, 1H, -N*H*NO_2), 9.32 (s, 1H, -N*H*-), 7.27 (s, 1H, -NH_2), 7.08 (s, 1H, -NH_2). ^{13}C{^{1}H} NMR ([d6]-DMSO): δ = 153.8 (-*C*O-NH_2), 148.8 (-*C*O-NHNO_2). ^{14}N NMR ([d6]-DMSO): δ = -41.7 (-NH-*N*O_2, $\Delta\nu_{1/2}$ = 0.5 Hz), -296.1 (-*N*H-, -*N*H_2, $\Delta\nu_{1/2}$ = 160 Hz). ^{15}N NMR ([d6]-DMSO): δ = -41.5 (s, -NH-*N*O_2), -181.8 (s, -*N*H-NO_2), -254.8 (d, $^{1}J_{NH}$ = 90.4Hz, -*N*H-), 294.2 (t, $^{1}J_{NH}$ = 89.3Hz, -*N*H_2). *m/z* (EI^+) 148 [(M^+) (2)], 102 (15), 86 (11), 70 (12), 62 (3), 60 (5), 59 (2), 46 (19), 45 (3), 44 (100) 43 (55), 42 (18), 41 (1), 32 (2), 31 (8), 30 (43), 29 (29), 28 (21), 27 (6), 26 (6), 18 (17), 17 (5), 16 (10), 15 (8), 14 (9), 12 (4). $C_2H_4N_4O_4$ (148.08): Calc. C, 16.22; H, 2.72; N, 37.84% ; Found: C, 16.52; H, 2.91; N, 37.63%.

1,5-Dinitrobiuret (114): To cooled 100% HNO_3 (-10°C, 10 ml), **MNB** (3.84g, 30 mmol) was added in small portion under stirring in such a way that the temperature was held at -10°C. After the addition the reaction mixture was allowed to rise to 0°C and stirred for 2 hours at this temperature, leaving a clear solution. After removing the excess of HNO_3 in vacuo at 0°C the white residue was kept over H_2SO_4/NaOH in an evacuated desiccator for 48 h. Recrystallization of the raw product form methanol yield pure **DNB**. Yield 2.65g (53%). m.p. 127 °C (dec.). IR $\tilde{\nu}$ (KBr) [cm^{-1}]: 3401(w), 3291(m), 3210(m), 3063(w), 2969 (w), 2805(vw), 1764(vs), 1630(m), 1618(s), 1568(s), 1484(w), 1464(m), 1336(m), 1318(s), 1261 (w), 1228 (w), 1154(m), 1080(m), 1015(m), 990(w), 829(vw), 755(w), 737(w), 654(m), 638(m). Raman (200 mW) $\tilde{\nu}$ [cm^{-1}]: 3290(11), 3212(7), 1760(72), 1615(19), 1566(7), 1465(20), 1349(12), 1325(100), 1223(6), 1056(92), 987(22), 828(8), 757(7), 733(2), 638 (5), 473(38), 258(27), 191(28), 161(2x 4). ^{1}H NMR ([d6]-acetone): δ = 10.96 (s, 1H, -N*H*NO$_2$), 9.19 (s, 1H, -N*H*-) ppm. $^{13}C\{^1H\}$ NMR ([d6]-acetone): δ = 145.5 (-*C*O-) ppm. ^{14}N NMR ([d6]-acetone): δ = -44.4 (-NH-*N*O$_2$, $\Delta\nu_{1/2}$ = 0.5Hz), -188.1 (-*N*H-NO$_2$, $\Delta\nu_{1/2}$ = 328Hz), -260.2 (-*N*H-, $\Delta\nu_{1/2}$ = 25Hz) ppm. ^{15}N NMR ([d6]-acetone): δ = -44.5 (s, -NH-*N*O$_2$), -182.7 (s, -*N*H-NO$_2$), -256.9 (d, $^1J_{NH}$ = 90.4Hz, -*N*H-) ppm. *m/z* (DEI$^+$) 193 [(M$^+$) (2)], 147 (7), 132 (1), 117 (5), 102 (2), 101 (6), 70 (6), 69 (5), 46 (78), 45 (4), 44 (100), 43 (53), 42 (11), 36 (2), 32 (2), 30 (96), 29 (26), 28 (34), 27 (4), 26 (5), 18 (15), 17 (6), 16 (15), 15 (6), 14 (14), 12 (6). *m/z* (*CI+, Isobutane*) 194 [M$^+$+1]; $C_2H_3N_5O_6$ (193.08): Calc. C, 12.44; H, 1.57; N, 36.27% ; Found: C, 12.38; H, 1.62; N, 36.53%.

Einleitung

Aufgrund eingehender Studien haben wir uns im ersten Teil dieses Projektes auf die Synthese neuartiger Oligo-/Poly-Nitramine beschränkt. Da bei den Synthesen das besondere Interesse auf der Substitution mit energiereichen Resten liegt, wobei bewusst auf Nitrogruppen (C-NO_2) verzichtet wurde, kommen als energiereiche Reste vorerst nur die Azid- (-N_3) und Nitratogruppe (-ONO_2) in Frage. Verbindungen mit Nitrato- und Azidgruppen erweisen sich als wesentlich günstiger, da sie bei Verbrennungsvorgängen wesentlich weniger Stickoxide bilden, im Gegensatz zu Nitroverbindungen, und dadurch eine bessere Umweltverträglichkeit versprechen. Ziel der Untersuchungen sind neuartige Nitramine, die als Komponenten für den Einsatz in TLP's Einsatz finden könnten. Hierbei ist besonders darauf Wert zu legen, dass diese neuartigen Verbindungen einen möglichst hohen Stickstoffgehalt mit gleichzeitig ausgewogenem Kohlenstoff-Sauerstoff Verhältnis besitzen und die Synthese solcher Verbindungen möglichst kurz, sicher und billig gestaltet werden kann, was in Hinsicht auf ein späteres „Up-scale"-Verfahren von besonderem Interesse ist.

Bekannt ist, dass Verbindungen mit **N**itrato**e**thyl**n**itr**a**minogruppen –$N(NO_2)$-CH_2CH_2-ONO_2, die sogenannten **NENA**s, als energieliefernde Weichmacher und Bestandteile von Sprengstoffen und Treibladungspulvern eingesetzt werden. Neben Diethanolnitramindinitrat **DINA** werden vor allem Methyl-, Ethyl- und Butyl-NENA eingesetzt, die eine energetische NENA-Gruppierung neben einem innerten Alkylrest enthalten. Diese sind allerdings in ihrem Energiegehalt aufgrund des Alkylrestes wesentlich reduziert. Wir erwarten nun eine Erhöhung der Leistung, bei hoffentlich vertretbarer Empfindlichkeit, durch die Kombination von NENA-Gruppierungen mit oben angeführten energiereichen Substituenten.

Die Herstellung von NENA-Verbindungen wird meist durch Umsetzung einer entsprechenden Hydroxyethylaminoverbindung mit Salpetersäure durchgeführt, wobei die entsprechenden -NH- bzw. -OH Gruppierungen nitriert werden (*Schema 1*). Auf diese Weise werden die bekannten Verbindungen DINA, Methyl-NENA, Ethyl-NENA und Butyl-NENA erhalten.

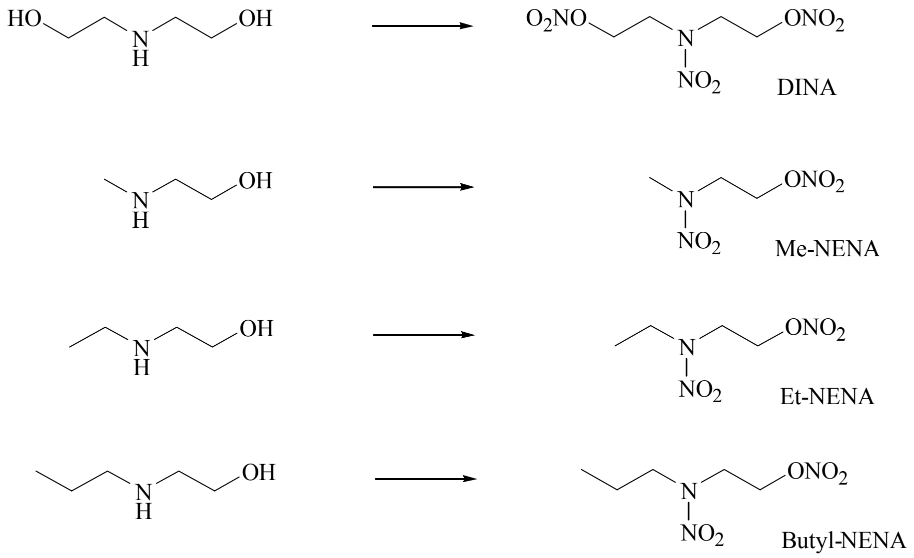

Schema 1

Kombinationen von NENAs mit Azidgruppen sind kaum untersucht oder nicht bekannt. Nach unserem Wissen gibt es gegenwärtig keine Verbindung, die neben einer NENA-Einheit eine Azidfunktion enthält. Beispiele (**1**,**2** und **3**) für denkbare Verbindungen sind in *Figur 1* aufgeführt.

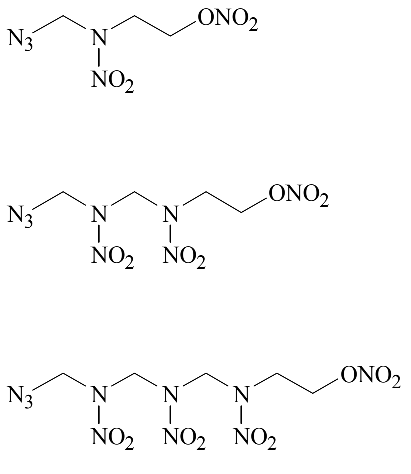

1 Ω = -31.1% N : 40.8%

2 Ω = -28.6% N : 40.0%

3 Ω = -27.1% N : 39.6%

Figur 1

Retrosynthetisch würde man die obigen Verbindungen aus den entsprechenden Chloriden **4** herstellen, welche man wiederrum aus den entsprechenden Acetoxymethylnitraminen **5** herhalten könnte (*Schema 2,* am Beispiel **1**). Allerdings ist bekannt, dass die Abbaureaktionen von solchen Acetoxymethylnitraminen in saurem Medium zu recht unterschiedlichen Produkten führen kann, was am folgenden Beispiel dargestellt werden soll (*Schema 2*).

Beispiel:

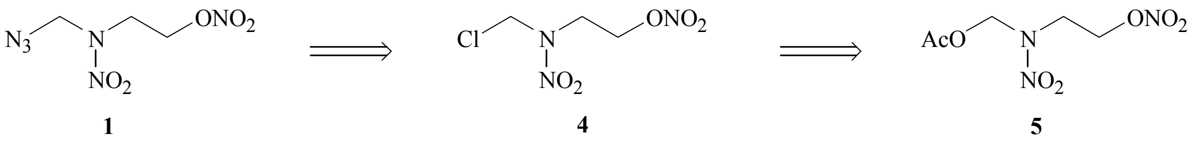

Schema 2

Die Nitrierung der Kondensationsprodukte (**9**, **10**) des Ethanolamins **7** mit Formaldehyd **8** führt je nach Reaktionsbedingungen zu unterschiedlichen Produkten. Dabei ist das Verhältnis der Reaktionsprodukte abhängig von der Abbaureaktion entsprechender Acetoxymethylen-nitramine im sauren Medium und führt unter stark sauren Bedingungen in der Regel zum Sechsring Hexogen **11** (Schema 3) oder bleibt auf der Stufe des 1-Acetoxy-4-nitrato-2-nitro-2-azabutans **12** oder 1-Acetoxy-8-nitrato-2,4,6-trinitro-2,4,6-triazaoctans **13** stehen.

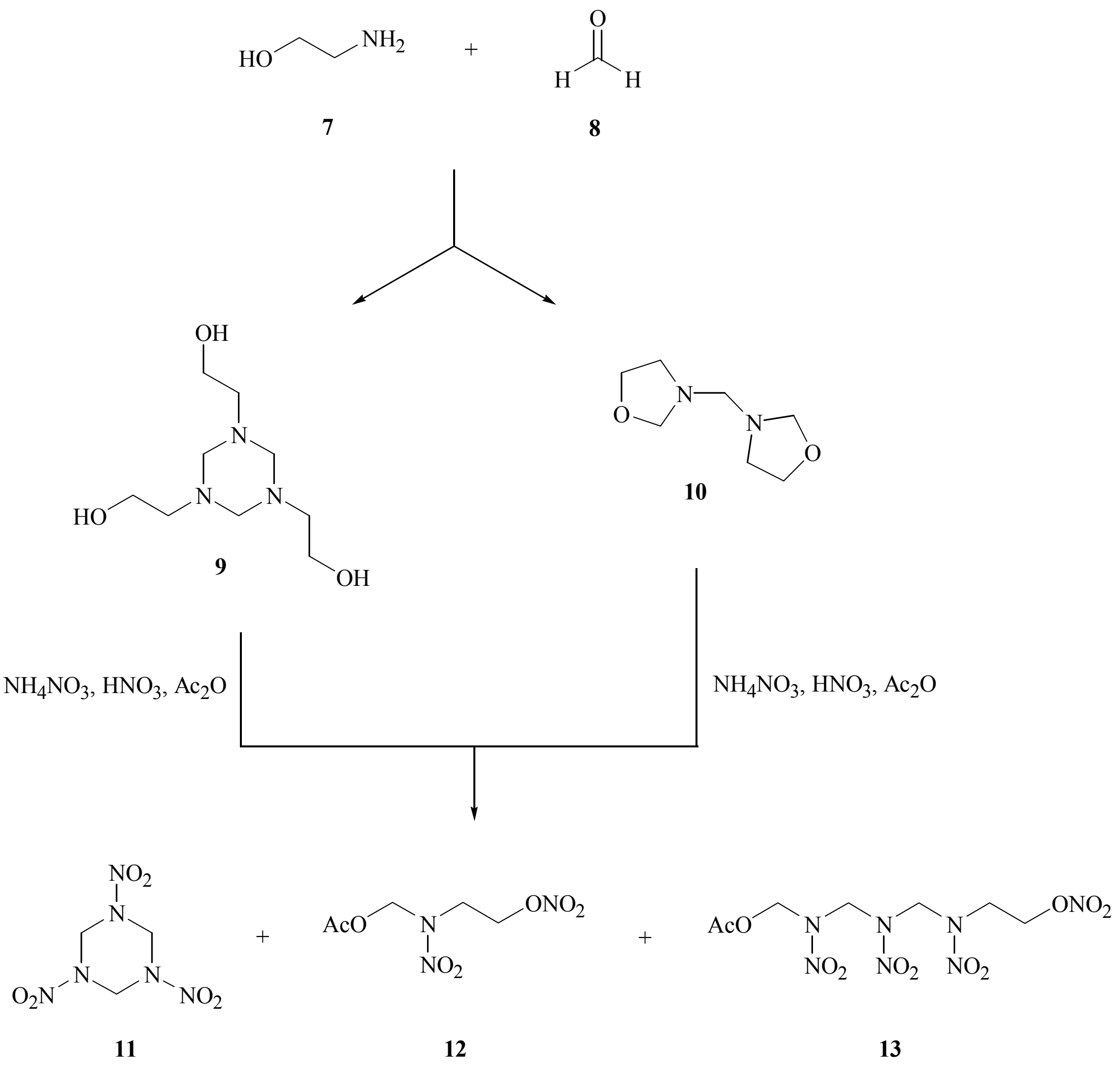

Schema 3

Verbindung **12** und **13** stellen geeignete Edukte für die Synthese von **1** und **3** dar. Es gibt einige Arbeiten, die sich mit dem Austausch einer Nitratogruppe gegen ein Chlor bzw. Bromatom in Gegenwart einer Acetoxymethylnitramingruppierung beschäftigen. Diese Reaktionen sind in der Regel nicht besonders selektiv und liefern die gewünschten Halogenverbindungen **14** oder **15** meist nur in schlechten Ausbeuten (< 35%). *Schema 4* zeigt eine solche Reaktion am Beispiel von **13**.

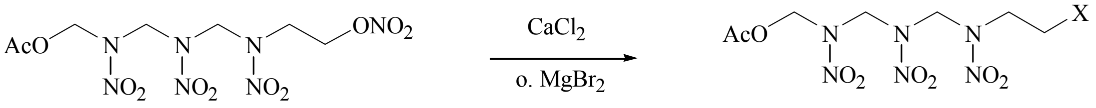

13

X = Cl (**14**), X = Br (**15**)

Schema 4

Untersuchungen bei der die Acetoxygruppierung einer Acetoxymethylnitramingruppierung gegen ein Halogenatom in Gegenwart von einer Nitratogruppe ausgetauscht werden kann, sind nicht bekannt (Schema 5).

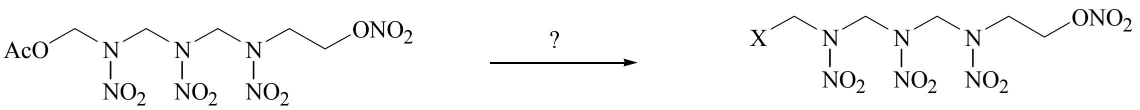

13

X = Cl (**16**), X = Br (**17**)

Schema 5

In diesem Zwischenbericht werden wir uns zunächst auf die Synthese von **3** und entsprechenden Modellverbindungen beschränken.

Synthese von 1-Azido-2,4,6-trinitro-2,4,6-triazaalkanen

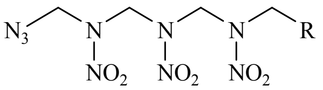

Die oben erwähnten Ergebnisse bezüglich der Kondensationsreaktion von Ethanolamin **7** und Formaldehyd **8**, stammen aus einer russischen Arbeit aus dem Jahre 1981 (Russ. J. Org. Chem. 1981, **17**, 623). Allerdings ließen sich die Ausbeuten bezüglich der dort vorgestellten Synthesen nur bedingt nachvollziehen, was dazu führte, eine andere jedoch ähnliche Synthese zu entwickeln. Bekannt ist, dass sich 1-methyl-3,5,7-triaza-1-azoniatricyclododecane nitrat **18** in HNO_3/Ac_2O zum entsprechenden 1-Methyl-2,4,6-trinitro-2,4,6-triazaheptan **21** umsetzen lässt (J. Denkstein, V. Kaderabek. Czech. 98,248, Jan. 15, 19661, Appl. Nov. 13, 1959). Die dabei erhaltenen Ausbeuten liegen in einem Bereich von mehr als 70%. In der Literatur ist kaum etwas beschrieben über andere alkylsubstituierte Hexametylentetramin Salze. Aus diesem Grund stellten wir die entsprechenden Urotropinium Salze des Ethyamins **19** sowie des Ethanolamins **20** erstmals her und untersuchten deren Verhalten gegenüber Nitrierungsreaktionen (*Schema 6*).

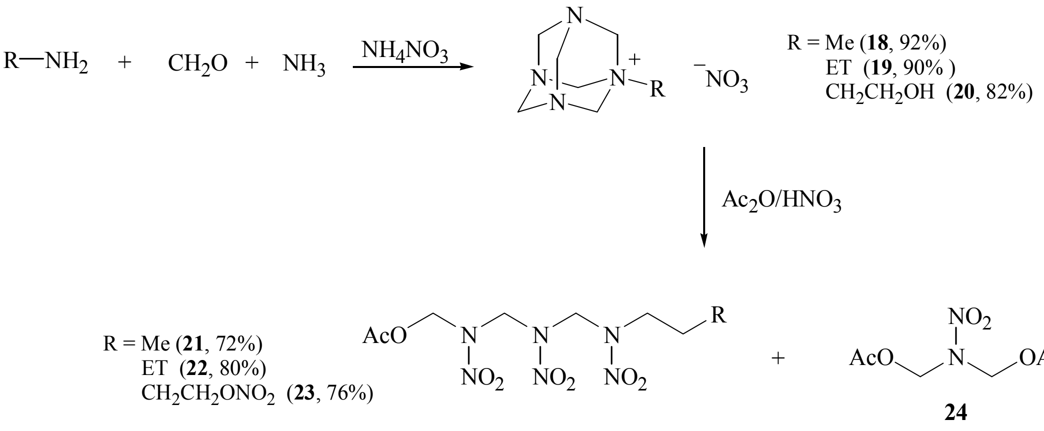

Schema 6

Die Kondensationsreaktion der entsprechenden Amine mit Formaldehyd und Ammoniumnitrat führte in allen Fällen zu den gut kristallisierbaren substituierten Urotropinium Nitraten **18**, **19** und **20** in guten bis sehr guten Ausbeuten. Sie bilden farblose, an Luft stabile, wenig hygroskopische Kristalle, die sich auch über längern Zeitraum nicht merklich zersetzen. Sie schmelzen allerdings unter Zersetzung. Die Nitrierung der Salze **18**, **19** und **20** führt in allen Fällen zu den entsprechenden 2,4,6-Trinitro-2,4,6-triazaalkanen **21**, **22** und **23** in guten Ausbeuten und dem 1,3-Diacetyl-2-nitro-2-azapropan **24** als

Nebenprodukt. **24** kann durch Extraktion mit DCM leicht abgetrennt und durch Destillation gereinigt werden und stellt ein sinnvolles Edukt für die Synthese entsprechender Mononitramine laut Leistungsbeschreibung dar. Das dem Ethanolamin zugrunde liegende Triazaalkan **23** wird als Nitratoderivat erhalten. Die Nitrierungsreaktionen verlaufen analog zur Darstellung von RDX und können deshalb in schon bestehende Prozesse direkt übernommen werden. Die Ausgangsmaterialien sind zudem großtechnische Produkte und billig. Bei den bekannten Prozessen wird das Hexamethylentetramin durch das entsprechende Nitrat ersetzt. Optimale Reaktionsbedingungen könnten sicherlich zu höheren Ausbeuten führen, liegen aber schon bei der hier zugrunde liegenden Arbeit zwischen 70 und 80% (**21**, 72%; **22**, 80%, **23**, 76%).

Aufgrund der hohen Reaktivität der Nitroaminomethylacetate **21**, **22** und **23** ist zu erwarten, dass sich die entsprechenden Verbindungen relativ leicht umestern (*Schema 7*, **I** z.B. mit 100% HNO_3 bei -40°C; wurde bisher noch nicht durchgeführt **25**, **26** u. **27**), oder in die entsprechenden Chloride **28**, **29** u. **30** überführen lassen sollten (*Schema 7,* **II**).

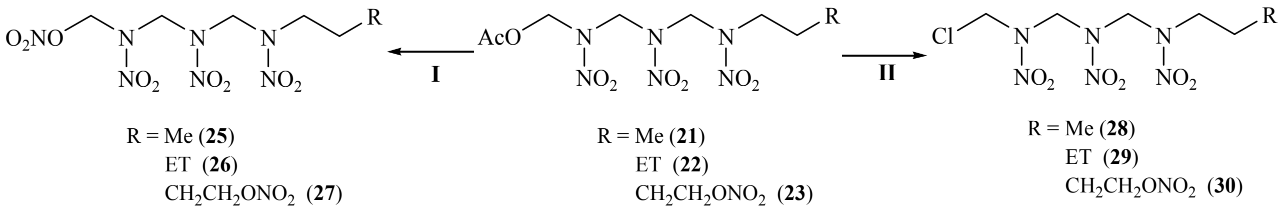

Schema 7

Die relative Reaktivität der säurekatalysierten Hydrolyse der Acetate **21**, **22** und **23** erklärt sich über die Stabilisierung des intermediär gebildeten Carbokations, entweder durch die p Orbitale des Aminostickstoffs oder eines Sauerstoff der Nitrogruppe (*Schema 8*).

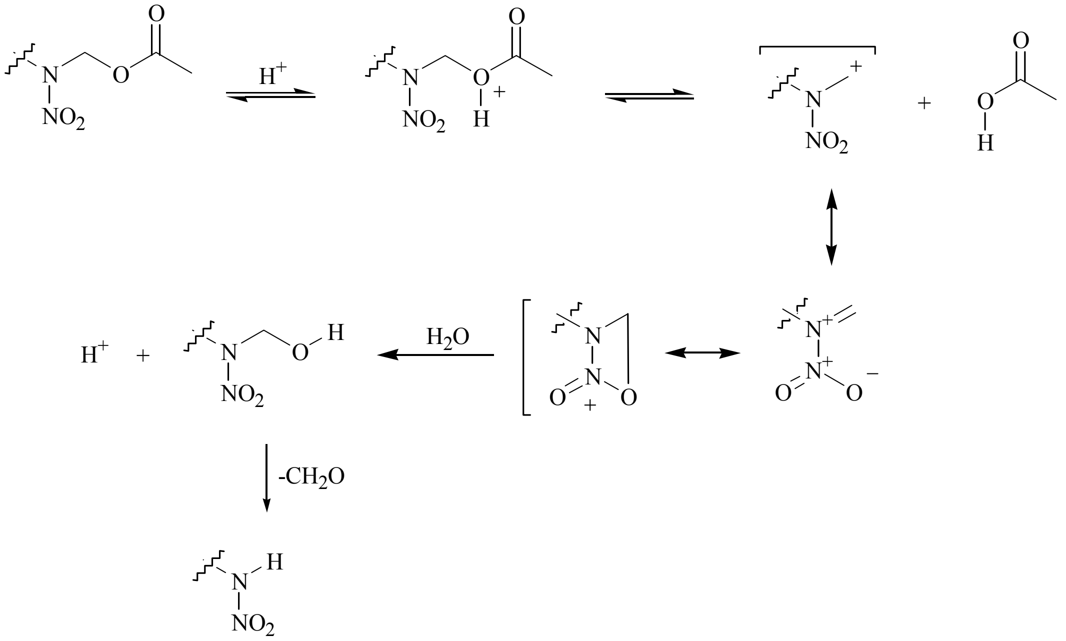

Schema 8

Diese Hydrolyseempfindlichkeit nimmt mit zunehmender stärker des elektronenziehende Charakters der Substituenten ab, d.h. die Stabilität der Acetate nimmt mit der Anzahl der Nitramideinheiten im Molekül zu und führt damit zu einer Verringerung der Mobilität der Acetylgruppe. Daraus folgt für spätere Syntheseplanungen, dass **12** wesentlich hydrolyseempfindlicher sein sollte als **13**.

Im Bezug auf die Transformierung der entsprechenden Nitroaminomethylacetate können verschieden Methoden angewendet werden. Im Falle der Methyl und Ethylverbindung erhält man die Chloride in sehr guten Ausbeuten durch Umsetzung der entsprechenden Acetat (**21**, **22**) durch Einleitung von trockenem HCl Gas in eine Suspension in wf. Dioxan. Die Reaktionszeit beträgt in der Regel ca. 6h und die Produkte können nach bekannten Methoden isoliert und gereinigt werden (*Schema 9*).

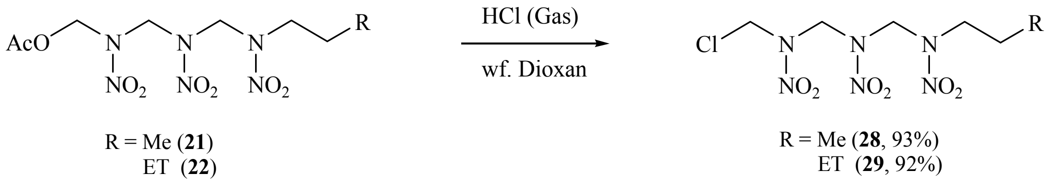

Schema 9

Im Falle des Nitrats **23** wurde diese Methode noch nicht getestet, da wir ebenfalls die Substitution der Nitratgruppe erwartet hatten. Allerdings gehen wir davon aus, dass durch

entsprechende Modifizierung auch hier mit der Isolierung des Monochlorproduktes **30** zu rechnen ist.

Die zweite Methode, die zur Substitution der Nitroaminomethylacetate **21**, **22** und **23** verwendet werden kann, ist die Umsetzung der Acetate in Trifluoressigsäure/conc. HCl (31%) (*Schema 10*).

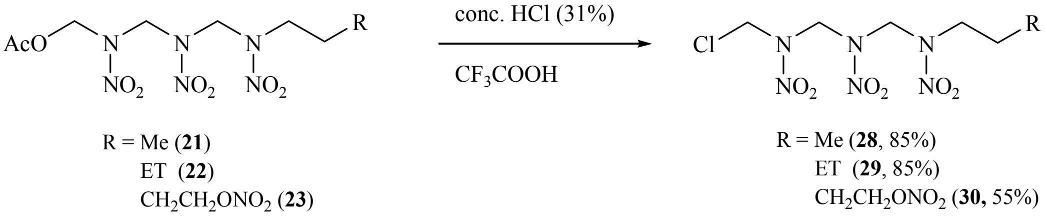

Schema 10

Der Vorteil dieser Reaktion liegt in den relativ kurzen Reaktionszeiten (in der Regel nach 2h beendet), der hohen Selektivität sowie der einfachen Aufarbeitung. Die Produkte fallen nach kurzer Zeit als feiner Niederschlag aus der Reaktionslösung aus und können durch einfache Saugfiltration abgetrennt werden. Waschen mit Wasser und Trocknung an Luft liefert schon sehr reine Produkte in moderaten bis guten Ausbeuten, die für weitere Umsetzungen eine ausreichende Reinheit aufweisen (**28**, 85%; **29**, 85%, **30**, 55%). Interessanterweise isoliert man im Falle von **23** tatsächlich das Monochlorierungsprodukt **30**, allerdings noch in moderater Ausbeute. Grund für die schlechtere Ausbeute im Vergleich zu **28** und **29** dürfte die wohl doch erhöhte Reaktivität der Nitratogruppe gegenüber der Reaktionsmischung sein, die zu den erwarteten Nebenreaktionen führt. Allerdings sollten kurze Reaktionszeiten und tiefe Temperaturen noch zu einer signifikanten Verbesserung der Ausbeuten führen. Entsprechende Modifikationen sind geplant und werden gegenwärtig Bearbeitet. Das entsprechende Dichlorprodukt **31** wurde bis jetzt noch nicht isoliert, allerdings bestehen auch hier starke Bemühungen, diese Produkt zu isolieren, da das entsprechende 1,8-Diazido-2,4,6-trinitro-2,4,6-nitrazaoctan **32** ebenfalls unbekannt ist (*Schema 11*).

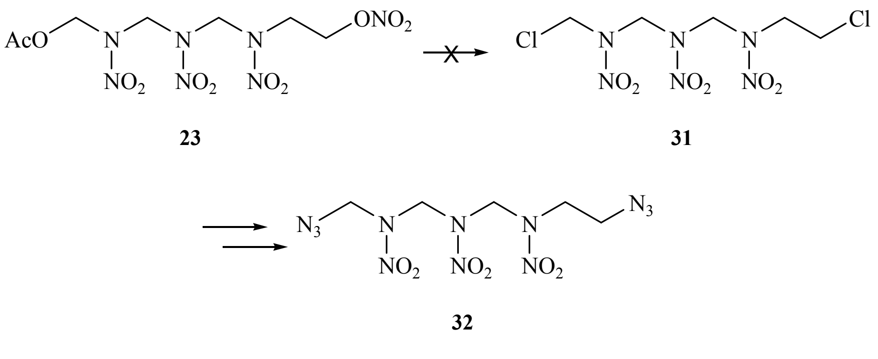

Schema 11

Die Überführung der so erhaltenen Chlorverbindungen in die Azide **33**, **34** und **35** erfolgt durch gewöhnliche Substitutionsreaktionen mit Natriumazid in Aceton/Wasser (*Schema 12*).

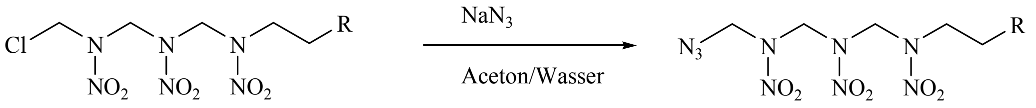

R = Me (**28**)
ET (**29**)
$CH_2CH_2ONO_2$ (**30**)

R = Me (**33**, 78%)
ET (**34**, 88%)
$CH_2CH_2ONO_2$ (**35**, 82%)

Schema 12

Dabei wird die entsprechende Chlorverbindung in Aceton gelöst und auf ca. 0°C gekühlt (Innenthermometer). Zu der Lösung wird eine wässrige Lösung von Natriumazid in der Art zugegeben, dass die Temperatur nicht über 10°C steigt. Das Aceton/Wasserverhältnis ist so zu wählen, dass nach Zugabe der gesamten Azidmenge (vorteilhaft ist die Zugabe von 1,5 eq) noch keine Fällung erfolgt. Der Ansatz wird danach für ca. 3h bei Raumtemperatur gerührt und dann mit der fünffachen Menge Wasser versetzt. Dabei scheiden sich die Produkte in der Regel erst ölig ab, erstarren dann aber nach ca. 10-15 min als feste weiße Masse. Die weiße Masse wird abgenutscht, mit Wasser gewaschen und nach Trocknung umkristallisiert. Die so erhaltenen Ausbeuten sind in der Regel höher als 75% (**33**, 78%; **34**, 88%, **35**, 82%).

Charakterisierung von 33, 34 und 35

Bei der Identifizierung der neuen Verbindungen waren neben der IR und Raman-Spektroskopie vor allem die NMR-Spektroskopie sowie die Massenspektroskopie dazu geeignet, bestimmte Strukturelemente eindeutig zu identifizieren.

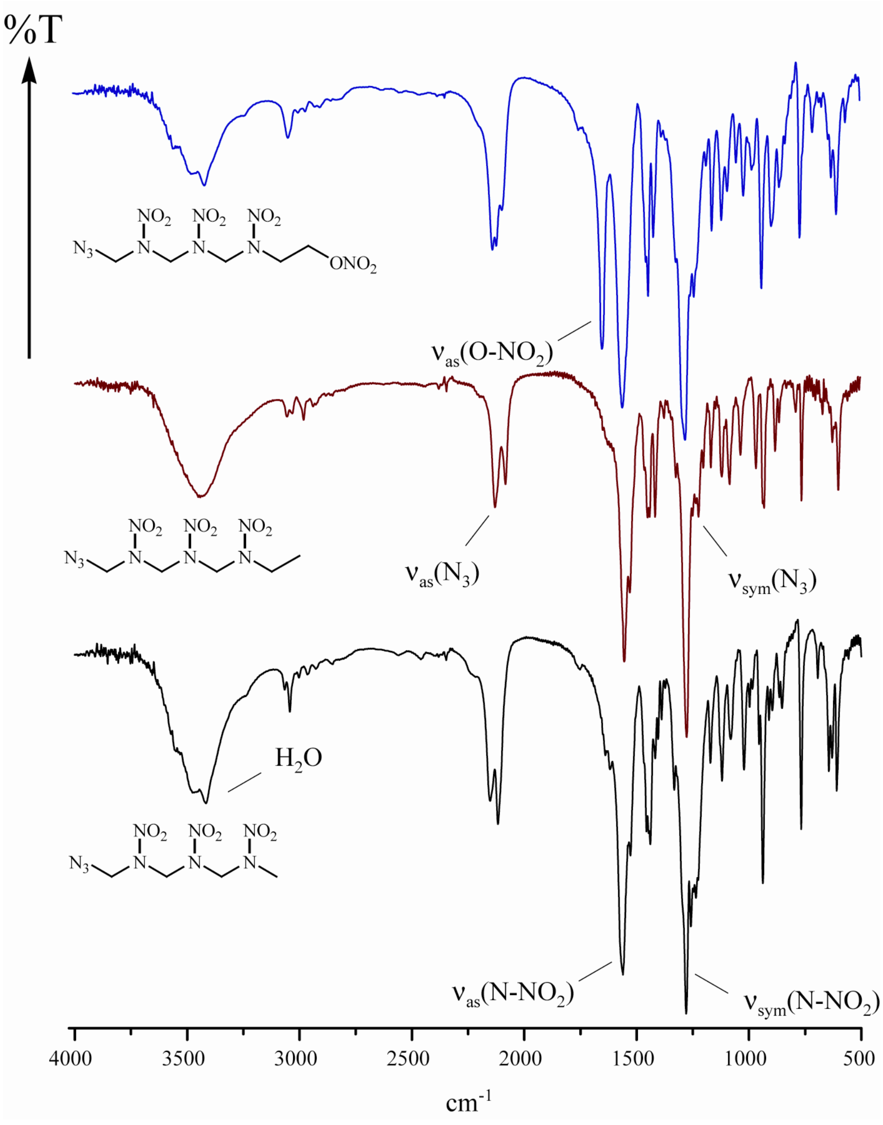

Abbildung 1. IR Spektren von **33**, **34** und **35**.

So zeigt der Vergleich der IR- und Raman-Spektren der Verbindungen **33**, **34** und **35** deutlich neben den Nitraminbanden (1555 cm^{-1} (ν_{as}), 1278 cm^{-1} (ν_{sym})) die Absorptionsbanden der Nitratogruppe in **35** (1645 cm^{-1} (ν_{as}), 1275 cm^{-1} (ν_{sym}), letztere überlagert sich mit der Niraminbande) sowie die in allen Verbindungen vorhandene Absorptionsbanden der Azidgruppe (2160-2120 cm^{-1} (ν_{as}), ~1300 cm^{-1} (ν_{sym})). Die weiteren Strukturelemente, wie CH_2, CH_3 Gruppen lassen sich dagegen nur schwer zuordnen, die Absorptionsbanden finden

sich allerdings in den zu erwartenden Bereichen (*Abbildung 1*, Die Proben waren aus Sicherheitsgründen nicht vollständig getrocknet).

Eindeutig lassen sich die Verbindungen mit Hilfe der Kernspinresonanz identifizieren. Aufgrund der unsymmetrischen Struktur erwartet man für Verbindung **33** vier und für Verbindungen **34** und **35** fünf charakteristische ^{1}H- sowie ^{13}C- Signale. *Tabelle 1* gibt eine Übersicht über die beobachten Signale und der Verschiebungen wieder.

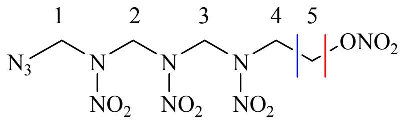

	1	2	3	4	5
33					
^{1}H	5.32 (s)	5.82 (s)	5.72 (s)	3.43 (s)	
^{13}C	65.9	66.4	67.1	40.4	
34					
^{1}H	5.33 (s)	5.82 (s)	5.75 (s)	3.86 (q)	1.20 (t)
^{13}C	65.9	66.38	66.42	48.3	12.3
35					
^{1}H	5.79 (s)	5.93 (s)	5.90 (s)	4.27 (t)	4.79 (t)
^{13}C	65.1	66.4	70.6	49.9	59.9

Tabell 1. ^{1}H- und ^{13}C-NMR-Daten von **33**, **34**, 35 in [d6]-DMSO; s = singulett, t = triplett, q = quartett

Alle Spektren wurden in [d6]-DMSO aufgenommen und die Zuordnung erfolget anhand entsprechender ^{1}H- bzw. ^{13}C-Inkrement-Systeme (auf aufwendige 2D Experimente zur exakten Zuordnung der einzelnen Verschiebungen wurde hier verzichtet). Von den Verbindungen wurden ebenfalls Protonen gekoppelte sowie entkoppelte ^{15}N Spektren aufgenommen (*Abbildung 2-4*). Dabei bezieht sich die ^{15}N-NMR-Skala auf reines Nitromethan als externen Standard ($\delta_N = 0$). Die chemische Verschiebung der beobachteten Resonanzen umfasst für die Verbindungen dabei einen Bereich von ca. 300 ppm. Für die Verbindungen **33** und **34** erwartet man 9 Resonanzen und im Falle von **35** 10.

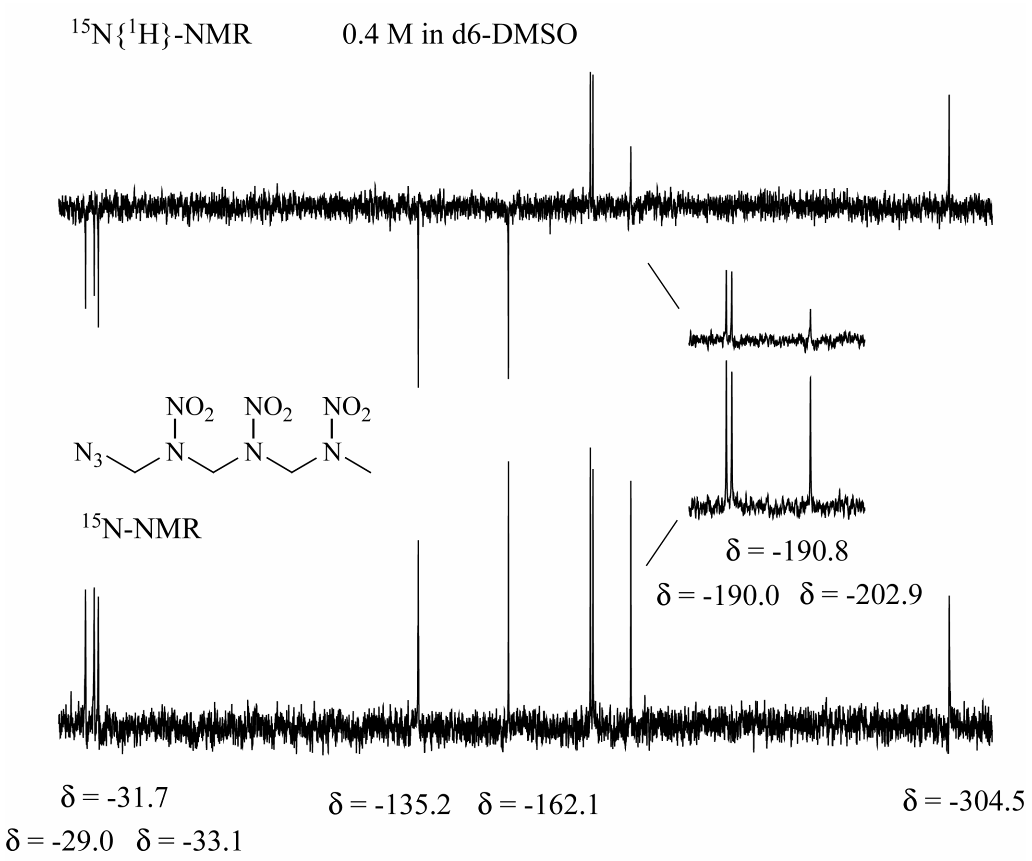

In gewisser Analogie zur ^{13}C-NMR-Spektroskopie liegen die Resonanzen der mit den elektronegativen substituierten N-Atome der Nitramineinheiten bei tieferem Feld zwischen -190 und -130 ppm. Die Nitrogruppen der Nitramineinheiten finden sich in einem engen Bereich um -32 ppm, wogegen die Nitratogruppe um ca. 10 ppm verschoben zu höherem Feld bei -42.5 ppm zu finden ist (**35**). Der Verschiebungsbereich der Azidgruppe (N_α = -304.5 ppm , N_β = -190.8 ppm, N_γ = ~ -200 ppm; Konnektivität : R-$N_\alpha N_\beta N_\gamma$) ist typische für kovalent gebundene Azide. Eine genaue Zuordnung der der einzelnen Nitramidgruppen bezüglich ihrer Position im Molekül wurde nicht getroffen. Mit Hilfe der NMR Spektren konnte die Struktur der einzelnen Nitraminen zweifelsfrei bestätigt werden.

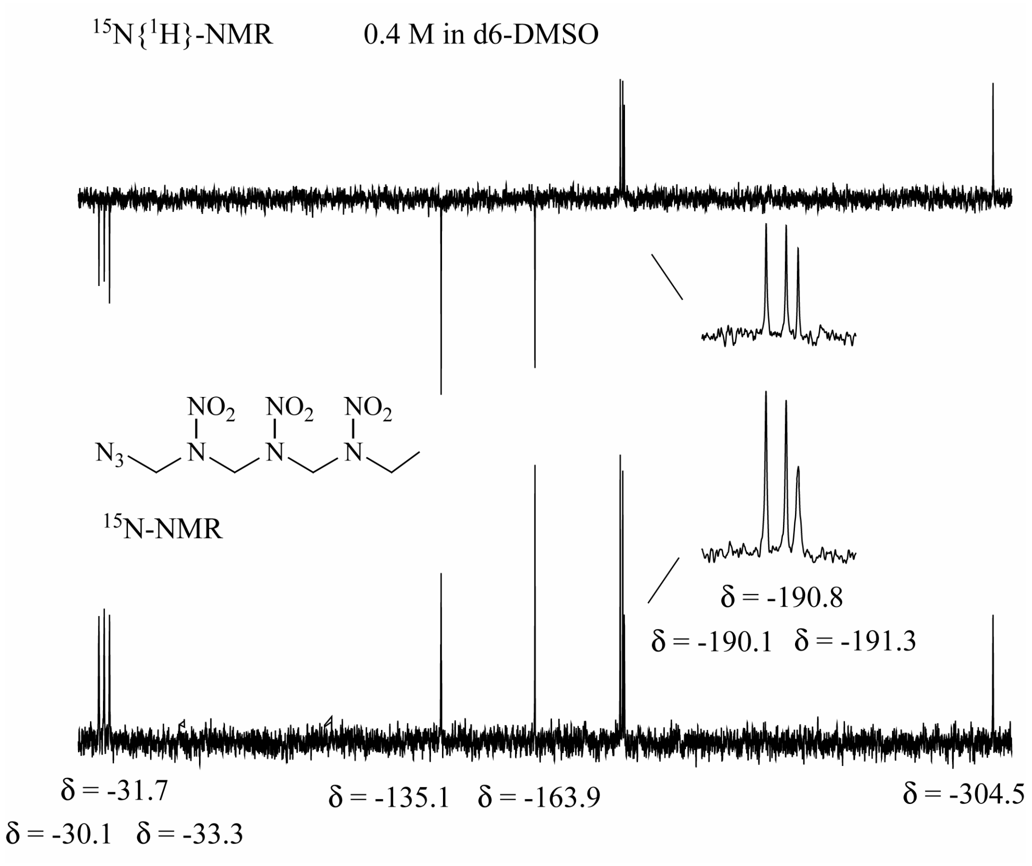

Abbildung 3

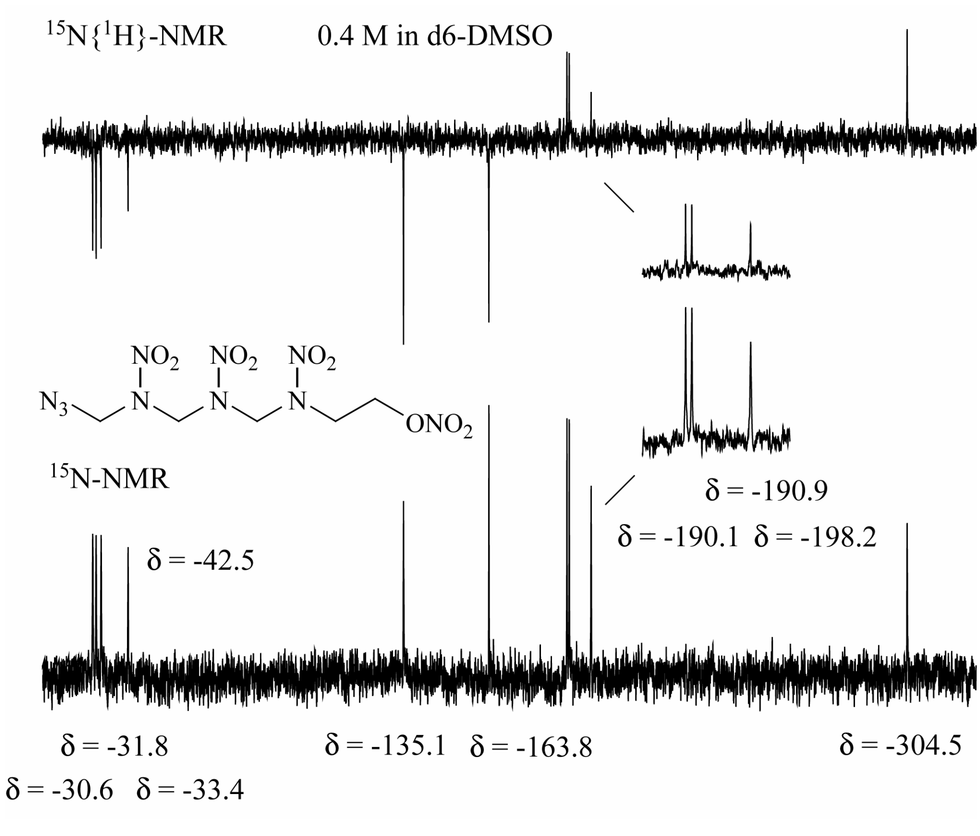

Abbildung 4

Massenspektroskopische Untersuchung von 33, 34 und 35.

Die erhaltenen Produkte wurden ebenfalls massenspektroskopisch mittels DEI und DCI untersucht. Im Falle der DCI Untersuchungen wurde als Stoßgas Ammoniak verwendet, was in allen drei Fällen zu der Beobachtung der $[M+NH_4]^+$ Ionen führte und damit zweifelsfrei als Bestätigung der entsprechenden Verbindungen angesehen werden kann (**33**, *m/z* 297; **34**, *m/z* 311; **35**, *m/z* 372). Die Elektronenstoß-Ionisation (EI) führte in allen drei Fällen nicht zur Beobachtung des Molekülpeaks, was mit der sehr leichten Fragmentierung der Verbindungen erklärt werden kann. In allen drei Fällen kommt es zu ähnlichen Fragmentierungen, die in *Abbildung 5* allgemein zusammengefasst wurden.

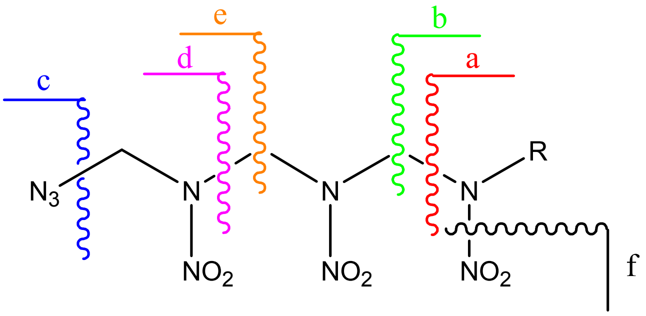

Abbildung 5. Fragmentierungsschema

In allen drei Fällen beobachtet man in den DEI Spektren von **33**, **34** und **35** vor allem die den Norrish-Typ-I-Reaktionen (α-Spaltung, a, c, d, f) entsprechenden Fragmentierungen, wobei die Spaltung bevorzugt an den Heteroatomen (hier Stickstoffen) erfolgt. Die Ladung wird dabei durch das Heteroatom stabilisiert. Die zu diesen Fragmentierungen beobachteten Massen sind in *Tabelle 2* aufgeführt.

	a (*m/z*)	b (*m/z*)	c (*m/z*)	d (*m/z*)	e (*m/z*)	f (*m/z*)
33	204 / 75	(190) / 89	237 / 42	163 / 116	(149) / 130	46
34	204 / 75[a]	(190) / 103	251 / 42	177 / (116)	(163) / 130	46
35	204 / 75	(190) / 164	312 / 42	238 / 116	(224) / 130	46 (groß)

Tabelle 2. Zahlen in Klammern, diese Massen werden entweder nicht oder nur mit sehr geringer Intensität beobachtet.
[a] Fragment m/z 89 wird nicht beobachtet, stabilisiert sich durch Abspaltung von CH_2.

Pfad b und e repräsentieren β-Spaltungen, wobei in den Massenspektren nur die entsprechend leichteren Fragmente gut beobachtet werden, d.h. die positive Ladung wird in diesen Fällen besser stabilisiert oder das schwerer Fragment hat nur eine geringe Stabilität und zerfällt augenblicklich zu leichtern Fragmenten. In allen Fällen beobachtet man die Massen mit *m/z* 46 und 43 was NO_2 (klein) und HN_3 zugeordnet werden kann. Der Zerfall von Nitramingruppen über die Bildung von N_2O wird in keinem Fall beobachtet, was darauf schließen lässt, dass Alkyl-substituierte Nitramine in der Gasphase nicht den postulierten Zerfallsweg über die Bildung von Distickstoffmonoxid eingehen können. Im Falle von **34** beobachtet man einen Peak bei *m/z* 57, der eventuell dem Methylazid zugeordnet werden kann, im Falle von **33** wir dieser Peak nicht und im Falle von **35** nur mit sehr schwacher Intensität beobachtet. Wie zu erwarten wird die α-Spaltung der Nitrogruppe im Nitrat **35** zum Hauptprozess (*m/z* 46 Peak mit höchster Intensität).

Kristallstruktur von 1-Azido-2,4,6-trinitro-2,4,6-triazaoctan 34

Bisher ist es uns nur im Falle des 1-Azido-2,4,6-trinitro-2,4,6-triazaoctan **34** gelungen dessen Identität auch durch ein Kristallstrukturanalyse zu belegen. Im Falle des Methylderivates **33** konnte auf Grund zu hoher Moazität der Kristalle keine Strukturlösung erfolgen. Im Falle des Nitratoderivates **35** haben wir bisher noch keine geeigneten Einkristalle züchten können.

1-Azido-2,4,6-trinitro-2,4,6-triazaoctan **34** kristallisiert in der triklinen Raumgruppe *P*-1 mit zwei Formeleinheiten in der Zelle. Aufgrund des ähnlichen Raumbedarfes der Azid- und Ethylgruppe kommt es im Kristall zu einer Fehlordnung dieser Gruppen. *Abbildung 6* zeigt den ORTEP Plot eines Moleküls ohne Berücksichtigung dieser Fehlordnung.

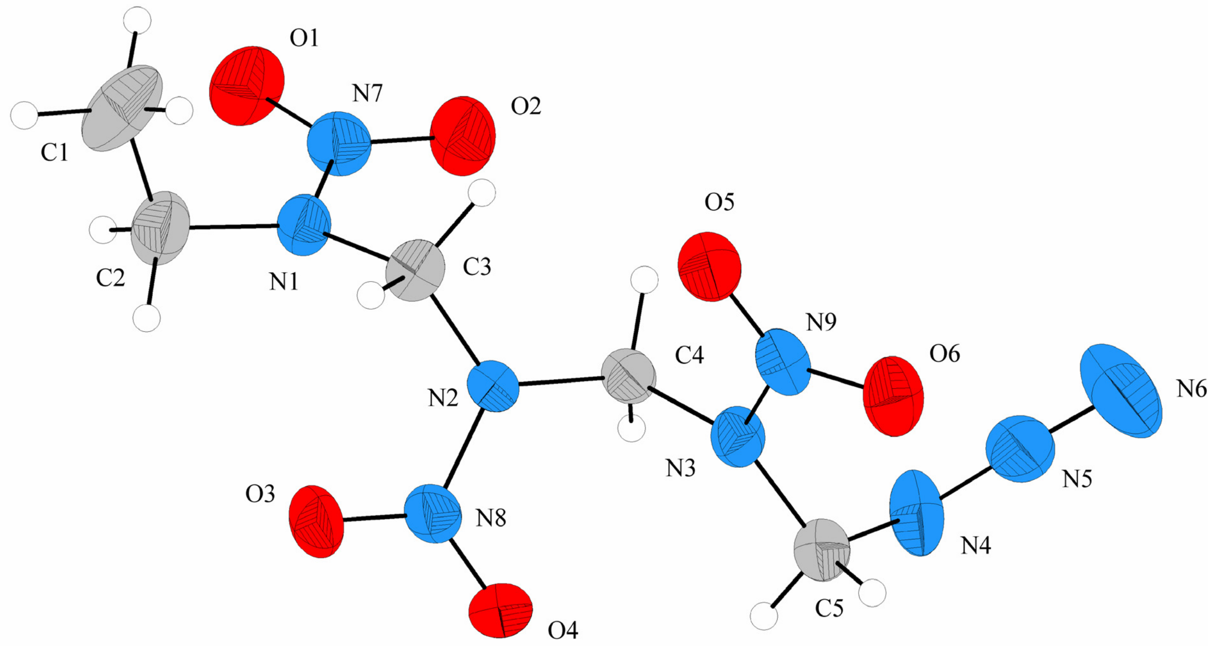

Abbildung 6. ORTEP plot of the molecular structure of compound **34** with thermal ellipsoid at 50% probability level and numbering scheme. Selceted bond length (Å) and angles (deg): O1-N7 1.230(2), O2-N7 1.229(3), O3-N8 1.226(2), O4-N8 1.225(3), O5-N9 1.231(3), O6-N9 1.231(2), N1-N7 1.348(3), N1-C2 1.449(3), N1-C3 1.450(3), N4-N5 1.215(4), N4-C5 1.460(4), N2-N8 1.366(3), N2-C3 1.445(3), N2-C4 1.443(3), N5-N6 1.129(4), N3-N9 1.362(3), N3-C4 1.456(3), N3-C5 1.444(3), C1-C2 1.527(7), N2-C3 1.445(3), N7-N1-C2 118.2(2), N7-N1-C3 116.6(2), C2-N1-C3 122.6(2), N5-N4-C5 118.2(3), N8-N2-C3 118.1(2), N8-N2-C4 117.3(2), C3-N2-C4 124.5(2), N4-N5-N6 170.8(3), O1-N7-O2 124.4(2), N9-N3-C4 117.1(2), N9-N3-C5 118.5(2), C4-N3-C5 122.3(2), O2-N7-N1 117.0(2), O1-N7 -O2 124.4(2), O1-N7-N1 118.5(2), O3-N8-N2 117.3(2), O3-N8-O4 125.7(2), O4-N8-N2 117.0(2), O5-N9-O6 124.8(2), O5-N9-N3 117.5(2), O6-N9-N3 117.7(2), N1-C2-C1 112.7(3), N1-C3-N2 114.6(2), N2-C4-N3 114.1(2), N4-C5-N3 114.3(2)

Die Abstände und Winkel sind für die dargestellte Graphik angegeben. Der andere Fall, bei dem die Ethylgruppe und die Azidgruppe den Platz tauschen, wird hier nicht besprochen, da es dabei zu keinen nennenswerten Änderungen in den Molekülparameter kommt. Die

gefunden Bindungsabstände sowie Winkel von **34** sind typisch für Nitraminen und Methylazidgruppen.

Alle drei Nitramine Fragmente sind planar, die Abweichung der Atome von der CNNOOC Ebene ist kleiner als ±0.03 Å. Die planare Konfiguration des Aminostickstoffes (sp^2-Hybridisierung) wird ebenfalls durch die Geometrie der Fragmente (Summe der Winkel um den Aminstickstoff liegt bei allen drei Nitramineinheiten bei ~360°) bewiesen und deutet auf die mögliche p-π* Orbital Überlappung zwischen den freien Elektronenpaaren des Aminostickstoffatoms und den unbesetzten Orbitalen der Nitrogruppe hin, was zu einer höheren Elektronendichte der Sauerstoffatome der Nitrogruppen führt. Diese erhöhte Elektronendichte führt zu einer stärkeren gegenseitigen Abstoßung der Nitrogruppen verschiedener Moleküle und einer Schwächung intermolecularer O···O Kontakte, was als Erklärung für die vergleichsweise geringe Dichte dieser Verbindung (ρ = 1.581 g cm^{-3}) herangezogen werden kann. Kurze intermolekular Wechselwirkung findet man zwischen $O4\cdots O4^{i}$ (2.867(3) Å; i: -x, -y, 1-z) sowie $O5\cdots O5^{ii}$ (2.940(3) Å; ii: 1-x, 1-y, 1-z), was die Anwesenheit, wenn auch nur schwacher dipolarer intermolekularer Wechselwirkungen bestätigt. Der kürzeste CH···O Abstand von 2.36(3) Å ($O2\cdots H21^{iii}$ 2.36(3) Å, H21–C2 0.94(4) Å, $O2\cdots C2^{iii}$ 3.166(4) Å, $O2–H21^{iii}–C2^{iii}$ 140.4(2) °; iii: 1+x, y, z) zeigt, dass es zwischen einzelnen Molekülen zu keinen merklichen Wasserstoffbrückenbindungen kommt, d.h. dass Wasserstoffbrückenbindungen nicht als strukturgebender Faktor in der Packung von **30** angesehen werden können. Die Azidgruppe trägt ebenfalls nicht, wie auch bei anderen Azidonitramiden, zu intermolekularen Wechselwirkungen bei.

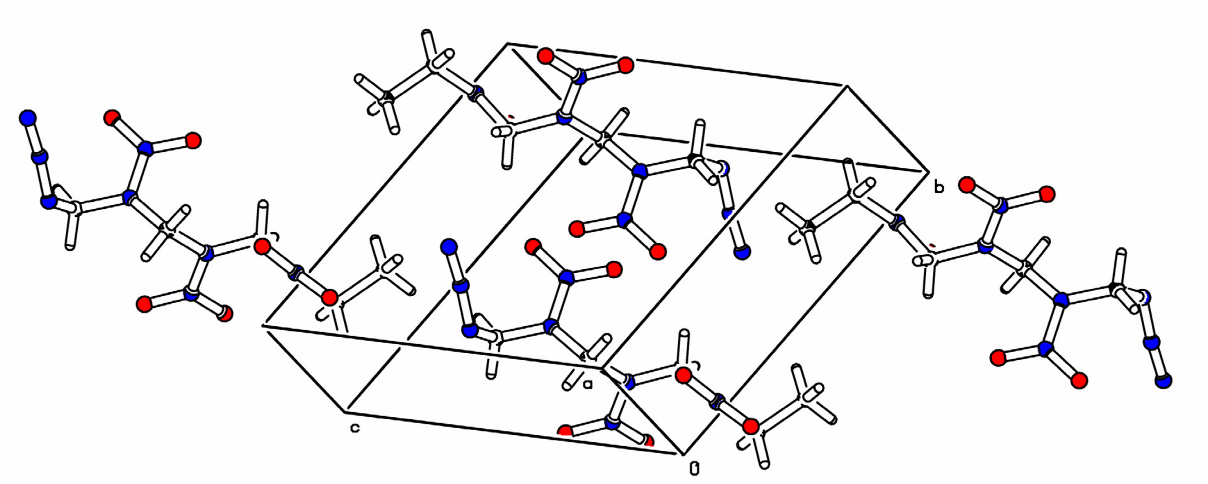

Abbildung 7. Darstellung der Packung in **34**.

Da die intermolekularen Wechselwirkungen hautsächlich auf die Nitrogruppen zurück zu führen sind, ist leicht zu verstehen, dass entlang der molekularen Achse dieser Verbindung es leicht zu Verschiebungen kommen kann, woraus ein höhere Platzbedarf resultiert. Kombiniert mit der dadurch verbundenen Fehlordnung im Bezug auf andere Moleküle, kommt es zu einer vergleichsweise geringen Dichte. Innerhalb der Moleküle liegen die Nitramineinheiten staggerd mit einem Winkel von ca. 120° um die Molekülachse angeordnet. Diese Anordnung minimiert ebenfalls die intermolekularen Wechselwirkungen. Wie man aus *Abbildung 7* ersehen kann liegen die Moleküle Seite an Seite gepackt im Molekül vor. Diese Anordnung führt zu einer parallelen Ausrichtung der Moleküle, die gestapelt zu einander liegen. Die Achsen dieser Ketten liegen dabei nahezu parallel zu der [001] Achse und sind aufgrund des vorhandenen Inversionszentrums alternierend zueinander angeordnet.

Thermisches Verhalten von **33**, **34** und **35**

Abbildungen 8 – 10 zeigen die DSC Thermogramme der Verbindungen **33**, **34** und **35**. Wie man deutlich aus den Graphiken entnehmen kann, besitzen alle drei Verbindungen einen endothermen Peak bei 102.5 – 104.3 °C (**33**, β = 2 °C/min), 121.5 – 122.8 °C (**34**, β = 2 °C/min) und 81.2 – 82.7 °C (**35**, β = 2 °C/min), was den Schmelzpunkt der entsprechenden Verbindungen repräsentiert. Alle drei Verbindungen zeigen einen starken exothermen Peak mit einem T_{max} von 199.5 (**33**), 197.3 (**34**) und 187.7 (**35**) °C.

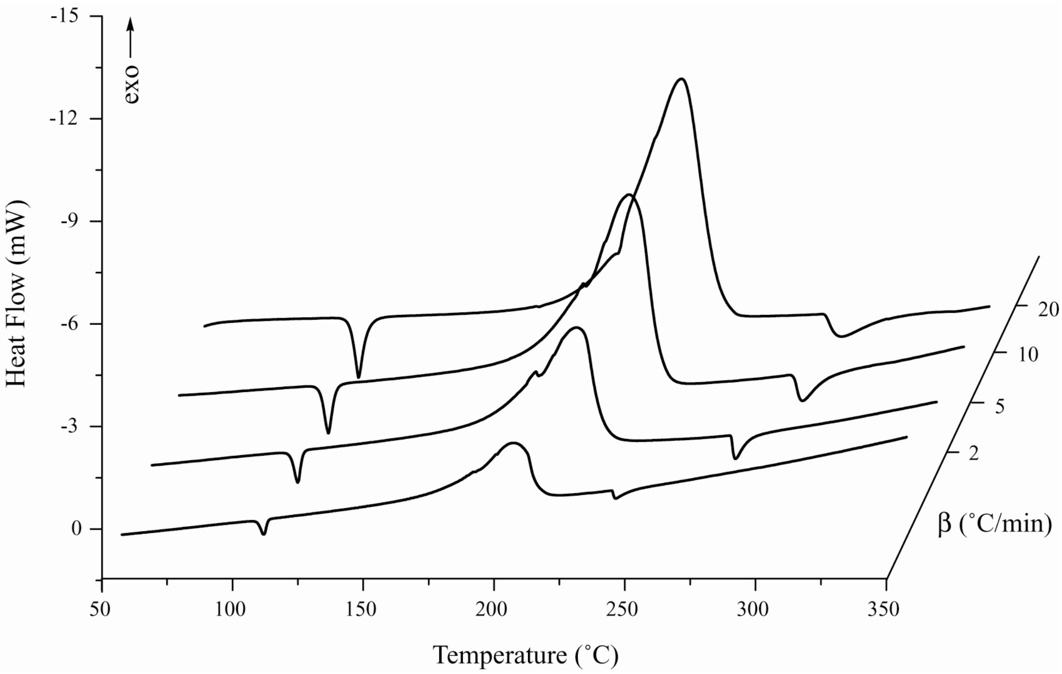

Abbildung 8. DSC Thermogramm von **33**.

Um den Prozess genauer zu verstehen, nach welchem Mechanismus diese Verbindungen zerfallen, haben wir mit Hilfe der Ozawa bzw. Kissinger Methode die Aktivierungsenergien abgeschätzt (*Tabelle 3*). Dabei stellt sich heraus, dass der Prozess der Zersetzung für alle

S. no.	β	T_p (°C)			E_a(Kcal/mol), Ozawa			E_a (Kcal/mol), Kissinger		
	(°C/min)	**33**	**34**	**35**	**33**	**34**	**35**	**33**	**34**	**35**
1	2	199.47	197.30	187.71	31.6	31.5	31.5	31.6	31.6	31.5
2	5	212.27	209.44	199.31						
3	10	222.24	218.86	208.50						
4	20	232.36	229.54	218.40						
5	40	242.61	240.16	229.02						

Table 3
Maximum exothermic responses of **33**, **34** and **35** as a function of scan speed

drei Verbindungen anscheinend nach dem gleichen Mechanismus abläuft. Für diese Verbindungen wurden Aktivierungsenergien (E_A) von ca. 31 kcal/mol bestimmt, wobei die Werte, bestimmt nach Ozawa ausgezeichnet mit den Werten nach Kissinger übereinstimmen.

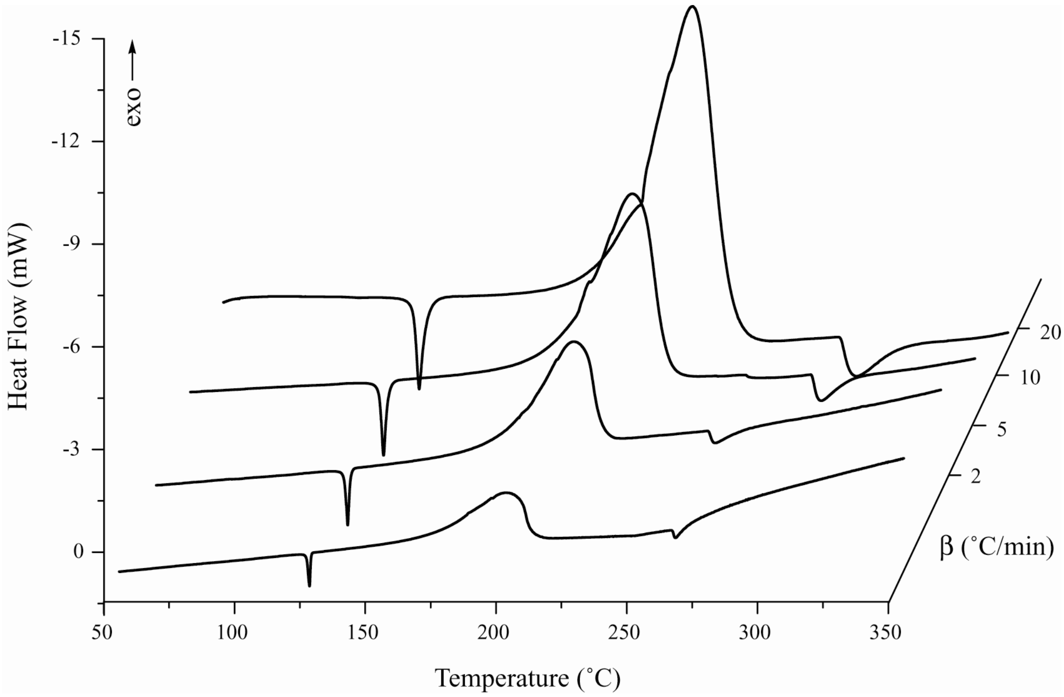

Abbildung 9. DSC Thermogramm von **34**.

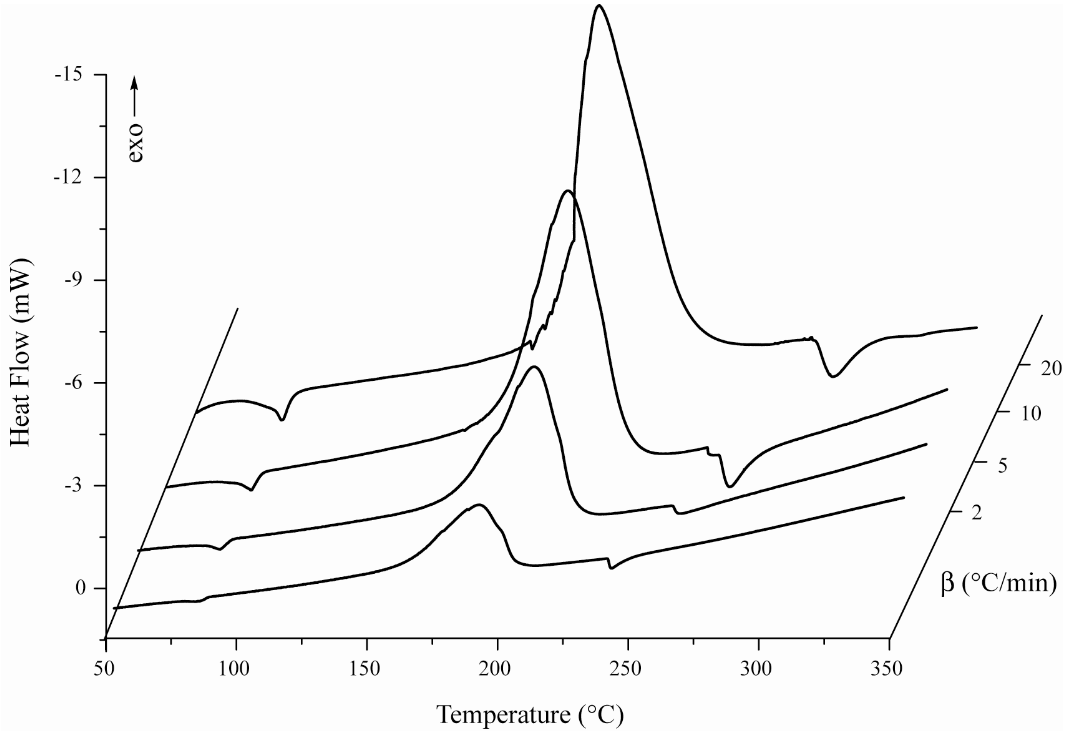

Abbildung 10. DSC Thermogramm von **35**.

Von Untersuchungen andere, vergleichbarer Nitramide ist bekannt, dass die Zersetzung wahrscheinlich initiiert wird durch den Bruch der N-NO_2 Einheit unter gleichzeitiger Freisetzung von NO_2. Dabei wird dieser Prozess unterstütz durch die Stickstoffabspaltung von der Azidgruppe (C-N_3 → CN + N_2) und der Zersetzung des verbleibenden Moleküls, mit der damit verbundenen Freisetzung von thermischer Energie. Diese Prozesse beschleunigen den Zersetzungsprozess, was durch die Beobachtung eines starken exothermen Peaks in der DSC belegt wird. Interessanterweise beobachtet man in den Massenspektren von **33** und **34** eine vergleichsweise geringe Neigung zu Spaltung der N-NO_2 Gruppe, was durch die relativ geringe Intensität des Massepeaks von *m/z* 46 beobachtet werden kann. Sicherlich spielen in der Massenspektroskopie andere Effekte eine tragende Rolle bezüglich der Fragmentierung, allerdings müssen auch thermische Reaktionen im Massenspektrometer in Betracht gezogen werden, da der Verdampfungsvorgang sowie Stoßreaktionen in der Gasphase eine Temperaturerhöhung und damit Energieerhöhung der Moleküle mit sich bringt, was unter anderem zu katalysierten thermische Zerfallsprozessen führen kann. Würde man von solchen Prozessen ausgehe, dann wäre der eigentliche Zersetzungsprozess in der Fragmentierung der Moleküle in kleinere Nitramineinheit, als primärer Prozess zu sehen. Zudem scheint es eigenartig zu sein, dass man im Falle der Nitratoverbindung **35** eine gleiche Aktivierungsenergie berechnet wird wie für **33** und **34**. Bekanntlich ist die N-O Bindung von Nitratoverbindungen leichter zu Spalten als die N-NO_2 Bindung in Nitramine. Da man nun für alle drei Verbindungen nahezu die gleiche Aktivierungsenergie berechnet, kann es sich bei dem primären Zersetzungsprozess nicht um die Spaltung der N-NO_2 Gruppe handeln.

Experimenteller Teil:

Preparation of 1-alkyl-3,5,7-triaza-1-azoniatricyclododecane nitrate **18**

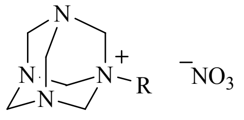

R = Me (**18**)
ET (**19**)
CH_2CH_2OH (**20**)

A 2.0 liter, three-neck round-bottom flask equipped with a reflux condenser, a mechanical stirrer, a thermometer, and a dropping funnel was charged with 100.0 g (1.25 moles) of ammonium nitrate (AN), and 1,25 moles of 50% aqueous solution of the corresponding amine (**18**: methylamine; **19**: ethylamine; **20**: 1-aminoethanole). To the above well-agitated mixture was slowly added 608.0 g (7.5 moles) of 37% aqueous formaldehyde, while maintaining the temperature between 45° and 50°C. After completion the addition and while continuing vigorous agitation, 175.0 g (3 moles) of 29% aqueous ammonia was introduced at such a rate as to maintain the temperature between 45° and 50°C. Stirring was continued for additional 2 hours while the temperature fell gradually to the ambient. The resulting water clear solution was concentrated until the precipitation of the salts (**18**: (92%); **19**: (90%); **20** (82%)). The so obtained salts are pure enough for further reaction. Further crops of product were obtained by evaporating of the mother liquor and crystallization.

Analytical data:

1-Methyl-3,5,7-triaza-1-azoniatricyclododecane nitrate **18**

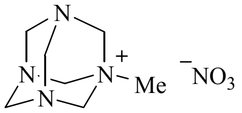

m.p. 185 °C (melts under decomp.); IR (KBr, cm^{-1}): $\tilde{\nu}$ = 3022 (vw), 2977 (vw), 2960 (w), (s), 2398 (vw), 1763 (vw), 1743 (vw), 1637 (w), 1618 (w), 1466 (m), 1384 (vs), 1354 (s, shoulder), 1264 (w), 1246 (s), 1148 (w), 1079 (vw), 1043 (s), 1015 (s), 995 (s), 958 (s), 817 (s), 787 (m), 649 (s), 501 (m); Raman (200mW, 25 °C, cm^{-1}): $\tilde{\nu}$ = 3024 (23), 2994 (67), 2964 (57), 2922 (26), 2867 (11), 1664 (3), 1469 (19), 1452 (16), 1369 (18), 1315 (11), 1266 (4), 1248 (5), 1149 (12), 1082 (5), 1041 (100), 1021 (9), 996 (6), 961 (28), 852 (4), 826 (16), 788 (16), 718 (53), 654 (13), 596 (17), 505 (21), 488(19), 451 (41), 407 (4), 290 (7); ^{1}H NMR (CD_3OD) δ: 2.55 (s, CH_3), 4.54 (d, 3H, ^{3}J = 12.5 Hz), 4.70 (d, 3H, ^{3}J = 12.5 Hz), 5.09 (s, 3xCH_2); ^{13}C NMR (CD_3OD, 25°C) δ: 41.8 (CH_3), 70.5 (CH_2), 80.5 (CH_2); ^{14}N NMR (CD_3OD, 25°C) δ: -4.2 (NO_3^-, $\Delta\nu_{1/2}$ = 72 Hz), -332.9 (N_{ring}, $\Delta\nu_{1/2}$ = 672 Hz), -351.3 (*N*-Me, $\Delta\nu_{1/2}$ = 82 Hz); *m/z* (FAB^+, xenon, 6keV, glycerin matrix) 155 $[C_6H_{12}N_4\text{-Me}]^+$; calcd. C, 38.70; H, 6.96; N, 32.24%; found: C, 38.56; H, 6.84; N, 32.25%.

1-Ethyl-3,5,7-triaza-1-azoniatricyclododecane nitrate **19**

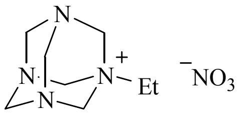

m.p. 132 °C (decomp.); IR (KBr, cm^{-1}): $\tilde{\nu}$ = 2997 (vw), 2964 (w), 2892 (vw), 2410 (vw), 1767 (vw), 1746 (vw), 1635 (vw), 1616 (vw), 1461 (m), 1384 (vs), 1370 (vs, shoulder), 1320 (s), 1293 (m), 1267 (s), 1226 (s), 1132 (s), 1116 (w), 1052 (m), 1041 (m), 1023 (s), 996 (vs), 902 (w), 858 (w), 827 (s), 781 (s), 705 (w), 651 (m), 578 (vw), 500 (m); Raman (200mW, 25 °C, cm^{-1}): $\tilde{\nu}$ = 3013 (38), 2997 (60), 2961 (72), 1663 (2), 1471 (12), 1446 (24), 1357 (22), 1321 (6), 1296 (7), 1270 (4), 1231 (4), 1153 (5), 1133 (14), 1117 (5), 1081 (4), 1042 (100), 1025 (10), 998 (19), 903 (12), 864 (4), 783 (16), 708 (56), 649 (7), 580 (21), 504 (23), 448 (29), 4123 (22), 337 (13), 207 (4); ^{1}H NMR (CD_3OD) δ: 1.29 (t, CH_3, ^{3}J = 7.4 Hz), 2.96 (q, CH_2, ^{3}J = 7.4 Hz), 4.58 (d, 3H, ^{3}J = 12.6 Hz), 4.70 (d, 3H, ^{3}J = 12.6 Hz), 5.13 (s, 3xCH_2); ^{13}C

NMR (CD_3OD, 25°C) δ: 4.5 (CH_3), 51.8 (CH_2), 70.8 (CH_2), 78.3 (CH_2); ^{14}N NMR (CD_3OD, 25°C) δ: -4.2 (NO_3^-, $\Delta\nu_{1/2}$ = 74 Hz), -339.9 (N_{ring}, $\Delta\nu_{1/2}$ = 722 Hz), -347.6 (*N*-Et, $\Delta\nu_{1/2}$ = 73 Hz); *m/z* (FAB^+, xenon, 6keV, NBA matrix) 169 $[C_6H_{12}N_4\text{-Et}]^+$; calcd. C, 41.55; H, 7.33; N, 30.31%; found: C, 41.42; H, 7.33; N, 30.31%.

1-(2-Hydroxyethyl)-3,5,7-triaza-1-azoniatricyclododecane nitrate **20**

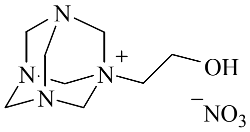

m.p. 133 °C (melts with decomp.); IR (KBr, cm^{-1}): $\tilde{\nu}$ = 3234 (s), 3010 (w), 2969 (w); 2938 (w), 2888 (w), 2396 (vw), 1763 (vw), 1753 (vw), 1636 (w), 1617 (w), 1475 (s), 1451 (w), 1384 (vs), 1357 (s, shoulder), 1295 (m), 1268 (s), 1225 (m), 1199 (m), 1128 (m), 1095 (w), 1073 (s), 1046 (m), 996 (s), 981 (s), 916 (m), 879 (w), 859 (w), 825 (s), 809 (s), 785 (m), 707 (w), 651 (s), 522 (w), 502 (m); Raman (200mW, 25 °C, cm^{-1}): $\tilde{\nu}$ = 3274 (2), 3016 (24), 2991 (44), 2965 (54), 1468 (19), 1452 (19), 1408 (7), 1387 (11), 1354 (17), 1331 (10), 1296 (11), 1256 (4), 1227 (6), 1208 (4), 1129 (15), 1086 (9), 1072 (9), 1047 (100), 1007 (9), 987 (12), 918 (24), 880 (7), 834 (12), 809 (12), 788 (19), 709 (69), 653 (11), 582 (23), 505 (31), 474 (14), 450 (27), 405 (7), 312 (10), 256 (6), 136 (5); ^1H NMR ([d6]-DMSO, 25°C) δ: 2.85 (t, CH_2, ^3J = 8 Hz), 3.79 (t, CH_2, ^3J = 8.0 Hz), 4.47 (d, 3H, ^3J = 12.7 Hz), 4.60 (d, 3H, ^3J = 12.7 Hz), 5.13 (s, $3xCH_2$), 5.38 (br, 1H); ^{13}C NMR ([d6]-DMSO, 25°C) δ: 53.7 (CH_2), 58.9 (CH_2), 70.5 (CH_2), 79.2 (CH_2); ^{14}N NMR ([d6]-DMSO, 25°C) δ: 1.5 (NO_3^-, $\Delta\nu_{1/2}$ = 85 Hz), -340.7 (*N*-CH_2CH_2OH, $\Delta\nu_{1/2}$ = 102 Hz); *m/z* (FAB^+, xenon, 6keV, NBA matrix) 185 $[C_6H_{12}N_4\text{-}CH_2CH_2OH]^+$; calcd. C, 38.86; H, 6.93; N, 28.32%; found: C, 38.62; H, 6.66; N, 28.38%.

1-Acetoxy-2,4,6-trinitro-2,4,6-triazaheptane **21**

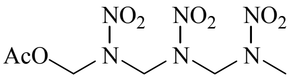

A mixture of 1-methyl-3,5,7-triaza-1-azoniatricyclododecane nitrate **19** (30 g, 138 mmol) and acetic acid (49 ml), was added within 30 minutes to a pale yellow solution of HNO_3 (52ml, 99%) and acetic anhydride (48 ml) below the temperature of 20°C. The temperature was raised under agitation to 75°C and kept there for 15 minutes. The product **21** precipitated out of solution by cooling to -5°C (23.8 g). The reaction mixture yields after dilution with water another crop of product (5.8 g) giving an all over yield of 72% calculated on **19**. m.p. 150-154 °C ; IR (KBr, cm^{-1}): $\tilde{\nu}$ = 3064 (vw), 3054 (vw), 3015 (vw), 3002 (vw), 2948 (vw), 1747 (s), 1660 (vw), 1567 (s), 1523 (m), 1545 (m), 1444 (s), 1417 (m), 1378 (w), 1282 (vs), 1253 (s), 1238 (m), 1222 (s), 1198 (m), 1137 (m), 1100 (w), 1049 (vw), 1027 (s), 1013 (m), 947 (w), 949 (m), 938 (s), 878 (w), 861 (w), 851 (vw), 826 (w), 767 (m), 720 (vw), 678 (w), 646 (m), 627 (w), 604 (w), 497 (vw), 471 (vw), 427 (vw); Raman (200mW, 25 °C, cm^{-1}): $\tilde{\nu}$ = 3066 (24), 3027 (34), 3001 (73), 2947 (59), 1751 (14), 1563 (14), 1527 (14), 1455 (31), 1418 (26), 1408 (26), 1379 (18), 1350 (25), 1333 (22), 1307 (69), 1274 (40), 1211 (10), 1196 (10), 1137 (8), 1102 (15), 1028 (16), 1013 (28), 970 (17), 950 (19), 878 (36), 864 (100), 853 (77), 830 (56), 775 (8), 724 (19), 681 (19), 644 (55), 605 (23), 487 (22), 450 (20), 428 (19), 361 (20), 258 (31), 246 (32), 141 (56); ^{1}H NMR ([d6]-DMSO, 25°C) δ: 2.05 (s, CH_3), 2.08 (s, CH_3), 5.73 (s, CH_2), 5.78 (s, CH_2), 5.87 (s, CH_2); ^{13}C NMR ([d6]-DMSO, 25°C) δ: 21.1 (CH_3), 31.2 (CH_3), 65.5 (CH_2), 66.9 (CH_2), 72.7 (CH_2), 170.8 (CO); ^{14}N NMR ([d6]-DMSO, 25°C) δ: -29.2 (NO_2, $\Delta\nu_{1/2}$ = 124 Hz), -33.1 (NO_2, $\Delta\nu_{1/2}$ = 173 Hz); *m/z* (DEI) 237 [M^+ - Acetyl (29)], 221 [M^+ - $MeNNO_2$ (4)], 163 (11), 148 (4), 147 (69), 117 (26), 116 (9), 90 (4), 89 (100), 73 (15), 59 (4), 45 (12), 43 (78), 42 (49), 30 (8), 28 (6), 15 (6); *m/z* (DCI, NH_3) 314 [M + NH_4^+ (19)], 163 (4), 147 (47), 117 (10), 116 (10), 106 (9), 94 (5), 90 (5), 89 (100), 73 (6), 60 (12), 59 (8), 47 (7), 46 (14), 43 (48), 42 (42), 41 (19).

1-Acetoxy-2,4,6-trinitro-2,4,6-triazaoctane **22**

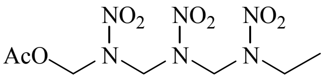

The preparation of this compound follows the same procedure as outlined for 1-acetoxy-2,4,6-trinitro-2,4,6-triazaheptane **21.** The product **22** also precipitated out of solution by cooling to -5°C. Yields range between 75 and 80%.

m.p. 115-117 °C ; IR (KBr, cm^{-1}): $\tilde{\nu}$ = 3051 (vw), 2997 (vw), 2987 (vw), 1748 (s), 1657 (vw), 1563 (vs), 1519 (m), 1447 (s), 1418 (m), 1384 (w), 1369 (w), 1281 (vs), 1256 (m), 1220 (s), 1186 (w), 1133 (w), 1103 (w), 1047 (w), 1025 (m), 994 (vw), 966 (w), 939 (m), 876 (vw), 865 (vw), 824 (vw), 788 (vw), 773 (w), 765 (m), 717 (vw), 672 (w), 645 (w), 620 (w), 599 (w), 497 (vw); Raman (200mW, 25 °C, cm^{-1}): $\tilde{\nu}$ = 3047 (39), 2997 (86), 2946 (72), 1752 (13), 1567 (14), 1529 (14), 1460 (41), 1414 (31), 1404 (26), 1384 (22), 1349 (26), 1335 (29), 1302 (76), 1272 (40), 1202 (8), 1136 (6), 1089 (17), 1053 (24), 1026 (16), 1011 (14), 968 (13), 941 (29), 868 (100), 827 (51), 776 (6), 720 (11), 676 (18), 643 (46), 617 (13), 602 (22), 498 (16), 469 (14), 406 (18), 345 (14), 231 (27), 139 (46); ^{1}H NMR ([d6]-DMSO, 25°C) δ: 1.20 (t, CH_3, ^{3}J = 8.0 Hz), 2.06 (s, CH_3), 3.87 (q, CH_2, ^{3}J = 8.0 Hz), 5.76 (s, CH_2), 5.79 (s, CH_3), 5.88 (s, CH_2); ^{13}C NMR ([d6]-DMSO, 25°C) δ: 12.3 (CH_3), 21.09 (CH_3), 48.4 (CH_2), 65.3 (CH_2), 65.6 (CH_2), 72.7 (CH_2), 170.7 (CO); ^{14}N NMR ([d6]-DMSO, 25°C) δ: -30.4 (NO_2, $\Delta\nu_{1/2}$ = 132 Hz), -32.9 (NO_2, $\Delta\nu_{1/2}$ = 124 Hz); *m/z* (DEI) 221 [M^+ - $EtNNO_2$ (5)], 177 (7), 148 (5), 147 (100), 130 (6), 117 (38), 103 (79), 73 (17), 57 (37), 56 (9), 46 (7), 43 (49), 42 (36), 30 (6), 29 (5), 28 (7); *m/z* (DCI, NH_3) 328 [M + NH_4^+ (23)], 177 (5), 147 (75), 130 (10), 120 (9), 118 (5), 117 (15), 103 (100), 84 (9), 82 (13), 73 (10), 60 (14), 58 (5), 57 (50), 56 (16), 47 (7), 46 (19), 43 (37), 42 (53); calcd. C, 27.10; H, 4.55; N, 29.09%; found: C, 26.43; H, 4.44; N, 27.32%.

1-Acetoxy-8-nitrato-2,4,6-trinitro-2,4,6-triazaoctane **23**

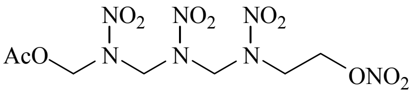

A mixture of 1-(2-hydroxyethyl)-3,5,7-triaza-1-azoniatricyclododecane nitrate **20** (34.12 g, 138 mmol) and acetic acid (49 ml), was added within 30 minutes to a pale yellow solution of HNO_3 (52ml, 99%) and acetic anhydride (48 ml) below the temperature of 20°C. The temperature was raised under agitation to 75°C and kept there for 15 minutes. Controlling of the temperature is important as reaction is exothermic and temperatures above 75°C have to be avoided (prepared ice bath). After cooling to ambient temperature the reaction mixture was quenched by pouring on ice and extracted with DCM. The collected DCM fractions were dried over $MgSO_4$ and all volatile components removed *in vacuo*. The product **20** precipitated after addition of Et_2O/EtOH to the oily residue as pale yellow powder (38.9 g, 76%). The ether solution contains 1,3-diacetoxy-2-nitro-2-azapropane **24**. m.p. 106.0-107.5 °C ; IR (KBr, cm^{-1}): $\tilde{\nu}$ = 3066 (vw), 3054 (vw), 3013 (vw), 1755 (s), 1633 (s), 1581 (s), 1531 (s), 1435 (m), 1412 (w), 1371 (w), 1280 (vs), 1244 (s), 1215 (s), 1199 (m), 1168 (m), 1121 (w), 1051 (vw), 1028 (m), 1008 (m), 987 (w), 974 (w), 929 (s), 890 (m), 857 (w), 846 (w), 830 (w), 768 (m), 711 (w), 643 (vw), 622 (w), 604 (w), 508 (vw); Raman (200mW, 25 °C, cm^{-1}): $\tilde{\nu}$ = 3067 (20), 3054 (25), 3017 (66), 2977 (36), 2941 (38), 1757 (18), 1625 (8), 1534 (18), 1457 (25), 1434 (26), 1407 (26), 1382 (36), 1361 (24), 1335 (18), 1305 (100), 1280 (28), 1267 (19), 1244 (15), 1220 (10), 1198 (8), 1170 (7), 1076 (10), 1052 (21), 1027 (16), 1011 (35), 989 (17), 929 (33), 888 (21), 859 (52), 847 (77), 832 (84), 772 (5), 713 (10), 672 (22), 658 (32), 645 (38), 622 (16), 605 (17), 562 (44), 495 (20), 464 (13), 436 (12), 396 (10), 362 (13), 295 (13), 247 (32), 194 (19), 131 (145); ^{1}H NMR ([d6]-DMSO, 25°C) δ: 2.07 (s, CH_3), 4.28 (t, CH_2, ^{2}J = 8.0 Hz), 4.79 (t, CH_2, ^{2}J = 8.0 Hz), 5.79 (s, 2xCH_2), 5.88 (s, CH_2); ^{13}C NMR ([d6]-DMSO, 25°C) δ: 21.1 (CH_3), 49.9 (CH_2), 65.5 (CH_2), 66.4 (CH_2), 70.6 (CH_2), 72.6 (CH_2), 170.8 (CO); ^{14}N NMR ([d6]-DMSO, 25°C) δ: -32.7 (NO_2/NO_3^-, $\Delta\nu_{1/2}$ = 278 Hz), -41.3 (NO_2, $\Delta\nu_{1/2}$ = 204 Hz); *m/z* (DEI) 238 [M^+ - $AcOCH_2NNO_2$ (2)], 221 [M^+ - $O_2NOCH_2NNO_2$ (4)], 164 (15), 147 (95), 117 (42), 116 (9), 89 (9), 85 (7), 83 (12), 73 (16), 60 (7), 46 (50), 45 (9), 44 (10), 43 (100), 42 (74), 30 (45), 29 (13), 28 (17); *m/z* (DCI, NH_3) 389 [M + NH_4^+ (19)], 191 (5), 190 (5), 164 (14), 148 (6), 147 (95), 119 (15), 117 (19), 89 (6), 87 (6), 73 (14), 72 (7), 60 (22), 47 (16), 46 (100) 45 (5), 44 (7), 43 (60), 42 (86), 41 (18); calcd. C, 22.65; H, 3.53; N, 26.41%; found: C, 22.69; H, 3.52; N, 26.52%.

1-Chloro-2,4,6-trinitro-2,4,6-triazaheptane **28**

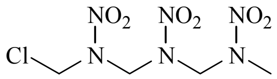

Method A:

To a mixture of trifluoroacetic acid (45,6 g, 0,4 mol) and conc. HCl (12 ml, 31%) was added in one portion 1-acetoxy-2,4,6-trinitro-2,4,6-triazaheptane **21** (6 g, 20 mmol). After stirring for a few minutes at room temperature the mixture became clear and shortly afterwards a heavy white precipitate was formed. Stirring was continued for another 2.5 hours at room temperature. The solid was collected by suction filtration, washed with distilled water, and dried *in vacuo*. Collected was 4,63 g (85 %) of **28**, recryst. from DCM/hexane.

Method B:

Hydrogen chloride was bubbled through a suspension of 1-acetoxy-2,4,6-trinitro-2,4,6-triazaheptane **21** (6 g, 20 mmol) in dioxane (30 ml) with stirring for 15-30 minutes. The reaction mixture was stirred at 0°C for 2 h and then at 20°C for 5 h. The solution was concentrated *in vacuo* and then water (60 ml) was added. The precipitated colorless solid was collected by suction filtration, washed with distilled water until acid free and dried *in vacuo*. Collected was 5,23 g (93 %) of **28**, recryst. from DCM/hexane.

m.p. 125-127 °C ; IR (KBr, cm^{-1}): $\tilde{\nu}$ = 3089 (vw), 3033 (vw), 2956 (vw), 2926 (vw), 1557 (s), 1570 (s), 1526 (s), 1457 (m), 1448 (m), 1413 (w), 1384 (vw), 1306 (m), 1281 (vs), 1257 (vs), 1220 (m), 1154 (w), 1108 (m), 1083 (w), 1022 (w), 946 (m), 915 (w), 765 (m), 670 (w), 650 (w), 621 (w), 602 (w); Raman (200mW, 25 °C, cm^{-1}): $\tilde{\nu}$ = 3089 (11), 3034 (28), 2996 (30), 2996 (45), 2955 (19), 2888 (7), 2766 (2), 1552 (9), 1450 (20), 1414 (19), 1386 (7), 1352 (17), 1313(36), 1283 (32), 1261 (15), 1157 (4), 1108 (15), 1085 (7), 1027 (11), 952 (16), 916 (19), 876 (18), 860 (100), 773 (5), 708 (13), 677 (63), 653 (28), 629 (41), 601 (17), 460 (16), 417 (18), 358 (14), 274 (14), 261 (16), 233 (21), 161 (36), 127 (22); ^{1}H NMR ([d6]-DMSO, 25°C) δ: 3.44 (s, CH_3), 5.75 (s, CH_2), 5.90 (s, CH_2), 5.93 (s, CH_2); ^{13}C NMR ([d6]-DMSO, 25°C) δ: 40.4 (CH_3), 59.9 (CH_2), 65.1 (CH_2), 67.0 (CH_2); ^{14}N NMR ([d6]-DMSO, 25°C) δ: -

29.0 (NO_2, $\Delta\nu_{1/2}$ = 126 Hz), -33.1 (NO_2, $\Delta\nu_{1/2}$ = 170 Hz), -35.2 (NO_2, $\Delta\nu_{1/2}$ = 152 Hz); *m/z* (DEI) 197 [M^+ - $MeNNO_2$ (22)], 163 (8), 125 (27), 123 (82), 116 (5), 89 (100), 46 (13), 43 (52), 42 (85), 30 (9), 28 (6); *m/z* (DCI, NH_3) 290 [M + NH_4^+ (13)], 143 (6), 125 (15), 123 (46), 116 (6), 106 (6), 98 (5), 94 (5), 89 (199), 78 (6), 59 (6), 46 (17), 45 (5), 43 (31), 42 (71); calcd. C, 17.62; H, 3.33; N, 30.83%; found: C, 17.93; H, 3.33; N, 30.61%.

1-Chloro-2,4,6-trinitro-2,4,6-triazaoctane **29**

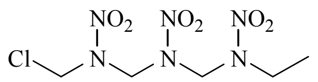

The preparation of this compound follows the same procedure as outlined for 1-chloro-2,4,6-trinitro-2,4,6-triazaheptane **28** according method 1 or 2**.** Yields range between 85 and 92%.

m.p. 109.0-112.2 °C ; IR (KBr, cm^{-1}): $\tilde{\nu}$ = 3085 (vw), 3032 (vw), 2982 (vw), 2939 (vw), 1559 (s), 1520 (s), 1442 (s), 1409 (m), 1382 (vw), 1275 (vs), 1249 (s), 1237 (m), 1205 (w), 1155 (w), 1106 (w), 1079 (m), 1041 (w), 971 (w), 938 (m), 913 (m), 871 (vw), 856 (vw), 790 (vw), 765 (m), 670 (w), 649 (w), 635 (vw), 619 (m), 597 (m), 476 (vw), 428 (vw); Raman (200mW, 25 °C, cm^{-1}): $\tilde{\nu}$ = 3020 (30), 2991 (53), 2940 (25), 2880 (10), 1557 (10), 1536 (19), 1452 (32), 1412 (20), 1391 (15), 1356 (30), 1336 (16), 1315 (43), 1271 (36), 1159 (6), 1105 (9), 1081 (29), 1044 (12), 934 (22), 919 (12), 859 (100), 831 (17), 791 (7), 770 (6), 702 (22), 673 (60), 650 (36), 637 (39), 619 (14), 596 (14), 476 (21), 433 (26), 380 (14), 357 (17), 258 (18), 219 (30), 162 (40), 135 (53); ^{1}H NMR ([d6]-DMSO, 25°C) δ: 1.20 (t, CH_3, ^3J = 8.0 Hz), 3.88 (q, CH_2, ^3J = 8.0 Hz), 5.78 (s, CH_2), 5.90 (s, CH_3), 5.94 (s, CH_2); ^{13}C NMR ([d6]-DMSO, 25°C) δ: 12.3 (CH_3), 48.3 (CH_2), 65.2 (CH_2), 66.3 (CH_2), 74.2 (CH_2); ^{14}N NMR ([d6]-DMSO, 25°C) δ: -30.3 (NO_2, $\Delta\nu_{1/2}$ = 127 Hz), -33.1 (NO_2, $\Delta\nu_{1/2}$ = 135 Hz); *m/z* (DEI) 197 [M^+ - $EtNNO_2$ (22)], 177 (5), 125 (33), 123 (100), 103 (67), 57 (39), 46 (10), 42 (75), 30 (6), 29 (6), 28 (8); *m/z* (DCI, NH_3) 304 [M + NH_4^+ (4)], 125 (19), 123 (60), 120 (5), 112 (9), 103 (93), 85 (15), 83 (23), 78 (6), 57 (49), 56 (15), 47 (6), 46 (26), 43 (100), 42 (5); calcd. C, 20.95; H, 3.87; N, 29.3%; found: C, 20.90; H, 3.86; N, 29.35%.

1-Chloro-8-nitrato-2,4,6-trinitro-2,4,6-triazaoctane **30**

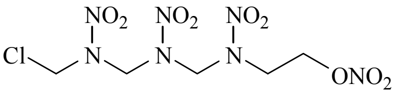

The preparation of this compound follows the same procedure as outlined for 1-chloro-2,4,6-trinitro-2,4,6-triazaheptane **28** according method 1**.** Yields range between 45 and 55%.

m.p. 85.9-88.6 °C ; IR (KBr, cm^{-1}): $\tilde{\nu}$ = 3074 (w), 3033 (w), 2952 (vw), 1643 (s), 1563 (s), 1554 (s), 1461 (m), 1440 (s), 1412 (m), 1387 (vw), 1363 (vw), 1275 (vs), 1236 (m), 1182 (w), 1144 (m), 1103 (m), 1071 (m), 1048 (m), 1016 (m), 980 (w), 938 (s), 910 (s), 895 (m), 853 (w), 766 (m), 714 (vw), 700 (vw), 672 (w), 646 (w), 630 (vw), 607 (m), 566 (w), 495 (vw), 474 (vw), 457 (vw), 426 (vw); Raman (200mW, 25 °C, cm^{-1}): $\tilde{\nu}$ = 3073 (11), 3033 (25), 3012 (33), 2991 (54), 2904 (6), 1561 (14), 1527 (9), 1462 (20), 1444 (22), 1410 (19), 1389 (18), 1349 (23), 1313 (48), 1280 (38), 1146 (7), 1103 (10), 1072 (13), 1052 (16), 1017 (8), 982 (9), 939 (18), 909 (20), 858 (100), 770 (7), 701 (18), 673 (50), 650 (42), 632 (27), 567 (29), 496 (29), 457 (15), 405 (20), 362 (18), 303 (12), 241 (22), 198 (22), 163 (43), 142 (44); ^{1}H NMR ([d6]-DMSO, 25°C) δ: 4.27 (t, CH_2, ^{3}J = 8.2 Hz), 4.79 (t, CH_2, ^{3}J = 8.2 Hz), 5.79 (s, CH_2), 5.90 (s, CH_3), 5.93 (s, CH_2); ^{13}C NMR ([d6]-DMSO, 25°C) δ: 49,9 (CH_2), 59.9 (CH_2), 65.1 (CH_2), 66.4 (CH_2), 70.6 (CH_2); ^{14}N NMR ([d6]-DMSO, 25°C) δ: -31.2 (NO_2, $\Delta\nu_{1/2}$ = 282 Hz), -41.2 (-ONO_2, $\Delta\nu_{1/2}$ = 143 Hz); *m/z* (DEI) 271 [M^+ - $ClCH_2$ (2)], 238 (5), 199 (6), 197 (47), 164 (33), 147 (7), 125 (40), 123 (100), 117 (5), 76 (7), 46 (62), 44 (12), 43 (8), 42 (99), 41 (8), 30 (24), 29 (11); calcd. C, 17.28; H, 2.90; N, 28.20%; found: C, 17.61; H, 2.96; N, 27.40%.

1-Azido-2,4,6-trinitro-2,4,6-triazaheptane **33**

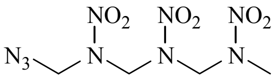

1-Chloro-2,4,6-trinitro-2,4,6-triazaheptane **28** (2.726 g, 10 mmol) was dissolved in 30 ml acetone under nitrogen and cooled. A solution of sodium azide (1.035 g, 16 mmol) water (5 ml) was added at such a rate that the temperature did not exceed 10°C. After 4 hours the clear solution was diluted with water (50 ml) and the precipitated solid collected by suction filtration, washed with distilled water, and dried *in vacuo*. Recryst from acetone/diethyl ether yielded **33** as colorless plates (2.17 g, 78%).

m.p. 102.5-104.3 °C ; IR (KBr, cm^{-1}): $\tilde{\nu}$ = 3060 (vw), 3042 (w), 2997 (vw), 2956 (vw), 2151 (m), 2116 (m), 1638 (w), 1615 (m), 1559 (vs), 1526 (s), 1455 (m), 1438 (m), 1416 (w), 1403 (w), 1388 (w), 1331 (m), 1278 (vs), 1257 (s), 1235 (s), 1170 (m), 1119 (m), 1080 (w), 1021 (m), 996 (m), 984 (w), 954 (w), 937 /s), 910 (w), 895 (w), 864 (w), 852 (w), 766 (s), 693 (vw), 643 (m), 629 (m), 608 (m), 480 (vw), 436 (vw); Raman (200mW, 25 °C, cm^{-1}): $\tilde{\nu}$ = 3066 (12), 3031 (29), 3044 (34), 300 (45), 2965 (36), 2136 (4), 2109 (9), 1532 (15), 1455 (29), 1417 (16), 1404 (24), 1389 (33), 1360 (22), 1301 (41), 1235 (35), 1174 (6), 1128 (6), 1085 (12), 943 (15), 913 (17), 895 (18), 858 (100), 704 (8), 657 (22), 644 (30), 610 (9), 481 (13), 459 (12), 416 (9), 358 (16), 263 (18), 246 (26), 218 (44); ^{1}H NMR ([d6]-DMSO, 25°C) δ: 3.43 (s, CH_3), 5.32 (s, CH_2), 5.72 (s, CH_2), 5.81 (s, CH_2); ^{13}C NMR ([d6]-DMSO, 25°C) δ: 40.4 (CH_3), 65.9 (CH_2), 66.4 (CH_2), 67.1 (CH_2); ^{14}N NMR ([d6]-DMSO, 25°C) δ: -28.7 (NO_2, $\Delta\nu_{1/2}$ = 99 Hz), -31.5 (NO_2, $\Delta\nu_{1/2}$ = 156 Hz), -134.2 (N_β, $\Delta\nu_{1/2}$ = 280 Hz), -167.1 (N_γ, $\Delta\nu_{1/2}$ = 1240 Hz); *m/z* (DEI) 237 [M^+ - N_3 (3)], 204, [M^+ - $MeNNO_2$ (3)], 163 [M^+ - $N_3CH_2NNO_2$ (27)], 147 (4), 130 (8), 116 (4), 89 (100), 75 (21), 59 (4), 46 (23), 43 (46), 42 (36), 30 (16), 29 (5), 28 (27), 27 (5), 18 (27), 17 (6), 15 (5); *m/z* (DCI, NH_3) 297 [M + NH_4^+ (2)], 237 (3), 204 (2), 163 (4), 147 (5), 130 (3), 106 (10), 89 (100), 75 (10); calcd. C, 17.21; H, 3.325; N, 45.16%; found: C, 17.38; H, 3.25; N, 45.13%.

1-Azido-2,4,6-trinitro-2,4,6-triazaoctane **34**

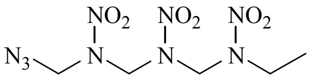

The preparation of this compound follows the same procedure as outlined for 1-azido-2,4,6-trinitro-2,4,6-triazaheptane **33.** Recryst. from MeOH/diethyl ether yields **34** as colorless plates (88%).

m.p. 121.5-122.8 °C ; IR (KBr, cm^{-1}): $\tilde{\nu}$ = 3055 (vw), 3031 (vw), 2981 (vw), 2939 (vw), 2130 (m), 2083 (m), 1555 (vs), 1530 (s), 1451 (m), 1417 (m), 1378 (vw), 1325 (w), 1277 (vs), 1249 (m), 1224 (m), 1203 (w), 1169 (w), 1121 (w), 1086 (m), 1038 (w), 968 (w), 932 (m), 883 (w), 866 (vw), 792 (vw), 766z (m), 629 (vw), 602 (m); Raman (200mW, 25 °C, cm^{-1}): $\tilde{\nu}$ = 3055 (14), 3037 (29), 2995 (52), 2943 (23), 2883 (10), 2133 (3), 2084 (3), 1561 (10), 1536 (12), 1516 (7), 1454 (28), 1418 (17), 1395 (19), 1380 (16), 1355 (24), 1331 (18), 1300 (18), 1281 (24), 1246 (14), 1223 (17), 1084 (25), 1041 (12), 973 (9), 934 (9), 884 (28), 854 (100), 837 (15), 679 (7), 645 (22), 616 (8), 474 (16), 445 (12), 429 (9), 383 (12), 257 (19), 238 (35), 192 (29), 167 (29), 137 (20); ^{1}H NMR ([d6]-DMSO, 25°C) δ: 1.20 (t, CH_3, ^{3}J = 8.0 Hz), 3.86 (q, CH_2, ^{3}J = 8.0 Hz), 5.33 (s, CH_2), 5.75 (s, CH_3), 5.82 (s, CH_2); ^{13}C NMR ([d6]-DMSO, 25°C) δ: 12.3 (CH_3), 48.4 (CH_2), 65.9 (CH_2), 66.38 (CH_2), 66.42 (CH_2); ^{14}N NMR ([d6]-DMSO, 25°C) δ: -26.3 (NO_2, $\Delta\nu_{1/2}$ = 245 Hz), -130.4 (N_β, $\Delta\nu_{1/2}$ = 284 Hz), -162.4 (N_γ, $\Delta\nu_{1/2}$ = 1293 Hz); *m/z* (DEI) 251 [M^+ - N_3 (2)], 204, [M^+ - $EtNNO_2$ (7)], 177 [M^+ - $N_3CH_2NNO_2$ (23)], 130 (19), 103 (100), 75 (45), 57 (53), 56 (11), 45 (27), 43 (5), 42 (48), 30 (18), 29 (11), 28 (34), 27 (5), 18 (12), 17 (3), 15 (3); *m/z* (DCI, NH_3) 311 [M + NH_4^+ (2)], 247 (4), 204 (4), 177 (9), 130 (7), 120 (11), 108 (10), 103 (100), 75 (10), 57 (45), 46 (41), 42 (52); calcd. C, 20.48; H, 3.78; N, 43.00%; found: C, 20.48; H, 3.62; N, 43.21%.

1-Azido-8-nitrato-2,4,6-trinitro-2,4,6-triazaoctane **35**

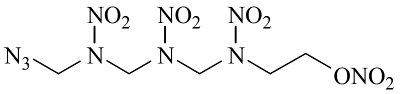

The preparation of this compound follows the same procedure as outlined for 1-azido-2,4,6-trinitro-2,4,6-triazaheptane **33.** Recryst. from MeOH/diethyl ether yields **35** as colorless plates (82%).

m.p. 81.2 – 82.7 °C ; IR (KBr, cm^{-1}): $\tilde{\nu}$ = 3074 (w), 3033 (w), 2952 (vw), 1643 (s), 1563 (s), 1554 (s), 1461 (m), 1440 (s), 1412 (m), 1387 (vw), 1363 (vw), 1275 (vs), 1236 (m), 1182 (w), 1144 (m), 1103 (m), 1071 (m), 1048 (m), 1016 (m), 980 (w), 938 (s), 910 (s), 895 (m), 853 (w), 766 (m), 714 (vw), 700 (vw), 672 (w), 646 (w), 630 (vw), 607 (m), 566 (w), 495 (vw), 474 (vw), 457 (vw), 426 (vw); Raman (200mW, 25 °C, cm^{-1}): $\tilde{\nu}$ = 3073 (11), 3033 (25), 3012 (33), 2991 (54), 2904 (6), 1561 (14), 1527 (9), 1462 (20), 1444 (22), 1410 (19), 1389 (18), 1349 (23), 1313 (48), 1280 (38), 1146 (7), 1103 (10), 1072 (13), 1052 (16), 1017 (8), 982 (9), 939 (18), 909 (20), 858 (100), 770 (7), 701 (18), 673 (50), 650 (42), 632 (27), 567 (29), 496 (29), 457 (15), 405 (20), 362 (18), 303 (12), 241 (22), 198 (22), 163 (43), 142 (44); ^{1}H NMR ([d6]-DMSO, 25°C) δ: 4.27 (t, CH_2, ^{3}J = 8.2 Hz), 4.79 (t, CH_2, ^{3}J = 8.2 Hz), 5.79 (s, CH_2), 5.90 (s, CH_3), 5.93 (s, CH_2); ^{13}C NMR ([d6]-DMSO, 25°C) δ: 49,9 (CH_2), 59.9 (CH_2), 65.1 (CH_2), 66.4 (CH_2), 70.6 (CH_2); ^{14}N NMR ([d6]-DMSO, 25°C) δ: -31.2 (NO_2, $\Delta\nu_{1/2}$ = 282 Hz); *m/z* (DEI) 312 [M^+ - N_3 (3)], 278 (2), 238 (30), 204 (17), 164 (74), 147 (11), 130 (24), 120 (6), 119 (9), 117 (6), 102 (4), 89 (3), 88 (6), 87 (3), 75 (61), 73 (8), 71 (5), 60 (3), 58 (3), 56 (6), 55 (3), 46 (100), 44 (29), 43 (12), 42 (93), 30 (51), 29 (30), 28 (44), 27 (4), 15 (4); *m/z* (DCI, NH_3) 372 [M + NH_4^+ (3)], 181 (5), 169 (3), 164 (16), 147 (4), 130 (4), 119 (18), 117 (4), 116 (3), 89 (4), 88 (3), 87 (4), 75 (12), 74 (7), 73 (8), 72 (10), 71 (6), 70 (4), 59 (3), 57 (4), 56 (3), 55 (3), 47 (15), 46 (100), 45 (8), 44 (9), 43 (15), 42 (76), 41 (19), 39 (4), 35 (19), 33 (41), 32 (24), 31 (28), 30 (84), 29 (16) 28 (13); calcd. C, 16.95; H, 2.85; N, 39.55%; found: C, 17.57; H, 2.85; N, 39.00%.

4. References

[1] Köhler, J.; Meyer, R., 'Explosivstoffe', Wiley-VCH, D-Weinheim, D, 9. Auflage, 1998.

[2] Engineering Design Hand Book: *Properties of Explosives of Military Interest, Army Material Command, AMC Pamphlet AMCP 706-117*, January 1971.

[3] Deal, W. E. *J. Chem. Phys.* **1957** , *27(1)*, 796.

[4] Mader, C. L. Report LA-2900, *Los Alomos Scientific Laboratory, Fortran BKW Code for computing the detonation properties of explosives*, Los Alamos, NM, July 1963.

[5] a) Hammerl, A.; Holl, G.; Kaiser, M.; Klapötke, T. M.; Mayer, P.; Nöth, H.; Piotrowski, H.; Suter, M. *Z. Naturforsch.* **2001**, *56 b*, 857; b) Hammerl, A.; Holl, G.; Klapötke, T. M.; Mayer, P.; Noth, H.; Piotrowski, H.; Warchhold, M. *Eur. J. Inorg. Chem.* **2002**, *4*, 834; c) Geith, J; Klapötke, T. M.; Weigand, J.; Holl, G. *Prop. Explos. Pyrotech.* **2004**, *29(1)*, 3; Klapötke, T. M.; Mayer, P. ; Schulz, A.; Weigand, J. J. *Prop. Explos. Pyrotech.* **2004**, *29(5)*, 325.

[6] a) Klapötke, T. M.; Mayer, P. ; Schulz, A.; Weigand, J. J. *J. Am. Chem. Soc.* **2005**, *127,* 2032; b) Gálvez-Ruiz, J. C.; Holl, G.; Karaghiosoff, K.; Klapötke, T. M.; Löhnwitz, K.; Mayer, P.; Nöth, H.; Polborn, K.; Rohbogner, C. J.; Suter, M.; Weigand, J. J. *Inorg. Chem.* **2005**, in press; c) Fischer, G.; Holl, G.; K.; Klapötke, Weigand, J. J. *Thermochim. Acta* **2005**, *in press*.

[7] a) Willer, R. L. *Synthesis of High-Nitrogen Content Heterocyclic Nitramines and Energetic Internal Plasticizers, Technical Report*, ADA182898, Morton Thiokol, Elkton, **1987**; b) Brill, T. B. *Proc. NATO-ASI on Chemistry and Physics of the Molecular Processes in Energetic Materials*, Bulusu, S. N. (eds.) Kluwer Academic Publisher, Dordrecht, Netherlands **1989**, 277.

[8] Gao, A.; Rheingold, A. L.; Brill, T. B. *Prop. Explos. Pyrotech.* **2004**, *29(1)*, 3

[9] Katritzky, A. R; Rogovoy, B. V.; Kovalenko, K. V. *J. Org. Chem.* **2003**, *68*, 4941 and references cited therein.

[10] a) Willer, R. L.; Henry, R. A. *J. Org. Chem.* **1988**, *53*, 5371; b) Butler, R. N.; Scott, F. L. *J. Org. Chem.* **1966**, 3182.

[11] a) Loeppky, R. N.; Outram, J. R. *N-Nitroso Compounds: Occurrence and Biological Effects* **1982**, IARC Scientific Publisher, Lion; b) Wang, P. G.; Xian, M.; Tang, X.; Wu, X.; Wen, Z.; Cai, T.; Janczuk, J. *Chem. Rev.* **2002**, *102*, 1091.

[12] a) Butler, R. N.; Lambe, T. L.; Tobin, J. C.; Scott, F. L.; *J. Chem. Soc., Perkin Trans. 1* **1973**, 1357; Catton, R.; Butler, R. N. *Can. J. Chem.* **1974**, *52*, 1248.

[13] Ford, R. E.; Knowles, P.; Lunt, E.; Marshall, S. M.; Penrose, A. J.; Ramsden, C. A.; Summers, A. J. H.; Walker, J. L.; Wright, D. E. *J. Med. Chem*. **1986**, *29*, 538.

[14] a) Peet, N. P. *J. Heterocycl. Chem.* **1987**, *24*, 223; b) Kato, T.; Chiba, T.; Daneshtalab, M. *Chem. Pharm. Bull.* **1976**, *24*, 2549.

[15] Andrus, A.; Partridge, B.; Heck, J. V.; Christensen, B. G. Tetrahedron Lett. **1984**, *25*, 911.

[16] Butler, R. N.; Scott, F. L. *J. Org. Chem.* **1966**, *31*, 3182.

[17] a) Klich, M.; Teutsch, G. *Tetrahedron* **1986**, *42*, 2677; b) Barlin, G. B. *J. Chem. Soc. B* **1967**, 641.

[18] a) Percival, D. F.; Herbst, R. M. *J. Org. Chem.* **1957**, *22*, 925; b) Ding, Y.-X.; Weber, W. P. *Synthesis* **1987**, 823.

[19] a) Moderhack, D.; Goos, K.-H.; Preu, L. *Chem. Ber.* **1990**, *123*, 1575; b) Garbrecht, W. L.; Herbst, R. M. *J. Org. Chem.* **1953**, *18*, 1014; c) Herbst, R. M.; Roberts, C. W.; Harvill, E. J. *J. Org. Chem.* **1951**, *16*, 139; d) Marchalin, M.; Martvon, A. *Collect. Czech. Chem. Commun.* **1980**, *45*, 2329.

[20] Ried, W.; Erle, H.-E. *Liebigs Ann. Chem.* **1982**, 201.

[21] a) Finnegan, W. G.; Henry, R. A.; Lieber, E. *J. Org. Chem.* **1953**, *18*, 779; b) Jensen, K. A.; Holm, A.; Rachlin, S. *Acta Chem. Scand.* **1966**, *20*, 2795.

[22] Garrison, J. A.; Herbst, R. M. J. Org. Chem. **1956**, *21*, 988.

[23] Willer, R. L.; Henry, R. A. *J. Org. Chem.* **1988**, *53*, 5371.

[24] Shustov, G. V.; Rauk, A. *J. Org. Chem.* **1995**, *60*, 5891.

[25] a) Lyakhov, A. S.; Vorobiov, A. N.; Gaponik, P. N.; Ivashkevich, L. S.; Matulis, V. E.; Ivashkevich, O. A; *Acta Cryst.* **2003**, *C59*, o690; b) Lyakhov, A. S.; Voitekhovich, S. V.; Gaponik, P. N.; Ivashkevich, L. S. *Acta Cryst.* **2004**, *C60*, o293; c) Ohno, Y.; Akutsu, Y.; Arai, M.; Tamura, M.; Matsunaga, T. *Acta Cryst.* **2004**, *C60*, 1014.

[26] a) Gdaniec, M., Milewska, M. J. & PoøonÂ ski, T. *J. Org. Chem.* **1995**, *60*, 7411; b) Olszewska, T., Milewska, M. J., Gdaniec, M., Małuszyńska, H. & Połoński, T. *J. Org. Chem.* **2001**, *66*, 501.

[27] a) Ohwada, T.; Miura, M.; Tamaka, H.; Sakamoto, S.; Yamaguclin, K.; Ikeda, H.; Inagaki, S. *J. Am. Chem. Soc.* **2001**, *133*, 10164; b) Chakrabarti, P.; Venkatesan, K. *J. Chem. Soc., Perkin Trans. 1* **1981**, 206; c) Constable, A. G.; Mc Donald, W. S.; Shaw, B. L. *J. Chem. Soc., Dalton Trans.* **1980**, 2282.

[28] (a) Filhohl, A.; Bravic, G.; Rey-Lafon, M.; Thomas, M. *Acta Cryst.* **1980**, *B36*, 575; (b) Ejsmont, K.; Kyziol, J.; Daszkiewicz, Z.; Bujak, M. *Acta Cryst.* **1998**, *C54*, 672.

[29] a) Reed, A. E.; Curtiss, L. A.; Weinhold, F. *Chem. Rev*. **1988**, *88*, 899; b) Reed, A. E.; Weinstock R. B.; Weinhold, F. *J. Chem. Phys.* **1985**, *83*, 735.

[30] a) Claramunt, R. M.; Sanz, D.; López, C; Jiménez J. A.; Jimeno, M. L.; Elguero, J.; Fruchier, A. *Magn. Reson. Chem.* **1997**, *35*, 35; b) Koren, A. O.; Gaponik, P. N. *Khim. Geterosikl. Soedin.* **1990**, 1643; c) Begtrup, M.; Elquero, J.; Faure, R.; Camps, P.; Estopa, C.; Ilavsky, D.; Fruchier, A.; Marzin, C.; Mendoza, J. de *Magn. Reson. Chem.* **1988** ,*26*, 134.

[31] Nelson, J. H.; Takach, N. E.; Henry, R. A.; Moore, D. W.; Tolles W. M.; Gray, G. A. *Magn. Reson. Chem.* **1986**, *24*, 984, and references cited therein.

[32] a) Kricheldorf, H. R. *Org. Magn. Reson.* **1980**, *13*, 52; b) Sogn, J. A.; Gibbon, Randall**,** E. W. *Biochemistry* **1973**, *12*, 2100.

[33] Frisch, M. J.; Trucks, G. W.; Schlegel, H. B.; Scuseria, G. E.; Robb, M. A.; Cheeseman, J. R.; Zakrzewski, V. G.; Montgomery, J. A.; Stratmann, Jr., R. E.; Burant, J. C.; Dapprich, S.; Millam, J. M.; Daniels, A. D.; Kudin, K. N.; Strain, M. C.; Farkas, O.; Tomasi, J.; Barone, V.; Cossi, M.; Cammi, R.; Mennucci, B.; Pomelli, C.; Adamo, C.; Clifford, S.; Ochterski, J.; Petersson, G. A.; Ayala, P. Y.; Cui, Q.; Morokuma, K.; Malick, D. K.; Rabuck, A. D.; Raghavachari, K.; Foresman, J. B.; Cioslowski, J.; Ortiz, J. V.; Stefanov, B. B.; Liu, G.; Liashenko, A.; Piskorz, P.; Komaromi, I.; Gomperts, R.; Martin, R. L.; Fox, D. J.; Keith, T.; Al-Laham, M. A.; Peng, C. Y.; Nanayakkara, A.; Gonzalez, C.; Challacombe, M.; Gill, P. M. W.; Johnson, B.; Chen, W.; Wong, M. W.; Andres, J. L.; Gonzalez, C.; Head-Gordon, M.; Replogle, E. S.; Pople, J. A. Gaussian 98, Revision A.6, Gaussian, Inc., Pittsburgh PA, **1998**.

[34] Wiberg, K. B.; Raben, P. R. *J. Comput. Chem.* **1993**, *14*, 1504.

[35] a) Bonnett, R.; Holleyhead, R.; Johnson, B. L.; Randall, E. W. *J. Chem. Soc.* **1964**, *86*, 5564; b) Gouesnard, J. P.; Martin, G. J. *Org. Magn. Reson.* **1979**, *12*, 263; c) Willer, R. L.; Lowe-Ma, C. K; Moore, D. W. *J. Org. Chem.* **1984**, *49*, 1481; d) Witanowski, M.; Biedrzycka, Z.; Sicinska, W.; Grabowski, Z. *J. Magn. Reson.* **2003**, *164*, 212.

[36] Gouesnard, J. P.; Martin, G. J. *Org. Magn. Reson.* **1979**, *12*, 263.

[37] Kupper, R.; Hilton, B. D.; Kroeger-Koepke, M. B.; Koepke, S. R.; Michejda, C. J. *J. Org. Chem.* **1984**, *49*, 3781.

[38] Witanowski, M.; Stefaniak, L.; Webb, G. A., *Ann. Reports NMR Spectrosc.* **1993**, 25.

[39] Witanowski, M.; Biedrzycka, Z.; Sicinska, W.; Grabowski, Z. *J. Mol Struct.* **2002**, *602*, 199.

[40] Wang, P. G.; Xian, M.; Tang, X.; Wu, X.; Wen, Z.; Cai, T.; Janczuk, J. *Chem. Rev.* **2002**, *102*, 1091.

[41] Daszkiewicz, Z.; Nowakowska, E. M. Preżdo, W. W.; Kyzioł, J. B. *Pol. J. Chem.* **1995**, *69*, 1437.

[42] Lunazzi, L; Cerioni, G.; Ingold, K. U.; *J. Am. Chem. Soc.* **1976**, *98*, 7484.

[43] Freeman, J. P.; Graham, W. H.; *J. Am. Chem. Soc.* **1967**, *89*, 1761.

[44] a) Loeppky, R. N.; Michejda, C. J. *N-Nitrosamines and Related N-Nitroso Compounds*; ACS Symposium Series 553; American Chemical Society: Washington, DC, 1994; b) Oh, S. M. N. Y. F.; Williams, D. L. H. *J. Chem. Soc., Perkin Trans. 2* **1989**, 755; c) Castro, A.; Leis, J. R.; Pena, M. E. *J. Chem. Soc., Perkin Trans. 2* **1989**, 1861; d) Galtress, C. L.; Morrow, P. R.; Nag, S.; Smalley, T. L.; Tschantz, M. F.; Vaughn, J. S.; Wichems, D. N.; Ziglar, S. K.; Fishbein, J. C. *J. Am. Chem. Soc.* **1992**, *114* 1406; e) Santala, T.; Fishbein, J. C. *J. Am. Chem. Soc.* **1992**, *114*, 8852.

[45] a) Gropen, O.; Skancke, P. N. *Acta Chem. Scand.* **1971**, *25*, 1241; b) Gdaniec, M.; Milewska, M. J.; Polonski, T. *J. Org. Chem.* **1995**, *60*, 7411.

[46] a) Harris, R. K.; Pryce-Jones, T.; Swinbourne, F. J. *J. Chem. Soc.,Perkin Trans. 2* **1980**, 476; b) *N*-Nitrosoindoline and *N*-methyl-*N*-phenylnitrosamine exist as a single conformational isomer, see: Looney, C. E.; Phillips, W. D.; Reilly, E. L. *J. Am. Chem. Soc.* **1957**, *79*, 6136; The rotational barrier of an aromatic *N*-nitrosamine, *N*-nitrosodiphenylamine, was reported to be 19.1 kcal/mol by Forlani et al.: Forlani, L.; Lunazzi, L.; Macciantelli, D.; Minguzzi, B. *Tetrahedron Lett.* **1979**, 1451.

[47] Kintzinger, J. P.; Lehn, J. M.; Williams, R. L. *Mol. Phys.,* **1969**, *17(1)*, 137.

[48] a) Habibollahzadeh, D.; Murray, J. S.; Redfern, P. S.; Politzer, P. *J. Phys. Chem.,* **1991**, *95*, 7702; b) Habibollahzadeh, D.; Murray, J. S.; Grice, M. E.; Politzer, P. *Int. J. Quantum Chem.,* **1993**, *45*, 15.

[49] *ICT – Thermdynamic Code*, Version 1.0, Frauenhofer-Institut für Chemische Technologie (ICT). Pfinztal/Berghausen, Germany 1988-2000.

[50] Kistiakoswky, G. B.; Romeyn, H. Jr.; Ruhoff, J. R.; Smith, A. H.; Vaughan, W. E. *J. Am. Chem. Soc.* **1935**, *56*, 1112.

[51] a) Kamlet, M. J.; Jacobs, S. J. *J. Chem. Phys.* **1968**, *48*, 23; b) Kamlet, M. J.; Ablard, J. E. *J. Chem. Phys.* **1968**, *48*, 36; c) Kamlet, M. J.; Dickinson, C. *J. Chem. Phys.* **1968**, *48*, 43; d) Eremenko, L. T.; Nesterenko, D. A. *Chem. Phys. Reports.* **1997**, *16*, 1675; e) Astakhov, A. M.; Stepanov, R. S.; Babushkin, A. Y. *Combust. Explos. Shock Waves.* **1998**, *34*, 85, (Engl. Transl.).

[52] With K = 15.58, ρ [g cm^{-3}]; $\varphi = N\sqrt{M(-\Delta_E H)}$; N = moles of gases per g of explosives; M = average molar mass of formed gases; $\Delta_E H$ = calculated enthalpy of detonation (in cal g^{-1}); A = 1.01; B = 1.30.

[53] Mader, C. L.; “Detonation Properties of Condensed Explosives Computed Using the Becker-Kistiakowsky-Wilson Equation of State,” *Los Alamos Scientific Laboratory* **1963**, Rept. LA-2900.

[54] Willer, R. L.; Chafin, A. P.; Doyle, J. P.; *Energy – A Computer Program for Calculated the Density, Detonation Velocety, and Detonation Pressure of Proposed Energetic Materials*, NWC Technical Memorandum 5144, August **1983**.

[55] Weigand, J. J. *1,4-Bis(1’-methyltetrazolyl)-1,4-dimethyl-2-tetrazene and other nitrogen rich high energy density materials* Diploma thesis, Ludwig-Maximilian University, **2002**.

[56] Meihong, X.; Quizheng, Y. Therory and Practice of Energetic Materials, in: *Proceedings of 3rd Beijing International Symposium on Pyrotechniques and Explosives*, Beijing, China, 6-9 November 1995, pp. 180.

[57] a) Ritter, H.; Braun, S.; Schäfer, M.; Aerni, H. R.; Bircher, H. R.; Berger, B.; Mathieu, J.; Gupta, A. *32th International Annual Conference of ICT,* Karlsruhe, **2001**, 91/1; b) Pogoria, P. F.; Mitchell, A. R.; Jessop, E. S. Prop. Explos. Pyrotech. **1996**, *21(1)*, 14.

[58] Fedoroff, T. B.; Sheffield, O. E. *Encyclopedia of Explosives and Related Items, Vol. 6*, Picatinny Arsenal, Dover, NJ, **1974**, pp. G117.

[59] a) Lobanova, A. A.; Il’yasov, S. G.; Popov, N. I.; Sataev, R. R. *Russ. J. Org. Chem.* **2002**, *38(1)*, 1; b) Lobanova, A. A.; Sataev, R. R.; Popov, N. I.; Il’yasov, S. G. *Russ. J. Org. Chem.* **2000**, *36(2)*, 1163.

[60] Lobanova, A. A.; Il’yasov, S. G.; Popov, N. I.; Sataev, R. R. *Russ. J. Org. Chem.* **2002**, *38(12)*, 1793.

[61] Boileau, J.; Emeury, J. M. L.; Kehren, J. P. USA Patent 4,487,938 **1974**.

[62] Agrawal, J. P. *Prog. Energy Combust. Sci.* **1998**, *24*, 1.

[63] Mitchell, A. R.; Pagoria, P. F.; Coon, C. L.; Jessop, E. S.; Poco, J.F.; Tarver, C. M.; Breithaupt, R. D.; Moody, G. L. Propell. Explos. Pyrotech. 1994, 19, 232.

[64] Souers, P. C.; Forbes, J. W.; Fried, L. E.; Howard, W. M.; Anderson, S.; Dawson, S.; Vitello, P.; Garza, R. Prop. Explos. Pyrotech. **2001**, *26*, 180.

[65] a) Klapötke, T. M.; Ang, H.-G. *Prop. Explos. Pyrotch.* **2001**, *26(5)*, 221; b) Goede, G.; Wingborg, W.; Bergmann, H.; Latypov, N. V. Prop. Explos. Pyrotch. **2001**, 26(1), 17; b) Geith, J.; Holl, G.; Klapötke, T. M.; Weigand, J. J. *Combustion and Flame* **2004**, *139*, 358.

[66] a) Thiele, J.; Uhlfelder, E. Lieb. Ann. **1898**, *303*, 93; b) Davis, T. L.; Blanchard L. C. *J. Am. Chem. Soc.* 1929, *51*, 1801.

[67] Fogarasi, G.; Balaz, A. *J. Mol. Struct.* **1985**, *113*, 105.

[68] Räsänen, M. *J. Mol. Struct.* **1983**, *101*, 275.

[69] Evans, J. C. *J. Chem. Phys.* **1954**, *22*, 1228.

[70] Evans, J. C. *J. Chem. Phys.* **1959**, *31*, 1435.

[71] Suzuki, I. *Bull. Chem. Soc. Jpn.* **1960**, *33*, 1359.

[72] Uno, T.; Machida, K.; Saito, Y. *Chem. Soc. Jpn.* **1969**, *42*, 1539.

[73] Saito, Y.; Machida, K.; Uno, T. *Spectrochim. Acta, Part A* **1969**, *26*, 2089.

[74] Kricheldorf, H. R. *Org. Reson. Chem.* **1980**, *14(3)*, 198.

[75] Prezhdo, V. V.; Bykova, A. S.; Glowiak, T.; Koll, A.; Kyziol, J. *Zh. Strukt. Khim.* **2001**, *42*, 611.

[76] Hughes E. W.; Yakel, H. Freeman H. C. Acta Cryst 1961, 14, 345.

[77] Bondi, A. *J. Phys. Chem*. **1964**, **68,** 441.

[78] a) Eckert-Maksic, M.; Maskill, H.; Zirinski, I. *J. Chem. Soc., Perkin Trans.* **2001**, *2*, 2147; b) Cox, R. A. *Can. J. Chem.* **1996**, *74*, 1779.

[79] Dewhurst, F.; Lamberton, A. H. *J. Chem. Soc (B)* **1971**, 788.

[80] Frèjacques, M. *Chim. Ind.* **1948**, *60(1)*, 29.

[81] Authentic sample (Aldrich).

[82] F. Börner, PhD thesis, Freie Universität Berlin, **1999**.

[83] Ozawa, T. *Bull. Chem. Soc. Jpn.* **1965**, *38*, 1881

[84] Kissinger, H. E. *Anal. Chem.* **1957**, *29*, 1702

[85] a) Standard Test Methods for Arrhenius Kinetic Constants for Thermally Unstable Materials. *ASTM designation E698-99*, **1999**; b) Rocco, J. A. F. F.; , Lima, J. E. S; Frutuoso, A. G.; Iha, K.; Ionashiro, M.; Matos, J. R.; Suárez-Iha, M. E. V. *J. Therm. Anal. Cal.* **2004**, *75*, 551.

[86] Steiner, D. A.; Polo, S. R.; McCubbin, T. K.; Wishah, K. A. *Can. J. Phys.* **1981**, *59*, 1313.

[87] a) Nakamoto, K. *Infrared and Raman Spectra of Inorganic an Coodination Compounds*, 4th ed.; Wiley & Sons: New York, Chichester, Brisbane, Toronto, Singapore, 1986; b) Mecke, R.; Langenbucher, F. *Infrared Spectra*, Heyden & Son, 1965, London, Serial *No. 106*.

[88] Mecke, R.; Langenbucher, F. *Infrared Spectra*, Heyden & Son, 1965, London, Serial *No. 6*.

[89] Shimanouchi, T. *Tables of Molecular Vibrational Frequencies Consolidated Volume I*, National Bureau of Standards, (1972) 1-160.

[90] Bosshardt, H.; Hesse, M. Angew. Chem. **1974**, *86*, 256.

[91] a) Chen, J. P.; Isa, K. *J. Mass. Spectrom. Soc. Jpn.* **1998**, *46(4)*, 299; b) Galperin, V. A.; Finkel'shtein, A. I.; Shishkin, N. P. *Zh. Vses. Khim. Ova.* 1972, *17(3)*, 359; c) Langer, H. G.; Brady, T. P. *Thermochim. Acta* **1973**, *5*, 391.

[92] Stradella, L.; Argentero, M. *Thermochim. Acta* **1993**, *219*, 315.

[93] Sikder, N.; Bulakh, N. R.; Sikder, A. K.; Sarwade, D. B. *J. Hazard. Mat.* **2003**, *A96*, 109.

APPENDIX A

COMPUTATIONAL DETAILS

Chapter III, 2

The structural and vibrational data of all considered species were calculated by using the hybrid density functional theory (B3LYP) with the program package Gaussian 98.[1] Different types of basis sets were used: aug-cc-pvYZ (Y = D, T). Both basis sets gave essentially the same results. Here, the focus has been mainly that on the B3LYP/aug-cc-pvTZ results with respect to the structural data. All stationary points were characterized by a frequency analysis at the B3LYP/aug-cc-pvDZ level. The computed frequencies for all species and approximate assignments are given in *Tables A1-3*. NBO[2] analyses and MO analyses were carried out to investigate the bonding at the aug-cc-pvDZ level utilizing the optimized B3LYP/aug-cc-pvTZ geometry (*Table A-4*). *Note:* There may well be significant differences among gas-phase, solution, and solid-state data.

Table A-1. Frequency analysis of **CIT** dianion (**33**): B3LYP/aug-cc-pvDZ.[a,b]

#	symmetry	Wave number [cm^{-1}]	IR intensity [km $mole^{-1}$]	Raman activity [$Å^4$/amu]	Approx. assign.
1	A'	78.9192	3.8304	0.2278	γ N_4C-NCN
2	A'	140.7846	5.3885	9.3542	δ N_4C-NCN
3	A"	330.2255	1.9292	3.6212	γ N_4C-NCN
4	A'	441.7789	6.0610	10.6096	δ N_4C-NCN
5	A'	550.0069	0.5861	5.1018	δ N_4C-NCN
6	A"	581.0759	6.4400	2.8953	γNCN, NCN
7	A"	731.7222	0.0010	0.0390	γNNNN, N_4C
8	?A	757.9463	12.8732	9.1257	δNCN, NCN
9	?A	768.5212	4.8446	0.6824	γNCN, N_4C
10	A'	1002.7240	6.7036	17.1445	ν_{oop}NN, N_4C
11	A'	1041.0467	1.6107	13.5452	δNCN, N_4C
12	A'	1114.5413	10.9189	10.9372	ν_{oop}NN, N_4C
13	A'	1125.1043	4.4977	12.2219	ν_{ip}NN, N_4C
14	A'	1194.5724	26.4712	25.5281	νN2N3, N_4C
15	A'	1245.7092	9.2964	1.2812	νCN, N-CN + ν_{ip}CN, N_4C
16	A'	1350.8385	66.4477	9.3865	ν_{oop}NCN, N_4C
17	A'	1513.0517	699.3810	171.5100	νCN, C-NCN
18	A'	2137.3550	1411.2991	228.6968	νCN, CNC-N

[a] ip = in phase, oop = out-of-phase, [b] for numbering scheme see *Figure 3.7 (Chapter III)*

Table A-2. Frequency analysis of Cs_2CIT (**33**): B3LYP/aug-cc-pvDZ.[a,b]

#	**Wave number [cm^{-1}]**	**IR intensity [km mole^{-1}]**	**Raman activity [Å^4/amu]**	**Approx. assign.**
1	25.8899	28.7020	0.3636	γ Cs-CIT
2	59.1460	11.3162	0.3701	δ Cs-CIT
3	73.5744	0.8058	3.9523	γ all
4	87.6685	20.0206	0.0149	δ all
5	98.8395	3.2954	0.1961	γ all
6	121.4175	3.2500	0.2829	δ all
7	150.8811	76.2516	0.2877	νCs-N
8	188.5583	13.7678	6.3482	δ N_4C-NCN
9	335.9261	0.5951	0.9856	γN_4C-NCN
10	437.5899	3.2081	5.9868	δ CIT
11	579.0460	0.2129	6.6400	δ CIT
12	594.1566	7.6087	0.1165	γNCN, NCN
13	734.3617	0.0003	0.2475	γNNNN, N_4C
14	772.8719	5.6383	0.7887	γNCN, N_4C
15	799.1775	4.3785	2.9348	δNCN, NCN
16	1023.7755	10.3321	5.5804	ν_{oop}NN, N_4C
17	1070.0532	5.1799	5.1056	δNCN, N_4C
18	1118.2668	6.9052	8.1806	νN2N5, N_4C
19	1122.8167	10.3181	5.1320	νN3N4, N_4C
20	1230.8993	30.9216	4.7051	νCN, N-CN + νN2N3, N_4C
21	1272.9695	6.8557	14.4751	νN2N3, N_4C
22	1404.8822	90.6536	9.4679	νNCN, N_4C
23	1497.5531	521.1193	101.6795	νCN, C-NCN
24	2197.9778	907.9263	145.9248	νCN, CNC-N

[a] ip = in phase, oop = out-of-phase, [b] for numbering scheme see *Figure 3.7 (Chapter III)*

Table A-3. Frequency analysis of CIT•SO_3 (**37**): B3LYP/aug-cc-pvDZ.[a,b]

#	Wave number [cm^{-1}]	IR intensity [km $mole^{-1}$]	Raman activity [$Å^4$/amu]	Approx. assign.
1	26.9789	0.0002	1.2490	γall
2	79.3075	6.5780	3.3838	γall
3	93.8184	2.3201	4.3252	δall
4	119.2595	0.0923	0.6100	γall
5	176.6699	2.4730	6.1266	δ all
6	255.4018	11.3446	11.6013	δ all
7	274.7550	0.2128	0.5381	γall
8	283.0548	5.8386	7.2535	δ all
9	349.9590	2.6950	0.8306	γall
10	454.2033	19.2543	9.4068	δ all
11	500.1190	19.4296	1.4597	δSO_3
12	508.5516	4.2114	2.3128	δ all
13	561.7957	339.3190	1.0832	ν SN + δSO_3
14	577.4616	6.8417	0.0465	γNCN, NCN
15	579.3746	24.0113	13.7352	δN_4C,NCN
16	692.8165	2.2190	0.1308	γNNNN, N_4C
17	746.4333	6.4215	0.0405	γNCN, N_4C
18	777.2932	0.3167	8.0122	δNCN, NCN
19	948.2741	194.1638	44.6246	$ν_{ip}$SO
20	994.1525	4.0411	7.6154	ν N_4C
21	1065.1707	133.4219	19.6916	ν N_4C
22	1101.4984	0.6036	4.6696	νN3N6, N_4C
23	1136.0139	15.1459	14.6451	νN2N5, N_4C
24	1173.3389	197.7116	5.6857	$ν_{oop}$SO
25	1176.9733	295.7906	8.9949	$ν_{oop}$SO
26	1246.6248	37.9325	16.3647	$ν_{ip}$CN, N4C + νCN, N-CN
27	1307.8301	85.5381	38.0480	νN2N3, N_4C
28	1348.3833	79.4370	8.2532	$ν_{oop}$NCN, N_4C
29	1589.1918	971.7955	24.5763	νCN, C-NCN
30	2195.9401	1062.8321	374.3944	νCN, CNC-N

[a] ip = in phase, oop = out-of-phase, [b] for numbering scheme see *Figure 3.7 (Chapter III)*

Table A-4. NPA Charges (B3LYP/aug-cc-pvDZ) [e]

	CIT (32)	CIT-SO_3 (37)
C 1	0.48772	0.58528
C 2	0.50689	0.50807
N 1	-0.48757	-0.45406
N 2	-0.23922	-0.14644
N 3	-0.24034	-0.11930
N 4	-0.48328	-0.49418
N 5	-0.77149	-0.71950
N 6	-0.7727	-0.67108
S 1	-	2.45395
O 1	-	-0.98565
O 2	-	-0.97856
O 3	-	-0.97852

Chapter IV, 2.7.2

In order to analyze the chemical bonding in **61c** the theory of Atoms in Molecules was used to define the atomic contribution within **61c**.[3] AIM and NBO analyses[4] were carried out to investigate the charge transfer from the dinitramide (DN) anion to the tetrazolium cation at the SCF level (B3LYP/6-6311+G(3d,2p) utilizing the geometry obtained from the X-ray structure analysis. Details of the NBO charges and AIM charges are summarized in *Table A-5*. The numbering scheme of **61c** is different from that of the structure determination and is depicted in *Figure A-1*. *Table A-6* gives the Cartesian coordinates of the molecular model obtained from crystals structure analysis and *Table A-7* gives the parameters of the important critical points (CP's) of **61c**. The electron density plot, ρ (r), and the Laplacian plot ρ (r), $-\nabla^2\rho$ (r), of the projection of the (**61c)** molecular graph onto the N2-N4-O3 plane is depicted in *Figure A-2*.

Table A-5. AIM and NBO charges.

	AIM charges B3LYP/6-311+G(3d,2p)	NBO charges B3LYP/6-311+G(3d,2p)
O1	-0,49743	-0,4428
N2	0,62742	0,5699
O3	-0,50015	-0,4501
N4	-0,14682	-0,2631
N5	0,64061	0,5824
O6	-0,54736	-0,4738
O7	-0,55789	-0,5049
N8	-0,41601	-0,0765
N9	0,00912	0,0135
N10	0,00725	0,0111
N11	-0,62501	-0,5553
C12	1,44031	0,6409
H13	0,38173	0,3546
H14	0,43781	0,3705
N15	-0,70428	-0,1954
N16	-1,04831	-0,6758
C17	1,18670	-0,2906
H18	0,43897	0,3839
H19	0,45312	0,3983
H20	-0,12336	0,1987
H21	-0,26660	0,2025
H22	-0,17951	0,2020

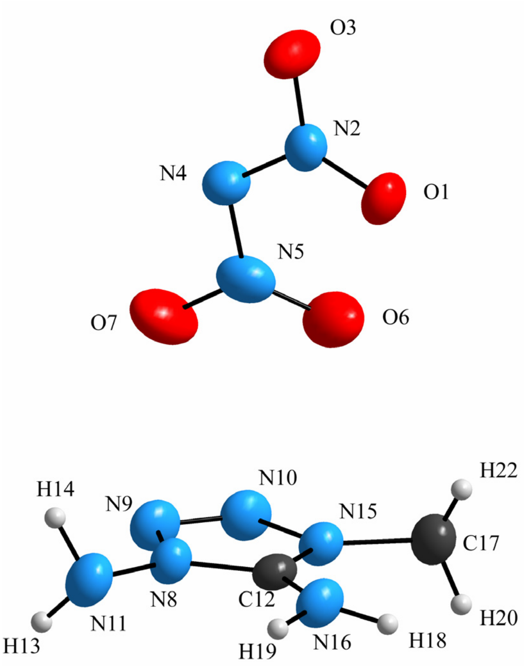

Figure A-1. Numbering scheme of **61c** used in calculation.

Table A-6. Cartesian coordinates from X-ray structure determination as input for the calculations.

Atomic Type		Coordinates (Angstroms)	
	x	y	z
O	-3.25028700	1.03480600	0.92032700
N	-3.57281600	0.10523900	0.18208800
O	-4.77269700	-0.17578400	0.00427200
N	-2.73726000	-0.73571300	-0.46430300
N	-1.40445000	-0.34028600	-0.49999500
O	-0.99960400	0.78987900	-0.26964300
O	-0.66737400	-1.26012800	-0.86427900
N	2.19827300	-1.01150800	0.25288900
N	2.33393300	-1.02117500	-1.10089000
N	2.32795900	0.18823300	-1.50119000
N	2.13765000	-2.16375200	1.04847200
C	2.08565400	0.24336500	0.69339300
H	2.86360400	-2.66012200	0.80064700
H	1.40938600	-2.64417900	0.80582100
N	2.17804400	0.98848600	-0.41116600
N	1.91728700	0.63922500	1.93575400
C	2.09930600	2.42793900	-0.51590100
H	2.06883900	1.49003500	2.15785400
H	1.99391900	0.02452600	2.60034900
H	2.85698900	2.82676500	-0.23814000
H	2.26922200	2.60977500	-1.30330400
H	1.29763700	2.67395200	-0.30521300

Table A-7. Parameters of the critical point analysis

CP1 between N4-O3:

```
(3, -1) critical point of RHO, electron density:
Coordinates:( 1.62891025, -2.01193462, -1.50340591)
VALUES
Rho(r) 8.33752507e-003
|GRAD(Rho(r))| 4.27829156e-018
GRAD(Rho(r)) x 3.57786717e-018
GRAD(Rho(r)) y 2.26327204e-018
GRAD(Rho(r)) z -6.16639986e-019
(-1/4)Del**2(Rho(r)) -7.41275639e-003
G(r) 6.45411734e-003
K(r) -9.58639046e-004
L(r) -7.41275639e-003
```

CP2 between N2-O4:

```
(3, -1) critical point of RHO, electron density:
Coordinates:( 1.15736661, 1.51012015, -0.54587990)
VALUES
Rho(r) 6.76168106e-003
|GRAD(Rho(r))| 2.57736370e-018
GRAD(Rho(r)) x -1.72455908e-018
GRAD(Rho(r)) y -1.45181447e-018
GRAD(Rho(r)) z -1.24937360e-018
(-1/4)Del**2(Rho(r)) -5.45507232e-003
G(r) 4.70918273e-003
K(r) -7.45889591e-004
L(r) -5.45507232e-003
V(r) -3.96329314e-003
```

CP3 between O3-O1:

```
(3, -1) critical point of RHO, electron density:
Coordinates:( -4.00636017, 1.70639039, 0.61083447)
VALUES
Rho(r) 2.12394179e-002
|GRAD(Rho(r))| 9.14850795e-018
GRAD(Rho(r)) x -8.67361738e-018
GRAD(Rho(r)) y 1.30104261e-018
GRAD(Rho(r)) z 2.60208521e-018
(-1/4)Del**2(Rho(r)) -2.23288399e-002
G(r) 2.02752931e-002
K(r) -2.05354678e-003
L(r) -2.23288399e-002
V(r) -1.82217463e-002
```

```
(3, -3) critical point of RHO, electron density:
Corresponding atom: O 1
Coordinates:( -6.14215407, 1.95549083, 1.73915961)

(3, -3) critical point of RHO, electron density:
Corresponding atom: O 6
Coordinates:( -1.88898071, 1.49264340, -0.50955417)

(3, -3) critical point of RHO, electron density:
Corresponding atom: O 7
Coordinates:( -1.26115998, -2.38128787, -1.63324606)

(3, -3) critical point of RHO, electron density:
Corresponding atom: N 9
Coordinates:( 4.41049164, -1.92972726, -2.08036995)

(3, -3) critical point of RHO, electron density:
Corresponding atom: N 15
Coordinates:( 4.11590749, 1.86796564, -0.77699214)
```

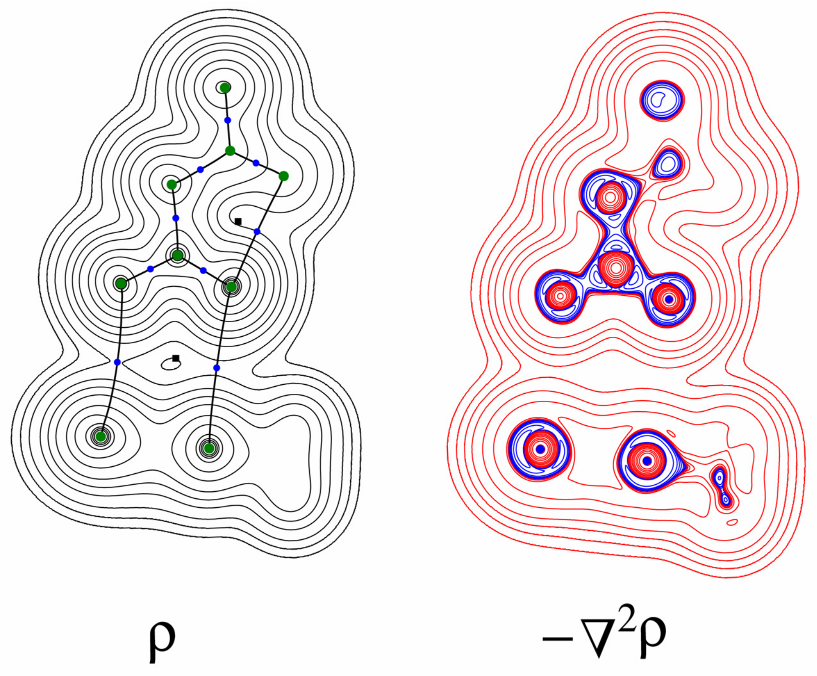

Figure A-2. The electron density plot, ρ (r), and the Laplacian plot ρ (r), - $\nabla^2 \rho$ (r), of the projection of the **61c** molecular graph onto the N2-N4-O3 plane

Chapter IV, 2.8

Table A-8a G2/G3 method

	DAT	$HDAT^+$	MeDAT	$HMeDAT^+$	ClO_4^-	$HClO_4$
point group	C_1	C_s	C_s	C_s	T_d	C_s
ZPE[a]	0.079389	0.091559	0.105743	0.118056	0.015252	0.026449
NIMAG	0	0	0	0	0	0
E_0 (G2)[a]	-368.396819	-368.738380	-407.603452	-407.972034	-760.115976	-760.591452
E_0 (G3)[a]	-368.718381	-369.061258	-407.970890	-408.340207	-760.631127	-761.106607
E_{298} (G2)[a]	-368.390688	-368.732110	-407.595421	-407.963903	-760.111942	-760.586685
E_{298} (G3)[a]	-368.712250	-369.054989	-407.962859	-408.332077	-760.627092	-761.101841
H_{298} (G2)[a]	-368.389744	-368.731166	-407.594477	-407.962959	-760.110998	-760.585741
H_{298} (G3)[a]	-368.711306	-369.054045	-407.961915	-408.331132	-760.626148	-761.100897
$\Delta_fH°$(exp.)[b]						
P_A (G2)[a]		214.25		231.23		297.91
P_A (G3)[a]		215.07		231.69		297.91
P_A (exp.)[a]						292.6 ± 8.4[5]

a) a.u. (atomic energy unit) = 1 Hartree = 627.509 kcal mol^{-1}
b) kcal mol^{-1}

Table A-8b

	NO_3^-	HNO_3	$N_3O_4^-$	HN_3O_4	N_3^-
point group	D_{3h}	C_s	C_2	C_s	$D_{\infty h}$
ZPE[a]	0.014506	0.026815	0.028806	0.041787	0.011035
NIMAG	0	0	0	0	0
E_0 (G2)[a]	-280.044857	-280.558755	-464.444405	-464.935204	-164.017017
E_0 (G3)[a]	-280.234048	-280.748610	-464.772241	-465.262982	-164.153878
E_{298} (G2)[a]	-280.041714	-280.555298	-464.438773	-464.929237	-164.014421
E_{298} (G3)[a]	-280.230906	-280.745153	-464.766608	-465.257014	-164.151282
H_{298} (G2)[a]	-280.040770	-280.554254	-464.437828	-464.928293	-164.013477
H_{298} (G3)[a]	-280.229962	-280.744209	-464.765664	-465.256070	-164.150338
$\Delta_fH°$(exp.)[b]		-32.1[6]		29.9[7]	
P_A (G2)[a]		322.22		307.77	
P_A (G3)[a]		322.69		307.73	
P_A (exp.)[a]		324.50 ± 0.20[8]		297.0 ± 0.20[9]	

a) a.u. (atomic energy unit) = 1 Hartree = 627.509 kcal mol^{-1}
b) kcal mol^{-1}

Table A-8c

	HN_3	HCl	CH_4	C_2H_6	N_2
point group	C_s	$C_{\infty v}$	T_d	D_{3d}	$D_{\infty h}$
ZPE[a]	0.020720	0.006481	0.ß42658	0.071216	0.005610
NIMAG	0	0	0	0	0
E_0 (G2)[a]	-164.560422	-460.340176	-40.410891	-79.630881	-109.392625
E_0 (G3)[a]	-164.698609	-460.654665	-40.457626	-79.723394	-109.484021
E_{298} (G2)[a]	-164.557181	-460.337816	-40.408020	-79.627340	-109.390264
E_{298} (G3)[a]	-164.695368	-460.652304	-40.454755	-79.719854	-109.481661
H_{298} (G2)[a]	-164.556237	-460.336872	-40.407075	-79.626396	-109.389320
H_{298} (G3)[a]	-164.694424	-460.651360	-40.453810	-79.718910	-109.480717
$\Delta_fH°$(exp.)[b]	71.1[10]	-22.30[11]	-17.89[12]	-20.04[13]	0
P_A (G2)[a]	340.59				
P_A (G3)[a]	341.42				
P_A (exp.)[a]	343.9 ± 2.2[14]				

a) a.u. (atomic energy unit) = 1 Hartree = 627.509 kcal mol^{-1}
b) kcal mol^{-1}

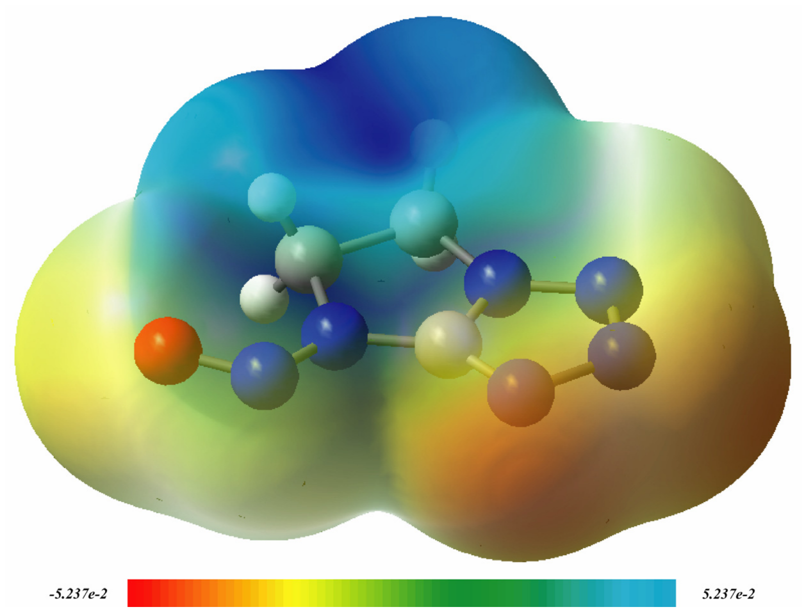

Figure A-3. ESP mapped onto electron density surface of **111c**

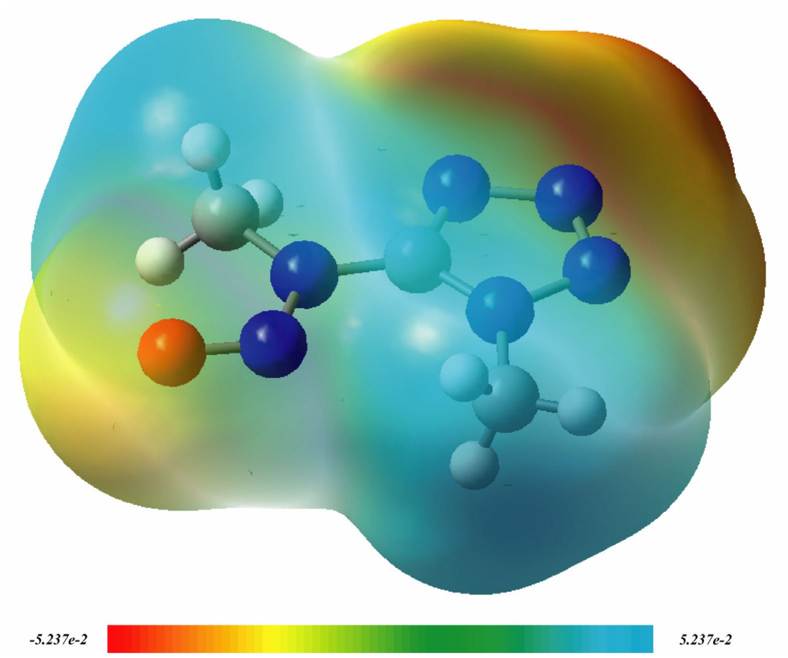

Figure A-4. ESP mapped onto electron density surface of **111a**

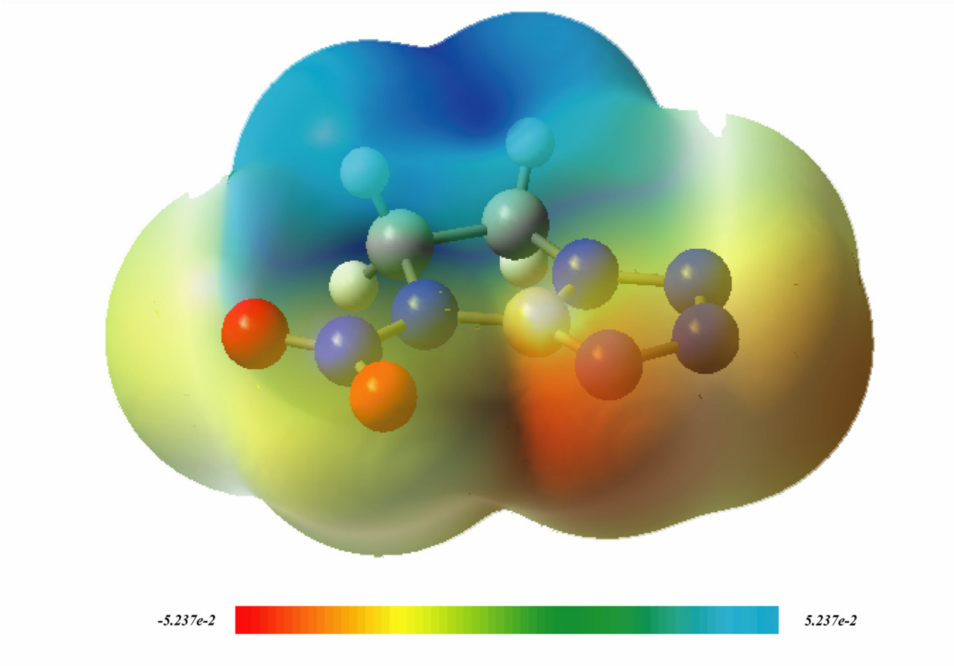

Figure A-5. ESP mapped onto electron density surface of **112c**

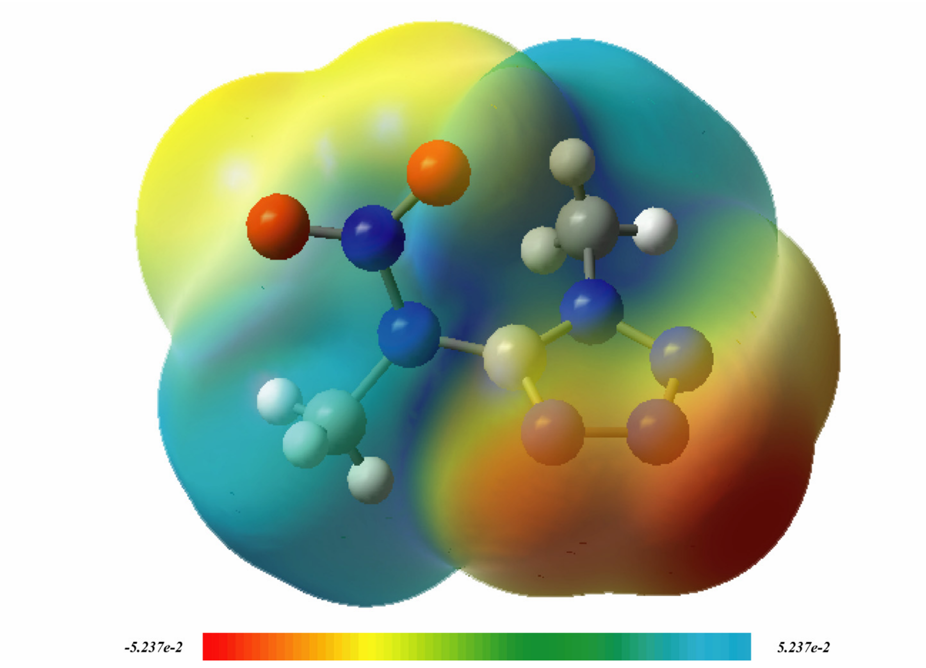

Figure A-6. ESP mapped onto electron density surface of **112a**

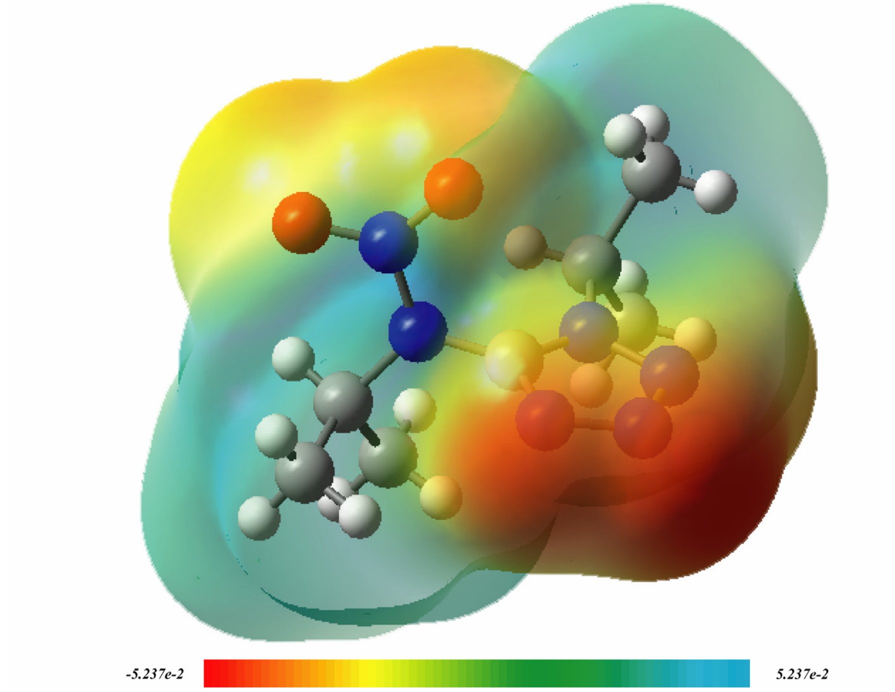

Figure A-7. ESP mapped onto electron density surface of **112b**.

Table A-9a. Mullican and NBO (in brackets) charges [*e*] for **109a,c**, **111a,c** and **112a-c**.[a]

	N-1	N-2	N-3	N-4	C-1	C-2[a]	E
109a	-0.332	-0.069	-0.095	-0.367	0.649	0.258	0.045
	(-0.253)	(-0.088)	(-0.059)	(-0.384)	(0.549)	(0.258)	(0.023)
109c	-0.321	-0-071	-0.093	-0.375	0.678	0.258	0.076
	(-0.261)	(-0.074)	(-0.061)	(-0.367)	(0.546)	(0.242)	(0.025)
111a	-0.333	-0.051	-0.078	-0.354	0.730	0.293	0.207
	(-0.227)	(-0.067)	(-0.051)	(-0.354)	(0.536)	(0.290)	(0.127)
111c	-0.338	-0.054	-0.081	-0.334	0.779	0.273	0.245
	(-0.236)	(-0.058)	(-0.051)	(-0.321)	(0.540)	(0.259)	(0.133)
112a	-0.280	-0.050	-0.085	-0.315	0.659	0.292	0.221
	(-0.197)	(-0.060)	(-0.059)	(-0.320)	(0.507)	(0.292)	(0.162)
112b	-0.334	-0.052	-0.081	-0.323	0.747	0.278	0.235
	(-0.238)	(-0.056)	(-0.050)	(-0.310)	(0.528)	(0.260)	(0.134)
112c	-0.275	-0.054	-0.083	-0.313	0.656	0.305	0.236
	(-0.196)	(-0.068)	(-0.061)	(-0.320)	(0.510)	(0.304)	(0.169)

[a] Mullican and NBO charges from the optimized structures calculated at B3LYP/6-31G(d,p); [b] hydrogen atoms summed into the heavy atoms; [c] hydrogen atom summed into heavy atom (N)

Table A-9a. Mulliken and NBO (in brackets) charges [*e*] for **109a,c**, **111a,c** and **112a-c**.[a]

	N-5	N-6	O-1	O-2	C-3[a]	E
109a	-0.263[c]	–	–	–	0.217	-0.045
	(-0.253)				(0.230)	(-0.023)
109c	-0.260[c]	–	–	–	0.182	-0.076
	(-0.238)				(0.214)	(-0.025)
111a	-0.325	0.169	-0.340	–	0.288	-0.207
	(-0.245)	(0.203)	(-0.358)		(0.271)	(-0.127)
111c	-0.375	0.192	-0.331	–	0.267	-0.245
	(-0.266)	(0.261)	(-0.365)		(0.237)	(-0.133)
112a	-0.377	0.628	-0.373	-0.393	0.294	-0.221
	(-0.324)	(0.670)	(-0.381)	(-0.408)	(0.281)	(-0.162)
112b	-0.395	0.623	-0.383	-0.344	0.264	-0.235
	(-0.310)	(0.673)	(-0.401)	(-0.352)	(0.256)	(-0.134)
112c	-0.394	0.636	-0.381	-0.397	0.303	0.236
	(-0.332)	(0.674)	(-0.393)	(-0.412)	(0.294)	(-0.169)

[a] Mulliken and NBO charges from the optimized structures calculated at B3LYP/6-31G(d,p); [b] hydrogen atoms summed into the heavy atoms; [c] hydrogen atom summed into heavy atom (N)

Table A-10. Absolute Energies (in au) for Ground State and Transition States for rotation as Optimized at the corresponding Level of Theory.

Theroretical method	**111a_iso1**	**111a_iso2**	**111a_*sp*_ts**	**111a_*ap*_ts**
-E_{tot}				
B3LYP/6-31G(d,p)	521.539532	521.537093	521.505501	521.499358
B3LYP/6-311+G(3df,2p)	521.712895	521.711023	521.679253	521.674844
ΔE				
B3LYP/6-31G(d,p)		-1.5	-21.4	-25.2
B3LYP/6-311+G(3df,2p)		-1.2	-21.1	-23.9
-E_0(6-31G(d,p))	521.422376	521.417594	521.389298	521.385733
-H^{298}(6-31G(d,p))	521.411962	521.407261	521.379148	521.375505
-G^{298}(6-31G(d,p))	521.4580375	521.452444	521.424202	521.420895
$\Delta H^{\ddagger}$		-2.9	-20.6	-22.8
$\Delta G^{\ddagger}$		-3.5	-21.2	-23.3

[a] At 298 K: **$\Delta H^{\ddagger}$** and **$\Delta G^{\ddagger}$** in kcal mol^{-1}

Table A-11. Absolute Energies (in au) for Ground State and Transition States for rotation as Optimized at the corresponding Level of Theory.

Theroretical method	**111c_iso1**	**111c_iso2**	**111c_*sp*_ts**	**111c_*ap*_ts**
-E_{tot}				
B3LYP/6-31G(d,p)	520.305804	520.299963	520.277137	520.272227
B3LYP/6-311+G(3df,2p)	520.479444	520.473416	520.451912	520.445549
ΔE				
B3LYP/6-31G(d,p)		-3.7	-18.0	-21.1
B3LYP/6-311+G(3df,2p)		-3.8	-17.3	-21.3
-E_0(6-31G(d,p))	520.209726	520.204082	520.182146	520.177070
-H^{298}(6-31G(d,p))	520.200969	520.195258	520.173938	520.168871
-G^{298}(6-31G(d,p))	520.243552	520.238149	520.214877	520.209666
$\Delta H^{\ddagger}$		-3.6	-17.0	-20.1
$\Delta G^{\ddagger}$		-3.4	-18.0	-21.3

[a] At 298 K: **$\Delta H^{\ddagger}$** and **$\Delta G^{\ddagger}$** in kcal mol^{-1}

Table A-12.. Absolute Energies (in au) for Ground State and Transition States for rotation as Optimized at the corresponding Level of Theory.

Theroretical method	**112a**	**112a_ts**	**112c**	**112c_ts**
-E_{tot}				
B3LYP/6-31G(d,p)	596.722138	596.701800	595.486083	595.471423
B3LYP/6-311+G(3df,2p)	596.924042	596.906893	595.690348	595.676786
ΔE				
B3LYP/6-31G(d,p)		-12.8		-9.2
B3LYP/6-311+G(3df,2p)		-10.8		-8.5
-E_0(6-31G(d,p))	596.596719	596.580065	595.384026	595.370146
-H^{298}(6-31G(d,p))	596.585655	596.569694	595.374808	595.361709
-G^{298}(6-31G(d,p))	596.633017	596.615461	595.418268	595.403306
$\Delta H^{\ddagger}$		-10.0		-8.2
$\Delta G^{\ddagger}$		-11.0		-9.4

[a] At 298 K: **$\Delta H^{\ddagger}$** and **$\Delta G^{\ddagger}$** in kcal mol^{-1}

Chapter VI, 2.2

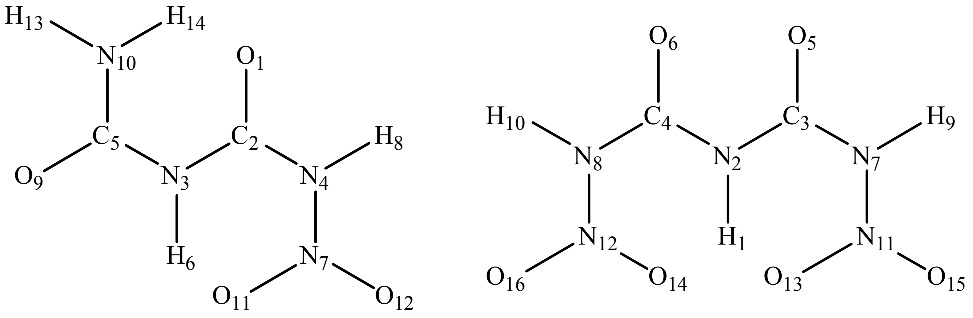

(a) (b)

Figure A-8. Labeling of the atoms in (a) MNB (**113**), (b) DNB (**114**).

Densitiy Functional Theory (DFT)[15] methods were carried out with the standard Pople 6-31G(d,p) basis set. As DFT methods, the Becke exchange functional (B)[16] and Becke's three-parameter exchange functional (B3)[17,18] in combination with both the correlational functional of Lee, Yang and Parr (LYP),[19] and with the P86[20,21] were selected. These procedures are implemented in the Gaussian-98 A11 program package.[1] The ground state minimum geometry and vibrational frequencies were determined, with the keyword OPT, by minimising the energy with respect to all geometrical parameters without imposing molecular symmetry constrains in the case of MNB (**113**). In the gas phase DNB (**113**) was found out to posses C_2 symmetry.

Table A-13. Calculated and experimental IR and Raman frequencies of **MNB**

Vib. No.	approx. assignment	calcd.[a]	IR int.[b]	Raman act.[b]	calcd.[c]	IR int.[d]	Raman act.[d]	**MNB** obs. IR[e,f]	Raman[g]
									-
ν_1	ν (NH_2)	3737	124.7	62.1	3640	112.4	92.4	3433	-
ν_2	ν (N-H)	3629	103.6	65.5	3520	81.0	87.6	3291	3291
ν_3	ν (N-H)	3562	70.2	137.7	3424	107.7	166.9	3146	3233
ν_4	ν (N-H)	3560	167.0	2.3	3421	139.6	1.6	-	-
ν_5	ν (C9=O)	1855	467.6	10.6	1802	387.6	14.9	1739vs	-
ν_6	ν (C2=O)	1803	245.2	19.6	1741	196.3	21.4	1714m[g]	1714
ν_7	ν_{asym} ($N7O_2$)	1706	324.4	2.2	1639	251.4	2.7	1630vs	1631
ν_8	δ_{sym} ($N10H_2$)	1610	249.2	11.7	1549	256.2	14.6	1572s	1577
ν_9	in plane bend (N3-H)	1540	554.8	16.2	1478	558.8	29.1	1490m	1522
ν_{10}	ν_{asym} (N3-C5-N10) + ν (N4-NO_2)	1395	128.7	13.0	1328	120.4	16.2	1431m	1425
ν_{11}	in plane bend (N4-H)	1385	31.1	11.1	1319	17.4	5.5	1383m	-
ν_{12}	ν_{sym} ($N7O_2$)	1366	424.7	2.5	1309	334.2	6.6	1335s	1352
ν_{13}	ν_{asym} (N3-C2-N4) + ν (N7-O11) + in plane bend (N3-H)	1206	268.4	1.6	1148	224.4	3.2	1200s	1194
ν_{14}	ρ (N4-H, C-$N5H_2$, rocking)	1142	9.2	3.3	1103	5.7	3.9	1117w	1119
ν_{15}	ν_{sym} (N3-C2-N4) + □ (C-$N5H_2$, rocking)	1074	101.0	4.8	1018	60.3	6.8	1072w	1074
ν_{16}	ν_{sym} (N7-NO_2)	1006	63.4	7.2	939	147.1	11.6	1015w	1011
ν_{17}	in plane bend (C5-N3)	951	16.0	15.0	918	11.2	19.6	956w	961
ν_{18}	in plane bend (C2-N4-NO_2)	780	17.6	3.3	751	19.8	3.2	777w	770
ν_{19}	out of plane bend (N-H)	776	30.2	0.4	750	19.6	1.1	756m	758
ν_{20}	out of plane bend (N-H)	764	14.6	1.0	729	2.8	0.9	717w	728
ν_{21}	out of plane bend (N-H)	734	8.6	1.0	706	2.6	0.9		-
ν_{22}	δ (C5-N3-C2)	728	4.9	0.6	696	5.1	1.2	654w	-
ν_{23}	out of plane bend (N3-H)	699	73.7	0.7	670	71.9	0.8	598m	-
ν_{24}	ω ($N10H_2$)	626	5.6	2.1	620	6.1	1.9	-	-
ν_{25}	out of plane bend (N4-H)	559	35.2	0.6	550	145.9	3.2	556m	-
ν_{26}	δ	552	150.1	2.0	533	22.9	1.1	502w	498
ν_{27}	δ	481	10.3	3.8	459	12.5	5.1	-	435
ν_{28}	δ	416	4.4	2.7	399	6.7	3.6	-	380
ν_{29}	δ	362	2.7	2.3	349	3.7	2.5	-	-
ν_{30}	out of plane bend ($N10H_2$)	338	226.5	1.8	315	212.3	2.3	-	301
ν_{31}	δ	289	36.5	1.6	278	34.4	2.2	-	212
ν_{32}	δ	151	0.6	0.3	147	0.6	0.6	-	176
ν_{33}	δ	133	1.0	0.9	127	1.8	0.7	-	141
ν_{34}	δ	94	0.1	0.3	94	0.7	0.6	-	-
ν_{35}	δ	69	0.5	0.4	62	1.8	0.3	-	-
ν_{36}	δ	27	0.1	0.5	44	0.2	0.7	-	-

[a] Calculated at Becke3LYP/6-31G(d,p); unscaled.
[b] Calculated infrared intensities [km/mole] and Raman activities [$Å^4$/amu] obtained from the Becke3LYP/6-31G(d,p).
[c] Calculated at BP86/6-31G(d,p); unscaled
[d] Calculated infrared intensities [km/mole] and Raman activities [$Å^4$/amu] obtained from the BP86/6-31G(d,p).
[e] Observed IR [KBr] and Raman spectra in solid state.
[f] vs = 90-100%, s = 70-90%, m = 40-70%, w = 10-40%, vw <10%.
[f] Shoulder

Table A-14. Calculated and experimental IR and Raman frequencies of **DNB**

Vib. No.	approx. assignment	calcd.[a]	IR int.[b]	Raman act.[b]	calcd.[c]	IR int.[d]	Raman act.[d]	DNB obs. IR[e,f]	Raman[e]
ν_1	ν (N-H)	3620	49.8	124.1	3514	41.5	162.0	3291m	3290
ν_2	ν (N-H)	3619	164.4	8.9	3513	133.0	10.4	3210m	3212
ν_3	ν (N-H)	3422	191.5	73.9	3253	167.8	107.3	3063w	3061
ν_4	ν_{sym}(C=O)	1892	479.5	44.3	1823	386.3	57.3	1764s	1760
ν_5	ν_{asym} (C=O)	1818	51.4	51.4	1755	68.9	0.3	-	-
ν_6	ν_{asym} (NO_2)	1713	7.9	7.9	1647	359.3	7.4	1630s	-
ν_7	ν_{asym} (NO_2)	1712	467.6	6.0	1646	6.2	1.1	1618s	1615
ν_8	in plane bend (N2-H)	1546	1457.9	13.2	1483	1406.8	12.9	1568s	1566
ν_9	in plane bend ν_{asym} (N7(8)-H)	1399	7.6	3.8	1331	74.8	25.9	1484w	-
ν_{10}	in plane bend ν_{sym} (N7(8)-H)	1398	46.9	1.6	1326	4.7	6.6	1464m	1465
ν_{11}	ν_{sym} (NO_2) + ν_{sym} (C4-N2-C3)	1393	249.2	39.1	1325	83.0	12.1	1336m	1349
ν_{12}	ν_{sym} (NO_2) + in plane bend (N-H)	1379	99.8	1.9	1312	93.0	1.3	1318s	1325
ν_{13}	ν_{sym} (N2-C3(4)-N7(8))	1275	539.6	2.7	1214	518.2	4.5	1228w	1223
ν_{14}	ν_{asym} (C4-N2-C3)	1143	89.9	0.8	1087	64.8	1.4	1162m[g]	-
ν_{15}	ν_{asym} (C3(4)-N7(8)	1061	119.9	5.1	1012	72.7	7.6	1154m	-
ν_{16}	ν_{sym} (N-NO_2)	1048	116.5	1.9	977	84.3	2.6	1080m	-
ν_{17}	ν_{asym} (N-NO_2)	995	53.2	0.6	923	111.2	41.6	1056m	1056
ν_{18}	δ (C4-N2-C3) + ν_{sym} (N-NO_2)	978	32.4	31.7	917	136.8	1.3	990w	987
ν_{19}	out of plane bend (N2-H) + δ (NO_2)	794	6.9	1.9	764	0.2	2.5	829vw	828
ν_{20}	δ (C4-N2-C3)	791	0.5	1.3	762	6.9	1.1	-	-
ν_{21}	out of plane bend (N2-H)	785	9.3	0.2	761	17.4	1.1	-	-
ν_{22}	δ (N-NO_2)	770	19.1	5.3	735	10.3	5.8	-	762
ν_{23}	γ_{asym} (N11(12))	759	0.3	0.2	719	0.8	0.2	-	-
ν_{24}	out of plane bend (N2-H)	749	38.6	0.6	719	21.1	0.7	755w	757
ν_{25}	γ_{sym} (N11(12))	737	95.2	0.0	700	78.2	0.3	737w	733
ν_{26}	γ_{asym} (N3(4))	701	0.0	0.6	671	0.0	0.6	-	-
ν_{27}	δ	611	97.6	0.8	586	206.0	0.4	654m	-
ν_{28}	out of plane bend (N7(9)-H)	591	0.2	2.5	581	1.0	2.7	-	-
ν_{29}	out of plane bend ν_{asym} (N7(9)-H)	589	225.1	3.3	573	86.6	6.0	638m	638
ν_{30}	out of plane bend ν_{sym} ($N10H_2$)	450	0.1	5.8	422	0.4	9.2	-	-
ν_{31}	δ	435	16.1	1.0	410	18.8	1.7	-	473
ν_{32}	δ	376	7.3	3.2	360	5.8	3.6	-	-
ν_{33}	δ	348	4.8	2.1	334	5.1	2.7	-	-
ν_{34}	δ	270	0.2	2.2	256	0.1	2.8	-	258
ν_{35}	δ	220	25.9	0-1	209	21.9	0.3	-	191
ν_{36}	γ_{sym} (N2)	158	2.2	0.5	151	3.4	0.4	-	161
ν_{37}	δ	98	0.4	0.2	103	0.5	0.4	-	-
ν_{38}	δ	87	0.0	0.8	86	0.1	0.6	-	-

[a] Calculated at Becke3LYP/6-31G(d,p); unscaled.
[b] Calculated infrared intensities [km/mole] and Raman activities [Å^4/amu] obtained from the Becke3LYP/6-31G(d,p).
[c] Calculated at BP86/6-31G(d,p); unscaled.
[d] Calculated infrared intensities [km/mole] and Raman activities [Å^4/amu] obtained from the BP86/6-31G(d,p).
[e] Observed IR [KBr] and Raman spectra in solid state.
[f] vs = 90-100%, s = 70-90%, m = 40-70%, w = 10-40%, vw <10%.
[g] Shoulder

References

[1] Frisch, M. J.; Trucks, G. W.; Schlegel, H. B.; Scuseria, G. E.; Robb, M. A.; Cheeseman, J. R.; Zakrzewski, V. G.; Montgomery, J. A.; Stratmann, Jr., R. E.; Burant, J. C.; Dapprich, S.; Millam, J. M.; Daniels, A. D.; Kudin, K. N.; Strain, M. C.; Farkas, O.; Tomasi, J.; Barone, V.; Cossi, M.; Cammi, R.; Mennucci, B.; Pomelli, C.; Adamo, C.; Clifford, S.; Ochterski, J.; Petersson, G. A.; Ayala, P. Y.; Cui, Q.; Morokuma, K.; Malick, D. K.; Rabuck, A. D.; Raghavachari, K.; Foresman, J. B.; Cioslowski, J.; Ortiz, J. V.; Stefanov, B. B.; Liu, G.; Liashenko, A.; Piskorz, P.; Komaromi, I.; Gomperts, R.; Martin, R. L.; Fox, D. J.; Keith, T.; Al-Laham, M. A.; Peng, C. Y.; Nanayakkara, A.; Gonzalez, C.; Challacombe, M.; Gill, P. M. W.; Johnson, B.; Chen, W.; Wong, M. W.; Andres, J. L.; Gonzalez, C.; Head-Gordon, M.; Replogle, E. S.; Pople, J. A. Gaussian 98, Revision A.6, Gaussian, Inc., Pittsburgh PA, **1998**.

[2] a) Reed, A. E.; Curtiss, L. A.; Weinhold, F. *Chem. Rev.* **1988**, *88*, 899; b) Reed, A. E.; Weinstock R. B.; Weinhold, F. *J. Chem. Phys.* **1985**, *83*, 735.

[3] Bader, R. F. W. *Atoms in Molecules: A Quantum Theory*; The international Series of Monographs of Chemistry; Oxford University Press, **1990**.

[4] a) NBO Version 3.1, Glendening, E. D.; Reed, A. E.; Carpenter, J. E.; Weinhold, F; b) Carpenter, J. E.; Weinhold, F. *J. Mol. Struc. (Theochem)* **1988**, *169*, 41; c) Foster, J. P.; Weinhold, F. *J. Am. Chem. Soc.* **1980**, *102*, 7211; d) Reed, A. E.; Weinhold, F. *J. Chem. Phys.* **1983**, *78*, 4066; e) Reed, A. E.; Weinstock, R. B.; Weinhold, F. *J. Chem. Phys.* **1985**, *83*, 735; f) Reed, A. E.; Schleyer, P. v. R. *J. Am. Chem. Soc.* **1987**, *109*, 7362; g) Reed, A. E.; Schleyer, P. v. R. *Inorg. Chem.* **1988**, *27*, 3969; h) Weinhold, F.; Carpenter, J. E. *The Structure of Small Molecules and Ions*, Plenum Press, **1988**, 227.

[5] a) Marcus, Y., *The Thermodynamics of Solvation of Ions. 2. The Enthalpy of Hydration at 298.15K, J. Chem. Soc. Farad. Trans. I* **1987**, *83*, 339; b) Kopel, I. A: ; Molder, U. H.; Palm, V. A. *Org. React.* **1985**, *22*, 3.

[6] Chase, M.W., Jr., *NIST-JANAF Themochemical Tables, Fourth Edition*, *J. Phys. Chem. Ref. Data, Monograph 9*. **1998**, 1.

[7] Michels, H. H.; Montgomery, Jr. J. A. *J. Phys. Chem.* **1993**, *97*, 6602.

[8] Davidson, J.A.; Fehsenfeld, F.C.; Howard, C.J., *The heats of formation of NO_3^- and NO_3^- association complexes with HNO_3 and HBr*, *Int. J. Chem. Kinet.* **1977**, *9*, 17.

[9] Schmitt, R.J.; Krempp, M.; Bierbaum, V.M. *Gas Phase Chemistry of Dinitramide and Nitroacetylide Ions*, *Int. J. Mass Spectrom. Ion Proc.* **1992**, *117*, 621.

[10] a) Franklin, J. L.; Dibeler, V. H.; Reese, R. M.; Krauss, M. *J. Am. Chem. Soc.* **1958**, *80(2)* 298; b) D'Orazio, L. A.; Wood, R. H. *J. Phys. Chem.* **1963**, *67(7)*, 1435.

[11] Cox, J.D.; Wagman, D.D.; Medvedev, V.A., CODATA Key Values for Thermodynamics, Hemisphere Publishing Corp., New York, **1984**, 1

[12] a) Chase, M.W., Jr., *NIST-JANAF Themochemical Tables, Fourth Edition*, *J. Phys. Chem. Ref. Data, Monograph 9*, ***1998***, 1-1951; b) Cox, J. D.; Wagmann, D. D.; Medvedev, *CODATA Key Values for Thermodynamics*, Hemisphere Publishing Corp., New York, **1984**, p.1.

[13] Pittam, D.A.; Pilcher, G., *Measurements of heats of combustion by flame calorimetry. Part 8.-Methane, ethane, propane, n-butane and 2-methylpropane*, *J. Chem. Soc. Faraday Trans. 1* **1972**, *68*, 2224.

[14] Illenberger, E.; Comita, P.; Brauman, J.I.; Fenzlaff, H.-P.; Heni, M.; Heinrich, N.; Koch, W.; Frenking, G., *Experimental and theoretical investigation of the azide anion (N_3^-) in the gas phase*, *Ber. Bunsen-Ges. Phys. Chem.* **1985**, *89*, 1026.

[15] Seminaro, J. M.; Politzer P. (Eds.), *Modern Density Functional Theory: a Tool for Chemistry*, vol. 2, Elsevier, Amsterdam, **1995**.

[16] Becke, A. D. *Phys. Rev.* **1988**, *A38,* 3098.

[17] Becke, A. D. *J. Chem. Phys.* **1992**, *97*, 9173.

[18] Becke, A. D. *J. Chem. Phys.* **1993**, *98*, 5648.

[19] Lee, C.; Yang, W.; Parr, R. G. *Phys. Rev.* **1988**, *A37*, 785.

[20] Perdew, J. P. *Phys. Rev.* **1986**, *B33*, 8822.

[21] Perdew, J. P. *Phys. Rev.* **1986**, *B34*, 7406.

APPENDIX B

CRYSTAL DATA

	13	**19**	**21**
Formula	$CH_4N_6O_3$	$C_4H_8N_2$	$C_4H_{16}N_{18}O$
Formula weight (g mol^{-1})	148.10	336.30	332.35
Crystal system	monoclinic	monoclinic	monoclinic
Space group	$P2_1$/c	$P\ 2_1$/n	C 2/c
Color / habit	coloress plate	yellow/organg plate	yellow rod
Size	0.30 x 0.20 x 0.10	0.57 x 0.43 x 0.20	0.40 x 0.05 x 0.03
a, Å	7.109(2)	9.928(2)	19.421(4)
b, Å	7.299(2)	6.9088(8)	3.7296(7)
c, Å	11.649(2)	10.026(2)	20.570(4)
a,deg.	90.0	90.0	90.0
β,deg.	96.990(3)	90.16(2)	108.14(3)
y,deg.	90.0	90.0	90.0
V, $Å^3$	599.9(2)	687.6(2)	1415.9(5)
Z	4	2	4
$\rho_{calc.}$, g cm^{-3}	1.640	1.624	1.559
μ, mm^{-1}	0.153	0.129	0.125
$\lambda_{MoK\alpha}$Å	0.71073	0.71073	0.71073
T, K	192(2)	295(2)	200(2)
Reflection collected	3061	2357	13402
Independent reflection	1017	1070	1617
R_{int}	0.089	0.0105	0.1034
Observed reflection	611	1052	956
F(000)	304	344	696
R_1[a] (obs)	0.0940	0.0449	0.0998
wR_2[b] (all data)	0.1035	0.1167	0.1197
Weighting scheme[b]	0.0388, 0.0000	0.0217, 1.8189	0.0614, 0.0000
GooF	0.993	1.049	1.010
No. parameters	107	110	148
Device type	Siemens P4	Nonius Mach3	Kappa CCD
Solution	SHELXS−97	SHELXS−86	SHELXS−97
Refinement	SHELXL−97	SHELXL−97	SHELXL−97
Absorption correction	−	psi-scan	−
CCDC	−	266607	266608

[a] $R_1 = \sum \| F_0 | - | F_c \| / \sum |F_0|$. [b] $wR_2 = \left[\sum [w (F_0^2 - F_c^2)^2] / \sum [w (F_0)^2] \right]^{1/2}$, where $w = \left[\sigma_c^2 (F_0^2) + (xP)^2 + yP \right]^{-1}$, $P = (F_0^2 - 2F_c^2) / 3$

APPENDIX B

CRYSTAL DATA

	34	**35**	**36**
Formula	$C_2Cs_2N_6$	$C_9H_{24}N_8O$	$C_2H_{11}N_9OPd$
Formula weight (g mol^{-1})	373.90	260.36	283.60
Crystal system	monoclinic	triclinic	monoclinic
Space group	$P2_1$/n	P-1	$P2_1$/n
Color / habit	colorless block	colorless plate	yellow parallelepipel
Size	0.25 x 0.09 x 0.07	0.57 x 0.40 x 0.33	0.53 x 0.47 x 0.20
a, Å	7.345(2)	7.141(2)	7.988(2)
b, Å	9.505(2)	9.539(2)	8.375(2)
c, Å	10.198(2)	12.817(4)	13.541(3)
a,deg.	90.0	72.51(2)	90.0
β,deg.	93.12(3))	85.21(2)	104.56(3)
y,deg.	90.0	67.39(2)	90.0
V, Å^3	710.9(2)	768.3(3)	876.8(3)
Z	4	2	4
$\rho_{calc.}$, g cm^{-3}	3.493	1.125	2.148
μ, mm^{-1}	10.185	0.080	2.098
$\lambda_{MoK\alpha}$Å	0.71073	0.71073	0.71073
T, K	200(2)	295(2)	295(2)
Reflection collected	11869	2520	1846
Independent reflection	1612	2396	1719
R_{int}	0.0430	0.0080	0.0079
Observed reflection	1524	1977	1668
F(000)	656	284	560
R_1[a] (obs)	0.0175	0.0529	0.0195
wR_2[b] (all data)	0.0405	0.1104	0.0533
Weighting scheme[b]	0.0107, 0.4285	0.0545, 0.2685	0.0286, 0.9463
GooF	1.224	0.995	1.157
No. parameters	91	170	119
Device type	Kappa CCD	Nonius Mach3	Nonius Mach3
Solution	SHELXS−97	SHELXS−86	SHELXS−97
Refinement	SHELXL−97	SHELXL−93	SHELXL−97
Absorption correction	numerical	psi-scan	psi-scan
CCDC	267201	267216	267217

[a] $R_1 = \sum \|F_0\| - \|F_c\| / \sum \|F_0\|$. [b] $wR_2 = \left[\sum[w(F_0^2 - F_c^2)^2] / \sum[w(F_0)^2]\right]^{1/2}$, where $w = \left[\sigma_c^2(F_0^2) + (xP)^2 + yP\right]^{-1}$, $P = (F_0^2 - 2F_c^2)/3$

APPENDIX B

CRYSTAL DATA

	37	**38**	**38**
Formula	$C_2Cs_2N_6O_5S_2$	$NaC_4H_5N_{18}$*$3H_2O$	$CsC_2H_2N_9$*H_2O
Formula weight (g mol^{-1})	518.02	382.30	303.05
Crystal system	monoclinic	orthorhombic	triclinic
Space group	$P2_1$	$P2_12_12_1$	P-1
Color / habit	coloreless platelet	colorless plate	colorless plate
Size	0.20 x 0.10 x 0.03	0.27 x 0.40 x 0.57	0.30 x 0.25 x 0.10
a, Å	8.0080(2)	6.3914(5)	5.477(1)
b, Å	8.0183(2)	12.445(1)	6.992(1)
c, Å	9.8986(3)	18.482(3)	10.917(2)
a,deg.	90.0	90	104.61(3)
β,deg.	108.619(1)	90	90.91(3)
y,deg.	90.0	90	98.02(3)
V, Å^3	602.33(3)	1470.1(3)	400.0(1)
Z	2	4	2
$\rho_{calc.}$, g cm^{-3}	2.856	1.727	2.516
μ, mm^{-1}	6.417	0.168	4.607
$\lambda_{MoK\alpha}$Å	0.71073	0.71073	0.71073
T, K	200(2)	293(2)	213(2)
Reflection collected	7607	2743	1475
Independent reflection	2752	2316	1322
R_{int}	0.069	0.077	0.0128
Observed reflection	2583	2201	1201
F(000)	472	784	284
R_1[a] (obs)	0.0287	0.0426	0.0404
wR_2[b] (all data)	0.0605	0.1253	0.0978
Weighting scheme[b]	0.0206, 0.000	0.0687, 0.9271	0.0814, 0.000
GooF	1.019	1.125	1.040
No. parameters	154	236	130
Device type	Kappa CCD	Nonius Mach3	Siemens P4
Solution	SIR97	SHELXS−93	SHELXS−97
Refinement	SHELXL−97	SHELXL−97	SHELXL−97
Absorption correction	numerical	psi-scan	SADABS
CCDC	267200	−	−

[a] $R_1 = \sum \| F_0| - |F_c\| / \sum |F_0|$. [b] $wR_2 = \left[\sum [w(F_0^2 - F_c^2)^2] / \sum [w(F_0)^2] \right]^{1/2}$, where $w = \left[\sigma_c^2(F_0^2) + (xP)^2 + yP \right]^{-1}$, $P = (F_0^2 - 2F_c^2)/3$

A P P E N D I X B

CRYSTAL DATA

	40	**42**	**43**
Formula	$Li_2C_2HN_9*5H_2O$	$Na_2C_2HN_9*2H_2O$	$Rb_2C_2HN_9*H_2O$
Formula weight (g mol^{-1})	255.08	233.13	340.07
Crystal system	monoclinic	monoclinic	orthorhombic
Space group	$P2_1/n$	$P2_1/m$	*P*ba2
Color / habit	colorless prism	coloreless platelet	colorless plate
Size	0.20 x 0.40 x 0.53	0.07 x 0.40 x 0.53	0.07 x 0.27 x 0.53
a, Å	8.311(2)	5.9316(4)	24.900(3)
b, Å	10.538(3)	6.480(1)	9.614(1)
c, Å	12.882(3)	10.807(2)	3.9332(9)
a,deg.	90	90	90
β,deg.	91.89(2)	97.116(9)	90
y,deg.	90	90	90
V, Å^3	1127.4 (4)	412.2(1)	941.5(3)
Z	4	2	4
$\rho_{calc.}$, g cm^{-3}	1.502	1.878	1.727
μ, mm^{-1}	0.132	0.242	2.399
$\lambda_{MoK\alpha}$Å	0.71073	0.71073	0.71073
T, K	293(2)	293(2)	293(2)
Reflection collected	1900	1500	1836
Independent reflection	1767	712	1472
R_{int}	0.004	0.008	0.0095
Observed reflection	1550	680	1257
F(000)	528	236	640
R_1^a (obs)	0.0447	0.0261	0.0331
wR_2^b (all data)	0.1049	0.0691	0.0682
Weighting scheme[b]	0.0534, 0.6178	0.0418, 0.2070	0.0434, 0.0682
GooF	1.098	1.064	1.001
No. parameters	164	99	140
Device type	Nonius Mach3	Nonius Mach3	Nonius Mach3
Solution	SHELXS−93	SHELXS−93	SHELXS−93
Refinement	SHELXL−97	SHELXL−97	SHELXL−97
Absorption correction	psi-scan	psi-scan	psi-scan
CCDC	–	–	–

[a] $R_1 = \sum \left\| F_0 \right| - \left| F_c \right\| / \sum \left| F_0 \right|$. [b] $wR_2 = \left[\sum [w(F_0^2 - F_c^2)^2] / \sum [w(F_0)^2] \right]^{1/2}$, where $w = \left[\sigma_c^2(F_0^2) + (xP)^2 + yP \right]^{-1}$, $P = (F_0^2 - 2F_c^2)/3$

APPENDIX B

CRYSTAL DATA

	44	**45**	**46**
Formula	$Cs_2C_2HN_9*5H_2O$	$CaC_2HN_9*5H_2O$	$BaC_2HN_9*5H_2O$
Formula weight (g mol^{-1})	434.95	281.28	360.52
Crystal system	orthorhombic	monoclinic	triclinic
Space group	Pmc2$_1$	P2/n	P-1
Color / habit	colorless plate	colorless plate	colorless plate
Size	0.27 x 0.27 x 0.04	0.10 x 0.27 x 0.53	0.10 x 0.27 x 0.33
a, Å	4.119(2)	11.809(1)	6.7410(9)
b, Å	12.378(2)	6.964(1)	9.084(1)
c, Å	10.065(2)	13.572(2)	9.488(7)
a,deg.	90	90	97.702(9)
β,deg.	90	101.08	103.514(8)
y,deg.	90	90	108.19(1)
V, Å^3	513.2(3)	1095.3(3)	518.7(1)
Z	2	4	2
$\rho_{calc.}$, g cm^{-3}	2.815	1.706	2.308
μ, mm^{-1}	7.092	0.606	3.850
$\lambda_{MoK\alpha}$Å	0.71073	0.71073	0.71073
T, K	293(2)	293(2)	293(2)
Reflection collected	1218	1805	1937
Independent reflection	1148	1773	1817
R_{int}	0.0241	0.0093	0.0064
Observed reflection	1141	1489	1795
F(000)	392	584	344
R_1[a] (obs)	0.0348	0.0392	0.0125
wR_2[b] (all data)	0.0908	0.0964	0.0350
Weighting scheme[b]	0.0785, 0.3568	0.0496, 1.3286	0.0198, 0.5474
GooF	1.088	1.024	1.085
No. parameters	186	156	171
Device type	Nonius Mach3	Nonius Mach3	Nonius Mach3
Solution	SHELXS−93	SHELXS−93	SHELXS−93
Refinement	SHELXL−97	SHELXL−97	SHELXL−97
Absorption correction	psi-scan	psi-scan	psi-scan
CCDC	–	–	–

[a] $R_1 = \sum \|F_0\| - \|F_c\| / \sum \|F_0\|$. [b] $wR_2 = \left[\sum [w(F_0^2 - F_c^2)^2] / \sum [w(F_0)^2]\right]^{1/2}$, where $w = \left[\sigma_c^2(F_0^2) + (xP)^2 + yP\right]^{-1}$, $P = (F_0^2 - 2F_c^2)/3$

A P P E N D I X B

CRYSTAL DATA

	47	**48**	**50**
Formula	$CuC_2H_7N_{11}$	$CuC_2H_9N_{11}O$	$CuC_2H_5N_9Cl_2O*5H_2O$
Formula weight (g mol^{-1})	248.70	266.71	341.62
Crystal system	monoclinic	monoclinic	triclinic
Space group	$P2_1$/n	$P2_1$/c	*P*-1
Color / habit	blue rods	blue prism	blue stick
Size	0.25 x 0.10 x 0.06	0.30 x 0.25 x 0.15	0.57 x 0.33 x 0.27
a, Å	6.3778(5)	7.596(2)	7.2027(8)
b, Å	9.1886(7)	13.056(3)	8.289(3)
c, Å	14.2064(9)	9.170(2)	9.998(2)
a,deg.	90	90	79.47(2)
β,deg.	93.633(8)	94.20(3)	78.948(8)
y,deg.	90	90	82.097(1)
V, Å^3	830.9(1)	907.0(3)	573.1(2)
Z	4	4	2
$\rho_{calc.}$, g cm^{-3}	1.9882	1.953	1.980
μ, mm^{-1}	2.611	2.407	2.387
$\lambda_{MoK\alpha}$Å	0.71073	0.71073	0.71073
T, K	200(2)	213(2)	295(2)
Reflection collected	6667	4087	2490
Independent reflection	1992	1741	2322
R_{int}	0.0395	0.00234	0.0152
Observed reflection	1595	1557	2183
F(000)	500	540	342
R_1^a (obs)	0.0241	0.0294	0.0235
wR_2^b (all data)	0.0561	0.0695	0.0615
Weighting scheme^b	0.0339, 0.0000	0.0436, 0.3853	0.0302, 0.3383
GooF	0.950	1.058	1.130
No. parameters	155	172	166
Device type	STOE IPDS	Siemens P4	Nonius Mach3
Solution	SIR97	SHELXS−97	SHELXS−93
Refinement	SHELXL−97	SHELXL−97	SHELXL−97
Absorption correction	numerical	SADABS	psi-scan
CCDC	269320	269321	−

$^a R_1 = \sum\|F_0|-|F_c\|/\sum|F_0|$. $^b wR_2 = \left[\sum[w(F_0^2-F_c^2)^2]/\sum[w(F_0)^2]\right]^{1/2}$, where $w = \left[\sigma_c^2(F_0^2)+(xP)^2+yP\right]^{-1}$, $P=(F_0^2-2F_c^2)/3$

A P P E N D I X B

CRYSTAL DATA

	51	**52**	**53**
Formula	$CuC_4H_6N_{18}Cl_2$	$CuC_4H_6N_{18}Cl_2*2H_2O$	$CuC_4H_8N_{18}Cl_2O_9$
Formula weight (g mol^{-1})	440.71	447.74	586.72
Crystal system	triclinic	monoclinic	triclinic
Space group	P-1	$P2_1$/n	P-1
Color / habit	blue plate	pale-blue plate	blue platelet
Size	0.30 x 0.27 x 0.10	0.27 x 0.20 x 0.07	0.47 x 0.37 x 0.23
a, Å	7.561(1)	9.749(3)	7.620(2)
b, Å	10.612(2)	6.822(4)	11.930(2)
c, Å	11.299(2)	12.347(5)	12.076(2)
a,deg.	115.88(2)	90	113.39(3)
β,deg.	96.806(1)	96.83(3)	103.27(3)
y,deg.	106.82(2)	90	103.33(3)
V, $Å^3$	748.5(2)	815.3(6)	914.9(5)
Z	2	2	2
$\rho_{calc.}$, g cm^{-3}	1.9955	1.942	2.130
μ, mm^{-1}	1.854	1.719	1.581
$\lambda_{MoK\alpha}$Å	0.71073	0.71073	0.71073
T, K	295(2)	295(2)	295(2)
Reflection collected	2477	1336	3828
Independent reflection	2342	1273	3543
R_{int}	0.0085	0.0430	0.0095
Observed reflection	2178	1118	3267
F(000)	438	478	586
R_1[a] (obs)	0.0252	0.0392	0.0426
wR_2[b] (all data)	0.0589	0.0318	0.0394
Weighting scheme[b]	0.0275, 0.6072	0.00391, 1.2099	0.0621, 1.2531
GooF	1.063	1.115	1.046
No. parameters	226	124	356
Device type	STOE IPDS	Nonius Mach3	Nonius Mach3
Solution	SHELXS−93	SHELXS−93	SHELXS−93
Refinement	SHELXL−97	SHELXL−97	SHELXL−97
Absorption correction	psi-scan	psi-scan	psi-scan
CCDC	–	–	–

[a] $R_1 = \sum \left\| F_0 \right| - \left| F_c \right\| / \sum \left| F_0 \right|$. [b] $wR_2 = \left[\sum [w(F_0^2 - F_c^2)^2] / \sum [w(F_0)^2] \right]^{1/2}$, where $w = \left[\sigma_c^2(F_0^2) + (xP)^2 + yP \right]^{-1}$, $P = (F_0^2 - 2F_c^2)/3$

A P P E N D I X   B

CRYSTAL DATA

	54	**59a**	**59b**
Formula	$CoC_6H_8N_{27}Cl_2$	$CH_5N_6^+NO_3^-$	$CH_5N_6^+ClO_4^-$
Formula weight (g mol^{-1})	588.22	163.12	200.56
Crystal system	tetragonal	monoclinic	monoclinic
Space group	*I*-4	*C*2/c	*P*2$_1$/n
Color / habit	red rhomb	colorless plate	colorless rhomb
Size	0.16 x 0.28 x 0.45	0.53 x 0.47 x 0.20	0.30 x 0.30 x 0.20
a, Å	10.4773(6)	17.898(3)	9.063(3)
b, Å	10.4773(6)	5.2292(8)	5.013(1)
c, Å	17.9842(11)	14.479(2)	15.659(4)
a,deg.	90	90	90
β,deg.	90	112.23(1)	100.022(5)
y,deg.	90	90	90
V, Å^3	1974.2(2)	1254.5(3)	700.5(4)
Z	4	8	4
$\rho_{calc.}$, g cm^{-3}	1.979	1.727	1.902
μ, mm^{-1}	1.209	0.159	0.537
$\lambda_{MoK\alpha}$Å	0.71073	0.71073	0.71073
T, K	200(2)	293(2)	193(2)
Reflection collected	8608	1027	3744
Independent reflection	2374	981	1447
R_{int}	0.047	0.015	0.0731
Observed reflection	2225	900	1225
F(000)	1176	672	408
R_1[a] (obs)	0.0248	0.0346	0.0466
wR_2[b] (all data)	0.0539	0.0861	0.1061
Weighting scheme[b]	0.0315, 0.0000	0.00446, 1.452	0.0598, 0.1484
GooF	1.020	1.050	1.068
No. parameters	176	101	129
Device type	Kappa CCD	Nonius Mach3	Siemens P4
Solution	SHELXL−97	SHELXS−86	SHELXS−97
Refinement	SHELXL−97	SHELXL−93	SHELXL−97
Absorption correction	−	psi-scan	SADABS
CCDC	−	261253	261252

[a] $R_1 = \sum \| F_0 | - | F_c \| / \sum | F_0 |$. [b] $wR_2 = \left[\sum [w(F_0^2 - F_c^2)^2] / \sum [w(F_0)^2] \right]^{1/2}$, where $w = \left[\sigma_c^2(F_0^2) + (xP)^2 + yP \right]^{-1}$, $P = (F_0^2 - 2F_c^2)/3$

CRYSTAL DATA

	61a	**61b**	**61c**
Formula	$C_2H_7N_6^+I^-$	$C_2H_7N_6^+NO_3^-$	$CH_5N_6^+N(NO_2)_4^-$
Formula weight (g mol^{-1})	227.12	163.12	221.17
Crystal system	orthorhombic	orthorhombic	orthorhombic
Space group	Pna2$_1$	Fdd2	$P2_12_12_1$
Color / habit	colorless prism	colorless plate	colorless block
Size	0.20 x 0.20 x 0.10	0.40 x 0.20 x 0.10	0.23 x 0.15 x 0.05
a, Å	8.9104(9)	18.547(2)	5.2632(2)
b, Å	16.506(2)	30.709(8)	12.3766(5)
c, Å	5.4554(6)	5.4554(2)	13.1225(6)
a,deg.	90	90	90
β,deg.	90	90	90
y,deg.	90	90	90
V, Å^3	802.35(2)	3125.8(5)	854.81(6)
Z	4	16	4
$\rho_{calc.}$, g cm^{-3}	1.880	1.506	1.719
μ, mm^{-1}	3.910	0.134	0.156
$\lambda_{MoK\alpha}$Å	0.71073	0.71073	0.71073
T, K	200(2)	213(2)	200(2)
Reflection collected	4473	4017	8108
Independent reflection	1612	1230	1513
R_{int}	0.0549	0.0861	0.067
Observed reflection	1104	983	1192
F(000)	452	1472	456
R_1[a] (obs)	0.0488	0.0587	0.0363
wR_2[b] (all data)	0.0740	0.1176	0.0888
Weighting scheme[b]	0.0430, 0.000	0.0736, 0.000	0.0510, 0.000
GooF	0.868	1.050	1.020
No. parameters	93	137	129
Device type	Siemens P4	Siemens P4	Kappa CCD
Solution	SHELXS−97	SHELXS−97	SIR97
Refinement	SHELXL−97	SHELXL−97	SHELXL−97
Absorption correction	SADABS	SADABS	−
CCDC	261254	261255	258034

[a] $R_1 = \sum \| F_0 | - | F_c \| / \sum | F_0 |$. [b] $wR_2 = \left[\sum [w(F_0^2 - F_c^2)^2] / \sum [w(F_0)^2] \right]^{1/2}$, where $w = \left[\sigma_c^2(F_0^2) + (xP)^2 + yP \right]^{-1}$, $P = (F_0^2 - 2F_c^2)/3$

A P P E N D I X   B

CRYSTAL DATA

	61d	**88a**	**88b**
Formula	$C_2H_7N_6^+N_3^-$	$C_2H_6N_6*H_2O$	$C_3H_8N_6$
Formula weight (g mol^{-1})	157.17	132.14	128.14
Crystal system	orthorhombic	monoclinic	orthorhombic
Space group	Pna2_1	$P2_1$/c	Pbca
Color / habit	colorless rod	colorless plate	colorless block
Size	0.26 x 0.05 x 0.02	0.20 x 0.43 x 0.57	0.11 x 0.15 x 0.18
a, Å	7.815(2)	6.2614(6)	11.4361(3)
b, Å	17.913(4)	13.655(2)	7.4653(2)
c, Å	5.262(1)	7.063(1)	14.5448(4)
a,deg.	90	90	90
β,deg.	90	98.662(9)	90
y,deg.	90	90	90
V, Å^3	736.7(3)	597.0(1)	1241.75(6)
Z	4	4	8
$\rho_{calc.}$, g cm^{-3}	1.417	1.470	1.371
μ, mm^{-1}	0.111	0.119	0.101
$\lambda_{MoK\alpha}$Å	0.71073	0.71073	0.71073
T, K	200(2)	293(2)	200(2)
Reflection collected	6387	2302	9213
Independent reflection	1157	1048	1098
R_{int}	0.1045	0.0262	0.046
Observed reflection	705	916	862
F(000)	328	280	544
R_1[a] (obs)	0.1172	0.0439	0.0369
wR_2[b] (all data)	0.1290	0.1233	0.0927
Weighting scheme[b]	0.0504, 0.0000	0.0693, 01.779	0.0440, 0.2661
GooF	0.976	1.098	1.060
No. parameters	113	81	115
Device type	STOE IPDS	Nonius Mach3	Kappa CCD
Solution	SHELXL−97	SHELXS−86	SIR97
Refinement	SHELXL−97	SHELXL−93	SHELXL−97
Absorption correction	numerical	psi-scan	numerical
CCDC	261459	−	−

[a] $R_1 = \sum \| F_0 | - | F_c \| / \sum | F_0 |$. [b] $wR_2 = \left[\sum [w(F_0^2 - F_c^2)^2] / \sum [w(F_0)^2] \right]^{1/2}$, where $w = \left[\sigma_c^2(F_0^2) + (xP)^2 + yP \right]^{-1}$, $P = (F_0^2 - 2F_c^2)/3$

A P P E N D I X   B

CRYSTAL DATA

	105a	**106a**	**84d**
Formula	$C_2H_6N_5{}^+Br^-$	$C_2H_6N_5$	$C_{16}H_{28}N_{12}$
Formula weight (g mol^{-1})	180.03	99.11	388.50
Crystal system	monoclinic	monoclinic	monoclinic
Space group	$P2_1$/n	$P2_1$/n	$P2_1$/n
Color / habit	colorless plate	colorless plate	colorless rod
Size	0.20 x 0.20 x 0.10	0.20 x 0.40 x 0.57	0.22 x 0.05 x 0.03
a, Å	5.5296(7)	4.948(1)	5.442(1)
b, Å	8.929(1)	13.737(5)	12.598(3)
c, Å	12.849(2)	6.912(1)	14.262(3)
a,deg.	90	90	90
β,deg.	102.069(9)	108.73(2)	94.89(2)
y,deg.	90	90	90
V, Å^3	620.3(1)	445.0(2)	974.2(3)
Z	4	4	2
$\rho_{calc.}$, g cm^{-3}	1.928	1.479	1.324
μ, mm^{-1}	6.529	0.112	0.090
$\lambda_{MoK\alpha}$Å	0.71073	0.71073	0.71073
T, K	193(2)	293(2)	292(2)
Reflection collected	2700	757	10917
Independent reflection	850	698	1714
R_{int}	0.0331	0.0293	0.1497
Observed reflection	679	534	783
F(000)	352	208	416
$R_1{}^a$ (obs)	0.0495	0.0644	0.0969
w$R_2{}^b$ (all data)	0.1100	0.1383	0.1676
Weighting scheme[b]	0.0896, 0.000	0.0811, 0.1448	0.0310, 0.0000
GooF	0.957	1.084	0.891
No. parameters	77	66	184
Device type	Siemens P4	Nonius Mach3	Kappa CCD
Solution	SHELXS−97	SHELXS−86	SHELXL−97
Refinement	SHELXL−97	SHELXL−93	SHELXL−97
Absorption correction	SADABS	psi-scan	numerical
CCDC	–	–	–

[a] $R_1 = \sum\|F_0| - |F_c\| / \sum|F_0|$. [b] $wR_2 = \left[\sum[w(F_0^2 - F_c^2)^2] / \sum[w(F_0)^2]\right]^{1/2}$, where $w = \left[\sigma_c^2(F_0^2) + (xP)^2 + yP\right]^{-1}$, $P = (F_0^2 - 2F_c^2)/3$

A P P E N D I X   B

CRYSTAL DATA

	104	**109a**	**109b**
Formula	$K_2C_4H_6N_{12}*3H_2O$	$C_4H_7N_5$	$C_3H_5N_5$
Formula weight (g mol^{-1})	354.46	113.12	111.12
Crystal system	monoclinic	orthorhombic	monoclinic
Space group	*C*2/c	*P*bca	$P2_1$/n
Color / habit	colorless rods	colorless rods	Yellow plate
Size	0.27 x 0.33 x 0.57	0.20 x 0.06 x 0.06	0.53 X 0.47 x 0.27
a, Å	18.756(5)	9.9999(4)	7.4471(9)
b, Å	10.248(2)	7.6682(3)	6.8100(6)
c, Å	7.2643(2)	14.192(5)	10.200(1)
a,deg.	90	90	90
β,deg.	90.02(3)	90	110.613(9)
y,deg.	90	90	90
V, Å^3	1396.3(6)	1088.24(7)	484.19(9)
Z	4	8	4
$\rho_{calc.}$, g cm^{-3}	1.686	1.381	1.524
μ, mm^{-1}	0.712	0.101	0.122
$\lambda_{MoK\alpha}$Å	0.71073	0.71073	0.71073
T, K	293(2)	200(2)	295(2)
Reflection collected	1138	10739	897
Independent reflection	1102	1240	847
R_{int}	0.0196	0.0655	0.0029
Observed reflection	1055	822	749
F(000)	728	480	232
R_1[a] (obs)	0.0263	0.0861	0.0417
wR_2[b] (all data)	0.0709	0.1477	0.1023
Weighting scheme[b]	0.0392, 0.0000	0.0921, 0.0260	0.0507, 0.1298
GooF	1.030	1.030	1.097
No. parameters	96	101	78
Device type	Nonius Mach3	Kappa CCD	Nonius Mach3
Solution	SHELXS−86	SHELXL−97	SHELXS−86
Refinement	SHELXL−93	SHELXL−97	SHELXL−93
Absorption correction	psi-scan	numerical	psi-scan
CCDC	–	269259	269260

[a] $R_1 = \sum\|F_0| - |F_c\| / \sum|F_0|$. [b] $wR_2 = \left[\sum[w(F_0^2 - F_c^2)^2] / \sum[w(F_0)^2]\right]^{1/2}$, where $w = \left[\sigma_c^2(F_0^2) + (xP)^2 + yP\right]^{-1}$, $P = (F_0^2 - 2F_c^2)/3$

APPENDIX B

CRYSTAL DATA

	111a	**111c**	**112a**
Formula	$C_4H_6N_6O$	$C_3H_4N_6O$	$C_4H_6N_6O_2$
Formula weight (g mol^{-1})	142.14	140.10	158.12
Crystal system	monoclinic	monoclinic	orthorhombic
Space group	$P2_1$/c	$P2_1$/c	*P*bca
Color / habit	colorless plates	colorless plate	colorless plate
Size	0.53 x 0.37 x 0.20	0.20 x 0.35 x 0.13	0.24 X 0.10 x 0.04
a, Å	14.045(2)	6.0853(2)	5.9553(4)
b, Å	5.788(2)	8.1184(3)	13.284(1)
c, Å	8.231(5)	11.6028(4)	17.444(2)
a,deg.	90	90	90
β,deg.	102.28(2)	99.647(2)	90
y,deg.	90	90	90
V, Å^3	653.8(3)	565.11(3)	1380.0(2)
Z	4	4	8
$\rho_{calc.}$, g cm^{-3}	1.444	1.647	1.522
μ, mm^{-1}	0.115	0.132	0.128
$\lambda_{MoK\alpha}$Å	0.71073	0.71073	0.71073
T, K	295(2)	200(2)	200(2)
Reflection collected	1107	8273	6175
Independent reflection	1023	1289	1199
R_{int}	0.0213	0.0338	0.0508
Observed reflection	854	1089	1486
F(000)	296	288	456
R_1[a] (obs)	0.0566	0.0505	0.0735
wR_2[b] (all data)	0.1221	0.1170	0.0943
Weighting scheme[b]	0.0630, 0.2299	0.0734, 0.0931	0.0534, 0.0000
GooF	1.042	1.057	0.878
No. parameters	93	108	124
Device type	Nonius Mach3	Kappa CCD	Kappa CCD
Solution	SHELXS−86	SIR97	SIR97
Refinement	SHELXL−93	SHELXL−97	SHELXL−97
Absorption correction	psi-scan	numerical	numerical
CCDC	269261	269262	269263

[a] $R_1 = \sum \| F_0 | - | F_c \| / \sum | F_0 |$. [b] $wR_2 = \left[\sum [w (F_0^2 - F_c^2)^2] / \sum [w (F_0)^2] \right]^{1/2}$, where $w = \left[\sigma_c^2 (F_0^2) + (xP)^2 + yP \right]^{-1}$, $P = (F_0^2 - 2F_c^2) / 3$

APPENDIX B

CRYSTAL DATA

	112b	**112c**	**113**
Formula	$C_7H_{14}N_6O_2$	$C_3H_4N_6O_2$	$C_2H_4N_4O_4$
Formula weight (g mol^{-1})	214.23	156.12	148.08
Crystal system	monoclinic	monoclinic	monoclinic
Space group	$P2_1$/n	$P2_1$/c	*P*21/c
Color / habit	colorless plates	colorless plate	colorless plates
Size	0.42 x 0.14 x 0.04	0.20 x 0.47 x 0.53	0.23 x 0.10 x 0.04
a, Å	8.609(1)	6.2083(8)	16.6440(8)
b, Å	12.5135(9)	8.683(1)	10.5023(5)
c, Å	10.579(1)	11.651(2)	6.3862(4)
a,deg.	90	90	90
β,deg.	106.90(1)	102.31(1)	106.353(2)
y,deg.	90	90	90
V, Å^3	1090.5(2)	613.7(2)	1071.2(1)
Z	4	4	8
$\rho_{calc.}$, g cm^{-3}	1.305	1.690	1.837(2)
μ, mm^{-1}	0.100	0.143	0.175
$\lambda_{MoK\alpha}$Å	0.71073	0.71073	0.71073
T, K	200(2)	295(2)	200(2)
Reflection collected	9229	1049	12484
Independent reflection	2544	953	2343
R_{int}	0.0508	0.0100	0.0529
Observed reflection	1486	753	1951
F(000)	456	320	608
R_1[a] (obs)	0.0837	0.0711	0.0594
wR_2[b] (all data)	0.0976	0.1384	0.1006
Weighting scheme[b]	0.0522, 0.0000	0.0463, 0.8519	0.0463, 0.5709
GooF	0.877	1.041	1.093
No. parameters	192	100	212
Device type	STOE IPDS	Nonius Mach3	Kappa CCD
Solution	SIR97	SHELXS−86	SIR97
Refinement	SHELXL−97	SHELXL−93	SHELXL−97
Absorption correction	numerical	psi-scan	numerical
CCDC	269264	269265	–

[a] $R_1 = \sum \|F_0| - |F_c\| / \sum |F_0|$. [b] $wR_2 = \left[\sum[w(F_0^2 - F_c^2)^2] / \sum[w(F_0)^2]\right]^{1/2}$, where $w = \left[\sigma_c^2(F_0^2) + (xP)^2 + yP\right]^{-1}$, $P = (F_0^2 - 2F_c^2)/3$

A P P E N D I X   B

CRYSTAL DATA

	114	**114a**	**117**
Formula	$C_2H_3N_5O_6$*H_2O	$C_2H_3N_5O_6$	$K_2C_2HN_5O_6$*H_2O
Formula weight (g mol^{-1})	211.09	193.08	287.27
Crystal system	monoclinic	orthorhombic	triclinic
Space group	*I*2/a	$P2_12_12_1$	*P*-1
Color / habit	colorless plates	colorless block	colorless prism
Size	0.29 x 0.08 x 0.03	0.40 x 0.15 x 0.10	0.07 x 0.11 x 0.17
a, Å	16.516(2)	4.6497(9)	6.8514(2)
b, Å	4.5873(3)	9.805(2)	6.8965(2)
c, Å	20.657(2)	13.990(3)	10.5849(4)
a,deg.	90	90	105.713(1)
β,deg.	105.44(1)	90	106.048(1)
y,deg.	90	90	97.328(1)
V, $Å^3$	1508.6(3)	637.8(2)	451.48(3)
Z	8	4	2
$\rho_{calc.}$, g cm^{-3}	1.859(4)	2.011	2.113(2)
μ, mm^{-1}	0.186	0.199	1.085
$\lambda_{MoK\alpha}$Å	0.71073	0.71073	0.71073
T, K	200(2)	213(2)	200(2)
Reflection collected	5094	2945	6794
Independent reflection	1775	1512	2038
R_{int}	0.0463	0.0526	0.037
Observed reflection	1085	793	1720
F(000)	864	392	288
R_1[a] (obs)	0.0753	0.0457	0.0381
wR_2[b] (all data)	0.0811	0.0833	0.0644
Weighting scheme[b]	0.0415, 0.0000	0.0305, 0.0000	0.0161, 0.1785
GooF	0.852	0.852	1.077
No. parameters	147	130	157
Device type	STOE IPDS	Siemens P4	Kappa CCD
Solution	SHELXL−97	SHELXS−97	SIR97
Refinement	SHELXL−97	SHELXL−97	SHELXL−97
Absorption correction	numerical	SADABS	numerical
CCDC	–	–	–

[a] $R_1 = \sum \lVert F_0 \rvert - \lvert F_c \rVert / \sum \lvert F_0 \rvert$. [b] $wR_2 = \left[\sum [w(F_0^2 - F_c^2)^2] / \sum [w(F_0)^2]\right]^{1/2}$, where $w = \left[\sigma_c^2(F_0^2) + (xP)^2 + yP\right]^{-1}$, $P = (F_0^2 - 2F_c^2)/3$

APPENDIX B

CRYSTAL DATA

	34 (Sachstands-bericht)
Formula	$C_5H_{11}N_9O_6$
Formula weight (g mol^{-1})	293.23
Crystal system	triclinic
Space group	*P*-1
Color / habit	colorless plates
Size	0.05 x 0.18 x 0.25
a, Å	6.4156(3)
b, Å	9.6462(5)
c, Å	11.2536(8)
a,deg.	112.136(2)
β,deg.	105.175(2)
y,deg.	91.8209(2)
V, Å^3	615.95(6)
Z	2
$\rho_{calc.}$, g cm^{-3}	1.581(3)
μ, mm^{-1}	0.141
$\lambda_{MoK\alpha}$Å	0.71073
T, K	200(2)
Reflection collected	6737
Independent reflection	2119
R_{int}	0.043
Observed reflection	1415
F(000)	304
R_1[a] (obs)	0.0780
wR_2[b] (all data)	0.1177
Weighting scheme[b]	0.00609, 0.0000
GooF	1.035
No. parameters	231
Device type	STOE IPDS
Solution	SHELXL−97
Refinement	SHELXL−97
Absorption correction	numerical
CCDC	–

[a] $R_1 = \sum \| F_0 | - | F_c \| / \sum | F_0 |$. [b] $wR_2 = \left[\sum [w (F_0^2 - F_c^2)^2] / \sum [w (F_0)^2] \right]^{1/2}$,

where $w = \left[\sigma_c^2 (F_0^2) + (xP)^2 + yP \right]^{-1}$, $P = (F_0^2 - 2F_c^2) / 3$

Full List of Publications:

<u>22</u>

BTA Transition Metal Complexes – Anriferromagnetic Coupling in a Chain-Type Copper(II) Complex with a disguised End-to-End Azido Bridge; Jan J. Weigand; Manfred Friedrich; Juan Carlos Galvez-Ruiz; Thomas M. Klapötke; Peter Mayer, Birgit Weber; *Inorg. Chem.* **2005**, *submitted for publication*.

<u>21</u>

N-Nitroso- and *N*-Nitraminotetrazoles; Jan J. Weigand; Stefan Berger; Konstantin Karaghiosoff; Thomas M. Klapötke; Peter Mayer, Holger Piotrowski, Kurt Polborn; Rodney L. Willer; *J. Org. Chem.* **2005**, *submitted for publication*.

<u>20</u>

The Dianion of 5-Cyanoiminotetrazoline: $C_2N_6^{2-}$; Jan J. Weigand; Axel Schulz; Thomas M. Klapötke; Christian Kuffer; Peter Mayer; Kurt Polborn; *Inorg. Chem.* **2005**, *in press*.

<u>19</u>

Azidoformamidinium and Guanidinium 5,5'-Azotetrazolate Salts; Jan J. Weigand; Michael Hiskey; Anton Hammer; Gerhard Holl; Thomas M. Klapötke; Kurt Polborn; Jörg Stierstorfer; *Chem. Mater.* **2005**, *17*, 3784-3793.

<u>18</u>

Properties of a highly friction sensitive derivative of 1,5-Diamino-1H-tetrazole (DAT): 1,5-Diamino-4-Methyltetrazolium dinitramide; Jan J. Weigand; Gerd Fischer; Gerdard Holl, Thomas M. Klapötke; Peter Mayer; *New Trends in Research of Energetic Materials, Proceedings of the Seminar, 8th,* Pardubice, Czech Republic, Arp. 19-21, **2005**, 190-201.

<u>17</u>

3,5-Dimethyl-2,4,6-triketo-1,3,5-oxadiazine: short intermolecular contacts determining the crystal packing; Jan J. Weigand; Janna Geith; Thomas M. Klapötke; Peter Mayer; Axel Schulz; *Acta Cryst.* **2005**, *submitted for publication*.

16

Dodecahydroxycyclohexane Dihydrate; Jan J. Weigand; Thomas M. Klapötke; Kurt Polborn; *Acta Cryst.* **2005**, *E61*, o1396-o1397.

15

Nitro(nitroso)cyanomethanides; Harald Brand; Peter Mayer; Axel Schulz, Jan J. Weigand; *Angew. Chem.* **2005**, 3998-4001.

14

A study on the thermal decomposition behavior on derivatives of 1,5-diamino-1*H*-tetrazole; a new familiy of energetic heterocyclic-based salts; Jan J. Weigand; Gerd Fischer; Gerhard Holl, Thomas M. Klapötke; *Thermochim. Acta.* **2005**, *in press*.

13

Derivatives of 1,5-Diamino-1*H*-tetrazole; A New Familiy of Energetic Heterocyclic-based Salts; Jan J. Weigand; Juan Carlos Galvez-Ruiz; Gerhard Holl, Konstantin Karaghiosoff, Thomas M. Klapötke; Karolin Lönwitz; Peter Mayer; Heinrich Nöth; Kurt Polborn; Christoph J. Rohbogner; *Inorg. Chem.* **2005**, 4237-4253.

12

Mono-, Di and Tri-Coordinated Phosphorus Attached to a N-N Unit: An Experimental And Theoretical Study; Gerd Fischer; Sebastian Herler; Peter Mayer; Axel Schulz; Alexander Villinger; Jan J. Weigand; *Inorg. Chem.* **2005**, *44(6),* 1740-1751.

11

1,5-Diamino-4-methyltetrazolium dinitramide; Jan J. Weigand; Axel Schulz; Thomas M. Klapötke; Peter Mayer; *J. Am. Chem. Soc.* **2005**, *127*, 2032-2033

10

Blue Alkali Dinitrosomethanides: Synthesis, Structure, and Bonding; Harald Brand; Peter Mayer; Kurt Polborn; Axel Schulz; Jan J. Weigand; *J. Am. Chem. Soc.* **2005**, *127(5)*, 1360-1361.

<u>9</u>

Synthesis, Structure, Molecular Orbital Calculations and Decomposition Mechanism for Tetrazolylazide CHN_7, its Phenyl Derivative $PhCN_7$ and Tetrazolylpentazole CHN_9; Anton Hammerl; Thomas M. Klapötke; Peter Mayer; Jan J. Weigand, *Propellants, Explosives and Pyrotechnics* **2005**, *30(1)*, 17-26.

<u>8</u>

1,4-Bis-[1-Methyltetrazol-5-yl]-1,4-Dimethyl-2-Tetrazene: A Stable, Highly Energetic Hexamer of Diazo methane $(CH_2N_2)_6$; Jan J. Weigand; Thomas M. Klapötke; Peter Mayer; Axel Schulz; *Propellants, Explosives and Pyrotechnics* **2004**, *29(6)*, 325-332.

<u>7</u>

Pyrolysis experiments and thermochemistry of mononitrobiuret (MNB) and 1,5-dinitrobiuret (DNB); Jan J. Weigand; Janna Geith; Gerhard Holl; Thomas M. Klapötke; *Combustion and Flame* **2004**, *139(1)*, 358-366.

<u>6</u>

Thermal Decomposition of MNB and DNB - A Thermogravimetric, IR Gasphase Spectroscopic and Mass Spectrometric Study; Jan J. Weigand; Janna Geith; Gerhard Holl; Thomas M. Klapötke; *35th International Annual Conference ICT, Karlsruhe June 29 - July 2th,* **2004** 175/1-175/17.

<u>5</u>

Dinitrobiuret and its Salts; Janna Geith; Konstantin Karaghiosoff; Thomas M. Klapötke; Peter Mayer; Jan J. Weigand; *New Trends in Research of Energetic Materials, Proceedings of the Seminar, 7th, Pardubice*, Czech Republic, Arp. 20-22, **2004**, *2*, 476-479.

<u>4</u>

New High Explosives and Propellants Based on Biuret and Tetrazole Compounds; Janna Geith; Anton Hammerl; Gerhard Holl; Thomas M. Klapötke; Jan J. Weigand, *New Trends in Research of Energetic Materials, Proceedings of the Seminar, 7th, Pardubi ce*, Czech Republic, Arp. 20-22, **2004**, *1*, 25-36.

3

Calculation of the Detonation Velocities and detonation Pressure of Dinitrobiuret (DNB) and Diaminotetrazole Nitrate (HDAT-NO3); Janna Geith; Gerhard Holl; Thomas M. Klapötke; Jan J. Weigand, *Propellants, Explosives and Pyrotechnics* **2004**, *29(1)*, 3-8.

2

Synthesis, Characterization and Crystal Structure of 1,3-Dipentafluorophenyl- 2,2,2,4,4,4-hexaazido-1,3-diaza-2,4-diphosphetidine; Christoph Aubauer; Gernot Kramer; Konstantin Karaghiosoff; Thomas M. Klapötke; Axel Schulz; Jan J. Weigand, *Z. Anorg. Allg. Chem.* **2001**, 2547-2552.

1

1,3-Diphenyl-2,4-hexaazido-1,3-diaza-2,4-diphosphetidine: synthesis and structural characterization of the first nitrogen-penta-coordinated phosphorus with three azide groups; Christoph Aubauer; Thomas M. Klapötke; Heinrich Nöth; Axel Schulz; Max Suter; Jan J. Weigand; *J. Chem. Soc., Chem. Commun.* **2000**, 2491-2492.

Patent:

Verfahren zur Herstellung von Explosivstoffen; Gerhard Holl, Thomas M. Klapötke, Jan J. Weigand, (2004/2005), 10 2004 014 044, *pending*.

Poster:

8

Crystal Structure of the Potassium and Silver Salts of Nitroform; Michael Göbel, Thomas M. Klapötke; Peter Mayer; Jan J. Weigand; *New Trends in Research of Energetic Materials, Proceedings of the Seminar*, 8th, Pardubice, Czech Republic, April 19. – 21th, **2005**.

<u>**7**</u>

Mono-, Di and Tri-Coordinated Phosphorus Attached to a N-N Unit: An Experimental And Theoretical Study; Sebastian Herler; Axel Schulz; Alexander Villinger; Jan J. Weigand; *Münchner Industrie-Tag*, October 15th, **2004**.

<u>**6**</u>

Thermal Decomposition of MNB and DNB - A Thermogravimetric, IR Gasphase Spectroscopic and Mass Spectrometric Study; Jan J. Weigand; Janna Geith ; Gerhard Holl; Thomas M. Klapötke; *35th International Annual Conference ICT, Karlsruhe,* June 29. – July 2th, **2004**.

<u>**5**</u>

Dinitrobiuret and its Salts; Jan J. Weigand; Janna Geith; Konstantin Karaghiosoff; Thomas M. Klapötke; Peter Mayer; *New Trends in Research of Energetic Materials, Proceedings of the Seminar, 7th, Pardubice*, Czech Republic, April 20. – 22th, **2004**.

<u>**4**</u>

Nitraminotetratzoles Synthesis, Molecular Structures and NMR Spectroscopy; Jan J. Weigand; Janna Geith; Konstatin Karaghiosoff; Thomas M. Klapötke; Peter Mayer; Kurt Polborn; *GDCh Annual Conference, Munich,* October 6. – 11th, **2003**.

<u>**3**</u>

Mono- and Dinitrobiuret; Jan J. Weigand; Janna Geith; Konstatin Karaghiosoff; Thomas M. Klapötke; Peter Mayer; *GDCh Annual Conference, Munich,* October 6. – 11th, **2003**.

<u>**2**</u>

Nitraminotetratzoles Synthesis, Molecular Structures and NMR Spectroscopy; Jan J. Weigand; Janna Geith; Konstatin Karaghiosoff; Thomas M. Klapötke; Peter Mayer; Kurt Polborn; Jan J. Weigand; *34th International Annual Conference ICT, Karlsruhe,* June 24. – 27th, **2003**.

1

1,3-Diphenyl- and 1,3-Dipentafluorophenyl-2,2,2,4,4,4-hexaazido-1,3-diaza-2,4-diphosphetidine: synthesis and structural characterization of the first nitrogen-penta-coordinated phosphorus with three azide groups; Jan J. Weigand; Christoph Aubauer; Konstantin Karaghiosoff; Thomas M. Klapötke; Heinrich Nöth; Axel Schulz; Max Suter; *SFC Eurochem, Toulouse,* July 08. – 11th, **2002**.

Book Chapters:

Formulation of Novel Energetic Materials, in: Novel Energetic Materials and Applications, L. T. DeLuca, L. Galfetti, R. A. Pesce-Rodriguez (eds.), T. M. Klapötke, J. Geith, A. Hammerl, J. Weigand, G. Holl, *9th IWCPON Novel Energetic Materials and Application*, Lerici (Pisa), Italy, September 14. – 18th, **2003**, 02-01 – 02-11.

Conferences:

10

New Trends in Research of Energetic Materials, Proceedings of the Seminar, 8th, Pardubice, Czech Republic, **2005** April 19. – 21th.

9

Chemiedozenten-Tagung 2005, Munich, Germany, **2005** March 6. – 9th.

8

Münchner Industrie-Tag, Munich, Germany, **2004** October 15th.

7

35th International Annual Conference ICT, Karlsruhe, Germany, **2004** June 29. – July 2th.

__**6**__

New Trends in Research of Energetic Materials, Proceedings of the Seminar, 7th, Pardubice, Czech Republic*,* **2004** April 20. – 22th.

__**5**__

Chemiedozenten-Tagung 2004, Dortmund, Germany, **2004** March 7. – 10th.

__**4**__

GDCh Annual Conference, Munich, Germany, **2003** October 6. – 9th.

__**3**__

34th International Annual Conference ICT, Karlsruhe, Germany, **2003** June 24. – 27th.

__**2**__

SFC Eurochem, Toulouse, France, **2002** July 8. – 11th.

__**1**__

AGICHEM, Munich, Germany, **2002** April 7. – 10th.

Curriculum Vitae

Name:	Jan J. Weigand
Adresse:	Thalkirchnerstr. 16 80337 München E-Mail: jjwch@cup.uni-muenchen.de
Geburtsdatum:	25. Mai 1974
Geburtsort:	Kronach (Oberfranken)
Staatsangehörigkeit:	deutsch
Familienstand:	ledig
Schulausbildung:	September 1988 – Juli 1991 Mittlere Reife, Herzog-Tassilo-Realschule Dingolfing
	September 1994 – Juli 1996 Fachgebunden Hochschulreife, BOS Regensburg Auszeichnung der Stadt Regensburg
Berufsausbildung:	September 1991 – Juli 1994 Ausbildung zum Chemielaborant, BMW Dingolfing Ausbildungsabschluss mit Auszeichnung
Hochschulausbildung:	November 1997 – August 2002 Studiengang Chemie Diplom, LMU München Diplomarbeit unter Anleitung von Prof. T. Klapötke „1,4-Bis(1'-methyltetrazolyl)-1,4-dimethyl-2-tetrazene and other nitrogen rich high energy density materials"
	September 2002 – Mai 2005 Promotion unter Anleitung von Prof. T. Klapötke „High Energy Density Materials Based on Tetrazoles and Nitramine Compounds – Synthesis, Scale-up and Testing"
Ersatzdienst:	August 1996 – August 1997 Zivildienst, Krankenhaus Schwabing München
Berufserfahrung, Praktika und Nebentätigkeiten:	Juli 1994 – September 1994 Chemielaborant, Angestellter bei BMW Dingolfing
	Juli 1995 – September 1995 Chemielaborant, Angestellter bei Peroxid-Chemie in Pullach
	Februar 1996 – Mai 1997 Institut und Polyklinik für Arbeits- und Umweltmedizin der LMU München „Messung der Schadstoffbelastung im Straßenverkehr"

	Juni 1998 – März 2000 ESF-Entwicklungslabor in München „Labor- und Kundenbetreuung“
	August 2000 – November 2000 Organisches Forschungspraktikum im Arbeitskreis von Prof. Richard Hartley, University of Glasgow/Scotland
	Februar 2000 – September 2001 Wissenschaftliche Hilfskraft, AK Prof. H. Zipse „Quantenchemische Berechnungen“
	September 2002 – Februar 2003 Wissenschaftliche Hilfskraft, AK Prof. T. Klapötke „Aufbau und Betreuung der Autoklavenstation“
Lehrerfahrung:	September 2002 – Februar 2003 Betreuung des Grundpraktikums Anorganische Chemie I
	Betreuung von 6 Forschungspraktikanten und 1 Bachelorarbeit
Stipendien und Mitgliedschaften:	August – November 2000 SOCRATES/ERASMUS „student mobility program“
	seit November 2000 e-fellows.net Stipendiat
	März 2003 – März 2005 Stipendiat des Fonds der Chemischen Industrie (FCI)
	seit 1997 Mitglied der Gesellschaft Deutscher Chemiker (GDCh)
	seit Februar 2005 Mitglied der Amerikanischen Chemischen Gesellschaft (ACS)
Sonstiges:	März 2005 Mithilfe bei der Chemiedozenten-Tagung an der LMU München
Sprachkenntnisse:	Deutsch Muttersprache Englisch fließend in Wort und Schrift